Plasma Physics Reports, Vol. 29, No. 6, 2003, pp. 449–458. Translated from Fizika Plazmy, Vol. 29, No. 6, 2003, pp. 483–493.

PLASMA INSTABILITY

Tearing Instability of a Force-Free Magnetic Configuration in a Collisionless Plasma

N. A. Bobrova[1], S. V. Bulanov[2], G. E. Vekstein[3], J.-I. Sakai[4], K. Machida[4], and T. Haruki[4]

[1]*Institute of Theoretical and Experimental Physics, Bol'shaya Cheremushkinskaya ul. 25, Moscow, 117259 Russia*

[2]*Prokhorov Institute of General Physics, Russian Academy of Sciences, ul. Vavilova 38, Moscow, 119991 Russia*

[3]*Manchester University, PO Box 88, Manchester M60 IQD, United Kingdom*

[4]*Laboratory of Plasma Astrophysics, Faculty of Engineering, Toyama University, Gofuku 3190, Toyama 930-8555, Japan*

Received October 24, 2002; in final form, December 10, 2002

Abstract—The equilibrium and stability of a sheared force-free magnetic field in a collisionless plasma are investigated, and the main features of charged particle motion in such a field are analyzed. A steady solution is derived to the Vlasov–Maxwell equations for the charged particle distribution function that describes different equilibrium configurations. The tearing instability of the magnetic field configurations is studied both analytically and by particle-in-cell simulations. © *2003 MAIK "Nauka/Interperiodica".*

1. INTRODUCTION

The equilibrium and stability of plasma configurations in force-free magnetic fields have been studied for many years [1]. The force-free magnetic field approximation is used to describe the equilibrium of magnetic configurations in both space and laboratory plasmas [2–4]. Such magnetic configurations are considered to play an important role, e.g., in stellar atmospheres and active regions emerging on the Sun, because the plasma pressure there is much lower than the magnetic field pressure, $\beta = 8\pi p/B^2 \ll 1$.

By force-free magnetic fields are meant those that have no force effect on the plasma. In a low-pressure plasma in an MHD equilibrium state, force-free magnetic fields satisfy the equations

$$\mathbf{B} \times (\nabla \times \mathbf{B}) = 0, \quad \nabla \cdot \mathbf{B} = 0. \tag{1}$$

These equations admit a broad class of solutions, which have been thoroughly investigated in the literature [3]. The equilibrium and stability of plasmas in force-free magnetic fields have been studied mainly in the MHD approximation. However, the MHD approach fails to hold for many problems, especially in astrophysical applications. Hence, the plasma should be described in terms of a collisionless model, in which it is necessary to determine the equilibrium particle distribution functions satisfying the Vlasov–Maxwell equations [5–7]. For the simplest force-free magnetic configuration, this problem was solved in [8], in which the question about the tearing instability of the configuration was also discussed.

Here, we continue the investigations that were begun in [8, 9] and report the new results achieved in this area. In [8], a general solution was obtained that describes the trajectories of charged particles in a one-dimensional force-free magnetic field and is expressed in terms of elliptic functions. In [9], the nontrivial features of the motion of charged particles were discussed in light of the fact that, in such a field, they undergo no centrifugal or gradient drifts. In the present paper, we analyze the main features of charged particle motion in more detail and present a wider class of exact solutions to the Vlasov–Maxwell equations in comparison with that studied in [8, 9]. For clarity in describing the results obtained here and in comparing them with the previously published results, we solve the problem by the same approach as in [8, 9] and keep the same notation. Note that, in recent papers [10, 11], an analogous approach was employed to find exact solutions to the Vlasov–Maxwell equations in the problem of the structure of relativistically strong electromagnetic waves in a collisionless plasma.

We begin by considering a solution to the Vlasov–Maxwell equations for the simplest force-free magnetic field:

$$\mathbf{B}(y) = B_0(\cos\alpha y\mathbf{e}_x + \sin\alpha y\mathbf{e}_z), \tag{2}$$

where α is a constant. This field is a solution to Eqs. (1) in one-dimensional geometry, in which **B** depends only on the *y* coordinate. Solution (2) is a particular solution admitted by the Vlasov–Maxwell equations for force-free magnetic fields. Below, we will find a more complicated solution describing the plasma equilibrium in a force-free field.

It is well known that the tearing instability plays a very important role in magnetic field reconnection in both astrophysical and laboratory plasmas [12, 13]. The present work focuses on the linear stage of this instability in magnetic field (2). In the nonlinear stage of the instability, the plasma and magnetic field usually evolve in an extremely complicated fashion [14–18]. In order to study the nonlinear stage of the tearing insta-

1063-780X/03/2906-0449$24.00 © 2003 MAIK "Nauka/Interperiodica"

bility, we carried out numerical simulations with a 2D3V particle-in-cell (PIC) code. In contrast to [8], we use the initial electron distribution that makes it possible to analyze namely the tearing instability. Since, in [8], the electron drift velocity was chosen to be fairly high, simulations showed the simultaneous development of a tearing and a bending instability; hence, it was rather difficult to compare the numerical results to theoretical predictions. In the computations reported here, the electron drift velocity was chosen to be much lower, thereby making it possible to simulate the tearing instability, resulting in the formation of magnetic islands. The growth rate calculated numerically for the linear instability stage coincides with that obtained analytically.

It should also be noted that, in simulating the nonlinear stage of the instability of plasma configurations in a magnetic field, the boundary conditions are often assumed to be periodic. The analytic solutions obtained in [8] and in the present paper for plasma equilibrium in a periodic magnetic field in the collisionless approximation may be useful for the proper choice of the initial and boundary conditions when simulating collisionless plasmas.

2. CHARGED PARTICLE MOTION IN A PERIODIC SHEARED FORCE-FREE MAGNETIC FIELD

The charged particle motion in force-free magnetic field (2) is described by the equations

$$\frac{\partial v_x}{dt} = \frac{e_a}{cm_a} v_y B_z, \tag{3}$$

$$\frac{dv_y}{dt} = \frac{e_a}{cm_a}(v_z B_x - v_x B_z) + \frac{e_a}{m_a} E_y(y), \tag{4}$$

$$\frac{dv_z}{dt} = -\frac{e_a}{cm_a} v_y B_x. \tag{5}$$

Here, (v_x, v_y, v_z) are the velocity components of a charged particle, the subscript a stands for the particle species ($a = e, i$), and m_a and e_a are the mass and electric charge of a particle. Note that the only nonzero component of the equilibrium electric field **E** is the y component, because, in magnetic field (2), all of the quantities depend solely on the y coordinate. Since the Lorentz force also depends only on y, the electric field can only arise as a result of charge separation in the plasma. In what follows, we will assume that charge separation does not occur and, hence, the electric field is zero.

The general solution to these equations [8] describes the trajectories of charged particles and can be expressed in terms of elliptic functions. Below, we derive an approximate solution to these equations that makes it possible to analyze the particle motion.

The vector potential of magnetic field (2) is equal to

$$\mathbf{A} = -B_0\alpha^{-1}(\cos\alpha y\mathbf{e}_x + \sin\alpha y\mathbf{e}_z). \tag{6}$$

The independence of the vector potential on the x and z coordinates implies the conservation of the corresponding components of the generalized momentum:

$$P_x = m_a v_x + \frac{e_a}{c}A_x = m_a v_x - \frac{m_a\omega_{Ba}}{\alpha}\cos\alpha y = C_1, \tag{7}$$

$$P_z = m_a v_z + \frac{e_a}{c}A_z = m_a v_z - \frac{m_a\omega_{Ba}}{\alpha}\sin\alpha y = C_2, \tag{8}$$

where $\omega_{Ba} = e_a B_0/cm_a$ is the gyrofrequency of the particles of species a.

Expressions (7) and (8) and the energy integral

$$v_x^2 + v_y^2 + v_z^2 = C_3 \tag{9}$$

are the integrals of motion and thus determine the trajectory of a particle. We assume that, at the initial instant, the particle is at the coordinate origin and that its velocity components along and across the magnetic field are equal to $v_x(0) = v_{0\|}$ and $v_y(0) = v_{0\perp}$, respectively. For such a particle, expressions (7) and (8) yield

$$v_x = v_{0\|} - \frac{\omega_{Ba}}{\alpha}(1 - \cos\alpha y), \tag{10}$$

$$v_z = \frac{\omega_{Ba}}{\alpha}\sin\alpha y. \tag{11}$$

Substituting expressions (10) and (11) into the energy integral, we obtain

$$v_y^2 + \frac{2\omega_{Ba}^2}{\alpha^2}\left(1 - \frac{\alpha v_{0\|}}{\omega_{Ba}}\right)(1 - \cos\alpha y) = v_{0\perp}^2, \tag{12}$$

which shows that the effective potential energy of a particle moving in the y direction is equal to

$$U(y) = \frac{\omega_{Ba}^2}{\alpha^2}\left(1 - \frac{\alpha v_{0\|}}{\omega_{Ba}}\right)(1 - \cos\alpha y). \tag{13}$$

Now, we consider some general features of the charged particle motion. When the initial velocity $v_{0\perp}$ of a particle across the magnetic field is sufficiently high, i.e., when the particle energy is higher than the maximum effective potential energy,

$$v_{0\perp}^2 > \frac{4\omega_{Ba}^2}{\alpha^2}\left(1 - \frac{\alpha v_{0\|}}{\omega_{Ba}}\right), \tag{14}$$

the particle executes infinite motion along the y-axis. Particles of this kind are called transit particles. A particle with $v_{0\|} = 0$ becomes transit when $v_{0\perp} > 2\omega_{Ba}/\alpha$, i.e., when its gyroradius becomes larger than the characteristic scale on which the magnetic field varies. When the energy of a charged particle is much higher than the maximum effective potential energy, the mag-

netic field does not affect the particle motion in the y direction and the particle trajectory is a helix with the radius $r_{Ba} = v_{0\perp}/\omega_{Ba}$, $r = \omega_{Ba}/v_{0\perp}\alpha^2$ and a pitch of $2\pi\alpha^{-1}$. The helix moves as a whole along the x-axis with a constant speed equal to $-\omega_{Ba}/\alpha$.

When inequality (14) fails to hold, the particle motion in a magnetic field is finite; such particles are called trapped particles. We first consider the case in which the particle energy is much lower than the effective potential energy. If the initial particle velocity along the magnetic field is zero, $v_{0\parallel} = 0$, then potential energy (13) is approximately equal to $U(y) \approx \omega_{Ba}^2 y^2/2$. In this case, expressions (11) and (12) become

$$v_y = v_{0\perp}\cos\omega_{Ba}t, \quad v_z = v_{0\perp}\sin\omega_{Ba}t. \tag{15}$$

We can see that, in the (y, z) plane, the particles move in the same manner as in a uniform magnetic field. Due to the nonuniformity of magnetic field (2), the field-aligned component of the particle velocity is nonzero and equal to

$$v_x = -\frac{\omega_{Ba}}{\alpha}(1-\cos\alpha y) \approx -\frac{\alpha v_{0\perp}^2}{2\omega_{Ba}}\sin^2(\omega_{Ba}t). \tag{16}$$

Averaging over the period of gyration yields

$$\langle v_x\rangle = -v_{0\perp}\frac{\alpha v_{0\perp}}{4\omega_{Ba}} \sim v_{0\perp}\frac{\alpha r_{Ba}}{2\pi}. \tag{17}$$

We thus arrive at the same dependence as that for the gradient and centrifugal drifts, the only difference being that, in sheared magnetic field (2), the particle drifts along the magnetic field lines rather than across them.

Now, we consider how the motion of a particle changes when its initial velocity along the magnetic field is nonzero. First, according to expression (13), the particle gyrofrequency will change: for low $v_{0\perp}$, the effective gyrofrequency is equal to $\tilde{\omega}_{Ba} = \omega_{Ba}(1 - \alpha v_{0\parallel}/\omega_{Ba})^{1/2}$. Second, the particle moves along an elliptical (rather than circular) trajectory whose semiaxes are in the ratio $(1 - \alpha v_{0\parallel}/\omega_{Ba})^{1/2}$. The motion of a particle with a sufficiently high initial velocity along the magnetic field, $v_{0\perp} \sim \omega_{Ba}/\alpha$, is rather complicated. For the projection of the particle trajectory onto the (y, z) plane, expression (12) gives

$$\frac{dy}{dt} = \pm\frac{\omega_{Ba}}{\alpha}\left(\frac{\alpha^2 v_{0\perp}^2}{\omega_{Ba}^2} - 2\left(1-\frac{\alpha v_{0\parallel}}{\omega_{Ba}}\right)(1-\cos\alpha y)\right)^{1/2}. \tag{18}$$

From expression (11), we obtain

$$\frac{dz}{dy} = \pm\sin\alpha y\left(\frac{\alpha^2 v_{0\perp}^2}{\omega_{Ba}^2} - 2\left(1-\frac{\alpha v_{0\parallel}}{\omega_{Ba}}\right)(1-\cos\alpha y)\right)^{-1/2}. \tag{19}$$

Integrating this equation, we determine the trajectory of a charged particle in the (y, z) plane:

$$\alpha^2\left(1-\frac{\alpha v_{0\parallel}}{\omega_{Ba}}\right)^2\left(z - \frac{v_{0\perp}}{\omega_{Ba}\left(1-\frac{\alpha v_{0\parallel}}{\omega_{Ba}}\right)}\right)^2 = \frac{\alpha^2 v_{0\perp}^2}{\omega_{Ba}^2} - 2\left(1-\frac{\alpha v_{0\parallel}}{\omega_{Ba}}\right)(1-\cos\alpha y). \tag{20}$$

Note that, for $v_{0\perp} \ll \omega_{Ba}\alpha^{-1}$, we arrive at the circular and elliptical trajectories discussed above. However, even when $v_{0\perp}$ is high, the trajectory deviates from being elliptical only slightly. The characteristic feature of the particle motion in the case at hand is that the particles do not undergo centrifugal and gradient drifts [9].

3. SOLUTION TO THE VLASOV EQUATION FOR A PLASMA IN A FORCE-FREE MAGNETIC FIELD

The equilibrium of a plasma in a force-free magnetic field $\mathbf{B} = (B_x, 0, B_z)$ is described by the time-independent ($\partial/\partial t = 0$) Vlasov equation

$$v_y\frac{\partial f_a}{\partial y} + \frac{e_a}{m_a}\left[\frac{v_y B_z}{c}\frac{\partial f_a}{\partial v_x} + \left(E_y + \frac{v_z B_x - v_x B_z}{c}\right)\frac{\partial f_a}{\partial v_y} - \frac{v_y B_x}{c}\frac{\partial f_a}{\partial v_z}\right] = 0, \tag{21}$$

where f_a is the distribution function of the particles of species a. The integrals of motion of the Vlasov equation are the energy of a particle,

$$W = m_a(v_x^2 + v_y^2 + v_z^2)/2 + e_a\varphi, \tag{22}$$

and the components of its canonical momentum,

$$p_x = m_a v_x + e_a A_x/c, \tag{23}$$

$$p_z = m_a v_z + e_a A_z/c. \tag{24}$$

The solution to Eq. (21) for the equilibrium distribution function can be searched for as a function of the integrals of motion:

$$f_a = f_a(W, p_x, p_z). \tag{25}$$

We choose a reference point y_0 at which $\varphi(y_0) = 0$, $A_x(y_0) = 0$, and $A_z(y_0) = A_0$, where A_0 is a constant. We

assume that, at $y = y_0$, the particle distribution is described by a Maxwellian function with an anisotropic temperature ($T_{a\parallel} \neq T_{a\perp}$) and the drift velocity $\mathbf{V}_d^{a0} = (V_{dx}^{a0}, 0, V_{dz}^{a0})$:

$$f_a(y_0, \mathbf{v}_0) = C_a \exp\left\{-\frac{m_a}{2}\left[\frac{v_{0y}^2}{T_{a\perp}} + \frac{(v_{0x} - V_{dx}^{a0})^2 + (v_{0z} - V_{dz}^{a0})^2}{T_{a\parallel}}\right]\right\}. \quad (26)$$

Now, we express the distribution function at the point y_0 in terms of the integrals of motion. To do this, we determine the dependence of $\mathbf{v}_0$ on these integrals and insert it into (26). As a result, we arrive at the following dependence of the distribution function on the integrals of motion:

$$f_a = f_a\left(\frac{W}{T_{a\perp}} - \frac{\Delta T_a}{2m_a T_{a\perp} T_{a\parallel}}(p_x^2 + p_z^2)\right), \quad (27)$$

where $\Delta T_a = T_{a\parallel} - T_{a\perp}$. Consequently, the distribution of the particles of species a can be described by the function

$$f_a(y, \mathbf{v}) = \frac{m_a^{3/2} n_a}{(2\pi m_a)^{3/2} T_{a\parallel} T_{a\perp}^{1/2}} \exp\left\{-\frac{m_a}{2}\left[\frac{v_y^2}{T_{a\perp}} + \frac{(v_x - V_{dx}^a)^2 + (v_z - V_{dz}^a)^2}{T_{a\parallel}}\right] - \left[\frac{e_a}{T_{a\perp}}\varphi(y) - \frac{1}{2}\frac{e_a^2}{c^2 m_a}\frac{\Delta T_a}{T_{a\perp}^2}A^2(y)\right]\right\}, \quad (28)$$

where the drift velocity is equal to

$$\mathbf{V}_d^a = \frac{e_a}{m_a c}\frac{\Delta T_a}{T_{a\perp}}\mathbf{A}. \quad (29)$$

In deriving distribution function (28), we took into account the relationships

$$\int_{-\infty}^{\infty} f_a d\mathbf{v} = n_a(y) = n_a \exp\left(-\frac{e_a\varphi(y)}{T_{a\perp}} + \frac{1}{2}\frac{e_a^2}{c^2 m_a}\frac{\Delta T_a}{T_{a\perp}^2}A^2(y)\right). \quad (30)$$

In a steady state, Maxwell's equations for the vector and scalar potentials, $\mathbf{A}$ and φ, reduce to

$$\frac{d^2\varphi}{dy^2} = -4\pi\rho_e, \quad (31)$$

$$\frac{d^2\mathbf{A}}{dy^2} = -\frac{4\pi}{c}\mathbf{j}, \quad (32)$$

where the electric-charge and electric-current densities have the form

$$\rho_e = \sum_a e_a \int_{-\infty}^{\infty} f_a d\mathbf{v}_a = \sum_a e_a n_a \exp\left(-\frac{e_a\varphi}{T_{a\perp}} + \frac{1}{2}\frac{e_a^2}{c^2 m_a}\frac{\Delta T_a}{T_{a\perp}^2}A^2\right), \quad (33)$$

$$\mathbf{j} = \sum_a e_a \int_{-\infty}^{\infty} f_a \mathbf{v}_a d\mathbf{v}_a = \sum_a \frac{e_a^2 n_a}{c m_a}\frac{\Delta T_a}{T_{a\perp}}\mathbf{A}\exp\left(-\frac{e_a\varphi}{T_{a\perp}} + \frac{1}{2}\frac{e_a^2}{c^2 m_a}\frac{\Delta T_a}{T_{a\perp}^2}A^2\right). \quad (34)$$

It is easy to show that Eqs. (31) and (32) with charge and current densities (33) and (34) have the first integral

$$\frac{1}{2}\left(\frac{d\varphi}{dy}\right)^2 - \frac{1}{2}\left(\frac{d\mathbf{A}}{dy}\right)^2 - 4\pi\sum_a n_a T_{a\perp}\exp\left(-\frac{e_a\varphi}{T_{a\perp}} + \frac{1}{2}\frac{e_a^2}{c^2 m_a}\frac{\Delta T_a}{T_{a\perp}^2}A^2\right) = \text{const}. \quad (35)$$

We assume that the plasma consists of electrons and ions of one species and that the quasineutrality condition is satisfied. Let us consider the case in which $\varphi(y) = 0$ and $A^2 = A_0^2$ is constant. In this case, Eq. (32) becomes

$$\frac{d^2\mathbf{A}}{dy^2} + \alpha^2\mathbf{A} = 0. \quad (36)$$

Here,

$$\alpha = \left[\frac{4\pi e^2}{c^2 m_e} n\left(\frac{\Delta T_e}{T_{e\perp}} + \frac{m_e}{m_i}\frac{\Delta T_i}{T_{i\perp}}\right)\right]^{1/2}, \quad (37)$$

where m_e is the mass of an electron, m_i is the mass of an ion, and $e_i = -e_e = e$. Note that the above definition of the temperature anisotropy differs from the definition used in [8]; as a result, the second term on the right-hand side of Eq. (36) is opposite in sign to the corresponding term in the equation for the vector potential in [8]. The solution to Eq. (36) describes a one-dimensional force-free magnetic field, which is the subject of our analysis. As we have already shown, a one-dimensional equilibrium force-free magnetic configuration can exist only when the plasma temperature is anisotro-

pic in the directions along and across the magnetic field. The weaker the anisotropies of the electron and ion temperatures, the larger the constant α^{-1}. In the limiting case of isotropic temperatures, the magnetic field becomes uniform.

The above solution is clearly a particular case of the solutions admitted by Eqs. (31) and (32) with charge and current densities (33) and (34). In order to find solutions describing more complicated equilibrium states of the plasma in a magnetic field, we impose the following condition on the electron-to-ion temperature anisotropy ratio:

$$\frac{e^2\Delta T_e}{T_{e\perp}^2 m_e} = \frac{e_i^2\Delta T_i}{T_{i\perp}^2 m_i}, \quad (38)$$

which is an analogue of the electroneutrality condition for a collisionless current sheet in the solution obtained by Harris [5]. Using condition (38) and the quasineutrality condition $\varphi(y) = 0$, we reduce the first integral (35) to

$$\frac{1}{2}\left(\frac{d\mathbf{A}}{dy}\right)^2 + k^2\exp\left(\frac{1}{2}\frac{e^2}{c^2 m_e}\frac{\Delta T_e}{T_{e\perp}^2}A^2\right) = \text{const}, \quad (39)$$

where $k^2 = 4\pi\sum_a n_a T_{a\perp}$.

We represent the vector potential $\mathbf{A}$ in a complex form, $\mathbf{A} = A_x + iA_z = R\exp(i\Psi)$, to obtain the equations

$$\left(\frac{d^2R}{dy^2}\right)^2 - \frac{M^2}{R^3} + q^2 R\exp\left(\frac{1}{2}\frac{e^2}{c^2 m_e}\frac{\Delta T_e}{T_{e\perp}^2}R^2\right) = 0, \quad (40)$$

$$\frac{d\Psi}{dy} = \frac{M}{R^2}, \quad (41)$$

where M is a constant and $q^2 = 4\pi\sum_a n_a T_{a\perp}\frac{e^2}{c^2 m_e}\frac{\Delta T_e}{T_{e\perp}^2}$.

The M value for which Eq. (40) with $R = R_0$ and, accordingly, Eq. (36) with constant (37) have a solution uniform along the y coordinate is equal to

$$M = qR_0^2\exp\left(\frac{1}{4}\frac{e^2}{c^2 m_e}\frac{\Delta T_e}{T_{e\perp}^2}R_0^2\right). \quad (42)$$

We can see that $M = \alpha$.

A more general case is that in which the functions R and Ψ (the amplitude and the phase) are not constant. The amplitude varies between $R_{\min}$ and $R_{\max}$, and the phase in the complex representation of the vector potential also varies between its minimum and maximum values. Figure 1 illustrates the behavior of the solution to Eqs. (41) and (39) in the form of a trajectory along which the particle moves in the (A_x, A_z) plane as the y coordinate of the particle varies from $-10/k$ to $10/k$. The solution was obtained by integrating Eqs. (39) and (41) numerically for $R(0) = q/k = 2$, $R'(0) = 0$, $\Psi(0) = 0$, and $M = 1$. We see nonlinear oscillations from the minimum to the maximum amplitude and back again. Because of the nonlinear dependence of the phase on the coordinate, the trajectory precesses in the (A_x, A_z) plane.

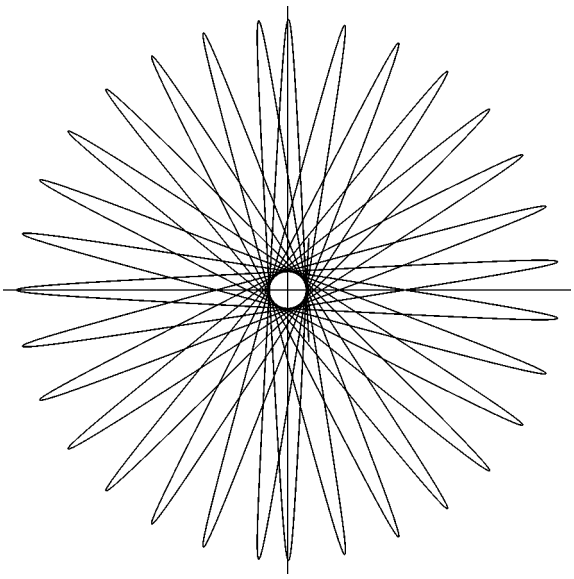

Fig. 1. Trajectory along which a particle moves in the (A_x, A_z) plane as the y coordinate of the particle varies from $-10/k$ to $10/k$ for $R(0) = q/k = 2$, $R'(0) = 0$, $\Psi(0) = 0$, and $M = 1$.

4. TEARING INSTABILITY

The equilibrium configuration under analysis is unstable against various instabilities, e.g., the Buneman instability, the tearing instability, drift instabilities, and some others. We restrict our analysis to the tearing instability because it plays an important role in the magnetic field reconnection. Below, we investigate the stability of equilibrium distribution function (28) in magnetic field (2) against perturbations that depend on x, y, z, and t.

Based on the results obtained in [19–23], we estimate the instability growth rate $\gamma(\mathbf{k})$. We consider the evolution of the following perturbations of the vector potential:

$$A_1(x, y, z, t) = A_1(y)\exp\{i(k_x x + k_z z) + \gamma t\}, \quad (43)$$

where $\mathbf{k} = (k_x, k_z)$ is the wave vector and γ is the growth rate. The perturbation $\mathbf{A}_1(x, y, z, t)$ of the vector potential is described by the equation

$$\frac{\partial^2\mathbf{A}_1}{\partial y^2} - k^2\mathbf{A}_1 = \frac{4\pi}{c}\left(\frac{\partial\mathbf{j}_0}{\partial\mathbf{A}_0}\mathbf{A}_1 + \mathbf{j}_1\right), \quad (44)$$

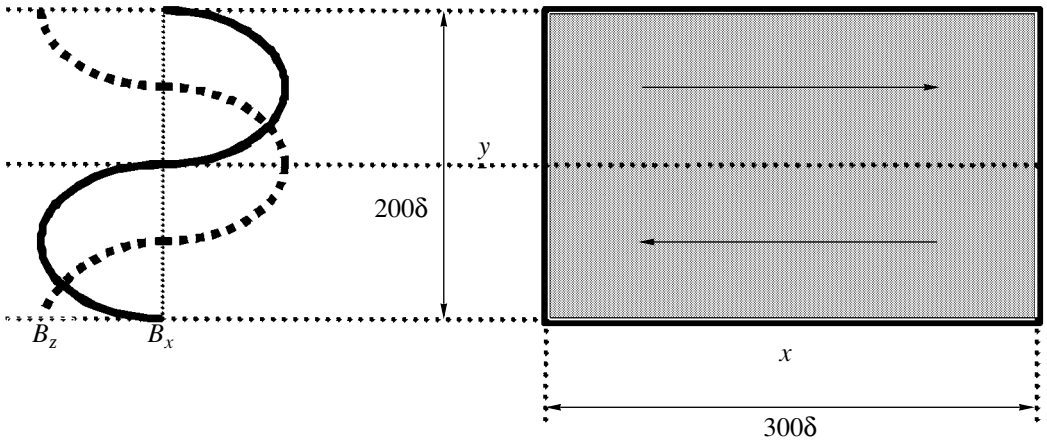

Fig. 2. Computation region and initial magnetic field distribution.

where $(\partial \mathbf{j}_0/\partial \mathbf{A}_0)\mathbf{A}_1$ is the adiabatic component of the perturbation of the electric current density and $\mathbf{j}_1$ is the nonadiabatic component.

It is well known [12] that the problem of the tearing instability should be solved in the outer region and also in the inner region near the surface at which $\mathbf{k} \cdot \mathbf{B} = 0$. In the outer region, the problem reduces to that of analyzing adiabatic (slow) perturbations. In this case, kinetic effects can be neglected and Eq. (44) reduces to the following equation for the function $\Psi = B_{1y}/B_0 = i(k_x A_{1z} - k_z A_{1x})/B_0$:

$$\Psi'' + (1 - \kappa^2)\Psi = 0, \tag{45}$$

where $\kappa = k\alpha^{-1}$, $k^2 = k_x^2 + k_z^2$, and the prime stands for the differentiation with respect to the dimensionless variable $\mu = \alpha y$.

The position of the resonance surface is determined by the condition

$$k_x \cos\mu + k_z \sin\mu = 0, \tag{46}$$

which holds on the planes $\mu_j = -\arctan k_x/k_z + j\pi$, $j = 0, \pm 1, \pm 2, \ldots$.

The solution to Eq. (45) depends on the wavenumber κ and thus can be represented as a linear combination of the functions $\Psi_1 = \sin\sqrt{1-\kappa^2}\mu$ and $\Psi_2 = \cos\sqrt{1-\kappa^2}\mu$ for $\kappa < 1$, the functions $\Psi_1 = 1$ and $\Psi_2 = \mu$ for $\kappa = 1$, and the functions $\Psi_1 = \sinh\sqrt{\kappa^2-1}\mu$ and $\Psi_2 = \cosh\sqrt{\kappa^2-1}\mu$ for $\kappa > 1$.

The solution to the Vlasov–Maxwell equations near the resonance surface in the inner region was considered in [19, 24–26], and the solution for the inner region of the plasma in a sheared magnetic field was derived by Drake and Lee [14, 27]. In the latter case, the width of the inner region is governed by the thermal motion of electrons along the magnetic field and the dispersion relation has the form

$$\Delta' = \frac{\Psi'_{\mu_j+0}}{\Psi_{\mu_j+0}} - \frac{\Psi'_{\mu_j-0}}{\Psi_{\mu_j-0}} = \frac{\gamma}{\kappa v_{Te}\alpha}(d_e\alpha)^{-2}, \tag{47}$$

where v_{Te} is the electron thermal velocity, $d_e = c/\omega_{pe}$ is the collisionless skin depth, and $\omega_{pe} = \sqrt{4\pi n_e e^2/m_e}$ is the plasma frequency.

We consider a plasma configuration infinite in the y direction. Matching the solutions for the outer and inner regions, we obtain the equation

$$\Psi'' + (1 - \kappa^2)\Psi - \sum_j \Delta'\delta(\mu - \mu_j)\Psi = 0, \tag{48}$$

in which the possible discontinuity of the derivative at the resonance surface is accounted for by δ functions. Note that this equation coincides with the Schrödinger equation for a particle moving in a periodic potential. According to the Floquet theorem, the solutions in the neighboring intervals differ only in a factor whose absolute value is equal to unity:

$$\Psi(\mu) = C_1\Psi(\mu) + C_2\Psi(\mu), \quad \mu_{j-1} < \mu < \mu_j, \tag{49}$$

$$\Psi(\mu) = \exp(iQ\pi)(C_1\Psi(\mu - \pi) + C_2\Psi(\mu - \pi)), \quad \mu_j < \mu < \mu_{j+1}, \tag{50}$$

where Q is a real number that characterizes the phase difference between the neighboring resonance surfaces and whose absolute value is less than or equal to unity. Taking into account the fact that, at the resonance surface, the function $\Psi(\mu)$ is continuous while its logarith-

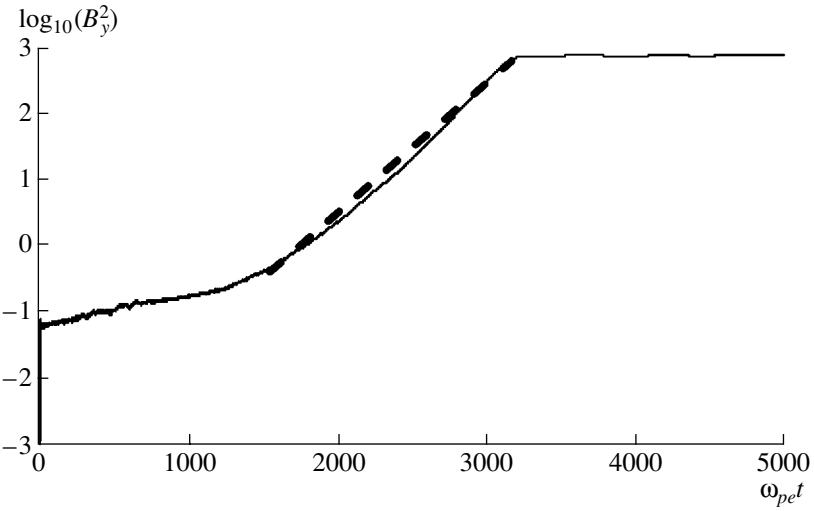

Fig. 3. Time evolution of $\log(B_y^2)$.

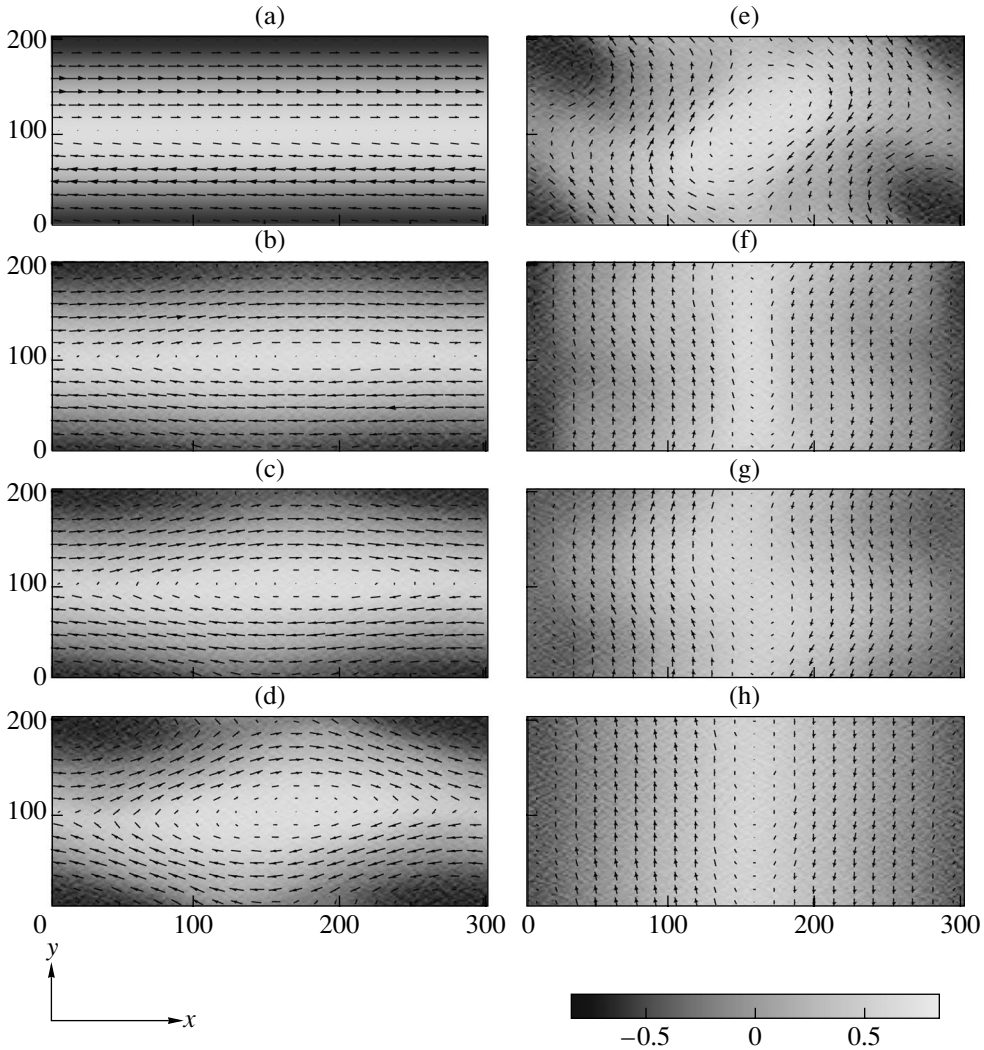

Fig. 4. Magnetic field distributions in the (x, y) plane at different times $\omega_{pe}t$ = (a) 0, (b) 2500, (c) 2750, (d) 3000, (e) 3250, (f) 3500, (g) 3750, and (h) 5000. The components B_x and B_y are represented as a vector field, and the component B_z is shown by shades of gray.

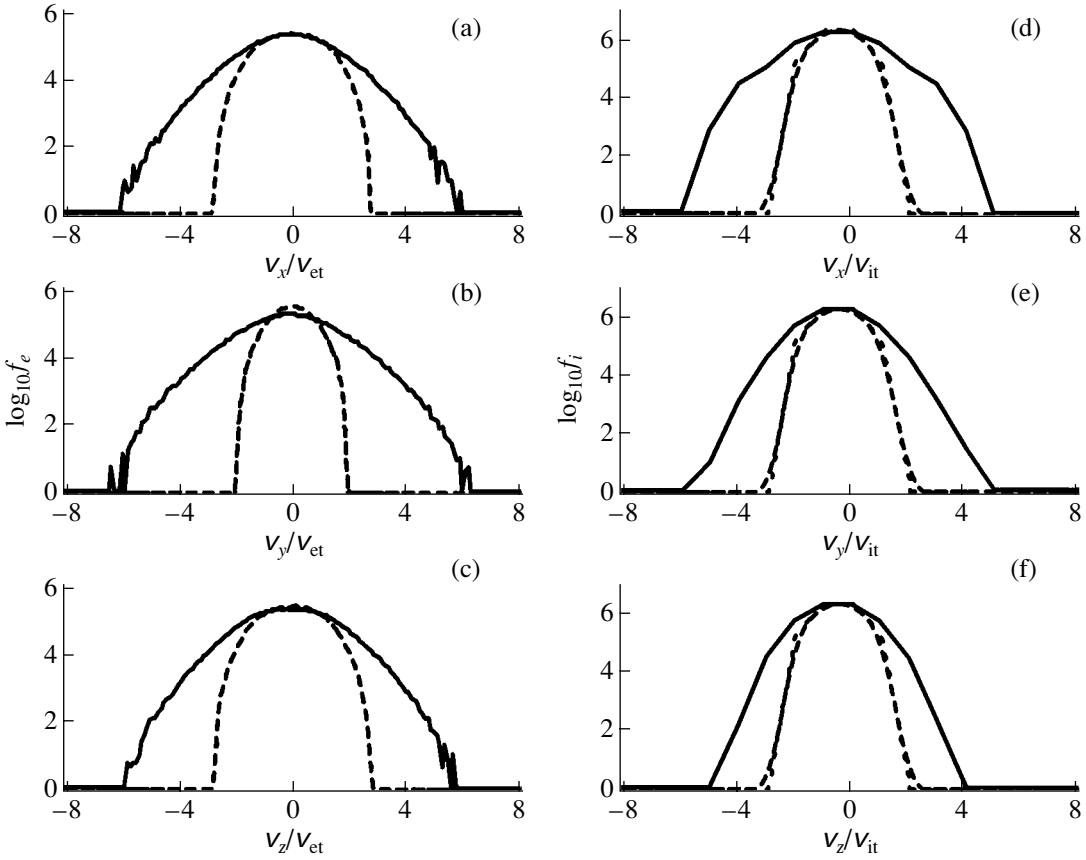

Fig. 5. Electron and ion distribution functions over (a, d) v_x, (b, e) v_y, and (c, f) v_z at the times $\omega_{pe}t = 0$ (dashed curves) and $\omega_{pe}t = 290$ (solid curves).

mic derivative jumps by an amount Δ', we arrive at the equations

$$\exp(iQ\pi)(C_1\Psi(\mu_j - \pi) + C_2\Psi(\mu_j - \pi)) = (C_1\Psi(\mu_j) + C_2\Psi(\mu_j)), \quad (51)$$

$$\exp(iQ\pi)(C_1\Psi'(\mu_j - \pi) + C_2\Psi'(\mu_j - \pi)) = (C_1\Psi'(\mu_j) + C_2\Psi'(\mu_j)) + \Delta'(C_1\Psi(\mu_j) + C_2\Psi(\mu_j)). \quad (52)$$

The condition that Eqs. (51) and (52) have a nontrivial solution yields the following expressions for the jump Δ':

$$\cos Q\pi = \cos\sqrt{1-\kappa^2}\pi + \Delta'\frac{\sin\sqrt{1-\kappa^2}\pi}{2\sqrt{1-\kappa^2}}, \quad \kappa < 1; \quad (53)$$

$$-4\sin^2 Q\pi/2 = \pi\Delta', \quad \kappa = 1; \quad (54)$$

$$\cos Q\pi = \cosh\sqrt{\kappa^2-1}\pi + \Delta'\frac{\sinh\sqrt{\kappa^2-1}\pi}{2\sqrt{\kappa^2-1}}, \quad \kappa > 1. \quad (55)$$

Substituting Δ' into expression (47), we obtain a dispersion relation between γ, κ, and the longitudinal wavenumber Q. The equilibrium state in question is unstable when $\kappa^2 + Q^2 < 1$. The instability growth rate is equal to

$$\gamma = \frac{2(\cos Q\pi - \cos\sqrt{1-\kappa^2}\pi)\kappa\sqrt{1-\kappa^2}}{\sin\sqrt{1-\kappa^2}\pi}(d_e\alpha)^2\alpha v_{Te}. \quad (56)$$

The growth rate is seen to be fastest at $Q = 0$.

5. NUMERICAL SIMULATIONS OF MAGNETIC RECONNECTION IN A FORCE-FREE MAGNETIC FIELD

We have considered above the linear stage of the tearing instability. The nonlinear stage of the instability in a force-free magnetic field was simulated with the 2D3V Tristan PIC electromagnetic code [28]. The dimensions of the computation region were chosen to be 300δ in the x direction and 200δ in the y direction, where $\delta = V_d^e/\omega_{pe}$ (Fig. 2). The initial electron distribution was described by function (28). The electron tem-

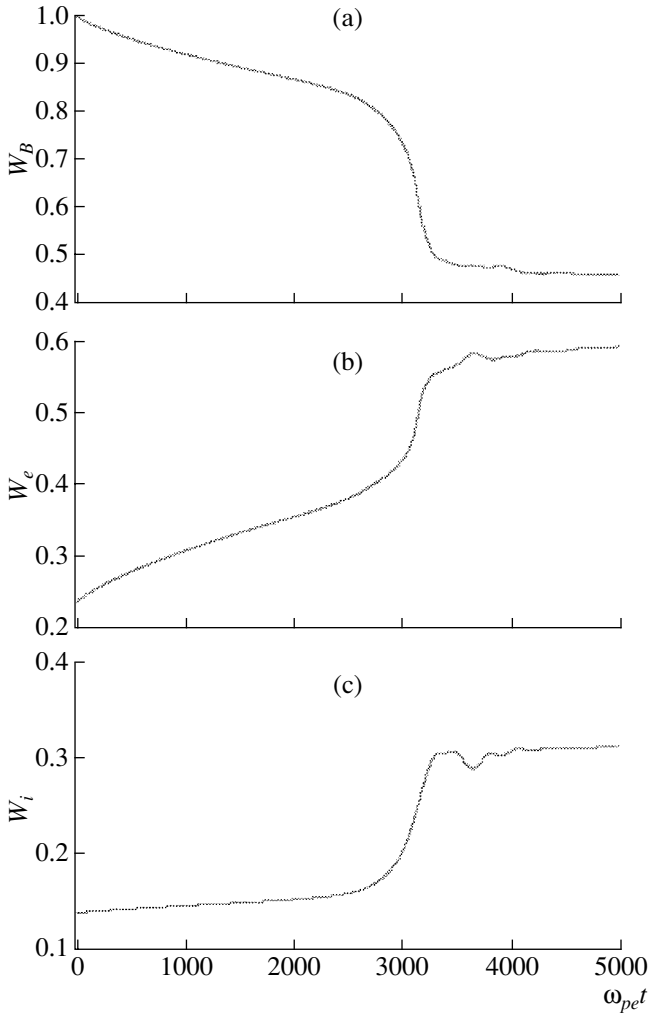

Fig. 6. Time evolutions of (a) the magnetic field energy, (b) the electron kinetic energy, and (c) the ion kinetic energy.

perature anisotropy was $T_{e\|}/T_{e\perp} = 1.12$ and the drift velocity was $V_d^e = 0.8v_{Te}$.

The ion distribution function was assumed to be isotropic, the ion temperature being $T_i = T_{e\|}$. The ion-to-electron mass ratio was set to be $m_i/m_e = 1836$. The total number of particles in the simulations was 1.2×10^7. The initial magnetic field was described by expression (2), in which the magnetic field strength corresponded to the ratio $\omega_{pe}/\omega_{Be} = 3.7$ and its characteristic scale length was $\alpha = 0.0314\delta^{-1}$ (Fig. 2). Note that the dimension of the computation region in the *y* direction coincides with the spatial field period. The boundary conditions were periodic in both the *x* and *y* directions.

Figure 3 illustrates how the squared *y* component of the magnetic field evolves during the development of the instability. According to the time evolution of $\log(B_y^2)$, the instability growth rate is equal to $\gamma/\omega_{pe} = 0.0023$ for $\omega_{pe}t > 1500$ and, for $\omega_{pe}t > 3100$, the instability saturates. The growth rate $\gamma/\omega_{pe} = 0.0023$ corresponds to the linear reconnection stage. The dashed line in Fig. 3 is the time evolution of $\log(B_y^2)$ corresponding to growth rate (56).

Figure 4 presents the magnetic field distributions in the (x, y) plane at different times $\omega_{pe}t$ = (a) 0, (b) 2500, (c) 2750, (d) 3000, (e) 3250, (f) 3500, (g) 3750, and (h) 5000. The components B_x and B_y are presented as a vector field, and the component B_z is shown by shades of gray. We see that the tearing instability produces a magnetic island. For $\omega_{pe}t > 3000$ (Figs. 4d, 4e), both the deviation of the resonance surface from its initial position and the width of the island become on the order of the dimension of the computation region in the *y* direction and the instability saturates, in which case the magnetic field topology changes in the way shown in Figs. 4f–4h. The instability can saturate for two different reasons. The first reason is the isotropization of the electron velocity distribution. This is confirmed by Fig. 5, which shows that, during the instability, the electron velocity distribution becomes isotropic. The ion velocity distribution remains isotropic from the very beginning. The second reason is the finite length of the computation region in the *y* direction: the effective length of the magnetic configuration becomes too large for the long-wavelength perturbations characteristic of the tearing instability [12] to develop.

Figure 6 displays time evolutions of the (a) magnetic field energy, (b) electron kinetic energy, and (c) ion kinetic energy. We can see that, for $\omega_{pe}t \sim 3000$, the magnetic field energy is rapidly dissipated and the plasma electrons and ions are accelerated.

6. CONCLUSION

We have investigated the behavior of a plasma in a force-free magnetic field using the collisionless approximation. An analysis of the particle trajectories shows that only two kinds of plasma particles can exist in such a field: transit particles and trapped ones. Knowing the integrals of motion of the charged particles, we have obtained an equilibrium solution to the Vlasov–Maxwell equations. This solution describes the particle distribution function in force-free magnetic field (2). The equilibrium is possible only when the plasma temperatures along and across the magnetic field are different. The characteristic scale length of the magnetic field is determined by the degree to which the plasma temperature is anisotropic. By taking into account the possible plasma nonquasineutrality, we have obtained a wider class of solutions describing equilibrium magnetic configurations.

We have investigated the stability of an equilibrium plasma configuration in force-free magnetic field (2) and have shown that a configuration that is infinite in the *y* direction is unstable against the tearing instability.

We have determined the growth rate of the tearing instability in its linear stage. The results from numerical simulations of this stage have been found to agree well with analytical predictions. We have also numerically investigated the nonlinear stage of the tearing instability.

REFERENCES

1. V. D. Shafranov, in *Reviews of Plasma Physics*, Ed. by M. A. Leontovich (Gosatomizdat, Moscow, 1963; Consultants Bureau, New York, 1966), Vol. 2.
2. B. B. Kadomtsev, Rev. Plasma Phys. **22**, 1 (2000).
3. H. K. Moffat, *Magnetic Field Generation in Electrically Conducting Fluids* (Cambridge Univ. Press, Cambridge, 1978).
4. E. R. Priest, *Solar Magnetohydrodynamics* (Reidel, Dordrecht, 1984).
5. E. G. Harris, Nuovo Cimento **23**, 117 (1962).
6. N. Attico and F. Pegoraro, Phys. Plasmas **6**, 767 (1999).
7. S. M. Mahaian and R. D. Hazeltine, Phys. Plasmas **7**, 1287 (2000).
8. N. A. Bobrova, S. V. Bulanov, J. I. Sakai, and D. Sugiyama, Phys. Plasmas **8**, 759 (2001).
9. G. E. Vekstein, N. A. Bobrova, and S. V. Bulanov, J. Plasma Phys. **67**, 215 (2002).
10. M. Lontano, S. Bulanov, J. Koga, *et al.*, Phys. Plasmas **9**, 2562 (2002).
11. M. Lontano, S. Bulanov, J. Koga, and M. Passoni, Phys. Plasmas **10** (2003) (in press).
12. H. P. Furth, J. K. Killen, and M. N. Rosenbluth, Phys. Fluids **6**, 459 (1963).
13. D. Biskamp, *Cambridge Monographs on Plasma Physics*, Vol. 1: *Nonlinear Magnetohydrodynamics* (Cambridge Univ. Press, Cambridge, 1993).
14. J. F. Drake and Y. C. Lee, Phys. Rev. Lett. **39**, 453 (1977).
15. K. Swartz and R. D. Hazeltine, Phys. Fluids **27**, 2043 (1984).
16. L. M. Zelenyĭ and A. L. Taktakishvili, Fiz. Plazmy **10**, 50 (1984) [Sov. J. Plasma Phys. **10**, 26 (1984)].
17. R. Horiuchi and T. Sato, Phys. Plasmas **4**, 277 (1977).
18. K. Schindler, J. Geophys. Res. **79**, 2803 (1974).
19. B. Coppi, G. Laval, and R. Pellat, Phys. Rev. Lett. **16**, 1207 (1966).
20. A. A. Galeev and L. M. Zelenyĭ, Zh. Éksp. Teor. Fiz. **69**, 882 (1975) [Sov. Phys. JETP **42**, 450 (1975)].
21. V. S. Berezinskii, S. V. Bulanov, V. A. Dogel, *et al.*, *Astrophysics of Cosmic Rays* (North-Holland, Amsterdam, 1990).
22. N. A. Bobrova and S. I. Syrovatskiĭ, Pis'ma Zh. Éksp. Teor. Fiz. **30**, 567 (1979) [JETP Lett. **30**, 535 (1979)].
23. N. A. Bobrova and S. I. Syrovatskiĭ, Fiz. Plazmy **6**, 104 (1980) [Sov. J. Plasma Phys. **6**, 59 (1980)].
24. G. Laval, R. Pellat, and M. Vuillemin, Plasma Phys. Controlled Nucl. Fusion **2**, 259 (1966).
25. T. M. O'Neil, Phys. Fluids **8**, 2255 (1965).
26. S. V. Bulanov and P. V. Sasorov, Fiz. Plazmy **4**, 640 (1978) [Sov. J. Plasma Phys. **4**, 357 (1978)].
27. J. F. Drake and Y. C. Lee, Phys. Fluids **20**, 1341 (1977).
28. O. Buneman, *Computer Space Plasma Physics, Simulation Techniques and Software*, Ed. by H. Matsumoto and Y. Omura (Terra Scientific, Tokio, 1993), p. 67.

Translated by O.E. Khadin

Plasma Physics Reports, Vol. 29, No. 6, 2003, pp. 459–465. Translated from Fizika Plazmy, Vol. 29, No. 6, 2003, pp. 494–500.

PLASMA INSTABILITY

Suppression of the Rayleigh–Taylor Instability of a Low-Density Imploding Liner by a Longitudinal Magnetic Field

A. V. Gordeev

Russian Research Centre Kurchatov Institute, pl. Kurchatova 1, Moscow, 123182 Russia

Received May 23, 2002; in final form, December 6, 2002

Abstract—The possibility of suppressing the Rayleigh–Taylor instability in a low-density plasma, $\Pi = \omega_{pi}^2\Delta^2/c^2 \ll 1$ (where Δ is the thickness of the current-carrying slab), is investigated for the case in which the electron currents are much higher than the ion currents. The suppression of this instability in an imploding cylindrical liner by an axial external magnetic field B_{0z} is considered. It is shown that, for the instability to be suppressed, the external magnetic field B_{0z} should be stronger than the magnetic field $B_{0\theta}$ of the current flowing through the liner. © *2003 MAIK "Nauka/Interperiodica".*

1. In recent years, the implosion of thin current-carrying plasma shells has been recognized as offering great promise for generating high levels of pulsed power in the form of electromagnetic radiation and neutrons [1–3]. In such implosion processes, the Rayleigh–Taylor (RT) instability is one of the most dangerous instabilities preventing the compression of a current-carrying plasma shell to small dimensions [4, 5]. As a magnetic piston converges toward the axis of the system, it inevitably becomes subject to RT instability, which violates the compactness of the converging plasma shell and reduces the parameters of the source of radiation and neutrons. In order to increase the efficiency of a magnetic piston, it is necessary to reduce the effect of instability on the imploding current-carrying plasma shell. Hence, the investigation of RT instability is important from the technological standpoint.

RT instability [6] certainly exists in one-fluid magnetohydrodynamics, when the influence of the Hall effect can be neglected by virtue of the smallness of the parameter $\Pi^{-1} \ll 1$, where $\Pi = 4\pi e^2 Zn\Delta^2/Mc^2$, with Δ the characteristic dimension of a plasma slab. When $\Pi \ll 1$ and the Hall effect plays an important role, opinions in the literature are divided regarding the possibility of RT instability in two-fluid magnetohydrodynamics (see [7, 8]). However, in view of the analogy between the RT instability in magnetohydrodynamics and the instability of a heavy liquid supported by a lighter liquid, it is natural to suppose that RT instability should also take place in two-fluid magnetohydrodynamics. RT instability has been studied in many papers (see, e.g., [9, 10]). In my recent works [11, 12], it was shown that, in the limit $\Pi \ll 1$, the linear equation for this instability can be integrated for arbitrary density and pressure profiles in the accelerated plasma slab. According to the solution obtained in [11, 12], the shapes of the density and pressure profiles have no effect on the instability growth rate.

Further analysis will be carried out based on a particular version of the two-fluid MHD model—a so-called Hall plasma model, in which the plasma ions are assumed to be unmagnetized [13].

2. The most widely used method for the stabilization of an imploding liner consists in imposing an external magnetic field parallel to the liner axis. This field makes the liner more "rigid" and thus can, in principle, retard the development of constrictions that grow from the perturbations associated with the longitudinal plasma inhomogeneity. It is known from experiments that the instability can be suppressed even by a comparatively weak longitudinal magnetic field B_{0z}, which is substantially weaker than the azimuthal magnetic field $B_{0\theta}$ [14, 15]. That is why, in order to provide better insight into the possibility of suppressing the instability, it is worthwhile to develop a simple analytic approach. Although the general case of arbitrary parameter values is difficult to investigate analytically, the problem can be greatly simplified by examining it in the limit of small values of the parameter $\Pi = \omega_{pi}^2\Delta^2/c^2 \ll 1$. The analytic solutions obtained in [11, 12] made it possible to draw some conclusions about RT instability in the absence of a longitudinal magnetic field in the parameter range $\Pi \ll 1$. It was shown that, for a low-density plasma, the standard formula for the instability growth rate is valid for an arbitrary density profile $n(x)$ inside the slab and an arbitrary pressure profile of the form $p = p(n)$. In other words, in such a plasma, RT instability in the linear stage cannot be suppressed by appropriately choosing the plasma density profile. Below, the approach developed previously will be generalized to study the possibility of suppressing RT instability with a longitudinal magnetic field.

1063-780X/03/2906-0459$24.00

In further analysis, the characteristic current in the liner and the characteristic liner radius will be assumed to be $J \geq 1$ MA and $r \leq 1$ cm, respectively (which correspond to a magnetic field of $B > 10^5$ G), and the characteristic plasma density will be assumed to be $n_e \sim 10^{17}$–10^{18} cm^{-3}.

Note that, in [12], RT instability was considered with allowance for the finite plasma pressure. However, to simplify matters, the gas-kinetic pressure effects will be neglected below. This indicates that the approach to be developed is valid for the stage before the complete collapse of the liner toward its axis. In this stage, the thickness of the plasma shell can be assumed to be much smaller than the characteristic liner radius, so that we can use the plane plasma slab approximation.

3. In a number of papers, it was shown clearly that the Hall effect cannot suppress RT instability [16–18]. At the same time, it was found that the one- and two-fluid MHD equations describe the instability in different ways. However, in those papers, the instability was modeled by introducing a fictitious gravitational field. Here, as in [11, 12], the model equations are derived by passing directly into the moving frame of reference, which makes the statement of the problem more adequate.

We start with the set of two-fluid MHD equations. Taking the sum of the equations of motion for ions and electrons and accounting for the quasineutrality condition, we can obtain an equation for the plasma mass velocity. We assume that the plasma is, on the one hand, cold enough for the gas-kinetic pressure to be much lower than the magnetic pressure, and, on the other, hot enough for the dissipation associated with the plasma resistivity to be negligible. Combining the two conditions $B^2 \gg 8\pi nT$ and $\sigma B \gg enc$ and using the conductivity estimated in [19], $\sigma \simeq 0.5 \times 10^{31} T^{3/2}$ (where T is expressed in ergs) [19], we arrive at the following necessary condition for the density of the accelerated plasma:

$$B^2 \gg 1.9 \times 10^{-14} n^{5/4}, \tag{1}$$

where the magnetic field and density are expressed in G and cm^{-3}, respectively.

This condition is fairly restrictive: it is satisfied only for sufficiently strong magnetic fields. Note that a comparatively low temperature (in the stage of the acceleration of a plasma shell in a liner, it is about 10^2 eV or even lower) may be associated with a strong emission from the shell.

Then, taking the curl of the equation of electron motion and neglecting electron inertia (which is justified because the scale c/ω_{pe} is much smaller than the characteristic spatial scale Δ of the accelerated shell), we obtain an equation for the magnetic field evolution.

As a result, we arrive at the following set of equations describing the dynamics of a plasma shell accelerated by the magnetic field:

$$\rho \frac{d\mathbf{V}}{dt} = -\frac{1}{4\pi}[\mathbf{B} \times [\nabla \times \mathbf{B}]], \tag{2}$$

$$\frac{\partial \rho}{\partial t} + \nabla \cdot (\rho \mathbf{V}) = 0, \tag{3}$$

$$\frac{\partial \mathbf{B}}{\partial t} = [\nabla \times [\mathbf{V} \times \mathbf{B}]] + \frac{c}{4\pi e}\left[\nabla \times \frac{1}{n}[\mathbf{B} \times [\nabla \times \mathbf{B}]]\right] - \frac{c^2}{4\pi}\left[\nabla \times \frac{1}{\sigma}[\nabla \times \mathbf{B}]\right]. \tag{4}$$

Here, we formally retain the finite plasma conductivity in order to stress its possible role in establishing the initial equilibrium.

We treat the problem in plane geometry, regarding the motion along the radial coordinate r as the motion in the x direction, in which case the θ-component of the magnetic field becomes the B_y component. We assume that, at the instant the magnetic field begins to accelerate the plasma, all of the quantities depend only on the x coordinate.

The equations for the initial configuration of a plasma slab accelerated by the magnetic field have the form

$$\rho_0 \frac{dV_0}{dt} = -\frac{1}{4\pi}\left(B_{0y}\frac{\partial B_{0y}}{\partial x} + B_{0z}\frac{\partial B_{0z}}{\partial x}\right), \tag{5}$$

$$\frac{\partial \rho_0}{\partial t} + \frac{\partial}{\partial x}(\rho_0 V_0) = 0, \tag{6}$$

$$\frac{\partial B_{0y}}{\partial t} + \frac{\partial}{\partial x}(B_{0y} V_0) = \frac{c^2}{4\pi}\frac{\partial}{\partial x}\left(\frac{1}{\sigma}\frac{\partial B_{0y}}{\partial x}\right). \tag{7}$$

The field component B_{0z} is described by an equation analogous to Eq. (7).

The equations for perturbations are

$$\rho_0 \frac{dV_x}{dt} + \rho \frac{dV_0}{dt} = -\frac{1}{4\pi}\left\{\frac{\partial}{\partial x}(B_{0y}B_y) + \frac{\partial}{\partial x}(B_{0z}B_z) - B_{0z}\frac{\partial}{\partial z}B_x\right\}, \tag{8}$$

$$\rho_0 \frac{dV_z}{dt} = -\frac{1}{4\pi}\left(B_{0y}\frac{\partial B_y}{\partial z} - B_x\frac{\partial B_{0z}}{\partial x}\right), \tag{9}$$

$$\rho_0 \frac{dV_y}{dt} = -\frac{1}{4\pi}\left(-B_{0z}\frac{\partial B_y}{\partial z} - B_x\frac{\partial B_{0y}}{\partial x}\right), \tag{10}$$

$$\frac{\partial \rho}{\partial t} + \frac{\partial}{\partial x}(\rho_0 V_x + \rho V_0) + \frac{\partial}{\partial z}(\rho_0 V_z) = 0, \tag{11}$$

$$\frac{\partial B_y}{\partial t} + \frac{\partial}{\partial x}(V_0 B_y + V_x B_{0y}) + \frac{\partial}{\partial z}(V_z B_{0y} - V_y B_{0z})$$

$$= \frac{c}{4\pi e n_0}\frac{\partial}{\partial z}\left\{\frac{\partial}{\partial x}(B_{0y}B_y) + \frac{\partial}{\partial x}(B_{0z}B_z) - B_{0z}\frac{\partial B_x}{\partial z}\right\} \quad (12)$$

$$- \frac{c}{4\pi e n_0^2}\frac{\partial n}{\partial z}\left(B_{0y}\frac{\partial B_{0y}}{\partial x} + B_{0z}\frac{\partial B_{0z}}{\partial x}\right)$$

$$- \frac{c}{4\pi e}\frac{\partial}{\partial x}\left\{\frac{1}{n_0}\left(B_{0y}\frac{\partial B_y}{\partial z} - B_x\frac{\partial B_{0z}}{\partial x}\right)\right\}.$$

Here, the vector potential A, in terms of which the magnetic field components B_x and B_z are expressed,

$$B_z = \frac{\partial A}{\partial x}, \quad B_x = -\frac{\partial A}{\partial z},$$

satisfies the equation

$$\frac{\partial A}{\partial t} + V_0\frac{\partial A}{\partial x} - \frac{c}{4\pi e n_0}\frac{\partial B_{0y}}{\partial x}\frac{\partial A}{\partial z}$$

$$= -B_{0z}\left(V_x + \frac{c}{4\pi e n_0}\frac{\partial B_y}{\partial z}\right). \quad (13)$$

In the equations for the perturbed quantities, we have omitted the dissipative term by virtue of the condition $h = \sigma B/enc \gg 1$. Note that, hereinafter, the quantities without subscripts refer to perturbations.

We simplify the above equations by using the compactness condition, which implies that the macroscopic velocity V_0 of the accelerated plasma slab is independent of x and depends only on time. This condition can be written as [13]

$$\frac{\partial V_0}{\partial t} = -a_0(t), \quad (14)$$

where the acceleration a_0 of a current-carrying plasma slab depends weakly on time.

We now transform the equations to an accelerated frame of reference, i.e., to a frame moving with the accelerated plasma slab in the negative x direction; this indicates that, in the original (cylindrical) coordinate system, the frame moves toward the liner axis. In order to pass to the accelerated frame, we must switch to a new spatial variable s:

$$s = x - \int_0^t V_0(t')dt'. \quad (15)$$

Using the relationship

$$\left.\frac{\partial}{\partial t}\right|_s = \left.\frac{\partial}{\partial t}\right|_x + V_0\left.\frac{\partial}{\partial x}\right|_t, \quad (16)$$

we obtain the equilibrium condition

$$\rho_0 a_0 = \frac{B_{0y}}{4\pi}\frac{\partial B_{0y}}{\partial s} + \frac{B_{0z}}{4\pi}\frac{\partial B_{0z}}{\partial s}, \quad (17)$$

where

$$\left.\frac{\partial \rho_0}{\partial t}\right|_s = 0, \quad \left.\frac{\partial B_{0y}}{\partial t}\right|_s = \frac{c^2}{4\pi}\frac{\partial}{\partial s}\left(\frac{1}{\sigma}\frac{\partial B_{0y}}{\partial s}\right).$$

The field component B_{0z} satisfies an analogous equation.

It can be seen that the characteristic spatial scale of the structure of the field component B_{0y} that forms in a plasma with a high (but finite) conductivity σ is the skin depth. However, when the characteristic dimension Δ of the plasma slab is sufficiently large, we can neglect the time variation of B_{0y} and describe this component by the equation

$$\left.\frac{\partial B_{0y}}{\partial t}\right|_s = 0.$$

For a Hall plasma ($\Pi \ll 1$), this yields the following lower bound on the Hall parameter h:

$$h^2 \gg \frac{1}{\Pi}. \quad (18)$$

In further analysis, we will assume that the stabilizing magnetic field B_{0z} produced by external coils is constant, in which case its spatial derivatives can be neglected.

Of course, during the implosion of a current-carrying plasma shell, in which the longitudinal magnetic field remains constant because the conductivity σ is sufficiently high, the magnetic flux density inside the shell increases and the magnetic field at its inner boundary becomes stronger. As the shell thickness decreases, the growing longitudinal magnetic field penetrates into the shell; as a result, the spatial gradients of the longitudinal field in the shell may be nonzero. However, this effect becomes important only in the final stage of the implosion of the shell, when it approaches the axis of the system.

Changing to the moving frame, we arrive at the following final set of equations:

$$\frac{\partial \rho}{\partial t} + \frac{\partial}{\partial s}(\rho_0 V_x) + \rho_0\frac{\partial V_z}{\partial z} = 0, \quad (19)$$

$$\rho_0\frac{\partial V_z}{\partial t} = -\frac{1}{4\pi}B_{0y}\frac{\partial B}{\partial z}, \quad (20)$$

$$\rho_0\frac{\partial V_y}{\partial t} = -\frac{1}{4\pi}\left(-B_{0z}\frac{\partial B}{\partial z} + \frac{\partial A}{\partial z}\frac{\partial B_{0y}}{\partial s}\right), \quad (21)$$

$$\rho_0\frac{\partial V_x}{\partial t} - \rho a_0 = -\frac{1}{4\pi}\left\{\frac{\partial}{\partial s}(B_{0y}B) + B_{0z}\left(\frac{\partial^2 A}{\partial s^2} + \frac{\partial^2 A}{\partial z^2}\right)\right\}, \quad (22)$$

$$\frac{\partial B}{\partial t} - \frac{B_0}{n_0}\frac{\partial n}{\partial t} + v_0\left(\frac{\partial B}{\partial z} - \frac{B_0}{n_0}\frac{\partial n}{\partial z}\right) = -\frac{\partial}{\partial s}\left(\frac{B_0}{n_0}\right)\left(n_0 V_x + \frac{c}{4\pi e}\frac{\partial B}{\partial z}\right) + B_{0z}\frac{\partial}{\partial z}\left\{V_y + \frac{c}{4\pi e n_0}\left(\frac{\partial^2 A}{\partial s^2} + \frac{\partial^2 A}{\partial z^2}\right)\right\}, \quad (23)$$

$$\frac{\partial A}{\partial t} + v_0\frac{\partial A}{\partial z} = -B_{0z}\left(V_x + \frac{c}{4\pi e n_0}\frac{\partial B}{\partial z}\right), \quad (24)$$

where

$$v_0 = -\frac{c}{4\pi e n_0}\frac{\partial B_{0y}}{\partial s}, \quad \rho = n\frac{M}{Z}.$$

Here, the time derivative is taken at fixed s. Also, the subscript in the y component of the perturbed magnetic field is dropped, because the remaining magnetic field components are expressed in terms of the perturbation of the vector potential A.

We take the Fourier transformation of the final set in the time t (changing into the frequency ω) and in the z coordinate (changing into the wave vector k_z) and nondimensionalize the equations according to the relationships

$$a = \frac{A}{\Delta \bar{B}_0}, \quad b_0 = \frac{B_0}{\bar{B}_0}, \quad b = \frac{B}{\bar{B}_0}, \quad \nu_0 = \frac{n_0}{\bar{n}_0},$$

$$\nu = \frac{n}{\bar{n}_0}, \quad s = \Delta\xi, \quad \kappa = k_z\Delta, \quad \Lambda = \frac{B_{0z}}{\bar{B}_0},$$

$$a_0 = \frac{\bar{V}_0^2}{\Delta}, \quad \bar{V}_0^2 = \frac{Z\bar{B}_0^2}{4\pi M\bar{n}_0}, \quad \omega = \Omega\frac{\bar{V}_0}{\Delta},$$

$$\tilde{\Omega} = \Omega + \frac{\kappa}{\sqrt{\Pi}}\frac{1}{\nu_0}\frac{db_0}{d\xi}, \quad \Pi = \frac{4\pi e^2\bar{n}_0 Z\Delta^2}{Mc^2},$$

where Δ is the thickness of the accelerated slab in the x direction, $\bar{B}_0$ is the characteristic strength of the magnetic field B_0, and $\bar{n}_0$ is the characteristic electron density.

As a result, we obtain the following basic set of dimensionless equations:

$$\frac{d\nu}{d\xi} - \Omega^2\nu = \frac{d^2}{d\xi^2}(b_0 b) - \kappa^2 b_0 b + \Lambda\frac{d}{d\xi}\hat{\Delta}a, \quad \hat{\Delta} \equiv \frac{d^2}{d\xi^2} - \kappa^2, \quad (25)$$

$$\Omega\tilde{\Omega}\left(b - \frac{b_0}{\nu_0}\nu\right) = \frac{d}{d\xi}\left(\frac{b_0}{\nu_0}\right)\left\{\Omega\frac{\kappa}{\sqrt{\Pi}}b + \nu - \frac{d}{d\xi}(b_0 b) - \Lambda\hat{\Delta}a\right\} + \Lambda^2\kappa^2\frac{1}{\nu_0}b - \Lambda\kappa^2\frac{1}{\nu_0}\frac{db_0}{d\xi}a - \Lambda\Omega\frac{\kappa}{\sqrt{\Pi}}\frac{1}{\nu_0}\hat{\Delta}a, \quad (26)$$

$$\Omega\tilde{\Omega}a + \Lambda^2\frac{1}{\nu_0}\hat{\Delta}a = \frac{\Lambda}{\nu_0}\left\{\nu - \frac{d}{d\xi}(bb_0) + \Omega\frac{\kappa}{\sqrt{\Pi}}b\right\}, \quad (27)$$

where ν_0 and b_0 are related by

$$\nu_0 = b_0 b_0'. \quad (28)$$

In these equations, the constant longitudinal component of the equilibrium magnetic field is neglected and the prime denotes the derivative with respect to the independent variable ξ.

4. Equations (25)–(28) describe the RT instability in a reference frame moving with the acceleration a_0 in the negative x direction. Since, in their general form, the equations are not amenable to analytic study, we restrict ourselves here to considering the limiting case $\Pi \ll 1$, in which Eqs. (26) and (27) will contain the terms proportional to $1/\sqrt{\Pi} \gg 1$ and also all of the terms with the parameter Λ.

In this limit, we use equilibrium relationship (28) to reduce Eq. (26) to

$$\nu = b\frac{\nu_0'}{b_0'} - \kappa^2\chi b + \Lambda\hat{\Delta}a + \Lambda\frac{\sqrt{\Pi}}{\Omega\kappa}\left\{\nu_0\frac{d}{d\xi}\left(\frac{b_0}{\nu_0}\right)\hat{\Delta}a + \kappa^2\frac{db_0}{d\xi}a\right\}, \quad (29)$$

$$\chi = \frac{\Lambda^2\sqrt{\Pi}}{\kappa\Omega}.$$

We introduce the function $w = bb_0$ and insert the expression for ν in (29) into Eq. (25) to get

$$\frac{d}{d\xi}\left(\frac{dw}{d\xi} - w\frac{\nu_0'}{\nu_0}\right) = w\left(\kappa^2 - \Omega^2\frac{\nu_0'}{\nu_0}\right)$$
$$- \kappa^2\chi\left\{\frac{d}{d\xi}\left(\frac{w}{b_0}\right) - \Omega^2\frac{w}{b_0}\right\} - \Lambda\Omega^2\hat{\Delta}a \qquad (30)$$
$$+ \Lambda\frac{\sqrt{\Pi}}{\Omega\kappa}\left(\frac{d}{d\xi} - \Omega^2\right)\left\{\nu_0\frac{d}{d\xi}\left(\frac{b_0}{\nu_0}\right)\hat{\Delta}a + \kappa^2\frac{db_0}{d\xi}a\right\}.$$

Here, the expressions for a and $\hat{\Delta}a$ can be derived from Eq. (27). We substitute expression (29) for ν into Eq. (27) and, in the resulting equation, take into account all the terms containing the parameter Λ. Then, we introduce the function $\varphi = w/\nu_0$ to obtain

$$a = \Lambda\varphi - \frac{\Lambda\sqrt{\Pi}}{\Omega\kappa}\frac{b_0\varphi'}{1 - \frac{\Lambda^2\Pi}{\Omega^2}}$$
$$+ \frac{\Lambda^2\Pi}{\Omega^2\kappa^2}\frac{1}{1 - \frac{\Lambda^2\Pi}{\Omega^2}}b_0\frac{d}{d\xi}\left(\frac{b_0}{\nu_0}\right)\hat{\Delta}a, \qquad (31)$$

$$\hat{\Delta}a = \Lambda\hat{L}\hat{\Delta}\varphi - \frac{\Lambda\sqrt{\Pi}}{\Omega\kappa}\frac{1}{1 - \frac{\Lambda^2\Pi}{\Omega^2}}\hat{L}\hat{\Delta}(b_0\varphi'), \qquad (32)$$

where the operator $\hat{L}$ is defined as

$$\hat{L} = \sum_{l=0}^{\infty}(\lambda\hat{\Delta}e_0)^l, \quad \lambda = \frac{\Lambda^2\Pi}{\Omega^2\kappa^2}\frac{1}{1 - \frac{\Lambda^2\Pi}{\Omega^2}}, \qquad (33)$$
$$e_0 = b_0\frac{d}{d\xi}\left(\frac{b_0}{\nu_0}\right).$$

In expression (33) for the operator $\hat{L}$, the two-dimensional Laplace operator $\hat{\Delta}$ applies to all ξ functions to the right of it; i.e., $\hat{L}$ is an integral operator. Substituting expressions (31) and (32) into Eq. (30), we arrive at the final equation for the function φ:

$$\nu_0\hat{\Delta}\varphi + \nu_0'(\varphi' + \Omega^2\varphi)$$
$$= -\frac{\Lambda^2\Pi}{\Omega^2}\frac{1}{1 - \frac{\Lambda^2\Pi}{\Omega^2}}\left(\frac{d}{d\xi} - \Omega^2\right)(\nu_0\varphi')$$
$$- \Lambda^2\Omega^2\hat{L}\hat{\Delta}\varphi + \frac{\Lambda^2\sqrt{\Pi}}{\kappa}\frac{\Omega}{1 - \frac{\Lambda^2\Pi}{\Omega^2}}\hat{L}\hat{\Delta}(b_0\varphi') \qquad (34)$$
$$+ \left(\frac{d}{d\xi} - \Omega^2\right)\left\{\nu_0\frac{d}{d\xi}\left(\frac{b_0}{\nu_0}\right)\left[\frac{\Lambda^2\sqrt{\Pi}}{\kappa\Omega}\frac{1}{1 - \frac{\Lambda^2\Pi}{\Omega^2}}\hat{L}\hat{\Delta}\varphi\right.\right.$$
$$\left.\left. - \frac{\Lambda^2\Pi}{\Omega^2\kappa^2}\frac{1}{\left(1 - \frac{\Lambda^2\Pi}{\Omega^2}\right)^2}\hat{L}\hat{\Delta}(b_0\varphi')\right]\right\}.$$

Here, in contrast to earlier studies [11, 12], $\mathbf{k}\cdot\mathbf{B}_0 \equiv k_z B_{0z} \neq 0$. For $\Lambda = 0$, this equation describes the RT instability in the frame of reference comoving with an accelerated current-carrying plasma slab, in which case the unstable solution has a maximum in the region where $\mathbf{a}_0\cdot\nabla n_0 < 0$. In the geometry adopted here, this condition reduces to $n_0' < 0$, which corresponds to the outer boundary of the accelerated slab.

For $\Lambda^2 \leq 1$, the basic assumption of our analysis allows us to neglect all terms in Eq. (34) that are proportional to different powers of Π; as a result, Eq. (34) becomes similar in structure to the equations derived in [11, 12], thereby indicating that RT instability is again possible.

The most important point in Eq. (34) is that we have retained all of the terms that contain the parameter Λ, thus providing a correct transition to the limit of a strong external stabilizing magnetic field B_{0z} such that $\Lambda^2\Pi \gg \Omega^2$. In taking the limit, we can omit the last two terms on the right-hand side of Eq. (34). In fact, for $\Lambda^2\Pi \gg \Omega^2$, the last term formally vanishes because it is proportional to $\Omega^2/(\Lambda^2\Pi) \ll 1$. As for the next to last term, it includes $\hat{\Delta}\varphi$ and, in the limit to be taken, is much smaller than the term $\Lambda^2\Omega^2\hat{L}\hat{\Delta}\varphi$. For the same reason, the term $\nu_0\hat{\Delta}\varphi$ on the left-hand side can also be omitted. Hence, in the limit at hand, Eq. (34) simplifies to

$$\nu_0'(\varphi' + \Omega^2\varphi) - \left(\frac{d}{d\xi} - \Omega^2\right)(\nu_0\varphi')$$
$$+ \Lambda^2\Omega^2\hat{L}\hat{\Delta}\varphi + \frac{\Omega^3}{\kappa\sqrt{\Pi}}\hat{L}\hat{\Delta}(b_0\varphi') = 0. \qquad (35)$$

Using the definition of the operator $\hat{L}$, we can readily verify that Eq. (35) reduces to a fourth-order

differential equation for φ. Now, we consider the perturbations whose characteristic spatial scale is small in comparison with the dimension of the plasma slab, $\kappa \equiv k_z\Delta \gg 1$. For $\Lambda^2\Pi \gg \Omega^2$, the largest term in Eq. (35) is $\Lambda^2\Omega^2\hat{L}\hat{\Delta}\varphi$, which requires that $\hat{\Delta}\varphi = 0$. Then, neglecting the first term in comparison with the second term and taking into account the condition $|\kappa| \gg 1$, we can represent Eq. (35) in the form

$$-b_0(|\kappa| - \Omega^2) + \frac{2\Omega^3}{\kappa\sqrt{\Pi}} = 0. \tag{36}$$

This equation implies that, for $\sqrt{\Pi} \longrightarrow 0$, the instability growth rate vanishes. However, it should be kept in mind that the growth rate estimated from this equation, $\Omega \sim (\kappa\sqrt{\Pi})^{1/3}$, is not very small because of the restricted range of variations of the parameter $\Pi \gg m/M$, where m is the mass of an electron.

Hence, the criterion for the stabilization of RT instability in a low-density plasma by a magnetic field directed along the axis of an imploding liner has the form

$$\Lambda^2\Pi \gg \Omega^2. \tag{37}$$

Note that the quasiclassical approximation based on Eq. (36) is also valid for the most dangerous mode with $|\kappa| = \pi$, when the slab thickness is half the perturbation wavelength. The stabilization criterion shows that, even at the boundary of applicability of the quasiclassical approximation, $\Pi \sim 1$, the constant external stabilizing longitudinal magnetic field should be stronger than the magnetic field of the current flowing through the liner.

5. Following papers [11, 12], it is worthwhile to discuss whether the pressure balance is satisfied at the boundaries of the accelerated plasma slab. Under the above assumptions, the approximate momentum conservation law has the form

$$\frac{\partial}{\partial t}\left(NMV_i + \frac{1}{4\pi}[\mathbf{E}\times\mathbf{B}]_i\right) + \frac{\partial}{\partial x_k}\left\{MNV_iV_k + \delta_{ik}\frac{1}{8\pi}(\mathbf{E}^2 + \mathbf{B}^2) - \frac{1}{4\pi}(E_iE_k + B_iB_k)\right\} = 0. \tag{38}$$

We take into account the fact that the electric field is much weaker than the magnetic field and switch to the moving frame in accordance with the procedure described in Section 3. As a result, we obtain the pressure balance equation

$$\frac{\partial}{\partial t}(MNV_i)\Big|_s + \frac{\partial}{\partial z}\left(MNV_iV_z + \delta_{iz}\frac{\mathbf{B}^2}{8\pi}\right) + \frac{\partial}{\partial s}\left\{MNV_i(V_x - V_0) + \delta_{ix}\frac{\mathbf{B}^2}{8\pi}\right\} = 0. \tag{39}$$

Integrating this equation over s yields the pressure balance condition at each of the slab boundaries in the x direction:

$$\left\langle MNV_x(V_x - V_0) + \frac{\mathbf{B}^2}{4\pi}\right\rangle = 0, \tag{40}$$

where $\langle\ldots\rangle$ denotes the difference between the values of the quantities on both sides of each boundary.

Let us prove that, in condition (40), the first term, which is associated with plasma inertia, undergoes no jump at the plasma boundary. Since $V_0 \equiv V_0(t)$, it is sufficient to prove this assertion only for the factor $N\delta V_x$, where $\delta V_x \equiv V_x - V_0$. In dimensionless form, this factor can be found from the Fourier transformed equation (22):

$$-i\Omega\nu_0\delta V_x = \nu - \frac{\partial}{\partial\xi}(b_0b) + \Lambda\hat{\Delta}a.$$

Equation (25) can be rewritten as

$$\frac{d}{d\xi}\left\{\nu - \frac{d}{d\xi}(b_0b) + \Lambda\hat{\Delta}a\right\} = \Omega^2\nu - \kappa^2b_0b.$$

Since the right-hand side of this equation is finite, the quantity $\nu - d(b_0b)/d\xi + \Lambda\hat{\Delta}a$ undergoes no jumps at the slab boundaries and, therefore, vanishes there; i.e., the quantity $\nu_0\delta V_x$ also equals zero at the boundaries.

The second term in condition (40) accounts for the magnetic field and contains the zero-order component; accordingly, in order for this condition to be satisfied, it is necessary that there be no surface currents in the equilibrium state.

It should be kept in mind that, to first order in the perturbations, the term with the magnetic field in condition (40) coincides with the solution $w = \nu_0\varphi$ to within a numerical factor. Consequently, for a plasma slab with zero density ($\nu_0 = 0$) at the boundaries, evolutionary condition (40) is always satisfied, provided that the function φ is regular.

ACKNOWLEDGMENTS

This study was supported in part by the Russian Foundation for Basic Research, project no. 00-02-16305.

REFERENCES

1. H. Sze, P. Coleman, B. Failor, *et al.*, in *Proceedings of 13th International Conference on High Power Particle Beams, Nagaoka, 2000* (Nagaoka Univ. of Technology, Nagaoka, 2001), Vol. 1, p. 36.
2. P. Blinov, A. Chernenko, A. Chesnokov, *et al.*, in *Proceedings of 13th International Conference on High Power Particle Beams, Nagaoka, 2000* (Nagaoka Univ. of Technology, Nagaoka, 2001), Vol. 1, p. 76.
3. V. V. Aleksandrov, A. V. Branitskiĭ, G. S. Volkov, *et al.*, Fiz. Plazmy **27**, 99 (2001) [Plasma Phys. Rep. **27**, 89 (2001)].
4. H. Dickinson, W. H. Bostick, J. N. DiMarko, and S. Koslov, Phys. Fluids **5**, 1048 (1962).
5. N. F. Roderick, T. W. Hussey, R. J. Faehl, and R. W. Boyd, Appl. Phys. Lett. **32**, 273 (1978).
6. N. A. Inogamov, Prikl. Mekh. Tekh. Fiz., No. 5, 110 (1985).
7. L. I. Rudakov, in *Proceedings of 2nd International Conference on Dense Z-Pinches, Laguna Beach, California, 1989*; AIP Conf. Proc. **195**, 290 (1989).
8. L. I. Rudakov and A. A. Sevast'yanov, Fiz. Plazmy **22**, 1095 (1996) [Plasma Phys. Rep. **22**, 993 (1996)].
9. A. B. Budko, A. L. Velikovich, A. I. Kleev, *et al.*, Zh. Éksp. Teor. Fiz. **94**, 496 (1989) [Sov. Phys. JETP **68**, 279 (1989)].
10. A. B. Budko, A. L. Velikovich, M. A. Liberman, *et al.*, Zh. Éksp. Teor. Fiz. **96**, 140 (1989) [Sov. Phys. JETP **69**, 76 (1989)].
11. A. V. Gordeev, Fiz. Plazmy **25**, 76 (1999) [Plasma Phys. Rep. **25**, 70 (1999)].
12. A. V. Gordeev, Fiz. Plazmy **25**, 227 (1999) [Plasma Phys. Rep. **25**, 202 (1999)].
13. A. V. Gordeev, A. S. Kingsep, and L. I. Rudakov, Phys. Rep. **243**, 215 (1994).
14. F. J. Wessel, F. S. Felber, N. C. Wild, and H. U. Rahman, Appl. Phys. Lett. **48**, 1119 (1986).
15. A. V. Luchinskiĭ, I. A. Ratakhin, S. A. Sorokin, and S. A. Chaĭkovskiĭ, Pis'ma Zh. Tekh. Fiz. **15** (18), 83 (1989) [Sov. Tech. Phys. Lett. **15**, 739 (1989)].
16. A. B. Hassam and J. D. Huba, Phys. Fluids **31**, 318 (1988).
17. J. D. Huba, A. B. Hassam, and P. Satyanerayana, Phys. Fluids B **1**, 931 (1989).
18. A. L. Velikovich, Phys. Fluids B **3**, 492 (1991).
19. S. I. Braginskii, in *Reviews of Plasma Physics*, Ed. by M. A. Leontovich (Gosatomizdat, Moscow, 1963; Consultants Bureau, 1965), Vol. 1.

Translated by I.A. Kalabalyk

Plasma Physics Reports, Vol. 29, No. 6, 2003, pp. 466–472. Translated from Fizika Plazmy, Vol. 29, No. 6, 2003, pp. 501–507.

PLASMA OSCILLATIONS AND WAVES

Small-Scale Alfvén Waves Localized near an Extremum in the Finite-Amplitude Perturbation of the Radial Plasma Density Profile

I. O. Girka and P. P. Rutkevich

Karazin National University, pl. Svobody 4, Kharkov, 61077 Ukraine

Received July 10, 2002; in final form, October 24, 2002

Abstract—A study is made of electromagnetic waves localized in the region where the radial plasma density profile has an extremum between two local Alfvén resonances. Analytic expressions for the eigenfrequencies and eigenmodes are obtained. It is shown that kinetic and inertial Alfvén waves can propagate in the vicinity of a maximum and a minimum in the density profile, respectively. Passage to the limiting case in which the plasma density is nonuniform and has a parabolic profile is considered. *© 2003 MAIK "Nauka/Interperiodica".*

1. INTRODUCTION

The production and heating of plasma in controlled fusion devices initiated active research on the processes of conversion and absorption of electromagnetic waves near Alfvén resonance [1–6]. It is well known that the absorption of waves with frequencies $\omega < \omega_{ci}$ is accompanied by significant plasma heating near the Alfvén resonance point $r = r_A$, at which the following relationship is satisfied:

$$\varepsilon_1(r_A) \approx (ck_\parallel/\omega)^2. \quad (1)$$

Here, $\varepsilon_1 = 1 + \sum_\alpha \omega_{p\alpha}^2/(\omega_{c\alpha}^2 - \omega^2)$ is the component of the dielectric tensor of a cold collisionless plasma, with the subscript α indicating the ions (i) and the electrons (e); $k_\parallel$ is the projection of the wave vector onto the direction of a constant magnetic field; c is the speed of light in vacuum; ω is the wave frequency; and $\omega_{c\alpha}$ and $\omega_{p\alpha}$ are the cyclotron and Langmuir frequencies of the particles of species α, respectively. The coordinate dependence enters the expression for ε_1 through two physical quantities: the external magnetic field $B_0(r)$ and the plasma density $n(r)$. In what follows, it is assumed that only the plasma density depends on the radial coordinate. However, when the possible radial nonuniformity of the external magnetic field is taken into account, the method for solving the problem and the final results remain essentially the same. It is well known [1] that the RF power absorbed in the Alfvén resonance region is inversely proportional to dn/dr. That is why the case in which $n(r)$ has an extremum near Alfvén resonance is of particular interest [7–10].

The density perturbation (nonuniformity) that has an extremum is usually described by a squared parabola (see, e.g., [7–10]). This approach is justified for electromagnetic oscillations localized in the immediate vicinity of the point of extreme density, where the density profile deviates only slightly from a squared parabola, or for a sufficiently large density perturbation. The dispersion properties of electromagnetic oscillations in these cases have been studied fairly well. Thus, the spectrum of oscillations in related problems is known to have an infinite number of levels, because the branches of a squared parabola are infinitely high. Hence, approximating the density profile by a parabola is equivalent to modeling a sufficiently deep potential well. However, the depth of the well is actually finite, so that the dispersion properties of the oscillations differ considerably from those in the problem with an infinitely deep potential well [11]. For this reason, modeling a plasma density perturbation by a squared parabola alone may be insufficient. In what follows, by analogy with quantum mechanics, a density perturbation will be referred to as a "potential well."

2. FORMULATION OF THE PROBLEM

We consider a plasma cylinder that is uniform in both the axial and azimuthal directions and is placed in a constant uniform axial magnetic field. The radial plasma density profile is modeled by the expression (see Fig. 1)

$$\varepsilon_1(r) = N_z^2[1 + M + A/\cosh^2((r - r_0)/a)]. \quad (2)$$

Here, $N_z = ck_z/\omega$ is the axial refractive index, k_z is the axial component of the wave vector, r is the radial variable in cylindrical coordinates, r_0 is the radial position of the density extremum, a is the characteristic width of the region where the density is perturbed, MN_z^2 is the deviation of the quantity ε_1 from the resonant value N_z^2 far from the position r_0 of the extremum ($|r - r_0| \gg a$),

1063-780X/03/2906-0466$24.00

and AN_z^2 is the perturbation amplitude at the profile $\varepsilon_1(r)$. We assume that the quantities A and M may be positive or negative.

It is convenient to use function (2), which provides a fairly good approximation of the radial density profile not only in the vicinity of but also far from its maximum, because, at large distances from r_0, the term with the hyperbolic cosine can be neglected. Near the resonance point r_0, a constant plasma density is perturbed (nonuniform) in an axisymmetric fashion, the radial width a of the perturbation being prescribed. The sign of each of the terms depends on the plasma parameters. Given the density far from the point r_0 (or the value of the parameter M), we look for the eigensolutions to Maxwell's equations. Starting from the corresponding eigenvalues, we determine the parameter range where Alfvén eigenmodes can exist, specifically, the range of values of the plasma parameters (in particular, the density perturbation amplitude) in the vicinity of the perturbation.

3. BASIC EQUATION

The equation for the radial component $\tilde{E_r}$ of the field of a wave can be derived from Maxwell's equations with allowance for electron inertia and finite ion Larmor radius (see, e.g., [1, 8, 10]). Setting $\tilde{E_r} = E_r(r)\exp[i(k_z z + m\vartheta - \omega t)]$, we obtain

$$\left[\varepsilon_1 - N_z^2 + \left(\varepsilon_T + \frac{\varepsilon_1}{\varepsilon_3}\frac{c^2}{\omega^2}\right)\frac{d^2}{dr^2}\right]E_r = -i\varepsilon_2 E_\vartheta - \frac{cm}{\omega r}B_z, \quad (3)$$

where ε_i are the components of the dielectric tensor of a collisionless magnetized plasma. The term ε_T, which accounts for finite ion Larmor radius effects [12], has the form

$$\varepsilon_T = \sum_\alpha \frac{3\omega_{p\alpha}^2(r)v_{T\alpha}^2(r)}{(\omega^2 - \omega_{c\alpha}^{(0)^2})(\omega^2 - 4\omega_{c\alpha}^{(0)^2})}. \quad (4)$$

The coefficient in front of the second derivative in Eq. (3) is equal in order of magnitude to $N_z^2\rho_{Li}^2$, where $\rho_{L\alpha} = v_{T\alpha}/\omega_{c\alpha}$ is the Larmor radius of the particles of species α and $v_{T\alpha}$ is their thermal velocity. Following [1], we apply the so-called "narrow-slab" approach, which implies that, in the resonance region, the plasma parameters change gradually and the wave fields depend strongly on the radial coordinate. Assuming that the radial variations of the quantities ε_T and $\varepsilon_1/\varepsilon_3$ are gradual in this approximation, we introduce the notation

$$\varepsilon_T + \frac{\varepsilon_1}{\varepsilon_3}\frac{c^2}{\omega^2} \equiv \pm N_z^2\rho^2. \quad (5)$$

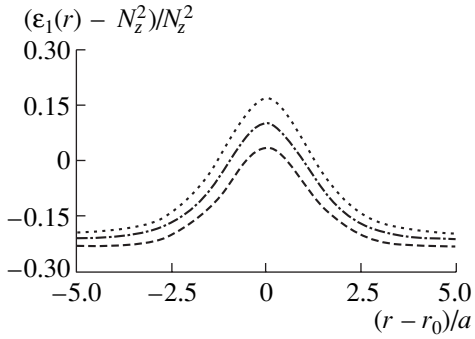

Fig. 1. Radial profiles of the quantity $(\varepsilon_1 - N_z^2)/N_z^2$ calculated for the fixed values $\delta = 10$ and $\rho/a = 0.05$ in the case of a maximum in the density profile. The dashed curve is for the eigenmode with the radial number $n = 0$, the dashed-and-dotted curve is for the mode with $n = 1$, and the dotted curve is for the mode with $n = 2$.

We emphasize that the quantity ρ in formula (5) has the dimensionality of length: it serves to normalize the coefficient in front of the second derivative in Eq. (3) and is of the same order of magnitude as (but not identical to) the ion Larmor radius.

Since, in the frequency range under consideration, the component ε_3 is negative and the component ε_T is positive, the coefficient in front of the second derivative may have different signs. The sign of the coefficient in front of the highest derivative in Eq. (3) is very important because it determines the conditions (a local maximum or a local minimum in the plasma density) in which the eigenmodes can exist. Since the quantity ε_T depends on the temperature of the plasma particles [see formula (4)], it is of considerable interest to determine the conditions under which quantity (5), being a function of the electron and ion temperatures, changes its sign. It is convenient to plot the curve along which quantity (5) is zero in the plane of the ion and electron thermal velocities (see Fig. 2). For a plasma in which both the ions and electrons are cold, $v_{Ti} \ll \omega/|k_z|$ and $v_{Te} \ll \omega/|k_z|$, coefficient (5) is negative. Physically, this indicates that the thermal velocities of the plasma particles can be neglected; hence, in expression (5), the second term, which accounts for electron inertia, is dominant. According to the generally accepted terminology [13], the waves in such a plasma are called inertial waves. On the contrary, for a plasma in which both the ions and electrons are hot, coefficient (5) is positive because it is primarily contributed by the ion thermal motion, in which case the waves are called kinetic waves.

Although, in the vicinity of Alfvén resonance, the azimuthal electric field E_ϑ and the axial magnetic field B_z have logarithmic singularities, $E_\vartheta, B_z \propto \ln|\varepsilon_1 - N_z^2|$, the combination $i\varepsilon_2 E_\vartheta + (cm/\omega r)B_z$ on the right-hand side of Eq. (3) is continuous and changes gradually.

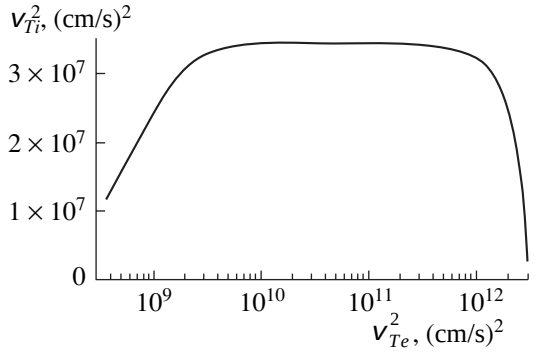

Fig. 2. Curve along which the quantity $\varepsilon_T + \frac{\varepsilon_1 c^2}{\varepsilon_3 \omega^2}$ in formula (5) changes sign in the coordinate plane (v_{Te}^2, v_{Ti}^2). Above the curve, this quantity is positive and, below the curve, it is negative. The calculations were carried out for a deuterium plasma of density 3×10^{13} cm^{-3} and a magnetic field of 39 kG.

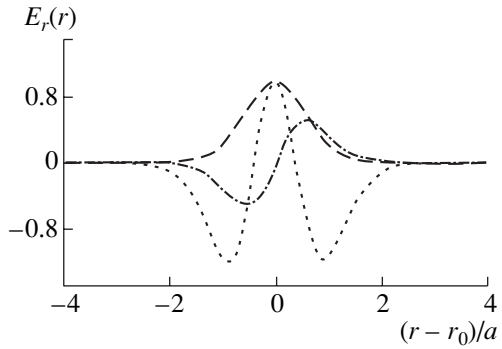

Fig. 3. Radial profiles of E_r for $n = 0$, 1, and 2. The parameters and notation are the same as in Fig. 1.

That is why this combination is usually set to be a constant and is attributed to the pump wave [1, 8, 10]. Since we are interested in the eigensolutions to Eq. (3) that are localized in the vicinity of $r = r_0$, we can assume that the wave fields are negligible far away from r_0 and, thus, we can set the combination to be zero.

4. KINETIC ALFVÉN WAVES

Here, we consider the case of a hot plasma, in which the coefficient in front of the second derivative in Eq. (3) is positive. In order for the solution to be localized, i.e., to decrease exponentially away from r_0, the quantity $\varepsilon_1 - N_z^2$ should be negative at $|r - r_0| \gg a$, which corresponds to $M < 0$. In the above notation, we rewrite Eq. (3) as

$$\left[- M + A\cosh^{-2}\left(\frac{r - r_0}{a}\right) + \rho^2 \frac{d^2}{dr^2}\right] E_r = 0. \qquad (6)$$

Recall that the coefficient A may have different signs. However, Eq. (6) has localized eigensolutions only when $A > 0$, i.e., when the density profile has a maximum (Fig. 1). This conclusion agrees with the results of a numerical analysis carried out by Appert *et al.* [14] for a plasma with hot electrons, $v_{Te} > \omega/|k_z|$.

Following [11], we introduce the notation

$$M = -\frac{\rho^2}{a^2}\delta^2, \quad A = \frac{\rho^2}{a^2}s(s+1). \qquad (7)$$

The replacement $\xi = \tanh\left(\frac{r - r_0}{a}\right)$ reduces Eq. (6) to a hypergeometric equation, whose solution is expressed in terms of a hypergeometric function [15]:

$$E_r(r) = \cosh^{-\delta}\left(\frac{r - r_0}{a}\right) F\left(\delta - s, \delta + s + 1, \delta + 1, \frac{1}{2}(1 - \xi)\right). \qquad (8)$$

At $r - r_0 \gg a$, function (8) is finite only when the quantities δ and s are related by $s = \delta + n$ (the number $n = 0$, 1, 2, … corresponds to the number of zeros of the function E_r). By the quantity δ, we mean the arithmetical square root of δ^2. Figure 3 shows the radial field component E_r calculated as a function of the radius from expression (8) at $n = 0$, 1, and 2.

For different n, the values of ε_1 at the point r_0 are equal to

$$\varepsilon_1(r_0) = N_z^2\left\{1 + \frac{\rho^2}{a^2}[\delta(2n+1) + n(n+1)]\right\}. \qquad (9)$$

The frequency for which resonance condition (1) is satisfied corresponds to the Alfvén continuum [5, 13] and is equal to $\omega = |k_z| v_A$, where v_A is the Alfvén speed. Assuming that the correction to N_z^2 on the right-hand side of expression (9) is small and retaining only the first term in the expansion in this correction, we find the frequencies of the eigenmodes with different values of n:

$$\omega_n = |k_z| v_A\left(1 + \frac{\rho^2}{2a^2}[\delta(2n+1) + n(n+1)]\right). \qquad (10)$$

In order to determine to which type of waves in a homogeneous plasma the waves localized between two Alfvén resonances belong, we solve Eq. (6) in the Wentzel–Kramers–Brillouin (WKB) approximation. Setting $E_r^{\sim} \propto \exp(i\int k_r dr)$ ($k_r a \gg 1$), we obtain the fol-

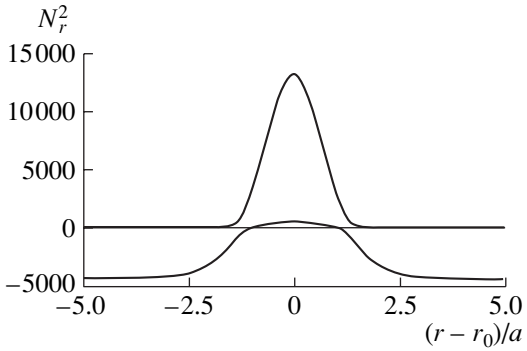

Fig. 4. Radial dependence of the radial refractive index in the case of a maximum in the density profile (which corresponds to the propagation of kinetic Alfvén waves).

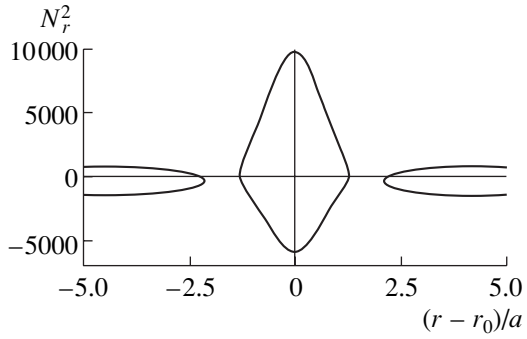

Fig. 5. Radial dependence of the radial refractive index in the case of a minimum in the density profile (which corresponds to the propagation of inertial Alfvén waves).

lowing expression for the squared radial refractive index $N_r^2 = c^2k_r^2/\omega^2$:

$$N_{r\pm}^2 = \frac{\varepsilon_1 - N_z^2}{2k_z^2\rho^2}\left[1 \pm \sqrt{1 - 4\frac{k_z^2\rho^2}{\varepsilon_1 - N_z^2}\left(N_\perp^2 - \frac{c^2m^2}{\omega^2 r_0^2}\right)}\right]. \quad (11)$$

This expression is plotted in Fig. 4 for the same parameters as in Figs. 1 and 3. In deriving expression (11), we have introduced the notation

$$N_\perp^2 = [(\varepsilon_1 - N_z^2)^2 - \varepsilon_2^2]/(\varepsilon_1 - N_z^2). \quad (12)$$

Far from the resonance region, the wave in question is a fast magnetosonic wave, whereas, near the resonance, it becomes an Alfvén wave. Far from the density perturbation, the squared radial refractive index is negative, $N_r^2 < 0$; hence, the waves do not exist. In the vicinity of the maximum in the perturbation, we have $N_r^2 > 0$, which indicates the existence of localized kinetic Alfvén waves.

5. INERTIAL ALFVÉN WAVES

For a cold plasma, coefficient (5) in front of the second derivative is negative, which corresponds to inertial waves. The problem for such a system possesses localized solutions only when the quantity $\varepsilon_1(r)$ far from the point r_0 (at infinity) is larger than its resonant value (1) ($M > 0$) and has a minimum ($A < 0$) in the vicinity of the point r_0. The radial dependence of the quantity $(\varepsilon_1(r) - N_z^2)/N_z^2$ differs from that shown in Fig. 1 only in sign (note that the zero on the vertical axis in Fig. 1 is chosen to correspond to the value N_z^2). Hence, using the replacement

$$M = +\frac{\rho^2}{a^2}\delta^2, \quad A = -\frac{\rho^2}{a^2}s(s+1), \quad (13)$$

we obtain, instead of Eq. (6), the following equation describing the eigenmodes when the density profile has a minimum:

$$\left[+\delta^2 - s(s+1)\cosh^{-2}\left(\frac{r - r_0}{a}\right) - a^2\frac{d^2}{dr^2}\right]E_r = 0. \quad (14)$$

Since Eq. (14) differs from Eq. (6) only in a constant factor, its solutions are also represented by formula (8); hence, the solutions for the first three eigenmodes behave in the same manner as those shown in Fig. 3.

The eigenfrequencies of the inertial Alfvén waves are equal to

$$\omega_n = |k_z|v_A\left\{1 - \frac{\rho^2}{a^2}[\delta(2n+1) + n(n+1)]\right\}. \quad (15)$$

Figure 5 shows the radial dependence of squared radial refractive index (11) calculated for the same plasma parameters as in Fig. 4. We can see that this dependence has discontinuities in the intervals where the imaginary part of N_r^2 is nonzero.

6. DISCUSSION OF THE RESULTS

It is known from the theory of Alfvén resonance [1, 8–10] that, in the vicinity of the resonance point at which condition (1) is satisfied, the field E_r diverges as $\propto(\varepsilon_1 - N_z^2)^{-1}$. When electron inertia and finite ion Larmor radius are taken into account, the solution becomes finite but changes radically. As has been shown above, the condition that the quantity ε_1 reaches its resonant value at only one point is not sufficient for the existence of the localized perturbations. A necessary condition for small-scale perturbations to be localized between two points is that the quantity $\varepsilon_1 - N_z^2$ at these points vanishes. Moreover, at the point of maximum density, $r = r_0$, the tensor component ε_1 should take on a certain value,

$$\varepsilon_1 - N_z^2 = N_z^2[(\delta + n)(\delta + n + 1) - \delta^2]. \quad (16)$$

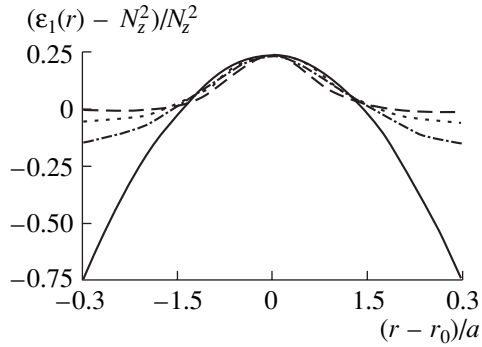

Fig. 6. Modeling of the profile of the quantity $(\varepsilon_1(r) - N_z^2)/N_z^2$, which depends linearly on the plasma density, by parabola (18) (solid curve) and hyperbolic cosine (2) in the case of a maximum in the density profile. The calculations were carried out for the mode with $n = 3$ and for different δ values: $\delta = 1$ (dashed curve), $\delta = 3$ (dotted curve), and $\delta = 7$ (dashed-and-dotted curve).

The amount by which the quantity ε_1 exceeds its resonant value depends on the δ value corresponding to the plasma density far from the resonance point.

The quantity $\varepsilon_1(r_0)$ given by expression (9) has a minimum value $N_z^2(1 + \delta\rho^2/a^2)$ at $n = 0$. In the model developed here, the eigenmodes do not exist for $\varepsilon_1 - N_z^2 < \delta N_z^2 \rho^2/a^2$.

On the other hand, for sufficiently small δ values, the amount by which the tensor component at hand should exceed its resonant value in the case $n = 0$ can be made arbitrarily small. This conclusion agrees with the well-known result from quantum mechanics [11]: in the corresponding quantum mechanical problem, the zero radial mode can exist in a potential well (2) of arbitrarily small depth. For higher modes, quantity (9) is finite (nonzero) for any δ value.

Note also that the applicability condition of the narrow-slab approach, $\rho \ll a$, can easily be satisfied in experiments. In the vicinity of Alfvén resonance, the characteristic parameter $k_r^2\rho^2$ is small, $k_r^2\rho^2 \sim \rho/a \ll 1$; hence, a description of the plasma in terms of the dielectric tensor turns out to be justified.

In deriving basic equation (6) from general equation (3), we imposed the corresponding boundary conditions and set the combination on the right-hand side of Eq. (3) to zero. In other words, we assumed that this combination is small in comparison with the retained terms that arise, e.g., from the finite ion Larmor radius and electron inertia. A comparison of the omitted term with the retained terms yields the following strong inequalities:

$$(\omega/\omega_{ci})N_\vartheta N_z,\ N_\vartheta^2,\ (\omega/\omega_{ci})^2 N_z^2 \ll c^2/(a\omega)^2. \quad (17)$$

Parenthetically, for a linear plasma density profile, these inequalities are weaker because of the large additional factor $(a/\rho)^{2/3}$ on the right-hand side. The first and third of these strong inequalities can be satisfied because they contain small factors (ω/ω_{ci}) and $(\omega/\omega_{ci})^2$ on the left-hand sides. The remaining inequality can also be satisfied because the characteristic radial scale a on which the plasma density varies is small in comparison with the value of the coordinate r_0 of the density extremum, $a \ll r_0$. It is clear that the first two of the inequalities are strictly satisfied for symmetric pulses ($m = 0$).

7. COMPARISON WITH EARLIER RESULTS

If the function $\varepsilon_1(r)$ approaches a large value far from the resonance point (this corresponds to large δ values and, consequently, to large plasma density perturbations), then potential well (2) in the vicinity of its minimum can be approximated by a parabola. This enables us to compare the above results with the results obtained in [9, 10], where the plasma density perturbation was modeled by a parabolic profile. To be specific, we consider the case in which the density profile has a maximum (see the solid curve in Fig. 6):

$$\varepsilon_1(r) = N_z^2\left(1 + B - \left(\frac{r - r_0}{b}\right)^2\right). \quad (18)$$

Neglecting absorption, the eigensolutions to Eq. (3) with profile (18), i.e., the solutions to this equation with zero on the right-hand side, can be found analytically. They are expressed in terms of Hermite polynomials [15]:

$$E_r(r) = \exp\left(-\frac{(r - r_0)^2}{2\rho b}\right)H_n\left(\frac{r - r_0}{\sqrt{2\rho b}}\right). \quad (19)$$

These solutions exist only for certain values of B:

$$B = \frac{\rho}{b}(2n + 1), \quad (20)$$

in which case the eigenfrequencies are equal to

$$\omega_n = k_z v_A\left(1 + \left(n + \frac{1}{2}\right)\frac{\rho}{b}\right). \quad (21)$$

Let us compare the eigenfrequencies corresponding to the parabolic density profile (18) with eigenfrequencies (10). To do this, we assume that the electron and ion temperatures (i.e., the values of the parameter ρ) are the same in both cases. We also require that the values of the quantity ε_1 in profiles (2) and (18) should coincide at the point of extreme density:

$$\frac{\rho^2}{a^2}[\delta(2n + 1) + n(n + 1)] = \frac{\rho}{b}(2n + 1). \quad (22)$$

The same requirement on the second derivative of this quantity yields

$$\frac{\rho^2}{a^4}(\delta + n)(\delta + n + 1) = \frac{1}{b^2}. \quad (23)$$

In both problems, we number the eigensolutions by consecutive positive integers n and require that equalities (22) and (23) be satisfied for the corresponding n values. It is easy to show that these equalities can be consistent only when $\delta \gg n$. Then, in equality (22), we can neglect n in comparison with δ to obtain the following relationship between the density perturbation widths in the cases of hyperbolic cosine (2) and parabolic profile (18):

$$a^2 = b\rho\delta. \quad (24)$$

It is seen that the width a of the region where density perturbation (2) is localized changes depending on the ε_1 value, which is determined by the value of ε_1 far from the point r_0. In the limit $\delta \gg n$, eigenfrequencies (21) with the values of b satisfying relationship (24) coincide with eigenfrequencies (10). For small n, the last term in expression (9) can be neglected.

Now, we fix the width b of the parabolic profile and approximate the potential well $\varepsilon_1(r)$ by a parabola and a hyperbolic cosine with different δ values and with a fixed value of n, which is taken to be $n = 3$. Figure 6 shows the potential well in the form of a parabola (solid curve) and hyperbolic cosine (2) with different δ values: $\delta = 1$ (dashed curve), $\delta = 3$ (dotted curve), and $\delta = 7$ (dashed-and-dotted curve). All the curves were calculated under conditions (22) and (23), implying that the values of the function, as well as of its second derivative, coincide at the point $r = r_0$. The eigenmodes in the cases at hand are illustrated in Fig. 7. As δ increases, the potential well (2) of finite depth is seen to become closer in shape to parabolic density profile (18). Analogously, from Fig. 7, we can see that, with increasing δ, the radial profile of the field component $E_r(r)$ in the case of a density perturbation of finite depth approaches the curve corresponding to a parabolic density profile.

Let us compare eigenfrequencies (10) and (21). The neighboring eigenfrequencies in spectrum (21) differ by a small amount proportional to ρ/a. The spectrum of eigenfrequencies (10) contains the square of the small parameter ρ/a. However, at a given density value far from r_0, or, equivalently, at a fixed value of M, the quantity δ is proportional to a/ρ (see Fig. 7). Consequently, for $\delta \gg n$, the intervals between the eigenfrequencies of the modes with neighboring radial numbers are the same in both problems.

Near the curve along which quantity (5) is zero (see Fig. 2), it is insufficient to retain only the small term proportional to $\rho_{Li}^2 d^2/dr^2$ in Eq. (3); it is also necessary to take into account higher order terms proportional to $\rho_{Li}^4 d^4/dr^4$.

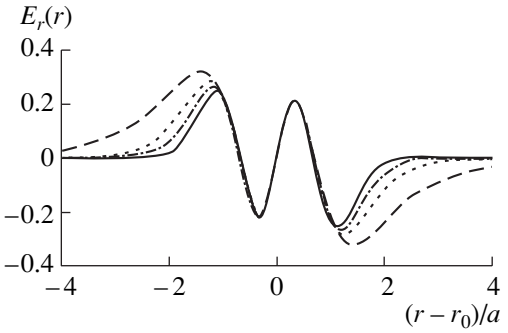

Fig. 7. Solutions to Eq. (6) with the density profiles shown in Fig. 6. The notation is the same as in Fig. 6.

8. CONCLUSION

We have analytically investigated electromagnetic eigenmodes localized in the region where the radial density profile of a hot plasma has a maximum (minimum) of the finite height (depth) between two local Alfvén resonances.

It is shown that, in a hot plasma, kinetic Alfvén waves can propagate near a maximum in the plasma density profile. The waves that can exist in the vicinity of a minimum in the density profile in a cold plasma are inertial Alfvén waves. This situation is analogous to that with an infinitely deep parabolic potential well, which was considered earlier, e.g., in [9, 10].

For an arbitrary value of the plasma density far from the region where the density perturbation is localized (or, in other words, for an arbitrary δ value), there exists a critical value of the maximum (minimum) density at which the eigenmodes can propagate. When the plasma density at the point r_0 of the maximum (minimum) exceeds its resonant value determined by condition (1) by an arbitrarily small amount, the necessary condition for the existence of localized eigenmodes is that the plasma density far from r_0 be sufficiently close to the resonant value.

We have determined the eigenfrequencies (10) and (15) of Alfvén waves and have shown that they are higher than the Alfvén continuum frequency in the case of a maximum in the density profile and are lower than this frequency when the density profile has a minimum. We have also obtained an analytic expression for the field of the eigenmodes [see formula (8) and Fig. 3].

The results of our analysis have been compared with those obtained for a parabolic plasma density profile. In the limit of an infinitely deep potential well ($\delta \gg n$), the eigenmodes and their eigenfrequencies have been found to be the same in both problems.

REFERENCES

1. V. V. Dolgopolov and K. N. Stepanov, Nucl. Fusion **5**, 276 (1965).
2. C. Uberoi, Phys. Fluids **15**, 1673 (1972).
3. J. Tataronis and W. Grossman, Z. Phys. **261**, 203 (1973).
4. L. Chen and A. Hasegawa, Phys. Fluids **17**, 1399 (1974).
5. J. Vaclavik and K. Appert, Nucl. Fusion **31**, 1945 (1991).
6. *High-Frequency Plasma Heating*, Ed. by A. G. Litvak (Am. Inst. of Physics, New York, 1992).
7. V. I. Lapshin, K. N. Stepanov, and E. A. Fedutenko, in *Proceedings of the Joint Varenna–Abastumani International School and Workshop on Plasma Astrophysics, Varenna, 1988*; ESA SP-285 **1**, 111 (1988).
8. I. O. Girka, S. V. Kasilov, V. I. Lapshin, and K. N. Stepanov, Probl. At. Sci. Technol., Ser. Plasma Phys. (Kharkov), No. 1/2, 148 (1999).
9. S. M. Mahajan, Phys. Fluids **27**, 2238 (1984).
10. I. O. Girka and P. P. Rutkevich, J. Kharkiv Nat. Univ., Phys. Ser.: Nuclei, Particles, Fields **3/15** (529), 43 (2001).
11. L. D. Landau and E. M. Lifshitz, *Quantum Mechanics: Non-Relativistic Theory* (Nauka, Moscow, 1989; Pergamon Press, New York, 1977).
12. *Plasma Electrodynamics*, Ed. by A. I. Akhiezer *et al.* (Nauka, Moscow, 1974; Pergamon Press, Oxford, 1975).
13. T. H. Stix, *Theory of Plasma Waves* (McGrow-Hill, New York, 1962; Atomizdat, Moscow, 1965).
14. K. Appert, T. Hellsten, H. Luetjens, *et al.*, in *Proceedings of International Conference on Plasma Physics, Invited Papers, Kiev, 1987* (World Scientific, Singapore, 1987), Vol. 2, p. 1230.
15. *Handbook of Mathematical Functions with Formulas, Graphs, and Mathematical Tables*, Ed. by M. Abramowitz and I. Stegun (National Bureau of Standards, Washington, 1964; Nauka, Moscow, 1979).

Translated by I.A. Kalabalyk

Plasma Physics Reports, Vol. 29, No. 6, 2003, pp. 473–479. Translated from Fizika Plazmy, Vol. 29, No. 6, 2003, pp. 508–515.

DUSTY PLASMA

Numerical Simulations of Ion and Electron Transport in a Low-Temperature Dusty Plasma

Yu. V. Petrushevich

Troitsk Institute for Innovation and Fusion Research, State Scientific Center of the Russian Federation, Troitsk, Moscow oblast, 142092 Russia

Received May 30, 2002; in final form, December 18, 2002

Abstract—Charged particle transport and kinetic processes in a low-temperature dusty plasma are numerically simulated. Dust grains are represented as spheres with a given radius. The self-consistent electric field in the plasma surrounding a charged dust grain is calculated taking into account the perturbations of plasma quasineutrality near the grains. It is shown that applying an external electric field leads to a rearrangement of the plasma space charge and a break of the spherical symmetry of the electron and ion density distributions around the grain. The mutual influence of two identical charged dust grains is considered, and the energy of the electrostatic interaction between the grains is calculated. It is shown that this energy has a minimum at a certain finite distance between the grains. *© 2003 MAIK "Nauka/Interperiodica".*

1. INTRODUCTION

The interaction between dust grains in a dusty plasma is one of the most important phenomena determining the properties of this system. In particular, this interaction results in the formation of dusty crystal structures, which have been observed under various conditions. A review of the studies on dusty plasma structures is presented in [1]. In many experiments, it was demonstrated that dust grains in a dusty plasma usually acquire a negative electric charge. One of the key problems is to find out the nature of the attraction forces between likely charged dust grains. The attraction is usually explained by the electrostatic interaction between the grains and the polarized ambient plasma [2–5]. In those papers, the medium polarization was analyzed under the assumption that the charged plasma particles (electrons and ions) obey a Boltzmann distribution. However, simulations of the grain charging process in a dusty plasma [6] showed that the electron and ion spatial distributions near the grain's surface were nonmonotonic and the equilibrium plasma particle distributions were not established. In [7], it was shown that the departure from the equilibrium distribution was more pronounced for the ions.

Simulations of [8, 9], in which the ions were modeled by the Monte Carlo method, showed that a positive space charge arose in the plasma region between the grains, which resulted in their mutual attraction.

We note that, near the grain's surface, where the quasineutrality is disturbed, the electric field caused by the grain charge is fairly strong and can attain 10^3–10^4 esu, depending on the plasma parameters (in particular, the grain size). Because of the strong electric field near the grain's surface and the spatial inhomogeneity of the field in this region, the electron temperature significantly differs from the gas temperature. This circumstance explains why the charged particle densities observed in numerical simulations [7] substantially deviate from a Boltzmann distribution.

Thus, although the mechanism for the interaction between dust grains under laboratory conditions is quite clear, the value of the interaction energy needs additional study. An adequate plasma model should accurately take into account the dynamics of charged plasma particles. Moreover, the problem of the interaction of two dust grains should be considered at least in two-dimensional geometry.

In this paper, we propose a model describing charged particle transport in a dusty plasma produced by an electron beam and present the results of simulations of the interaction between charged dust grains in such a plasma.

2. PROBLEM FORMULATION AND BASIC EQUATIONS OF THE CHARGED PARTICLE DYNAMICS IN A LOW-TEMPERATURE DUSTY PLASMA

We study the phenomena occurring in a dusty plasma with the dust component consisting of solid metal or dielectric grains. The problems under investigation are the process of grain charging and the formation of the charge distribution in the ambient plasma. We consider a model problem in which dust grains are assumed to be spheres with a given radius. The grains can be either metal or dielectric; however, in this paper, we present the results of calculations in which the grains are assumed to be dielectric and the charge is distributed uniformly over the grain's surface. The numerical model also includes the surrounding plasma region. The plasma consists of electrons and ions (in the gen-

1063-780X/03/2906-0473$24.00

eral case, there may be several ion species). In experiments, an external electric field is usually applied to the dusty plasma, which favors the formation of spatial dusty structures. For this reason, the self-consistent (including the external) electric field should also be taken into account. In view of the axial symmetry of the system under consideration, it is reasonable to solve the problem in spherical coordinates in two-dimensional geometry.

The proposed model of a low-temperature plasma includes the continuity equations for charged particles. The particle velocities are determined by the local value of the electric field. The electron diffusion is also taken into account, which is necessary because, under the given conditions, the dust grains are negatively charged and it is precisely the diffusion term that provides the electron flow onto a grain. The ion flow near a dust grain is provided by the ion drift in an electric field, which is fairly high in this region. Under these conditions, the contribution of the diffusive ion flow is insignificant. The model is valid when the characteristic dimensions of the problem are larger than the mean free path of the charged particles, which amounts to 10^{-5} cm at atmospheric pressure. Therefore, for grains with a size of 10^{-4}–10^{-3} cm, the model proposed can be regarded as quite adequate.

The basic equations have the form

$$\begin{aligned} \frac{\partial n_e}{\partial t} + \nabla \cdot (\mathbf{w}_e n_e) &= \nabla \cdot (D \nabla n_e) + Q_e, \\ \frac{\partial n_i}{\partial t} + \nabla \cdot (\mathbf{w}_i n_i) &= Q_i, \\ \Delta \varphi &= 4\pi e (n_e - n_i), \end{aligned} \tag{1}$$

where n_e and n_i are the densities of the electrons and positive ions, respectively; $\mathbf{w}_e$ and $\mathbf{w}_i$ are the electron and ion drift velocities; Q_e and Q_i are the terms describing the production and loss of electrons and ions; D is the electron diffusion coefficient; and φ is the electric potential.

We use a spherical coordinate system whose origin coincides with the center of a spherical dust grain with a radius R_d. Equations (1) should be supplemented with the boundary conditions, which can be deduced from the following considerations. If the charge of the sphere is positive, then the ion drift velocity is directed outward from the sphere. In this case, the density of the positive ions is assumed to be zero at the grain's surface. For a negatively charged sphere, no boundary conditions for the ions on the grain's surface apply.

The electron transport equation contains the diffusion term. Hence, the boundary conditions on the grain's surface must be imposed for either sign of the grain charge. In view of the low efficiency of the known mechanisms of electron production on the grain's surface in a low-temperature dusty plasma, we will assume that the electron density near the grain's surface is zero. At infinity (far from the grain), the ion and electron densities are assumed to be equal to their equilibrium values, determined by plasmochemical processes.

Simulations were performed with allowance for the external electric field. As a boundary condition for the electric field, we assume that the field at infinity is equal to the external field. Summarizing all the assumptions, the boundary conditions can be written in the form

$$\begin{aligned} n_i(r = R_d) &= 0; \quad \text{for} \quad E(r = R_d) > 0; \\ n_i(r \longrightarrow \infty) &= n_i^{(\mathrm{eq})}; \\ n_e(r = R_d) &= 0; \quad n_e(r \longrightarrow \infty) = n_e^{(\mathrm{eq})}; \end{aligned} \tag{2}$$

$$\begin{aligned} \nabla \varphi(r = R_d) &= -Qe/R_d^2, \\ \nabla \varphi(r \longrightarrow \infty) &= -E_0(r), \end{aligned} \tag{3}$$

where Q is the grain charge in atomic units and E_0 is the external electric field, which depends on the specific conditions of the problem.

We consider a nitrogen dusty plasma produced by a high-power electron beam ionizing the gas with an ionization rate of $\sim 10^{16}$ s^{-1} cm^{-3}. Under the given conditions, the ion density attains $\sim 10^{11}$ cm^{-3}. We assume that the plasma consists of positive ions and electrons. The charge particle balance is determined by plasmochemical reactions, including both the gas ionization by the electron beam and electron–ion recombination:

$$Q_e = Q_i = q - \beta n_e n_i,$$

where q is the ionization rate and β is the recombination coefficient. In calculations, the recombination coefficient depended on the electric field and was on the order of $\beta \sim 10^{-6}$ cm^3/s.

The dielectric dust grains were spheres with the radius $R_d = 12$ μm. We considered the gas at atmospheric pressure ($p = 1$ atm) and room temperature ($T = 300$ K). The dust density was assumed to be low enough for the dust charge to have no effect on the average density of charged plasma particles. The known dependences of the plasma kinetic coefficients on the electric field for nitrogen were used. The grain charge was determined by the balance of the currents of the plasma electrons and ions. Simulations were performed until the calculated quantities reached their steady state values.

Two-dimensional simulations require considerable computational resources; hence, the choice of an efficient algorithm is of great importance for this kind of problem. The algorithm used in this study is described in detail in [10]. The simulations were separated into several steps. The transport equations were solved using a standard implicit scheme, and Poisson's equation was solved using the expansion of the electric potential in Legendre polynomials. The main problem arising when using this method is providing the convergence of the expansion series; therefore, the expansion

terms should be regularly checked for the convergence. Simulations showed that in the modeling of a real plasma with spherical dust grains, it is quite sufficient to take into account six harmonics.

3. RESULTS OF SIMULATIONS OF A DUSTY PLASMA IN AN EXTERNAL ELECTRIC FIELD

The charging of a spherical grain with a radius of 12 μm in a nitrogen plasma and the establishment of the spatial charge distribution around the grain were investigated. The ionization source power was taken to be 2×10^{16} cm^{-3} s^{-1}.

Simulations were performed both without an external electric field and in the presence of a fairly strong external electric field with a strength of $E_0 = 900$ V/cm. The results of calculations are presented in Fig. 1.

It can be seen in the figure that applying the electric field results in a significant redistribution of the space charge around the grain. The electron density profile shifts toward the grain's surface, and a slight local maximum appears on the profile. The ion density profile shifts in the opposite direction. As a result, the length of the region in which the plasma quasineutrality is disturbed changes substantially. Moreover, in the presence of the electric field, a region appears in which the space charge changes its sign. We note that, far from the grain (in the quasineutral plasma), the plasma density increases because the recombination coefficient decreases considerably when the external electric field is applied. Figure 2 shows the spatial profile of the self-consistent electric field. It can be seen that, in the presence of the external field, the radial component of the electric field changes its sign far from the grain's surface.

We also note that the region where quasineutrality is disturbed is fairly large. The simulations were performed for the Debye radius $R_{Db} \approx 4$ μm. It can be seen in Fig. 1 that, in the absence of an external electric field, the region where quasineutrality is disturbed is about $R_a \sim 25$ μm. From Fig. 2, it is seen that R_a corresponds to the distance at which the electric field significantly decreases. Similar results in the absence of an external field were obtained in [6, 7].

The calculated dependence of the grain charge on the external electric field is shown in Fig. 3. The grain charge is negative and its value agrees with the results of calculations presented in [1, 6]. The negative sign of the grain charge in a gas-discharge plasma was pointed out by many authors; it is explained by the higher mobility of electrons in plasma in comparison with that of ions. It follows from the simulation results that the grain charge can be increased severalfold by increasing the external electric field within reasonable limits.

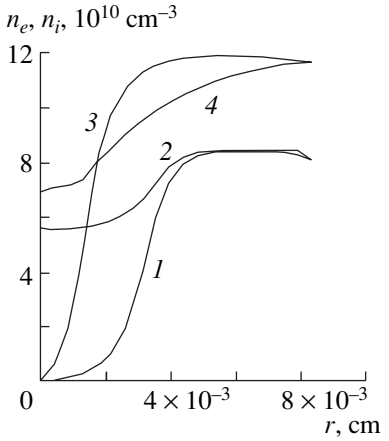

Fig. 1. Radial profiles of the (*1*, *3*) electron and (*2*, *4*) ion densities in the plasma surrounding the grain (*1*, *2*) in the absence of an external electric field and (*3*, *4*) in the presence of an external field of 900 V/cm. The density profiles are shown for the angle θ = 36° with respect to the direction of the external field (Here and in the subsequent figures, the radial coordinate is measured from the grain's surface).

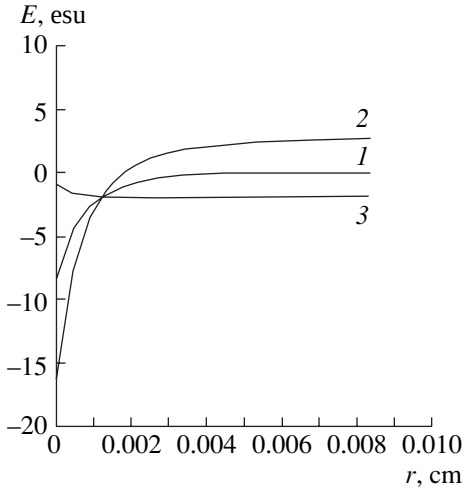

Fig. 2. (*1*) Radial profile of the electric field in the plasma surrounding the grain in the absence of an external electric field and the profiles of the (*2*) radial and (*3*) tangential components of the self-consistent electric field in the presence of an external electric field of 900 V/cm for the angle θ = 36° with respect to the direction of the external field.

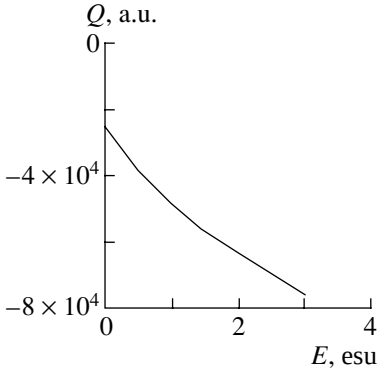

Fig. 3. Charge of a spherical grain as a function of the external electric field.

4. CHARGE DISTRIBUTION AND INTERACTION IN A TWO-GRAIN SYSTEM

The presence of attraction forces between dust grains in a dusty plasma was unambiguously demonstrated in the experiments of [11]. The shift of one of the interacting grains by a laser beam results in a similar shift of the second grain. The problem of the interaction between two charged dust grains was considered in [12]. In that paper, the electrostatic potential was accurately calculated by using appropriate curvilinear coordinates. However, in that paper, as well as in the papers mentioned above, it was assumed that the plasma particles obey a Boltzmann distribution. However, the numerical results obtained using more adequate models show that the real plasma particle distributions should differ significantly from a Boltzmann one.

In [13], the interaction energy of two grains and its dependence on the distance between these grains were calculated. The interaction energy was found to be minimum at the distance $r_{12} = 2.73R_{\mathrm{Db}}$. This means that the grains efficiently interact at a distance larger then the Debye radius, i.e., in the region where the plasma substantially screens the grain charge. On the one hand, this result is important because it corresponds to experimental observations. On the other hand, in that paper, a mechanism for the appearance of the attraction force between likely charged grains in the polarized surrounding medium was proposed based on a rather simple model. Unfortunately, the applicability of the results of [13] is limited to the case of small grains with the radii $R_d \ll R_{\mathrm{Db}}$; moreover, that paper also used the Debye screening model, which has a limited applicability range, as has been discussed above.

The conclusion of [14] about the repulsion of likely charged grains in plasma was made based on the collisionless plasma model assuming the mirror reflection of charged particles from the grain's surface. In that paper, the limited applicability of this model was also indicated. In particular, this model is inapplicable to a low-temperature dusty plasma of a high-pressure gas discharge, which is considered in the present paper. Hence, along with the interaction mechanism associated with anisotropy of gas-kinetic pressure in a two-grain system [14, 15], the electrostatic interaction must also be taken into account. We note that the possibility of attraction between likely charged grains due to plasma polarization was shown in [4, 8].

In the present paper, an evident symmetry of the problem was used to calculate the charge distribution in the system of two grains in plasma in the absence of an external electric field. When the grains are identical and have the same electric charge, there is a symmetry plane lying halfway between the grains. In this case, the solution of the problem reduces to the calculation of the dynamics of charged plasma particles in the half-space adjacent to one of the grains, and the electric field is determined as a sum of the fields produced by the electric charges in both half-spaces:

$$\begin{aligned}\varphi(\mathbf{r}) &= \varphi_1(\mathbf{r}) + \varphi_2(\mathbf{r}) \\ &= \left(\int_{V_1}\frac{\rho(\mathbf{r}_1)dV_1}{|\mathbf{r}-\mathbf{r}_1|} + \int_{S_1}\frac{\sigma(\mathbf{r}_1)ds_1}{|\mathbf{r}-\mathbf{r}_1|}\right) \\ &+ \left(\int_{V_2}\frac{\rho(\mathbf{r}_2)dV_2}{|\mathbf{r}-\mathbf{r}_2|} + \int_{S_2}\frac{\sigma(\mathbf{r}_2)ds_2}{|\mathbf{r}-\mathbf{r}_2|}\right),\end{aligned} \tag{4}$$

where $\rho(\mathbf{r})$ is the charge density; $\sigma(\mathbf{r})$ is the surface charge density; S_1 and S_2 are the grain surface areas; V_1 and V_2 are the symmetric plasma regions adjacent to the first and second dust grains, respectively, and together covering the entire region under consideration; and the components of the electric potential $\varphi(\mathbf{r})$ are equal to the corresponding expressions in parentheses.

We note that, when the field is defined in such a fashion, the electric field component perpendicular the symmetry plane vanishes on this plane: $E_\perp = 0$.

The energy of a system of point charged particles can be determined by the formula [16]

$$W_t = \frac{1}{2}\sum_i \rho_i\varphi_i, \tag{5}$$

where the potential φ_i in the position of the charge ρ_i is determined by all of the charges except for the given one. Such an exclusion is necessary because the self-energy of a charged particle increases without bound with decreasing radius.

In the model under consideration, the charge distribution is continuous and the charge density at any point is finite. In numerical simulations, the space is divided into the computational cells, in which the plasma space charge, as well as other quantities, can be assumed to be uniform. In this case, the self-energy of the small spatial cells decreases with decreasing their size; therefore, the expression defining the total energy of the system of electric charges is finite.

Actually, to solve the problem of the interaction between dust grains, we should consider the interaction energy of the parts of the system of electric charges (electrically charged grains together with adjacent polarized plasma regions), rather than the total energy of the electric charges. In view of the symmetry of the problem, the interaction energy can be determined from the formula

$$W = \int_{V_1}\rho(\mathbf{r}_1)\varphi_2(\mathbf{r}_1)dV_1 + \int_{S_1}\sigma(\mathbf{r}_1)\varphi_2(\mathbf{r}_1)ds_1, \tag{6}$$

where the potential $\varphi_2(\mathbf{r}_1)$ is calculated by formula (4). According to expression (6), the interaction energy is determined by the interaction of charges located in one

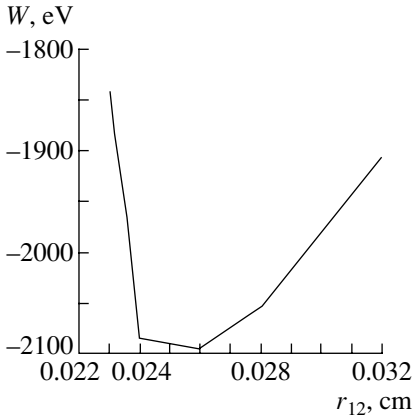

Fig. 4. Electrostatic interaction energy as a function of the distance between two grains in a dusty plasma.

half-space with the electric field produced by charges located in the other half-space. If the interaction energy is negative, then one can speak of the tendency toward the formation of a complex (quasi-molecule). In this case, the dependence of the bond energy on the intergrain distance may be identified with a term of this quasi-molecule.

To determine W as a function the intergrain distance, we performed a series of calculations of the steady charge density distribution and the self-consistent electric field in a two-grain system in the model described above. All other conditions, such as the ionization source power and the medium composition, were the same as in the case of one grain.

Figure 4 shows the results of calculations. It can be seen from the dependence $W(r_{12})$ that the interaction energy is negative and the depth of the potential well is $\sim 10^3$ eV. For comparison, this energy corresponds to the kinetic energy of a dust grain of mass $\sim 10^{-8}$ g moving at a velocity of ~0.5 cm/s. As is seen from the figure, the calculations were performed for a relatively small number of the distances r_{12}, because each calculation version required a fairly long computation time. Nevertheless, the results of calculations clearly demonstrate the presence of a minimum in the electrostatic interaction energy. Along with the negative value of the calculated energy, this testifies to the possibility of the existence of a bound state in this system. The attraction force can be estimated by the formula

$$F = -\frac{\partial W}{\partial r_{12}}. \quad (7)$$

According to this estimate, we have $F \sim 10^{-6}$–10^{-7} dyn, which is much smaller than the grain weight in the Earth's gravity field. We remember that the simulations were performed in the absence of an external electric field and the plasma was produced by an external source. When analyzing the applicability of formula (7), it should be taken into account that our model includes the process of grain charging, which is associated with the work done by external sources (plasma ionizers). Hence, the negative potential of the grain obtained in the calculations reflects the work done by these sources. At the same time, the force calculated by formula (7) neglects the interaction associated, e.g., with the plasma pressure [14, 15]; therefore, no final conclusion

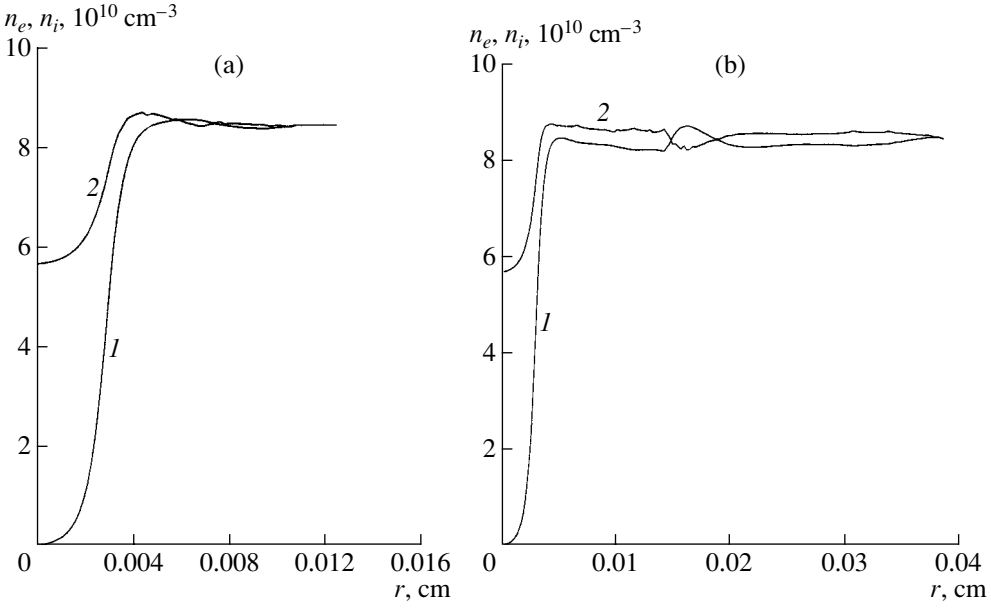

Fig. 5. Radial profiles of the (*1*) electron and (*2*) ion densities in the plasma surrounding one of the two interacting grains (a) in the direction toward the second grain and (b) in the opposite direction.

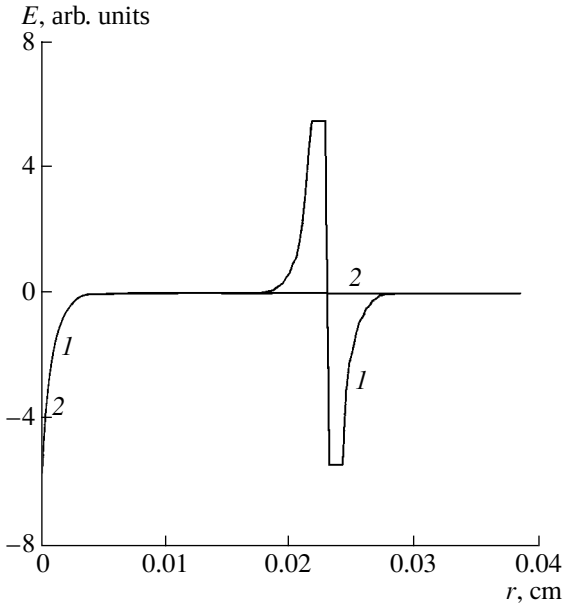

Fig. 6. Radial profiles of the electric field in the plasma surrounding two interacting grains (*1*) in the direction toward the second interacting grain and (*2*) in the opposite direction.

about the formation of a bound state in a two-grain system can be made based on formula (7) only.

Figure 5 shows the spatial distributions of the charged particle densities in the direction toward the second dust grain and in the opposite direction. We can see that the charge density distributions differ from those in the case of one grain (Fig. 1, curve *2*). Toward the second grain (Fig. 5a), the ion density at a distance of ~40 μm from the grain's surface substantially exceeds the electron density and there is a slight maximum in the ion density profile. This agrees qualitatively with the results of [8], in which an ion cloud between the interacting grains was observed in numerical simulations of a microwave-discharge dusty plasma. In view of the symmetry of the problem, a similar cloud should also form in the region adjacent to the second grain. In the opposite direction (Fig. 5b), the distributions of the charged particle densities are markedly different. A characteristic feature of these distributions is the formation of regions with an alternating sign of the space charge.

In the region immediately adjacent to the grain, the electric field changes only slightly as compared to the case of one grain, because, in this region, it is mainly determined by the grain charge. Figure 6 shows the spatial distributions of the electric field in the direction toward the second dust grain and in the opposite direction. The curves coincide near the grain's surface and are different at a distance of 240 μm, where the second dust grain is situated.

5. CONCLUSION

The interaction of charged grains in a low-temperature dusty plasma has been investigated numerically. To calculate the grain charge and the polarization of the surrounding plasma, the self-consistent electrostatic problem has been solved with allowance for charged particle transport in a plasma. Minimal simplifications were adopted when formulating the problem: the symmetry of the problem allowed us to use two-dimensional geometry, and the equations for charged particle transport were reduced to the continuity equations, which is quite justified under the given conditions.

We have also simulated the interaction between two dust grains in a nitrogen plasma produced by an external ionization source in the absence of an external electric field. Under the given conditions, the energy of interaction between the grains (including the energy of interaction with the polarized surrounding plasma) is found to be negative and is minimum at a distance of ~250 μm between the grains. The attraction force between two grains, which can be estimated from the calculated dependence of the electrostatic interaction energy on the intergrain distance, turns out to be weaker than the weight of a grain in the Earth's gravity field.

It has been found that, when the Debye plasma model is used to calculate the grain charge screening, significant errors are introduced for the most important region near the grain's surface. It turns out that the region where the plasma quasineutrality is disturbed is much larger than the Debye radius, because the equilibrium conditions, which are required for a Boltzmann distribution to be established, are not satisfied there due to the boundary effects.

The spatial distributions of the charged particle densities and the self-consistent electric field were calculated for individual dust grains in the presence of an external electric field. The break of spherical symmetry in the presence of an external electric field leads to an asymmetry of the charged particle distribution. It has been shown that the grain charge depends on the external electric field. Applying the external electric field increases the grain charge by a factor of up to 4, which should naturally increase the interaction force between the grains.

The simulations have shown that the plasma particle distribution in a system of two interacting grains is nonuniform. In the direction toward the second interacting grain, a positive space charge arises at a distance of about one-sixth of the intergrain distance from the first grain. (In view of the symmetry of the problem, a similar positive space charge forms in the region adjacent to the second grain.) In other words, the plasma charges are redistributed so that the positive space charge in this region increases in comparison with the spherically symmetric case of one grain. This redistribution corresponds to the plasma polarization, resulting in the attraction of likely charged grains. In the opposite

direction, the plasma polarization markedly differs and charged layers are formed.

ACKNOWLEDGMENTS

I am grateful to A.N. Starostin for his interest in this work and fruitful discussions. This work was supported by the Russian Foundation for Basic Research, project no. 00-15-96539.

REFERENCES

1. A. P. Nefedov, O. F. Petrov, and V. E. Fortov, Usp. Fiz. Nauk **167**, 1215 (1997) [Phys. Usp. **40**, 1163 (1997)].
2. S. V. Vladimirov and M. Nambu, Phys. Rev. E **52**, 2172 (1995).
3. F. Melandso and J. Goree, Phys. Rev. E **52**, 5312 (1995).
4. S. I. Yakovlenko, Pis'ma Zh. Tekh. Fiz. **25** (16), 83 (1999) [Tech. Phys. Lett. **25**, 670 (1999)].
5. Peilong Chen and C.-Y. D. Lu, Phys. Rev. E **61**, 824 (2000).
6. A. F. Pal', A. O. Serov, A. N. Starostin, *et al.*, Zh. Éksp. Teor. Fiz. **119**, 272 (2001) [JETP **92**, 235 (2001)].
7. A. F. Pal', D. V. Sivokhin, A. N. Starostin, *et al.*, Fiz. Plazmy **28**, 32 (2002) [Plasma Phys. Rep. **28**, 28 (2002)].
8. V. A. Schweigert, I. V. Schweigert, A. Melzer, *et al.*, Phys. Rev. E **54**, 4155 (1996).
9. V. I. Vladimirov, L. V. Deputatova, V. I. Molotkov, *et al.*, Fiz. Plazmy **27**, 37 (2001) [Plasma Phys. Rep. **27**, 36 (2001)].
10. Yu. V. Petrushevich, Preprint No. 0088-A (TRINITI, Troitsk, 2002).
11. A. Melzer, V. A. Schweigert, and A. Piel, Phys. Rev. Lett. **83**, 3194 (1999).
12. V. A. Gundienkov and S. I. Yakovlenko, Kratk. Soobshch. Fiz., No. 12 (2001).
13. A. S. Ivanov, Phys. Lett. A **290**, 304 (2001).
14. A. M. Ignatov, Fiz. Plazmy **24**, 731 (1998) [Plasma Phys. Rep. **24**, 677 (1998)].
15. A. M. Ignatov, Usp. Fiz. Nauk **171**, 213 (2001) [Phys. Usp. **44**, 199 (2001)].
16. I. E. Tamm, *The Principles of Electricity Theory* (Nauka, Moscow, 1976).

Translated by N.F. Larionova

Plasma Physics Reports, Vol. 29, No. 6, 2003, pp. 480–484. Translated from Fizika Plazmy, Vol. 29, No. 6, 2003, pp. 516–520.

PLASMA OPTICS

Space-Charge Lens for Focusing a Negative-Ion Beam

A. M. Zavalov, V. N. Gorshkov, V. P. Goretskiĭ, and I. A. Soloshenko

Institute of Physics, National Academy of Sciences of Ukraine, pr. Nauki 144, Kiev, 03039 Ukraine

Received November 19, 2002

Abstract—Results are presented from experimental and theoretical studies of a space-charge lens for focusing a negative-ion beam. The space-charge field and the beam ion trajectories are numerically calculated for the lens used in the experiments. The results of calculations are compared with the experimental data. It is shown theoretically and experimentally that the proposed device allows one to achieve the main operating conditions of the space-charge lens: the inertial confinement of positive ions and the removal of electrons by an external electric field. The focusing field of the lens attains ~100 V/cm, which provides a focal length of <20 cm. © *2003 MAIK "Nauka/Interperiodica"*.

1. INTRODUCTION

The concept of a space-charge lens for focusing a positive-ion beam was first proposed by Gabor [1] and then was further developed by Morozov [2, 3]. The efficiency of such a lens was confirmed in many experiments (see, e.g., [4]). The focusing field of the lens is produced by a space charge of electrons that are injected by a separate emitter or come from the lens electrodes due to ion-induced emission and are confined within the beam by an external magnetic field.

In [5], a space-charge lens for focusing a negative-ion beam was proposed. In this case, the focusing space charge is produced by positive ions that are generated through the ionization of the working gas by an ion beam and are confined within the beam by inertial forces. It was proposed that the electrons produced in this process be removed from the system by a longitudinal electric field. Preliminary experiments showed the high efficiency of such a lens.

This paper is devoted to a detailed study of the device proposed in [5]. In particular, the space charge field and trajectories of the beam ions are numerically calculated for the lens used in experiment. The time evolution of the particles produced due to the ionization of argon by the beam is also studied. The results of calculations are compared with the experimental data. The theoretical and experimental results show that, under our experimental conditions, it is possible to achieve the main operating conditions of the space-charge lens: the inertial confinement of positive ions and the removal of electrons by an external electric field. The ratio between the positive-ion and electron densities in the lens varies within the range 10^1–10^3 and the focusing field attains ~100 V/cm, which provides a focal length of <20 cm.

2. EXPERIMENTAL RESULTS

The space-charge lens for focusing a negative-ion beam was investigated using the experimental setup shown schematically in Fig. 1a. A beam of negative ions with energies of ~10–12 keV and a current of ~10–30 mA was extracted from surface-plasma source *1* through a 0.5 × 15-mm slit. The beam was preformed and directed to lens *3–5* by an ≈2-kG magnetic field produced by deflecting magnets *2*. The beam diameter was limited by the entrance aperture of the lens. The beam current was measured by collector *7* with a diameter of 10 cm. The beam compression ration was determined from a change in the current at collector *6* with a diameter of 2 cm. The lens was placed ≈20 cm from the source slit. The distance from the lens exit plane to the collector was ≈30 cm. In the given configuration, the beam radius at the collector should be minimum for a lens focal length of ≈12 cm.

The lens was designed as follows. Lens chamber *4* was a metal cylinder 15 cm in diameter and 10 cm in length with two grounded diaphragms with an inner diameter of 5 cm at the ends. Removable metal grid cylinder *5* with a diameter of 5 cm and length of 10 cm was installed inside the lens chamber on its axis and was at the potential of the lens chamber. The lens chamber was insulated from the chamber walls; during operation, the chamber potential can be varied from 0 to –2000 V. Grounded electrodes *3* with a thickness of 1.5 cm and an inner diameter of 5 cm were installed 0.5 cm from the ends of the lens chamber. The working gas (argon) was admitted through the end wall of the lens chamber. The gas pressure in the lens could be varied in the range 10^{-4}–1.5×10^{-3} torr. With such a lens design, the pressure in the lens was higher than the pressure in the beam-drift region by a factor of nearly 10.

A positive space charge in the lens was produced through the ionization of the working gas by a negative-ion beam. It was proposed that the electrons produced by ionization and detachment from negative ions in col-

1063-780X/03/2906-0480$24.00

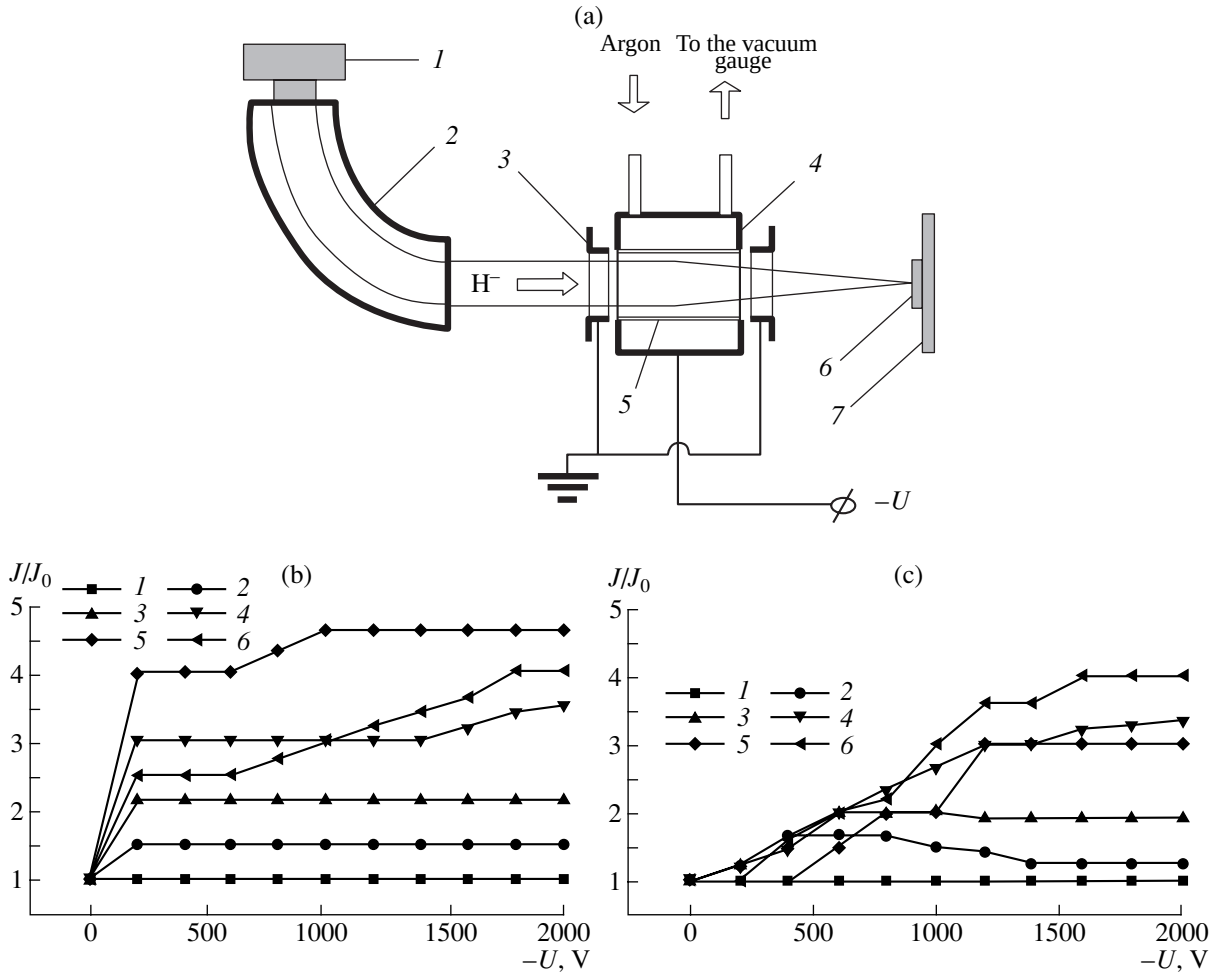

Fig. 1. (a) Schematic of the experiment: (*1*) pulsed source of negative hydrogen ions, (*2*) deflecting magnets, (*3*) grounded inlet and outlet electrodes, (*4*) lens chamber, (*5*) removable grid electrode, (*6*) collector for determining the beam density, and (*7*) beam-current collector; (b) the H^- beam compression ratio as a function of the negative potential of the lens chamber in the presence of the grid electrode at different argon pressures p = (*1*) 1.8×10^{-4}, (*2*) 4.2×10^{-4}, (*3*) 6.2×10^{-4}, (*4*) 8×10^{-4}, (*5*) 1.1×10^{-3}, and (*6*) 1.7×10^{-3} torr; and (c) the H^- beam compression ratio as a function of the negative potential of the lens chamber without a grid electrode at different argon pressures p = (*1*) 1.2×10^{-4}, (*2*) 4.1×10^{-4}, (*3*) 6×10^{-4}, (*4*) 7.9×10^{-4}, (*5*) 1.2×10^{-3}, and (*6*) 1.7×10^{-3} torr. The beam current is 10 mA and the beam ion energy is 12 keV.

lision with neutral particles be expelled along the lens axis by applying a negative potential to the chamber.

Experiments were carried out for two lens configurations. In the first version, the lens contained grid electrode *5* (Fig. 1a), and in the second version, this electrode was absent (the numerical experiment was performed for the second version).

The results of measurements are presented in Figs. 1b and 1c. The figures show the beam compression ratio (the ratio of the maximum current J of the H^- beam at collector *6* in the regime of focusing to the maximum beam current J_0 at collector *6* in the regime without focusing) in the collector plane as a function of the negative potential of the lens chamber at different values of the argon pressure in the lens.

It can be seen from the figures that the beam compression ratio depends on both the gas pressure in the lens and the potential at its central electrode. (The gas pressure determines the value of the positive ion space charge, whereas the negative potential determines the efficiency of the removal of electrons from the lens in the longitudinal direction.) The maximum beam compression ratio is the same for both versions (with and without grid *5*). However, with the grid, the optimal compression of the beam is reached even at a lens potential of –200 V, whereas without a grid, it is reached at a much lower potential; i.e., in the former case, the removal of electrons from the lens is more efficient.

Thus, it has been demonstrated experimentally that the space-charge lens proposed can be very efficient

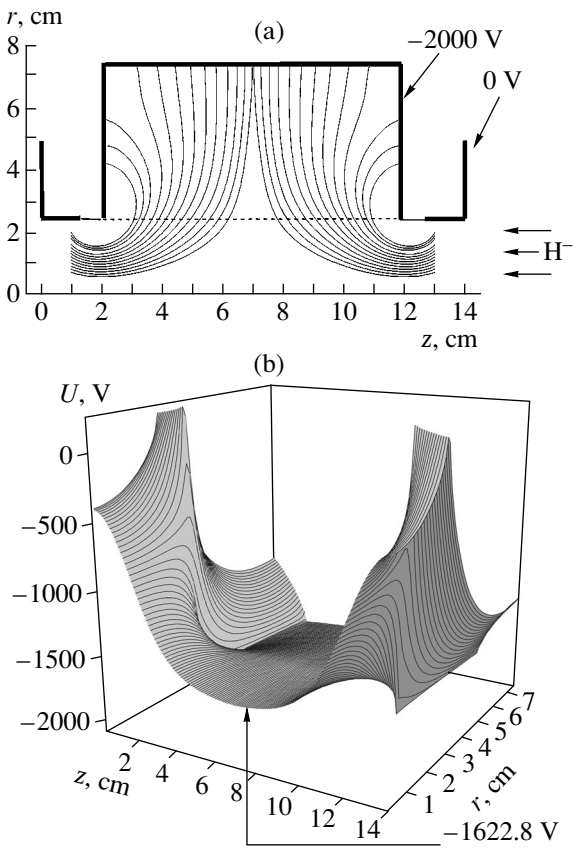

Fig. 2. (a) Schematic of the numerical experiment and the lines of the electric field generated by the electrodes inside the lens; the main ionization region in the lens extends from the axis to the dashed line; the arrows show the trajectories of the beam ions and the atoms of the working gas (argon) entering the lens. (b) Steady-state distribution of the electric potential in the lens at $t = 10^{-5}$ s.

and can provide a focal length of <20 cm. The lens efficiency is determined by the gas pressure (by the value of the positive space charge), provided that the electrons are removed from the system by the longitudinal electric field. The geometry of the lens only has an effect on the efficiency with which the electrons are removed from the lens.

3. NUMERICAL EXPERIMENT

We calculated the electric field and trajectories of the beam particles in the space-charge lens for focusing a negative-ion beam and investigated the time evolution of the electrons and Ar^+ ions produced by ionization. The numerical studies were performed using the particle-in-cell (PIC) method [6, 7]; the plasma was assumed to be collisionless.

A schematic of the numerical experiment is shown in Fig. 2a. A uniform beam of negative H^- ions with a current of 10 mA and an energy of 12 keV entered the lens through the entrance plane along the lens axis. The beam diameter coincided with the diameter of the lens entrance aperture and was equal to 5 cm. The potential of the lens chamber was assumed to be –2000 V, and the argon pressure in the lens transmission line was 1.5×10^{-3} torr (the parameters corresponding to the regime of optimal focusing in the experiment).

In the calculations, it was taken into account that, during the interaction of the beam with the working gas, the positive argon ions are produced through ionization, whereas the electrons are produced through both ionization and the neutralization of negative ions in collisions with neutral particles (the probability of the latter process is several orders of magnitude higher). The lifetimes of the produced particles are proportional to their path lengths and are limited by the time required for the particles to leave the calculation region.

At each time step, we introduced $N_+ = \Delta t J_I V_I \sigma_I N$ positive ions and $N_e = \Delta t J_I V_I (\sigma_I + \sigma_{-0}) N$ electrons (in the proportion 1 : 11) into the lens region occupied by the beam. Here, Δt is the time step, J_I is the ion flux density at the lens inlet, V_I is the volume of the ionization region, σ_I is the cross section for the ionization of the gas by the beam ions, σ_{-0} is the cross section for the neutralization of the beam ions in collisions with gas atoms, and N is the number of neutral particles in the ionization region. The initial electron energies were specified according to the calculated energy distribution (see [8]), and the initial directions of the electron velocities were taken according to the angular distribution from [9]; the maximum of this distribution was in the range 85°–95° with respect to the lens axis. The coordinates of the new particles in the ionization region were specified with the help of a random number generator. The trajectories of the new particles and the particles already occurring in the lens were calculated from the equation of motion

$$m\frac{d}{dt}\mathbf{v} = q(\mathbf{E}_{\mathrm{ION}} + \mathbf{E}_{\mathrm{E}} + \mathbf{E}_{\mathrm{B}} + \mathbf{E}_{\mathrm{EL}}),$$

where m, $\mathbf{v}$, and q are the mass, velocity, and charge of a particle, respectively, and $\mathbf{E}_{\mathrm{ION}}$, $\mathbf{E}_{\mathrm{E}}$, $\mathbf{E}_{\mathrm{B}}$, and $\mathbf{E}_{\mathrm{EL}}$ are the components of the electric field produced by the plasma ions, plasma electrons, beam ions, and electrodes, respectively. The time step was $\Delta t = 10^{-11}$ s. After a time of $\Delta T = 10^{-9}$ s, using the coordinates of all the particles, we calculated the distribution of the space charges of electrons, Ar^+ ions, and H^- beam ions by the cloud-in-cell method [7]. The radial and longitudinal dimensions of the spatial cell were equal to 0.1 cm. Using the distribution of the total space charge $\rho(z, r)$, we calculated the potential $U(z, r)$. Then, the particle motion in the new electric field was calculated and a new group of charged particles was introduced. The calculation continued until the steady-state distribution of the electric potential was established. The simulation time was no longer than 10^{-5} s. Figure 2b shows a typ-

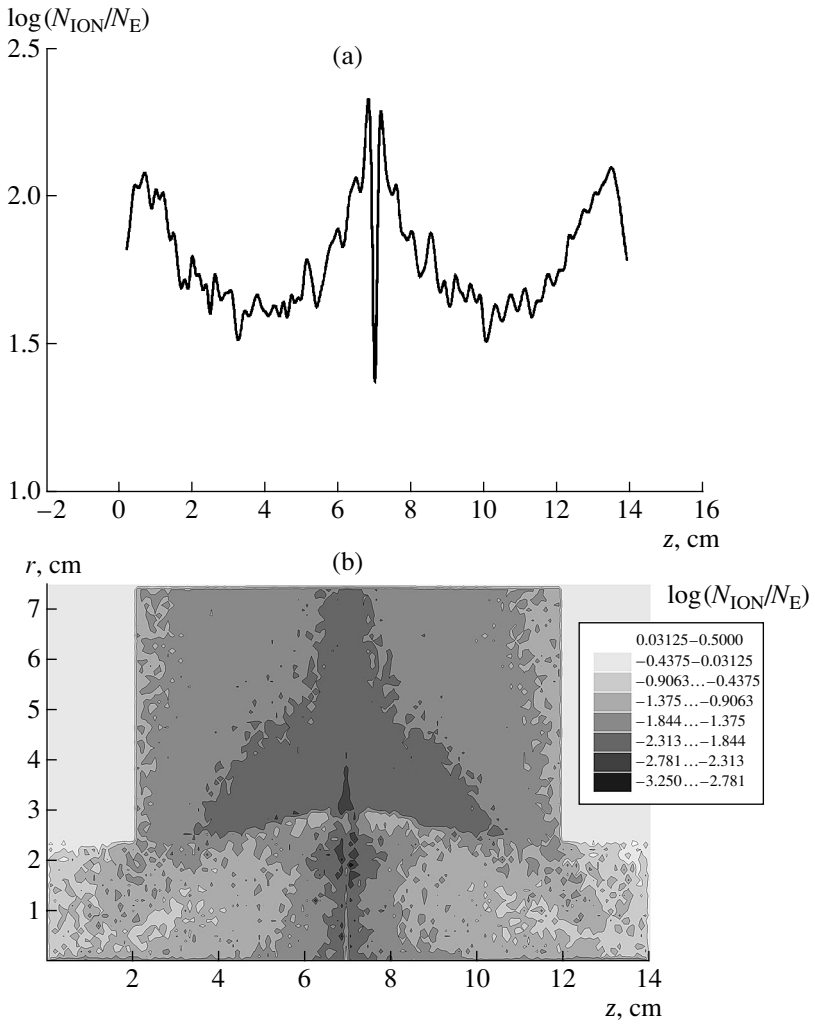

Fig. 3. (a) Axial profile and (b) spatial distribution of the ratio between the steady-state ion and electron densities in the lens at $t = 10^{-5}$ s.

ical steady-state potential distribution. The increase in the potential in the center of the system due to the filling of the working region with a positive charge is ≈300 V.

In the course of the lens formation, the positive argon ions go away from the lens axis along the trajectories close to the electric field lines (Fig. 2a) and occupy the entire lens cavity with time. The electrons in the working region move toward the lens axis and leave the calculation region in the axial direction. Figures 3a and 3b show the ratio between the steady-state electron and positive-ion densities on the lens axis and in the lens volume, respectively. In Fig. 3a, one can see three minima associated with characteristic features of the formation of the ion flow. A deep valley can be seen in the central peak, which is explained by the fact that the ion flux density in the central cross section is the highest and the electrons bunch there due to the lens symmetry. The positive-ion density exceeds the electron density at least by one order of magnitude (the light areas in Fig. 3b), and it is by two to three orders of magnitude higher than the electron density in the region adjacent to the central cross section (the dark areas in Fig. 3b), which testifies that the ion component is predominant during the formation of the space charge distribution.

Figure 4 shows the calculated trajectories of the negative-beam ions in the field of the lens in the steady-state regime. The lens has a high focal power, but there are significant aberrations caused by edge fluxes, which can be avoided under real conditions by limiting the diameter of the output beam and by reducing the influence of the electrodes. The focal length of the lens is 18 cm. At a collector radius of 1 cm, the beam compression ratio attains a value of ≈25, which is substantially higher than that observed in the experiment (about 5). However, this discrepancy can easily be explained taking into account the considerable phase space occupied by the real beam and the initial asymmetry of the beam emerging from the source slit.

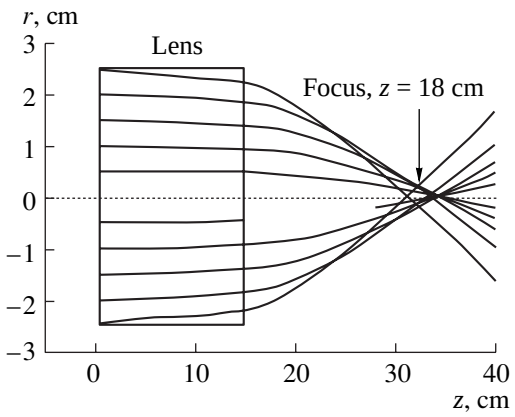

Fig. 4. Calculated trajectories of the negative beam ions in the field of the lens in the steady-state regime.

Thus, we have calculated the distributions of the potential and charged particle densities in the working region of the space-charge lens for focusing a negative-ion beam. The assumptions that the electron density is substantially reduced in the presence of a longitudinal electric field and that an excess positive charge is produced in the lens have been confirmed. The calculated value of the focal length of the lens is close to that measured in the experiment.

4. CONCLUSIONS

(i) The distributions of the space charge and electric field in the space-charge lens for focusing a negative-ion beam have been calculated numerically. The calculations demonstrate the high efficiency of both the inertial confinement of positive ions in the lens and the removal of electrons from the focusing region by a longitudinal electric field. As a result, the density of the positive ions in the lens is two to three orders of magnitude higher than the electron density. The focal length of the lens observed in calculations attains ≈20 cm.

(ii) It has been shown that the calculated values of the focusing electric field and the focal length agree well with the measured values.

(iii) It has been shown experimentally that the geometry of the lens significantly affects the removal of electrons from the lens.

REFERENCES

1. D. Gabor, Nature (London) **160**, 89 (1947).
2. A. I. Morozov, Dokl. Akad. Nauk SSSR **163**, 1363 (1965) [Sov. Phys. Dokl. **10**, 775 (1966)].
3. A. I. Morozov and S. V. Lebedev, *Reviews of Plasma Physics*, Ed. by M. A. Leontovich (Atomizdat, Moscow, 1974; Consultants Bureau, New York, 1980), Vol. 8.
4. A. A. Goncharov, A. N. Dobrovolskiĭ, A. N. Kotsarenko, *et al.*, Fiz. Plazmy **20**, 499 (1994) [Plasma Phys. Rep. **20**, 449 (1994)].
5. V. P. Goretskiĭ, I. A. Soloshenko, and A. I. Shchedrin, Fiz. Plazmy **27**, 356 (2001) [Plasma Phys. Rep. **27**, 335 (2001)].
6. B. I. Volkov and S. A. Yakunin, *Mathematical Problems of Plasma Optics* (Znanie, Moscow, 1982), p. 64.
7. D. Potter, *Computational Physics* (Wiley, New York, 1973; Mir, Moscow, 1975).
8. P. M. Golovinskiĭ and A. I. Shchedrin, Zh. Tekh. Fiz. **59** (2), 51 (1989) [Sov. Phys. Tech. Phys. **34**, 159 (1989)].
9. N. Mott and H. Massey, *Theory of Atomic Collisions* (Clarendon, Oxford, 1965; Mir, Moscow, 1969).

Translated by E.L. Satunina

Plasma Physics Reports, Vol. 29, No. 6, 2003, pp. 485–490. Translated from Fizika Plazmy, Vol. 29, No. 6, 2003, pp. 521–526.

NONIDEAL PLASMA

Oscillations of a Helical Plasma Crystal

N. G. Guseĭn-zade and A. M. Ignatov

Prokhorov Institute of General Physics, Russian Academy of Sciences, ul. Vavilova 38, Moscow, 119991 Russia

Received September 26, 2002

Abstract—Oscillations and the stability of the helical structures of likely charged particles undergoing Coulomb interactions and confined in an axisymmetric potential well are studied theoretically. © *2003 MAIK "Nauka/Interperiodica".*

1. INTRODUCTION

A typical example of a strongly nonideal plasma is provided by ordered structures of charged particles confined by external fields. In plasma physics, such structures are sometimes called quasi-crystals, although they lack the quasi-crystalline order known in solid-state physics [1]. One of the first experimentally observed ordered structures was a system of micron-sized iron and aluminum charged particles in a certain configuration of an alternating and a static field [2]. In later experimental investigations involving laser cooling techniques, Coulomb crystals were observed to form in various types of devices, e.g., in a Penning trap [3, 4], an RF Paul trap [5–7], and storage rings [8, 9]. From a practical standpoint, interest in such systems is associated with a new type of atomic clock [10] and the schemes proposed for implementing a quantum computer [11]. Crystals may also form in a purely electron plasma [12] and a dusty plasma [13].

The nature of ordered structures that arise in various devices is largely governed by the parameters of the external confining field. In this paper, we investigate quasi-one-dimensional structures that form in linear Paul traps and storage rings. The simplest approximation for such structures is to describe them as a system of singly charged ions that is uniform or periodic in a certain direction (e.g., along the z-axis) and whose transverse spreading is prevented by an external parabolic potential. During the laser cooling process, the ion kinetic energy T decreases; as a result, the plasma parameter e^2/aT (where a is the characteristic distance between the particles) amounts to about 10^4. As the parameters of the confining potential change, various structures that form during the cooling process undergo numerous phase transitions. The behavior of such structures has received much experimental, numerical, and analytical study [15]. On the other hand, virtually nothing is known about the oscillations and stability of Coulomb crystals in linear devices.

Here, we develop a theory of linear oscillations of Coulomb crystals exhibiting helical symmetry. We begin with a review of the different equilibrium configurations of charges in a linear device. Then, we derive a general set of linearized equations. Finally, we use these equations to calculate the spectra of oscillations of the five simplest types of crystals.

2. STEADY STATES OF A CRYSTAL

We consider a system consisting of a large number of likely charged particles confined in an external field with the potential $U_{\text{ext}}(\mathbf{r})$, which prevents the system from spreading in the transverse direction. We restrict ourselves to considering the case in which the external potential can be assumed to be independent of one of the coordinates (the z coordinate) and harmonic in the transverse coordinate. This case corresponds to two experimental situations. First, in a Penning trap, as well as in a Paul trap, the shape of any axisymmetric potential well $U_{\text{ext}}(\mathbf{r}) \approx 1/2[K_z z^2 + K(x^2 + y^2)]$ near its bottom is often highly anisotropic, $K_z \ll K$. Accordingly, at $z \approx 0$, the longitudinal component of the external force can be neglected. Second, in a toroidal device or storage ring, charged particles are confined in the vicinity of the closed axis; in this case, toroidal effects can be neglected provided that particle excursions away from the axis are small in comparison with the major radius of the device.

It is acceptable to ignore the distinction between the toroidal and axisymmetric devices in analyzing the small oscillations of a crystal. However, in searching for the spatial configurations of charges that would be most advantageous from the energy standpoint, doing so requires certain care. In a toroidal device, the line density (or the mean distance between the particles) is determined by the total number of particles and the major radius of the torus and is independent of K. On the other hand, in a highly anisotropic device, a decrease in the parameter K, which characterizes particle confinement in the transverse direction, may change the mean interparticle distance even near the bottom of the potential well [14]. In describing the states that are most favorable energetically, we neglect, for simplicity, the dependence of the mean distance between the particles on the confinement parameter K. This dependence

1063-780X/03/2906-0485$24.00

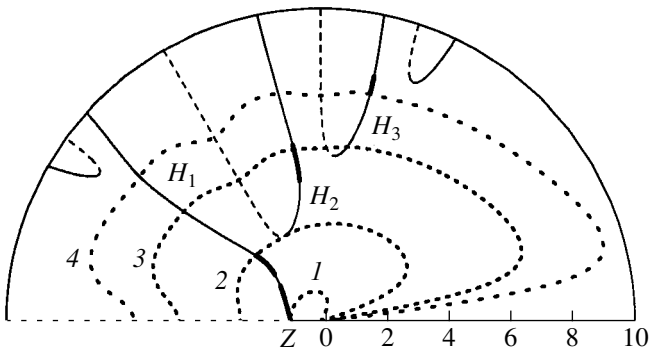

Fig. 1. Extrema of Madelung energy (7) in polar coordinates (u, θ). The solid and dashed curves represent the solutions to Eq. (8), and curves *1–4* are the solutions to Eq. (4) with $\mu =$ (*1*) 1.674, (*2*) 0.305, (*3*) 0.098, and (*4*) 0.058.

can be accounted for through an unessential renormalization of the dimensionless parameter μ, which will be introduced below.

The dynamics of the system is described by the equations

$$m\ddot{\mathbf{r}}_n = -K\mathbf{r}_{\perp n} + q^2 \sum_{\substack{m=-N \\ m\neq n}}^{N} \frac{\mathbf{r}_n - \mathbf{r}_m}{|\mathbf{r}_n - \mathbf{r}_m|^3}, \quad n = -N\ldots N, \quad (1)$$

where $\mathbf{r}_n = (x_n, y_n, z_n)$, $\mathbf{r}_{\perp n} = (x_n, y_n, 0)$, and q and m are the charge and mass of a particle. In writing the formulas, it is convenient to assume that the total number of particles is equal to $2N + 1$.

In the steady state, $\ddot{\mathbf{r}}_n = 0$; accordingly, the problem reduces to that of looking for the coordinates $\mathbf{r}_n$ of the particles with which the right-hand side of Newton's equation (1) vanishes. Let us list some of the simplest configurations that can take place at $N \longrightarrow \infty$. When the external potential is sufficiently high, all particles occur at the axis and form a linear chain (string), in which they have the coordinates

$$\mathbf{r}_n = (0, 0, na). \quad (2)$$

Recall that the distance a between the particles is assumed to be given. It is clear that, by virtue of the symmetry of the system, the total force acting on the nth particle in chain (2) is identically zero.

A somewhat more complicated case is that of a helical configuration, i.e., a helical chain (a helix) of particles with the coordinates

$$\mathbf{r}_n = [R\cos(n\theta), R\sin(n\theta), na]. \quad (3)$$

Substituting coordinates (3) into Eq. (1) and taking the limit $N \longrightarrow \infty$, we can readily see that the balance of the longitudinal forces and the balance of the angular momenta are satisfied exactly and that the condition for the radial force to vanish yields

$$u\left\{\frac{\mu}{4} - \sum_{m=1}^{\infty} \frac{\sin^2\left(\frac{m\theta}{2}\right)}{D_m^{3/2}}\right\} = 0, \quad (4)$$

where

$$D_m = m^2 + u^2\sin^2\left(\frac{m\theta}{2}\right). \quad (5)$$

Here, we have introduced the dimensionless diameter of the helix, $u = 2R/a$. The dimensionless quantity $\mu = Ka^3/q^2$ serves as a control parameter. Equation (4) and its trivial solution $u = 0$, which corresponds to configuration (2), represent only two relationships between the three quantities μ, θ, and u. In other words, the configuration of the system cannot be uniquely determined from the purely mechanical force-equilibrium condition. This ambiguity is resolved by imposing an additional requirement that the total energy of the system be minimum, which naturally applies to systems with dissipation and, in particular, to laser-cooled systems. The total potential energy of the system can be written as $U = \sum_n w_n$, where the energy w_n of an individual particle, which will be called, by analogy with solid-state physics, the Madelung energy, is equal to

$$w_n = \frac{1}{2}K\mathbf{r}_{\perp n}^2 + \frac{q^2}{2}\sum_{m\neq n}\frac{1}{|\mathbf{r}_n - \mathbf{r}_m|}. \quad (6)$$

For both linear chain (2) and helical chain (3), this energy diverges logarithmically as the total number of particles tends to infinity. However, the difference in the Madelung energies of each of these configurations is finite and is, of course, independent of n. In dimensionless form, it is convenient to write this difference as $w_{(h)n} - w_{(s)n} = (q^2/a)\varepsilon(u, \theta)$, where

$$\varepsilon(u, \theta) = \frac{1}{8}\mu u^2 + \sum_{m=1}^{\infty}\left(\frac{1}{D_m^{1/2}} - \frac{1}{m}\right). \quad (7)$$

The values of u that make this function an extremum are given by Eq. (4), and the equation $\partial\varepsilon/\partial\theta = 0$ yields

$$\sum_{m=1}^{\infty}\frac{m\sin(m\theta)}{D_m^{3/2}} = 0. \quad (8)$$

Equations (4) and (8) uniquely determine the dependence of the free parameters u and θ on μ.

Some insight into the extreme points of function (7) is provided by Fig. 1, which presents the solutions to Eq. (8) in polar coordinates (u, θ). The positions of the maxima of $\varepsilon(u, \theta)$ are shown by solid curves, the continuations of which in the form of dashed curves correspond to the minima. The dotted curves refer to the

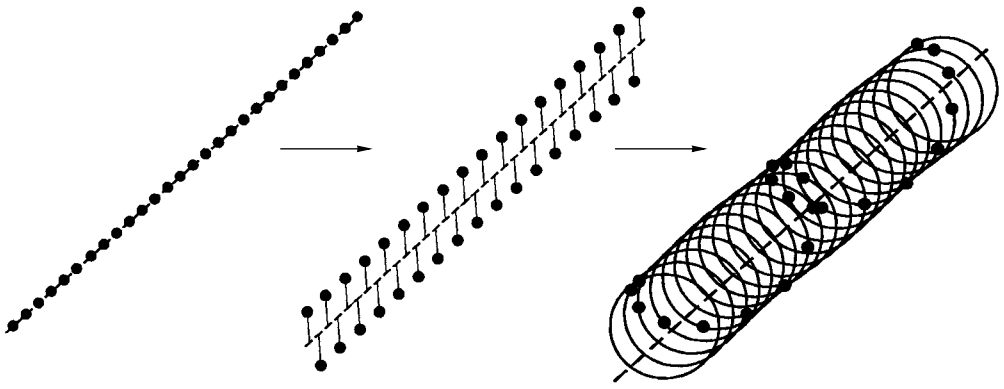

Fig. 2. Evolution of the structure of a Coulomb crystal as the confinement parameter of the device changes.

solutions to Eq. (4) that were obtained for different values of the parameter μ.

For a sufficiently high confining potential ($\mu > \mu_0 \approx 4.209$), the state that is most advantageous from the energy standpoint is that with linear chain (2), which is at the origin of the coordinates in Fig. 1. In the range $\mu_0 > \mu > \mu_1 \approx 1.674$, the most advantageous structure is a zigzag, i.e., structure (3) with $\theta = \pi$. In Fig. 1, the corresponding branch is marked with a *Z*. As μ increases, the size of the zigzag increases from zero to a maximum value of $u_{max} \approx 0.965$. Then, at $\mu < \mu_1$, the following bifurcation occurs: the maxima of Madelung energy (7) are now on the ray $u > u_{max}$, $\theta = \pi$ (Fig. 1) and the minima of this energy lie on the line H_1, corresponding to helical configuration (3) along which the angle θ depends in a certain fashion on μ. The transition from the zigzag to the first helix H_1 is continuous. The two transitions just described are illustrated schematically in Fig. 2.

As the confining potential decreases further, the system undergoes a series of phase transitions. Different helical branches H_2, H_3, … in Fig. 1 are separated from each other by potential barriers. As a rule, phase transitions occur through the formation of more complicated, tetrahedral structures. Altogether, there are ten phase transitions from one to another of the relatively simple structure, such as those shown in Fig. 2. All of these phase transitions are well captured numerically and many of them were observed experimentally. Finally, in the range $\mu \le 0.05$, a system forms that consists of several nested cylindrical shells. The details of the analysis of the Madelung energy for different configurations and the results of numerical simulations can be found in the review by Hasse and Schiffer [15].[1] Table 1 presents the ranges of variation of the parameter μ in which the Madelung energy in different helical structures has an absolute minimum. In Fig. 1, the corresponding portions of the curves are shown by heavy lines. In the gaps between the ranges given in Table 1, the minimum of energy corresponds to a tetrahedral configuration, which is not considered here. It should be noted that H_2 and H_3 helices are nearly isomeric: the difference between the energies in them is about 0.01.

[1] It should be noted that, in [15], the role of the external parameter is played by the dimensionless line particle density λ, which is related to the parameter μ used here by the relationship $\mu = 3/(2\lambda^3)$.

3. DISPERSION RELATION

In order to investigate oscillations of helical structure (3) and its stability, we represent the coordinate of each particle in the form

$$\mathbf{r}_n = a\left[\left(\frac{u}{2} + \delta\rho_n\right)\cos(n\theta + \delta\phi_n),\right.$$
$$\left.\left(\frac{u}{2} + \delta\rho_n\right)\sin(n\theta + \delta\phi_n),\ n + \delta z_n\right]. \quad (9)$$

We insert coordinates (9) into the equation of motion (1) and linearize the resulting equation in small deviations ($\delta\rho_n$, $\delta\phi_n$, δz_n) from the equilibrium positions. As a result, we obtain an infinite set of equations, which is too complicated to present here. Since the group of symmetries of unperturbed helix (3) is Abelian, the linearized set of equations is diagonalized by the substitution

Table 1. Structures with a minimum Madelung energy. Symbol *S* denotes linear chain (2)

Structure type	Intervals of μ
S	(4.207, ∞)
Z	(1.674, 4.207)
H_1	(0.768, 1.674)
H_1	(0.305, 0.559)
H_2	(0.094, 0.143)
H_3	(0.050, 0.058)

$$(\delta\rho_n, \delta\phi_n, \delta z_n) = \exp(-i\omega_p \nu t + isn)(\rho_0, \phi_0, z_0), \quad (10)$$

where we have introduced an analogue of the plasma frequency, $\omega_p = \sqrt{q^2/(ma^3)}$, and the dimensionless oscillation frequency ν. The dimensionless wave vector lies in the first Brillouin zone $-\pi < s < \pi$. Hence, we arrive at a homogeneous set of linear equations:

$$\begin{pmatrix} \nu^2 - \mu + Q_{11} & Q_{12} & Q_{13} \\ -Q_{12} & \frac{1}{4}u^2\nu^2 + Q_{22} & Q_{23} \\ -Q_{13} & Q_{23} & \nu^2 + Q_{33} \end{pmatrix} \begin{pmatrix} \delta r \\ \delta\phi \\ \delta z \end{pmatrix} = \begin{pmatrix} 0 \\ 0 \\ 0 \end{pmatrix}, \quad (11)$$

where the elements of the Hermitian matrix Q are equal to

$$\begin{aligned} Q_{11} &= 2\sum_{m=1}^{\infty} \frac{1-\cos(ms)\cos(m\theta)}{D_m^{3/2}} \\ &\quad - 12u^2 \sum_{m=1}^{\infty} \frac{\cos^2\left(\frac{ms}{2}\right)\sin^4\left(\frac{m\theta}{2}\right)}{D_m^{5/2}}, \\ Q_{22} &= u^2 \sum_{m=1}^{\infty} \frac{\cos(m\theta)\sin^2\left(\frac{ms}{2}\right)}{D_m^{3/2}} \\ &\quad - \frac{3}{4}u^4 \sum_{m=1}^{\infty} \frac{\sin^2(m\theta)\sin^2\left(\frac{ms}{2}\right)}{D_m^{5/2}}, \\ Q_{33} &= -8\sum_{m=1}^{\infty} \frac{\sin^2\left(\frac{ms}{2}\right)}{D_m^{3/2}} \\ &\quad + 12u^2 \sum_{m=1}^{\infty} \frac{\sin^2\left(\frac{ms}{2}\right)\sin^2\left(\frac{m\theta}{2}\right)}{D_m^{5/2}}, \\ Q_{12} &= iu \sum_{m=1}^{\infty} \frac{\sin(ms)\sin(m\theta)}{D_m^{3/2}} \\ &\quad - \frac{3}{2}iu^3 \sum_{m=1}^{\infty} \frac{\sin(ms)\sin(m\theta)\sin^2\left(\frac{m\theta}{2}\right)}{D_m^{5/2}}, \\ Q_{13} &= -6iu \sum_{m=1}^{\infty} \frac{m\sin(ms)\sin^2\left(\frac{m\theta}{2}\right)}{D_m^{5/2}}, \\ Q_{23} &= -3u^2 \sum_{m=1}^{\infty} \frac{m\sin^2(ms)\sin\left(\frac{m\theta}{2}\right)}{D_m^{5/2}}, \end{aligned} \quad (12)$$

and the quantity D_m is given by formula (5).

Equations (11) can be investigated analytically only for a linear chain. The results presented below were obtained from a numerical analysis of other types of chains. The numerical procedure consisted in finding the equilibrium radius u and pitch angle θ for certain values of μ and calculating the eigenvalues and eigenvectors of Eqs. (11) for wavenumbers in the range $0 \le s \le \pi$. Attention was largely focused on determining the intervals of stability of helical configurations, i.e., the intervals of μ values in which $\nu^2 > 0$ for any values of s. Such an analysis is required because a local or a global minimum in the Madelung energy automatically guarantees that the configuration is stable only against long-wavelength perturbations with $s = 0$ but does not guarantee its stability against arbitrary perturbations.

3.1. Linear Chain

For linear ion chain (2), the linearized equations of motion are easy to solve. Since the oscillations of the ions are symmetric, they can be resolved into longitudinal oscillations with $\rho_0 = 0$ and transverse oscillations with $z_0 = 0$ and an arbitrary plane of polarization. The dimensionless oscillation frequencies are determined by the expressions

$$\nu_\parallel^2(s) = 8\sum_{m=1}^{\infty} \frac{\sin^2(ms/2)}{m^3}, \quad (13)$$

$$\nu_\perp^2(s) = \mu - \frac{1}{2}\nu_\parallel^2(s). \quad (14)$$

The spectral curves of the longitudinal and transverse oscillations are shown in Fig. 3. The function $\nu_\parallel^2(s)$ is maximum at $s = \pi$, which indicates that, as the confinement parameter decreases to the value $\mu = \nu_\parallel^2(\pi)/2 = 7\zeta(3)/2 \approx 4.207$, the transverse oscillations with $s = \pi$ lose their stability and a linear chain continuously evolves into a zigzag. This μ value coincides with the stability boundary estimated for a linear chain from energy considerations (Table 1).

3.2. Zigzag

Zigzag chain (3) with $\theta = \pi$ is characterized by three oscillation branches. The polarization of one of them

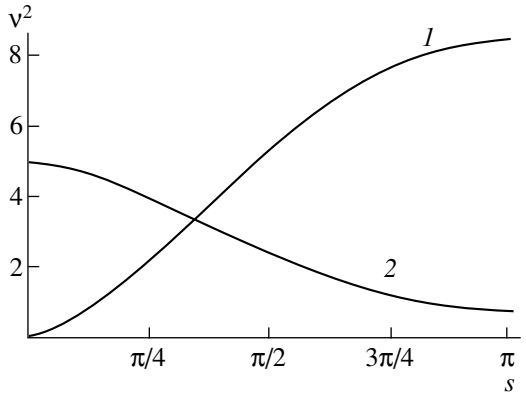

Fig. 3. Spectra (13) and (14) of (*1*) longitudinal and (*2*) transverse oscillations of a linear chain for $\mu = 5$.

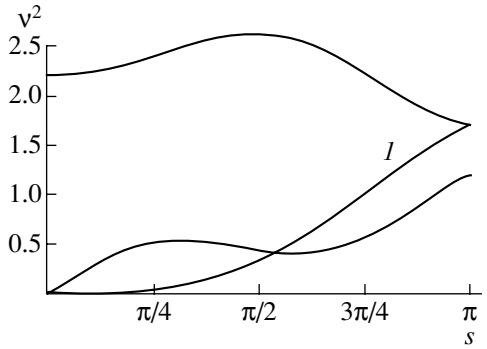

Fig. 4. Spectra of oscillations of a zigzag at the stability boundary for $\mu = 1.674$, $u = 0.965$, and $\theta = \pi$. Spectrum *1* refers to azimuthal oscillations.

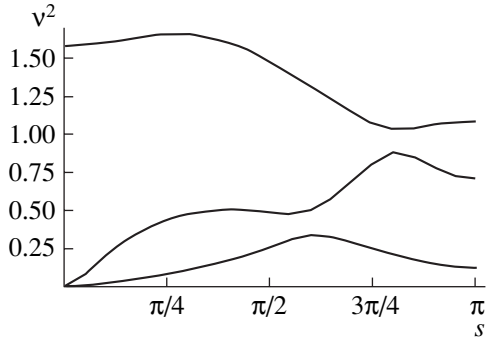

Fig. 5. Spectra of oscillations of helix H_1 for $\mu = 1.04$, $u = 1.405$, and $\theta = 2.548$. The upper curve at $s = 0$ corresponds to purely radial oscillations.

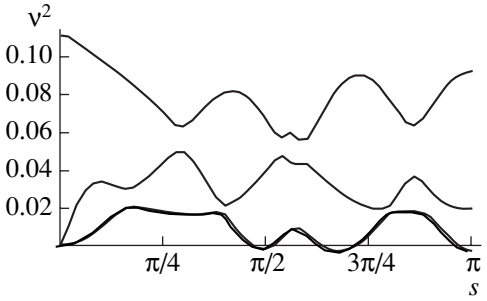

Fig. 6. Spectra of oscillations of helix H_2 for $\mu = 0.06$, $u = 7.264$, and $\theta = 1.753$.

corresponds to purely azimuthal oscillations with $\phi_0 \neq 0$, $\rho_0 = 0$, and $z_0 = 0$. The polarization of the remaining two corresponds to oscillations with $\delta_0 = 0$, $\rho_0 \neq 0$, and $z_0 \neq 0$.

Like a linear chain, a zigzag is stable over the entire range in which it exists. As the confinement parameter decreases to its minimum value $\mu \approx 1.674$, the group velocity of the long-wavelength azimuthal oscillations approaches zero. For $\mu < 1.674$, a long-wavelength instability develops, $(\nu^2/s^2)_{s \to 0} < 0$ (Fig. 4), which corresponds, obviously, to the continuous evolution of a zigzag into helix H_1.

3.3. Helix

As was noted above, there are three different helical configurations that are most advantageous from the energy standpoint; moreover, as the confinement parameter μ changes, the absolute minimum of Madelung energy (7) may jump from branch to branch (Fig. 1).

Helical configurations oscillate in a more complicated fashion than the configurations considered above do. As a rule, the oscillations of the particles are essentially three-dimensional ($\delta_0 \neq 0$, $\rho_0 \neq 0$, $z_0 \neq 0$). The only exception is uniform oscillations with $s = 0$ (i.e., purely radial oscillations), in which case the frequencies of the azimuthal and longitudinal oscillations become zero.

A characteristic example of the dispersion curves for oscillations of helix H_1 is shown in Fig. 5. The intervals of μ values where all of the configurations in question are stable are presented in Table 2. An important point is that, for all configurations, the intervals of stability either coincide with those in which the Madelung energy has an absolute minimum (*S* and *Z* configurations) or exceed them. As μ increases, the helix loses its stability in a more complicated way than the linear chain and zigzag do. As far as we can judge by the numerical results, in most cases, the oscillations that become unstable are those whose wavenumbers are incommensurable with π. A characteristic example of how helix H_2 loses its stability is illustrated in Fig. 6. This type of instability may give rise to more complicated structures, such as helices with additional modulation.

Table 2. Intervals of stability of different helical structures

Structure type	Intervals of μ
S	(4.207, ∞)
Z	(1.674, 4.207)
H_1	(0.708, 1.674)
H_2	(0.084, 0.170)
H_3	(0.033, 0.071)

4. CONCLUSION

The main qualitative conclusion from the above analysis may be formulated as follows. A helical structure whose potential energy has an absolute minimum is stable. On the other hand, as the confinement parameter changes, a crystal may remain stable even when its configuration becomes energetically unfavorable. Since different helical branches are separated from each other by the potential barriers, the crystals may, in principle, evolve into metastable states and the corresponding hysteresis effects may come into play. We can conclude by saying that, whereas the evolutions of a linear chain into a zigzag and of a zigzag into a helix are analogues of phase transitions of the second kind, the evolutions of helices from one configuration into another are analogous to phase transitions of the first kind.

ACKNOWLEDGMENTS

This work was supported in part by the Russian Foundation for Basic Research (project no. 02-02-16439) and the Netherlands Organization for Scientific Research (project no. NWO.047.008.013).

REFERENCES

1. M. Quilichini and T. Janssen, Rev. Mod. Phys. **69**, 277 (1997).
2. R. F. Wueker, H. Shelton, and R. V. Langmuir, J. Appl. Phys. **30**, 342 (1959).
3. S. L. Gilbert, J. J. Bollinger, and D. J. Wineland, Phys. Rev. Lett. **60**, 2022 (1988).
4. J. J. Bolinger, D. J. Wineland, and D. H. E. Dubin, Phys. Plasmas **1**, 1403 (1994).
5. G. Birkl, S. Kassner, and H. Walther, Nature (London) **357**, 310 (1992).
6. J. D. Prestage, G. J. Dick, and L. Maleki, J. Appl. Phys. **66**, 1013 (1989).
7. M. G. Raizen, J. M. Gilligan, J. C. Bergquist, *et al.*, Phys. Rev. A **45**, 6493 (1992).
8. N. Kjærgaard, K. Mølhave, and M. Drewsen, Phys. Rev. E **66**, 015401 (2002).
9. U. Schramm, T. Schätz, and D. Habs, Phys. Rev. E **66**, 036501 (2002).
10. M. E. Poitzesch *et al.*, Rev. Sci. Instrum. **67**, 129 (1996).
11. J. I. Cirac and P. Zoller, Phys. Rev. Lett. **74**, 4091 (1995).
12. J. H. Malmberg and T. M. O'Neil, Phys. Rev. Lett. **39**, 1333 (1977).
13. G. Morfill, H. Tomas, and V. N. Tsytovich, Fiz. Plazmy **28**, 675 (2002).
14. D. H. E. Dubin, Phys. Rev. Lett. **71**, 2753 (1993).
15. R. W. Hasse and J. P. Schiffer, Ann. Phys. (N.Y.) **203**, 419 (1990).

Translated by O.E. Khadin

Plasma Physics Reports, Vol. 29, No. 6, 2003, pp. 491–502. Translated from Fizika Plazmy, Vol. 29, No. 6, 2003, pp. 527–539.

PLASMA ELECTRONICS

Microwave Generation by a Superluminal Source at Limiting Current Densities

Yu. N. Lazarev, P. V. Petrov, and Yu. G. Syrtsova

Zababakhin All-Russia Research Institute of Technical Physics, Russian Federal Nuclear Center, Snezhinsk, Chelyabinsk oblast, 456770 Russia

Received August 12, 2002

Abstract—It is well known that high-power directed wideband electromagnetic radiation in the microwave range can be generated by a superluminal pulse of the electron emission current. The operation of a simple emitting element driven by a superluminal current pulse and consisting of an accelerating diode with a photocathode and a source of ionizing radiation that initiates electron emission from the cathode is considered. It is shown that the parameters of an elementary superluminal source obey scaling relations that are determined by the growth rate of the electron emission current from the photocathode and the parameters of the accelerating diode. The limiting anode current density and the limiting values of the characteristics of electromagnetic radiation achievable in such a system are determined. The effect of the finite dimensions of the accelerating system on the parameters of the emitter is investigated, and the spatiotemporal characteristics of the generated electromagnetic fields are obtained. © *2003 MAIK "Nauka/Interperiodica".*

1. INTRODUCTION

High-power directed wideband electromagnetic (EM) radiation in the microwave range can be generated by means of a superluminal electron emission current pulse [1, 2] produced when the front of the electron emission from the interface between a vacuum and a medium propagates with a velocity v_{ph} higher than the speed of light c. In particular, a superluminal current pulse is generated when a plane metal surface is irradiated by a plane flux of radiation capable of producing electron emission, in which case the phase velocity of the moving emission front is equal to

$$v_{ph} = c/\sin\theta, \quad (1)$$

where θ is the angle of incidence of the radiation.

The spatiotemporal distribution of the electron emission current near the surface is phased in such a way that an emitted EM wave propagates in the same direction as the reflected wave of the ionizing radiation (Fig. 1). At sufficiently large distances R from the source, the amplitude of the emitted EM field is proportional to the second derivative of the surface density of the dipole moment P with respect to time; in turn, this derivative is proportional to the energy of the electrons emitted and the area S of the emitter surface [1, 2]:

$$E^w \sim H^w \sim \ddot{P}S/c^2R, \quad \ddot{P} = \left|d^2\mathbf{P}/dt^2\right|,$$
$$\mathbf{P}(\mathbf{r}, t) = \int dV'(\mathbf{r}-\mathbf{r}')\rho(\mathbf{r}', t), \quad (2)$$

where $\rho(\mathbf{r}, t)$ is the electron density in the dipole layer.

According to formulas (2), the higher the energy of the emitted electrons, the higher the intensity and total energy of the emitted EM radiation. Estimates [2] show that, in order for the energy and intensity of the generated EM radiation be of interest for practical purposes, the energy of the emitted electrons should be on the order of tens of kiloelectronvolts or higher. Under laboratory conditions, the emission current of the high-energy electrons can be generated by separating the processes of the electron production and the formation of the emitting dipole layer. Light or ionizing radiation capable of producing electron emission is used only to initiate the emission of electrons with the minimum possible energy; the electrons emitted are then accelerated to their final energies from hundreds to thousands

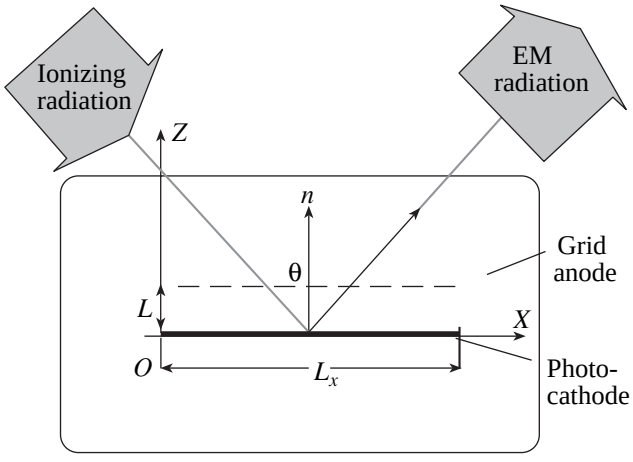

Fig. 1. Elementary microwave source in a vacuum chamber evacuated to a pressure of $p < 0.005$ mm Hg.

1063-780X/03/2906-0491$24.00 © 2003 MAIK "Nauka/Interperiodica"

of kiloelectronvolts by an external electric field. Schematically, an EM radiation source supplied by a superluminal current pulse is a plane accelerating diode with a grid anode irradiated at a certain angle by a plane flux of ionizing or light radiation (Fig. 1). The plane front of the ionizing radiation generates a superluminal current pulse of the electrons emitted from a photocathode. Then, the electrons are accelerated in the interelectrode gap, pass through the grid anode, and form a superluminal current pulse above it. The current pulse so produced generates a high-power directed EM pulse near the anode.

In the theory of a superluminal source [1, 2], the main results were obtained in studying the operating modes of an emitter in which the generated electromagnetic wave did not have any significant effect on the parameters of the accelerating system. However, it is clear that, for high current densities of the accelerated electrons, this effect should be taken into account: when the current density is sufficiently high, the characteristics of the generated EM radiation depend on the parameters of the accelerated diode and, primarily, on the parameters of the limiting current that can be produced above the anode. Although there are many papers devoted to the problem of limiting currents (see [3–5] and the literature cited therein), some features of the generation of EM radiation by a superluminal emission current pulse that do not manifest themselves in the classical schemes of microwave generation remain uninvestigated. In particular, since the EM radiation pulse forms at the front of the emission current, the achievement of high current densities at the anode is determined not by the current density of the emitted electrons but by the growth rate of the emission current.

Our objective here is to investigate the limiting characteristics of the EM radiation generated by an elementary superluminal source. We present analytic estimates and the results of numerical calculations of the parameters of a superluminal current pulse and EM radiation generated when the emission electrons are accelerated in a plane diode operating at high current densities.

2. ANALYTIC MODEL OF THE FORMATION OF AN EMITTING DIPOLE LAYER IN AN ELEMENTARY EMITTER

The feature of an emitting element (Fig. 1) based on the generation of EM radiation by a superluminal current pulse of the electrons accelerated in a plane diode is that it generates two electromagnetic waves, which will be referred to as "directed" and "guided" waves. The interaction of these waves with the emitted electrons governs the magnitude of the anode current and the dipole moment above the anode.

In the free half-space above the anode ($z > L$), the directed electromagnetic wave propagates in the direction in which the ionizing radiation is reflected (Fig. 1). The parameters of the directed wave are determined by the dynamics of the dipole layer of the electrons accelerated in the diode [see Eq. (2)]. It can be assumed that this wave does not affect the anode current amplitude because of the screening effect of the metal grid anode.

A superluminal current pulse produced by the electrons moving in the interelectrode gap also generates an electromagnetic wave that propagates in a plane waveguide formed by the cathode and anode. Being added to the field of the space charge of the emitted electrons, the field of this guided electromagnetic wave reduces the effective accelerating field in the diode and, accordingly, lowers the limiting current density at the anode and the density of the dipole moment of the electrons above it.

The processes of the generation of EM radiation, the formation of the dipole layer, and the electron motion in the accelerating gap should be considered together because they are closely related to each other. A theoretical study of such systems is based mainly on numerical simulations. However, in some cases, the problem of the initial stage of the formation of a dipole layer (before the electron flow velocity becomes multivalued [6]) can be investigated by approximate analytic methods, which make it possible to obtain scaling relations for the main parameters of the electron current and to estimate the limiting current densities at the anode operating in a dynamic mode.

We consider the process of the formation of an electron dipole layer above the grid anode of an infinite plane capacitor in the one-dimensional approximation. We assume that the anode is transparent to electrons and denote by L and φ_0 the distance and the voltage between the electrodes. It is well known that, when the voltage φ_0 is not too high, $e\varphi_0/(mc^2) = \gamma_0 - 1 \ll 1$, the electron motion can be treated as nonrelativistic. In such a diode, the steady-state limiting current density is described by the expression [5]

$$J_0 = \frac{\varphi_0^{3/2}}{9\pi L^2}\sqrt{\frac{2e}{m}}. \quad (3)$$

We assume that, under the action of ionizing radiation incident on the emitting element, the cathode emits electrons with a current density $J_c(t)$ and a zero initial velocity.

2.1. The Case of Normal Incidence of the Ionizing Radiation ($\theta = 0$, $v_{ph} = \infty$)

The normal incidence of ionizing radiation on an emitting element is an exceptional case in which an electromagnetic wave is not generated ($v_{ph} = \infty$) and, accordingly, there is no need to take into account the effect of the fields of the directed and guided electromagnetic waves on the electron motion. Nevertheless, this problem, even being considerably simplified, is of interest because it makes it possible to derive the main

scaling relations for the parameters of the electron current.

Let the cathode ($z = 0$) start emitting electrons into the accelerating gap at the time $t = 0$. We consider only the initial stage of the formation of a dipole layer, up to the time τ_r at which the emitted electrons begin to return to the cathode and the electron flow velocity becomes multivalued. In this stage, the space charge that arises above the cathode by the time τ is equal to

$$Q = \int_0^\tau J_c(t)dt. \tag{4}$$

Since the space charge produced changes the accelerating electric field of the capacitor, the motion of the electrons injected at the time $\tau < \tau_r$ is described by the equation

$$\frac{d^2z(t,\tau)}{dt^2} = \frac{e}{m_e}E(\tau, z), \tag{5}$$

where e and m_e are the charge and mass of an electron. The electric field $E_z(\tau, z)$ acting on an electron emitted from the cathode at the time τ has the form

$$E(\tau, z) = \begin{cases} E_0 - 4\pi\int_0^\tau J_c(t')dt', & 0 < z < L, \\ -\eta[\tau - T^*(\tau)]4\pi\int_{T^*(\tau)}^\tau J_c(t')dt', & z > L. \end{cases} \tag{6}$$

Here, $E_0 = \varphi_0/L$ is the initial accelerating electric field in the diode; $\eta(t) = 0$ ($t < 0$) and 1 ($t \geq 0$) is the Heaviside step function; and $T^*(\tau)$ is the transit time of an electron from the cathode to the anode, so an electron emitted from the cathode at the time τ reaches the anode at the time $t = \tau + T^*(\tau)$.

Since the accelerating field decreases as the space change increases, the electron transit time from the cathode to the anode becomes longer. As a result, the electrons injected from the cathode during the time interval $\Delta\tau$ reach the anode during the time interval $\Delta t = \Delta\tau\left(1 + \left|\frac{dT^*}{d\tau}\right|\right)$. Accordingly, the current density at the anode J_a is related to the current density at the cathode $J_c(\tau)$ by

$$J_a(t) = \frac{J_c(\tau)}{1 + \left|\frac{dT^*}{d\tau}\right|}, \quad t = \tau + T^*(\tau). \tag{7}$$

Of course, for $\left|\frac{dT^*}{d\tau}\right| \ll 1$, the current density may be regarded as conserved: the current density above the anode is equal to that at the cathode and the electron velocity at the anode does not depend on time and is equal to

$$v_0 = \sqrt{\frac{2eLE_0}{m_e}}. \tag{8}$$

In this case, the characteristic time of the formation of the dipole layer, T_p, can be estimated from the current density at the cathode.

If we assume that the current density at the cathode changes linearly with time (at least over the time interval $0 < \tau < \tau_r$),

$$J_c(\tau) = J_t\tau, \tag{9}$$

then we obtain

$$T^*(\tau) = \frac{T_0T_m}{\sqrt{T_m^2 - \tau^2}}, \quad \frac{dT^*(\tau)}{d\tau} = \frac{T_0T_m\tau}{(T_m^2 - \tau^2)^{3/2}},$$
$$T_m = \sqrt{\frac{E_0}{2\pi J_t}}, \quad T_0 = \sqrt{\frac{2m_eL}{eE_0}}. \tag{10}$$

The condition $\left|\frac{dT^*}{d\tau}\right| \ll 1$ is satisfied when

$$a = T_0/T_m \ll 1, \tag{11}$$

i.e., when the transit time of an electron through the interelectrode gap is much shorter than the time scale on which the electric field in the gap changes. This condition can be rewritten in terms of the growth rate of the emission current from the cathode:

$$J_t \ll \frac{J_{0t}}{4\pi} = \frac{J_0}{4\pi T_0} = \frac{eE_0^2}{4\pi m_eL}. \tag{12}$$

Under conditions (11) and (12), the characteristic time of the formation of the dipole layer is $T_p = \left(\frac{m_ev_0}{4\pi eJ_t}\right)^{1/3} = \left(\frac{1}{2\pi J_t}\sqrt{\frac{m_eLE_0}{2e}}\right)^{1/3}$, the surface density of the dipole moment is $P_0 = \frac{mv_0^2}{8\pi e} = \frac{LE_0}{4\pi}$, the time derivatives of the dipole moment density are equal to $\dot{P}_0 = \frac{P_0}{T_p}$ and $\ddot{P}_0 = \frac{P_0}{T_p^2}$, and the characteristic wavelength of the generated EM radiation is $\lambda = 2\pi\lambda\!\!\!^{-} = 2\pi cT_p$.

When the current density at the cathode changes at a high rate, $J_t \sim J_{0t}$, the time scale on which the accelerated field in the interelectrode gap changes is comparable with the electron transit time, $T_m \sim T_0$. The space charge of the electrons emitted from the cathode during the time interval $0 < \tau < T_m$ completely neutralizes the external accelerating field; i.e., the electrons emitted at the times $\tau > T_m$ do not contribute to the anode current. Only after the time $\tau = \tau_r$, at which the electrons begin

to return to the cathode, is the anode current again contributed by the emission from the photocathode. Accordingly, the time scales on which the anode current and the dipole moment density change are determined by the times T_m and T_0.

We assume that the current density changes linearly with time [see expression (9)] and switch to the new dimensionless variables

$$\tau' = \tau/T_m, \quad j_c(\tau') = J_c(\tau)/(J_t T_m),$$
$$\dot{p} = \dot{P}/(J_t T_m^2 v_0), \quad \ddot{p} = \ddot{P}/(J_t T_m v_0), \tag{13}$$
$$v' = v/v_0, \quad a = T_0/T_m.$$

Substituting these variables into equation of motion (5), we obtain the following parametric expressions for the density of the current flowing through the anode and for the time derivatives of the dipole moment density:

$$j_a(\tau') = \frac{j_c(\tau')(1-\tau'^2)^{3/2}}{(1-\tau'^2)^{3/2} + a\tau'}, \tag{14}$$

$$\dot{p} = 1 + \frac{(\tau'^2 - 1 - \tau'^4/4)}{\sqrt{1-\tau'^2}} - \frac{\tau'^5}{20a},$$
$$\ddot{p} = \tau'\sqrt{1-\tau'^2} - \frac{\tau'^5}{4(1-\tau'^2)^{3/2}} - \frac{\tau'^4}{4a}, \tag{15}$$

where the time at which an electron is emitted from the cathode and the time at which it reaches the anode are related by

$$t' = \tau' + a/\sqrt{1-\tau'^2}. \tag{16}$$

Using formulas (14) and (15), we can estimate the maximum values of the anode current and of the time derivatives of the dipole moment density, as well as the times at which the maximum values are achieved:

$$(j_a)_{\max} \approx \frac{1}{2(1 + 4\sqrt{3}a/9)}, \quad t_f' \approx 0.7; \tag{17}$$

$$\dot{p}_{\max} \approx 0.22 - \frac{0.01}{a}, \quad t_f' \approx 0.97a + 0.66; \tag{18}$$

$$\ddot{p}_{\max} \approx \frac{0.36}{1 + 0.52a}, \quad t_f' \approx 0.5 + 0.1a. \tag{19}$$

Figures 2–4 show the electron current and the derivatives of the dipole moment density above the anode, calculated from analytic expressions (17)–(19) and obtained in the one-dimensional numerical modeling with the two-dimensional EMC2D code [7], in which Maxwell's equations and the equations of electron motion are solved self-consistently by a particle-in-cell (PIC) method.

In dimensional form, expressions (17)–(19) become

$$(J_a)_{\max} \approx \frac{\sqrt{J_t E_0}}{2\sqrt{2\pi}\left(1 + \frac{8}{9E_0}\sqrt{\frac{3\pi J_t L m_e}{e}}\right)},$$
$$t_f \approx 0.7T_m = 0.7\sqrt{\frac{E_0}{2\pi J_t}}, \tag{20}$$

$$\dot{P}_{\max} \approx \frac{0.22}{\pi}\sqrt{\frac{eL}{2m_e}E_0^{3/2}}, \quad t_f \approx 0.97T_0 + 0.66T_m, \tag{21}$$

$$\ddot{P}_{\max} \approx \frac{0.36E_0}{1 + \frac{1}{E_0}\sqrt{\frac{\pi m_e L J_t}{e}}}\sqrt{\frac{eLJ_t}{\pi m_e}},$$
$$t_f \approx 0.5T_m + 0.1T_0. \tag{22}$$

Expressions (17)–(22) show that, when the generated EM radiation (the directed and guided waves) has a negligible effect on the motion of accelerated electrons, such parameters as the anode current, the dipole moment, and the EM radiation intensity obey certain scaling relations and their asymptotic values are determined by the parameters of the accelerated diode.

2.2. The Case of Oblique Incidence of the Ionizing Radiation ($\theta \neq 0$, $v_{\text{ph}} < \infty$)

In the case of obliquely incident ionizing radiation, the phase velocity of the emission current from the cathode surface is finite, $c < v_{\text{ph}} < \infty$, which results in the generation of EM waves (directed and guided waves). The field of the guided mode affects the process of electron acceleration in the interelectrode gap, and the field of the directed mode influences the dynamics of the dipole layer above the anode.

We consider the effect of a directed EM wave on the dipole moment above the anode under the assumption that the EM field of the directed wave is screened by the anode and thus has no impact on electron motion in the interelectrode gap. It is clear that the field E^w of the emitted wave can be neglected when it is lower than space-charge field E^{sch}:

$$E^w < E^{\text{sch}}.$$

Near the emitting surface, the component E_z^w of the electric field of the EM wave is determined by the first derivative of the dipole moment [2]:

$$E_z^w \approx \frac{4\pi}{c}\frac{\sin^2\theta}{\cos\theta}\dot{P}(t) \approx \frac{v_0}{c}\frac{\sin^2\theta}{\cos\theta}E_0. \tag{23}$$

In order of magnitude, we have

$$E_z^w \sim \frac{\varepsilon_0}{\chi\tan\theta}, \quad E^{\text{sch}} \sim \frac{\varepsilon_0}{\lambda_D},$$

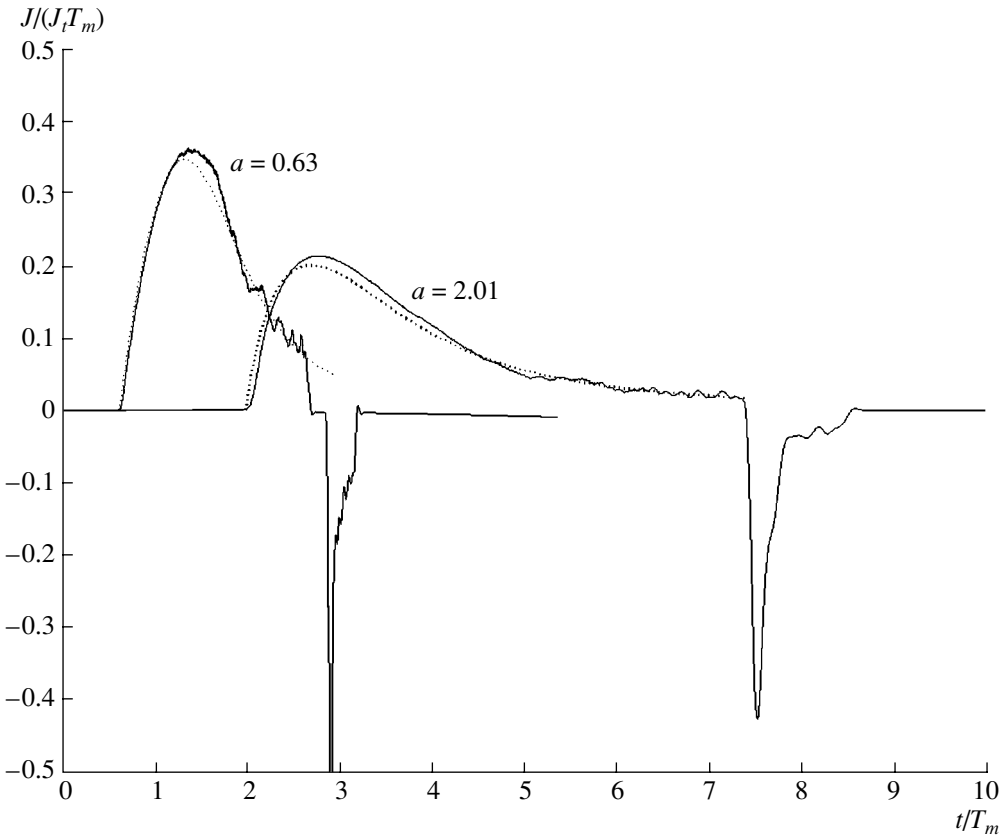

Fig. 2. Time evolutions of the anode current for different growth rates of the current density at the cathode. The solid curves show the results of numerical calculations, and the dotted curves are analytical results.

where $\varepsilon_0 = \dfrac{m_e v_0^2}{2}$ is the maximum energy of the electrons accelerated in the diode and $\lambda_D = v_0 T_m$ is the characteristic dimension of the electron dipole layer.

Consequently, when the angle of incidence of the ionizing radiation satisfies the condition

$$\theta > \arccos\left(\frac{1}{\sqrt{1 + v_0^2/c^2}}\right), \tag{24}$$

the field of the EM wave has a significant effect on the process under consideration: it decreases the derivatives of the dipole moment density and somewhat reduces the duration of the generated EM pulse.

The guided mode of the EM radiation has a greater effect because it influences the electron acceleration process. The reason is that the accelerating field of the diode decreases not only because of the increase in the space charge of the emitted electrons [see expression (6)] but also because of the generation of the EM field component E_z^w. Accordingly, in equation of motion (5), the electric field should be taken in the form

$$E(\tau, z) = E_0 - 4\pi\int_0^\tau J_c(t')dt' - E_z^w(z, \tau), \quad 0 < z < L. \tag{25}$$

Self-consistent PIC computations (Fig. 5) show that, in the case of oblique incidence of the ionizing radiation on an accelerating diode (when EM radiation is generated), the total field of the EM wave and of the space charge increases at a much faster rate and to a greater value than does the space charge field alone in the case of normal incidence. Hence, the guided EM radiation leads to the following effects:

(i) the shortening of the electron transit time T_m from the cathode to the anode and

(ii) the weakening of the accelerating electric field in the interelectrode gap.

Accordingly, both the anode current and the derivatives of the dipole moment decrease.

The amount by which the anode current decreases can be estimated by assuming that the electron acceleration in a diode with the guided mode of the EM radiation is determined not by the initial accelerating electric field E_0 but by a certain effective electric field E_{eff} =

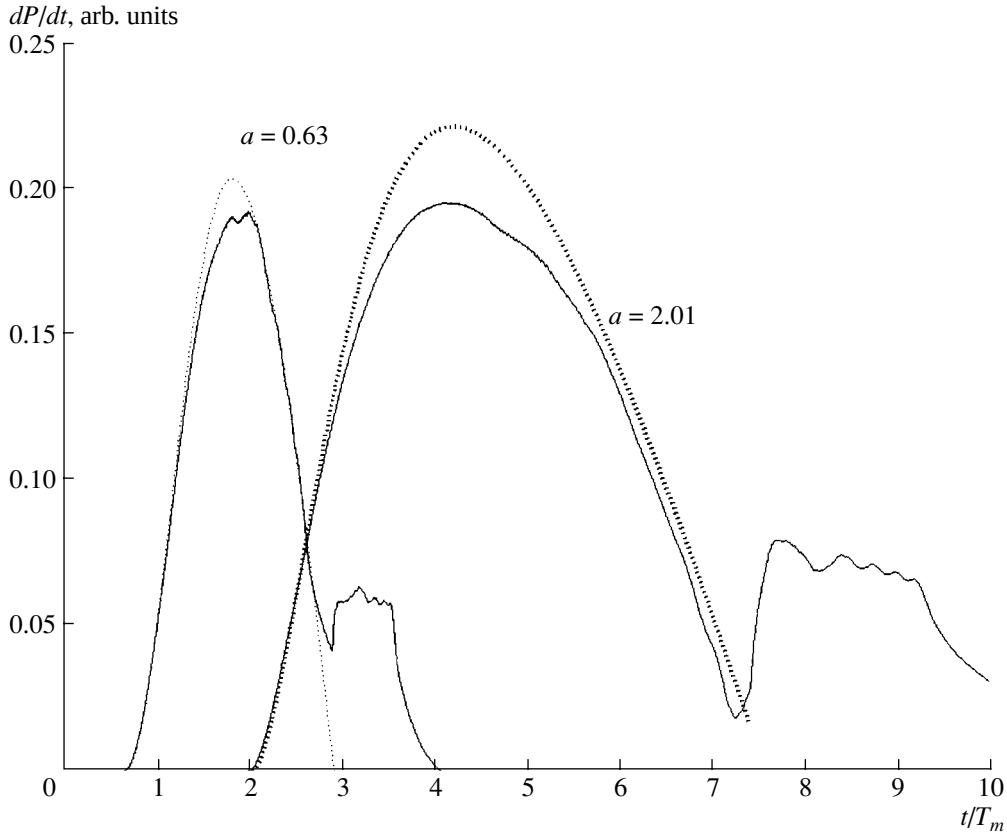

Fig. 3. Time evolutions of the first time derivative of the surface density of the dipole moment for different growth rates of the current density at the cathode. The solid curves show the results of numerical calculations, and the dotted curves are analytical results.

$E_0 - E_z^w$, where the field component E_z^w is given by formula (23):

$$E_{\text{eff}} = E_0\left(1 - \frac{v_0}{c}\frac{\sin^2\theta}{\cos\theta}\right). \tag{26}$$

We assume that the angle of incidence is not too large, $\pi/4 < \theta < \pi/3$, and that the electron motion is nonrelativistic, $\beta_0 = v_0/c \approx 0.5$. Then, we insert E_{eff} into formulas (20)–(22) to see that the amplitude of the anode current and the second derivative of the dipole moment density decrease by a factor of approximately two:

$$(J_a^w)_{\max} \approx \left(1 - \frac{v_0}{c}\frac{\sin^2\theta}{\cos\theta}\right)^{1/2}(J_a)_{\max} \approx 0.5(J_a)_{\max},$$
$$\ddot{P}^w_{\max} \approx \left(1 - \frac{v_0}{c}\frac{\sin^2\theta}{\cos\theta}\right)\ddot{P}_{\max} \approx 0.25\ddot{P}_{\max}. \tag{27}$$

This result is confirmed by numerical calculations with the EMC2D code (Figs. 6, 7).

The above analytic estimates obtained for the generation of microwaves by a superluminal electron emission current pulse formed by a plane diode allow us to draw the following conclusions:

(i) The anode current density and the time derivatives of the dipole moment in an emitting element are determined by the parameters of an accelerating diode and by the growth rate of the electron emission current from the cathode; in turn, this rate depends on the rate of change of the ionizing radiation flux intensity.

(ii) The limiting current at the anode, $(J_a)_{\max}$, is lower than the steady-state limiting current J_0 and the limiting values of the derivatives of the dipole moment are smaller than the corresponding steady-state limiting values because the electron current is limited by not only the space charge field but also by the field of the generated EM wave.

(iii) In a half-space above the anode, the parameters of the anode current and the derivatives of the electron dipole moment obey scaling relations (13), (17)–(19), and (27).

(iv) An increase in the rate of electron emission from the cathode changes not only the amplitude values of the parameters of the dipole layer but also the time dependence of the derivatives of the dipole moment density: the characteristic time scale of the dipole moment and the associated wavelength $\lambda = 2\pi c T_m$ both decrease. This indicates that the spectrum of the gener-

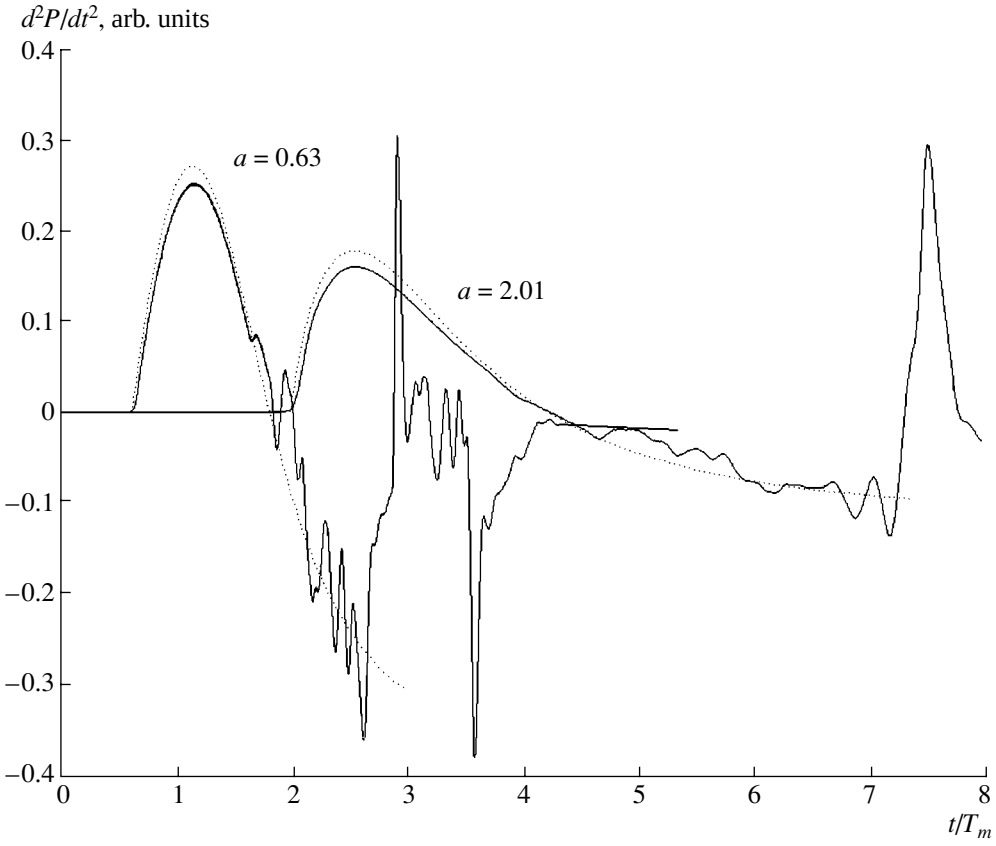

Fig. 4. Time evolutions of the second time derivative of the surface density of the dipole moment for different growth rates of the emission current density at the cathode. The solid curves show the results of numerical calculations, and the dotted curves are analytical results.

ated radiation can be changed by changing the electron emission rate.

3. NUMERICAL SIMULATIONS OF THE MICROWAVE GENERATION AT A HIGH EMISSION RATE

The above estimates have been obtained from a one-dimensional model of an infinitely long emitting element. In actuality, the dimensions of a capacitor used to form superluminal current pulses are usually too small for it to be treated as a plane one with an infinite length and an infinite width. Thus, in [8], the experiments on microwave generation by superluminal current pulses initiated by the front of soft X radiation from a laser–plasma source were carried out with a capacitor with voltage $\varphi_0 = 80$ kV, length $L_x = 80$ cm, width 5 cm, and interelectrode distance $L = 2$ cm. The configuration of this accelerating system was used as the basis for our numerical investigations of the effect of the finite dimensions of an emitter on the parameters of a superluminal source. The investigations were carried out with the EMC2D PIC code [7]. The geometry of the system corresponded to that shown schematically in Fig. 1. The initial electrostatic field of the capacitor were computed by the finite-element method with the help of the MATLAB software package [9] and then were used as the input to the EMC2D code for calculating the dynamics of an electron cloud. It was assumed that electron emission is initiated by the plane front of the ionizing radiation incident at an angle of 60° and that the current density changes linearly according to the law $J_t = 2.5 \times 10^{10}$–5×10^{11} $\frac{\text{A}}{\text{cm}^2\ \text{s}}$ ($a = 0.45$–2.0).

3.1. Effects of the Finite Length of the Emitting Element

Figures 8–10 illustrate the results of calculations of the anode current, the second derivative of the dipole moment, and the rise time of the second derivative [all normalized to their maximum values determined by Eqs. (20)–(22)] as functions of the longitudinal coordinate. The main effect of the finite length of an emitting element is the spatial nonuniformity of the profiles of the anode current and dipole moment density along the capacitor; this effect is associated with the influence of the generated radiation on the electron motion. At the left end of the capacitor (Fig. 1), the EM radiation has an insignificant effect on the formation of the current pulse. However, the larger the distance from the left

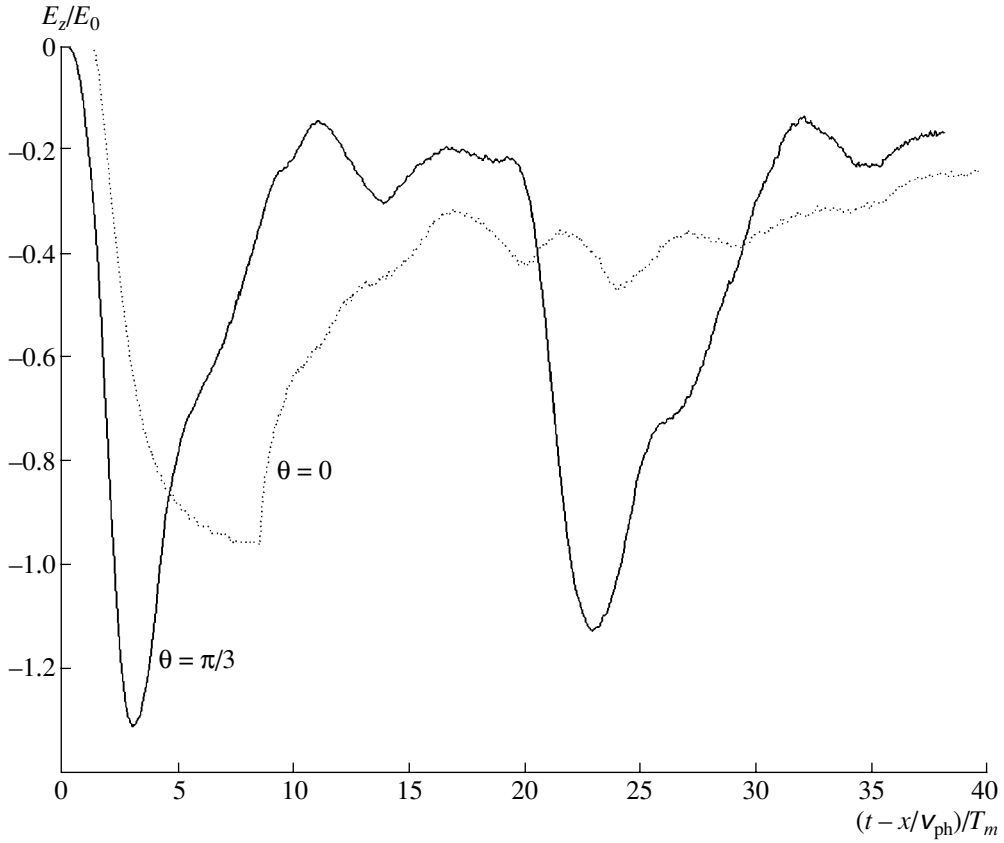

Fig. 5. Time evolutions of the electric field E_z in the middle of the accelerating gap in the case of the oblique ($\theta = \pi/3$) incidence of the ionizing radiation on an infinitely long (one-dimensional) emitting element (with allowance for the generation of EM waves) and in the case of normal ($\theta = 0$) incidence (with no generation of EM waves). The calculations were carried out for $a = 2$.

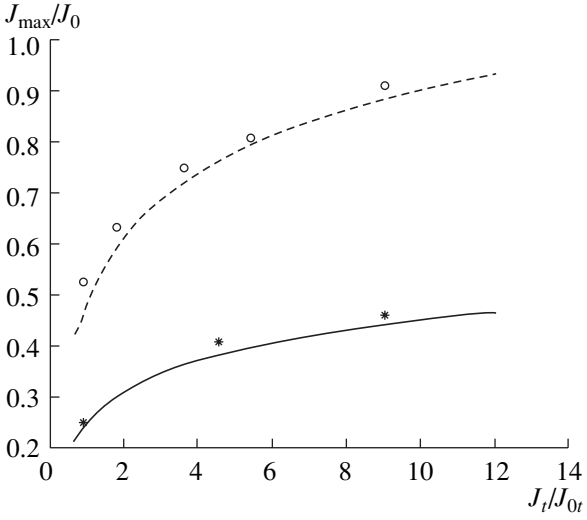

Fig. 6. Anode current density as a function of the growth rate of the emission current density at the cathode in the case of the oblique ($\theta = \pi/3$) incidence of the ionizing radiation on an infinitely long (one-dimensional) emitting element [with allowance for the generation of EM waves, formula (27)] and in the case of normal ($\theta = 0$) incidence [with no generation of EM waves, formula (17)]. The symbols show the results of numerical calculations.

end, the larger the amplitude of the generated EM wave and the closer the parameters of the superluminal current pulse to their limiting values corresponding to an infinitely long emitter (Figs. 6, 7). For an emitter of fixed length, an increase in the rate of electron emission from the cathode is seen to somewhat reduce the degradation of the parameters of the electron dipole moment due to the effect of the guided EM wave (Fig. 9); however, as the length of the emitting surface increases, the parameters in question always approach their asymptotic values given by formulas (27).

3.2. Effects of the Finite Transverse Dimensions of the Emitting Element

For the width of an accelerating diode not to significantly distort the spatiotemporal distribution of the electrons over the dipole layer, it should be much larger than the distance between the electrodes. Calculations show that the anode current and the derivatives of the dipole moment are essentially the same as those predicted by the one-dimensional model. The difference between the numerical and analytical results is the largest at distances from the capacitor edge that are shorter than the distance between the electrodes.

Since the intensity of radiation generated in a distant source region is determined by the second derivative of the surface density of the dipole moment and the emitter area, which is the anode area, the boundary effects associated with the finite width of the capacitor reduce the effective width of the emitting surface by an amount of about $(1–2) \times L$.

3.3. Calculation of the EM Fields

Recall that an elementary microwave source supplied by a superluminal emission current pulse that is formed by an accelerating diode generates two wideband radiation pulses—a directed pulse and a guided pulse.

At sufficiently large distances R from the emitting region, the amplitude of the EM field of the directed wave can be estimated in terms of the delayed potentials. The magnetic field is easier to estimate:

$$\mathbf{H} \simeq \frac{1}{c^2 R}\int dV' \left[\frac{\partial}{\partial t}\mathbf{j}\left(t - \frac{|\mathbf{r}-\mathbf{r}'|}{c}, \mathbf{r}'\right), \frac{\mathbf{r}-\mathbf{r}'}{|\mathbf{r}-\mathbf{r}'|}\right] \approx \frac{1}{c^2 R}\int_{S_a} dS[\ddot{\mathbf{P}} \times \mathbf{n}], \quad (28)$$

where S_a is the anode area.

For an emitting element of infinite width ($-\infty < y < \infty$), this expression yields the following estimate for the magnetic field:

$$H_0 = \frac{L_x \sin\theta}{\sqrt{R}(cT_0)^{3/2}} P_0. \quad (29)$$

Figure 11 presents the results of two-dimensional calculations of the magnetic field in a distant region of the microwave source, $-\infty < y < \infty$ and $R/D = 5$, where $D = L_x \cos\theta$ is the effective length of the radiating element. We can see that, since the parameters of the generated radiation (the derivatives of the dipole moment in Figs. 7, 8) approach their asymptotic values as the growth rate of the emission current increases, the amplitude of the directed EM radiation pulse and its characteristic rise time also approach their limiting values, in which case the field amplitude reaches its maximum and the characteristic wavelength reaches its minimum. A change in the characteristic wavelength of the EM radiation alters its directional pattern, which is characterized by the diffractional divergence angle

$$\theta_D = \frac{\lambda}{D} = \frac{2\pi c T_0}{D}. \quad (30)$$

Figure 12 shows the angular distributions of the maximum radiation flux density with respect to the direction in which the ionizing radiation is reflected for different growth rates of the emission current. As can be seen, an increase in the emission rate and the corresponding decrease in the characteristic radiation wavelength increases the directionality of the EM emission from the source, which radiates energy into a cone with a solid angle of about $2\theta_D$ (Fig. 13).

The characteristic wavelength of the EM radiation generated in the accelerating gap is far longer than the

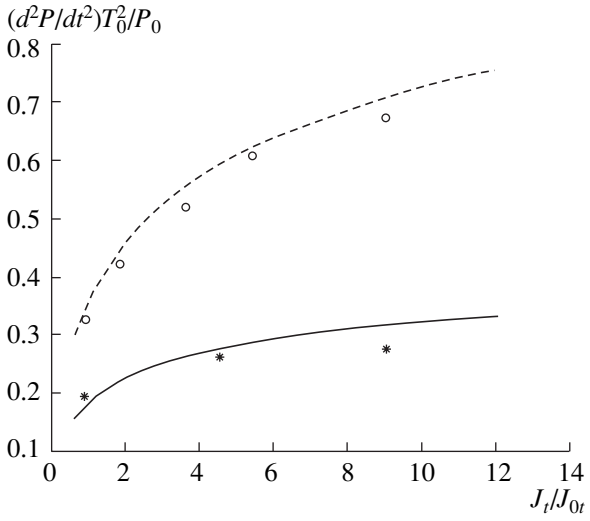

Fig. 7. Second derivative of the electron dipole moment in the half-space above the anode as a function of the growth rate of the emission current density at the cathode in the case of the oblique ($\theta = \pi/3$) incidence of the ionizing radiation on an infinitely long (one-dimensional) emitting element [with allowance for the generation of EM waves, formula (25)] and in the case of normal ($\theta = 0$) incidence [with no generation of EM waves, formula (19)]. The symbols show the results of numerical calculations.

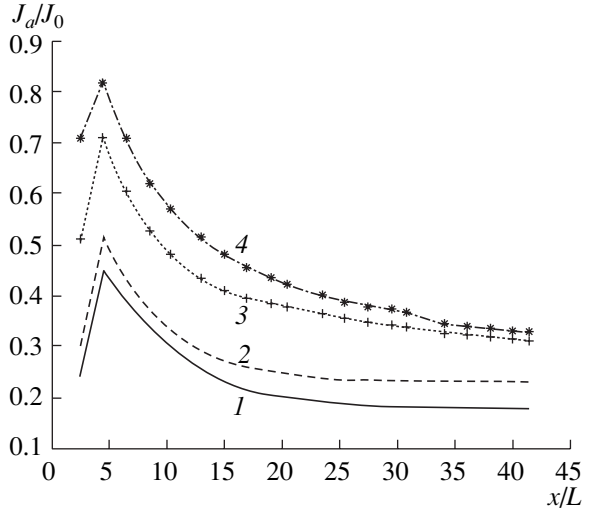

Fig. 8. Profiles of the second derivative of the electron dipole moment along a capacitor in the case of the oblique ($\theta = \pi/3$) incidence of the ionizing radiation for different growth rates of the emission current density at the cathode: a = (*1*) 0.45, (*2*) 0.64, (*3*) 1.42, and (*4*) 2.0.

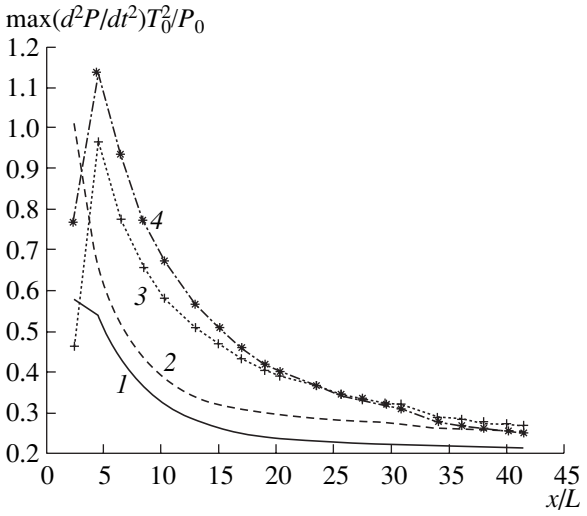

Fig. 9. Profiles of the anode current along a capacitor in the case of the oblique ($\theta = \pi/3$) incidence of the ionizing radiation for different growth rates of the emission current density at the cathode: a = (*1*) 0.45, (*2*) 0.64, (*3*) 1.42, and (*4*) 2.0.

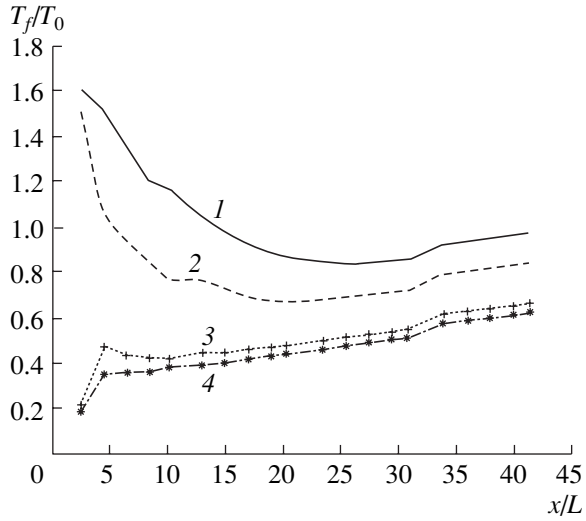

Fig. 10. Rise time of the second derivative of the electron dipole moment as a function of the longitudinal coordinate in the case of the oblique ($\theta = \pi/3$) incidence of the ionizing radiation for different growth rates of the emission current density at the cathode: a = (*1*) 0.45, (*2*) 0.64, (*3*) 1.42, and (*4*) 2.0.

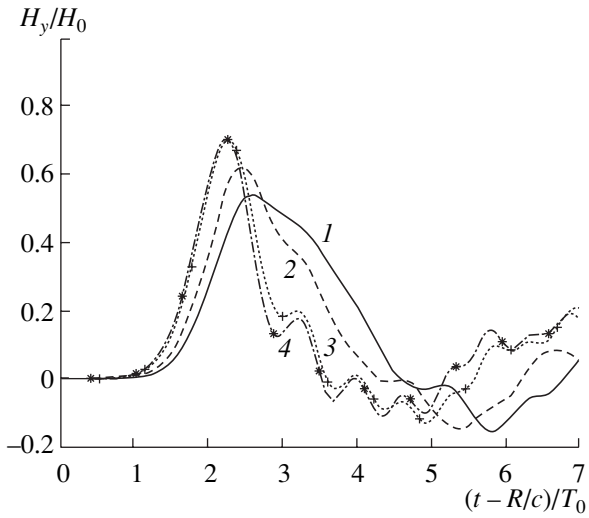

Fig. 11. Time evolutions of the magnetic field of the generated EM radiation propagating in the direction in which obliquely ($\theta = \pi/3$) incident ionizing radiation is reflected for R/D = 5 and for different growth rates of the emission current density at the cathode: a = (*1*) 0.45, (*2*) 0.64, (*3*) 1.42, and (*4*) 2.0.

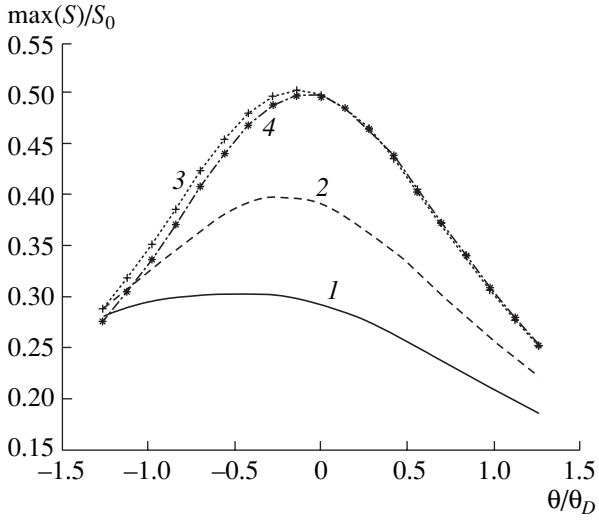

Fig. 12. Angular distributions of the maximum EM radiation flux density for different growth rates of the emission current density at the cathode: a = (*1*) 0.45, (*2*) 0.64, (*3*) 1.42, and (*4*) 2.0.

critical wavelength; i.e., the waveguide formed by the cathode and anode is overcritical. Nevertheless, a guided EM wave can propagate in the waveguide because of the propagation of the emission current along the cathode. As a result, the EM field emitted through the open end of the waveguide is dipolar and coherent with the directed EM wave emitted by a superluminal current source (both of them are generated by the same ionizing radiation pulse and are in phase with one another). Figure 14 illustrates the results from two-dimensional simulations of the generation of EM radiation and its propagation away from an elementary emitter with (a) a screened and (b) an open waveguide end. In both figures, we see the directed EM radiation

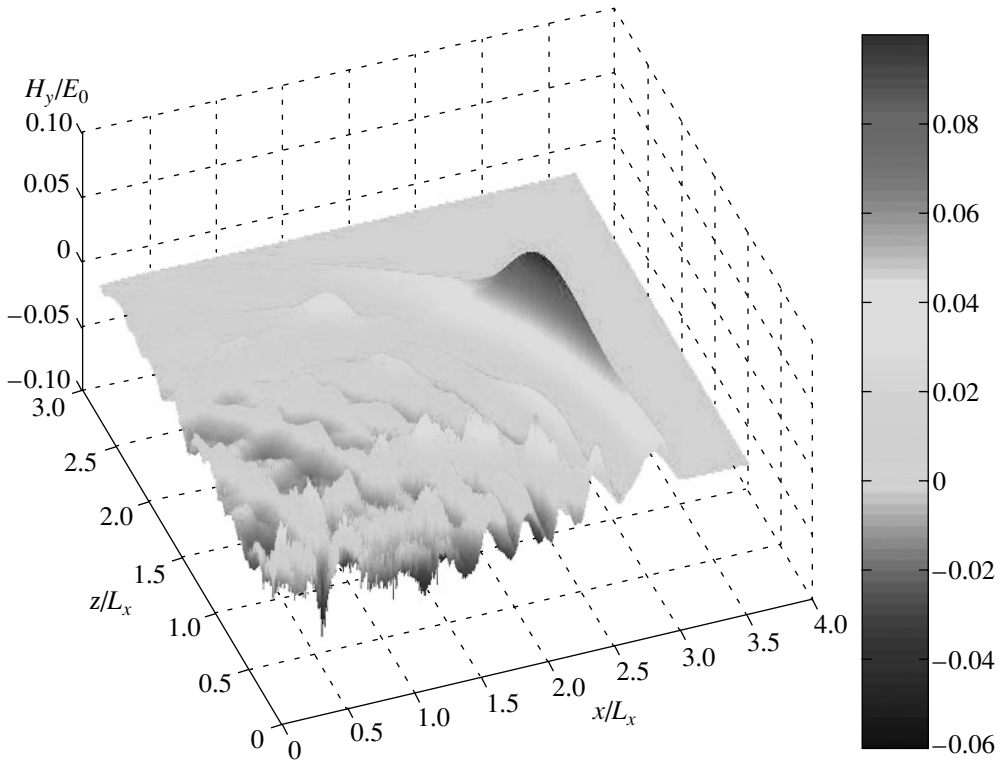

Fig. 13. Spatial distribution of the magnetic field of a directed EM pulse generated by an elementary emitter at the time $t = 5$ ns. The emission current from the cathode increases according to the law $J_t = 5 \times 10^{11}$ A/(cm^2 s) ($a = 2.0$).

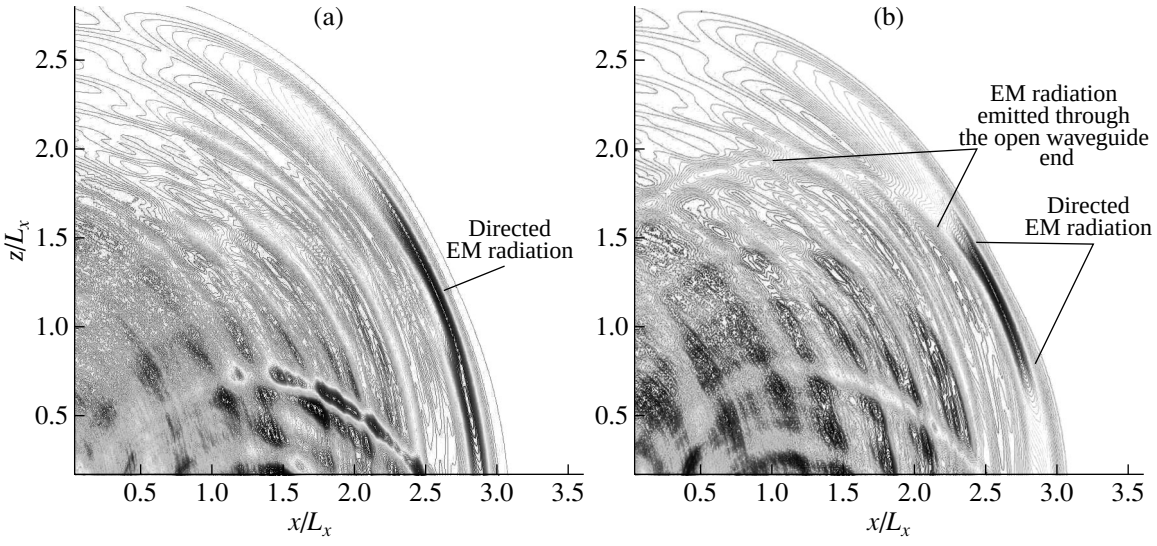

Fig. 14. Spatial distribution of the magnetic field at the time $t = 5$ ns for two versions of an elementary emitter: (a) with a screened and (b) with an open end of the waveguide structure. The emission current from the cathode increases according to the law $J_t = 5 \times 10^{11}$ A/(cm^2 s) ($a = 2.0$).

from a superluminal current source. In Fig. 14b, we also see a cylindrical EM wave emitted through the open end of the waveguide structure. Accordingly, in an emitter with an open waveguide end, the EM field amplitude and the energy flux in the direction in which the radiation is emitted most intensely are seen to sub-

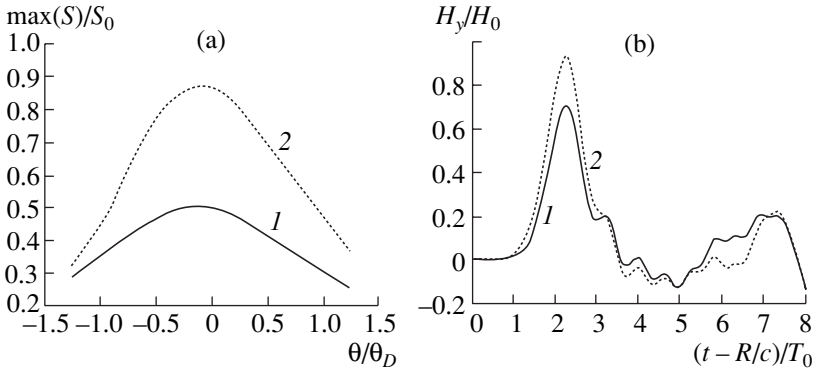

Fig. 15. (a) Angular distributions of the EM radiation flux density and (b) temporal profiles of an EM radiation pulse for two versions of an elementary emitter: (*1*) with a screened and (*2*) an open end of the waveguide structure for $a = 1.42$ and $R/D = 5$. The emission current from the cathode increases according to the law $J_t = 5 \times 10^{11}$ A/(cm^2 s).

stantially exceed those in a system with a screened waveguide end (Fig. 15).

4. CONCLUSION

Our studies have shown that the parameters of an elementary superluminal source obey scaling relations in terms of the growth rate of the electron emission current from the cathode and the parameters of the accelerating diode (the voltage and the distance between the electrodes). The limiting anode current density and the limiting intensity and energy of the EM radiation that can be achieved in such a source have been determined. The maximum achievable anode current density is substantially lower than the steady-state limiting current density because of the additional restrictions on the electron current dynamics that are associated with the influence of the field of the generated EM radiation. The effect of the finite dimensions of the accelerating system on the parameters of the emitter has been investigated. The spatiotemporal characteristics of the emitted EM fields have been obtained as functions of the parameters of the configuration of an accelerating system and the rate of electron emission from the cathode.

ACKNOWLEDGMENTS

This work was supported in part by the International Science and Technology Center (project no. 1158-2000) and the Russian Foundation for Basic Research (project no. 01-02-17629).

REFERENCES

1. Yu. N. Lazarev and P. V. Petrov, Pis'ma Zh. Éksp. Teor. Fiz. **60** (9), 625 (1994) [JETP Lett. **60**, 634 (1994)].
2. Yu. N. Lazarev and P. V. Petrov, Zh. Éksp. Teor. Fiz. **115** (5), 1689 (1999) [JETP **88**, 926 (1999)].
3. A. A. Rukhadze, L. S. Bogdankevich, S. E. Rosinskiĭ, and V. G. Rukhlin, *Physics of High-Current Relativistic Electron Beams* (Atomizdat, Moscow, 1981).
4. L. S. Bogdankevich and A. A. Rukhadze, Usp. Fiz. Nauk **103**, 609 (1971) [Sov. Phys. Usp. **14**, 163 (1971)].
5. A. A. Rukhadze, P. V. Rybak, Ya. K. Khodataev, and V. Shokri, Fiz. Plazmy **22**, 358 (1996) [Plasma Phys. Rep. **22**, 326 (1996)].
6. A. E. Dubinov, Fiz. Plazmy **26**, 439 (2000) [Plasma Phys. Rep. **26**, 409 (2000)].
7. E. V. Diyankova and P. V. Petrov, Preprint No. 99 (All-Russia Research Institute of Experimental Physics, Russian Federal Nuclear Center, Sarov, 1996).
8. A. V. Bessarab, A. V. Kunin, S. P. Martynenko, *et al.*, Tr. RFYaTs–VNIIÉF (Nauchno-Issledovatel'skoe Izd., Sarov, 2001), No. 1, p. 518.
9. *Partial Differential Equation Toolbox User's Guide* (The Mathworks Inc., 1997).

Translated by G.V. Shepekina

Plasma Physics Reports, Vol. 29, No. 6, 2003, pp. 503–511. Translated from Fizika Plazmy, Vol. 29, No. 6, 2003, pp. 540–549.

NONLINEAR PHENOMENA

Nonlinear Scattering of Two Counterpropagating Laser Pulses in an Underdense Plasma

A. A. Frolov

Institute for High Energy Densities, Associated Institute for High Temperatures, Russian Academy of Sciences, Izhorskaya ul. 13/19, Moscow, 125412 Russia

Received November 5, 2002

Abstract—A study is made of the interaction ("collision") of two laser pulses with the same frequency but different durations, propagating toward one another in a low-density plasma. It is found that, in the interaction region, the excitation of small-scale plasma fields localized within a distance on the order of the length of the longer pulse is accompanied by the backscattering of each of the pulses. The frequency shift of the backscattered radiation and its duration depend strongly on the lengths of the interacting pulses. It is shown that the spectrum of the long backscattered radiation "tail" that arises behind the shorter pulse as a result of its interaction with the longer pulse contains satellites shifted from the laser frequency by the plasma frequency. *© 2003 MAIK "Nauka/Interperiodica".*

INTRODUCTION

In recent years, increased attention has been given to the nonlinear effects accompanying the propagation of laser pulses in plasmas. Of particular interest is the investigation of the physical processes occurring in the interaction (collision) between two laser pulses propagating in a plasma toward one another, with the focus on such issues as the amplification of pulses [1, 2], the acceleration of electron bunches [3, 4], the excitation of superstrong wake fields [5], the generation of Bragg mirrors [6], the possibility of deriving information about the structure of the pulses [7], and some other problems [8–11].

In this paper, the nonlinear scattering of two laser pulses during their interaction in an underdense plasma is investigated in one-dimensional geometry. It is shown that, in the interaction region, laser pulses with the same frequency but different lengths generate small-scale plasma perturbations localized within a distance on the order of the length of the longer pulse. In interacting with the small-scale perturbations, each of the laser pulses is backscattered; the frequency shift and duration of the backscattered radiation depend strongly on the lengths of the colliding pulses. In the interaction of two long laser pulses, each of them is backscattered into a pulse whose frequency is equal to the laser carrier frequency and whose duration is determined by the length of the laser pulse propagating in the opposite direction. In the case of short laser pulses, the spectrum of the backscattered pulses contains satellites whose frequencies are shifted from the laser frequency by an amount determined by the plasma frequency and the ratio between the durations of the interacting pulses. In the case of interaction of a long laser pulse with a short counterpropagating laser pulse, the duration of the radiation pulse scattered in the propagation direction of the shorter pulse is determined by the length of the longer pulse. The spectrum of the long backscattered radiation tail that arises behind the shorter laser pulse as a result of scattering contains satellites shifted from the laser frequency by the plasma frequency.

1. SMALL-SCALE PLASMA DENSITY PERTURBATIONS GENERATED IN THE INTERACTION BETWEEN TWO COUNTERPROPAGATING LASER PULSES

We consider two laser pulses with the same frequency but different durations, propagating toward one another along the z-axis in a low-density plasma with the electron density N_{0e} (Fig. 1a). The electric field of laser radiation can be represented as

$$\mathbf{E}_L(z,t) = \frac{1}{2}\exp(-i\omega_0 t) \times [\mathbf{E}_+(z,t)\exp(ik_0 z) + \mathbf{E}_-(z,t)\exp(-ik_0 z)] + \text{c.c.}, \quad (1.1)$$

where $k_0 = (\omega_0/c)\sqrt{\varepsilon(\omega_0)}$; $\varepsilon(\omega) = 1 - \omega_p^2/\omega^2$ is the plasma dielectric function, ω_0 is the laser frequency, $\omega_p = \sqrt{4\pi e^2 N_{0e}/m_e}$ is the plasma frequency ($\omega_0 \gg \omega_p$), e and m_e are the charge and mass of an electron, and c is the speed of light. The amplitudes $\mathbf{E}_\pm(z,t)$ of the electric fields of laser pulses propagating from left to right (the plus sign) and from right to left (the minus sign) are assumed to vary slowly on the spatial and time scales k_0^{-1} and ω_0^{-1}.

When laser pulses begin to overlap, they generate small-scale electron density perturbations $\delta N_e(z,t)$. In

1063-780X/03/2906-0503$24.00

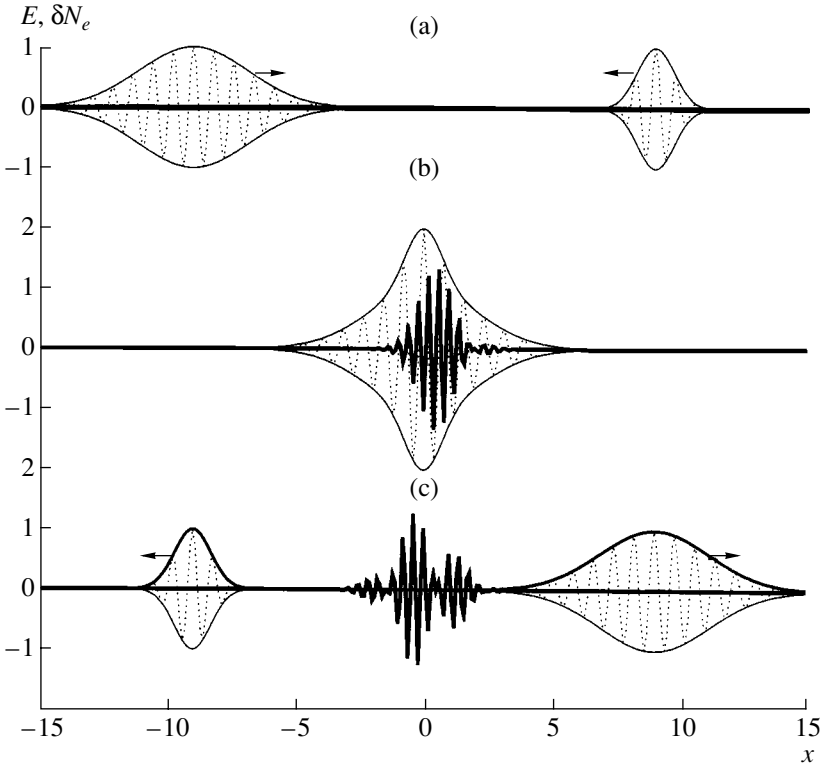

Fig. 1. Schemes illustrating the interaction between a long laser pulse and a short counterpropagating laser pulse and the generation of small-scale plasma fields at different times. The envelopes of the laser electric field and high-frequency oscillations within the laser pulses are represented by light solid curves and dotted curves, respectively. The field amplitudes are given in dimensionless units. The heavy solid curves show the reduced amplitude of the density perturbations, $\frac{\delta N_e}{N_{0e}}\frac{m_e^2\omega_0^2\omega_p^2}{2e^2k_0^2|\mathbf{E}_{0+}\mathbf{E}_{0-}|}$, calculated as a function of the dimensionless coordinate $x = \frac{z}{\sqrt{2}L_-}$ from expression (1.5) at $\omega_p = 0.25\omega_0$ for two laser pulses with the same intensities but different durations $\omega_p\tau_- = \sqrt{2}$, $\tau_+ = 3\tau_-$. Plots (a), (b), and (c) refer to the dimensionless times $\frac{t}{\sqrt{2}\tau_-} = -9$, 0, and 9.

the linear approximation ($\delta N_e \ll N_{0e}$) and under the condition

$$\frac{e^2|\mathbf{E}_{0+}\mathbf{E}_{0-}|}{m_e^2\omega_0^2c^2} \ll \frac{\omega_p^2}{\omega_0^2}, \tag{1.2}$$

the perturbations can be described by the equation [6]

$$\left(\frac{\partial^2}{\partial t^2} + \omega_p^2\right)\frac{\delta N_e}{N_{0e}} = \frac{e^2}{4m_e^2\omega_0^2} \times \frac{\partial^2}{\partial z^2}[(\mathbf{E}_+\mathbf{E}_-^*)\exp(2ik_0z) + (\mathbf{E}_+^*\mathbf{E}_-)\exp(-2ik_0z)]. \tag{1.3}$$

We solve Eq. (1.3) assuming that, in the interaction region, the pulses are Gaussian in shape:

$$\mathbf{E}_+(z,t) = \mathbf{E}_{0+}\exp(-\xi^2/2L_+^2), \quad \mathbf{E}_-(z,t) = \mathbf{E}_{0-}\exp(-\eta^2/2L_-^2), \tag{1.4}$$

where $\xi = z - V_gt$ and $\eta = z + V_gt$ are the spatial coordinates in the comoving frames of reference of the propagating pulses, $V_g = (k_0/\omega_0)c^2$ is the group velocity of the pulses, $L_\pm$ are their lengths, and the vectors $\mathbf{E}_{0\pm}$ characterize their polarization and the maximum amplitudes of their electric fields. The coordinate system is chosen in such a way that, at the initial instant $t = 0$, the functions $\mathbf{E}_+(z,t)$ and $\mathbf{E}_-(z,t)$ are maximum at the point $z = 0$ (Fig. 1b).

With allowance for relationships (1.4), the solution to Eq. (1.3) that satisfies the condition for the electron density to be unperturbed before the two linearly polarized laser pulses start to interact has the form

$$\frac{\delta N_e(z,t)}{N_{0e}} = -\frac{2e^2k_0^2\mathbf{E}_{0+}\mathbf{E}_{0-}}{m_e^2\omega_0^2\omega_p^2} \times \exp\left(-\frac{2z^2}{L_+^2 + L_-^2}\right)\Phi\left(\frac{t}{\tau} + \frac{z}{L}\frac{\tau_+^2 - \tau_-^2}{\tau_+^2 + \tau_-^2}, \omega_p\tau\right)\cos(2k_0z), \tag{1.5}$$

where $\tau = \frac{\sqrt{2}\tau_+\tau_-}{\sqrt{\tau_+^2 + \tau_-^2}}$, $L = V_g\tau = \frac{\sqrt{2}L_+L_-}{\sqrt{L_+^2 + L_-^2}}$, and $\tau_\pm = L_\pm/V_g$ is the duration of the pulses. The time dependence enters solution (1.5) through the function $\Phi(x, a)$ [6]:

$$\Phi(x, a) = a\int_{-\infty}^{x} dy \sin[a(x-y)]\exp(-y^2). \quad (1.6)$$

It should be noted that the amplitude of the density perturbations (1.5) depends on the polarization of the laser pulses and is maximum when the vectors $\mathbf{E}_{0+}$ and $\mathbf{E}_{0-}$ are parallel or antiparallel to each other. When the electric fields of the pulses are mutually orthogonal, $\mathbf{E}_{0+}\mathbf{E}_{0-} = 0$, small-scale electron density perturbations (1.5) are not generated. The reason is that, in this case, the Lorentz force vanishes, because, in the field of either pulse, the electrons move along the magnetic field of the other pulse.

Now, using asymptotic expansions of the function $\Phi(x, a)$, we investigate the spatiotemporal evolution of density perturbations (1.5) generated by laser pulses with different durations τ_+ and τ_-.

In the case of collision between two long laser pulses ($\omega_p\tau_\pm \gg 1$), the parameter $\omega_p\tau$ is large and function (1.6) is described by the asymptotic formula [6]

$$\Phi(x, a) = \frac{a^2}{a^2 + 4x^2}\exp(-x^2) + \frac{\sqrt{\pi}}{2}a\exp\left(-\frac{a^2}{4}\right)\sin(ax), \quad (1.7)$$

which is valid for $a \gg 1, x$. As a result, we arrive at the following expression for density perturbations (1.5):

$$\frac{\delta N_e(z, t)}{N_{0e}} = -\frac{2e^2k_0^2\mathbf{E}_{0+}\mathbf{E}_{0-}}{m_e^2\omega_0^2\omega_p^2} \times \left\{\exp\left(-\frac{2t^2}{\tau_+^2 + \tau_-^2} - \frac{1}{L^2}\left(z + V_g t\frac{\tau_+^2 - \tau_-^2}{\tau_+^2 + \tau_-^2}\right)^2\right) + \frac{\sqrt{\pi}}{2}\omega_p\tau\exp\left(-\frac{2z^2}{L_+^2 + L_-^2} - \frac{\omega_p^2\tau^2}{4}\right) \times \sin\left(\omega_p t + k_p z\frac{\tau_+^2 - \tau_-^2}{\tau_+^2 + \tau_-^2}\right)\right\}\cos(2k_0z). \quad (1.8)$$

The first term in parentheses in expression (1.8) describes quasistatic electron density perturbations, which are excited only during the time interval $\Delta t \approx \sqrt{(\tau_+^2 + \tau_-^2)/2}$ and disappear after the interaction. During the entire interaction process, the amplitude of the density perturbations excited in the interaction between two pulses with the same duration ($\tau_+ = \tau_-$) is maximum at $z = 0$. In the case of pulses with different durations ($\tau_+ \neq \tau_-$), the position of maximum amplitude moves at the velocity $V = -V_g\frac{\tau_+^2 - \tau_-^2}{\tau_+^2 + \tau_-^2}$ in the propagation direction of the shorter pulse. The second term in parentheses in expression (1.8) implies that the plasma oscillations remaining in the interaction region after the interaction process has come to an end are exponentially small.

In the case of collision between two short laser pulses ($\omega_p\tau_\pm \leq 1$) or between a short pulse ($\omega_p\tau_- \leq 1$) and a long pulse ($\omega_p\tau_+ \gg 1$), the parameter $\omega_p\tau$, characterizing the time during which the pulses overlap, is small, $\omega_p\tau \leq 1$. In this case, small-scale plasma perturbations are excited by a short-term driving force (in a shocklike fashion). Using the asymptotic representation [6]

$$\Phi(x, a) = \sqrt{\pi}a\exp(-a^2/4)\sin(ax), \quad (1.9)$$

which is valid for $x > 0$ such that $x \gg 1, a$, we arrive at the following expression for the density perturbations that remain in the interaction region after the interaction process has come to an end:

$$\frac{\delta N_e(z, t)}{N_{0e}} = -2\sqrt{\pi}\omega_p\tau\frac{e^2k_0^2\mathbf{E}_{0+}\mathbf{E}_{0-}}{m_e^2\omega_0^2\omega_p^2} \times \exp\left(-\frac{2z^2}{L_+^2 + L_-^2} - \frac{\omega_p^2\tau^2}{4}\right)\sin\left(\omega_p t + k_p z\frac{\tau_+^2 - \tau_-^2}{\tau_+^2 + \tau_-^2}\right) \times \cos(2k_0z). \quad (1.10)$$

The plasma oscillations that are excited in the interaction of two pulses with the same duration ($\tau_+ = \tau_-$) are long-lived small-scale standing waves. The spatiotemporal evolution of the plasma perturbations generated by two laser pulses with different durations is more complicated. In the interaction between a short and a long laser pulse, small-scale wake plasma fields are excited behind the shorter pulse (Fig. 1b). The small-scale plasma oscillations that remain in the interaction region after the interaction process has come to an end are localized within a distance on the order of the length of the longer pulse (Fig. 1c). In this case, the positions of the zeros of the density perturbation amplitude and of its maxima and minima are determined by the function $\cos(2k_0z)$ and are fixed in space, and the envelope of the small-scale perturbations moves in the propagation direction of the shorter pulse.

2. SCATTERING OF LASER PULSES BY SMALL-SCALE PLASMA FIELDS

In interacting with one another, two laser pulses generate small-scale plasma fields and are backscattered by them. For the pulse propagating from left to right, the electric field $\mathbf{E}_S^+(z, t)$ of the backscattered radiation satisfies the conventional equation of scattering theory [12]:

$$\left(\frac{\partial^2}{\partial t^2} + \omega_p^2 - c^2\frac{\partial^2}{\partial z^2}\right)\mathbf{E}_S^+(z, t) = -\omega_p^2\frac{\delta N_e}{N_{0e}}\left[\frac{1}{2}\mathbf{E}_+\exp(-i\omega_0 t + ik_0 z) + \text{c.c.}\right], \quad (2.1)$$

where the density perturbations δN_e are given by expression (1.5). An analogous equation is valid for a laser pulse propagating in the opposite direction.

To solve Eq. (2.1), we apply the Fourier transformation in time and in the longitudinal coordinate:

$$\mathbf{E}_S^+(z, t) = \int\frac{d\omega dk}{(2\pi)^2}\exp(-i\omega t + ikz)\mathbf{E}_S^+(\omega, k),$$
$$\mathbf{E}_S^+(\omega, k) = \int dt dz\exp(i\omega t - ikz)\mathbf{E}_S^+(z, t). \quad (2.2)$$

With allowance for expressions (1.4), the Fourier transformed electric field of the scattered pulse has the form

$$\mathbf{E}_S^+(\omega, k) = \frac{1}{2}\mathbf{E}_{0+}(2\pi)^{3/2}L_+\frac{\omega_p^2}{\omega^2\varepsilon(\omega) - c^2k^2} \times\int\frac{d\omega' dk'}{(2\pi)^2}\frac{\delta N_e(\omega - \omega', k - k')}{N_{0e}} \times\left\{\delta[\omega' - \omega_0 - (k' - k_0)V_g]\exp\left(-\frac{(\omega' - \omega_0)^2\tau_+^2}{2}\right)\right.$$
$$\left. + \delta[\omega' + \omega_0 - (k' + k_0)V_g]\exp\left(-\frac{(\omega' + \omega_0)^2\tau_+^2}{2}\right)\right\}, \quad (2.3)$$

in which the Fourier transformed density perturbations $\delta N_e(\omega, k)$ can be found from Eq. (1.3):

$$\frac{\delta N_e(\omega, k)}{N_{0e}} = \frac{e^2\mathbf{E}_{0+}\mathbf{E}_{0-}}{4m_e^2\omega_0^2}\frac{\pi k^2 V_g\tau_+\tau_-}{\omega^2\varepsilon(\omega)}\exp\left(-\frac{\omega^2\tau^2}{4}\right) \times\left\{\exp\left[-\left(k - 2k_0 + \frac{\omega}{V_g}\frac{\tau_+^2 - \tau_-^2}{\tau_+^2 + \tau_-^2}\right)^2\frac{L_+^2 + L_-^2}{8}\right]\right.$$
$$\left. + \exp\left[-\left(k + 2k_0 + \frac{\omega}{V_g}\frac{\tau_+^2 - \tau_-^2}{\tau_+^2 + \tau_-^2}\right)^2\frac{L_+^2 + L_-^2}{8}\right]\right\}. \quad (2.4)$$

Taking into account expression (2.4), we integrate over the frequencies ω' and wavenumbers k' in formula (2.3) to obtain

$$\mathbf{E}_S^+(\omega, k) = \frac{ie^2\mathbf{E}_{0+}(\mathbf{E}_{0+}\mathbf{E}_{0-})\pi^{3/2}k_p\tau_-}{16\sqrt{2}m_e^2\omega_0^2[\omega^2\varepsilon(\omega) - c^2k^2]} \times\left\{\exp\left[-\left(k + k_0 - \frac{\omega - \omega_0}{V_g}\right)^2\frac{L_+^2 + L_-^2}{8}\right]\exp\left[-\frac{(\omega - \omega_0)^2\tau_+^2}{2}\right]\right.$$
$$\times\left[L_+^2\left(k - k_0 - \frac{\omega - \omega_0 + \omega_p}{V_g}\right)^2[1 - \text{erf}(i\alpha_-)]\right.$$
$$\left.\times\exp\left(-\frac{\omega_p\tau_+^2}{2}[3(\omega - \omega_0) + 2\omega_p - (k + k_0)V_g]\right)\right.$$
$$\left. - L_+^2\left(k - k_0 - \frac{\omega - \omega_0 - \omega_p}{V_g}\right)^2[1 - \text{erf}(i\alpha_+)]\right.$$
$$\left.\times\exp\left(\frac{\omega_p\tau_+^2}{2}[3(\omega - \omega_0) - 2\omega_p - (k + k_0)V_g]\right)\right] \quad (2.5)$$
$$+\exp\left[-\left(k - k_0 - \frac{\omega + \omega_0}{V_g}\right)^2\frac{L_+^2 + L_-^2}{8} - \frac{(\omega + \omega_0)^2\tau_+^2}{2}\right]$$
$$\times\left[L_+^2\left(k + k_0 - \frac{\omega + \omega_0 + \omega_p}{V_g}\right)^2[1 - \text{erf}(i\beta_-)]\right.$$
$$\left.\times\exp\left(-\frac{\omega_p\tau_+^2}{2}[3(\omega + \omega_0) + 2\omega_p - (k - k_0)V_g]\right)\right.$$
$$\left. - L_+^2\left(k + k_0 - \frac{\omega + \omega_0 - \omega_p}{V_g}\right)^2[1 - \text{erf}(i\beta_+)]\right.$$
$$\left.\times\exp\left(\frac{\omega_p\tau_+^2}{2}[3(\omega + \omega_0) - 2\omega_p - (k - k_0)V_g]\right)\right]\right\},$$

where $k_p = \omega_p/V_g$ is the wavenumber of the plasma oscillations, $\text{erf}(z) = \frac{2}{\sqrt{\pi}}\int_0^z dt\exp(-t^2)$ is the error function of the complex argument, $\alpha_\pm = \frac{\tau_+}{4}[(k + k_0)V_g - 3(\omega - \omega_0) \pm 4\omega_p]$, and $\beta_\pm = \frac{\tau_+}{4}[(k - k_0)V_g - 3(\omega + \omega_0) \pm 4\omega_p]$.

The spectral density $\mathbf{E}_S^+(\omega, z)$ of the electric field of the scattered pulse can be solved for by taking the inverse Fourier transformation of expression (2.5) in the longitudinal coordinate [see the first of formulas (2.2)]. Applying the saddle point method, we find that the main contribution to the integral over the wavenumbers comes from the residue at the pole $k = -\omega\sqrt{\varepsilon(\omega)}/c$, which corresponds to backscattering.

Then, at large distances $z < 0$ from the region where the density perturbations are localized, the Fourier transformed backscattered field has the form

$$\mathbf{E}_S^+(\omega, z) = \frac{\pi^{3/2}\omega_p\tau_+\tau_-}{2\sqrt{2}}k_0L_+\frac{e^2\mathbf{E}_{0+}(\mathbf{E}_{0+}\mathbf{E}_{0-})}{4m_e^2\omega_0^2c^2}$$

$$\times\left\{\exp\left[-i\frac{\omega}{c}\sqrt{\varepsilon(\omega)}z-\frac{(\omega-\omega_0)^2\tau_-^2}{2}\right]\right.$$

$$\times\{[1+\mathrm{erf}(i[\omega-\omega_0+\omega_p]\tau_+)]$$

$$\times\exp(-[\omega-\omega_0+\omega_p]^2\tau_+^2)$$

$$-[1+\mathrm{erf}(i[\omega-\omega_0-\omega_p]\tau_+)]$$

$$\left.\times\exp(-[\omega-\omega_0-\omega_p]^2\tau_+^2)\right\} \qquad (2.6)$$

$$+\exp\left[i\frac{\omega}{c}\sqrt{\varepsilon(\omega)}z-\frac{(\omega+\omega_0)^2\tau_-^2}{2}\right]$$

$$\times\{[1+\mathrm{erf}(i[\omega+\omega_0+\omega_p]\tau_+)]$$

$$\times\exp(-[\omega+\omega_0+\omega_p]^2\tau_+^2)$$

$$-[1+\mathrm{erf}(i[\omega+\omega_0-\omega_p]\tau_+)]$$

$$\times\exp(-[\omega+\omega_0-\omega_p]^2\tau_+^2)\}\}.$$

For the pulse propagating from left to right, the spatiotemporal structure of the backscattered radiation can be evaluated by taking the inverse Fourier transformation of formula (2.6) in time:

$$\mathbf{E}_S^+(z, t) = \sqrt{\pi}k_0L_+\frac{e^2\mathbf{E}_{0+}(\mathbf{E}_{0+}\mathbf{E}_{0-})}{4m_e^2\omega_0^2c^2}$$

$$\times\exp\left[-\frac{\eta^2}{2(L_-^2+2L_+^2)}\right] \qquad (2.7)$$

$$\times\Phi\left(\frac{\eta}{\sqrt{2}L_-\sqrt{1+\tau_-^2/2\tau_+^2}},\frac{\sqrt{2}\omega_p\tau_-}{\sqrt{1+\tau_-^2/2\tau_+^2}}\right)\sin(\omega_0t+k_0z).$$

In deriving expression (2.7) from formula (2.6), we used the following expansion in the small deviation $\Omega = \omega - \omega_0$ from the laser frequency:

$$\frac{\omega}{c}\sqrt{\varepsilon(\omega)}\approx k_0+\frac{\Omega}{V_g}.$$

In this expansion, we neglected the terms of the second order in Ω, which indicates the smallness of the dispersive spreading of the backscattered radiation pulse and is justified under the condition

$$z < k_0L_-^2\frac{\omega_0^2}{\omega_p^2}.$$

Expression (2.7) can also be obtained directly by solving a reduced version of Eq. (2.1) with allowance for relationship (1.5).

For the pulse propagating from right to left, the electric field of the backscattered radiation is obtained in an analogous manner. At large distances $z > 0$ from the interaction region, it has the form

$$\mathbf{E}_S^-(z, t) = \sqrt{\pi}k_0L_-\frac{e^2\mathbf{E}_{0-}(\mathbf{E}_{0+}\mathbf{E}_{0-})}{4m_e^2\omega_0^2c^2}$$

$$\times\exp\left[-\frac{\xi^2}{2(L_+^2+2L_-^2)}\right] \qquad (2.8)$$

$$\times\Phi\left(-\frac{\xi}{\sqrt{2}L_+\sqrt{1+\tau_+^2/2\tau_-^2}},\frac{\sqrt{2}\omega_p\tau_+}{\sqrt{1+\tau_+^2/2\tau_-^2}}\right)\sin(\omega_0t-k_0z),$$

where the function $\Phi(x, a)$ is given by formula (1.6).

Electric fields (2.7) and (2.8) depend on the polarization of laser pulses. The fields have maximum amplitudes when the vectors $\mathbf{E}_{0+}$ and $\mathbf{E}_{0-}$ are parallel or antiparallel to each other and vanish when the vectors $\mathbf{E}_{0+}$ and $\mathbf{E}_{0-}$ are mutually orthogonal.

It follows from expressions (2.7) and (2.8) that, for each of the laser pulses, the ratio of the amplitude of the electric field of the backscattered radiation to the laser field amplitude contains the product of the large quantity $k_0L_\pm$, which is proportional to the number of spatial periods of small-scale plasma perturbations, and the parameter $e^2(\mathbf{E}_{0+}\mathbf{E}_{0-})/4m_e^2\omega_0^2c^2$, which is small by virtue of condition (1.2). In deriving expression (1.5) for density perturbations, the contribution of the scattered fields was assumed to be small and, accordingly, was neglected. Thus, the condition $|\mathbf{E}_S^\pm| < |\mathbf{E}_{0\pm}|$ and inequality (1.2) yield the following restriction on the parameters of the plasma and the laser pulses:

$$\frac{\pi}{4}\frac{\omega_p}{\omega_0}\omega_p\tau_\pm \le 1.$$

Let us analyze how electric fields (2.7) and (2.8) depend on the duration of laser pulses. In the case of a collision between two long laser pulses ($\omega_p\tau_\pm \gg 1$), the

electric field of the backscattered radiation with allowance for asymptotic formula (1.7) has the form

$$\mathbf{E}_S^{\pm}(z,t) = \sqrt{\pi}k_0 L_{\pm}\frac{e^2\mathbf{E}_{0\pm}(\mathbf{E}_{0+}\mathbf{E}_{0-})}{4m_e^2\omega_0^2c^2} \times \exp\left\{-\frac{(z\pm V_g t)^2}{2L_{\mp}^2}\right\}\sin(\omega_0 t \pm k_0 z). \quad (2.9)$$

The small-scale density perturbations excited in the collision are quasistatic, and each of the two laser pulses is backscattered into a radiation pulse whose duration is determined by the length of the laser pulse propagating in the opposite direction and whose frequency is equal to the laser frequency.

An interaction between two short laser pulses ($\omega_p\tau_{\pm} \le 1$) or between a long pulse ($\omega_p\tau_+ \gg 1$) and a short pulse ($\omega_p\tau_- \le 1$) is accompanied by the excitation of plasma oscillations in the interaction region. In this case, the electric fields of the backscattered radiation pulses can be found by using asymptotic representation (1.9):

$$\mathbf{E}_S^{\pm}(z,t) = \frac{\pi k_0 L_+\omega_p\tau_-}{\sqrt{2+\tau_{\mp}^2/\tau_{\pm}^2}}\frac{e^2\mathbf{E}_{0\pm}(\mathbf{E}_{0+}\mathbf{E}_{0-})}{4m_e^2\omega_0^2c^2} \times \exp\left\{-\frac{\omega_p^2\tau_+^2\tau_-^2}{\tau_{\mp}^2+2\tau_{\pm}^2}-\frac{(z\pm V_g t)^2}{2(L_{\mp}^2+2L_{\pm}^2)}\right\} \times\left\{\cos\left[\left(\omega_0-\frac{\omega_p}{1+\tau_{\mp}^2/2\tau_{\pm}^2}\right)t\pm\left(k_0-\frac{k_p}{1+\tau_{\mp}^2/2\tau_{\pm}^2}\right)z\right]\right. \left.-\cos\left[\left(\omega_0+\frac{\omega_p}{1+\tau_{\mp}^2/2\tau_{\pm}^2}\right)t\pm\left(k_0+\frac{k_p}{1+\tau_{\mp}^2/2\tau_{\pm}^2}\right)z\right]\right\}. \quad (2.10)$$

In the case of a collision between short laser pulses, we see from expressions (2.10) that the frequency and wavenumber of each of the backscattered radiation pulses are shifted from the frequency and wavenumber of the laser radiation by the amounts $\omega_0 \pm \frac{\omega_p}{1+\tau_{\mp}^2/2\tau_{\pm}^2}$ and $k_0 \pm \frac{k_p}{1+\tau_{\mp}^2/2\tau_{\pm}^2}$, respectively. The frequency shift is strongly dependent on the ratio between the durations of the laser pulses.

An analysis of the interaction of a long ($\omega_p\tau_+ \gg 1$) and a short ($\omega_p\tau_- \le 1$) laser pulse reveals the following interesting effect. According to formula (2.10), the backscattered electric field of the longer pulse at $\frac{\eta}{L_-} \gg 1$, $\omega_p\tau_-$ has the form

$$\mathbf{E}_S^{+}(z,t) = \frac{\pi k_0 L_+\omega_p\tau_-}{\sqrt{2}}\frac{e^2\mathbf{E}_{0+}(\mathbf{E}_{0+}\mathbf{E}_{0-})}{4m_e^2\omega_0^2c^2} \times \exp\left\{-\frac{\omega_p^2\tau_-^2}{2}-\frac{\eta^2}{4L_+^2}\right\} \times\{\cos[(\omega_0-\omega_p)t+(k_0-k_p)z] -\cos[(\omega_0+\omega_p)t+(k_0+k_p)z]\}. \quad (2.11)$$

According to the same formula, the backscattered electric field of the shorter pulse at $\frac{\xi}{L_+} \gg \frac{\tau_+}{\tau_-}$, $\omega_p\tau_+$ is expressed as

$$\mathbf{E}_S^{-}(z,t) = \pi k_0 L_-\omega_p\tau_-\frac{e^2\mathbf{E}_{0-}(\mathbf{E}_{0+}\mathbf{E}_{0-})}{4m_e^2\omega_0^2c^2} \times \exp\left\{-\omega_p^2\tau_-^2-\frac{\xi^2}{2L_+^2}\right\} \times\left\{\cos\left[\left(\omega_0-2\omega_p\frac{\tau_-^2}{\tau_+^2}\right)t-\left(k_0-2k_p\frac{\tau_-^2}{\tau_+^2}\right)z\right]\right. \left.-\cos\left[\left(\omega_0+2\omega_p\frac{\tau_-^2}{\tau_+^2}\right)t-\left(k_0+2k_p\frac{\tau_-^2}{\tau_+^2}\right)z\right]\right\}. \quad (2.12)$$

The frequency of backscattered electric field (2.12) of the shorter pulse is close to the laser frequency ω_0, the pulse length being comparable with the length L_+ of the longer laser pulse. Consequently, after the interaction, this field has an insignificant impact on the spectral parameters of the longer laser pulse and on its shape. On the other hand, backscattered electric field (2.11) of the longer pulse propagates in the direction of the shorter laser pulse, thereby distorting the shape of the latter and changing its spectrum. As a result, from formula (2.11), we can see that, after the interaction, the spectrum of the backscattered pulse propagating from right to left contains not only the fundamental harmonic at the laser carrier frequency ω_0 but also satellite harmonics at the frequencies $\omega_0 \pm \omega_p$ and the pulse length is determined by the duration of the longer laser pulse. Such an increase in the backscattered pulse length is explained as being due to the scattering of the laser field by the small-scale plasma oscillations that are generated over a distance comparable to the length of the longer laser pulse. The radiation pulse into which the longer laser pulse is backscattered is also long. As a result, when this long backscattered pulse overlaps with

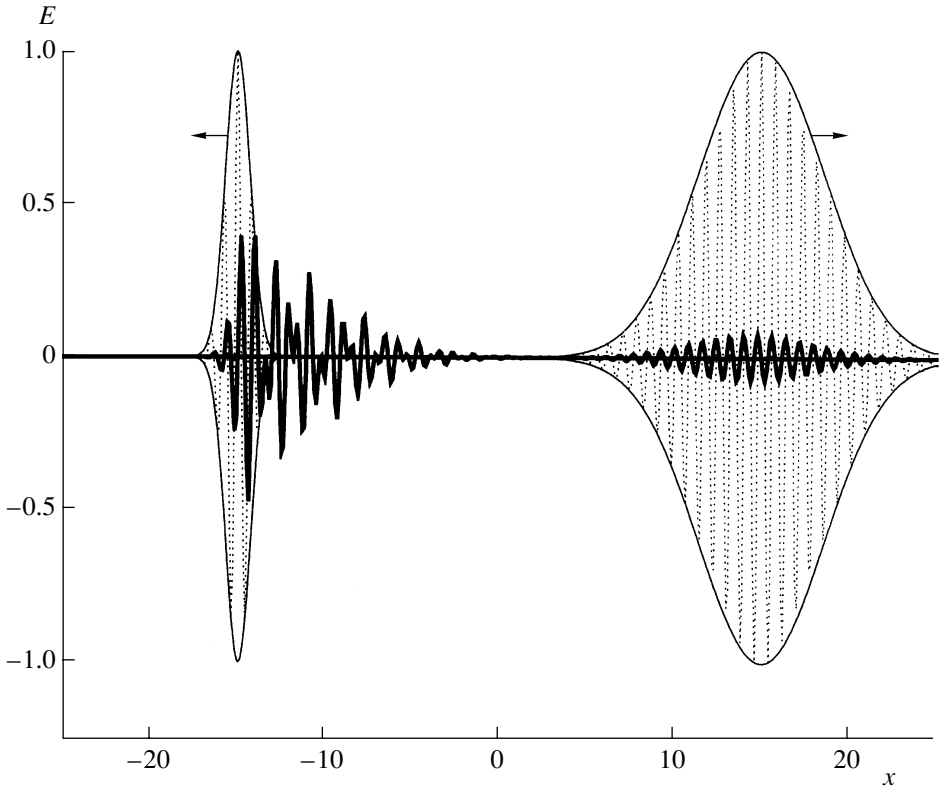

Fig. 2. Laser fields calculated numerically from formulas (1.4), (2.7), and (2.8) as functions of the dimensionless coordinate $x = \frac{z}{\sqrt{2}L_-}$ at the time $\frac{t}{\sqrt{2}\tau_-} = 15$. The electric fields of the laser pulses and backscattered radiation are normalized to the electric fields $E_{0\pm}$ and are shown by light solid curves (and the dotted curves within) and a heavy solid curve, respectively. The calculations were carried out for laser pulses with intensities $I_+ = I_- = 5.1 \times 10^{16}$ W/cm^2 and durations $\omega_p\tau_- = \sqrt{2}$, $\tau_+ = 5\tau_-$ and for a plasma with $\omega_p = 0.25\omega_0$.

the field of the shorter laser pulse, it gives rise to a long radiation tail behind the latter. The results of numerical calculations based on formulas (2.7) and (2.8) are illustrated in Fig. 2, which shows that a long backscattered radiation tail actually arises behind a short laser pulse after its interaction with a long laser pulse.

The spectral features of backscattered laser radiation can be derived from a straightforward analysis of expression (2.6). Simple transformations of this expression in the range of positive frequencies ($\omega > 0$) yield

$$\mathbf{E}_S^+(\omega, z) = \frac{\pi^{3/2}\omega_p\tau_+\tau_-}{2\sqrt{2}}k_0L_+\frac{e^2\mathbf{E}_{0+}(\mathbf{E}_{0+}\mathbf{E}_{0-})}{4m_e^2\omega_0^2c^2} \times \exp\left(-i\frac{\omega}{c}\sqrt{\varepsilon(\omega)}z\right)G_+(\omega), \quad (2.13)$$

where the frequency dependence of the electric field of the backscattered laser radiation is determined by the function $G_+(\omega)$,

$$G_+(\omega) = \exp\left(-\frac{\omega_p^2\tau_+^2\tau_-^2}{\tau_-^2 + 2\tau_+^2}\right) \times \left\{\exp\left[-\left(\omega - \omega_0 + \frac{\omega_p}{1 + \tau_-^2/2\tau_+^2}\right)^2(\tau_+^2 + \tau_-^2/2)\right] \times [1 + \mathrm{erf}(i[\omega - \omega_0 + \omega_p]\tau_+)]\right. \quad (2.14)$$
$$\left. - \exp\left[-\left(\omega - \omega_0 - \frac{\omega_p}{1 + \tau_-^2/2\tau_+^2}\right)^2(\tau_+^2 + \tau_-^2/2)\right] \times [1 + \mathrm{erf}(i[\omega - \omega_0 - \omega_p]\tau_+)]\right\}.$$

Resulting formulas (2.13) and (2.14) show that the spectrum of the backscattered radiation contains satellites at the frequencies $\omega = \omega_0 \pm \frac{\omega_p}{1 + \tau_-^2/2\tau_+^2}$, which depend on the ratio between the durations of the interacting laser pulses.

From expression (2.13) for the electric field, we can find the backscattered radiation energy dW_S^+ per frequency interval $d\omega$:

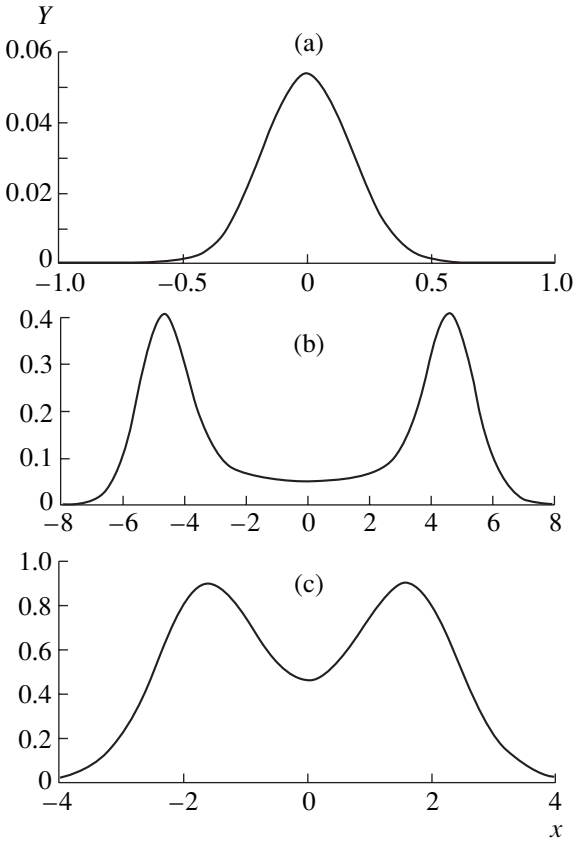

Fig. 3. Dependence of the function $Y = |G_+(\omega)|^2$ on the dimensionless frequency $X = (\omega - \omega_0)\tau_+$ for different ratios between the lengths of the interacting laser pulses: (a) the interaction of two long pulses with the durations $\omega_p\tau_+ = 5$ and $\omega_p\tau_- = 20$, (b) the interaction of a long ($\omega_p\tau_+ = 5$) and a short ($\omega_p\tau_- = 1$) pulse, and (c) the interaction of two short pulses with the durations $\omega_p\tau_+ = 2$ and $\omega_p\tau_- = 0.5$.

$$\frac{dW_S^+}{d\omega} = \frac{\pi^{3/2}\omega_p^2\tau_-^2k_0^2L_+^2}{4}\tau_+W_L^+\frac{e^4(\mathbf{E}_{0+}\mathbf{E}_{0-})^2}{16m_e^4\omega_0^4c^4}|G_+(\omega)|^2, \quad (2.15)$$

where W_L^+ is the energy of the laser pulse propagating from left to right.

The total energy W_S^+ of the backscattered radiation is obtained by integrating expression (2.15) over frequency. For a collision between a long pulse ($\omega_p\tau_+ \gg 1$) and a short counterpropagating pulse ($\omega_p\tau_- \leq 1$), the integral over the frequency spectrum can be taken analytically,

$$\int_0^\infty d\omega|G_+(\omega)|^2 = \frac{2\sqrt{2\pi}}{\tau_+}\exp(-\omega_p^2\tau_-^2), \quad (2.16)$$

and the total backscattered radiation energy is equal to

$$W_S^+ = \frac{\pi^2\omega_p^2\tau_-^2k_0^2L_+^2}{\sqrt{2}}W_L^+\frac{e^4(\mathbf{E}_{0+}\mathbf{E}_{0-})^2}{16m_e^4\omega_0^4c^4}\exp(-\omega_p^2\tau_-^2). \quad (2.17)$$

Figure 3 shows the backscattered radiation spectra calculated for different ratios between the durations of the interacting laser pulses. For two long laser pulses, the frequency of the backscattered radiation coincides with the laser carrier frequency (Fig. 3a). In the case of a collision between a long and a short laser pulse, the backscattering spectrum contains two satellites shifted from the laser frequency by the plasma frequency (Fig. 3b). In the case of two short laser pulses, the spectrum of the backscattered field contains satellites at the frequencies $\omega = \omega_0 \pm \frac{\omega_p}{1 + \tau_-^2/2\tau_+^2}$; however, the spectral peaks are close to one another and partially overlap, which is a consequence of the short pulse lengths (Fig. 3c).

It should be noted that the cold plasma approximation used here is valid for small-scale plasma oscillations under the assumption of a negligible spatial dispersion, i.e., only under the condition

$$\delta^2 = 12\frac{V_T^2}{c^2}\frac{\omega_0^2}{\omega_p^2} \ll 1, \quad (2.18)$$

where $V_T = \sqrt{\frac{T_e}{m_e}}$ is the electron thermal velocity and T_e is the electron temperature. Additionally, the condition that the Landau damping of small-scale plasma oscillations is insignificant during the entire interaction process yields the restrictions

$$\omega_p\tau_\pm < \frac{\delta^3}{3}\exp\left(\frac{3}{2\delta^2} + \frac{3}{2}\right), \quad (2.19)$$

which relate the durations of the laser pulses to the electron temperature.

CONCLUSION

In this paper, a simple one-dimensional hydrodynamic model has been applied to study the nonlinear scattering of two counterpropagating laser pulses in their interaction in a plasma and to investigate the shape of the backscattered radiation pulses and their spectral parameters. In particular, it has been shown that a long backscattered radiation tail arises behind a short laser pulse after its collision with a long laser pulse and that the length of the tail is comparable to the length of the longer pulse. It has also been found that the backscattered radiation spectrum contains satellites shifted from the laser frequency by nearly the plasma frequency. The presence of such satellites may provide the basis for

diagnosing both the plasma and the interacting laser pulses.

Note that the results obtained in one-dimensional geometry change only slightly when the finite transverse dimensions of the laser pulses are taken into account. The difference is that, in three-dimensional geometry, the electromagnetic radiation is scattered in the near-backward (rather than backward) direction, i.e., at such angles θ to the pulse propagation direction that are close to π: $\pi - \theta \le 1/k_0 D$, where D is the diameter of the focal spot of laser light. Another difference lies in the dependence of the amplitude of the electric field of the backscattered laser radiation on the spatial coordinates. However, the main conclusions of the one-dimensional theory, specifically, those concerning the spectral parameters of the backscattered radiation and its longitudinal structure, remain valid in three-dimensional geometry.

Let us estimate the electric field and the energy of radiation backscattered in the interaction of a long laser pulse with intensity $I_+ = 1.2 \times 10^{15}$ W/cm^2, duration $\tau_+ = 330$ fs, and wavelength $\lambda_0 = 0.8$ μm and a counterpropagating, less intense, short laser pulse with intensity $I_- = 1.2 \times 10^{14}$ W/cm^2, duration $\tau_- = 14$ fs, and the same wavelength in a low-density plasma with electron temperature $T_e = 20$ eV and electron density $N_{0e} = 3.2 \times 10^{18}$ cm^{-3}. The amplitude of the plasma density perturbations excited in the interaction region is about $\delta N_e \approx 0.2 N_{0e}$. After the interaction, the radiation pulse propagating from right to left is longer by a factor of 30 times than the original length of the shorter pulse because of the contribution of the backscattered radiation of the longer pulse. Although the electric field amplitude is small, $E_S^+ \approx 0.13 E_{0-}$, backscattered radiation energy (2.17) amounts to about 50% of the energy of the shorter laser pulse. In this case, inequalities (2.18) and (2.19) are satisfied, because the parameter δ^2 is approximately equal to 0.28 and, thus, the small-scale plasma oscillations in question can be described in the cold plasma approximation.

Since the above analysis assumes that the small-scale density perturbations are linear [see Eq. (1.3) and condition (1.2)], it is restricted to laser pulse intensities of 10^{15}–10^{16} W/cm^2 at $\lambda_0 \cong 1$ μm. In fact, however, present-day laser devices can operate at far higher intensities, in which case the electron density perturbations are strongly nonlinear. It can be expected that the backscattering efficiency will increase with laser intensity; hence, it makes sense to speak of the possible reflection of laser pulses from the interaction region.

The above analysis deals exclusively with the excitation of radiation at a frequency close to the laser carrier frequency. However, two interacting laser pulses can also generate low-frequency radiation at a frequency twice the plasma frequency. This issue will be addressed in a separate paper.

ACKNOWLEDGMENTS

I am grateful to L.M. Gorbunov for fruitful discussions and useful remarks. I also thank N.E. Andreev for critical comments and A.N. Vasil'ev and S.V. Kuznetsov for their help in carrying out simulations. This work was supported in part by the Russian Foundation for Basic Research, project nos. 01-02-16723 and 02-02-16110.

REFERENCES

1. V. M. Malkin, G. Shvets, and N. J. Fisch, Phys. Plasmas **7**, 2232 (2000); Phys. Rev. Lett. **84**, 1208 (2000).
2. Y. Ping, I. Geltner, N. J. Fisch, *et al.*, Phys. Rev. E **62**, 4532 (2000).
3. G. Shvets, N. J. Fisch, A. Pukhov, and J. Meyer-ter-Vehn, Phys. Rev. E **60**, 2218 (1999).
4. C. B. Schroeder, P. B. Lee, and J. S. Wurtele, Phys. Rev. E **59**, 6037 (1999).
5. K. Nagashima, J. Koga, and M. Kando, Phys. Rev. E **64**, 066403 (2001).
6. L. M. Gorbunov and A. A. Frolov, Zh. Éksp. Teor. Fiz. **120**, 583 (2001) [JETP **93**, 510 (2001)].
7. I. Y. Dodin and N. J. Fish, Phys. Rev. Lett. **88**, 165001 (2002).
8. G. Shvets and A. Pukhov, Phys. Rev. E **59**, 1033 (1999).
9. B. Shen and J. Meyer-ter-Vehn, Phys. Rev. E **65**, 016405 (2002).
10. Yu. Tsidulko, V. M. Malkin, and N. J. Fisch, Phys. Rev. Lett. **88**, 235004 (2002).
11. L. M. Gorbunov and A. A. Frolov, Fiz. Plazmy **29**, 440 (2003) [Plasma Phys. Rep. **29**, 407 (2003)].
12. L. D. Landau and E. M. Lifshitz, *Electrodynamics of Continuous Media* (Nauka, Moscow, 1982; Pergamon Press, New York, 1984).

Translated by O.E. Khadin

Plasma Physics Reports, Vol. 29, No. 6, 2003, pp. 512–516. Translated from Fizika Plazmy, Vol. 29, No. 6, 2003, pp. 550–554.

PLASMA TURBULENCE

Effect of the External Magnetic Field on the MHD Turbulence Spectra

E. Golbraikh*, S. S. Moiseev†, and A. Eidelman*****

**Center for MHD Studies, Ben-Gurion University of the Negev, Beer-Sheva, Israel*

***Institute for Space Research, Russian Academy of Sciences, Profsoyuznaya ul. 84/32, Moscow, 117810 Russia*

****Mechanical Engineering Department, Ben-Gurion University of the Negev, Beer-Sheva, Israel*

Received September 26, 2002; in final form, January 4, 2003

Abstract—The turbulent properties of conducting fluids in an external constant magnetic field are known to change with increasing field strength. A study is made of the behavior of the second-order structural function of the velocity field in a homogeneous incompressible turbulent fluid in the presence of an external uniform magnetic field. It is shown that, depending on the magnetic field strength, there may be different governing parameters of the system in both the inertial and dissipative intervals of turbulence. This leads to new spectral scalings that are consistent with experimental ones. © *2003 MAIK "Nauka/Interperiodica".*

1. INTRODUCTION

Numerous investigations of turbulent flows of conducting fluids at low Reynolds numbers in an external uniform magnetic field $\mathbf{B}_0$ (see [1] and the literature cited therein) show that the fluid properties charge substantially as the field strength increases. Here, we investigate the behavior of the second-order structural function for the velocity field in a homogeneous incompressible turbulent fluid in the presence of the magnetic field $\mathbf{B}_0$. The one-dimensional second-order structural function is defined by the formula

$$D(r) = \langle [u'(r + r') - u'(r')]^2 \rangle, \quad (1)$$

where u' is the velocity of turbulent fluctuations. In the inertial interval of turbulence, the structural function D is a power function of r:

$$D(r) \sim Ar^{\alpha}, \quad (2)$$

where A is a parameter and α is the scaling index.

As was shown in [2, 3], the α values observed experimentally at different magnitudes of the interaction parameter $N = Ha^2/Re = \sigma B_0^2 L/\rho U$ (where σ is the conductivity of the fluid, ρ is its density, $Ha = B_0(\sigma/\rho\nu)^{1/2}$ is the Hartmann number, $Re = LU/\nu$ is the Reynolds number, L and U are the characteristic length and characteristic velocity, ν is the kinematic viscosity, and B_0 is the strength of the external magnetic field) are equal to 2/3, 4/3, 2, and 8/3. Note that, from a morphological point of view, this sequence forms an arithmetic progression with a difference of 2/3. Below, we will see that, in each turbulent regime, characterized by its own scaling index α, the turbulent energy is transferred along the spectrum by a certain mechanism and there are corresponding governing parameters in the inertial interval of turbulence and the viscous interval of small-scale turbulence.

2. KOLMOGOROV REGIMES OF TURBULENCE

We begin with the most thoroughly studied Kolmogorov turbulent spectrum, which was obtained more than 60 years ago by Kolmogorov under the assumption that, for a developed steady-state homogeneous turbulent flow of an incompressible fluid at a high Reynolds number, the governing parameter in the inertial and viscous intervals is the energy flux along the spectrum. In the viscous interval, there are two governing parameters: the energy flux ε and the viscosity ν, which serves as an additional governing parameter of the turbulent cascade. If the characteristic scale length L_F of an external force that maintains turbulence is much larger than the characteristic length λ_i of the inertial interval, $L_F \gg \lambda_i$, then the structural function of turbulent fluctuations of the velocity field has the form

$$D(r) \sim U^2 f\left(\frac{r}{\lambda}\right), \quad (3)$$

where U is the characteristic velocity of the turbulent fluctuations and λ is their spatial scale.

In the inertial interval, in which the parameters of the system are independent of ν (i.e., we can set $\nu = 0$ in the Navier–Stokes equation), the energy is an integral of motion. Consequently, the energy flux ε along the spectrum is the governing parameter. In essence, Kolmogorov's first hypothesis extends this property to the dissipative interval of turbulent pulsations.

† Deceased.

1063-780X/03/2906-0512$24.00 © 2003 MAIK "Nauka/Interperiodica"

In the dissipative interval, the velocity of turbulent pulsations and their characteristic scale length are equal to $U_\nu = U_k \sim (\varepsilon\nu)^{1/4}$ and $\lambda_\nu = \lambda_k \sim (\nu^3/\varepsilon)^{1/4}$. In the inertial interval, the viscosity drops out of expression (3). As a result, we obtain

$$D(r) \sim \varepsilon^{2/3} r^{2/3}. \quad (4)$$

On the other hand, almost 20 years after the publication of Kolmogorov's works, it was shown that the Euler equation has another integral of motion, namely, the helicity [4],

$$He = \langle \mathbf{u}' \cdot (\nabla \times \mathbf{u}') \rangle, \quad (5)$$

which is associated with the violation of the mirror-image symmetry of homogeneous isotropic turbulence. A helical cascade in the regime of fully developed isotropic turbulence was first investigated by Brissaud *et al.* [5]. If there is a helicity flux η (which may be introduced by analogy with the energy flux ε) in the system, then it can be regarded (together with ε) as a governing parameter in the inertial interval of turbulence. At the same time, in [5], the fluxes ε and η were also assumed to be governing parameters in the dissipative interval. From the experimental and numerical data accumulated over the last 40 years, it has become clear that helical turbulence is encountered as often as conventional Kolmogorov turbulence; this may be attributed to the level of helicity of turbulent pulsations in the system [6]. Interest in helical turbulence increased considerably when it was recognized that it plays a fundamental role in the generation of moderately strong large-scale magnetic fields (see [7] and the references therein) and the formation of large-scale atmospheric vortices (see [1] and the references therein).

By analogy with Kolmogorov's hypothesis, we now consider another case—the one in which, first, the governing parameters for the development of turbulence in the inertial interval are ε and η and, second, in the dissipative interval, to these must be added the viscosity ν. In this case, according to the Π theorem, the characteristic scale of turbulence in the dissipative interval (when the viscosity ν should be accounted for) is equal to

$$\lambda_\eta \sim \varepsilon^\beta \nu^{3(1-\beta)/5} \eta^{-(1+4\beta)/5}, \quad (6)$$

where β is a free parameter.

We take into account the form of function (5) and the asymptotic behavior of the function $D(r)$ in the inertial interval of turbulence and, following conventional practice, set

$$D(r) \sim U_\eta^2 \left(\frac{r}{\lambda_\eta}\right)^\delta, \quad (7)$$

where the velocity scales as $U_\eta \sim \varepsilon^{-\beta} \eta^{-(1+4\beta)/5} \nu^{(2+3\beta)/5}$ (the dependence of the exponents in the formula for U_η on β stems from the fact that, in the dissipative interval, the Reynolds number is approximately equal to unity, $Re(\lambda_\eta) \sim 1$). As a result, we obtain the relationship between the parameters β and δ,

$$\beta = \frac{\delta - 4/3}{\delta + 2}, \quad (8)$$

and the scaling for the structural function,

$$D(r) \sim \left(\frac{\varepsilon^2}{\eta}\right)^{2/3} \left(\frac{\eta}{\varepsilon}\right)^\delta r^\delta. \quad (9)$$

Now, we consider two limiting cases in which, along with ν, either ε or η is a governing parameter in the dissipative interval. It should be noted that, in these cases, the characteristic scale $\lambda \sim \varepsilon/\eta$ of turbulent pulsations and the velocity $U \sim (\varepsilon^2/\eta)^{1/3}$ in the inertial interval depend on the two parameters ε and η, which are both nonzero.

We have derived that, in the first case (which corresponds to Kolmogorov turbulence), the helicity flux η is not a governing parameter; i.e., $\eta = \eta(\varepsilon)$. Therefore, Eq. (9) yields $\delta = 2/3$ and expression (6) gives $\beta = -1/4$. As a consequence, we arrive at Kolmogorov's dependence of the second-order moment in the inertial interval of turbulence:

$$D(r) \sim C_\varepsilon \varepsilon^{2/3} r^{2/3}. \quad (10)$$

In the second case (corresponding helical turbulence), the energy flux ε drops out of expression (6); i.e., $\beta = 0$ and $\delta = 4/3$, and the scaling of the structural function in the inertial interval has the form

$$D(r) = C_\eta \eta^{2/3} r^{4/3}. \quad (11)$$

In scalings (10) and (11), C_ε and C_η are constants. Note that these two scalings are actually observed in experiments (see [1] and the literature cited therein).

Now, using the above expressions for the characteristic scale and velocity of turbulent pulsations, we write the effective Reynolds number as

$$Re_{\text{eff}} \sim \frac{\varepsilon^{5/3}}{\nu \eta^{4/3}}. \quad (12)$$

Since the Reynolds number can be represented as the ratio of the turbulent to the kinematic viscosity (see, e.g., [8]), formula (12) leads to the following fundamentally important conclusion: as the helicity flux (and the helicity itself) increases, the turbulent viscosity in the system decreases according to the law $\eta^{-4/3}$. Note that this conclusion stems exclusively from the sufficiently high level of helical turbulence in the system. An analogous behavior of turbulent fields was also observed in [9].

Hence, when ε is not a governing parameter in the dissipative interval, we obtain $\delta = 4/3$, which corresponds to the helical scaling of the structural function $D(r)$ in the inertial interval. Since such scalings are typical of helical turbulent fields [6], we can conclude that the situation in question, namely, that with $\varepsilon(\eta)$, takes

place in real media. This conclusion is somewhat unexpected in view of the fact that, since Kolmogorov's time, it has become customary to think that ε is the governing parameter in the dissipative interval. For helical turbulence, however, the conclusion reached here is quite natural. In fact, as was shown in many papers (see [1] and the literature cited therein), helical turbulence slows the direct energy transfer from large to small scales, gives rise to reverse energy cascades, reduces turbulent viscosity, etc. As a combined result of all of these processes, the energy flux ε in the dissipative interval depends on the helicity flux η in a way that reflects the behavior of the governing parameters at $\delta = 4/3$ in the inertial interval.

In addition, note that the above interpretation of the scalings obtained differs from the interpretation given in [5] (which, basically, is accepted today). In fact, according to [5], the helical scaling index $\delta = 4/3$ refers exclusively to the case $\varepsilon = 0$. However, this seems highly doubtful, because it is unclear how to treat the energy flux in the inertial interval, which plays the role of the energy source. It is important to take into account the fact that the parameter ε does not disappear in the case under consideration but merely drops out of the expression for the structural function $D(r)$.

3. EFFECT OF THE MAGNETIC FIELD ON THE SCALING FOR TURBULENCE

A growing external magnetic field has a significant effect on the properties of a turbulent flow of conducting fluid. In the presence of an external magnetic field $\mathbf{B}_0$, the homogeneous correlation (and, therefore, structural) function

$$Q(r) = \langle u'(0)u'(r)\rangle \tag{13}$$

depends on the parameter $N = \sigma B_0^2 L/\rho U$ (see, e.g., [7] and the references therein). However, for a magnetic field weak enough that its influence on $Q(r)$ can be neglected, we arrive at spectral scalings close to the Kolmogorov and helical scalings discussed above.

According to [7], the condition for the magnetic field to be sufficiently weak in the first approximation is formulated in terms of the harmonics of the Fourier transformed correlation function:

$$\frac{(\mathbf{k}\cdot\mathbf{B}_0)^2}{\mu\rho_0}\frac{2\eta\nu k^4 - 2\omega^2 + (\mathbf{k}\cdot\mathbf{B}_0)^2/\mu\rho_0}{(\nu_B^2 k^4 + \omega^2)(\nu^2 k^4 + \omega^2)} \ll 1, \tag{14}$$

where $\mathbf{k}$ is the wave vector of turbulent pulsations, $\mathbf{B}_0$ is the external magnetic field, ρ_0 is the fluid density, μ is the magnetic permeability, $\nu_B = 1/\mu_0\sigma$ is the magnetic viscosity, and σ is the electric conductivity of the fluid. However, even sufficiently weak magnetic fields may be important in the generation of helical turbulence [10, 11]. This fundamental effect should be taken into account in investigating helical turbulence since helicity plays an important role in the energy transfer along the spectrum and can substantially affect the magnetic viscosity. Consequently, as the magnetic field increases, condition (14) fails to hold, which, in turn, should change the form of the function $D(r)$.

Recall that, in the absence of an external magnetic field, the mean energy of the turbulent fluctuations and their helicity are the integrals of motion of the Euler equation. In the Euler equation in the inertial interval, a growing external magnetic field is accounted for by an additional term, namely, the Lorentz force:

$$\rho d\mathbf{V}/dt = -\nabla P + \mathbf{j}\times\mathbf{B}, \tag{15}$$

where $\mathbf{j}$ is the current density.

It is easy to show that, for $Re_m = \mu_0\sigma UB_0/\lambda \ll 1$, the Lorentz force and the associated Joule dissipation occur on all scales, in which case the energy and helicity fluxes both become dependent on the magnetic field and, therefore, fail to serve as the governing parameters in the inertial and viscous intervals. At present, there is a vast amount of experimental data obtained from laboratory investigations of turbulence in an external constant magnetic field. On the whole, these investigations were carried out in the two main directions: the fluctuations of the velocity field were measured along [2] and across [3] the magnetic field.

In the first case, the scaling index in correlation function (2) at a sufficiently strong field $\mathbf{B}_0$ was close to $\alpha = 2$, which was explained by the tendency of turbulence to become two-dimensional [2].

In the second case, the scaling index α was close to 8/3; in some papers (see [1] and the literature cited therein), this was attributed to the generation of superhelical turbulence (super-helicity), $\omega_s = \langle(\nabla\times\mathbf{u}')\cdot(\nabla\times\nabla\times\mathbf{u}')\rangle$. In our opinion, however, the difference in the properties of turbulent fluctuations along and across the magnetic field stems from an increase in the anisotropy of the turbulence in the presence of an external magnetic field. In fact, it is obvious from condition (14) that the character of the interaction is different for transverse modes (with $\mathbf{k}\cdot\mathbf{B}_0 = 0$) and longitudinal modes (with $\mathbf{k}\cdot\mathbf{B}_0 \neq 0$): the dissipation of transverse modes is minimal, while the dissipation of longitudinal modes is maximal.

Hence, the effect of Joule dissipation is greatest for the spectral modes whose wave vectors $\mathbf{k}$ are parallel to $\mathbf{B}_0$ and that thus correspond to the longitudinal harmonics of the correlation function. In this case, choosing the parameter $\gamma = \sigma B^2/\rho$, together with the viscosity ν, as a governing parameter in the dissipative interval seems quite logical. Then, using representation (7), we obtain the characteristic velocity of the turbulent pulsations and their characteristic scale, $U \approx (\gamma\nu)^{1/2}$ and $\lambda_B \sim (\nu/\gamma)^{1/2}$, and also arrive at the following scaling for the second-order structural function:

$$D(r) \sim (\gamma r)^2, \tag{16}$$

which corresponds to a α spectrum with a spectral density index of –3. Consequently, the spectral index –3 arises as a result of the increasing influence of the magnetic field on the longitudinal modes of the turbulent field. A similar line of reasoning was earlier suggested in [2].

Note that the spectral index –3 is usually identified with the transition of the turbulence to the two-dimensional regime. In fact, the spectral index –3 is associated with the enstrophy conservation and is characteristic of two-dimensional turbulence, in analogy to the spectral index –7/3, which is associated with the helical properties of a three-dimensional turbulent field. However, in the case of three-dimensional turbulence, the spectral index –3 is associated exclusively with the longitudinal modes.

A conducting fluid in which the turbulent fluctuations of the velocity field are transverse to the magnetic field should be studied in a different manner. In this situation, as the magnetic field increases, the scaling index α changes in a jumplike manner and instead of being equal to 2, it is equal to 8/3, which corresponds to a spectral density index of –11/3 (i.e., to the steeper spectra) [3]. In order to explain the value $\alpha = 8/3$, Branover *et al.* [3] assumed that, in this case, the governing parameter in the inertial interval is the super-helicity flux $\eta_s = d\omega_s/dt$. However, this assumption is based exclusively on the dimensionality of the quantity η_s. In addition, since this quantity is not an integral of motion, it is difficult to understand why it should be conserved and why all the remaining quantities should depend on it.

On the other hand, experimental data show that, as the magnetic field strength increases, the turbulence tends to become intermittent. As this occurs, the properties of the energy flux ε along the spectrum should change. Why we again discuss the behavior of the function ε may be explained as follows: as the magnetic field $\mathbf{B}_0$ increases, the field-aligned fluctuations can decouple from the cross-field fluctuations; i.e., in the first approximation, the longitudinal and transverse fluctuations occur independently of each other and Joule dissipation has essentially no effect on the transverse modes. As a consequence, the parameter γ introduced above ceases to be a governing parameter for describing the development of turbulence.

Now, we again turn to the case in which the energy and helicity fluxes can be the governing parameters in the inertial interval of turbulence. It should be noted, however, that, since the properties of the energy transfer along the spectrum change as the intermittent activity of turbulence increases, the energy flux ε should be treated as a function of the coordinates and time. In other words, instead of ε, it is necessary to consider the function $\varepsilon(\mathbf{x}, t)$, which was studied in many papers, the first being [12, 13]. Usually, this approach reduces to choosing a certain spatial region over which to average the function ε. On the other hand, the energy pumped into the small-scale fluctuations in the system by an external force is independent of the properties of the system. When ε depends on the coordinates, it is more meaningful to switch from the global parameters (such as the densities of the energy and helicity pumped into the system and dissipated there) to the local ones (such as, e.g., the energy and helicity flux densities).

The flux density of the energy pumped into the system is described by the equation

$$\frac{\partial}{\partial V}\left(\frac{dU'^2}{dt}\right) = \varepsilon_V,$$

where U' is the characteristic velocity of the turbulent fluctuations on the spatial scales on which an external force is acting and V is the volume. Under steady-state conditions, this flux density should be canceled by the energy flux density along the spectrum, $\varepsilon_V = -\partial\varepsilon/\partial V$. Consequently, in this case, the parameters ε_V and $\eta_V = \partial\eta/\partial V$ are the governing parameters for the formation of turbulent spectra.

Repeating the above arguments, we find that the expressions for the velocity field components perpendicular to the magnetic field yield the following form of the structural function in the inertial interval:

$$D_\perp(r) \sim (\varepsilon_V^5/\eta_V^4)^{2/3}(\eta_V/\varepsilon_V)^\delta r^\delta. \tag{17}$$

We thus arrive at the following possible scalings for turbulence in two limiting cases:

$$10/3 - \delta = 0 \longrightarrow D_\perp(r) \sim \eta_V^{2/3} r^{10/3}, \tag{18}$$

$$8/3 - \delta = 0 \longrightarrow D_\perp(r) \sim \varepsilon_V^{2/3} r^{8/3}, \tag{18a}$$

the latter of which is a transient one. In the situation in question, the effective Reynolds number analogous to that in formula (12) has the form

$$Re_{\text{eff}} = \frac{\varepsilon_V^{8/3}}{\eta_V^{7/3}\nu}. \tag{19}$$

In the dissipative interval, the scalings of the characteristic parameters differ from those in the inertial interval. In particular, the characteristic scale and velocity of turbulent pulsations obey the scalings

$$\begin{aligned} \lambda_t &\sim \varepsilon_V^\beta \eta_V^{-(1+7\beta)/8} \nu^{3(1-\beta)/8}, \\ U_t &\sim \varepsilon_V^{-\beta} \eta_V^{(1+7\beta)/8} \nu^{(5+3\beta)/8}, \end{aligned} \tag{20}$$

which were derived with allowance for the fact that, at the boundary of the dissipative interval, the Reynolds number is equal to unity. The two limiting cases are now treated as follows. For $\delta = 10/3$, we obtain $\alpha = 0$ and thus arrive at the above scalings for turbulent pulsations: $\lambda_{t\eta} = (\nu^3/\eta_V)^{1/8}$ and $U \sim (\nu^5/\eta_V)^{1/8}$. For $\delta = 8/3$, we obtain $\alpha = -1/7$; i.e., the characteristic scale and velocity of the turbulent pulsations obey the scalings $\lambda_{tV} \sim (\nu^3/\varepsilon_V)^{1/7}$ and $U_{tV} \sim (\nu^4\varepsilon_V)^{1/7}$.

4. CONCLUSION

The results of our study can be summarized as follows. Based on dimensionality considerations, we have investigated MHD turbulence in the different regimes that may occur depending on the relationships between the governing parameters of the system, namely, the energy and helicity fluxes, viscosity, etc. The classical and helical scalings that have been obtained for the second-order structural function are consistent with both the available experimental data on the generation of turbulence and the corresponding numerical results. We have demonstrated that the external magnetic field has a significant impact on the structural properties of turbulent fields in a conducting fluid. We have shown that the transient turbulent regime under analysis is not only peculiar to the dynamics of a conducting fluid in an external magnetic field but can also occur in response to some external action, such as externally induced rotation. The results obtained can be used to interpret the experimental data on MHD turbulence and simulate the generation of turbulence in conducting fluids, e.g., in plasmas.

REFERENCES

1. H. Branover, A. Eidelman, E. Golbraikh, and S. S. Moiseev, *Turbulence and Structures* (Academic, New York, 1999).
2. A. Alemany, R. Moreau, P. L. Sulem, and U. Frisch, J. Mec. **18** (2), 277 (1979).
3. H. Branover, A. Eidelman, M. Nagorny, and M. Kireev, *Progress in Turbulence Research*, Ed. by H. Branover and Y. Unger (AIAA, New York, 1994), Vol. 162, p. 64.
4. J. J. Moreau, C. R. Acad. Sci. (Paris) **252**, 2810 (1962).
5. A. Brissaud, U. Frisch, J. Leorat, *et al.*, Phys. Fluids **16**, 1366 (1973).
6. H. Branover, O. G. Chkhetiani, A. Eidelman, *et al.*, Magnetohydrodynamics **37**, 31 (2001).
7. F. Krause and K.-H. Radler, *Mean-Field Magnetohydrodynamics and Dynamo Theory* (Pergamon Press, Oxford, 1980), p. 321.
8. L. D. Landau and E. M. Lifshitz, *Fluid Mechanics* (Nauka, Moscow, 1986; Pergamon Press, New York, 1987).
9. A. V. Belyan, S. S. Moiseev, and O. G. Chkhetiani, Preprint No. Pr-1845 (Institute for Space Research, Russian Academy of Sciences, Moscow, 1992); A. V. Belyan, S. S. Moiseev, and O. G. Chkhetiani, Dokl. Akad. Nauk **334**, 34 (1994) [Phys. Dokl. **39**, 13 (1994)]; A. Belyan, O. Chkhetiani, E. Golbraikh, and S. Moiseev, Physica A (Amsterdam) **258**, 55 (1998).
10. O. G. Chkhetiani, S. S. Moiseev, and E. I. Gol'braikh, Zh. Éksp. Teor. Fiz. **114**, 946 (1998) [JETP **87**, 513 (1998)].
11. O. G. Chkhetiani and E. Gol'braikh, Zh. Éksp. Teor. Fiz. (in press).
12. A. M. Obukhov, J. Fluid Mech. **13**, 77 (1962).
13. A. N. Kolmogorov, *La Turbulence en Mecanique des Fluides*, Ed. by A. Favre, L. S. G. Kovasznay, R. Dumas, *et al.* (Gauthier-Villars, Paris, 1961), p. 447.

Translated by I.A. Kalabalyk

Plasma Physics Reports, Vol. 29, No. 6, 2003, pp. 517–527. Translated from Fizika Plazmy, Vol. 29, No. 6, 2003, pp. 555–565.

LOW-TEMPERATURE PLASMA

Nonthermal Decomposition of Nitrous Oxide in a High-Current Pulsed Discharge

D. V. Zatsepin, S. M. Starikovskaya, and A. Yu. Starikovskiĭ

Moscow Institute of Physics and Technology, Institutskiĭ proezd 9, Dolgoprudnyĭ, Moscow oblast, 141700 Russia

Received July 3, 2002; in final form, November 21, 2002

Abstract—The kinetics of the nonthermal decomposition of nitrous oxide (N_2O) in a nonequilibrium plasma is investigated experimentally. A numerical model of the process is constructed and used to simulate the decomposition of N_2O in a high-current pulsed discharge. The most important channels for decomposition are revealed by analyzing the results obtained. The role of the charged, electronically excited, and vibrationally excited components is examined. It is shown that the mechanism for the thermally nonequilibrium decomposition of N_2O in a high-current pulsed discharge is governed by the reactions involving ions and electronically excited molecules. © *2003 MAIK "Nauka/Interperiodica".*

1. INTRODUCTION

In recent years, increased attention has been given to the possibility of actively controlling burning process by means of nonequilibrium low-temperature gas-discharge plasmas [1–5]. In our earlier paper [6], we investigated the relative role of the excitation of the vibrational and electronic degrees of freedom of the gas, the ionization of molecules, and their dissociation in controlling the ignition of a H_2–air mixture. We showed that the main governing parameters for ignition under strongly nonequilibrium conditions are the distribution of the discharge energy over different degrees of freedom of the gas and the rate of the relaxation reactions in the initial ignition stage. In particular, we found that the key role in low-temperature oxidation is played by the production of vibrationally and electronically excited molecules in the discharge. Otherwise, as the temperature increases, the efficiency of the excitation of the internal degrees of freedom somewhat decreases, and the key role is played by the dissociation of molecules and the production of chemically active O and H atoms in the discharge stage. This circumstance leads to the idea of using oxygen-carrying polyatomic molecules, which are efficient sources of oxygen under the discharge conditions, as a means of an additional control in initiating ignition by a nonequilibrium pulsed discharge.

Note that one of the best known chemical compounds of this kind is nitrous oxide, N_2O, which is often used as a source of atomic oxygen both at high temperatures and in the processes of plasmochemical deposition of silicon films, in which N_2O is utilized in mixtures with silane [7].

The decomposition of nitrous oxide behind shock waves has been investigated quite thoroughly under both thermally equilibrium and weakly nonequilibrium conditions. The cross sections for the electron impact excitation of nitrous oxides are known fairly well and make it possible to model in detail both the discharge phase and the afterglow stage. That is why, in this study, we attempted to investigate the nonequilibrium regime of the decomposition of N_2O in a plasma of a nanosecond pulsed discharge in order to clarify the effect of reactions involving the electronically excited, charged, and vibrationally excited components on the decomposition kinetics.

In order to better understand the processes that occur in an N_2O plasma in the high-current discharge phase and the discharge afterglow in the pressure range from 1 to 8 torr at room temperature, we experimentally studied the decomposition of nitrous oxide in a system affected by a fast ionization wave. We carried out a numerical modeling of this decomposition process and, by comparing the measured data with the calculated results, analyzed the kinetics of the plasmochemical reactions in the system.

2. EXPERIMENTAL INVESTIGATIONS OF THE DECOMPOSITION OF N_2O IN A PULSED DISCHARGE

The experimental setup used in this study was described in detail in [6]. The discharges were initiated in a 47-mm-diameter and 20-cm-long quartz tube with a high-voltage plane stainless-steel electrode and a low-voltage ring stainless-steel electrode at its ends. The low-voltage electrode was short-circuited to a grounded shield of a feeding cable by eight wide brass bars and was equipped with a CaF_2 window for emission spectroscopy diagnostics. Negative voltage pulses with an amplitude $|U_{gen}| = 13$ kV, a full width at half-maximum (FWHM) of 25 ns, and a rise time of 2 ns were supplied to the high-voltage electrode of the discharge tube from a pulsed-voltage generator at a repetition rate $f = 40$ Hz

1063-780X/03/2906-0517$24.00

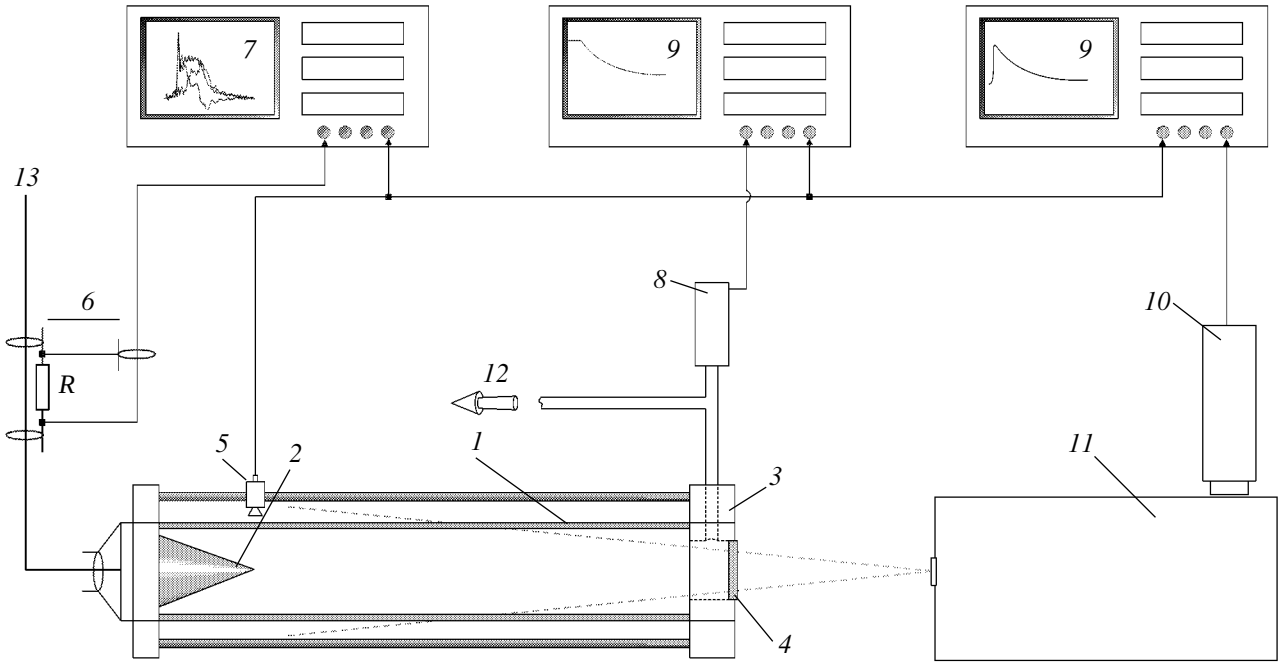

Fig. 1. Experimental device: (*1*) quartz discharge tube, (*2*) high-voltage electrode, (*3*) low-voltage electrode, (*4*) end CaF_2 window, (*5*) capacitive detector, (*6*) back-current shunt, (*7*) TDS-380 oscilloscope, (*8*) pressure gauge, (*9*) C9-8 digital oscilloscope, (*10*) photomultiplier, (*11*) MDR-23 monochromator, (*12*) to a system for pumping out and admitting gas mixtures, and (*13*) 50-Ω coaxial cable for supplying pulsed voltage.

(Fig. 1). In the initial discharge stage, when the conductivity of the discharge plasma is low, a current pulse propagating in a coaxial transmission line is reflected from the open end of the line (i.e., from the high-voltage electrode). As a result, in the stage in which the ionization wave propagates along the discharge gap, the voltage at the high-voltage electrode doubles.

In this stage, the amplitude and shape of the discharge current pulse were measured by a broadband calibrated back-current shunt.

The time-integrated emission signals from the end of the discharge tube were measured by an MDR-23 monochromator.

The absolute value of the pressure during the decomposition of N_2O molecules was measured by an MD × 4S mechanotron.

Figure 2 shows part of the recorded near-ultraviolet spectrum. One can clearly see the spectral bands of the γ system of nitrous oxide.

A complete set of spectroscopic data and the data on the dynamics of the total pressure in the system are illustrated in Fig. 3. Under the same initial conditions, we measured the emission intensities of the second positive system (the $C^3\Pi_u$ transition, $v' = 0 \longrightarrow B^3\Pi_g$, $v'' = 0$; $\lambda = 337.1$ nm) (Fig. 3) and the first negative system (the $B^2\Sigma_u^+$ transition, $v' = 0 \longrightarrow X^2\Sigma_g^+$, $v'' = 0$; $\lambda = 391.4$ nm) of molecular nitrogen, which is the main decomposition product of N_2O. These measurements made it possible to determine the characteristic time of production of molecular nitrogen in the decomposition of N_2O molecules (Fig. 4). The dynamics of the relative density of NO molecules during the decomposition process was measured from the emission intensity corresponding to the transition $NO(A^2\Sigma^+) \longrightarrow NO(X^2\Pi)$ with $\lambda = 237.02 \pm 0.02$ nm. The upper level for this transition is populated by direct electron impact from the ground state of NO molecules and also in chemical reactions involving electronically excited molecules. This circumstance substantially complicates the interpretation of the measured data. Figure 5 shows the half-times of the increase and decrease in the emission intensity of the γ system of NO. Because of the low mean power of the generator of the nanosecond pulses (0.6 W), the gas temperature in the discharge device did not differ appreciably from the temperature of the surrounding air and, in all experiments, was in the range $T = 300 \pm 5$ K.

The data from pressure measurements (Fig. 4) provide additional important information on the conversion rate of a triatomic reagent (N_2O) into bimolecular reaction products.

The total current through the discharge gap can be obtained as a sum of the currents of the incident and reflected pulses. Figure 6 shows the measured incident and reflected current pulses and the calculated transmitted current pulse at an initial gas pressure $p = 4.1$ torr.

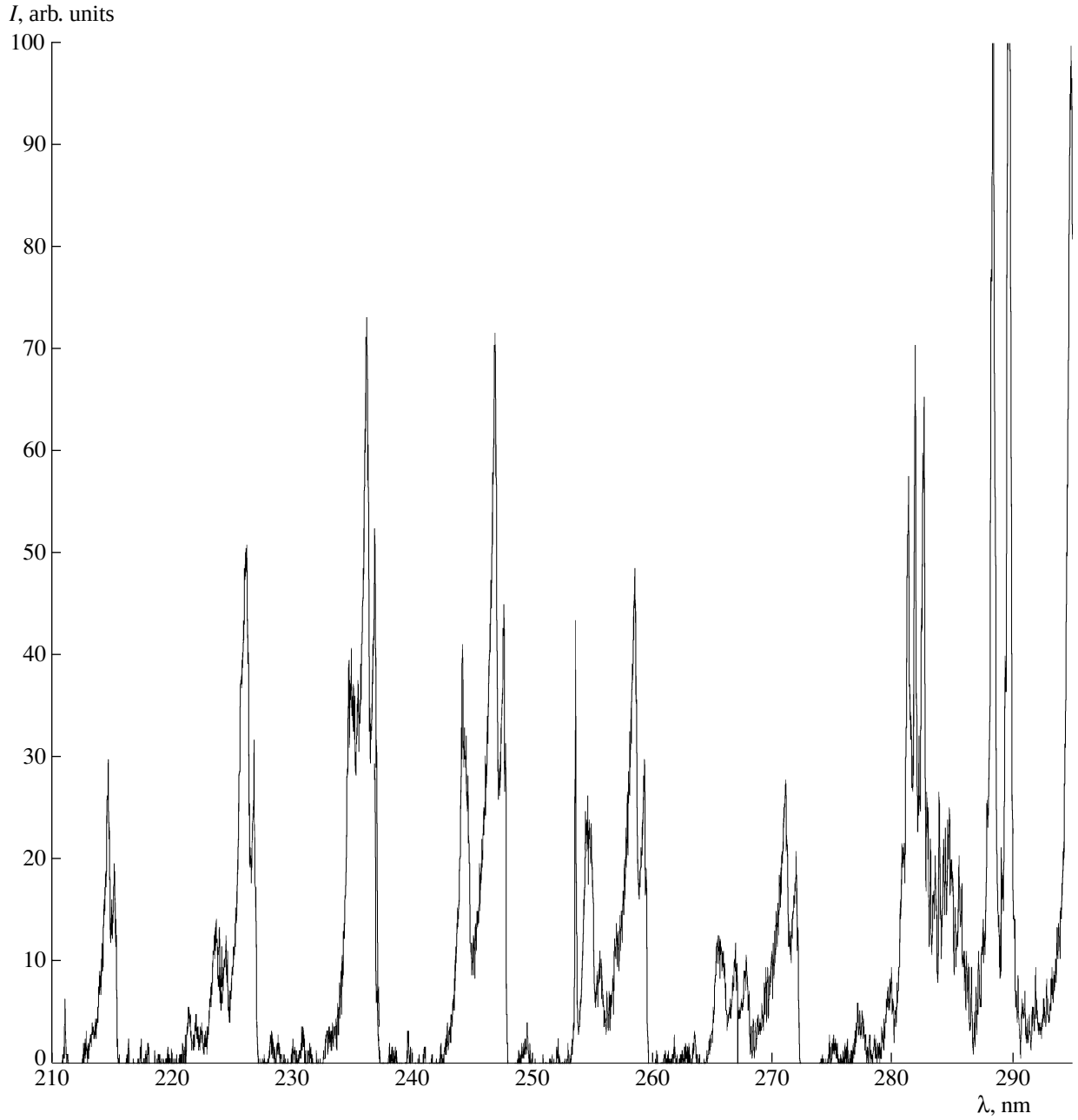

Fig. 2. Emission spectrum from a nanosecond discharge in N_2O at a total pressure of 4 torr 50 s after the start of the decomposition process.

For convenience in comparing the results obtained, the sign of the reflected current pulse is reversed.

Figure 7 displays the maximum amplitude I and the FWHM τ of the current pulse through the discharge gap as functions of pressure. In the pressure range under investigation, the current amplitude in the discharge gap changed from $I = 210$ A at $p = 3$ torr to $I = 110$ A at $p = 7.5$ torr.

The data from measurements of the discharge current and voltage drop across the discharge gap made it possible to estimate the electron density and the reduced electric field after the gap is bridged by a fast ionization wave (Fig. 8). The estimates were carried out in the drift approximation. The electron drift velocity v_d was calculated for a given pulse with allowance for the instantaneous gas composition by solving the Boltzmann equation in the two-term approximation. These data, together with the data on the time behavior of the current density $j = I/S$ through the discharge gap, enabled us to reconstruct the dynamics of the electron

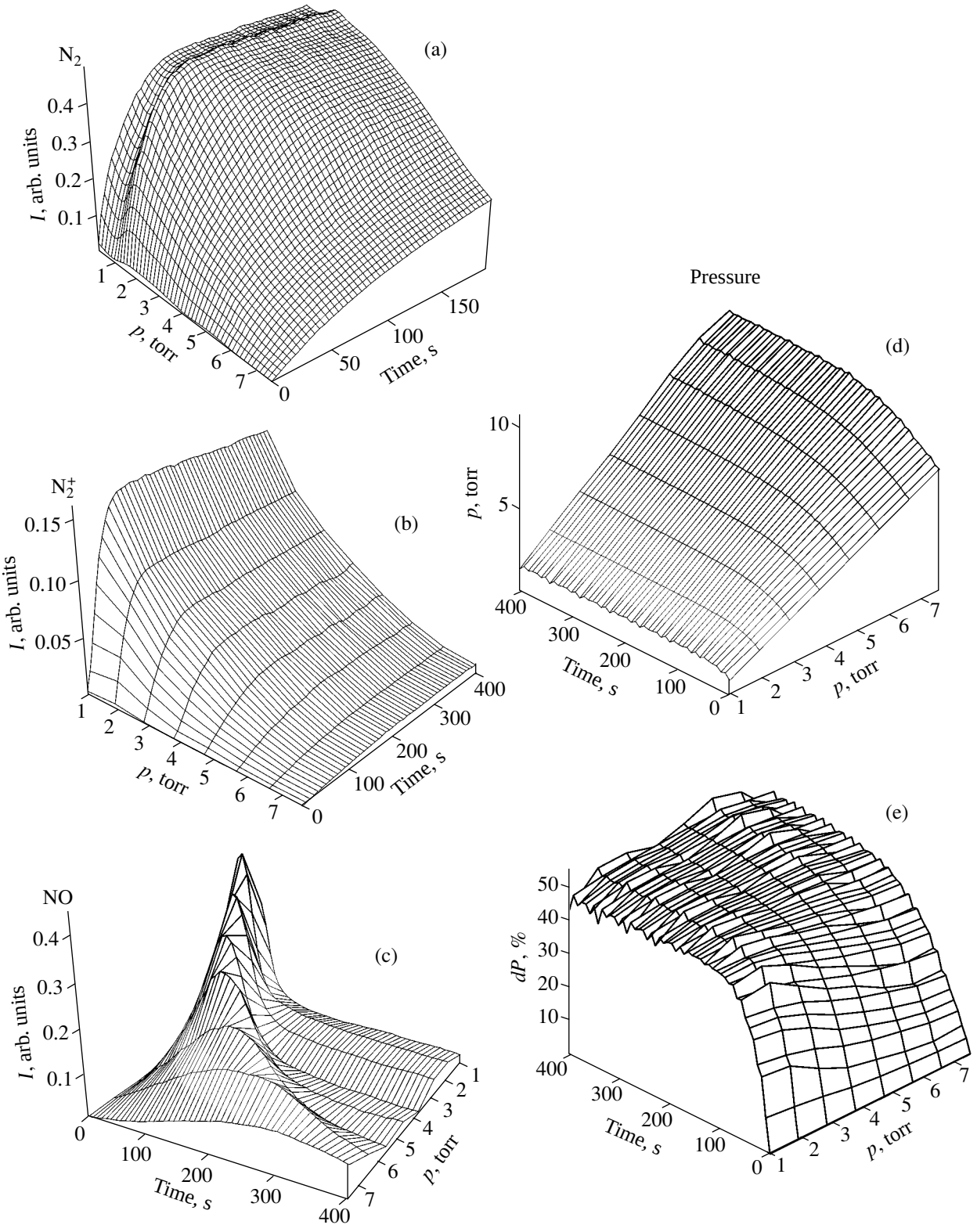

Fig. 3. The measured evolutions of the emission intensities in (a) the second positive nitrogen system (the transition from the $N_2(C^3\Pi_u)$ level), (b) the first negative nitrogen system (the $(N_2^+(B^2\Sigma_u^+))$ level), and (c) the γ system (the $NO(A^2\Sigma^+)$ level) and (d, e) the time evolutions of the gas pressure during the decomposition of N_2O at different initial gas pressures.

density in the high-current discharge phase, $n_e = j/(eV_d)$ (where e is an elementary charge).

In the parameter range under investigation, the reduced electric field in the discharge gap changed from E/n = 300 to 800 Td, which is close to the applicability limit of the two-term approximation for solving the Boltzmann equation in order to calculate the rates of the inelastic processes in the electron–molecule collisions at the lowest pressures in our experiments. The effect of the violation of the two-term approximation (which was observed, e.g., in our earlier paper [6]) should be taken into account when comparing the experimental data and numerical results.

The maximum electron densities were found to lie in the range $n_e \simeq (0.9–2.2) \times 10^{12}$ cm^{-3} (Fig. 8), which correlates well with the results from measurements carried out for other mixtures under similar conditions [8, 9, 6].

3. NUMERICAL MODEL OF THE NONTHERMAL DECOMPOSITION OF N_2O UNDER THE CONDITIONS OF A PULSED DISCHARGE

The calculations were carried out in a direct way; i.e., we computed all subsequent current pulses through the discharge gap with allowance for the changes in the mixture composition during and between the pulses.

The numerical scheme was constructed based on the model developed in [6]. In order to adequately describe the decomposition of N_2O in the presence of NO, N_2, and O_2 molecules, the energy distribution function (EDF) of the electrons was calculated with allowance for the electron-impact excitation of nitric oxide and nitrous oxide molecules. The cross sections for the corresponding processes were taken from [10].

The processes of the relaxation of the vibrationally and electronically excited states, as well as the ion–molecule and molecule–molecule processes, were included in the kinetic scheme in the same manner as was done in [6] in describing the nonthermal oxidation of hydrogen in a H_2–air mixture.

The dependence of the relaxation rate on the degree of vibrational excitation of the reagents and products was taken into account by using the model based on the vibronic-term approximation [11].

The role of the vibrational excitation was taken into account in all the processes involving N_2O, NO, N_2, and O_2 molecules. It was assumed that N_2O molecules are decomposed primarily through the excitation of antisymmetric vibrations (for high vibrational energies and because of the rapid mixing of vibrational modes in an anharmonic interaction, this assumption imposes essentially no restrictions on the dynamics of the EDF near the dissociation threshold).

In the kinetic scheme, every reaction is modeled by a sequence of elementary processes, each of which

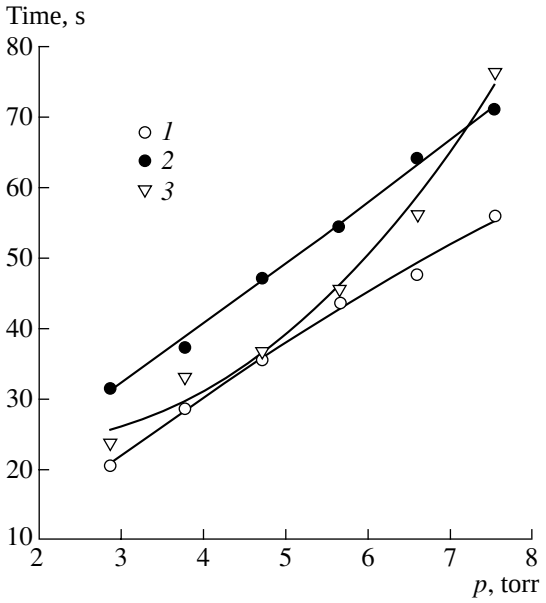

Fig. 4. Characteristic reaction times: the half-times of the increase in the densities of (*1*) $N_2(C^3\Pi_u)$ and (*2*) $N_2^+(B^2\Sigma_u^+)$ molecules and (*3*) the half-time of the increase in pressure. The symbols show the experimental data, and the curves show the calculated results.

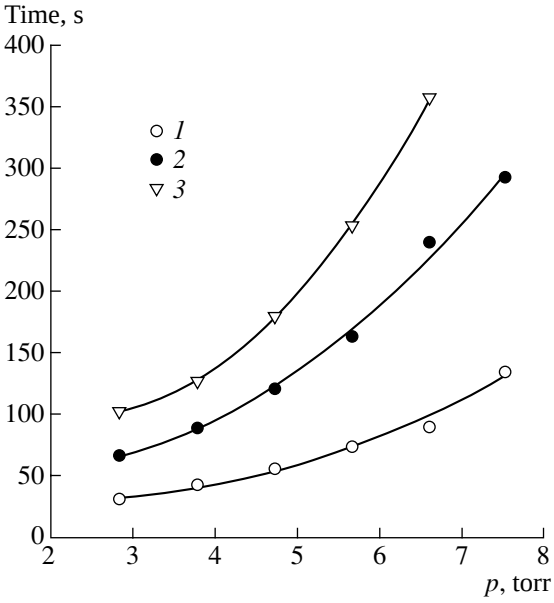

Fig. 5. Dynamics of the density of NO($A^2\Sigma^+$) molecules during the discharge: (*1*) the half-time of the increase in the density, (*2*) the time at which the density becomes maximum, and (*3*) the half-time of the decomposition of NO($A^2\Sigma^+$). The symbols show the experimental data. The curves were obtained by calculating the emission spectrum in the γ band under the assumption that the NO($A^2\Sigma^+$) state is mainly populated via the reaction $N^+ + O_2^- \longrightarrow NO(A^2\Sigma^+) + O$.

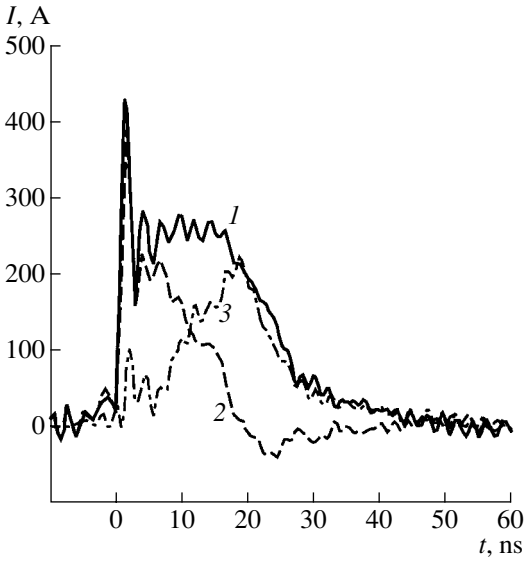

Fig. 6. (*1*) Incident, (*2*) reflected (with the opposite sign), and (*3*) transmitted current pulses at an initial pressure p = 4.1 torr and at U = 26 kV.

determines the rate of the reaction involving reagents in certain vibrationally excited states and producing reagents populated at certain levels.

As an example, the reaction

$$N_2O + O \longrightarrow NO + NO$$

was modeled by the following sequence of elementary processes:

$$N_2O(v_3 = 0) + O \longrightarrow NO(0) + NO(0),$$
$$N_2O(v_3 = 0) + O \longrightarrow NO(1) + NO(1),$$
$$\vdots$$
$$N_2O(v_3) + O \longrightarrow NO(w) + NO(w),$$

whose rate constants were calculated using the algorithm developed in [11].

The remaining reactions incorporated into the kinetic scheme were modeled in an analogous fashion.

The results from calculations of the population dynamics of the individual vibrational states of different molecules in the decomposition process show that the distributions depend nonmonotonically on the energy and that the upper levels are greatly overpopulated. The local peaks in the distributions are associated with the selective depopulation from the upper electronic states to the vibrational levels of the ground state and the recombination fluxes to the upper levels.

The time evolutions of the total pressure and the relative density of $N_2(C^3\Pi_u)$ molecules at an initial pressure p = 4.7 torr are given in Figs. 9 and 10, in which the solid curves show the experimental data and the

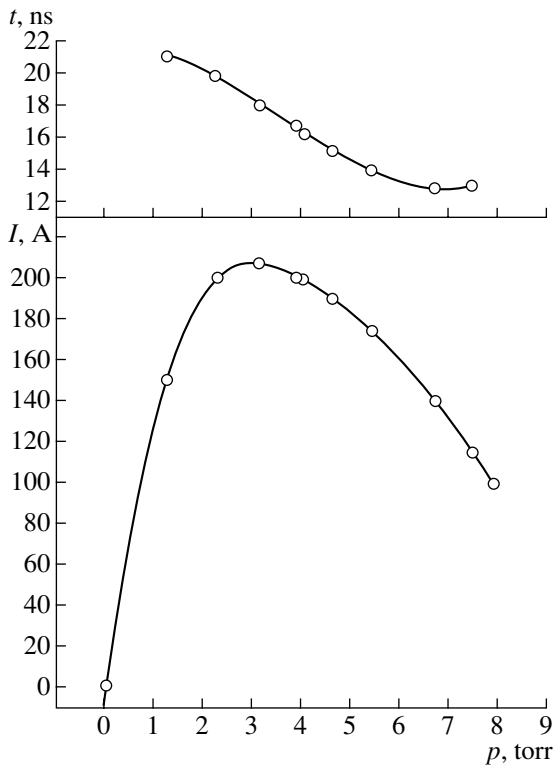

Fig. 7. Mean amplitude of the current pulse and its duration vs. pressure at U = 26 kV.

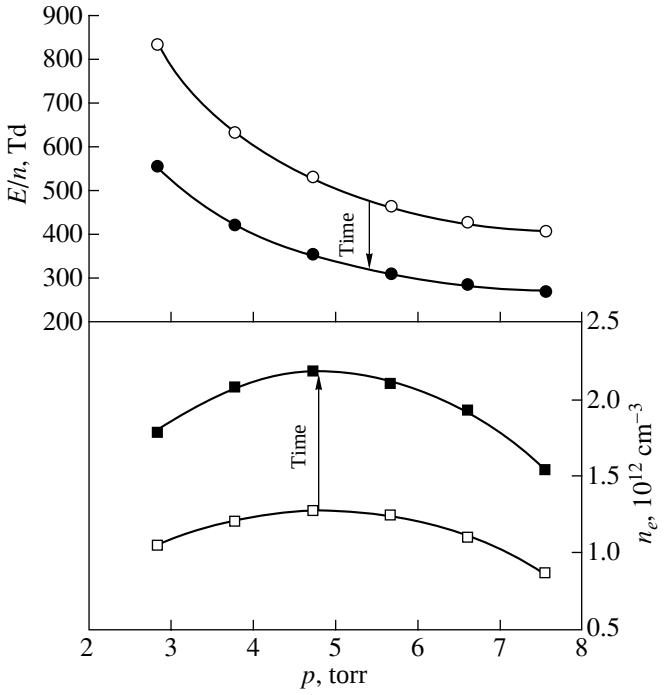

Fig. 8. Reduced electric field and electron density vs. initial pressure for U = 26 kV. The closed circles and closed squares show the initial values, and the open circles and open squares correspond to the values at the end of the decomposition of N_2O molecules.

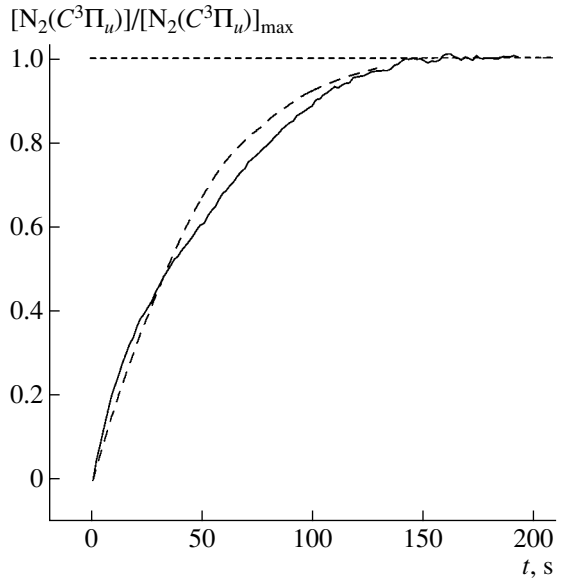

Fig. 9. Comparison between the calculations and the experiment: the measured (solid curve) and calculated (dashed curve) dynamics of the relative density of $N_2(C^3\Pi_u)$ molecules in an N_2O gas at an initial pressure $p = 4.7$ torr and at $U = 26$ kV. Both curves are normalized to the theoretical value of the density of $N_2(C^3\Pi_u)$ molecules in the case of the complete conversion of the initial gas into a mixture of N_2 and O_2 gases.

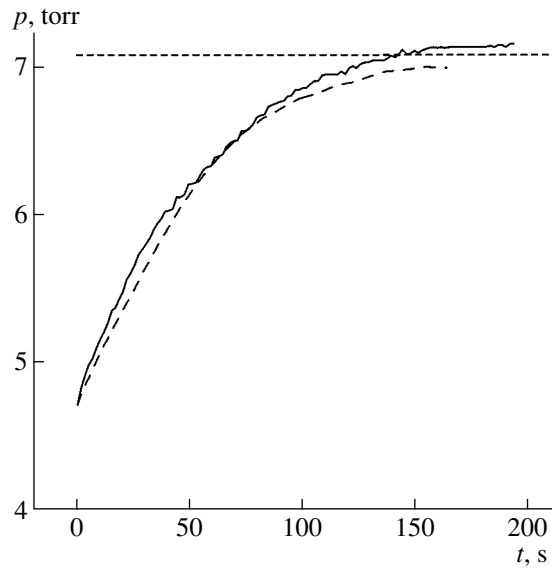

Fig. 10. Comparison between the calculations and the experiment: the measured (solid curve) and calculated (dashed curve) dynamics of the pressure in the mixture resulting from an N_2O gas at an initial pressure $p = 4.7$ torr and at $U = 26$ kV. The horizontal dashed line indicates the theoretical value of the total pressure in the mixture in the case of the complete conversion of the initial gas into a mixture of N_2 and O_2 gases.

dashed curves show the numerical results. The density of $N_2(C^3\Pi_u)$ in Fig. 9 is normalized to the maximum theoretical density of these molecules, and the horizontal dashed line in Fig. 10 indicates the total pressure in the mixture in the case of the complete conversion of the initial gas into a mixture of N_2 and O_2 gases.

Nearly the same shapes of the calculated and measured curves characterizing the production of $N_2(C^3\Pi_u)$ molecules allow us to conclude that, for the conditions of our experiments, the model based on solving the Boltzmann equation in the two-term approximation correctly describes the gas excitation by electron impact. Also, the almost exact coincidence of the time behavior of the experimental and numerical pressure profiles indicates that the model is capable of correctly reconstructing the kinetics of the decomposition of N_2O molecules in the afterglow stage.

The calculated and measured data on the time in which the densities of the main components recorded in our experiments change are compared in Figs. 4 and 5. One can clearly see that, over the entire pressure range under investigation, the proposed model well describes both the rate of conversion of triatomic nitrous oxide into diatomic reaction products (which is evidenced by an increase in pressure during the decomposition of the main reagent; see Fig. 4) and the time evolution of the population of the upper radiating states of nitrogen molecules and atoms.

The situation with the dynamics of the emission intensity of the γ band of NO (Fig. 3) is far more complicated. It is readily seen that the emission from NO increases over a substantially longer time in comparison with the emissions from $N_2(C^3\Pi_u)$ and $N_2^+(B^2\Sigma_u^+)$ (Fig. 5). As a result, the density of $NO(A^2\Sigma^+)$ becomes maximum when the bulk of N_2O molecules have already been decomposed and the density of NO molecules in the ground electronic state is low because of their decomposition in the late discharge stages. This circumstance makes it possible to assert that the $NO(A^2\Sigma^+)$ states are populated through the direct production of the electronically excited nitric oxide molecules rather than through the excitation of NO molecules, e.g., in the reactions $NO + e \longrightarrow NO(A^2\Sigma^+) + e$ or $NO + N_2(A^3\Sigma_u) \longrightarrow NO(A^2\Sigma^+) + N_2$, whose rates are proportional to the instantaneous density of NO molecules in the system. Unfortunately, there are no data on alternative channels of the production of $NO(A^2\Sigma^+)$ molecules. That is why we considered several energetically allowable channels for the production of these excited molecular states. The calculated results that are closest to the experimental data on the dynamics of the emission intensity of the γ band were obtained under the assumption that the $NO(A^2\Sigma^+)$ state is mainly populated in the reaction $N^+ + O_2^- \longrightarrow NO(A^2\Sigma^+) + O$. Since the density of negative oxygen ions O_2^- increases con-

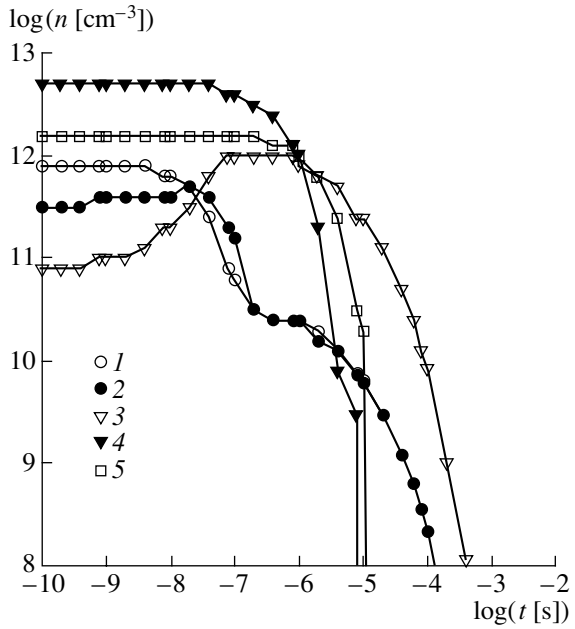

Fig. 11. Dynamics of the densities of the components involved into the fastest reactions in the initial decomposition stage in the discharge afterglow ($[N_2O]/[N_2O]_0 = 1$): (*1*) electrons, (*2*) O^-, (*3*) NO^-, (*4*) $N_2(A^3\Sigma_u^+)$, and (*5*) $N(^2D)$. The initial pressure of the N_2O gas is $p = 4.7$ torr.

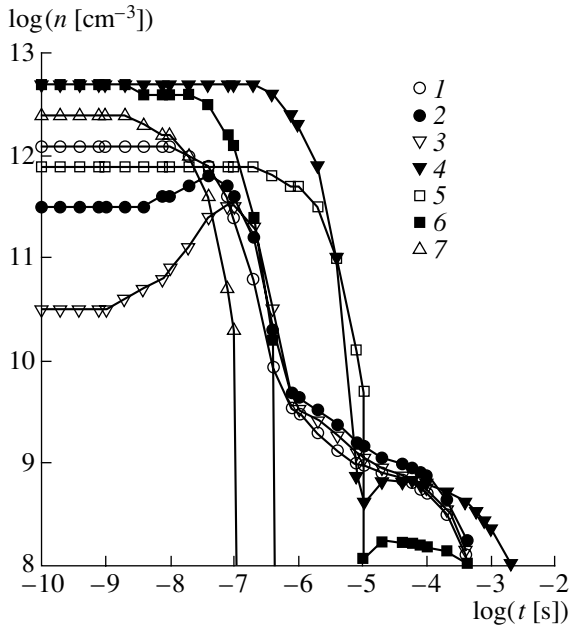

Fig. 12. Dynamics of the densities of the components involved into the fastest reactions in the final decomposition stage in the discharge afterglow ($[N_2O]/[N_2O]_0 = 0.5$): (*1*) electrons, (*2*) O^-, (*3*) NO^-, (*4*) $N_2(A^3\Sigma_u^+)$, (*5*) $N(^2D)$, (*6*) $N_2(B^3\Pi_g)$, and (*7*) $N_2(C^3\Pi_u)$. The initial pressure of the N_2O gas is $p = 4.7$ torr.

tinuously during the discharge, the population of the $NO(A^2\Sigma^+)$ state becomes maximum by the end of the decomposition process; simultaneously, because of a sharp decrease in the density of N^+ atoms after the decomposition of all N_2O molecules, this state is rapidly depopulated in the late discharge stages, which correlates well the experimentally observed population dynamics (Fig. 5). Nevertheless, the question about the possible channels of the excitation of the γ band under our experimental conditions apparently remains open.

4. FLUXES OF ACTIVE PARTICLES AND THE MAIN STAGES OF THE NONTHERMAL DECOMPOSITION OF N_2O IN A PULSED DISCHARGE

In order to single out the most important processes occurring in an afterglow discharge plasma, we analyzed the rates of reactions of the kinetic scheme for the conditions of the first current pulse propagating through the discharge gap originally filled with N_2O at a pressure of 4.7 torr and also for the conditions of the 1560th pulse, which corresponded to the decomposition of 50% of the initial nitrous oxide. To do this, in simulating the discharge kinetics, we calculated the instantaneous densities of the discharge plasma components simultaneously with the absolute rates of all of the reactions (i.e., the rate of the forward reaction minus the rate of the reverse reaction). The reactions that proceed at high absolute rates give rise to particle fluxes in the "reagents–final products" space. This approach allowed us to follow the sequence of the main reactions in which N_2O decomposed into N_2 and O_2.

Figures 11 and 12 show the kinetic curves for the components involved in the fastest reactions in the afterglow plasmas of the above two current pulses.

From these figures, we can clearly see that, in the initial stage of the decomposition of N_2O (when the densities of nitrogen and oxygen molecules in the mixture are low), the kinetics is characteristically different from the kinetics in the late stages (which are dominated by the processes of the excitation of the electronic levels of N_2 molecules in the discharge plasma and their dissociative deexcitation in collisions with N_2O molecules). In particular, the lifetime of the excited $N_2(A^3\Sigma_u)$ molecules increases because of the decrease in the rate of their deexcitation in collisions with N_2O molecules. The lifetime of the negative nitrogen monoxide ions decreases by almost three orders of magnitude because the density of molecular oxygen increases during the decomposition of N_2O and the charge-exchange rate increases. The density of the excited nitrogen atoms $N(^2D)$ decreases markedly for the following reason. In the initial stage, these atoms are efficiently produced in the dissociation of N_2O molecules by electron impact.

However, in the late stages, the density of N_2O molecules decreases; as a result, the rate of this process decreases, thereby reducing the density of $N(^2D)$ atoms. The conversion time of the electrons also becomes somewhat shorter.

The dynamics of the densities of the main neutral components in the afterglow of the first discharge pulse in an N_2O gas at an initial pressure $p = 4.7$ torr is illustrated in Fig. 13. It can be seen that the process proceeds in several stages that are accompanied by the slow decomposition of N_2O and the production of molecular nitrogen and oxygen. During the first pulse, the densities of NO molecules and oxygen atoms in the mixture are relatively high; then, during the decomposition of N_2O, these densities decrease.

As in the case of a system with a reacting H_2–air mixture, the time between the end of each current pulse and the beginning of the next pulse can be divided into four intervals: 0–10^{-7}, 10^{-7}–10^{-5}, 10^{-5}–10^{-3}, and 10^{-3}–25×10^{-3} s.

We performed an analysis of the fluxes of active particles in the fastest chemical conversion reactions during these intervals.

Let us consider the processes that are dominant in each of above four intervals in the afterglow of the first current pulse.

(i) In the first 10^{-7} s after the end of the pulse, the fastest processes are those involved in the electron transfer reactions

$$e^- + N_2O \longrightarrow O^- + N_2, \quad (1)$$

$$O^- + N_2O \longrightarrow NO^- + NO, \quad (2)$$

in which N_2O molecules are efficiently decomposed.

The second fast process is the dissociative quenching of the electronically excited level $N_2(A^3\Sigma_u^+)$ by N_2O molecules.

In this time interval, N_2O molecules are also decomposed in the reaction $N(^2D) + N_2O \longrightarrow NO + N_2$.

(ii) During the second interval (from 10^{-7} to 10^{-5} s), the rate of reactions (1) and (2) increases considerably. However, the decomposition of nitrous oxide is now dominated by the reaction of dissociative quenching of the electronically excited level $N_2(A^3\Sigma_u^+)$ by N_2O molecules.

(iii) The third interval (from 10^{-5} to 10^{-3} s) is characterized by an increasing influence of the secondary processes, namely, the reactions involving O and N atoms.

(iv) For longer times (from 10^{-3} to 25×10^{-3} s), the reactions responsible for the production of N_2 and O_2 molecules in the system become more intense. The most important of these reactions are those involving NO molecules:

$$NO + O + M \longrightarrow NO_2 + M,$$

$$NO_2 + O \longrightarrow NO + O_2,$$

$$NO + N \longrightarrow N_2 + O.$$

The general pattern of the decomposition kinetics changes substantially as the N_2O molecules decompose and the nitrogen, oxygen, and nitric oxide molecules are produced. Although the scheme of the main reactions remains the same, the role of the reactions involving electronically excited nitrogen molecules and oxygen ions increases considerably. The dynamics of the densities of the main reaction products—molecular nitrogen and oxygen—is clearly seen in Fig. 13b. The production of molecular oxygen in the mixture leads, in particular, to a decrease in the density of negative NO^- ions in fast charge-exchange reactions (Fig. 12).

Based on the above analysis, we can conclude that the reactions involving ions and electronically excited particles play a fundamental role in the decomposition of nitrous oxide in a high-current pulsed discharge at low temperatures.

The role of the reactions involving O atoms is relatively unimportant because of the high energy threshold of the reaction

$$N_2O + O \longrightarrow NO + NO.$$

In contrast to an H_2–air mixture, in which the vibrational excitation of H_2 molecules substantially intensifies the oxidation process, the vibrational excitation of the gas does not have any important effect on the decomposition of N_2O molecules.

Under the conditions in question, vibrational excitation cannot play any important role in the decomposition of nitrous oxide by the purely vibrational mechanism [11] for intensifying the monomolecular decomposition because of the high rates of the relaxation of the EDF via the deformation mode at high vibrational quantum numbers.

A decrease in the threshold ($\Theta \simeq 14000$ K) of the reaction $N_2O + O \longrightarrow NO + NO$ also cannot result in any significant (in comparison with other mechanisms) decomposition of N_2O molecules.

The above analysis shows that, under the conditions in question, the nonequilibrium character of the vibrational excitation manifests itself in a quite different manner.

On the one hand, the vibrational excitation of the gas substantially intensifies the reactions of the collisional detachment of electrons from O^-, O_2^-, and NO^- ions. As a result, the recombination of charged particles becomes somewhat more rapid, and reactions (1) and (2) proceed at a slower rate. On the other hand, the vibrational excitation of the gas somewhat increases the mean electron energy in the discharge (because of superelastic collisions) and, accordingly, the population rate of the electronically excited level $N_2(A^3\Sigma_u^+)$,

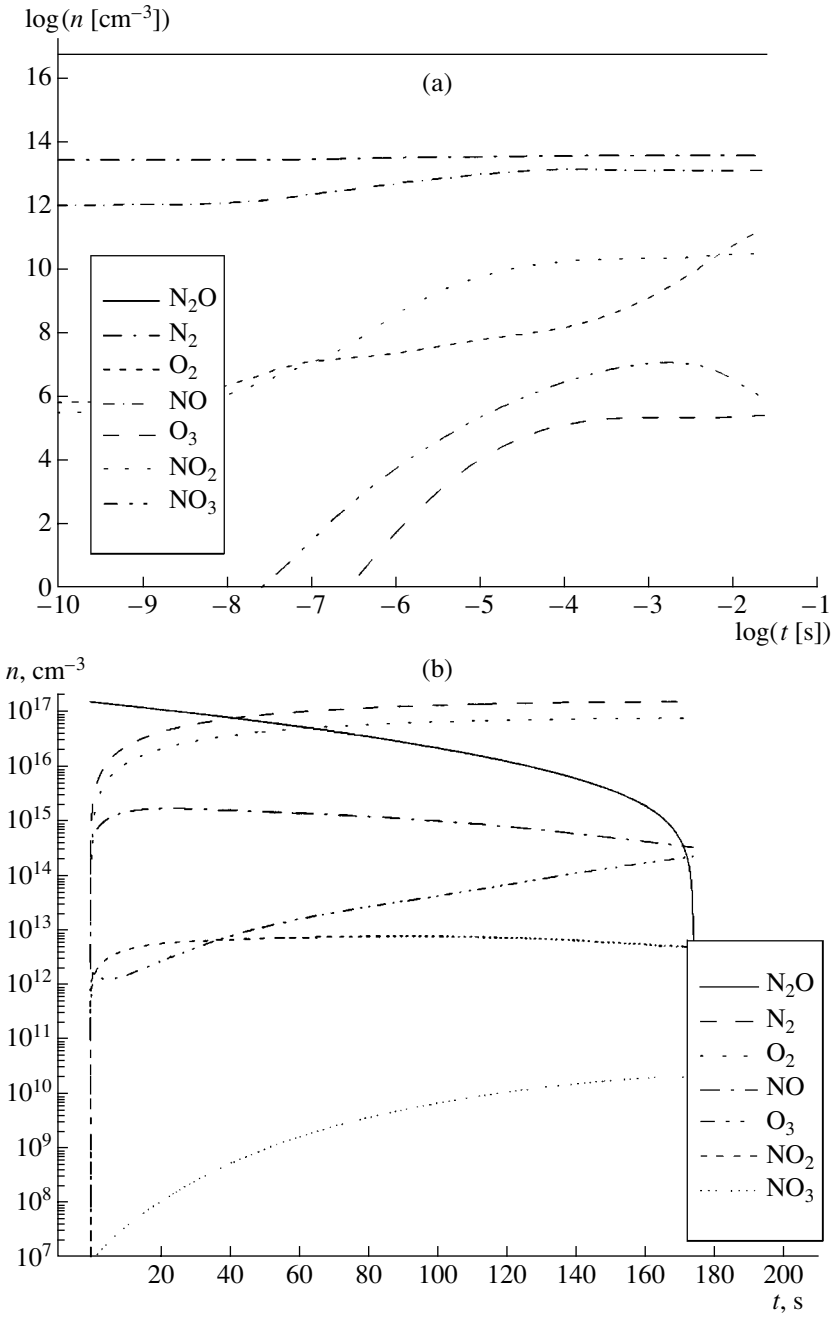

Fig. 13. Dynamics of the densities of the main components (a) in the afterglow of the first discharge pulse and (b) during the decomposition process (the values of the density at the end of each subsequent current pulse are presented): (*1*) molecules, (*2*) atoms, (*3*) electronically excited particles, (*4*) negatively charged particles, and (*5*) positively charged particles. The initial pressure of the N_2O gas is $p = 4.7$ torr.

thereby increasing the rate of the collisional dissociation of N_2O molecules. The rate of direct electron impact ionization of N_2O also increases.

Both of these mechanisms have only an indirect effect on the integral decomposition rate of N_2O molecules and, on the whole, do not significantly change the rate of the decomposition process.

Hence, based on the results obtained in this section, we can conclude that the mechanism for the thermally nonequilibrium decomposition of nitrous oxide (N_2O) in a high-current pulsed discharge is governed by reactions involving the ions and electronically excited molecules.

ACKNOWLEDGMENTS

This work was supported in part by the Ministry of Education of the Russian Federation (project nos. E00-

3.2-427 and E00-5.0-304), the Russian Foundation for Basic Research (project nos. 01-02-17785, 02-02-06523, and 02-03-33376), the International Scientific Technical Center (grant no. 1474), and the U.S. Civilian Research and Development Foundation for the Independent States of the Former Soviet Union (CRDF) (grant no. MO-011-0).

REFERENCES

1. A. F. Panteleev, G. A. Popkov, Yu. N. Shebeko, *et al.*, Fiz. Goreniya Vzryva **27** (1), 26 (1991).
2. N. I. Maiorov, Fiz. Goreniya Vzryva **21** (5), 48 (1985).
3. S. N. Cherepnin, Fiz. Goreniya Vzryva **26** (2), 58 (1990).
4. J. Vinogradov, E. Sher, I. Rutkevich, and M. Mond, Combust. Flame **127**, 2041 (2001).
5. M. Saito, A. Arai, and M. Arai, Combust. Flame **119**, 356 (1999).
6. D. V. Zatsepin, S. M. Starikovskaya, and A. Yu. Starikovskii, Khim. Fiz. **20** (7), 66 (2001).
7. M. Ceiler, B. Kohl, and S. Bidstrup, J. Electrochem. Soc. **142**, 2067 (1995).
8. N. B. Anikin, S. V. Pancheshnyi, S. M. Starikovskaia, and A. Yu. Starikovskii, J. Phys. D **31**, 826 (1998).
9. S. V. Pancheshnyi, S. M. Starikovskaya, and A. Yu. Starikovskii, Fiz. Plazmy **25**, 393 (1999) [Plasma Phys. Rep. **25**, 355 (1999)].
10. M. Hayashi, in *Swarm Studies and Inelastic Electron-Molecule Collisions*, Ed. by L. C. Pitchford, B. V. McKoy, A. Chutjian, and S. Trajmar (Springer-Verlag, New York, 1987).
11. A. M. Lashin and A. Yu. Starikovskii, in *Proceedings of the 26th International Symposium on Combustion, Naples, 1996* (Combustion Inst., Naples, 1996), Rep. 04-077.

Translated by G.V. Shepekina

Plasma Physics Reports, Vol. 29, No. 6, 2003, pp. 528–533. Translated from Fizika Plazmy, Vol. 29, No. 6, 2003, pp. 566–572.

LOW-TEMPERATURE PLASMA

Structure of a Discharge Induced by a Coaxial Microwave Plasmatron with a Gas-Supply Channel in the Inner Electrode

A. Ya. Kirichenko, A. P. Motornenko, and O. A. Suvorova

Usikov Institute of Radiophysics and Electronics, National Academy of Sciences of Ukraine, Kharkov, 61085 Ukraine

Received August 22, 2002; in final form, October 29, 2002

Abstract—The structure of a discharge induced by a coaxial microwave plasmatron with a gas-supply channel in the inner electrode of a coaxial waveguide is investigated. A plasmatron with a power of up to 10 W operates at a frequency of 10 GHz. Depending on the operation regime, the discharge takes either a filament or torch form. A plasma filament arises at low flow rates of the working gas (argon) and occurs at the border of the potential core of the gas jet. A torch discharge occurs at high flow rates and has the form of a hollow cone. In both cases, the discharge arises in the potential core of the gas jet and does not spread beyond it. The distribution of the microwave field in the discharge plasma is determined. © *2003 MAIK "Nauka/Interperiodica"*.

1. INTRODUCTION

The structure of a torch discharge induced by a conventional coaxial microwave plasmatron [1–3] is similar to that of an RF torch discharge [4, 5]. The main difference is that, in an RF torch discharge, the heated gas leaves the discharge region due to upward convection, whereas in a microwave torch, the working gas is blown through the interelectrode channel and then is let out into the atmosphere. When the working gas in a microwave plasmatron is supplied through a special channel in the central electrode [6–10] (rather than through the interelectrode space), the discharge takes a specific form. The plasmatrons of this type are called TIA (Torche á Injection Axiale) plasmatrons. In this case, the edge of the inner electrode (rather than the coaxial outer electrode) acts as a nozzle forming the gas flow. As a result, the microwave discharge is ignited not in the central region of the argon jet, but at the border between the potential core of the jet and the turbulent boundary layer, which contains (besides argon) molecules of the surrounding air. Because of the specific conditions of discharge formation, the discharge structure in such a plasmatron differs significantly from that in a conventional plasma torch [4].

The structure and dynamics of the discharge in various operating regimes of a plasmatron with a gas-supply channel in the central electrode were studied in [8–10]. In [8, 9], the specific features of such a discharge were attributed to the high electron density and the presence of a plasma skin layer, as well as to the effect of the surrounding air. In contrast, in [10], it was suggested that the discharge structure can be strongly affected by the structure of the cold gas jet. In all of these studies, argon at approximately the same flow rate was used as a plasma-forming gas; however, in [8, 9], the discharge was fed with a microwave power of ~1 kW at a frequency of 2.45 GHz, whereas in [10], the power supplied to the discharge did not exceed 10 W and the experiments were performed at a higher microwave frequency (10 GHz).

This paper is aimed at studying the general features of such discharges by a unified approach and acquiring additional data on the microwave field distribution in the discharge at a frequency of 10 GHz and an input power of several watts. Attention is focused mainly on investigating the discharge structure at different flow rates of the plasma-forming gas (argon).

2. EXPERIMENTAL SETUP

In our experiments, we used a plasmatron in which argon was supplied through an axial channel in the inner electrode [6]. The channel diameter was varied from 0.35 to 2 mm. The argon flow rate was no higher than 2 l/min. The output power of the 10-GHz continuous-wave magnetron exciting the discharge was up to 10 W. The discharge plasma was strongly nonequilibrium [6], and the electron energy distribution was far from Maxwellian [8, 9]. Taking into account relatively small plasma dimensions, this somewhat impedes the study of the plasma using conventional investigation techniques. To investigate the microwave field distribution in the discharge, we employed the method of a small perturbing body (vibrating metal string) [11, 12].

Figure 1 presents a schematic of the plasmatron and the block diagram of a system for measuring the microwave field distribution in a discharge. The microwave radiation is fed from magnetron *1* through ferrite valve *2* and attenuator *3* to a plasma torch in the form of coaxial waveguide *4* with nozzle *5* at its end. The end of the coaxial waveguide with an inner electrode 4 mm in diameter and outer electrode 10.5 mm in diameter is

1063-780X/03/2906-0528$24.00

tapered to a cone so that the output opening of the outer electrode decreases to 4 mm and that of the inner electrode decreases to 0.6–2 mm. The shape of the inner electrode apex can be varied by changing the diameter of the gas supply channel. In the feed circuit of the torch, directional coupler *6* is inserted, which receives the total microwave signal reflected from the matching elements of the coaxial waveguide, torch nozzle, and all of the other elements that reside in the surrounding space near the nozzle. The reflected signal is recorded with detector *7*, loading the measurement channel of the directional coupler. Since this signal is time-independent, the input capacitance of oscilloscope *8*, which displays the signal, does not allow it to pass to the oscilloscope input. In the measurements, this signal was used as a reference one.

When a small perturbing body (a sphere, disc, or cylinder) is placed in the microwave field created by the coaxial nozzle in the atmosphere or a discharge plasma, the signal reflected from the perturbing body is added to the reference signal. The amplitude of the reflected signal is proportional to the electric field strength at the position of the perturbing body, and the signal phase is determined by the phase difference between the microwave field at this point and the reference signal. If the perturbing body is immobile, there will be no reflected signal on the oscilloscope screen. However, when the perturbing body is displaced from one point to another, at which the electric field differs in amplitude or phase, the time variations in the electric field will be displayed on the oscilloscope screen.

In our experiment, vibrating steel string *9* (0.3 mm in diameter and 80–100 mm in length) serves as a perturbing body. The string is fixed at its upper end and hangs down freely. The string vibrations are excited with electromagnet *11*, which is placed near the string support and is fed from audio-frequency generator *10*. The audio-frequency oscillator is also used to synchronize the horizontal sweep of the oscilloscope. The signal reflected from the vibrating string provides information about the electric field strength at the string position, and, being superimposed on the reference signal, it also provides information about the phase difference between them.

The electric field profile across the discharge and the amplitude–phase characteristic of the wave propagating along plasma jet *12* are displayed on the oscilloscope screen.

Figure 1 schematically illustrates the string vibrations along the plasma axis. Obviously, such measurements allow us to reveal only the character of the spatial variations in the electric field or the change in the electric field at a given spatial point as the regime of plasmatron feeding is changed or the plasmatron design is modified. It should also be taken into account that the measurement results are averaged over the string segment located in the plasma jet. The abelianization of the measurement results, assuming the discharge to be

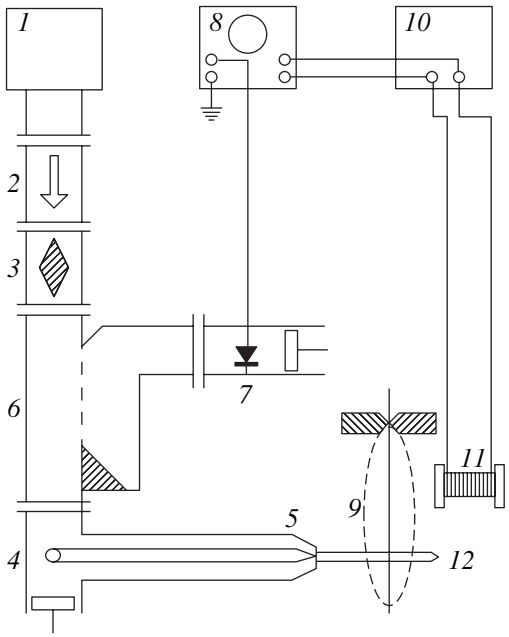

Fig. 1. Schematic of the experimental setup.

cylindrical in shape, allow us to determine the true electric field profile. Since the detector operates at the quadratic segment of its characteristic, the oscilloscope trace reflects the evolution of the electric field squared.

A cathetometer with a magnification of 15–20 was used to monitor the discharge structure and measure its dimensions. The discharge was also photographed.

3. EXPERIMENTAL RESULTS

Photographing the discharge and monitoring its structure with a cathetometer revealed the following features. In the middle of the torch, there is a constriction (waist), which divides the discharge into two parts—a conical part residing on the nozzle and a small cylindrical part, which then transforms into a kind of brush with a blurred end (Fig. 2a). The cone base diameter is determined by the nozzle diameter, i.e., by the diameter of the edge of the inner coaxial electrode. The inner electrode was tapered so that the thickness of the nozzle wall was as small as several tenths of a millimeter. As a result, the electric field at the nozzle edge is fairly strong and highly nonuniform, which leads to the ignition of a microwave discharge. Any eccentricity of the inner electrode with respect to the outer one violates the discharge symmetry.

A specific feature of the conical part of the discharge is that the discharge occurs only in a thin layer on the cone surface, the layer thickness being on the order of the skin depth. From the inside, this layer is adjacent to the conical region occupied by the unexcited working gas. In [8, 9], it was hypothesized that the increase in the electron density N_e, electron temperature T_e, and gas

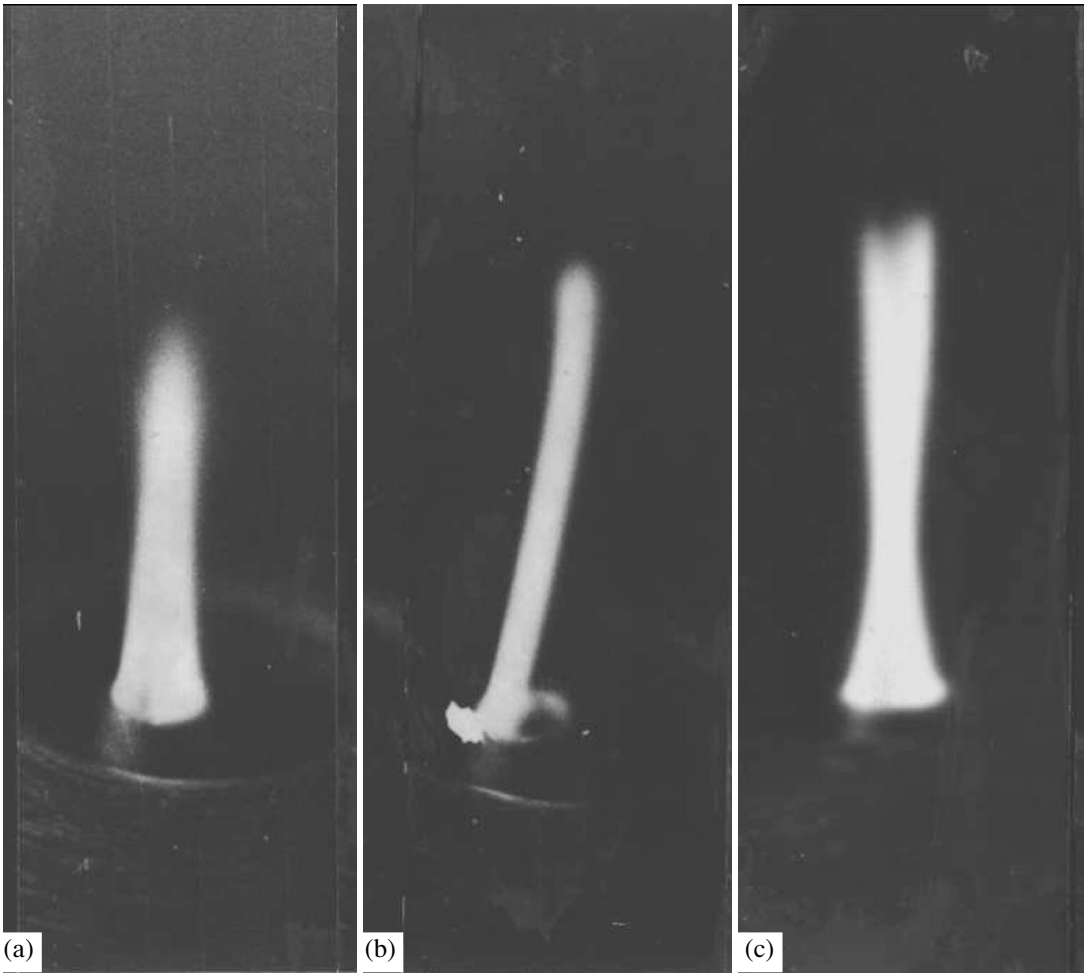

Fig. 2. Photograph of (a) a torch discharge and (b, c) a filament discharge.

temperature T_g at the border of the initial part of the discharge is only due to the penetration of nitrogen or oxygen through the surface of the potential core of the gas jet from the surrounding air. However, this hypothesis seems to be unconvincing; in particular, it does not explain the conical shape of this part of discharge.

It has been found that, in the power range of 2–10 W, the decrease in the argon flow rate to 1.0 l/min results in a qualitative change of the discharge, which converts into a steady-state filament discharge. The photograph of such a discharge is shown in Fig. 2b. The point on the nozzle edge on which the filament base resides is usually located closest to the outer coaxial electrode (it happens because of the violation of the axial electrode symmetry, which is very difficult to avoid in the experiments). It is natural to expect that the microwave field is maximum at this point. The filament is stretched not along the velocity vector of the gas outflowing from the nozzle but is inclined at a small angle (~6°) toward the axis of the inner electrode. The filament radius is around 0.15 mm. Assuming that the filament radius is equal to the skin depth in the discharge plasma, the electron density in the filament turns out to be higher than 10^{12} cm^{-3}, which agrees with the results of [6].

The increase in the argon flow rate at a fixed input power leads to an increase in the filament length until it reaches its maximum value at $Q \approx 1$ l/min.

After the filament has reached its maximum length, a similar filament (initially unstable) inclined at the same angle to the axis arises at the diametrically opposite point of the nozzle edge. The latter filament crosses the former one, forming a scissorlike figure (Fig. 2c). The number of filaments arising and vanishing at the nozzle edge gradually increases with the argon flow rate. At the same time, the rate of filament motion over the perimeter of the nozzle opening also increases. This motion is similar to that of an anode spot on the anode of a voltaic arc. However, the filaments move not in the nozzle plane but along the nozzle perimeter, thereby forming a conical part of the discharge. As a result, a hollow conical discharge region arises near the nozzle (Fig. 2a); such a discharge was previously observed in

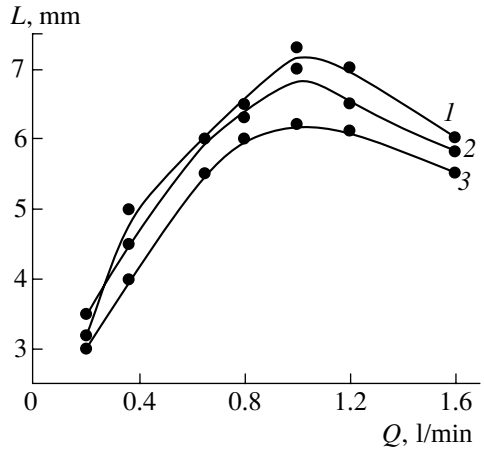

Fig. 3. Plasma filament length L vs. argon flow rate at input powers of (*1*) 5.9, (*2*) 4.5, and (*3*) 3.0 W.

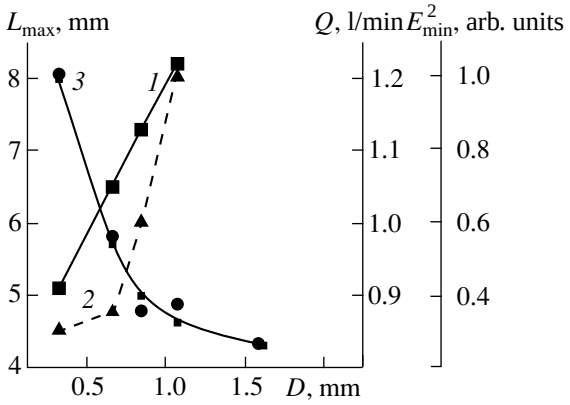

Fig. 4. Maximum discharge length L_{max} and the corresponding values of the argon flow rate Q and the electric field squared E^2 vs. nozzle diameter.

[8–10]. The angle between the cone generatrix and the discharge axis is again ~6°, as in the case with a solitary filament occurring at low argon flow rates. When comparing with the results of [8, 9], it should be remembered that, in those papers, the inclination angle was in the range 4°–8°, which does not contradict the results of our study.

After the filament length L has reached its maximum value, it begins to decrease. This is illustrated in Fig. 3, which shows the plasma filament length as a function of the argon flow rate Q at different input powers P. The dependences were measured for a nozzle with the diameter of the channel in the inner electrode equal to 0.8 mm. Whatever the power, the maximum length of the plasma filament is reached at the same argon flow rate of Q = 1 l/min. We note that a steady-state filament discharge occurs only at argon flow rates in the range Q = 0.2–1.0 l/min. A further increase in the argon flow rate leads to both filament instability and a change in the discharge structure.

The increase in the diameter D of the channel in the coaxial inner electrode (i.e., the diameter of the nozzle opening) leads to an increase in the maximum length of the plasma filament. Simultaneously, the argon flow rate at which this maximum is reached also somewhat increases. Figure 4 shows the maximum filament length L_{max} (curve *1*) and the argon flow rate Q (curve *2*) corresponding to this maximum versus the diameter D of the plasmatron nozzle opening. The dependences were measured at the fixed discharge input power P = 5.9 W. We note that the dependence of the maximum discharge length on the nozzle opening diameter is linear.

The measurements of the electric field profile along the filament show that a surface plasma wave propagates along the filament [11]. As an example, Fig. 5 presents the amplitude–phase characteristics of the wave propagating along the filament for plasmatrons with two different diameters (0.6 and 0.8 mm) of the channel in the inner electrode. In both cases, the input power is 5.3 W and the argon flow rate is 1.0 l/min. Under these conditions, the filament length amounts to 6.0 and 7.5 mm, respectively. It follows from these dependences that, in the latter case, the wave is slower by a factor of 1.25–1.5. In this case (as in the case of a surfatron [13]), the filament discharge is apparently sustained by a slowed-down traveling surface plasma wave. Since, under the same operating conditions, the discharge formed by a nozzle with D = 0.6 mm is shorter than that formed by a nozzle with D = 0.8 mm, the electric field strength in the latter case is somewhat lower.

The increase in the filament length is accompanied by a decrease in the electric field inside the filament. Figure 6 shows the maximum value of the electric field squared E^2 in the filament as a function of the gas flow rate at a fixed power of P = 5.3 W and different nozzle diameters. The electric field was measured at a distance of z = 0.5 mm from the nozzle. Stable plasma filaments

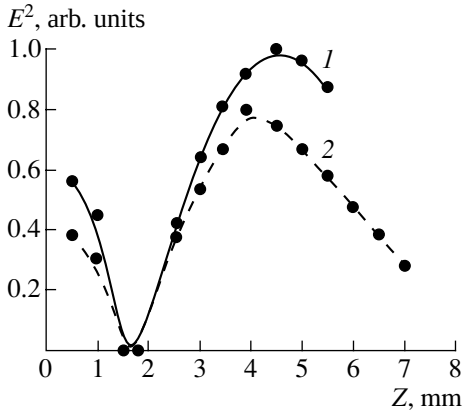

Fig. 5. Profile of the electric field squared E^2 along the discharge axis for nozzle-opening diameters of (*1*) 0.6 and (*2*) 0.8 mm.

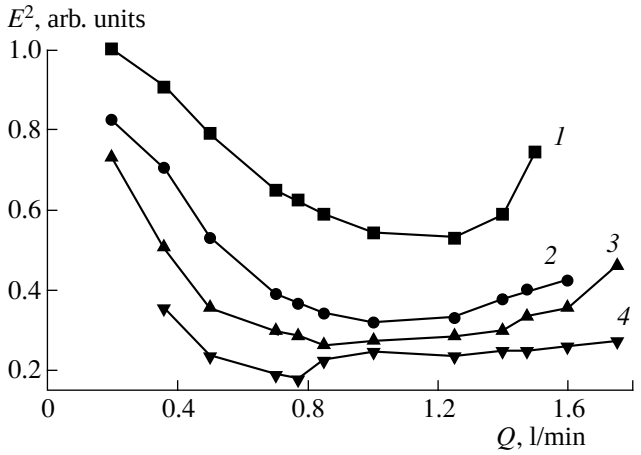

Fig. 6. Electric field squared E^2 in the filament discharge vs. argon flow rate for nozzles with opening diameters of (*1*) 0.35, (*2*) 0.6, (*3*) 0.8, and (*4*) 1.6 mm.

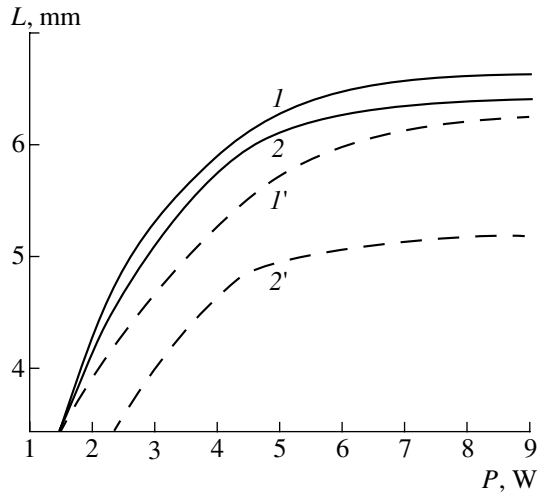

Fig.7. Discharge length L vs. input power P with (curves *1*, *2*) and without (curves *1'*, *2'*) an additional supply of argon through the interelectrode space for two rates of argon supply through the channel in the inner electrode: Q = (*1*, *1'*) 1.4 and (*2*, *2'*) 0.65 l/min.

exist only at the descending branches of these curves. After reaching the minimum on the curve $E = F(Q)$ (which corresponds to the maximum filament length), the filament becomes unstable and begins to move about the nozzle perimeter in a jumplike manner. It is interesting to note that, at the minimum of the curve, the electric field squared $E^2_{\min}$ is approximately inversely proportional to the diameter D of the nozzle opening. This can be seen in Fig. 4, in which the circles show the measured values of $E^2_{\min} = F(D)$ and curve *3* shows the dependence $E^2_{\min} \approx 1/D$. The fairly good agreement between the inversely proportional dependence and the experimental results indicates that the squared electric field E^2 in the filament is inversely proportional to the filament length.

As was noted in [8, 9], the length of the conical part of the discharge depends slightly on the microwave input power, although the total torch length can be varied by varying input power P. The study of the transformation of a filament into a torch shows that, as the input power P and/or argon flow rate Q increase, the length L of a stable steady-state plasma filament gradually increases until it saturates or reaches its maximum value, after which it begins to decrease. A further increase in Q results in the change of the discharge structure. As the input power increases, the dependence $L(P)$ at $Q < 1$ l/min saturates without an appreciable change in the filament structure except for the appearance at its end of an additional reddish glow, whose size increases with P. Seemingly, this extra glow is related to the excitation of nitrogen outside the potential core of argon jet.

4. DISCUSSION OF THE EXPERIMENTAL RESULTS

Observations of the dynamics of the gas jet flowing out of the nozzle [14] show that a potential core in the shape of a cone residing on the nozzle is formed in the jet. Inside the core, the outflowing gas (argon) is not mixed with the surrounding air. In the rest of the jet, intense turbulent mixing of the jet gas with the surrounding air occurs. The cone height is higher by a factor of nearly 4.4–5 than the diameter of the nozzle opening from which the jet is ejected. Hence, the cone half-angle of the potential core is 6°.

Therefore, the discharge filament does not stretch along the gas flow, as is the case of a torch discharge in other types of plasmatrons, but, originating at the nozzle edge, propagates along the conical border of the potential core of the jet. The filament length gradually increases with increasing argon flow rate Q or input power P. A significant fraction of the energy acquired from the microwave field is carried away by the gas flow not only along the filament but also across it. This is an extra channel for thermal energy losses into the surrounding space through the side surface of the filament, thereby appreciably contributing to the loss caused by diffusion. As was shown in [8, 9], the diffusion of the surrounding gas (particularly, nitrogen) into the discharge naturally results in an increase in the gas temperature on the surface of the conical part of the discharge.

In [8], a special chamber filled with argon was used to reduce the effect of nitrogen and oxygen penetrating into the discharge from the surrounding space. In our experiments, similar isolation of the discharge from the surrounding air was accomplished by simultaneously supplying argon through both the axial channel in the central electrode and the interelectrode space. Figure 7 shows the lengths of the filament and torch discharges

as functions of the input power P with (curves *1* and *2*) and without (curves *1*' and *2*') an additional supply of argon through the interelectrode space at a flow rate of $Q' = 1.5$ l/min. In the latter case, argon was supplied only through the channel in the central electrode. In both cases, the filament discharge occurred at $Q = 0.65$ l/min, whereas the torch discharge occurred at $Q = 1.4$ l/min. It can be seen that, when the filament discharge has not yet attained its maximum length, the supply of argon through the interelectrode space increases the discharge length by several tens of percent, whereas in the case of a torch discharge, the extra supply of argon increases the discharge length less significantly.

This result again confirms the influence of the structure of the working gas jet on the characteristics of the discharge under study. The plasma filament is formed at the border of the potential core of the gas jet and stops elongating after leaving the cone region. Then, extra filaments arise, which form the conical part of the discharge. An increase in the microwave power or the argon flow rate does not affect the height of this cone, because it is completely determined by the size of the potential core of the outflowing gas jet. A further increase in the argon flow rate leads to a shortening of the plasma torch because of an increase in the thermal energy losses from the discharge. In this case, the discharge diameter can somewhat increase far from the nozzle.

REFERENCES

1. J. D. Cobine and D. A. Wilbur, J. Appl. Phys. **22**, 835 (1951).
2. S. Murayama, J. Appl. Phys. **39** (12), 5478 (1968).
3. S. P. Martynyuk, A. P. Motornenko, and A. Yu. Usikov, Dokl. Akad. Nauk Ukr. SSR, Ser. A, No. 8, 734 (1975).
4. S. I. Zilitinkevich, Telefoniya i Telegrafiya bez Provodov, No. 6, 652 (1928).
5. R. Grigorovich and D. Kristesku, Opt. Spektrosk. **6** (2), 129 (1959).
6. S. P. Martynyuk and A. P. Motornenko, Dokl. Akad. Nauk Ukr. SSR, Ser. A, No. 2, 161 (1978).
7. M. Moisan, G. Sauve, Z. Zakrzewski, and J. Hubert, Plasma Sources Sci. Technol. **3**, 584 (1994).
8. J. Jonkers, L. J. M. Selen, J. A. M. van der Mullen, *et al.*, Plasma Sources Sci. Technol. **6**, 533 (1997).
9. J. Jonkers, A. Hartgers, L. J. M. Selen, *et al.*, Plasma Sources Sci. Technol. **8**, 49 (1999).
10. A. Ya. Kirichenko, A. P. Motornenko, and O. A. Suvorova, Radiofiz. Élektron. **6** (2), 252 (2001).
11. A. Ya. Kirichenko, A. P. Motornenko, A. F. Rusanov, *et al.*, Zh. Tekh. Fiz. **71** (4), 23 (2001) [Tech. Phys. **46**, 386 (2001)].
12. A. Ya. Kirichenko, A. P. Motornenko, and O. A. Suvorova, Ukr. Fiz. Zh. **46**, 689 (2001).
13. M. Moisan and Z. Zakrzewski, J. Phys. D: Appl. Phys. **24**, 1025 (1991).
14. Shih-I. Pai, *Viscous Flow Theory* (Van Nostrand, Prinston, 1957; Inostrannaya Literatura, Moscow, 1962), Vol. 2.

Translated by N.N. Ustinovskiĭ

Plasma Physics Reports, Vol. 29, No. 6, 2003, pp. 534–537. Translated from Fizika Plazmy, Vol. 29, No. 6, 2003, pp. 573–576.

LOW-TEMPERATURE PLASMA

High-Voltage Stage of a Vacuum Arc

A. V. Zharinov and V. P. Shumilin

Lenin All-Russia Electrotechnical Institute, Krasnokazarmennaya ul. 12, Moscow, 111250 Russia

Received October 31, 2002

Abstract—An elementary theory of the cathode region at the high-voltage stage of an arc discharge is proposed. The theory is based on the balance equations for the particles in an active plasma layer, the power balance at the cathode, and the equation for the Richardson–Dushman electron emission with allowance for the Schottky effect. The most characteristic features of this type of discharge are considered. A non-Langmuir cathode sheath model is proposed for a low-voltage arc on a tungsten electrode. © *2003 MAIK "Nauka/Interperiodica".*

The literature on arc-discharge physics is mainly devoted to low-voltage arcs at voltages on the order of the ionization potential u_i. It is obvious, however, that there is also a high-voltage arc stage (HVAS), which occurs, e.g., during vacuum breakdown, and after which the discharge inevitably transforms into a low-voltage arc.

Theoretical and experimental studies of the HVAS are of interest for the following reasons:

(i) A HVAS seems to be significantly simpler to investigate than a low-voltage arc because the cathode surface can be treated as plane and solid (unmelted). For high-melting cathodes (W, Ta, etc.), evaporation can be ignored in comparison with cathode sputtering. The electron emission is known to be described by the Richardson–Dushman–Schottky (RDS) theory.

(ii) It is likely that studying the HVAS will help to understand some amazing features of a low-voltage arc.

(iii) Experimental studies of the HVAS will allow one to verify the RDS theory within the record ranges of the current densities and electric fields, including those corresponding to the field emission.

(iv) The highest voltage in the HVAS occurs when the electric field at the cathode is zero and the value of i (the ratio of the ion current density at the cathode, j_i, to the density of the electron current at the cathode) is equal to $i_0 = \sqrt{m/M}$, where m and M are the electron and ion masses, respectively. In the regime of a zero electric field, the gas target density n_0 is minimum [1] and is determined by the formula $n_0\sigma_i R \approx i_0 \ll 1$, where σ_i is the ionization cross section and R is the cathode spot radius. For tungsten, we have $i_0 \approx 1.7 \times 10^{-3}$; hence, the mean square scattering angle of the cathode electrons is negligibly small. Thus, in the HVAS, a nearly collisionless electron beam, directed normally to the cathode spot surface, is produced.

As i increases ($i > i_0$) and the surface is deformed, the beam spreads out. Hence, it is possible to experimentally investigate the dynamics of a solid or fluid surface using a technique similar to the Muller electron projector.

(v) The HVAS can be used in various applications; apparently, it has long been used in pulsed accelerators.

All the above considerations inspire one to analyze the quasi-steady HVAS.

The quasi-steady HVAS is described by two elementary algebraic equations

$$jR \approx \frac{e v_0}{\sigma_i(1+\gamma_i)}, \tag{1}$$

$$i(\varphi_p + u_i - \varphi) \approx \varphi + \frac{\lambda T}{jR}. \tag{2}$$

Equation (1) is the existence condition, and Eq. (2) is the heat balance equation at the spot surface. Here, j is the current density in the RDS model at $i > i_0$, e is the elementary charge, v_0 is the mean velocity of the atoms produced due to the cathode self-sputtering (the flux density of these atoms is $q_0 = j_i(1+\gamma_i)/e$), γ_i is the self-sputtering coefficient, φ_p is the discharge voltage, $e\varphi = e\varphi_0 - e\Delta\varphi$ is the work function with allowance for the Schottky effect ($\varphi_0 = 4.5$ V), T is the surface temperature, and λ is the thermal conductivity.

Equation (1) takes into account that the angular expansion of the atomic flow with the flux density q_0 obeys the cosine law [2] and the electron beam is directed normally to the flat surface of the spot of area πR^2 and is practically not scattered. Hence, we have

$$j_i \le \sigma_i j \int_0^\infty n(x)dx \approx \sigma_i j n_0 R.$$

Since $i = j_i/j \ll 1$, then $j \approx$ const, $\sigma_i \approx$ const, and $i \le \sigma_i n_0 R$. Moreover, $n_0 = j_i(1+\gamma_i)/ev_0 = ij(1+\gamma_i)/ev_0$; hence, Eq. (1) is independent of n_0, i, and T (i.e., they can take any values) and depends only on the discharge voltage through $\sigma_i(\varphi_p)$, $v_0(\varphi_p)$, and $\gamma_i(\varphi_p)$. Condition (1) is valid at $R \ge 3d$, where d is the thickness of a one-

dimensional plane cathode sheath with the cathode fall voltage φ_p.

In contrast, when $d/R \geq 3$, the beam is highly diverging, as in the case of a spherical diode. However, even in this case, a condition of type (1) holds accurate to an arbitrary factor or correction function. This is also true for a deformed spot surface. In the general case, the rigorous derivation of the condition of type (1) is not an easy matter.

Below, in the qualitative analysis, we use approximate condition (1), which leads to the following formula for the HVAS minimum current

$$J \approx \frac{\pi}{j}\left[\frac{e v_0}{\sigma_i(1+\gamma_i)}\right]^2. \quad (3)$$

Obviously, the total discharge current is $J_p = \omega J$, where ω is the number of autonomous microarcs and J_p is determined by the load of the external electric circuit.

The literature data on the v_0 and γ_i values are fragmentary and inexact [3]. In a qualitative analysis, it can be assumed that, for tungsten, $\sigma_i \approx 2 \times 10^{-17}$ cm^2; $v_0 \approx 4 \times 10^5$ cm/s; and

$$\gamma_i \approx \frac{10^{-3}\varphi_p}{1 + 10^{-4}\varphi_p}, \quad (4)$$

where φ_p is in volts. Then, the HVAS minimum current (in amperes) is

$$J \approx \frac{3.2 \times 10^7 (1 + 10^{-4}\varphi_p)^2}{j(1 + 10^{-3}\varphi_p)^2},$$

where the electron current density is in A/cm^2.

If $j(T, \varphi_p) = \text{const}$, then the microarc current decreases with increasing voltage: an increase in the voltage φ_p from 10^3 to 5×10^4 V leads to a 24-fold decrease in the current due to the increase in the rate of cathode sputtering. At high voltages ($\varphi_p > 6 \times 10^3$ V), the regime of a zero electric field ($i = i_0 \approx 1.7 \times 10^{-3}$) is feasible. In this regime, the current density j_0 is determined by the Richardson–Dushman law, whereas the current J and radius R exponentially decrease with the voltage (Fig. 1). For example, they decrease from $J \approx 290$ A and $R \approx 0.15$ cm at $\varphi_p = 7230$ V (in this case, $T \approx 4000$ K) to $J \approx 11$ A and $R \approx 6.4 \times 10^{-3}$ cm at $\varphi_p = 8960$ V (in this case, $T \approx 5000$ K). At $i > i_0$, J and R decrease much more rapidly due to the Schottky effect.

It should be stressed that the energy density released at the anode under the action of the electron beam is extremely high. Accordingly, we assume that special measures are taken to prevent the effect of the anode material vapor.

In the literature, the terms "current per spot" and "threshold current" are sometimes used; in fact, these terms refer to the currents equivalent to current (3).

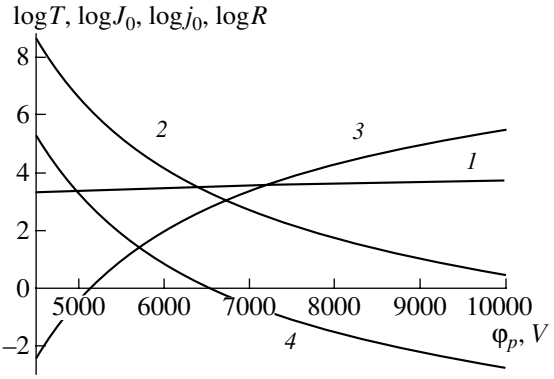

Fig. 1. Decimal logarithms of the (*1*) cathode spot temperature T [K], (*2*) arc current J_0 [A], (*3*) electron current density on the cathode j_0 [A/cm^2], and (*4*) spot radius R [cm] vs. voltage φ_p in the regime of a zero electric field at the cathode.

Even with allowance for the Schottky effect, the HVAS is feasible only at a sufficiently high temperature. For example, if $j > 600$ A/cm^2, then, at $\varphi = 3$ V, we should have $T > 2500$ K.

The Schottky effect leads to a sophisticated interrelation among the HVAS parameters. For a Langmuir cathode sheath, the electric field at the cathode (in volts per centimeter) is

$$E \approx 5700(\varphi_p M)^{1/4}[j(i - i_0)]^{1/2}.$$

Hence, for tungsten ($M \approx 184$ amu) at $\Delta\varphi \approx 3.8 \times 10^{-4}\sqrt{E}$, we have

$$\Delta\varphi \approx 0.055\varphi_p^{1/2} j^{1/4}(i - i_0)^{1/4}. \quad (5)$$

Here, the current density is determined by the formula

$$\vartheta = \tau\exp(-\tau/4), \quad (6)$$

where $\tau = \ln(j/j_0)$, $j_0 = 120T^2\exp(-11\,600\varphi_0/T)$, $\varphi_0 \approx 4.5$ V, and

$$\vartheta T \approx 640\varphi_p^{1/8} j_0^{1/4}(i - i_0)^{1/4}. \quad (7)$$

The values of ϑ lie in the range $0 \leq \vartheta \leq 1.4715$ (Fig. 2). At $\vartheta_{max} = 1.4715$, we have $\tau = 4$ and the current density corresponding to the maximum value of ϑ is equal to $j^* \approx 54.6j_0$; at $\vartheta \longrightarrow 0$, there are two asymptotic values: $j \longrightarrow j_0$ and $j \longrightarrow \infty$. In the range $\vartheta < \vartheta_{max}$, there are two solutions: $j_1 < j^*$ and $j_2 > j^*$. At $T = \text{const}$, the ϑ value increases with increasing $i - i_0$; in this case, we have $dj_1/di > 0$ and $dj_2/di < 0$. Thus, as i and ϑ increase, both solutions tend to j^*. As $i - i_0 \longrightarrow 0$, the current density j_2 tends to infinity because of the decrease in the work function and the transition to field emission becomes feasible. Experimental observations of this transition would be of fundamental importance; however, it is extremely difficult to observe.

One can eliminate T from Eqs. (1), (2), (4), and (7) and obtain the dependence $\vartheta(i)$ at a fixed φ_p. As a

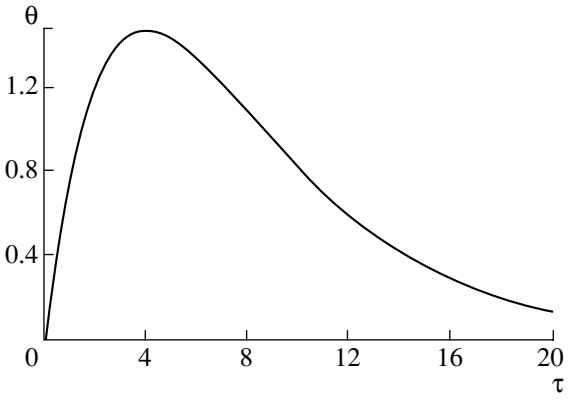

Fig. 2. Parameter θ vs. $\tau = \ln(j/j_0)$.

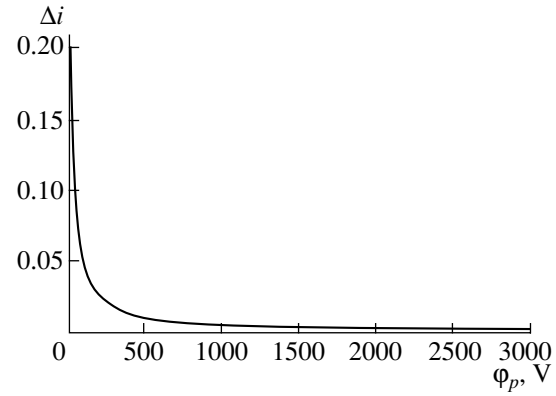

Fig. 3. Dispersion Δi vs. voltage φ_p.

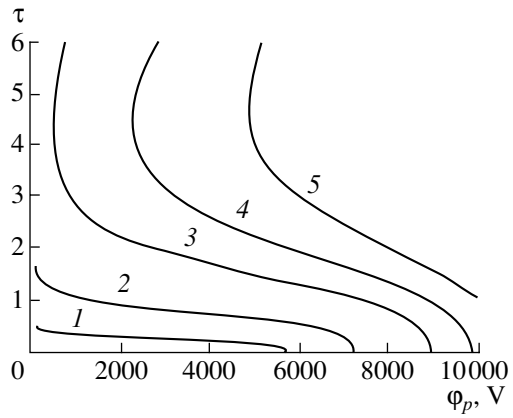

Fig. 4. Dependence of $\tau = \ln(j/j_0)$ on the voltage φ_p at the cathode spot temperatures T = (*1*) 3000, (*2*) 4000, (*3*) 5000, (*4*) 5500, and (*5*) 6000 K.

result, any fixed φ_p value corresponds to certain definite dispersions $\Delta i = i(\varphi_p) - i_0$ and $\Delta J(\varphi_p)$ characterizing the ranges of the admissible i and J values. The dispersions Δi and ΔJ rapidly decrease with increasing voltage. For example, when φ_p increases from 50 to 2000 V, Δi decreases from 0.11 to 2.6×10^{-3}, i.e., by a factor of about 40 (see the dependence in Fig. 3, which was obtained at $\lambda \approx 1.2$ W/(cm K)). Figure 4 presents the solutions to the set of Eqs. (1), (2), (4), and (7) at a fixed temperature. As φ_p increases, the dispersion tends to zero, the Schottky effect disappears, and the current density tends to j_0.

According to Eqs. (3) and (4), the HVAS evolution can start from a single spot with a current of $J \approx 290$ A and radius of $R \approx 0.15$ cm, corresponding to $\varphi_p \approx 7.2 \times 10^3$ V and $T \approx 4000$ K. As i increases, the number of microarcs increases in an avalanche-like manner; the voltage φ_p decreases; and the discharge current $J_p = \omega J$, dispersion, and current density $j = j_0 \exp(t)$ increase. Note that HVAS filamentation develops and J_p grows within the original spot with an initial temperature of 4000 K, rather than on the cold cathode surface.

Obviously, J_p and φ_p vary rapidly in time. Consequently, the filamentation dynamics strongly depends on the intrinsic variable reactance of the microarcs. Thus, the HVAS is also a very sophisticated phenomenon, and an exact non-steady-state theory of the HVAS is still lacking.

In conclusion, let us consider the problem of a field-emission microarc with a current density of $j \sim 10^8$ A/cm^2, which, until now, has been regarded as debatable.

As is the case of the HVAS, the low-voltage tungsten arc is feasible due to cathode sputtering. At the sputtering threshold (e.g., at $\gamma_i \approx 10^{-4}$), the sputtered atoms accumulate near the cathode due to ionization and resonant charge transfer [1]. Equations (1) and (2) also apply to a low-voltage arc at $i \ll 1$. The main distinctive feature of the field-emission arc is the intense Coulomb deceleration of the ions moving to the cathode against the electron flow. As a result, the ions decelerate and the electron beam rapidly spreads out because of scattering. Hence, the Langmuir model of the cathode sheath is not applicable here. In this case, a quasineutral cathode sheath described by the equation

$$\nabla^2 \phi = 4\pi(j/v_e - j_i/v_i) = 0 \qquad (8)$$

can arise. Then, we have $j(r) = \sigma_c d\phi/dr$, where σ_c is the Coulomb conductivity of the plasma,

$$\sigma_c \approx 13 T_e^{3/2}, \qquad (9)$$

with T_e being the electron temperature in eV. On the other hand, we have $j(r) \approx j_E R^2/r^2$ and $T_e(\phi) \approx (T_c + 2\phi/3)$, where T_c is the cathode temperature and j_E is the emission current density. Hence, we obtain

$$j_E \approx 13\left(T_c + \frac{2}{3}\phi\right)^{3/2}\frac{d\phi}{dr}. \qquad (10)$$

It follows from this that, at $\phi \longrightarrow 0$ and $r \sim R$, the electric field at the cathode is

$$\left.\frac{d\phi}{dr}\right|_c \approx \frac{j_E}{13T_c^{3/2}}. \quad (11)$$

At $T_c = 2500$ K ≈ 0.2 eV, we have $E \approx 0.8 j_E$; i.e., in accordance with the Fowler–Nordheim theory, $E \approx 8 \times 10^7$ V/cm at $j_E \approx 10^8$ A/cm^2. After integrating Eq. (10), we obtain

$$j_E R \approx 2.9\varphi_p^{5/2}. \quad (12)$$

According to Eq. (1), at $\varphi_p \ll 10^3$ V, we have

$$jR \approx 3.2 \times 10^3.$$

From here, we obtain $\varphi_p \approx 16.5$ V (for $j_E \approx 10^8$ A/cm^2) and $R \approx 3.2 \times 10^{-5}$ cm. Microspots with such dimensions were mentioned in review [4] and monograph [5].

It is possible that the above estimates are not sufficiently convincing. Nevertheless, the question of a quasineutral cathode sheath is worthy of detailed and comprehensive theoretical consideration.

To conclude, a qualitative analysis of the quasisteady HVAS can stimulate more comprehensive and systematic theoretical and experimental studies aimed at evaluating the fundamental processes in an arc discharge.

ACKNOWLEDGMENTS

We are grateful to A.N. Ermilov for his continuing interest in our study and support. This study was supported in part by the Russian Foundation for Basic Research, project no. 01-02-16014.

REFERENCES

1. A. V. Zharinov, in *Proceedings of XXV International Conference on Phenomena in Ionized Gases, Nagoya, 2001*, Ed. by T. Goto (Nagoya University, Nagoya, 2001), Vol. 3, p. 335.
2. A. V. Zharinov and V. P. Shumilin, Teplofiz. Vys. Temp. **40**, 181 (2002).
3. M. Kaminsky, *Atomic and Ionic Impact Phenomena on Metal Surfaces* (Springer-Verlag, Berlin, 1965; Mir, Moscow, 1967).
4. L. P. Harris, *Vacuum Arcs: Theory and Application*, Ed. by J. M. Lafferty (Wiley, New York, 1980; Mir, Moscow, 1982).
5. G. A. Mesyats, *Ectons* (Nauka, Ekaterinburg, 1993, 1994), Vols. 1–3.

Translated by N.N. Ustinovskiĭ

Plasma Physics Reports, Vol. 29, No. 6, 2003, pp. 449–458. Translated from Fizika Plazmy, Vol. 29, No. 6, 2003, pp. 483–493.

PLASMA INSTABILITY

Tearing Instability of a Force-Free Magnetic Configuration in a Collisionless Plasma

N. A. Bobrova[1], S. V. Bulanov[2], G. E. Vekstein[3], J.-I. Sakai[4], K. Machida[4], and T. Haruki[4]

[1]*Institute of Theoretical and Experimental Physics, Bol'shaya Cheremushkinskaya ul. 25, Moscow, 117259 Russia*

[2]*Prokhorov Institute of General Physics, Russian Academy of Sciences, ul. Vavilova 38, Moscow, 119991 Russia*

[3]*Manchester University, PO Box 88, Manchester M60 IQD, United Kingdom*

[4]*Laboratory of Plasma Astrophysics, Faculty of Engineering, Toyama University, Gofuku 3190, Toyama 930-8555, Japan*

Received October 24, 2002; in final form, December 10, 2002

Abstract—The equilibrium and stability of a sheared force-free magnetic field in a collisionless plasma are investigated, and the main features of charged particle motion in such a field are analyzed. A steady solution is derived to the Vlasov–Maxwell equations for the charged particle distribution function that describes different equilibrium configurations. The tearing instability of the magnetic field configurations is studied both analytically and by particle-in-cell simulations. © *2003 MAIK "Nauka/Interperiodica".*

1. INTRODUCTION

The equilibrium and stability of plasma configurations in force-free magnetic fields have been studied for many years [1]. The force-free magnetic field approximation is used to describe the equilibrium of magnetic configurations in both space and laboratory plasmas [2–4]. Such magnetic configurations are considered to play an important role, e.g., in stellar atmospheres and active regions emerging on the Sun, because the plasma pressure there is much lower than the magnetic field pressure, $\beta = 8\pi p/B^2 \ll 1$.

By force-free magnetic fields are meant those that have no force effect on the plasma. In a low-pressure plasma in an MHD equilibrium state, force-free magnetic fields satisfy the equations

$$\mathbf{B} \times (\nabla \times \mathbf{B}) = 0, \quad \nabla \cdot \mathbf{B} = 0. \tag{1}$$

These equations admit a broad class of solutions, which have been thoroughly investigated in the literature [3]. The equilibrium and stability of plasmas in force-free magnetic fields have been studied mainly in the MHD approximation. However, the MHD approach fails to hold for many problems, especially in astrophysical applications. Hence, the plasma should be described in terms of a collisionless model, in which it is necessary to determine the equilibrium particle distribution functions satisfying the Vlasov–Maxwell equations [5–7]. For the simplest force-free magnetic configuration, this problem was solved in [8], in which the question about the tearing instability of the configuration was also discussed.

Here, we continue the investigations that were begun in [8, 9] and report the new results achieved in this area. In [8], a general solution was obtained that describes the trajectories of charged particles in a one-dimensional force-free magnetic field and is expressed in terms of elliptic functions. In [9], the nontrivial features of the motion of charged particles were discussed in light of the fact that, in such a field, they undergo no centrifugal or gradient drifts. In the present paper, we analyze the main features of charged particle motion in more detail and present a wider class of exact solutions to the Vlasov–Maxwell equations in comparison with that studied in [8, 9]. For clarity in describing the results obtained here and in comparing them with the previously published results, we solve the problem by the same approach as in [8, 9] and keep the same notation. Note that, in recent papers [10, 11], an analogous approach was employed to find exact solutions to the Vlasov–Maxwell equations in the problem of the structure of relativistically strong electromagnetic waves in a collisionless plasma.

We begin by considering a solution to the Vlasov–Maxwell equations for the simplest force-free magnetic field:

$$\mathbf{B}(y) = B_0(\cos\alpha y\mathbf{e}_x + \sin\alpha y\mathbf{e}_z), \tag{2}$$

where α is a constant. This field is a solution to Eqs. (1) in one-dimensional geometry, in which **B** depends only on the *y* coordinate. Solution (2) is a particular solution admitted by the Vlasov–Maxwell equations for force-free magnetic fields. Below, we will find a more complicated solution describing the plasma equilibrium in a force-free field.

It is well known that the tearing instability plays a very important role in magnetic field reconnection in both astrophysical and laboratory plasmas [12, 13]. The present work focuses on the linear stage of this instability in magnetic field (2). In the nonlinear stage of the instability, the plasma and magnetic field usually evolve in an extremely complicated fashion [14–18]. In order to study the nonlinear stage of the tearing insta-

1063-780X/03/2906-0449$24.00 © 2003 MAIK "Nauka/Interperiodica"

bility, we carried out numerical simulations with a 2D3V particle-in-cell (PIC) code. In contrast to [8], we use the initial electron distribution that makes it possible to analyze namely the tearing instability. Since, in [8], the electron drift velocity was chosen to be fairly high, simulations showed the simultaneous development of a tearing and a bending instability; hence, it was rather difficult to compare the numerical results to theoretical predictions. In the computations reported here, the electron drift velocity was chosen to be much lower, thereby making it possible to simulate the tearing instability, resulting in the formation of magnetic islands. The growth rate calculated numerically for the linear instability stage coincides with that obtained analytically.

It should also be noted that, in simulating the nonlinear stage of the instability of plasma configurations in a magnetic field, the boundary conditions are often assumed to be periodic. The analytic solutions obtained in [8] and in the present paper for plasma equilibrium in a periodic magnetic field in the collisionless approximation may be useful for the proper choice of the initial and boundary conditions when simulating collisionless plasmas.

2. CHARGED PARTICLE MOTION IN A PERIODIC SHEARED FORCE-FREE MAGNETIC FIELD

The charged particle motion in force-free magnetic field (2) is described by the equations

$$\frac{\partial v_x}{dt} = \frac{e_a}{cm_a} v_y B_z, \tag{3}$$

$$\frac{dv_y}{dt} = \frac{e_a}{cm_a}(v_z B_x - v_x B_z) + \frac{e_a}{m_a} E_y(y), \tag{4}$$

$$\frac{dv_z}{dt} = -\frac{e_a}{cm_a} v_y B_x. \tag{5}$$

Here, (v_x, v_y, v_z) are the velocity components of a charged particle, the subscript a stands for the particle species ($a = e, i$), and m_a and e_a are the mass and electric charge of a particle. Note that the only nonzero component of the equilibrium electric field **E** is the y component, because, in magnetic field (2), all of the quantities depend solely on the y coordinate. Since the Lorentz force also depends only on y, the electric field can only arise as a result of charge separation in the plasma. In what follows, we will assume that charge separation does not occur and, hence, the electric field is zero.

The general solution to these equations [8] describes the trajectories of charged particles and can be expressed in terms of elliptic functions. Below, we derive an approximate solution to these equations that makes it possible to analyze the particle motion.

The vector potential of magnetic field (2) is equal to

$$\mathbf{A} = -B_0\alpha^{-1}(\cos\alpha y\mathbf{e}_x + \sin\alpha y\mathbf{e}_z). \tag{6}$$

The independence of the vector potential on the x and z coordinates implies the conservation of the corresponding components of the generalized momentum:

$$P_x = m_a v_x + \frac{e_a}{c}A_x = m_a v_x - \frac{m_a\omega_{Ba}}{\alpha}\cos\alpha y = C_1, \tag{7}$$

$$P_z = m_a v_z + \frac{e_a}{c}A_z = m_a v_z - \frac{m_a\omega_{Ba}}{\alpha}\sin\alpha y = C_2, \tag{8}$$

where $\omega_{Ba} = e_a B_0/cm_a$ is the gyrofrequency of the particles of species a.

Expressions (7) and (8) and the energy integral

$$v_x^2 + v_y^2 + v_z^2 = C_3 \tag{9}$$

are the integrals of motion and thus determine the trajectory of a particle. We assume that, at the initial instant, the particle is at the coordinate origin and that its velocity components along and across the magnetic field are equal to $v_x(0) = v_{0\|}$ and $v_y(0) = v_{0\perp}$, respectively. For such a particle, expressions (7) and (8) yield

$$v_x = v_{0\|} - \frac{\omega_{Ba}}{\alpha}(1 - \cos\alpha y), \tag{10}$$

$$v_z = \frac{\omega_{Ba}}{\alpha}\sin\alpha y. \tag{11}$$

Substituting expressions (10) and (11) into the energy integral, we obtain

$$v_y^2 + \frac{2\omega_{Ba}^2}{\alpha^2}\left(1 - \frac{\alpha v_{0\|}}{\omega_{Ba}}\right)(1 - \cos\alpha y) = v_{0\perp}^2, \tag{12}$$

which shows that the effective potential energy of a particle moving in the y direction is equal to

$$U(y) = \frac{\omega_{Ba}^2}{\alpha^2}\left(1 - \frac{\alpha v_{0\|}}{\omega_{Ba}}\right)(1 - \cos\alpha y). \tag{13}$$

Now, we consider some general features of the charged particle motion. When the initial velocity $v_{0\perp}$ of a particle across the magnetic field is sufficiently high, i.e., when the particle energy is higher than the maximum effective potential energy,

$$v_{0\perp}^2 > \frac{4\omega_{Ba}^2}{\alpha^2}\left(1 - \frac{\alpha v_{0\|}}{\omega_{Ba}}\right), \tag{14}$$

the particle executes infinite motion along the y-axis. Particles of this kind are called transit particles. A particle with $v_{0\|} = 0$ becomes transit when $v_{0\perp} > 2\omega_{Ba}/\alpha$, i.e., when its gyroradius becomes larger than the characteristic scale on which the magnetic field varies. When the energy of a charged particle is much higher than the maximum effective potential energy, the mag-

netic field does not affect the particle motion in the y direction and the particle trajectory is a helix with the radius $r_{Ba} = v_{0\perp}/\omega_{Ba}$, $r = \omega_{Ba}/v_{0\perp}\alpha^2$ and a pitch of $2\pi\alpha^{-1}$. The helix moves as a whole along the x-axis with a constant speed equal to $-\omega_{Ba}/\alpha$.

When inequality (14) fails to hold, the particle motion in a magnetic field is finite; such particles are called trapped particles. We first consider the case in which the particle energy is much lower than the effective potential energy. If the initial particle velocity along the magnetic field is zero, $v_{0\parallel} = 0$, then potential energy (13) is approximately equal to $U(y) \approx \omega_{Ba}^2 y^2/2$. In this case, expressions (11) and (12) become

$$v_y = v_{0\perp}\cos\omega_{Ba}t, \quad v_z = v_{0\perp}\sin\omega_{Ba}t. \tag{15}$$

We can see that, in the (y, z) plane, the particles move in the same manner as in a uniform magnetic field. Due to the nonuniformity of magnetic field (2), the field-aligned component of the particle velocity is nonzero and equal to

$$v_x = -\frac{\omega_{Ba}}{\alpha}(1-\cos\alpha y) \approx -\frac{\alpha v_{0\perp}^2}{2\omega_{Ba}}\sin^2(\omega_{Ba}t). \tag{16}$$

Averaging over the period of gyration yields

$$\langle v_x\rangle = -v_{0\perp}\frac{\alpha v_{0\perp}}{4\omega_{Ba}} \sim v_{0\perp}\frac{\alpha r_{Ba}}{2\pi}. \tag{17}$$

We thus arrive at the same dependence as that for the gradient and centrifugal drifts, the only difference being that, in sheared magnetic field (2), the particle drifts along the magnetic field lines rather than across them.

Now, we consider how the motion of a particle changes when its initial velocity along the magnetic field is nonzero. First, according to expression (13), the particle gyrofrequency will change: for low $v_{0\perp}$, the effective gyrofrequency is equal to $\tilde{\omega}_{Ba} = \omega_{Ba}(1 - \alpha v_{0\parallel}/\omega_{Ba})^{1/2}$. Second, the particle moves along an elliptical (rather than circular) trajectory whose semiaxes are in the ratio $(1 - \alpha v_{0\parallel}/\omega_{Ba})^{1/2}$. The motion of a particle with a sufficiently high initial velocity along the magnetic field, $v_{0\perp} \sim \omega_{Ba}/\alpha$, is rather complicated. For the projection of the particle trajectory onto the (y, z) plane, expression (12) gives

$$\frac{dy}{dt} = \pm\frac{\omega_{Ba}}{\alpha}\left(\frac{\alpha^2 v_{0\perp}^2}{\omega_{Ba}^2} - 2\left(1-\frac{\alpha v_{0\parallel}}{\omega_{Ba}}\right)(1-\cos\alpha y)\right)^{1/2}. \tag{18}$$

From expression (11), we obtain

$$\frac{dz}{dy} = \pm\sin\alpha y\left(\frac{\alpha^2 v_{0\perp}^2}{\omega_{Ba}^2} - 2\left(1-\frac{\alpha v_{0\parallel}}{\omega_{Ba}}\right)(1-\cos\alpha y)\right)^{-1/2}. \tag{19}$$

Integrating this equation, we determine the trajectory of a charged particle in the (y, z) plane:

$$\alpha^2\left(1-\frac{\alpha v_{0\parallel}}{\omega_{Ba}}\right)^2\left(z - \frac{v_{0\perp}}{\omega_{Ba}\left(1-\frac{\alpha v_{0\parallel}}{\omega_{Ba}}\right)}\right)^2 = \frac{\alpha^2 v_{0\perp}^2}{\omega_{Ba}^2} - 2\left(1-\frac{\alpha v_{0\parallel}}{\omega_{Ba}}\right)(1-\cos\alpha y). \tag{20}$$

Note that, for $v_{0\perp} \ll \omega_{Ba}\alpha^{-1}$, we arrive at the circular and elliptical trajectories discussed above. However, even when $v_{0\perp}$ is high, the trajectory deviates from being elliptical only slightly. The characteristic feature of the particle motion in the case at hand is that the particles do not undergo centrifugal and gradient drifts [9].

3. SOLUTION TO THE VLASOV EQUATION FOR A PLASMA IN A FORCE-FREE MAGNETIC FIELD

The equilibrium of a plasma in a force-free magnetic field $\mathbf{B} = (B_x, 0, B_z)$ is described by the time-independent ($\partial/\partial t = 0$) Vlasov equation

$$v_y\frac{\partial f_a}{\partial y} + \frac{e_a}{m_a}\left[\frac{v_y B_z}{c}\frac{\partial f_a}{\partial v_x} + \left(E_y + \frac{v_z B_x - v_x B_z}{c}\right)\frac{\partial f_a}{\partial v_y} - \frac{v_y B_x}{c}\frac{\partial f_a}{\partial v_z}\right] = 0, \tag{21}$$

where f_a is the distribution function of the particles of species a. The integrals of motion of the Vlasov equation are the energy of a particle,

$$W = m_a(v_x^2 + v_y^2 + v_z^2)/2 + e_a\varphi, \tag{22}$$

and the components of its canonical momentum,

$$p_x = m_a v_x + e_a A_x/c, \tag{23}$$

$$p_z = m_a v_z + e_a A_z/c. \tag{24}$$

The solution to Eq. (21) for the equilibrium distribution function can be searched for as a function of the integrals of motion:

$$f_a = f_a(W, p_x, p_z). \tag{25}$$

We choose a reference point y_0 at which $\varphi(y_0) = 0$, $A_x(y_0) = 0$, and $A_z(y_0) = A_0$, where A_0 is a constant. We

assume that, at $y = y_0$, the particle distribution is described by a Maxwellian function with an anisotropic temperature ($T_{a\parallel} \neq T_{a\perp}$) and the drift velocity $\mathbf{V}_d^{a0} = (V_{dx}^{a0}, 0, V_{dz}^{a0})$:

$$f_a(y_0, \mathbf{v}_0) = C_a \exp\left\{-\frac{m_a}{2}\left[\frac{v_{0y}^2}{T_{a\perp}} + \frac{(v_{0x} - V_{dx}^{a0})^2 + (v_{0z} - V_{dz}^{a0})^2}{T_{a\parallel}}\right]\right\}. \quad (26)$$

Now, we express the distribution function at the point y_0 in terms of the integrals of motion. To do this, we determine the dependence of $\mathbf{v}_0$ on these integrals and insert it into (26). As a result, we arrive at the following dependence of the distribution function on the integrals of motion:

$$f_a = f_a\left(\frac{W}{T_{a\perp}} - \frac{\Delta T_a}{2m_a T_{a\perp} T_{a\parallel}}(p_x^2 + p_z^2)\right), \quad (27)$$

where $\Delta T_a = T_{a\parallel} - T_{a\perp}$. Consequently, the distribution of the particles of species a can be described by the function

$$f_a(y, \mathbf{v}) = \frac{m_a^{3/2} n_a}{(2\pi m_a)^{3/2} T_{a\parallel} T_{a\perp}^{1/2}} \exp\left\{-\frac{m_a}{2}\left[\frac{v_y^2}{T_{a\perp}} + \frac{(v_x - V_{dx}^a)^2 + (v_z - V_{dz}^a)^2}{T_{a\parallel}}\right] - \left[\frac{e_a}{T_{a\perp}}\varphi(y) - \frac{1}{2}\frac{e_a^2}{c^2 m_a}\frac{\Delta T_a}{T_{a\perp}^2}A^2(y)\right]\right\}, \quad (28)$$

where the drift velocity is equal to

$$\mathbf{V}_d^a = \frac{e_a}{m_a c}\frac{\Delta T_a}{T_{a\perp}}\mathbf{A}. \quad (29)$$

In deriving distribution function (28), we took into account the relationships

$$\int_{-\infty}^{\infty} f_a d\mathbf{v} = n_a(y) = n_a \exp\left(-\frac{e_a\varphi(y)}{T_{a\perp}} + \frac{1}{2}\frac{e_a^2}{c^2 m_a}\frac{\Delta T_a}{T_{a\perp}^2}A^2(y)\right). \quad (30)$$

In a steady state, Maxwell's equations for the vector and scalar potentials, $\mathbf{A}$ and φ, reduce to

$$\frac{d^2\varphi}{dy^2} = -4\pi\rho_e, \quad (31)$$

$$\frac{d^2\mathbf{A}}{dy^2} = -\frac{4\pi}{c}\mathbf{j}, \quad (32)$$

where the electric-charge and electric-current densities have the form

$$\rho_e = \sum_a e_a \int_{-\infty}^{\infty} f_a d\mathbf{v}_a = \sum_a e_a n_a \exp\left(-\frac{e_a\varphi}{T_{a\perp}} + \frac{1}{2}\frac{e_a^2}{c^2 m_a}\frac{\Delta T_a}{T_{a\perp}^2}A^2\right), \quad (33)$$

$$\mathbf{j} = \sum_a e_a \int_{-\infty}^{\infty} f_a \mathbf{v}_a d\mathbf{v}_a = \sum_a \frac{e_a^2 n_a}{c m_a}\frac{\Delta T_a}{T_{a\perp}}\mathbf{A}\exp\left(-\frac{e_a\varphi}{T_{a\perp}} + \frac{1}{2}\frac{e_a^2}{c^2 m_a}\frac{\Delta T_a}{T_{a\perp}^2}A^2\right). \quad (34)$$

It is easy to show that Eqs. (31) and (32) with charge and current densities (33) and (34) have the first integral

$$\frac{1}{2}\left(\frac{d\varphi}{dy}\right)^2 - \frac{1}{2}\left(\frac{d\mathbf{A}}{dy}\right)^2 - 4\pi\sum_a n_a T_{a\perp}\exp\left(-\frac{e_a\varphi}{T_{a\perp}} + \frac{1}{2}\frac{e_a^2}{c^2 m_a}\frac{\Delta T_a}{T_{a\perp}^2}A^2\right) = \text{const}. \quad (35)$$

We assume that the plasma consists of electrons and ions of one species and that the quasineutrality condition is satisfied. Let us consider the case in which $\varphi(y) = 0$ and $A^2 = A_0^2$ is constant. In this case, Eq. (32) becomes

$$\frac{d^2\mathbf{A}}{dy^2} + \alpha^2\mathbf{A} = 0. \quad (36)$$

Here,

$$\alpha = \left[\frac{4\pi e^2}{c^2 m_e} n\left(\frac{\Delta T_e}{T_{e\perp}} + \frac{m_e}{m_i}\frac{\Delta T_i}{T_{i\perp}}\right)\right]^{1/2}, \quad (37)$$

where m_e is the mass of an electron, m_i is the mass of an ion, and $e_i = -e_e = e$. Note that the above definition of the temperature anisotropy differs from the definition used in [8]; as a result, the second term on the right-hand side of Eq. (36) is opposite in sign to the corresponding term in the equation for the vector potential in [8]. The solution to Eq. (36) describes a one-dimensional force-free magnetic field, which is the subject of our analysis. As we have already shown, a one-dimensional equilibrium force-free magnetic configuration can exist only when the plasma temperature is anisotro-

pic in the directions along and across the magnetic field. The weaker the anisotropies of the electron and ion temperatures, the larger the constant α^{-1}. In the limiting case of isotropic temperatures, the magnetic field becomes uniform.

The above solution is clearly a particular case of the solutions admitted by Eqs. (31) and (32) with charge and current densities (33) and (34). In order to find solutions describing more complicated equilibrium states of the plasma in a magnetic field, we impose the following condition on the electron-to-ion temperature anisotropy ratio:

$$\frac{e^2\Delta T_e}{T_{e\perp}^2 m_e} = \frac{e_i^2\Delta T_i}{T_{i\perp}^2 m_i}, \quad (38)$$

which is an analogue of the electroneutrality condition for a collisionless current sheet in the solution obtained by Harris [5]. Using condition (38) and the quasineutrality condition $\varphi(y) = 0$, we reduce the first integral (35) to

$$\frac{1}{2}\left(\frac{d\mathbf{A}}{dy}\right)^2 + k^2\exp\left(\frac{1}{2}\frac{e^2}{c^2 m_e}\frac{\Delta T_e}{T_{e\perp}^2}A^2\right) = \text{const}, \quad (39)$$

where $k^2 = 4\pi\sum_a n_a T_{a\perp}$.

We represent the vector potential $\mathbf{A}$ in a complex form, $\mathbf{A} = A_x + iA_z = R\exp(i\Psi)$, to obtain the equations

$$\left(\frac{d^2R}{dy^2}\right)^2 - \frac{M^2}{R^3} + q^2 R\exp\left(\frac{1}{2}\frac{e^2}{c^2 m_e}\frac{\Delta T_e}{T_{e\perp}^2}R^2\right) = 0, \quad (40)$$

$$\frac{d\Psi}{dy} = \frac{M}{R^2}, \quad (41)$$

where M is a constant and $q^2 = 4\pi\sum_a n_a T_{a\perp}\frac{e^2}{c^2 m_e}\frac{\Delta T_e}{T_{e\perp}^2}$.

The M value for which Eq. (40) with $R = R_0$ and, accordingly, Eq. (36) with constant (37) have a solution uniform along the y coordinate is equal to

$$M = qR_0^2\exp\left(\frac{1}{4}\frac{e^2}{c^2 m_e}\frac{\Delta T_e}{T_{e\perp}^2}R_0^2\right). \quad (42)$$

We can see that $M = \alpha$.

A more general case is that in which the functions R and Ψ (the amplitude and the phase) are not constant. The amplitude varies between $R_{\min}$ and $R_{\max}$, and the phase in the complex representation of the vector potential also varies between its minimum and maximum values. Figure 1 illustrates the behavior of the solution to Eqs. (41) and (39) in the form of a trajectory along which the particle moves in the (A_x, A_z) plane as the y coordinate of the particle varies from $-10/k$ to $10/k$. The solution was obtained by integrating Eqs. (39) and (41) numerically for $R(0) = q/k = 2$, $R'(0) = 0$, $\Psi(0) = 0$, and $M = 1$. We see nonlinear oscillations from the minimum to the maximum amplitude and back again. Because of the nonlinear dependence of the phase on the coordinate, the trajectory precesses in the (A_x, A_z) plane.

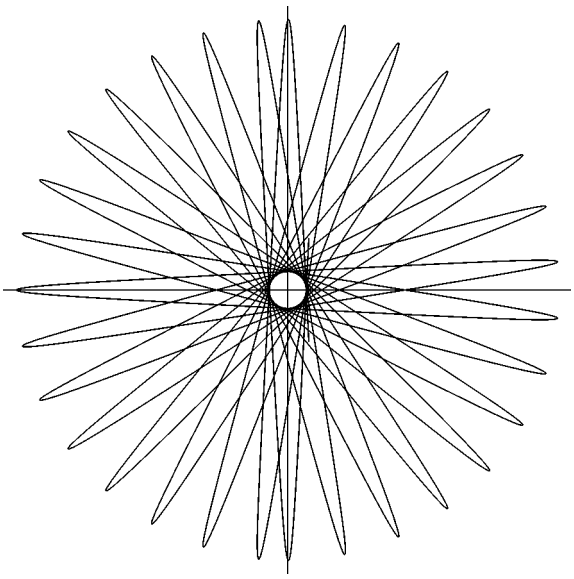

Fig. 1. Trajectory along which a particle moves in the (A_x, A_z) plane as the y coordinate of the particle varies from $-10/k$ to $10/k$ for $R(0) = q/k = 2$, $R'(0) = 0$, $\Psi(0) = 0$, and $M = 1$.

4. TEARING INSTABILITY

The equilibrium configuration under analysis is unstable against various instabilities, e.g., the Buneman instability, the tearing instability, drift instabilities, and some others. We restrict our analysis to the tearing instability because it plays an important role in the magnetic field reconnection. Below, we investigate the stability of equilibrium distribution function (28) in magnetic field (2) against perturbations that depend on x, y, z, and t.

Based on the results obtained in [19–23], we estimate the instability growth rate $\gamma(\mathbf{k})$. We consider the evolution of the following perturbations of the vector potential:

$$A_1(x, y, z, t) = A_1(y)\exp\{i(k_x x + k_z z) + \gamma t\}, \quad (43)$$

where $\mathbf{k} = (k_x, k_z)$ is the wave vector and γ is the growth rate. The perturbation $\mathbf{A}_1(x, y, z, t)$ of the vector potential is described by the equation

$$\frac{\partial^2\mathbf{A}_1}{\partial y^2} - k^2\mathbf{A}_1 = \frac{4\pi}{c}\left(\frac{\partial\mathbf{j}_0}{\partial\mathbf{A}_0}\mathbf{A}_1 + \mathbf{j}_1\right), \quad (44)$$

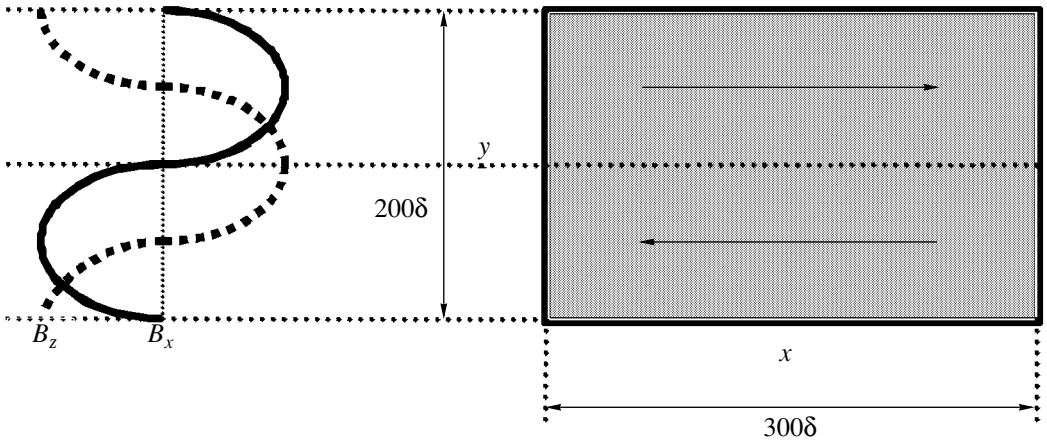

Fig. 2. Computation region and initial magnetic field distribution.

where $(\partial \mathbf{j}_0/\partial \mathbf{A}_0)\mathbf{A}_1$ is the adiabatic component of the perturbation of the electric current density and $\mathbf{j}_1$ is the nonadiabatic component.

It is well known [12] that the problem of the tearing instability should be solved in the outer region and also in the inner region near the surface at which $\mathbf{k} \cdot \mathbf{B} = 0$. In the outer region, the problem reduces to that of analyzing adiabatic (slow) perturbations. In this case, kinetic effects can be neglected and Eq. (44) reduces to the following equation for the function $\Psi = B_{1y}/B_0 = i(k_x A_{1z} - k_z A_{1x})/B_0$:

$$\Psi'' + (1 - \kappa^2)\Psi = 0, \tag{45}$$

where $\kappa = k\alpha^{-1}$, $k^2 = k_x^2 + k_z^2$, and the prime stands for the differentiation with respect to the dimensionless variable $\mu = \alpha y$.

The position of the resonance surface is determined by the condition

$$k_x \cos\mu + k_z \sin\mu = 0, \tag{46}$$

which holds on the planes $\mu_j = -\arctan k_x/k_z + j\pi$, $j = 0, \pm 1, \pm 2, \ldots$.

The solution to Eq. (45) depends on the wavenumber κ and thus can be represented as a linear combination of the functions $\Psi_1 = \sin\sqrt{1-\kappa^2}\mu$ and $\Psi_2 = \cos\sqrt{1-\kappa^2}\mu$ for $\kappa < 1$, the functions $\Psi_1 = 1$ and $\Psi_2 = \mu$ for $\kappa = 1$, and the functions $\Psi_1 = \sinh\sqrt{\kappa^2-1}\mu$ and $\Psi_2 = \cosh\sqrt{\kappa^2-1}\mu$ for $\kappa > 1$.

The solution to the Vlasov–Maxwell equations near the resonance surface in the inner region was considered in [19, 24–26], and the solution for the inner region of the plasma in a sheared magnetic field was derived by Drake and Lee [14, 27]. In the latter case, the width of the inner region is governed by the thermal motion of electrons along the magnetic field and the dispersion relation has the form

$$\Delta' = \frac{\Psi'_{\mu_j+0}}{\Psi_{\mu_j+0}} - \frac{\Psi'_{\mu_j-0}}{\Psi_{\mu_j-0}} = \frac{\gamma}{\kappa v_{Te}\alpha}(d_e\alpha)^{-2}, \tag{47}$$

where v_{Te} is the electron thermal velocity, $d_e = c/\omega_{pe}$ is the collisionless skin depth, and $\omega_{pe} = \sqrt{4\pi n_e e^2/m_e}$ is the plasma frequency.

We consider a plasma configuration infinite in the y direction. Matching the solutions for the outer and inner regions, we obtain the equation

$$\Psi'' + (1 - \kappa^2)\Psi - \sum_j \Delta'\delta(\mu - \mu_j)\Psi = 0, \tag{48}$$

in which the possible discontinuity of the derivative at the resonance surface is accounted for by δ functions. Note that this equation coincides with the Schrödinger equation for a particle moving in a periodic potential. According to the Floquet theorem, the solutions in the neighboring intervals differ only in a factor whose absolute value is equal to unity:

$$\Psi(\mu) = C_1\Psi(\mu) + C_2\Psi(\mu), \quad \mu_{j-1} < \mu < \mu_j, \tag{49}$$

$$\Psi(\mu) = \exp(iQ\pi)(C_1\Psi(\mu - \pi) + C_2\Psi(\mu - \pi)), \quad \mu_j < \mu < \mu_{j+1}, \tag{50}$$

where Q is a real number that characterizes the phase difference between the neighboring resonance surfaces and whose absolute value is less than or equal to unity. Taking into account the fact that, at the resonance surface, the function $\Psi(\mu)$ is continuous while its logarith-

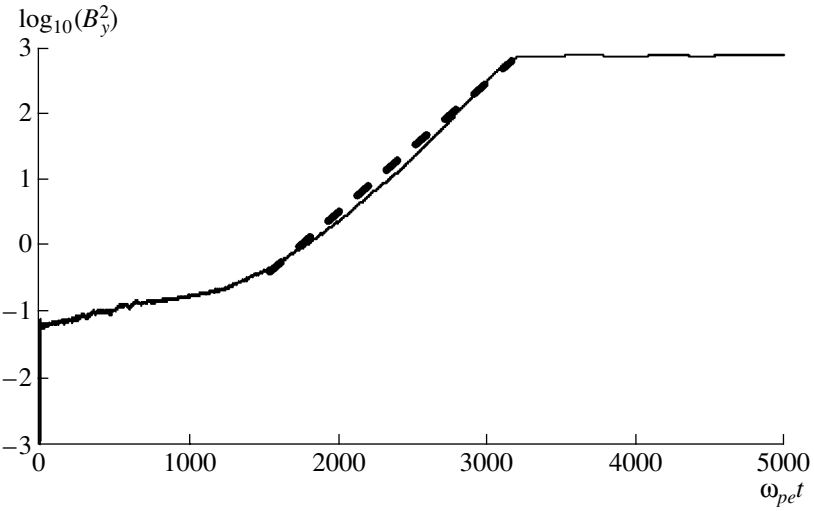

Fig. 3. Time evolution of $\log(B_y^2)$.

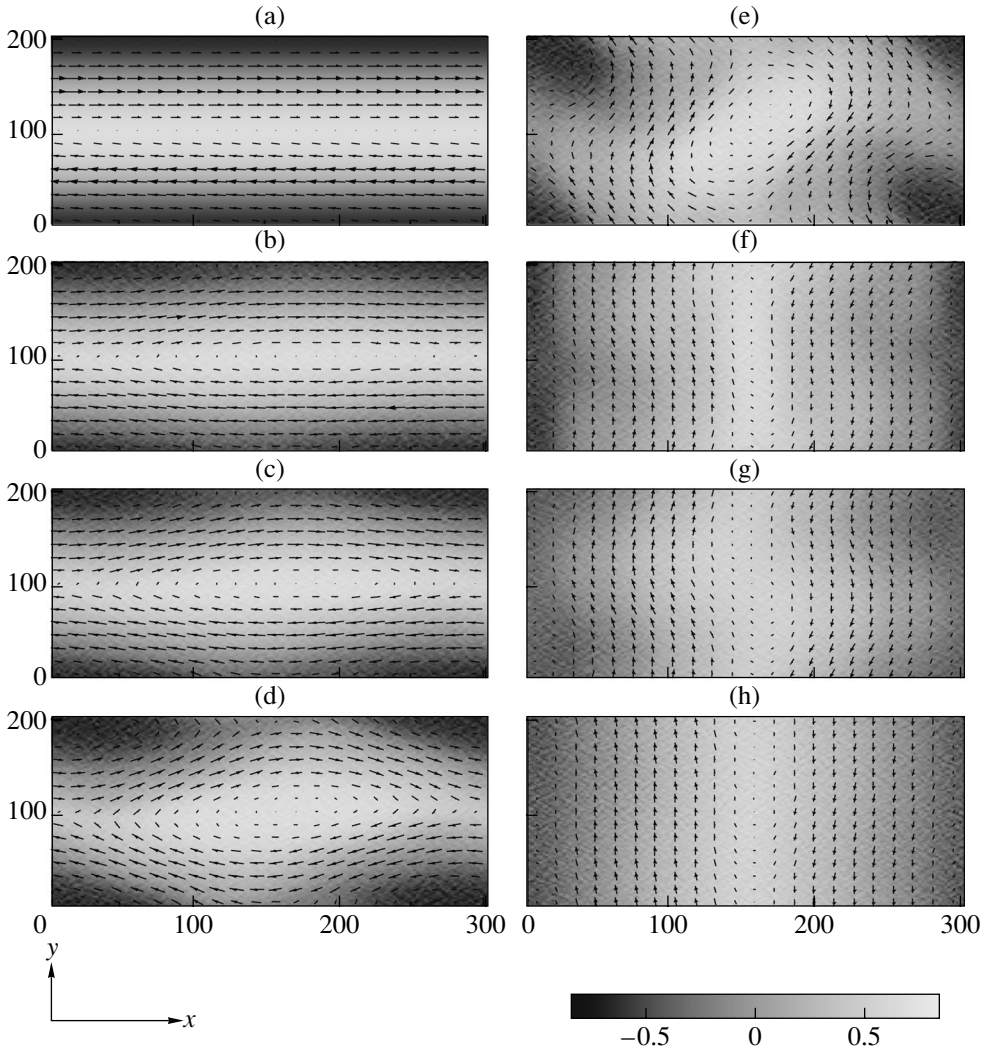

Fig. 4. Magnetic field distributions in the (x, y) plane at different times $\omega_{pe}t$ = (a) 0, (b) 2500, (c) 2750, (d) 3000, (e) 3250, (f) 3500, (g) 3750, and (h) 5000. The components B_x and B_y are represented as a vector field, and the component B_z is shown by shades of gray.

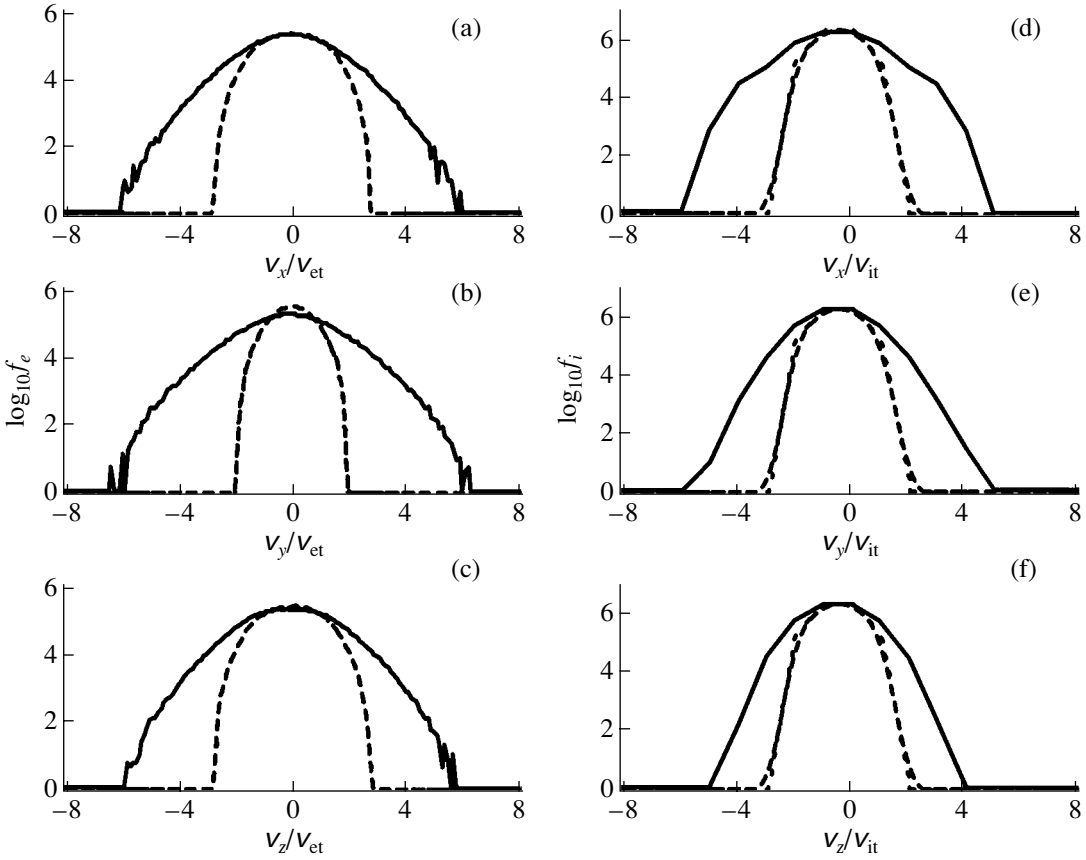

Fig. 5. Electron and ion distribution functions over (a, d) v_x, (b, e) v_y, and (c, f) v_z at the times $\omega_{pe}t = 0$ (dashed curves) and $\omega_{pe}t = 290$ (solid curves).

mic derivative jumps by an amount Δ', we arrive at the equations

$$\exp(iQ\pi)(C_1\Psi(\mu_j - \pi) + C_2\Psi(\mu_j - \pi)) = (C_1\Psi(\mu_j) + C_2\Psi(\mu_j)), \quad (51)$$

$$\exp(iQ\pi)(C_1\Psi'(\mu_j - \pi) + C_2\Psi'(\mu_j - \pi)) = (C_1\Psi'(\mu_j) + C_2\Psi'(\mu_j)) + \Delta'(C_1\Psi(\mu_j) + C_2\Psi(\mu_j)). \quad (52)$$

The condition that Eqs. (51) and (52) have a nontrivial solution yields the following expressions for the jump Δ':

$$\cos Q\pi = \cos\sqrt{1-\kappa^2}\pi + \Delta'\frac{\sin\sqrt{1-\kappa^2}\pi}{2\sqrt{1-\kappa^2}}, \quad \kappa < 1; \quad (53)$$

$$-4\sin^2 Q\pi/2 = \pi\Delta', \quad \kappa = 1; \quad (54)$$

$$\cos Q\pi = \cosh\sqrt{\kappa^2-1}\pi + \Delta'\frac{\sinh\sqrt{\kappa^2-1}\pi}{2\sqrt{\kappa^2-1}}, \quad \kappa > 1. \quad (55)$$

Substituting Δ' into expression (47), we obtain a dispersion relation between γ, κ, and the longitudinal wavenumber Q. The equilibrium state in question is unstable when $\kappa^2 + Q^2 < 1$. The instability growth rate is equal to

$$\gamma = \frac{2(\cos Q\pi - \cos\sqrt{1-\kappa^2}\pi)\kappa\sqrt{1-\kappa^2}}{\sin\sqrt{1-\kappa^2}\pi}(d_e\alpha)^2\alpha v_{Te}. \quad (56)$$

The growth rate is seen to be fastest at $Q = 0$.

5. NUMERICAL SIMULATIONS OF MAGNETIC RECONNECTION IN A FORCE-FREE MAGNETIC FIELD

We have considered above the linear stage of the tearing instability. The nonlinear stage of the instability in a force-free magnetic field was simulated with the 2D3V Tristan PIC electromagnetic code [28]. The dimensions of the computation region were chosen to be 300δ in the x direction and 200δ in the y direction, where $\delta = V_d^e/\omega_{pe}$ (Fig. 2). The initial electron distribution was described by function (28). The electron tem-

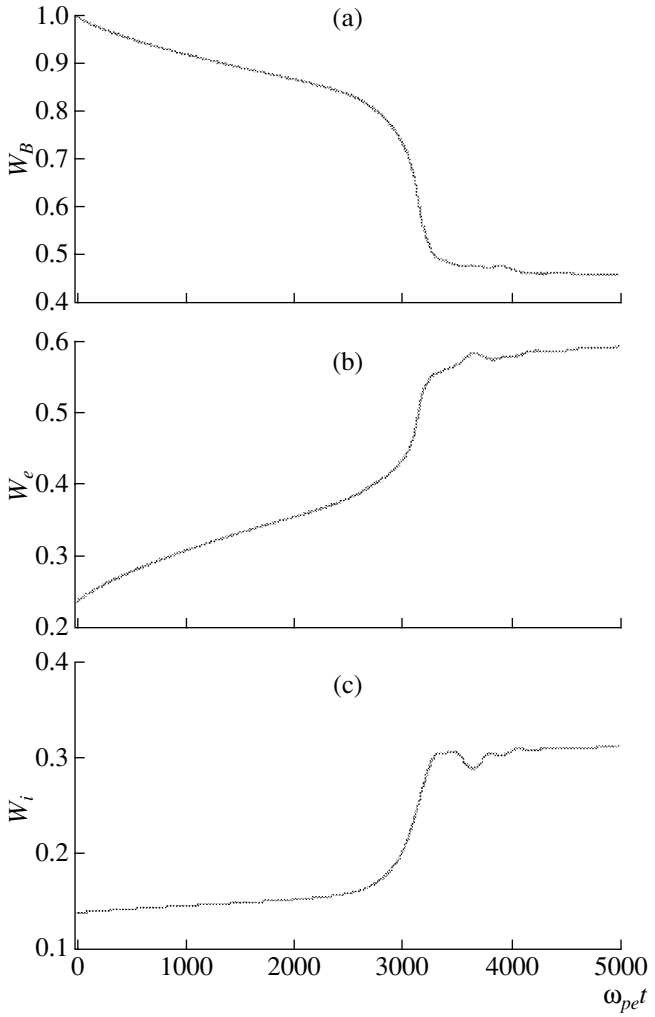

Fig. 6. Time evolutions of (a) the magnetic field energy, (b) the electron kinetic energy, and (c) the ion kinetic energy.

perature anisotropy was $T_{e\|}/T_{e\perp} = 1.12$ and the drift velocity was $V_d^e = 0.8v_{Te}$.

The ion distribution function was assumed to be isotropic, the ion temperature being $T_i = T_{e\|}$. The ion-to-electron mass ratio was set to be $m_i/m_e = 1836$. The total number of particles in the simulations was 1.2×10^7. The initial magnetic field was described by expression (2), in which the magnetic field strength corresponded to the ratio $\omega_{pe}/\omega_{Be} = 3.7$ and its characteristic scale length was $\alpha = 0.0314\delta^{-1}$ (Fig. 2). Note that the dimension of the computation region in the *y* direction coincides with the spatial field period. The boundary conditions were periodic in both the *x* and *y* directions.

Figure 3 illustrates how the squared *y* component of the magnetic field evolves during the development of the instability. According to the time evolution of $\log(B_y^2)$, the instability growth rate is equal to $\gamma/\omega_{pe} = 0.0023$ for $\omega_{pe}t > 1500$ and, for $\omega_{pe}t > 3100$, the instability saturates. The growth rate $\gamma/\omega_{pe} = 0.0023$ corresponds to the linear reconnection stage. The dashed line in Fig. 3 is the time evolution of $\log(B_y^2)$ corresponding to growth rate (56).

Figure 4 presents the magnetic field distributions in the (x, y) plane at different times $\omega_{pe}t$ = (a) 0, (b) 2500, (c) 2750, (d) 3000, (e) 3250, (f) 3500, (g) 3750, and (h) 5000. The components B_x and B_y are presented as a vector field, and the component B_z is shown by shades of gray. We see that the tearing instability produces a magnetic island. For $\omega_{pe}t > 3000$ (Figs. 4d, 4e), both the deviation of the resonance surface from its initial position and the width of the island become on the order of the dimension of the computation region in the *y* direction and the instability saturates, in which case the magnetic field topology changes in the way shown in Figs. 4f–4h. The instability can saturate for two different reasons. The first reason is the isotropization of the electron velocity distribution. This is confirmed by Fig. 5, which shows that, during the instability, the electron velocity distribution becomes isotropic. The ion velocity distribution remains isotropic from the very beginning. The second reason is the finite length of the computation region in the *y* direction: the effective length of the magnetic configuration becomes too large for the long-wavelength perturbations characteristic of the tearing instability [12] to develop.

Figure 6 displays time evolutions of the (a) magnetic field energy, (b) electron kinetic energy, and (c) ion kinetic energy. We can see that, for $\omega_{pe}t \sim 3000$, the magnetic field energy is rapidly dissipated and the plasma electrons and ions are accelerated.

6. CONCLUSION

We have investigated the behavior of a plasma in a force-free magnetic field using the collisionless approximation. An analysis of the particle trajectories shows that only two kinds of plasma particles can exist in such a field: transit particles and trapped ones. Knowing the integrals of motion of the charged particles, we have obtained an equilibrium solution to the Vlasov–Maxwell equations. This solution describes the particle distribution function in force-free magnetic field (2). The equilibrium is possible only when the plasma temperatures along and across the magnetic field are different. The characteristic scale length of the magnetic field is determined by the degree to which the plasma temperature is anisotropic. By taking into account the possible plasma nonquasineutrality, we have obtained a wider class of solutions describing equilibrium magnetic configurations.

We have investigated the stability of an equilibrium plasma configuration in force-free magnetic field (2) and have shown that a configuration that is infinite in the *y* direction is unstable against the tearing instability.

We have determined the growth rate of the tearing instability in its linear stage. The results from numerical simulations of this stage have been found to agree well with analytical predictions. We have also numerically investigated the nonlinear stage of the tearing instability.

REFERENCES

1. V. D. Shafranov, in *Reviews of Plasma Physics*, Ed. by M. A. Leontovich (Gosatomizdat, Moscow, 1963; Consultants Bureau, New York, 1966), Vol. 2.
2. B. B. Kadomtsev, Rev. Plasma Phys. **22**, 1 (2000).
3. H. K. Moffat, *Magnetic Field Generation in Electrically Conducting Fluids* (Cambridge Univ. Press, Cambridge, 1978).
4. E. R. Priest, *Solar Magnetohydrodynamics* (Reidel, Dordrecht, 1984).
5. E. G. Harris, Nuovo Cimento **23**, 117 (1962).
6. N. Attico and F. Pegoraro, Phys. Plasmas **6**, 767 (1999).
7. S. M. Mahaian and R. D. Hazeltine, Phys. Plasmas **7**, 1287 (2000).
8. N. A. Bobrova, S. V. Bulanov, J. I. Sakai, and D. Sugiyama, Phys. Plasmas **8**, 759 (2001).
9. G. E. Vekstein, N. A. Bobrova, and S. V. Bulanov, J. Plasma Phys. **67**, 215 (2002).
10. M. Lontano, S. Bulanov, J. Koga, *et al.*, Phys. Plasmas **9**, 2562 (2002).
11. M. Lontano, S. Bulanov, J. Koga, and M. Passoni, Phys. Plasmas **10** (2003) (in press).
12. H. P. Furth, J. K. Killen, and M. N. Rosenbluth, Phys. Fluids **6**, 459 (1963).
13. D. Biskamp, *Cambridge Monographs on Plasma Physics*, Vol. 1: *Nonlinear Magnetohydrodynamics* (Cambridge Univ. Press, Cambridge, 1993).
14. J. F. Drake and Y. C. Lee, Phys. Rev. Lett. **39**, 453 (1977).
15. K. Swartz and R. D. Hazeltine, Phys. Fluids **27**, 2043 (1984).
16. L. M. Zelenyĭ and A. L. Taktakishvili, Fiz. Plazmy **10**, 50 (1984) [Sov. J. Plasma Phys. **10**, 26 (1984)].
17. R. Horiuchi and T. Sato, Phys. Plasmas **4**, 277 (1977).
18. K. Schindler, J. Geophys. Res. **79**, 2803 (1974).
19. B. Coppi, G. Laval, and R. Pellat, Phys. Rev. Lett. **16**, 1207 (1966).
20. A. A. Galeev and L. M. Zelenyĭ, Zh. Éksp. Teor. Fiz. **69**, 882 (1975) [Sov. Phys. JETP **42**, 450 (1975)].
21. V. S. Berezinskii, S. V. Bulanov, V. A. Dogel, *et al.*, *Astrophysics of Cosmic Rays* (North-Holland, Amsterdam, 1990).
22. N. A. Bobrova and S. I. Syrovatskiĭ, Pis'ma Zh. Éksp. Teor. Fiz. **30**, 567 (1979) [JETP Lett. **30**, 535 (1979)].
23. N. A. Bobrova and S. I. Syrovatskiĭ, Fiz. Plazmy **6**, 104 (1980) [Sov. J. Plasma Phys. **6**, 59 (1980)].
24. G. Laval, R. Pellat, and M. Vuillemin, Plasma Phys. Controlled Nucl. Fusion **2**, 259 (1966).
25. T. M. O'Neil, Phys. Fluids **8**, 2255 (1965).
26. S. V. Bulanov and P. V. Sasorov, Fiz. Plazmy **4**, 640 (1978) [Sov. J. Plasma Phys. **4**, 357 (1978)].
27. J. F. Drake and Y. C. Lee, Phys. Fluids **20**, 1341 (1977).
28. O. Buneman, *Computer Space Plasma Physics, Simulation Techniques and Software*, Ed. by H. Matsumoto and Y. Omura (Terra Scientific, Tokio, 1993), p. 67.

Translated by O.E. Khadin

Plasma Physics Reports, Vol. 29, No. 6, 2003, pp. 459–465. Translated from Fizika Plazmy, Vol. 29, No. 6, 2003, pp. 494–500.

PLASMA INSTABILITY

Suppression of the Rayleigh–Taylor Instability of a Low-Density Imploding Liner by a Longitudinal Magnetic Field

A. V. Gordeev

Russian Research Centre Kurchatov Institute, pl. Kurchatova 1, Moscow, 123182 Russia

Received May 23, 2002; in final form, December 6, 2002

Abstract—The possibility of suppressing the Rayleigh–Taylor instability in a low-density plasma, $\Pi = \omega_{pi}^2\Delta^2/c^2 \ll 1$ (where Δ is the thickness of the current-carrying slab), is investigated for the case in which the electron currents are much higher than the ion currents. The suppression of this instability in an imploding cylindrical liner by an axial external magnetic field B_{0z} is considered. It is shown that, for the instability to be suppressed, the external magnetic field B_{0z} should be stronger than the magnetic field $B_{0\theta}$ of the current flowing through the liner. © *2003 MAIK "Nauka/Interperiodica".*

1. In recent years, the implosion of thin current-carrying plasma shells has been recognized as offering great promise for generating high levels of pulsed power in the form of electromagnetic radiation and neutrons [1–3]. In such implosion processes, the Rayleigh–Taylor (RT) instability is one of the most dangerous instabilities preventing the compression of a current-carrying plasma shell to small dimensions [4, 5]. As a magnetic piston converges toward the axis of the system, it inevitably becomes subject to RT instability, which violates the compactness of the converging plasma shell and reduces the parameters of the source of radiation and neutrons. In order to increase the efficiency of a magnetic piston, it is necessary to reduce the effect of instability on the imploding current-carrying plasma shell. Hence, the investigation of RT instability is important from the technological standpoint.

RT instability [6] certainly exists in one-fluid magnetohydrodynamics, when the influence of the Hall effect can be neglected by virtue of the smallness of the parameter $\Pi^{-1} \ll 1$, where $\Pi = 4\pi e^2 Zn\Delta^2/Mc^2$, with Δ the characteristic dimension of a plasma slab. When $\Pi \ll 1$ and the Hall effect plays an important role, opinions in the literature are divided regarding the possibility of RT instability in two-fluid magnetohydrodynamics (see [7, 8]). However, in view of the analogy between the RT instability in magnetohydrodynamics and the instability of a heavy liquid supported by a lighter liquid, it is natural to suppose that RT instability should also take place in two-fluid magnetohydrodynamics. RT instability has been studied in many papers (see, e.g., [9, 10]). In my recent works [11, 12], it was shown that, in the limit $\Pi \ll 1$, the linear equation for this instability can be integrated for arbitrary density and pressure profiles in the accelerated plasma slab. According to the solution obtained in [11, 12], the shapes of the density and pressure profiles have no effect on the instability growth rate.

Further analysis will be carried out based on a particular version of the two-fluid MHD model—a so-called Hall plasma model, in which the plasma ions are assumed to be unmagnetized [13].

2. The most widely used method for the stabilization of an imploding liner consists in imposing an external magnetic field parallel to the liner axis. This field makes the liner more "rigid" and thus can, in principle, retard the development of constrictions that grow from the perturbations associated with the longitudinal plasma inhomogeneity. It is known from experiments that the instability can be suppressed even by a comparatively weak longitudinal magnetic field B_{0z}, which is substantially weaker than the azimuthal magnetic field $B_{0\theta}$ [14, 15]. That is why, in order to provide better insight into the possibility of suppressing the instability, it is worthwhile to develop a simple analytic approach. Although the general case of arbitrary parameter values is difficult to investigate analytically, the problem can be greatly simplified by examining it in the limit of small values of the parameter $\Pi = \omega_{pi}^2\Delta^2/c^2 \ll 1$. The analytic solutions obtained in [11, 12] made it possible to draw some conclusions about RT instability in the absence of a longitudinal magnetic field in the parameter range $\Pi \ll 1$. It was shown that, for a low-density plasma, the standard formula for the instability growth rate is valid for an arbitrary density profile $n(x)$ inside the slab and an arbitrary pressure profile of the form $p = p(n)$. In other words, in such a plasma, RT instability in the linear stage cannot be suppressed by appropriately choosing the plasma density profile. Below, the approach developed previously will be generalized to study the possibility of suppressing RT instability with a longitudinal magnetic field.

1063-780X/03/2906-0459$24.00

In further analysis, the characteristic current in the liner and the characteristic liner radius will be assumed to be $J \geq 1$ MA and $r \leq 1$ cm, respectively (which correspond to a magnetic field of $B > 10^5$ G), and the characteristic plasma density will be assumed to be $n_e \sim 10^{17}$–10^{18} cm^{-3}.

Note that, in [12], RT instability was considered with allowance for the finite plasma pressure. However, to simplify matters, the gas-kinetic pressure effects will be neglected below. This indicates that the approach to be developed is valid for the stage before the complete collapse of the liner toward its axis. In this stage, the thickness of the plasma shell can be assumed to be much smaller than the characteristic liner radius, so that we can use the plane plasma slab approximation.

3. In a number of papers, it was shown clearly that the Hall effect cannot suppress RT instability [16–18]. At the same time, it was found that the one- and two-fluid MHD equations describe the instability in different ways. However, in those papers, the instability was modeled by introducing a fictitious gravitational field. Here, as in [11, 12], the model equations are derived by passing directly into the moving frame of reference, which makes the statement of the problem more adequate.

We start with the set of two-fluid MHD equations. Taking the sum of the equations of motion for ions and electrons and accounting for the quasineutrality condition, we can obtain an equation for the plasma mass velocity. We assume that the plasma is, on the one hand, cold enough for the gas-kinetic pressure to be much lower than the magnetic pressure, and, on the other, hot enough for the dissipation associated with the plasma resistivity to be negligible. Combining the two conditions $B^2 \gg 8\pi nT$ and $\sigma B \gg enc$ and using the conductivity estimated in [19], $\sigma \simeq 0.5 \times 10^{31} T^{3/2}$ (where T is expressed in ergs) [19], we arrive at the following necessary condition for the density of the accelerated plasma:

$$B^2 \gg 1.9 \times 10^{-14} n^{5/4}, \tag{1}$$

where the magnetic field and density are expressed in G and cm^{-3}, respectively.

This condition is fairly restrictive: it is satisfied only for sufficiently strong magnetic fields. Note that a comparatively low temperature (in the stage of the acceleration of a plasma shell in a liner, it is about 10^2 eV or even lower) may be associated with a strong emission from the shell.

Then, taking the curl of the equation of electron motion and neglecting electron inertia (which is justified because the scale c/ω_{pe} is much smaller than the characteristic spatial scale Δ of the accelerated shell), we obtain an equation for the magnetic field evolution.

As a result, we arrive at the following set of equations describing the dynamics of a plasma shell accelerated by the magnetic field:

$$\rho \frac{d\mathbf{V}}{dt} = -\frac{1}{4\pi}[\mathbf{B} \times [\nabla \times \mathbf{B}]], \tag{2}$$

$$\frac{\partial \rho}{\partial t} + \nabla \cdot (\rho \mathbf{V}) = 0, \tag{3}$$

$$\frac{\partial \mathbf{B}}{\partial t} = [\nabla \times [\mathbf{V} \times \mathbf{B}]] + \frac{c}{4\pi e}\left[\nabla \times \frac{1}{n}[\mathbf{B} \times [\nabla \times \mathbf{B}]]\right] - \frac{c^2}{4\pi}\left[\nabla \times \frac{1}{\sigma}[\nabla \times \mathbf{B}]\right]. \tag{4}$$

Here, we formally retain the finite plasma conductivity in order to stress its possible role in establishing the initial equilibrium.

We treat the problem in plane geometry, regarding the motion along the radial coordinate r as the motion in the x direction, in which case the θ-component of the magnetic field becomes the B_y component. We assume that, at the instant the magnetic field begins to accelerate the plasma, all of the quantities depend only on the x coordinate.

The equations for the initial configuration of a plasma slab accelerated by the magnetic field have the form

$$\rho_0 \frac{dV_0}{dt} = -\frac{1}{4\pi}\left(B_{0y}\frac{\partial B_{0y}}{\partial x} + B_{0z}\frac{\partial B_{0z}}{\partial x}\right), \tag{5}$$

$$\frac{\partial \rho_0}{\partial t} + \frac{\partial}{\partial x}(\rho_0 V_0) = 0, \tag{6}$$

$$\frac{\partial B_{0y}}{\partial t} + \frac{\partial}{\partial x}(B_{0y} V_0) = \frac{c^2}{4\pi}\frac{\partial}{\partial x}\left(\frac{1}{\sigma}\frac{\partial B_{0y}}{\partial x}\right). \tag{7}$$

The field component B_{0z} is described by an equation analogous to Eq. (7).

The equations for perturbations are

$$\rho_0 \frac{dV_x}{dt} + \rho \frac{dV_0}{dt} = -\frac{1}{4\pi}\left\{\frac{\partial}{\partial x}(B_{0y}B_y) + \frac{\partial}{\partial x}(B_{0z}B_z) - B_{0z}\frac{\partial}{\partial z}B_x\right\}, \tag{8}$$

$$\rho_0 \frac{dV_z}{dt} = -\frac{1}{4\pi}\left(B_{0y}\frac{\partial B_y}{\partial z} - B_x\frac{\partial B_{0z}}{\partial x}\right), \tag{9}$$

$$\rho_0 \frac{dV_y}{dt} = -\frac{1}{4\pi}\left(-B_{0z}\frac{\partial B_y}{\partial z} - B_x\frac{\partial B_{0y}}{\partial x}\right), \tag{10}$$

$$\frac{\partial \rho}{\partial t} + \frac{\partial}{\partial x}(\rho_0 V_x + \rho V_0) + \frac{\partial}{\partial z}(\rho_0 V_z) = 0, \tag{11}$$

$$\frac{\partial B_y}{\partial t} + \frac{\partial}{\partial x}(V_0 B_y + V_x B_{0y}) + \frac{\partial}{\partial z}(V_z B_{0y} - V_y B_{0z})$$

$$= \frac{c}{4\pi e n_0}\frac{\partial}{\partial z}\left\{\frac{\partial}{\partial x}(B_{0y}B_y) + \frac{\partial}{\partial x}(B_{0z}B_z) - B_{0z}\frac{\partial B_x}{\partial z}\right\} \quad (12)$$

$$- \frac{c}{4\pi e n_0^2}\frac{\partial n}{\partial z}\left(B_{0y}\frac{\partial B_{0y}}{\partial x} + B_{0z}\frac{\partial B_{0z}}{\partial x}\right)$$

$$- \frac{c}{4\pi e}\frac{\partial}{\partial x}\left\{\frac{1}{n_0}\left(B_{0y}\frac{\partial B_y}{\partial z} - B_x\frac{\partial B_{0z}}{\partial x}\right)\right\}.$$

Here, the vector potential A, in terms of which the magnetic field components B_x and B_z are expressed,

$$B_z = \frac{\partial A}{\partial x}, \quad B_x = -\frac{\partial A}{\partial z},$$

satisfies the equation

$$\frac{\partial A}{\partial t} + V_0\frac{\partial A}{\partial x} - \frac{c}{4\pi e n_0}\frac{\partial B_{0y}}{\partial x}\frac{\partial A}{\partial z}$$

$$= -B_{0z}\left(V_x + \frac{c}{4\pi e n_0}\frac{\partial B_y}{\partial z}\right). \quad (13)$$

In the equations for the perturbed quantities, we have omitted the dissipative term by virtue of the condition $h = \sigma B/enc \gg 1$. Note that, hereinafter, the quantities without subscripts refer to perturbations.

We simplify the above equations by using the compactness condition, which implies that the macroscopic velocity V_0 of the accelerated plasma slab is independent of x and depends only on time. This condition can be written as [13]

$$\frac{\partial V_0}{\partial t} = -a_0(t), \quad (14)$$

where the acceleration a_0 of a current-carrying plasma slab depends weakly on time.

We now transform the equations to an accelerated frame of reference, i.e., to a frame moving with the accelerated plasma slab in the negative x direction; this indicates that, in the original (cylindrical) coordinate system, the frame moves toward the liner axis. In order to pass to the accelerated frame, we must switch to a new spatial variable s:

$$s = x - \int_0^t V_0(t')dt'. \quad (15)$$

Using the relationship

$$\left.\frac{\partial}{\partial t}\right|_s = \left.\frac{\partial}{\partial t}\right|_x + V_0\left.\frac{\partial}{\partial x}\right|_t, \quad (16)$$

we obtain the equilibrium condition

$$\rho_0 a_0 = \frac{B_{0y}}{4\pi}\frac{\partial B_{0y}}{\partial s} + \frac{B_{0z}}{4\pi}\frac{\partial B_{0z}}{\partial s}, \quad (17)$$

where

$$\left.\frac{\partial \rho_0}{\partial t}\right|_s = 0, \quad \left.\frac{\partial B_{0y}}{\partial t}\right|_s = \frac{c^2}{4\pi}\frac{\partial}{\partial s}\left(\frac{1}{\sigma}\frac{\partial B_{0y}}{\partial s}\right).$$

The field component B_{0z} satisfies an analogous equation.

It can be seen that the characteristic spatial scale of the structure of the field component B_{0y} that forms in a plasma with a high (but finite) conductivity σ is the skin depth. However, when the characteristic dimension Δ of the plasma slab is sufficiently large, we can neglect the time variation of B_{0y} and describe this component by the equation

$$\left.\frac{\partial B_{0y}}{\partial t}\right|_s = 0.$$

For a Hall plasma ($\Pi \ll 1$), this yields the following lower bound on the Hall parameter h:

$$h^2 \gg \frac{1}{\Pi}. \quad (18)$$

In further analysis, we will assume that the stabilizing magnetic field B_{0z} produced by external coils is constant, in which case its spatial derivatives can be neglected.

Of course, during the implosion of a current-carrying plasma shell, in which the longitudinal magnetic field remains constant because the conductivity σ is sufficiently high, the magnetic flux density inside the shell increases and the magnetic field at its inner boundary becomes stronger. As the shell thickness decreases, the growing longitudinal magnetic field penetrates into the shell; as a result, the spatial gradients of the longitudinal field in the shell may be nonzero. However, this effect becomes important only in the final stage of the implosion of the shell, when it approaches the axis of the system.

Changing to the moving frame, we arrive at the following final set of equations:

$$\frac{\partial \rho}{\partial t} + \frac{\partial}{\partial s}(\rho_0 V_x) + \rho_0\frac{\partial V_z}{\partial z} = 0, \quad (19)$$

$$\rho_0\frac{\partial V_z}{\partial t} = -\frac{1}{4\pi}B_{0y}\frac{\partial B}{\partial z}, \quad (20)$$

$$\rho_0\frac{\partial V_y}{\partial t} = -\frac{1}{4\pi}\left(-B_{0z}\frac{\partial B}{\partial z} + \frac{\partial A}{\partial z}\frac{\partial B_{0y}}{\partial s}\right), \quad (21)$$

$$\rho_0\frac{\partial V_x}{\partial t} - \rho a_0 = -\frac{1}{4\pi}\left\{\frac{\partial}{\partial s}(B_{0y}B) + B_{0z}\left(\frac{\partial^2 A}{\partial s^2} + \frac{\partial^2 A}{\partial z^2}\right)\right\}, \quad (22)$$

$$\frac{\partial B}{\partial t} - \frac{B_0}{n_0}\frac{\partial n}{\partial t} + v_0\left(\frac{\partial B}{\partial z} - \frac{B_0}{n_0}\frac{\partial n}{\partial z}\right) = -\frac{\partial}{\partial s}\left(\frac{B_0}{n_0}\right)\left(n_0 V_x + \frac{c}{4\pi e}\frac{\partial B}{\partial z}\right) + B_{0z}\frac{\partial}{\partial z}\left\{V_y + \frac{c}{4\pi e n_0}\left(\frac{\partial^2 A}{\partial s^2} + \frac{\partial^2 A}{\partial z^2}\right)\right\}, \quad (23)$$

$$\frac{\partial A}{\partial t} + v_0\frac{\partial A}{\partial z} = -B_{0z}\left(V_x + \frac{c}{4\pi e n_0}\frac{\partial B}{\partial z}\right), \quad (24)$$

where

$$v_0 = -\frac{c}{4\pi e n_0}\frac{\partial B_{0y}}{\partial s}, \quad \rho = n\frac{M}{Z}.$$

Here, the time derivative is taken at fixed s. Also, the subscript in the y component of the perturbed magnetic field is dropped, because the remaining magnetic field components are expressed in terms of the perturbation of the vector potential A.

We take the Fourier transformation of the final set in the time t (changing into the frequency ω) and in the z coordinate (changing into the wave vector k_z) and nondimensionalize the equations according to the relationships

$$a = \frac{A}{\Delta \bar{B}_0}, \quad b_0 = \frac{B_0}{\bar{B}_0}, \quad b = \frac{B}{\bar{B}_0}, \quad \nu_0 = \frac{n_0}{\bar{n}_0},$$

$$\nu = \frac{n}{\bar{n}_0}, \quad s = \Delta\xi, \quad \kappa = k_z\Delta, \quad \Lambda = \frac{B_{0z}}{\bar{B}_0},$$

$$a_0 = \frac{\bar{V}_0^2}{\Delta}, \quad \bar{V}_0^2 = \frac{Z\bar{B}_0^2}{4\pi M\bar{n}_0}, \quad \omega = \Omega\frac{\bar{V}_0}{\Delta},$$

$$\tilde{\Omega} = \Omega + \frac{\kappa}{\sqrt{\Pi}}\frac{1}{\nu_0}\frac{db_0}{d\xi}, \quad \Pi = \frac{4\pi e^2\bar{n}_0 Z\Delta^2}{Mc^2},$$

where Δ is the thickness of the accelerated slab in the x direction, $\bar{B}_0$ is the characteristic strength of the magnetic field B_0, and $\bar{n}_0$ is the characteristic electron density.

As a result, we obtain the following basic set of dimensionless equations:

$$\frac{d\nu}{d\xi} - \Omega^2\nu = \frac{d^2}{d\xi^2}(b_0 b) - \kappa^2 b_0 b + \Lambda\frac{d}{d\xi}\hat{\Delta}a, \quad \hat{\Delta} \equiv \frac{d^2}{d\xi^2} - \kappa^2, \quad (25)$$

$$\Omega\tilde{\Omega}\left(b - \frac{b_0}{\nu_0}\nu\right) = \frac{d}{d\xi}\left(\frac{b_0}{\nu_0}\right)\left\{\Omega\frac{\kappa}{\sqrt{\Pi}}b + \nu - \frac{d}{d\xi}(b_0 b) - \Lambda\hat{\Delta}a\right\} + \Lambda^2\kappa^2\frac{1}{\nu_0}b - \Lambda\kappa^2\frac{1}{\nu_0}\frac{db_0}{d\xi}a - \Lambda\Omega\frac{\kappa}{\sqrt{\Pi}}\frac{1}{\nu_0}\hat{\Delta}a, \quad (26)$$

$$\Omega\tilde{\Omega}a + \Lambda^2\frac{1}{\nu_0}\hat{\Delta}a = \frac{\Lambda}{\nu_0}\left\{\nu - \frac{d}{d\xi}(bb_0) + \Omega\frac{\kappa}{\sqrt{\Pi}}b\right\}, \quad (27)$$

where ν_0 and b_0 are related by

$$\nu_0 = b_0 b_0'. \quad (28)$$

In these equations, the constant longitudinal component of the equilibrium magnetic field is neglected and the prime denotes the derivative with respect to the independent variable ξ.

4. Equations (25)–(28) describe the RT instability in a reference frame moving with the acceleration a_0 in the negative x direction. Since, in their general form, the equations are not amenable to analytic study, we restrict ourselves here to considering the limiting case $\Pi \ll 1$, in which Eqs. (26) and (27) will contain the terms proportional to $1/\sqrt{\Pi} \gg 1$ and also all of the terms with the parameter Λ.

In this limit, we use equilibrium relationship (28) to reduce Eq. (26) to

$$\nu = b\frac{\nu_0'}{b_0'} - \kappa^2\chi b + \Lambda\hat{\Delta}a + \Lambda\frac{\sqrt{\Pi}}{\Omega\kappa}\left\{\nu_0\frac{d}{d\xi}\left(\frac{b_0}{\nu_0}\right)\hat{\Delta}a + \kappa^2\frac{db_0}{d\xi}a\right\}, \quad (29)$$

$$\chi = \frac{\Lambda^2\sqrt{\Pi}}{\kappa\Omega}.$$

We introduce the function $w = bb_0$ and insert the expression for ν in (29) into Eq. (25) to get

$$\frac{d}{d\xi}\left(\frac{dw}{d\xi} - w\frac{\nu_0'}{\nu_0}\right) = w\left(\kappa^2 - \Omega^2\frac{\nu_0'}{\nu_0}\right)$$
$$- \kappa^2\chi\left\{\frac{d}{d\xi}\left(\frac{w}{b_0}\right) - \Omega^2\frac{w}{b_0}\right\} - \Lambda\Omega^2\hat{\Delta}a \qquad (30)$$
$$+ \Lambda\frac{\sqrt{\Pi}}{\Omega\kappa}\left(\frac{d}{d\xi} - \Omega^2\right)\left\{\nu_0\frac{d}{d\xi}\left(\frac{b_0}{\nu_0}\right)\hat{\Delta}a + \kappa^2\frac{db_0}{d\xi}a\right\}.$$

Here, the expressions for a and $\hat{\Delta}a$ can be derived from Eq. (27). We substitute expression (29) for ν into Eq. (27) and, in the resulting equation, take into account all the terms containing the parameter Λ. Then, we introduce the function $\varphi = w/\nu_0$ to obtain

$$a = \Lambda\varphi - \frac{\Lambda\sqrt{\Pi}}{\Omega\kappa}\frac{b_0\varphi'}{1 - \frac{\Lambda^2\Pi}{\Omega^2}}$$
$$+ \frac{\Lambda^2\Pi}{\Omega^2\kappa^2}\frac{1}{1 - \frac{\Lambda^2\Pi}{\Omega^2}}b_0\frac{d}{d\xi}\left(\frac{b_0}{\nu_0}\right)\hat{\Delta}a, \qquad (31)$$

$$\hat{\Delta}a = \Lambda\hat{L}\hat{\Delta}\varphi - \frac{\Lambda\sqrt{\Pi}}{\Omega\kappa}\frac{1}{1 - \frac{\Lambda^2\Pi}{\Omega^2}}\hat{L}\hat{\Delta}(b_0\varphi'), \qquad (32)$$

where the operator $\hat{L}$ is defined as

$$\hat{L} = \sum_{l=0}^{\infty}(\lambda\hat{\Delta}e_0)^l, \quad \lambda = \frac{\Lambda^2\Pi}{\Omega^2\kappa^2}\frac{1}{1 - \frac{\Lambda^2\Pi}{\Omega^2}}, \qquad (33)$$
$$e_0 = b_0\frac{d}{d\xi}\left(\frac{b_0}{\nu_0}\right).$$

In expression (33) for the operator $\hat{L}$, the two-dimensional Laplace operator $\hat{\Delta}$ applies to all ξ functions to the right of it; i.e., $\hat{L}$ is an integral operator. Substituting expressions (31) and (32) into Eq. (30), we arrive at the final equation for the function φ:

$$\nu_0\hat{\Delta}\varphi + \nu_0'(\varphi' + \Omega^2\varphi)$$
$$= -\frac{\Lambda^2\Pi}{\Omega^2}\frac{1}{1 - \frac{\Lambda^2\Pi}{\Omega^2}}\left(\frac{d}{d\xi} - \Omega^2\right)(\nu_0\varphi')$$
$$- \Lambda^2\Omega^2\hat{L}\hat{\Delta}\varphi + \frac{\Lambda^2\sqrt{\Pi}}{\kappa}\frac{\Omega}{1 - \frac{\Lambda^2\Pi}{\Omega^2}}\hat{L}\hat{\Delta}(b_0\varphi') \qquad (34)$$
$$+ \left(\frac{d}{d\xi} - \Omega^2\right)\left\{\nu_0\frac{d}{d\xi}\left(\frac{b_0}{\nu_0}\right)\left[\frac{\Lambda^2\sqrt{\Pi}}{\kappa\Omega}\frac{1}{1 - \frac{\Lambda^2\Pi}{\Omega^2}}\hat{L}\hat{\Delta}\varphi\right.\right.$$
$$\left.\left. - \frac{\Lambda^2\Pi}{\Omega^2\kappa^2}\frac{1}{\left(1 - \frac{\Lambda^2\Pi}{\Omega^2}\right)^2}\hat{L}\hat{\Delta}(b_0\varphi')\right]\right\}.$$

Here, in contrast to earlier studies [11, 12], $\mathbf{k}\cdot\mathbf{B}_0 \equiv k_z B_{0z} \neq 0$. For $\Lambda = 0$, this equation describes the RT instability in the frame of reference comoving with an accelerated current-carrying plasma slab, in which case the unstable solution has a maximum in the region where $\mathbf{a}_0\cdot\nabla n_0 < 0$. In the geometry adopted here, this condition reduces to $n_0' < 0$, which corresponds to the outer boundary of the accelerated slab.

For $\Lambda^2 \leq 1$, the basic assumption of our analysis allows us to neglect all terms in Eq. (34) that are proportional to different powers of Π; as a result, Eq. (34) becomes similar in structure to the equations derived in [11, 12], thereby indicating that RT instability is again possible.

The most important point in Eq. (34) is that we have retained all of the terms that contain the parameter Λ, thus providing a correct transition to the limit of a strong external stabilizing magnetic field B_{0z} such that $\Lambda^2\Pi \gg \Omega^2$. In taking the limit, we can omit the last two terms on the right-hand side of Eq. (34). In fact, for $\Lambda^2\Pi \gg \Omega^2$, the last term formally vanishes because it is proportional to $\Omega^2/(\Lambda^2\Pi) \ll 1$. As for the next to last term, it includes $\hat{\Delta}\varphi$ and, in the limit to be taken, is much smaller than the term $\Lambda^2\Omega^2\hat{L}\hat{\Delta}\varphi$. For the same reason, the term $\nu_0\hat{\Delta}\varphi$ on the left-hand side can also be omitted. Hence, in the limit at hand, Eq. (34) simplifies to

$$\nu_0'(\varphi' + \Omega^2\varphi) - \left(\frac{d}{d\xi} - \Omega^2\right)(\nu_0\varphi')$$
$$+ \Lambda^2\Omega^2\hat{L}\hat{\Delta}\varphi + \frac{\Omega^3}{\kappa\sqrt{\Pi}}\hat{L}\hat{\Delta}(b_0\varphi') = 0. \qquad (35)$$

Using the definition of the operator $\hat{L}$, we can readily verify that Eq. (35) reduces to a fourth-order

differential equation for φ. Now, we consider the perturbations whose characteristic spatial scale is small in comparison with the dimension of the plasma slab, $\kappa \equiv k_z\Delta \gg 1$. For $\Lambda^2\Pi \gg \Omega^2$, the largest term in Eq. (35) is $\Lambda^2\Omega^2\hat{L}\hat{\Delta}\varphi$, which requires that $\hat{\Delta}\varphi = 0$. Then, neglecting the first term in comparison with the second term and taking into account the condition $|\kappa| \gg 1$, we can represent Eq. (35) in the form

$$-b_0(|\kappa| - \Omega^2) + \frac{2\Omega^3}{\kappa\sqrt{\Pi}} = 0. \tag{36}$$

This equation implies that, for $\sqrt{\Pi} \longrightarrow 0$, the instability growth rate vanishes. However, it should be kept in mind that the growth rate estimated from this equation, $\Omega \sim (\kappa\sqrt{\Pi})^{1/3}$, is not very small because of the restricted range of variations of the parameter $\Pi \gg m/M$, where m is the mass of an electron.

Hence, the criterion for the stabilization of RT instability in a low-density plasma by a magnetic field directed along the axis of an imploding liner has the form

$$\Lambda^2\Pi \gg \Omega^2. \tag{37}$$

Note that the quasiclassical approximation based on Eq. (36) is also valid for the most dangerous mode with $|\kappa| = \pi$, when the slab thickness is half the perturbation wavelength. The stabilization criterion shows that, even at the boundary of applicability of the quasiclassical approximation, $\Pi \sim 1$, the constant external stabilizing longitudinal magnetic field should be stronger than the magnetic field of the current flowing through the liner.

5. Following papers [11, 12], it is worthwhile to discuss whether the pressure balance is satisfied at the boundaries of the accelerated plasma slab. Under the above assumptions, the approximate momentum conservation law has the form

$$\frac{\partial}{\partial t}\left(NMV_i + \frac{1}{4\pi}[\mathbf{E}\times\mathbf{B}]_i\right) + \frac{\partial}{\partial x_k}\left\{MNV_iV_k + \delta_{ik}\frac{1}{8\pi}(\mathbf{E}^2 + \mathbf{B}^2) - \frac{1}{4\pi}(E_iE_k + B_iB_k)\right\} = 0. \tag{38}$$

We take into account the fact that the electric field is much weaker than the magnetic field and switch to the moving frame in accordance with the procedure described in Section 3. As a result, we obtain the pressure balance equation

$$\frac{\partial}{\partial t}(MNV_i)\Big|_s + \frac{\partial}{\partial z}\left(MNV_iV_z + \delta_{iz}\frac{\mathbf{B}^2}{8\pi}\right) + \frac{\partial}{\partial s}\left\{MNV_i(V_x - V_0) + \delta_{ix}\frac{\mathbf{B}^2}{8\pi}\right\} = 0. \tag{39}$$

Integrating this equation over s yields the pressure balance condition at each of the slab boundaries in the x direction:

$$\left\langle MNV_x(V_x - V_0) + \frac{\mathbf{B}^2}{4\pi}\right\rangle = 0, \tag{40}$$

where $\langle\ldots\rangle$ denotes the difference between the values of the quantities on both sides of each boundary.

Let us prove that, in condition (40), the first term, which is associated with plasma inertia, undergoes no jump at the plasma boundary. Since $V_0 \equiv V_0(t)$, it is sufficient to prove this assertion only for the factor $N\delta V_x$, where $\delta V_x \equiv V_x - V_0$. In dimensionless form, this factor can be found from the Fourier transformed equation (22):

$$-i\Omega\nu_0\delta V_x = \nu - \frac{\partial}{\partial\xi}(b_0b) + \Lambda\hat{\Delta}a.$$

Equation (25) can be rewritten as

$$\frac{d}{d\xi}\left\{\nu - \frac{d}{d\xi}(b_0b) + \Lambda\hat{\Delta}a\right\} = \Omega^2\nu - \kappa^2b_0b.$$

Since the right-hand side of this equation is finite, the quantity $\nu - d(b_0b)/d\xi + \Lambda\hat{\Delta}a$ undergoes no jumps at the slab boundaries and, therefore, vanishes there; i.e., the quantity $\nu_0\delta V_x$ also equals zero at the boundaries.

The second term in condition (40) accounts for the magnetic field and contains the zero-order component; accordingly, in order for this condition to be satisfied, it is necessary that there be no surface currents in the equilibrium state.

It should be kept in mind that, to first order in the perturbations, the term with the magnetic field in condition (40) coincides with the solution $w = \nu_0\varphi$ to within a numerical factor. Consequently, for a plasma slab with zero density ($\nu_0 = 0$) at the boundaries, evolutionary condition (40) is always satisfied, provided that the function φ is regular.

ACKNOWLEDGMENTS

This study was supported in part by the Russian Foundation for Basic Research, project no. 00-02-16305.

REFERENCES

1. H. Sze, P. Coleman, B. Failor, *et al.*, in *Proceedings of 13th International Conference on High Power Particle Beams, Nagaoka, 2000* (Nagaoka Univ. of Technology, Nagaoka, 2001), Vol. 1, p. 36.
2. P. Blinov, A. Chernenko, A. Chesnokov, *et al.*, in *Proceedings of 13th International Conference on High Power Particle Beams, Nagaoka, 2000* (Nagaoka Univ. of Technology, Nagaoka, 2001), Vol. 1, p. 76.
3. V. V. Aleksandrov, A. V. Branitskiĭ, G. S. Volkov, *et al.*, Fiz. Plazmy **27**, 99 (2001) [Plasma Phys. Rep. **27**, 89 (2001)].
4. H. Dickinson, W. H. Bostick, J. N. DiMarko, and S. Koslov, Phys. Fluids **5**, 1048 (1962).
5. N. F. Roderick, T. W. Hussey, R. J. Faehl, and R. W. Boyd, Appl. Phys. Lett. **32**, 273 (1978).
6. N. A. Inogamov, Prikl. Mekh. Tekh. Fiz., No. 5, 110 (1985).
7. L. I. Rudakov, in *Proceedings of 2nd International Conference on Dense Z-Pinches, Laguna Beach, California, 1989*; AIP Conf. Proc. **195**, 290 (1989).
8. L. I. Rudakov and A. A. Sevast'yanov, Fiz. Plazmy **22**, 1095 (1996) [Plasma Phys. Rep. **22**, 993 (1996)].
9. A. B. Budko, A. L. Velikovich, A. I. Kleev, *et al.*, Zh. Éksp. Teor. Fiz. **94**, 496 (1989) [Sov. Phys. JETP **68**, 279 (1989)].
10. A. B. Budko, A. L. Velikovich, M. A. Liberman, *et al.*, Zh. Éksp. Teor. Fiz. **96**, 140 (1989) [Sov. Phys. JETP **69**, 76 (1989)].
11. A. V. Gordeev, Fiz. Plazmy **25**, 76 (1999) [Plasma Phys. Rep. **25**, 70 (1999)].
12. A. V. Gordeev, Fiz. Plazmy **25**, 227 (1999) [Plasma Phys. Rep. **25**, 202 (1999)].
13. A. V. Gordeev, A. S. Kingsep, and L. I. Rudakov, Phys. Rep. **243**, 215 (1994).
14. F. J. Wessel, F. S. Felber, N. C. Wild, and H. U. Rahman, Appl. Phys. Lett. **48**, 1119 (1986).
15. A. V. Luchinskiĭ, I. A. Ratakhin, S. A. Sorokin, and S. A. Chaĭkovskiĭ, Pis'ma Zh. Tekh. Fiz. **15** (18), 83 (1989) [Sov. Tech. Phys. Lett. **15**, 739 (1989)].
16. A. B. Hassam and J. D. Huba, Phys. Fluids **31**, 318 (1988).
17. J. D. Huba, A. B. Hassam, and P. Satyanerayana, Phys. Fluids B **1**, 931 (1989).
18. A. L. Velikovich, Phys. Fluids B **3**, 492 (1991).
19. S. I. Braginskii, in *Reviews of Plasma Physics*, Ed. by M. A. Leontovich (Gosatomizdat, Moscow, 1963; Consultants Bureau, 1965), Vol. 1.

Translated by I.A. Kalabalyk

Plasma Physics Reports, Vol. 29, No. 6, 2003, pp. 466–472. Translated from Fizika Plazmy, Vol. 29, No. 6, 2003, pp. 501–507.

PLASMA OSCILLATIONS AND WAVES

Small-Scale Alfvén Waves Localized near an Extremum in the Finite-Amplitude Perturbation of the Radial Plasma Density Profile

I. O. Girka and P. P. Rutkevich

Karazin National University, pl. Svobody 4, Kharkov, 61077 Ukraine

Received July 10, 2002; in final form, October 24, 2002

Abstract—A study is made of electromagnetic waves localized in the region where the radial plasma density profile has an extremum between two local Alfvén resonances. Analytic expressions for the eigenfrequencies and eigenmodes are obtained. It is shown that kinetic and inertial Alfvén waves can propagate in the vicinity of a maximum and a minimum in the density profile, respectively. Passage to the limiting case in which the plasma density is nonuniform and has a parabolic profile is considered. *© 2003 MAIK "Nauka/Interperiodica".*

1. INTRODUCTION

The production and heating of plasma in controlled fusion devices initiated active research on the processes of conversion and absorption of electromagnetic waves near Alfvén resonance [1–6]. It is well known that the absorption of waves with frequencies $\omega < \omega_{ci}$ is accompanied by significant plasma heating near the Alfvén resonance point $r = r_A$, at which the following relationship is satisfied:

$$\varepsilon_1(r_A) \approx (ck_\parallel/\omega)^2. \quad (1)$$

Here, $\varepsilon_1 = 1 + \sum_\alpha \omega_{p\alpha}^2/(\omega_{c\alpha}^2 - \omega^2)$ is the component of the dielectric tensor of a cold collisionless plasma, with the subscript α indicating the ions (i) and the electrons (e); $k_\parallel$ is the projection of the wave vector onto the direction of a constant magnetic field; c is the speed of light in vacuum; ω is the wave frequency; and $\omega_{c\alpha}$ and $\omega_{p\alpha}$ are the cyclotron and Langmuir frequencies of the particles of species α, respectively. The coordinate dependence enters the expression for ε_1 through two physical quantities: the external magnetic field $B_0(r)$ and the plasma density $n(r)$. In what follows, it is assumed that only the plasma density depends on the radial coordinate. However, when the possible radial nonuniformity of the external magnetic field is taken into account, the method for solving the problem and the final results remain essentially the same. It is well known [1] that the RF power absorbed in the Alfvén resonance region is inversely proportional to dn/dr. That is why the case in which $n(r)$ has an extremum near Alfvén resonance is of particular interest [7–10].

The density perturbation (nonuniformity) that has an extremum is usually described by a squared parabola (see, e.g., [7–10]). This approach is justified for electromagnetic oscillations localized in the immediate vicinity of the point of extreme density, where the density profile deviates only slightly from a squared parabola, or for a sufficiently large density perturbation. The dispersion properties of electromagnetic oscillations in these cases have been studied fairly well. Thus, the spectrum of oscillations in related problems is known to have an infinite number of levels, because the branches of a squared parabola are infinitely high. Hence, approximating the density profile by a parabola is equivalent to modeling a sufficiently deep potential well. However, the depth of the well is actually finite, so that the dispersion properties of the oscillations differ considerably from those in the problem with an infinitely deep potential well [11]. For this reason, modeling a plasma density perturbation by a squared parabola alone may be insufficient. In what follows, by analogy with quantum mechanics, a density perturbation will be referred to as a "potential well."

2. FORMULATION OF THE PROBLEM

We consider a plasma cylinder that is uniform in both the axial and azimuthal directions and is placed in a constant uniform axial magnetic field. The radial plasma density profile is modeled by the expression (see Fig. 1)

$$\varepsilon_1(r) = N_z^2[1 + M + A/\cosh^2((r - r_0)/a)]. \quad (2)$$

Here, $N_z = ck_z/\omega$ is the axial refractive index, k_z is the axial component of the wave vector, r is the radial variable in cylindrical coordinates, r_0 is the radial position of the density extremum, a is the characteristic width of the region where the density is perturbed, MN_z^2 is the deviation of the quantity ε_1 from the resonant value N_z^2 far from the position r_0 of the extremum ($|r - r_0| \gg a$),

1063-780X/03/2906-0466$24.00

and AN_z^2 is the perturbation amplitude at the profile $\varepsilon_1(r)$. We assume that the quantities A and M may be positive or negative.

It is convenient to use function (2), which provides a fairly good approximation of the radial density profile not only in the vicinity of but also far from its maximum, because, at large distances from r_0, the term with the hyperbolic cosine can be neglected. Near the resonance point r_0, a constant plasma density is perturbed (nonuniform) in an axisymmetric fashion, the radial width a of the perturbation being prescribed. The sign of each of the terms depends on the plasma parameters. Given the density far from the point r_0 (or the value of the parameter M), we look for the eigensolutions to Maxwell's equations. Starting from the corresponding eigenvalues, we determine the parameter range where Alfvén eigenmodes can exist, specifically, the range of values of the plasma parameters (in particular, the density perturbation amplitude) in the vicinity of the perturbation.

3. BASIC EQUATION

The equation for the radial component $\tilde{E_r}$ of the field of a wave can be derived from Maxwell's equations with allowance for electron inertia and finite ion Larmor radius (see, e.g., [1, 8, 10]). Setting $\tilde{E_r} = E_r(r)\exp[i(k_z z + m\vartheta - \omega t)]$, we obtain

$$\left[\varepsilon_1 - N_z^2 + \left(\varepsilon_T + \frac{\varepsilon_1}{\varepsilon_3}\frac{c^2}{\omega^2}\right)\frac{d^2}{dr^2}\right]E_r = -i\varepsilon_2 E_\vartheta - \frac{cm}{\omega r}B_z, \quad (3)$$

where ε_i are the components of the dielectric tensor of a collisionless magnetized plasma. The term ε_T, which accounts for finite ion Larmor radius effects [12], has the form

$$\varepsilon_T = \sum_\alpha \frac{3\omega_{p\alpha}^2(r)v_{T\alpha}^2(r)}{(\omega^2 - \omega_{c\alpha}^{(0)^2})(\omega^2 - 4\omega_{c\alpha}^{(0)^2})}. \quad (4)$$

The coefficient in front of the second derivative in Eq. (3) is equal in order of magnitude to $N_z^2\rho_{Li}^2$, where $\rho_{L\alpha} = v_{T\alpha}/\omega_{c\alpha}$ is the Larmor radius of the particles of species α and $v_{T\alpha}$ is their thermal velocity. Following [1], we apply the so-called "narrow-slab" approach, which implies that, in the resonance region, the plasma parameters change gradually and the wave fields depend strongly on the radial coordinate. Assuming that the radial variations of the quantities ε_T and $\varepsilon_1/\varepsilon_3$ are gradual in this approximation, we introduce the notation

$$\varepsilon_T + \frac{\varepsilon_1}{\varepsilon_3}\frac{c^2}{\omega^2} \equiv \pm N_z^2\rho^2. \quad (5)$$

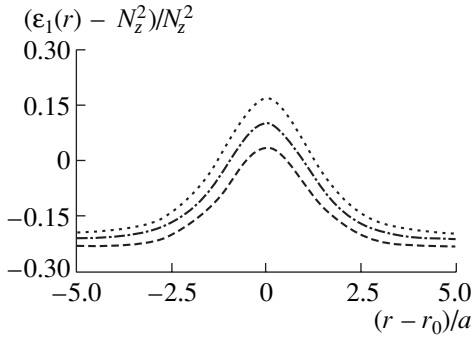

Fig. 1. Radial profiles of the quantity $(\varepsilon_1 - N_z^2)/N_z^2$ calculated for the fixed values $\delta = 10$ and $\rho/a = 0.05$ in the case of a maximum in the density profile. The dashed curve is for the eigenmode with the radial number $n = 0$, the dashed-and-dotted curve is for the mode with $n = 1$, and the dotted curve is for the mode with $n = 2$.

We emphasize that the quantity ρ in formula (5) has the dimensionality of length: it serves to normalize the coefficient in front of the second derivative in Eq. (3) and is of the same order of magnitude as (but not identical to) the ion Larmor radius.

Since, in the frequency range under consideration, the component ε_3 is negative and the component ε_T is positive, the coefficient in front of the second derivative may have different signs. The sign of the coefficient in front of the highest derivative in Eq. (3) is very important because it determines the conditions (a local maximum or a local minimum in the plasma density) in which the eigenmodes can exist. Since the quantity ε_T depends on the temperature of the plasma particles [see formula (4)], it is of considerable interest to determine the conditions under which quantity (5), being a function of the electron and ion temperatures, changes its sign. It is convenient to plot the curve along which quantity (5) is zero in the plane of the ion and electron thermal velocities (see Fig. 2). For a plasma in which both the ions and electrons are cold, $v_{Ti} \ll \omega/|k_z|$ and $v_{Te} \ll \omega/|k_z|$, coefficient (5) is negative. Physically, this indicates that the thermal velocities of the plasma particles can be neglected; hence, in expression (5), the second term, which accounts for electron inertia, is dominant. According to the generally accepted terminology [13], the waves in such a plasma are called inertial waves. On the contrary, for a plasma in which both the ions and electrons are hot, coefficient (5) is positive because it is primarily contributed by the ion thermal motion, in which case the waves are called kinetic waves.

Although, in the vicinity of Alfvén resonance, the azimuthal electric field E_ϑ and the axial magnetic field B_z have logarithmic singularities, $E_\vartheta, B_z \propto \ln|\varepsilon_1 - N_z^2|$, the combination $i\varepsilon_2 E_\vartheta + (cm/\omega r)B_z$ on the right-hand side of Eq. (3) is continuous and changes gradually.

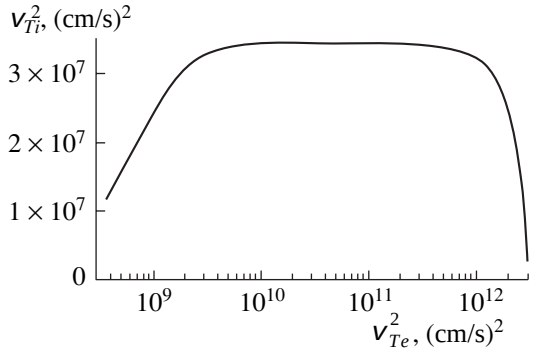

Fig. 2. Curve along which the quantity $\varepsilon_T + \frac{\varepsilon_1 c^2}{\varepsilon_3 \omega^2}$ in formula (5) changes sign in the coordinate plane (v_{Te}^2, v_{Ti}^2). Above the curve, this quantity is positive and, below the curve, it is negative. The calculations were carried out for a deuterium plasma of density 3×10^{13} cm^{-3} and a magnetic field of 39 kG.

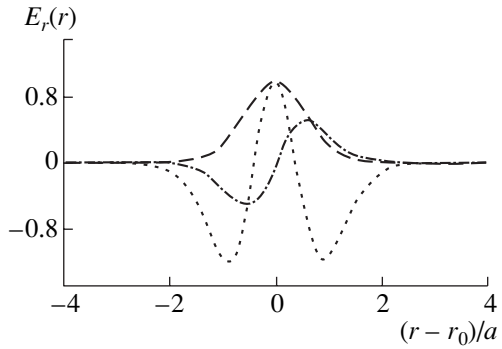

Fig. 3. Radial profiles of E_r for $n = 0$, 1, and 2. The parameters and notation are the same as in Fig. 1.

That is why this combination is usually set to be a constant and is attributed to the pump wave [1, 8, 10]. Since we are interested in the eigensolutions to Eq. (3) that are localized in the vicinity of $r = r_0$, we can assume that the wave fields are negligible far away from r_0 and, thus, we can set the combination to be zero.

4. KINETIC ALFVÉN WAVES

Here, we consider the case of a hot plasma, in which the coefficient in front of the second derivative in Eq. (3) is positive. In order for the solution to be localized, i.e., to decrease exponentially away from r_0, the quantity $\varepsilon_1 - N_z^2$ should be negative at $|r - r_0| \gg a$, which corresponds to $M < 0$. In the above notation, we rewrite Eq. (3) as

$$\left[- M + A\cosh^{-2}\left(\frac{r - r_0}{a}\right) + \rho^2 \frac{d^2}{dr^2}\right] E_r = 0. \qquad (6)$$

Recall that the coefficient A may have different signs. However, Eq. (6) has localized eigensolutions only when $A > 0$, i.e., when the density profile has a maximum (Fig. 1). This conclusion agrees with the results of a numerical analysis carried out by Appert *et al.* [14] for a plasma with hot electrons, $v_{Te} > \omega/|k_z|$.

Following [11], we introduce the notation

$$M = -\frac{\rho^2}{a^2}\delta^2, \quad A = \frac{\rho^2}{a^2}s(s+1). \qquad (7)$$

The replacement $\xi = \tanh\left(\frac{r - r_0}{a}\right)$ reduces Eq. (6) to a hypergeometric equation, whose solution is expressed in terms of a hypergeometric function [15]:

$$E_r(r) = \cosh^{-\delta}\left(\frac{r - r_0}{a}\right) F\left(\delta - s, \delta + s + 1, \delta + 1, \frac{1}{2}(1 - \xi)\right). \qquad (8)$$

At $r - r_0 \gg a$, function (8) is finite only when the quantities δ and s are related by $s = \delta + n$ (the number $n = 0$, 1, 2, … corresponds to the number of zeros of the function E_r). By the quantity δ, we mean the arithmetical square root of δ^2. Figure 3 shows the radial field component E_r calculated as a function of the radius from expression (8) at $n = 0$, 1, and 2.

For different n, the values of ε_1 at the point r_0 are equal to

$$\varepsilon_1(r_0) = N_z^2\left\{1 + \frac{\rho^2}{a^2}[\delta(2n+1) + n(n+1)]\right\}. \qquad (9)$$

The frequency for which resonance condition (1) is satisfied corresponds to the Alfvén continuum [5, 13] and is equal to $\omega = |k_z| v_A$, where v_A is the Alfvén speed. Assuming that the correction to N_z^2 on the right-hand side of expression (9) is small and retaining only the first term in the expansion in this correction, we find the frequencies of the eigenmodes with different values of n:

$$\omega_n = |k_z| v_A\left(1 + \frac{\rho^2}{2a^2}[\delta(2n+1) + n(n+1)]\right). \qquad (10)$$

In order to determine to which type of waves in a homogeneous plasma the waves localized between two Alfvén resonances belong, we solve Eq. (6) in the Wentzel–Kramers–Brillouin (WKB) approximation. Setting $E_r^{\sim} \propto \exp(i\int k_r dr)$ ($k_r a \gg 1$), we obtain the fol-

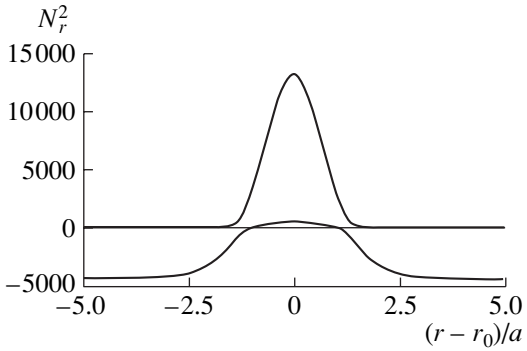

Fig. 4. Radial dependence of the radial refractive index in the case of a maximum in the density profile (which corresponds to the propagation of kinetic Alfvén waves).

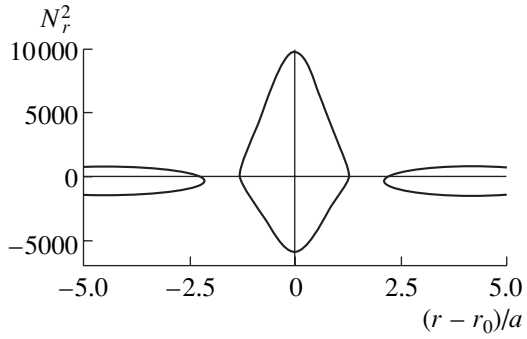

Fig. 5. Radial dependence of the radial refractive index in the case of a minimum in the density profile (which corresponds to the propagation of inertial Alfvén waves).

lowing expression for the squared radial refractive index $N_r^2 = c^2k_r^2/\omega^2$:

$$N_{r\pm}^2 = \frac{\varepsilon_1 - N_z^2}{2k_z^2\rho^2}\left[1 \pm \sqrt{1 - 4\frac{k_z^2\rho^2}{\varepsilon_1 - N_z^2}\left(N_\perp^2 - \frac{c^2m^2}{\omega^2 r_0^2}\right)}\right]. \quad (11)$$

This expression is plotted in Fig. 4 for the same parameters as in Figs. 1 and 3. In deriving expression (11), we have introduced the notation

$$N_\perp^2 = [(\varepsilon_1 - N_z^2)^2 - \varepsilon_2^2]/(\varepsilon_1 - N_z^2). \quad (12)$$

Far from the resonance region, the wave in question is a fast magnetosonic wave, whereas, near the resonance, it becomes an Alfvén wave. Far from the density perturbation, the squared radial refractive index is negative, $N_r^2 < 0$; hence, the waves do not exist. In the vicinity of the maximum in the perturbation, we have $N_r^2 > 0$, which indicates the existence of localized kinetic Alfvén waves.

5. INERTIAL ALFVÉN WAVES

For a cold plasma, coefficient (5) in front of the second derivative is negative, which corresponds to inertial waves. The problem for such a system possesses localized solutions only when the quantity $\varepsilon_1(r)$ far from the point r_0 (at infinity) is larger than its resonant value (1) ($M > 0$) and has a minimum ($A < 0$) in the vicinity of the point r_0. The radial dependence of the quantity $(\varepsilon_1(r) - N_z^2)/N_z^2$ differs from that shown in Fig. 1 only in sign (note that the zero on the vertical axis in Fig. 1 is chosen to correspond to the value N_z^2). Hence, using the replacement

$$M = +\frac{\rho^2}{a^2}\delta^2, \quad A = -\frac{\rho^2}{a^2}s(s+1), \quad (13)$$

we obtain, instead of Eq. (6), the following equation describing the eigenmodes when the density profile has a minimum:

$$\left[+\delta^2 - s(s+1)\cosh^{-2}\left(\frac{r - r_0}{a}\right) - a^2\frac{d^2}{dr^2}\right]E_r = 0. \quad (14)$$

Since Eq. (14) differs from Eq. (6) only in a constant factor, its solutions are also represented by formula (8); hence, the solutions for the first three eigenmodes behave in the same manner as those shown in Fig. 3.

The eigenfrequencies of the inertial Alfvén waves are equal to

$$\omega_n = |k_z|v_A\left\{1 - \frac{\rho^2}{a^2}[\delta(2n+1) + n(n+1)]\right\}. \quad (15)$$

Figure 5 shows the radial dependence of squared radial refractive index (11) calculated for the same plasma parameters as in Fig. 4. We can see that this dependence has discontinuities in the intervals where the imaginary part of N_r^2 is nonzero.

6. DISCUSSION OF THE RESULTS

It is known from the theory of Alfvén resonance [1, 8–10] that, in the vicinity of the resonance point at which condition (1) is satisfied, the field E_r diverges as $\propto(\varepsilon_1 - N_z^2)^{-1}$. When electron inertia and finite ion Larmor radius are taken into account, the solution becomes finite but changes radically. As has been shown above, the condition that the quantity ε_1 reaches its resonant value at only one point is not sufficient for the existence of the localized perturbations. A necessary condition for small-scale perturbations to be localized between two points is that the quantity $\varepsilon_1 - N_z^2$ at these points vanishes. Moreover, at the point of maximum density, $r = r_0$, the tensor component ε_1 should take on a certain value,

$$\varepsilon_1 - N_z^2 = N_z^2[(\delta + n)(\delta + n + 1) - \delta^2]. \quad (16)$$

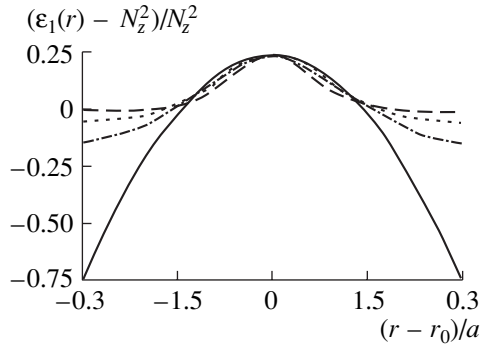

Fig. 6. Modeling of the profile of the quantity $(\varepsilon_1(r) - N_z^2)/N_z^2$, which depends linearly on the plasma density, by parabola (18) (solid curve) and hyperbolic cosine (2) in the case of a maximum in the density profile. The calculations were carried out for the mode with $n = 3$ and for different δ values: $\delta = 1$ (dashed curve), $\delta = 3$ (dotted curve), and $\delta = 7$ (dashed-and-dotted curve).

The amount by which the quantity ε_1 exceeds its resonant value depends on the δ value corresponding to the plasma density far from the resonance point.

The quantity $\varepsilon_1(r_0)$ given by expression (9) has a minimum value $N_z^2(1 + \delta\rho^2/a^2)$ at $n = 0$. In the model developed here, the eigenmodes do not exist for $\varepsilon_1 - N_z^2 < \delta N_z^2 \rho^2/a^2$.

On the other hand, for sufficiently small δ values, the amount by which the tensor component at hand should exceed its resonant value in the case $n = 0$ can be made arbitrarily small. This conclusion agrees with the well-known result from quantum mechanics [11]: in the corresponding quantum mechanical problem, the zero radial mode can exist in a potential well (2) of arbitrarily small depth. For higher modes, quantity (9) is finite (nonzero) for any δ value.

Note also that the applicability condition of the narrow-slab approach, $\rho \ll a$, can easily be satisfied in experiments. In the vicinity of Alfvén resonance, the characteristic parameter $k_r^2\rho^2$ is small, $k_r^2\rho^2 \sim \rho/a \ll 1$; hence, a description of the plasma in terms of the dielectric tensor turns out to be justified.

In deriving basic equation (6) from general equation (3), we imposed the corresponding boundary conditions and set the combination on the right-hand side of Eq. (3) to zero. In other words, we assumed that this combination is small in comparison with the retained terms that arise, e.g., from the finite ion Larmor radius and electron inertia. A comparison of the omitted term with the retained terms yields the following strong inequalities:

$$(\omega/\omega_{ci})N_\vartheta N_z,\ N_\vartheta^2,\ (\omega/\omega_{ci})^2 N_z^2 \ll c^2/(a\omega)^2. \quad (17)$$

Parenthetically, for a linear plasma density profile, these inequalities are weaker because of the large additional factor $(a/\rho)^{2/3}$ on the right-hand side. The first and third of these strong inequalities can be satisfied because they contain small factors (ω/ω_{ci}) and $(\omega/\omega_{ci})^2$ on the left-hand sides. The remaining inequality can also be satisfied because the characteristic radial scale a on which the plasma density varies is small in comparison with the value of the coordinate r_0 of the density extremum, $a \ll r_0$. It is clear that the first two of the inequalities are strictly satisfied for symmetric pulses ($m = 0$).

7. COMPARISON WITH EARLIER RESULTS

If the function $\varepsilon_1(r)$ approaches a large value far from the resonance point (this corresponds to large δ values and, consequently, to large plasma density perturbations), then potential well (2) in the vicinity of its minimum can be approximated by a parabola. This enables us to compare the above results with the results obtained in [9, 10], where the plasma density perturbation was modeled by a parabolic profile. To be specific, we consider the case in which the density profile has a maximum (see the solid curve in Fig. 6):

$$\varepsilon_1(r) = N_z^2\left(1 + B - \left(\frac{r - r_0}{b}\right)^2\right). \quad (18)$$

Neglecting absorption, the eigensolutions to Eq. (3) with profile (18), i.e., the solutions to this equation with zero on the right-hand side, can be found analytically. They are expressed in terms of Hermite polynomials [15]:

$$E_r(r) = \exp\left(-\frac{(r - r_0)^2}{2\rho b}\right)H_n\left(\frac{r - r_0}{\sqrt{2\rho b}}\right). \quad (19)$$

These solutions exist only for certain values of B:

$$B = \frac{\rho}{b}(2n + 1), \quad (20)$$

in which case the eigenfrequencies are equal to

$$\omega_n = k_z v_A\left(1 + \left(n + \frac{1}{2}\right)\frac{\rho}{b}\right). \quad (21)$$

Let us compare the eigenfrequencies corresponding to the parabolic density profile (18) with eigenfrequencies (10). To do this, we assume that the electron and ion temperatures (i.e., the values of the parameter ρ) are the same in both cases. We also require that the values of the quantity ε_1 in profiles (2) and (18) should coincide at the point of extreme density:

$$\frac{\rho^2}{a^2}[\delta(2n + 1) + n(n + 1)] = \frac{\rho}{b}(2n + 1). \quad (22)$$

The same requirement on the second derivative of this quantity yields

$$\frac{\rho^2}{a^4}(\delta + n)(\delta + n + 1) = \frac{1}{b^2}. \quad (23)$$

In both problems, we number the eigensolutions by consecutive positive integers n and require that equalities (22) and (23) be satisfied for the corresponding n values. It is easy to show that these equalities can be consistent only when $\delta \gg n$. Then, in equality (22), we can neglect n in comparison with δ to obtain the following relationship between the density perturbation widths in the cases of hyperbolic cosine (2) and parabolic profile (18):

$$a^2 = b\rho\delta. \quad (24)$$

It is seen that the width a of the region where density perturbation (2) is localized changes depending on the ε_1 value, which is determined by the value of ε_1 far from the point r_0. In the limit $\delta \gg n$, eigenfrequencies (21) with the values of b satisfying relationship (24) coincide with eigenfrequencies (10). For small n, the last term in expression (9) can be neglected.

Now, we fix the width b of the parabolic profile and approximate the potential well $\varepsilon_1(r)$ by a parabola and a hyperbolic cosine with different δ values and with a fixed value of n, which is taken to be $n = 3$. Figure 6 shows the potential well in the form of a parabola (solid curve) and hyperbolic cosine (2) with different δ values: $\delta = 1$ (dashed curve), $\delta = 3$ (dotted curve), and $\delta = 7$ (dashed-and-dotted curve). All the curves were calculated under conditions (22) and (23), implying that the values of the function, as well as of its second derivative, coincide at the point $r = r_0$. The eigenmodes in the cases at hand are illustrated in Fig. 7. As δ increases, the potential well (2) of finite depth is seen to become closer in shape to parabolic density profile (18). Analogously, from Fig. 7, we can see that, with increasing δ, the radial profile of the field component $E_r(r)$ in the case of a density perturbation of finite depth approaches the curve corresponding to a parabolic density profile.

Let us compare eigenfrequencies (10) and (21). The neighboring eigenfrequencies in spectrum (21) differ by a small amount proportional to ρ/a. The spectrum of eigenfrequencies (10) contains the square of the small parameter ρ/a. However, at a given density value far from r_0, or, equivalently, at a fixed value of M, the quantity δ is proportional to a/ρ (see Fig. 7). Consequently, for $\delta \gg n$, the intervals between the eigenfrequencies of the modes with neighboring radial numbers are the same in both problems.

Near the curve along which quantity (5) is zero (see Fig. 2), it is insufficient to retain only the small term proportional to $\rho_{Li}^2 d^2/dr^2$ in Eq. (3); it is also necessary to take into account higher order terms proportional to $\rho_{Li}^4 d^4/dr^4$.

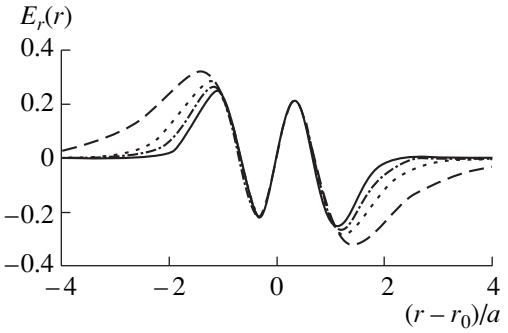

Fig. 7. Solutions to Eq. (6) with the density profiles shown in Fig. 6. The notation is the same as in Fig. 6.

8. CONCLUSION

We have analytically investigated electromagnetic eigenmodes localized in the region where the radial density profile of a hot plasma has a maximum (minimum) of the finite height (depth) between two local Alfvén resonances.

It is shown that, in a hot plasma, kinetic Alfvén waves can propagate near a maximum in the plasma density profile. The waves that can exist in the vicinity of a minimum in the density profile in a cold plasma are inertial Alfvén waves. This situation is analogous to that with an infinitely deep parabolic potential well, which was considered earlier, e.g., in [9, 10].

For an arbitrary value of the plasma density far from the region where the density perturbation is localized (or, in other words, for an arbitrary δ value), there exists a critical value of the maximum (minimum) density at which the eigenmodes can propagate. When the plasma density at the point r_0 of the maximum (minimum) exceeds its resonant value determined by condition (1) by an arbitrarily small amount, the necessary condition for the existence of localized eigenmodes is that the plasma density far from r_0 be sufficiently close to the resonant value.

We have determined the eigenfrequencies (10) and (15) of Alfvén waves and have shown that they are higher than the Alfvén continuum frequency in the case of a maximum in the density profile and are lower than this frequency when the density profile has a minimum. We have also obtained an analytic expression for the field of the eigenmodes [see formula (8) and Fig. 3].

The results of our analysis have been compared with those obtained for a parabolic plasma density profile. In the limit of an infinitely deep potential well ($\delta \gg n$), the eigenmodes and their eigenfrequencies have been found to be the same in both problems.

REFERENCES

1. V. V. Dolgopolov and K. N. Stepanov, Nucl. Fusion **5**, 276 (1965).
2. C. Uberoi, Phys. Fluids **15**, 1673 (1972).
3. J. Tataronis and W. Grossman, Z. Phys. **261**, 203 (1973).
4. L. Chen and A. Hasegawa, Phys. Fluids **17**, 1399 (1974).
5. J. Vaclavik and K. Appert, Nucl. Fusion **31**, 1945 (1991).
6. *High-Frequency Plasma Heating*, Ed. by A. G. Litvak (Am. Inst. of Physics, New York, 1992).
7. V. I. Lapshin, K. N. Stepanov, and E. A. Fedutenko, in *Proceedings of the Joint Varenna–Abastumani International School and Workshop on Plasma Astrophysics, Varenna, 1988*; ESA SP-285 **1**, 111 (1988).
8. I. O. Girka, S. V. Kasilov, V. I. Lapshin, and K. N. Stepanov, Probl. At. Sci. Technol., Ser. Plasma Phys. (Kharkov), No. 1/2, 148 (1999).
9. S. M. Mahajan, Phys. Fluids **27**, 2238 (1984).
10. I. O. Girka and P. P. Rutkevich, J. Kharkiv Nat. Univ., Phys. Ser.: Nuclei, Particles, Fields **3/15** (529), 43 (2001).
11. L. D. Landau and E. M. Lifshitz, *Quantum Mechanics: Non-Relativistic Theory* (Nauka, Moscow, 1989; Pergamon Press, New York, 1977).
12. *Plasma Electrodynamics*, Ed. by A. I. Akhiezer *et al.* (Nauka, Moscow, 1974; Pergamon Press, Oxford, 1975).
13. T. H. Stix, *Theory of Plasma Waves* (McGrow-Hill, New York, 1962; Atomizdat, Moscow, 1965).
14. K. Appert, T. Hellsten, H. Luetjens, *et al.*, in *Proceedings of International Conference on Plasma Physics, Invited Papers, Kiev, 1987* (World Scientific, Singapore, 1987), Vol. 2, p. 1230.
15. *Handbook of Mathematical Functions with Formulas, Graphs, and Mathematical Tables*, Ed. by M. Abramowitz and I. Stegun (National Bureau of Standards, Washington, 1964; Nauka, Moscow, 1979).

Translated by I.A. Kalabalyk

Plasma Physics Reports, Vol. 29, No. 6, 2003, pp. 473–479. Translated from Fizika Plazmy, Vol. 29, No. 6, 2003, pp. 508–515.

DUSTY PLASMA

Numerical Simulations of Ion and Electron Transport in a Low-Temperature Dusty Plasma

Yu. V. Petrushevich

Troitsk Institute for Innovation and Fusion Research, State Scientific Center of the Russian Federation, Troitsk, Moscow oblast, 142092 Russia

Received May 30, 2002; in final form, December 18, 2002

Abstract—Charged particle transport and kinetic processes in a low-temperature dusty plasma are numerically simulated. Dust grains are represented as spheres with a given radius. The self-consistent electric field in the plasma surrounding a charged dust grain is calculated taking into account the perturbations of plasma quasineutrality near the grains. It is shown that applying an external electric field leads to a rearrangement of the plasma space charge and a break of the spherical symmetry of the electron and ion density distributions around the grain. The mutual influence of two identical charged dust grains is considered, and the energy of the electrostatic interaction between the grains is calculated. It is shown that this energy has a minimum at a certain finite distance between the grains. *© 2003 MAIK "Nauka/Interperiodica".*

1. INTRODUCTION

The interaction between dust grains in a dusty plasma is one of the most important phenomena determining the properties of this system. In particular, this interaction results in the formation of dusty crystal structures, which have been observed under various conditions. A review of the studies on dusty plasma structures is presented in [1]. In many experiments, it was demonstrated that dust grains in a dusty plasma usually acquire a negative electric charge. One of the key problems is to find out the nature of the attraction forces between likely charged dust grains. The attraction is usually explained by the electrostatic interaction between the grains and the polarized ambient plasma [2–5]. In those papers, the medium polarization was analyzed under the assumption that the charged plasma particles (electrons and ions) obey a Boltzmann distribution. However, simulations of the grain charging process in a dusty plasma [6] showed that the electron and ion spatial distributions near the grain's surface were nonmonotonic and the equilibrium plasma particle distributions were not established. In [7], it was shown that the departure from the equilibrium distribution was more pronounced for the ions.

Simulations of [8, 9], in which the ions were modeled by the Monte Carlo method, showed that a positive space charge arose in the plasma region between the grains, which resulted in their mutual attraction.

We note that, near the grain's surface, where the quasineutrality is disturbed, the electric field caused by the grain charge is fairly strong and can attain 10^3–10^4 esu, depending on the plasma parameters (in particular, the grain size). Because of the strong electric field near the grain's surface and the spatial inhomogeneity of the field in this region, the electron temperature significantly differs from the gas temperature. This circumstance explains why the charged particle densities observed in numerical simulations [7] substantially deviate from a Boltzmann distribution.

Thus, although the mechanism for the interaction between dust grains under laboratory conditions is quite clear, the value of the interaction energy needs additional study. An adequate plasma model should accurately take into account the dynamics of charged plasma particles. Moreover, the problem of the interaction of two dust grains should be considered at least in two-dimensional geometry.

In this paper, we propose a model describing charged particle transport in a dusty plasma produced by an electron beam and present the results of simulations of the interaction between charged dust grains in such a plasma.

2. PROBLEM FORMULATION AND BASIC EQUATIONS OF THE CHARGED PARTICLE DYNAMICS IN A LOW-TEMPERATURE DUSTY PLASMA

We study the phenomena occurring in a dusty plasma with the dust component consisting of solid metal or dielectric grains. The problems under investigation are the process of grain charging and the formation of the charge distribution in the ambient plasma. We consider a model problem in which dust grains are assumed to be spheres with a given radius. The grains can be either metal or dielectric; however, in this paper, we present the results of calculations in which the grains are assumed to be dielectric and the charge is distributed uniformly over the grain's surface. The numerical model also includes the surrounding plasma region. The plasma consists of electrons and ions (in the gen-

1063-780X/03/2906-0473$24.00

eral case, there may be several ion species). In experiments, an external electric field is usually applied to the dusty plasma, which favors the formation of spatial dusty structures. For this reason, the self-consistent (including the external) electric field should also be taken into account. In view of the axial symmetry of the system under consideration, it is reasonable to solve the problem in spherical coordinates in two-dimensional geometry.

The proposed model of a low-temperature plasma includes the continuity equations for charged particles. The particle velocities are determined by the local value of the electric field. The electron diffusion is also taken into account, which is necessary because, under the given conditions, the dust grains are negatively charged and it is precisely the diffusion term that provides the electron flow onto a grain. The ion flow near a dust grain is provided by the ion drift in an electric field, which is fairly high in this region. Under these conditions, the contribution of the diffusive ion flow is insignificant. The model is valid when the characteristic dimensions of the problem are larger than the mean free path of the charged particles, which amounts to 10^{-5} cm at atmospheric pressure. Therefore, for grains with a size of 10^{-4}–10^{-3} cm, the model proposed can be regarded as quite adequate.

The basic equations have the form

$$\begin{aligned} \frac{\partial n_e}{\partial t} + \nabla \cdot (\mathbf{w}_e n_e) &= \nabla \cdot (D \nabla n_e) + Q_e, \\ \frac{\partial n_i}{\partial t} + \nabla \cdot (\mathbf{w}_i n_i) &= Q_i, \\ \Delta \varphi &= 4\pi e (n_e - n_i), \end{aligned} \tag{1}$$

where n_e and n_i are the densities of the electrons and positive ions, respectively; $\mathbf{w}_e$ and $\mathbf{w}_i$ are the electron and ion drift velocities; Q_e and Q_i are the terms describing the production and loss of electrons and ions; D is the electron diffusion coefficient; and φ is the electric potential.

We use a spherical coordinate system whose origin coincides with the center of a spherical dust grain with a radius R_d. Equations (1) should be supplemented with the boundary conditions, which can be deduced from the following considerations. If the charge of the sphere is positive, then the ion drift velocity is directed outward from the sphere. In this case, the density of the positive ions is assumed to be zero at the grain's surface. For a negatively charged sphere, no boundary conditions for the ions on the grain's surface apply.

The electron transport equation contains the diffusion term. Hence, the boundary conditions on the grain's surface must be imposed for either sign of the grain charge. In view of the low efficiency of the known mechanisms of electron production on the grain's surface in a low-temperature dusty plasma, we will assume that the electron density near the grain's surface is zero. At infinity (far from the grain), the ion and electron densities are assumed to be equal to their equilibrium values, determined by plasmochemical processes.

Simulations were performed with allowance for the external electric field. As a boundary condition for the electric field, we assume that the field at infinity is equal to the external field. Summarizing all the assumptions, the boundary conditions can be written in the form

$$\begin{aligned} n_i(r = R_d) &= 0; \quad \text{for} \quad E(r = R_d) > 0; \\ n_i(r \longrightarrow \infty) &= n_i^{(\mathrm{eq})}; \\ n_e(r = R_d) &= 0; \quad n_e(r \longrightarrow \infty) = n_e^{(\mathrm{eq})}; \end{aligned} \tag{2}$$

$$\begin{aligned} \nabla \varphi(r = R_d) &= -Qe/R_d^2, \\ \nabla \varphi(r \longrightarrow \infty) &= -E_0(r), \end{aligned} \tag{3}$$

where Q is the grain charge in atomic units and E_0 is the external electric field, which depends on the specific conditions of the problem.

We consider a nitrogen dusty plasma produced by a high-power electron beam ionizing the gas with an ionization rate of $\sim 10^{16}$ s^{-1} cm^{-3}. Under the given conditions, the ion density attains $\sim 10^{11}$ cm^{-3}. We assume that the plasma consists of positive ions and electrons. The charge particle balance is determined by plasmochemical reactions, including both the gas ionization by the electron beam and electron–ion recombination:

$$Q_e = Q_i = q - \beta n_e n_i,$$

where q is the ionization rate and β is the recombination coefficient. In calculations, the recombination coefficient depended on the electric field and was on the order of $\beta \sim 10^{-6}$ cm^3/s.

The dielectric dust grains were spheres with the radius $R_d = 12$ μm. We considered the gas at atmospheric pressure ($p = 1$ atm) and room temperature ($T = 300$ K). The dust density was assumed to be low enough for the dust charge to have no effect on the average density of charged plasma particles. The known dependences of the plasma kinetic coefficients on the electric field for nitrogen were used. The grain charge was determined by the balance of the currents of the plasma electrons and ions. Simulations were performed until the calculated quantities reached their steady state values.

Two-dimensional simulations require considerable computational resources; hence, the choice of an efficient algorithm is of great importance for this kind of problem. The algorithm used in this study is described in detail in [10]. The simulations were separated into several steps. The transport equations were solved using a standard implicit scheme, and Poisson's equation was solved using the expansion of the electric potential in Legendre polynomials. The main problem arising when using this method is providing the convergence of the expansion series; therefore, the expansion

terms should be regularly checked for the convergence. Simulations showed that in the modeling of a real plasma with spherical dust grains, it is quite sufficient to take into account six harmonics.

3. RESULTS OF SIMULATIONS OF A DUSTY PLASMA IN AN EXTERNAL ELECTRIC FIELD

The charging of a spherical grain with a radius of 12 μm in a nitrogen plasma and the establishment of the spatial charge distribution around the grain were investigated. The ionization source power was taken to be 2×10^{16} cm^{-3} s^{-1}.

Simulations were performed both without an external electric field and in the presence of a fairly strong external electric field with a strength of $E_0 = 900$ V/cm. The results of calculations are presented in Fig. 1.

It can be seen in the figure that applying the electric field results in a significant redistribution of the space charge around the grain. The electron density profile shifts toward the grain's surface, and a slight local maximum appears on the profile. The ion density profile shifts in the opposite direction. As a result, the length of the region in which the plasma quasineutrality is disturbed changes substantially. Moreover, in the presence of the electric field, a region appears in which the space charge changes its sign. We note that, far from the grain (in the quasineutral plasma), the plasma density increases because the recombination coefficient decreases considerably when the external electric field is applied. Figure 2 shows the spatial profile of the self-consistent electric field. It can be seen that, in the presence of the external field, the radial component of the electric field changes its sign far from the grain's surface.

We also note that the region where quasineutrality is disturbed is fairly large. The simulations were performed for the Debye radius $R_{Db} \approx 4$ μm. It can be seen in Fig. 1 that, in the absence of an external electric field, the region where quasineutrality is disturbed is about $R_a \sim 25$ μm. From Fig. 2, it is seen that R_a corresponds to the distance at which the electric field significantly decreases. Similar results in the absence of an external field were obtained in [6, 7].

The calculated dependence of the grain charge on the external electric field is shown in Fig. 3. The grain charge is negative and its value agrees with the results of calculations presented in [1, 6]. The negative sign of the grain charge in a gas-discharge plasma was pointed out by many authors; it is explained by the higher mobility of electrons in plasma in comparison with that of ions. It follows from the simulation results that the grain charge can be increased severalfold by increasing the external electric field within reasonable limits.

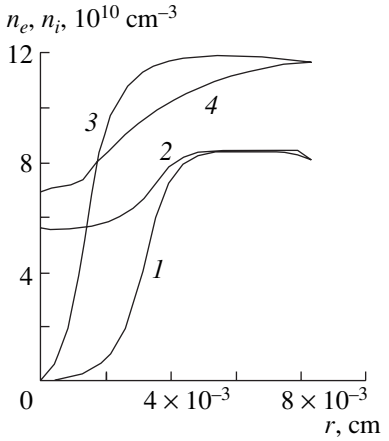

Fig. 1. Radial profiles of the (*1*, *3*) electron and (*2*, *4*) ion densities in the plasma surrounding the grain (*1*, *2*) in the absence of an external electric field and (*3*, *4*) in the presence of an external field of 900 V/cm. The density profiles are shown for the angle θ = 36° with respect to the direction of the external field (Here and in the subsequent figures, the radial coordinate is measured from the grain's surface).

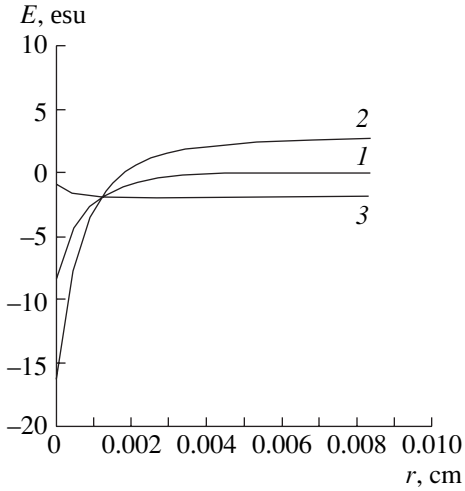

Fig. 2. (*1*) Radial profile of the electric field in the plasma surrounding the grain in the absence of an external electric field and the profiles of the (*2*) radial and (*3*) tangential components of the self-consistent electric field in the presence of an external electric field of 900 V/cm for the angle θ = 36° with respect to the direction of the external field.

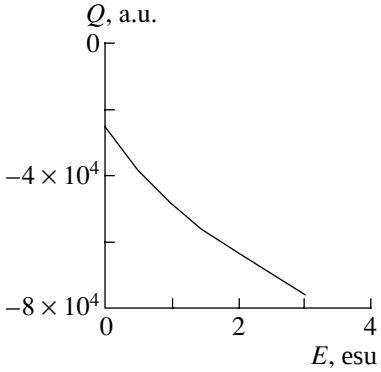

Fig. 3. Charge of a spherical grain as a function of the external electric field.

4. CHARGE DISTRIBUTION AND INTERACTION IN A TWO-GRAIN SYSTEM

The presence of attraction forces between dust grains in a dusty plasma was unambiguously demonstrated in the experiments of [11]. The shift of one of the interacting grains by a laser beam results in a similar shift of the second grain. The problem of the interaction between two charged dust grains was considered in [12]. In that paper, the electrostatic potential was accurately calculated by using appropriate curvilinear coordinates. However, in that paper, as well as in the papers mentioned above, it was assumed that the plasma particles obey a Boltzmann distribution. However, the numerical results obtained using more adequate models show that the real plasma particle distributions should differ significantly from a Boltzmann one.

In [13], the interaction energy of two grains and its dependence on the distance between these grains were calculated. The interaction energy was found to be minimum at the distance $r_{12} = 2.73R_{\mathrm{Db}}$. This means that the grains efficiently interact at a distance larger then the Debye radius, i.e., in the region where the plasma substantially screens the grain charge. On the one hand, this result is important because it corresponds to experimental observations. On the other hand, in that paper, a mechanism for the appearance of the attraction force between likely charged grains in the polarized surrounding medium was proposed based on a rather simple model. Unfortunately, the applicability of the results of [13] is limited to the case of small grains with the radii $R_d \ll R_{\mathrm{Db}}$; moreover, that paper also used the Debye screening model, which has a limited applicability range, as has been discussed above.

The conclusion of [14] about the repulsion of likely charged grains in plasma was made based on the collisionless plasma model assuming the mirror reflection of charged particles from the grain's surface. In that paper, the limited applicability of this model was also indicated. In particular, this model is inapplicable to a low-temperature dusty plasma of a high-pressure gas discharge, which is considered in the present paper. Hence, along with the interaction mechanism associated with anisotropy of gas-kinetic pressure in a two-grain system [14, 15], the electrostatic interaction must also be taken into account. We note that the possibility of attraction between likely charged grains due to plasma polarization was shown in [4, 8].

In the present paper, an evident symmetry of the problem was used to calculate the charge distribution in the system of two grains in plasma in the absence of an external electric field. When the grains are identical and have the same electric charge, there is a symmetry plane lying halfway between the grains. In this case, the solution of the problem reduces to the calculation of the dynamics of charged plasma particles in the half-space adjacent to one of the grains, and the electric field is determined as a sum of the fields produced by the electric charges in both half-spaces:

$$\begin{aligned}\varphi(\mathbf{r}) &= \varphi_1(\mathbf{r}) + \varphi_2(\mathbf{r}) \\ &= \left(\int_{V_1}\frac{\rho(\mathbf{r}_1)dV_1}{|\mathbf{r}-\mathbf{r}_1|} + \int_{S_1}\frac{\sigma(\mathbf{r}_1)ds_1}{|\mathbf{r}-\mathbf{r}_1|}\right) \\ &+ \left(\int_{V_2}\frac{\rho(\mathbf{r}_2)dV_2}{|\mathbf{r}-\mathbf{r}_2|} + \int_{S_2}\frac{\sigma(\mathbf{r}_2)ds_2}{|\mathbf{r}-\mathbf{r}_2|}\right),\end{aligned} \tag{4}$$

where $\rho(\mathbf{r})$ is the charge density; $\sigma(\mathbf{r})$ is the surface charge density; S_1 and S_2 are the grain surface areas; V_1 and V_2 are the symmetric plasma regions adjacent to the first and second dust grains, respectively, and together covering the entire region under consideration; and the components of the electric potential $\varphi(\mathbf{r})$ are equal to the corresponding expressions in parentheses.

We note that, when the field is defined in such a fashion, the electric field component perpendicular the symmetry plane vanishes on this plane: $E_\perp = 0$.

The energy of a system of point charged particles can be determined by the formula [16]

$$W_t = \frac{1}{2}\sum_i \rho_i\varphi_i, \tag{5}$$

where the potential φ_i in the position of the charge ρ_i is determined by all of the charges except for the given one. Such an exclusion is necessary because the self-energy of a charged particle increases without bound with decreasing radius.

In the model under consideration, the charge distribution is continuous and the charge density at any point is finite. In numerical simulations, the space is divided into the computational cells, in which the plasma space charge, as well as other quantities, can be assumed to be uniform. In this case, the self-energy of the small spatial cells decreases with decreasing their size; therefore, the expression defining the total energy of the system of electric charges is finite.

Actually, to solve the problem of the interaction between dust grains, we should consider the interaction energy of the parts of the system of electric charges (electrically charged grains together with adjacent polarized plasma regions), rather than the total energy of the electric charges. In view of the symmetry of the problem, the interaction energy can be determined from the formula

$$W = \int_{V_1}\rho(\mathbf{r}_1)\varphi_2(\mathbf{r}_1)dV_1 + \int_{S_1}\sigma(\mathbf{r}_1)\varphi_2(\mathbf{r}_1)ds_1, \tag{6}$$

where the potential $\varphi_2(\mathbf{r}_1)$ is calculated by formula (4). According to expression (6), the interaction energy is determined by the interaction of charges located in one

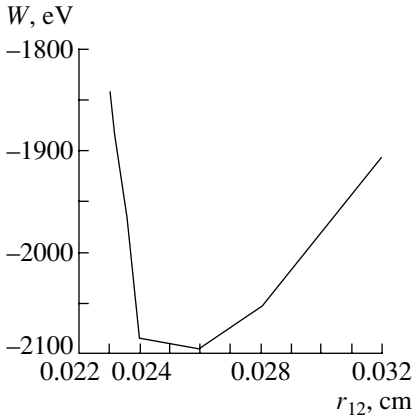

Fig. 4. Electrostatic interaction energy as a function of the distance between two grains in a dusty plasma.

half-space with the electric field produced by charges located in the other half-space. If the interaction energy is negative, then one can speak of the tendency toward the formation of a complex (quasi-molecule). In this case, the dependence of the bond energy on the intergrain distance may be identified with a term of this quasi-molecule.

To determine W as a function the intergrain distance, we performed a series of calculations of the steady charge density distribution and the self-consistent electric field in a two-grain system in the model described above. All other conditions, such as the ionization source power and the medium composition, were the same as in the case of one grain.

Figure 4 shows the results of calculations. It can be seen from the dependence $W(r_{12})$ that the interaction energy is negative and the depth of the potential well is $\sim 10^3$ eV. For comparison, this energy corresponds to the kinetic energy of a dust grain of mass $\sim 10^{-8}$ g moving at a velocity of ~0.5 cm/s. As is seen from the figure, the calculations were performed for a relatively small number of the distances r_{12}, because each calculation version required a fairly long computation time. Nevertheless, the results of calculations clearly demonstrate the presence of a minimum in the electrostatic interaction energy. Along with the negative value of the calculated energy, this testifies to the possibility of the existence of a bound state in this system. The attraction force can be estimated by the formula

$$F = -\frac{\partial W}{\partial r_{12}}. \quad (7)$$

According to this estimate, we have $F \sim 10^{-6}$–10^{-7} dyn, which is much smaller than the grain weight in the Earth's gravity field. We remember that the simulations were performed in the absence of an external electric field and the plasma was produced by an external source. When analyzing the applicability of formula (7), it should be taken into account that our model includes the process of grain charging, which is associated with the work done by external sources (plasma ionizers). Hence, the negative potential of the grain obtained in the calculations reflects the work done by these sources. At the same time, the force calculated by formula (7) neglects the interaction associated, e.g., with the plasma pressure [14, 15]; therefore, no final conclusion

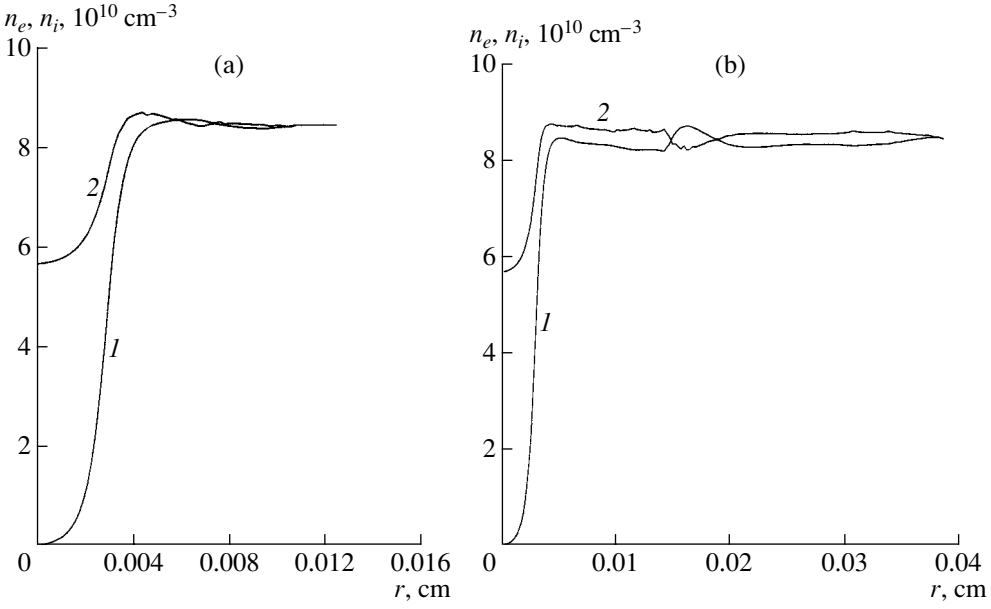

Fig. 5. Radial profiles of the (*1*) electron and (*2*) ion densities in the plasma surrounding one of the two interacting grains (a) in the direction toward the second grain and (b) in the opposite direction.

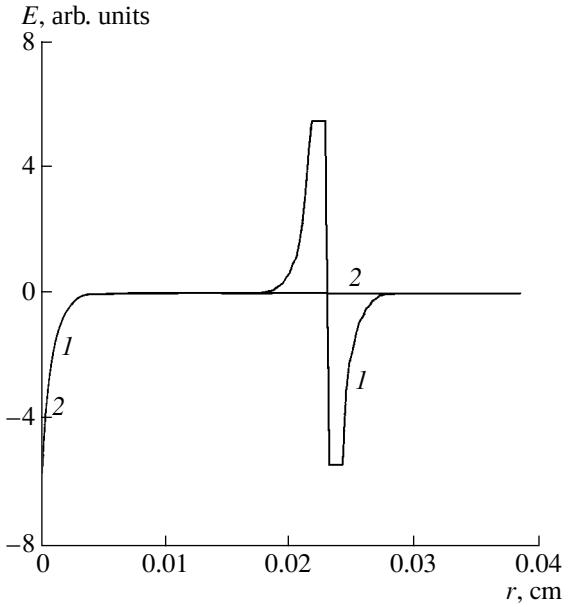

Fig. 6. Radial profiles of the electric field in the plasma surrounding two interacting grains (*1*) in the direction toward the second interacting grain and (*2*) in the opposite direction.

about the formation of a bound state in a two-grain system can be made based on formula (7) only.

Figure 5 shows the spatial distributions of the charged particle densities in the direction toward the second dust grain and in the opposite direction. We can see that the charge density distributions differ from those in the case of one grain (Fig. 1, curve *2*). Toward the second grain (Fig. 5a), the ion density at a distance of ~40 μm from the grain's surface substantially exceeds the electron density and there is a slight maximum in the ion density profile. This agrees qualitatively with the results of [8], in which an ion cloud between the interacting grains was observed in numerical simulations of a microwave-discharge dusty plasma. In view of the symmetry of the problem, a similar cloud should also form in the region adjacent to the second grain. In the opposite direction (Fig. 5b), the distributions of the charged particle densities are markedly different. A characteristic feature of these distributions is the formation of regions with an alternating sign of the space charge.

In the region immediately adjacent to the grain, the electric field changes only slightly as compared to the case of one grain, because, in this region, it is mainly determined by the grain charge. Figure 6 shows the spatial distributions of the electric field in the direction toward the second dust grain and in the opposite direction. The curves coincide near the grain's surface and are different at a distance of 240 μm, where the second dust grain is situated.

5. CONCLUSION

The interaction of charged grains in a low-temperature dusty plasma has been investigated numerically. To calculate the grain charge and the polarization of the surrounding plasma, the self-consistent electrostatic problem has been solved with allowance for charged particle transport in a plasma. Minimal simplifications were adopted when formulating the problem: the symmetry of the problem allowed us to use two-dimensional geometry, and the equations for charged particle transport were reduced to the continuity equations, which is quite justified under the given conditions.

We have also simulated the interaction between two dust grains in a nitrogen plasma produced by an external ionization source in the absence of an external electric field. Under the given conditions, the energy of interaction between the grains (including the energy of interaction with the polarized surrounding plasma) is found to be negative and is minimum at a distance of ~250 μm between the grains. The attraction force between two grains, which can be estimated from the calculated dependence of the electrostatic interaction energy on the intergrain distance, turns out to be weaker than the weight of a grain in the Earth's gravity field.

It has been found that, when the Debye plasma model is used to calculate the grain charge screening, significant errors are introduced for the most important region near the grain's surface. It turns out that the region where the plasma quasineutrality is disturbed is much larger than the Debye radius, because the equilibrium conditions, which are required for a Boltzmann distribution to be established, are not satisfied there due to the boundary effects.

The spatial distributions of the charged particle densities and the self-consistent electric field were calculated for individual dust grains in the presence of an external electric field. The break of spherical symmetry in the presence of an external electric field leads to an asymmetry of the charged particle distribution. It has been shown that the grain charge depends on the external electric field. Applying the external electric field increases the grain charge by a factor of up to 4, which should naturally increase the interaction force between the grains.

The simulations have shown that the plasma particle distribution in a system of two interacting grains is nonuniform. In the direction toward the second interacting grain, a positive space charge arises at a distance of about one-sixth of the intergrain distance from the first grain. (In view of the symmetry of the problem, a similar positive space charge forms in the region adjacent to the second grain.) In other words, the plasma charges are redistributed so that the positive space charge in this region increases in comparison with the spherically symmetric case of one grain. This redistribution corresponds to the plasma polarization, resulting in the attraction of likely charged grains. In the opposite

direction, the plasma polarization markedly differs and charged layers are formed.

ACKNOWLEDGMENTS

I am grateful to A.N. Starostin for his interest in this work and fruitful discussions. This work was supported by the Russian Foundation for Basic Research, project no. 00-15-96539.

REFERENCES

1. A. P. Nefedov, O. F. Petrov, and V. E. Fortov, Usp. Fiz. Nauk **167**, 1215 (1997) [Phys. Usp. **40**, 1163 (1997)].
2. S. V. Vladimirov and M. Nambu, Phys. Rev. E **52**, 2172 (1995).
3. F. Melandso and J. Goree, Phys. Rev. E **52**, 5312 (1995).
4. S. I. Yakovlenko, Pis'ma Zh. Tekh. Fiz. **25** (16), 83 (1999) [Tech. Phys. Lett. **25**, 670 (1999)].
5. Peilong Chen and C.-Y. D. Lu, Phys. Rev. E **61**, 824 (2000).
6. A. F. Pal', A. O. Serov, A. N. Starostin, *et al.*, Zh. Éksp. Teor. Fiz. **119**, 272 (2001) [JETP **92**, 235 (2001)].
7. A. F. Pal', D. V. Sivokhin, A. N. Starostin, *et al.*, Fiz. Plazmy **28**, 32 (2002) [Plasma Phys. Rep. **28**, 28 (2002)].
8. V. A. Schweigert, I. V. Schweigert, A. Melzer, *et al.*, Phys. Rev. E **54**, 4155 (1996).
9. V. I. Vladimirov, L. V. Deputatova, V. I. Molotkov, *et al.*, Fiz. Plazmy **27**, 37 (2001) [Plasma Phys. Rep. **27**, 36 (2001)].
10. Yu. V. Petrushevich, Preprint No. 0088-A (TRINITI, Troitsk, 2002).
11. A. Melzer, V. A. Schweigert, and A. Piel, Phys. Rev. Lett. **83**, 3194 (1999).
12. V. A. Gundienkov and S. I. Yakovlenko, Kratk. Soobshch. Fiz., No. 12 (2001).
13. A. S. Ivanov, Phys. Lett. A **290**, 304 (2001).
14. A. M. Ignatov, Fiz. Plazmy **24**, 731 (1998) [Plasma Phys. Rep. **24**, 677 (1998)].
15. A. M. Ignatov, Usp. Fiz. Nauk **171**, 213 (2001) [Phys. Usp. **44**, 199 (2001)].
16. I. E. Tamm, *The Principles of Electricity Theory* (Nauka, Moscow, 1976).

Translated by N.F. Larionova

Plasma Physics Reports, Vol. 29, No. 6, 2003, pp. 480–484. Translated from Fizika Plazmy, Vol. 29, No. 6, 2003, pp. 516–520.

PLASMA OPTICS

Space-Charge Lens for Focusing a Negative-Ion Beam

A. M. Zavalov, V. N. Gorshkov, V. P. Goretskiĭ, and I. A. Soloshenko

Institute of Physics, National Academy of Sciences of Ukraine, pr. Nauki 144, Kiev, 03039 Ukraine

Received November 19, 2002

Abstract—Results are presented from experimental and theoretical studies of a space-charge lens for focusing a negative-ion beam. The space-charge field and the beam ion trajectories are numerically calculated for the lens used in the experiments. The results of calculations are compared with the experimental data. It is shown theoretically and experimentally that the proposed device allows one to achieve the main operating conditions of the space-charge lens: the inertial confinement of positive ions and the removal of electrons by an external electric field. The focusing field of the lens attains ~100 V/cm, which provides a focal length of <20 cm. © *2003 MAIK "Nauka/Interperiodica"*.

1. INTRODUCTION

The concept of a space-charge lens for focusing a positive-ion beam was first proposed by Gabor [1] and then was further developed by Morozov [2, 3]. The efficiency of such a lens was confirmed in many experiments (see, e.g., [4]). The focusing field of the lens is produced by a space charge of electrons that are injected by a separate emitter or come from the lens electrodes due to ion-induced emission and are confined within the beam by an external magnetic field.

In [5], a space-charge lens for focusing a negative-ion beam was proposed. In this case, the focusing space charge is produced by positive ions that are generated through the ionization of the working gas by an ion beam and are confined within the beam by inertial forces. It was proposed that the electrons produced in this process be removed from the system by a longitudinal electric field. Preliminary experiments showed the high efficiency of such a lens.

This paper is devoted to a detailed study of the device proposed in [5]. In particular, the space charge field and trajectories of the beam ions are numerically calculated for the lens used in experiment. The time evolution of the particles produced due to the ionization of argon by the beam is also studied. The results of calculations are compared with the experimental data. The theoretical and experimental results show that, under our experimental conditions, it is possible to achieve the main operating conditions of the space-charge lens: the inertial confinement of positive ions and the removal of electrons by an external electric field. The ratio between the positive-ion and electron densities in the lens varies within the range 10^1–10^3 and the focusing field attains ~100 V/cm, which provides a focal length of <20 cm.

2. EXPERIMENTAL RESULTS

The space-charge lens for focusing a negative-ion beam was investigated using the experimental setup shown schematically in Fig. 1a. A beam of negative ions with energies of ~10–12 keV and a current of ~10–30 mA was extracted from surface-plasma source *1* through a 0.5 × 15-mm slit. The beam was preformed and directed to lens *3–5* by an ≈2-kG magnetic field produced by deflecting magnets *2*. The beam diameter was limited by the entrance aperture of the lens. The beam current was measured by collector *7* with a diameter of 10 cm. The beam compression ration was determined from a change in the current at collector *6* with a diameter of 2 cm. The lens was placed ≈20 cm from the source slit. The distance from the lens exit plane to the collector was ≈30 cm. In the given configuration, the beam radius at the collector should be minimum for a lens focal length of ≈12 cm.

The lens was designed as follows. Lens chamber *4* was a metal cylinder 15 cm in diameter and 10 cm in length with two grounded diaphragms with an inner diameter of 5 cm at the ends. Removable metal grid cylinder *5* with a diameter of 5 cm and length of 10 cm was installed inside the lens chamber on its axis and was at the potential of the lens chamber. The lens chamber was insulated from the chamber walls; during operation, the chamber potential can be varied from 0 to –2000 V. Grounded electrodes *3* with a thickness of 1.5 cm and an inner diameter of 5 cm were installed 0.5 cm from the ends of the lens chamber. The working gas (argon) was admitted through the end wall of the lens chamber. The gas pressure in the lens could be varied in the range 10^{-4}–1.5×10^{-3} torr. With such a lens design, the pressure in the lens was higher than the pressure in the beam-drift region by a factor of nearly 10.

A positive space charge in the lens was produced through the ionization of the working gas by a negative-ion beam. It was proposed that the electrons produced by ionization and detachment from negative ions in col-

1063-780X/03/2906-0480$24.00

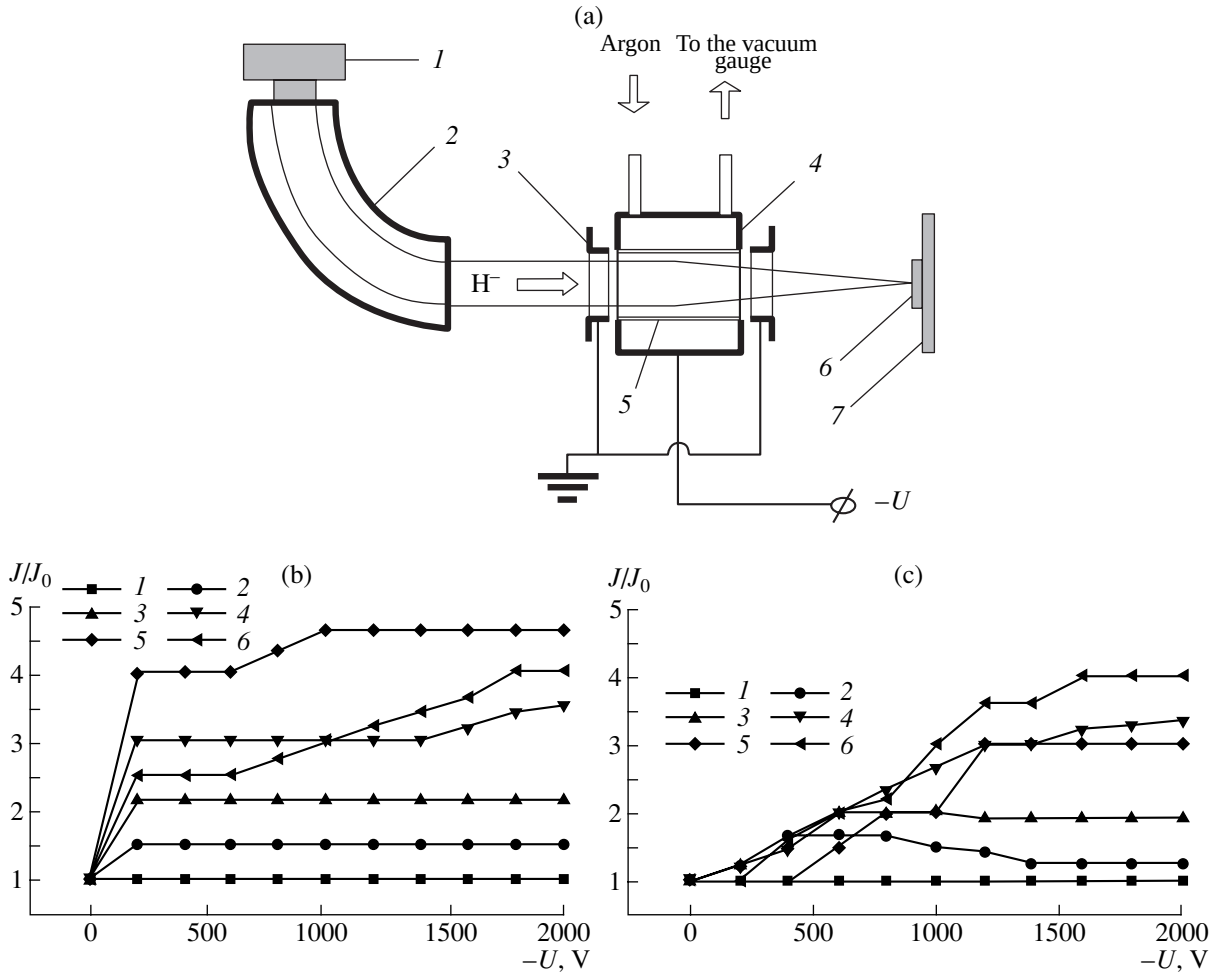

Fig. 1. (a) Schematic of the experiment: (*1*) pulsed source of negative hydrogen ions, (*2*) deflecting magnets, (*3*) grounded inlet and outlet electrodes, (*4*) lens chamber, (*5*) removable grid electrode, (*6*) collector for determining the beam density, and (*7*) beam-current collector; (b) the H^- beam compression ratio as a function of the negative potential of the lens chamber in the presence of the grid electrode at different argon pressures p = (*1*) 1.8×10^{-4}, (*2*) 4.2×10^{-4}, (*3*) 6.2×10^{-4}, (*4*) 8×10^{-4}, (*5*) 1.1×10^{-3}, and (*6*) 1.7×10^{-3} torr; and (c) the H^- beam compression ratio as a function of the negative potential of the lens chamber without a grid electrode at different argon pressures p = (*1*) 1.2×10^{-4}, (*2*) 4.1×10^{-4}, (*3*) 6×10^{-4}, (*4*) 7.9×10^{-4}, (*5*) 1.2×10^{-3}, and (*6*) 1.7×10^{-3} torr. The beam current is 10 mA and the beam ion energy is 12 keV.

lision with neutral particles be expelled along the lens axis by applying a negative potential to the chamber.

Experiments were carried out for two lens configurations. In the first version, the lens contained grid electrode *5* (Fig. 1a), and in the second version, this electrode was absent (the numerical experiment was performed for the second version).

The results of measurements are presented in Figs. 1b and 1c. The figures show the beam compression ratio (the ratio of the maximum current J of the H^- beam at collector *6* in the regime of focusing to the maximum beam current J_0 at collector *6* in the regime without focusing) in the collector plane as a function of the negative potential of the lens chamber at different values of the argon pressure in the lens.

It can be seen from the figures that the beam compression ratio depends on both the gas pressure in the lens and the potential at its central electrode. (The gas pressure determines the value of the positive ion space charge, whereas the negative potential determines the efficiency of the removal of electrons from the lens in the longitudinal direction.) The maximum beam compression ratio is the same for both versions (with and without grid *5*). However, with the grid, the optimal compression of the beam is reached even at a lens potential of –200 V, whereas without a grid, it is reached at a much lower potential; i.e., in the former case, the removal of electrons from the lens is more efficient.

Thus, it has been demonstrated experimentally that the space-charge lens proposed can be very efficient

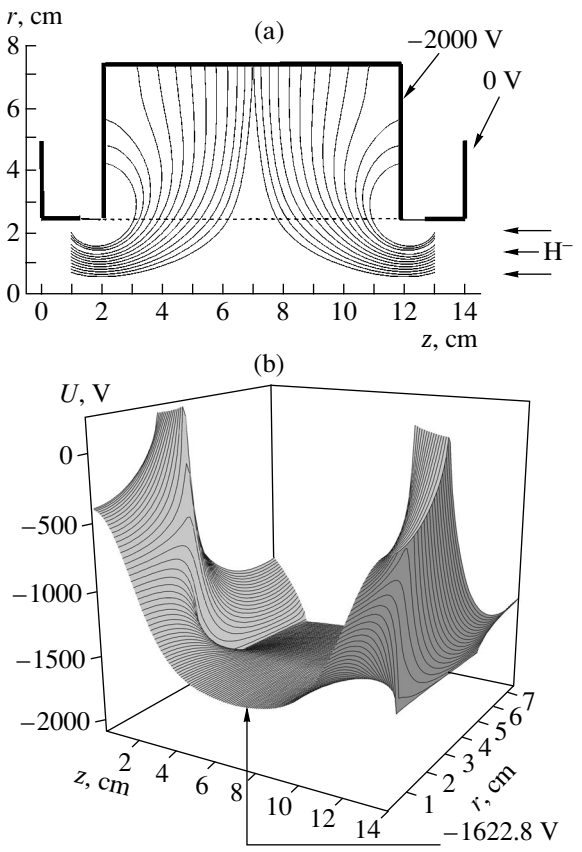

Fig. 2. (a) Schematic of the numerical experiment and the lines of the electric field generated by the electrodes inside the lens; the main ionization region in the lens extends from the axis to the dashed line; the arrows show the trajectories of the beam ions and the atoms of the working gas (argon) entering the lens. (b) Steady-state distribution of the electric potential in the lens at $t = 10^{-5}$ s.

and can provide a focal length of <20 cm. The lens efficiency is determined by the gas pressure (by the value of the positive space charge), provided that the electrons are removed from the system by the longitudinal electric field. The geometry of the lens only has an effect on the efficiency with which the electrons are removed from the lens.

3. NUMERICAL EXPERIMENT

We calculated the electric field and trajectories of the beam particles in the space-charge lens for focusing a negative-ion beam and investigated the time evolution of the electrons and Ar^+ ions produced by ionization. The numerical studies were performed using the particle-in-cell (PIC) method [6, 7]; the plasma was assumed to be collisionless.

A schematic of the numerical experiment is shown in Fig. 2a. A uniform beam of negative H^- ions with a current of 10 mA and an energy of 12 keV entered the lens through the entrance plane along the lens axis. The beam diameter coincided with the diameter of the lens entrance aperture and was equal to 5 cm. The potential of the lens chamber was assumed to be –2000 V, and the argon pressure in the lens transmission line was 1.5×10^{-3} torr (the parameters corresponding to the regime of optimal focusing in the experiment).

In the calculations, it was taken into account that, during the interaction of the beam with the working gas, the positive argon ions are produced through ionization, whereas the electrons are produced through both ionization and the neutralization of negative ions in collisions with neutral particles (the probability of the latter process is several orders of magnitude higher). The lifetimes of the produced particles are proportional to their path lengths and are limited by the time required for the particles to leave the calculation region.

At each time step, we introduced $N_+ = \Delta t J_I V_I \sigma_I N$ positive ions and $N_e = \Delta t J_I V_I (\sigma_I + \sigma_{-0}) N$ electrons (in the proportion 1 : 11) into the lens region occupied by the beam. Here, Δt is the time step, J_I is the ion flux density at the lens inlet, V_I is the volume of the ionization region, σ_I is the cross section for the ionization of the gas by the beam ions, σ_{-0} is the cross section for the neutralization of the beam ions in collisions with gas atoms, and N is the number of neutral particles in the ionization region. The initial electron energies were specified according to the calculated energy distribution (see [8]), and the initial directions of the electron velocities were taken according to the angular distribution from [9]; the maximum of this distribution was in the range 85°–95° with respect to the lens axis. The coordinates of the new particles in the ionization region were specified with the help of a random number generator. The trajectories of the new particles and the particles already occurring in the lens were calculated from the equation of motion

$$m\frac{d}{dt}\mathbf{v} = q(\mathbf{E}_{\mathrm{ION}} + \mathbf{E}_{\mathrm{E}} + \mathbf{E}_{\mathrm{B}} + \mathbf{E}_{\mathrm{EL}}),$$

where m, $\mathbf{v}$, and q are the mass, velocity, and charge of a particle, respectively, and $\mathbf{E}_{\mathrm{ION}}$, $\mathbf{E}_{\mathrm{E}}$, $\mathbf{E}_{\mathrm{B}}$, and $\mathbf{E}_{\mathrm{EL}}$ are the components of the electric field produced by the plasma ions, plasma electrons, beam ions, and electrodes, respectively. The time step was $\Delta t = 10^{-11}$ s. After a time of $\Delta T = 10^{-9}$ s, using the coordinates of all the particles, we calculated the distribution of the space charges of electrons, Ar^+ ions, and H^- beam ions by the cloud-in-cell method [7]. The radial and longitudinal dimensions of the spatial cell were equal to 0.1 cm. Using the distribution of the total space charge $\rho(z, r)$, we calculated the potential $U(z, r)$. Then, the particle motion in the new electric field was calculated and a new group of charged particles was introduced. The calculation continued until the steady-state distribution of the electric potential was established. The simulation time was no longer than 10^{-5} s. Figure 2b shows a typ-

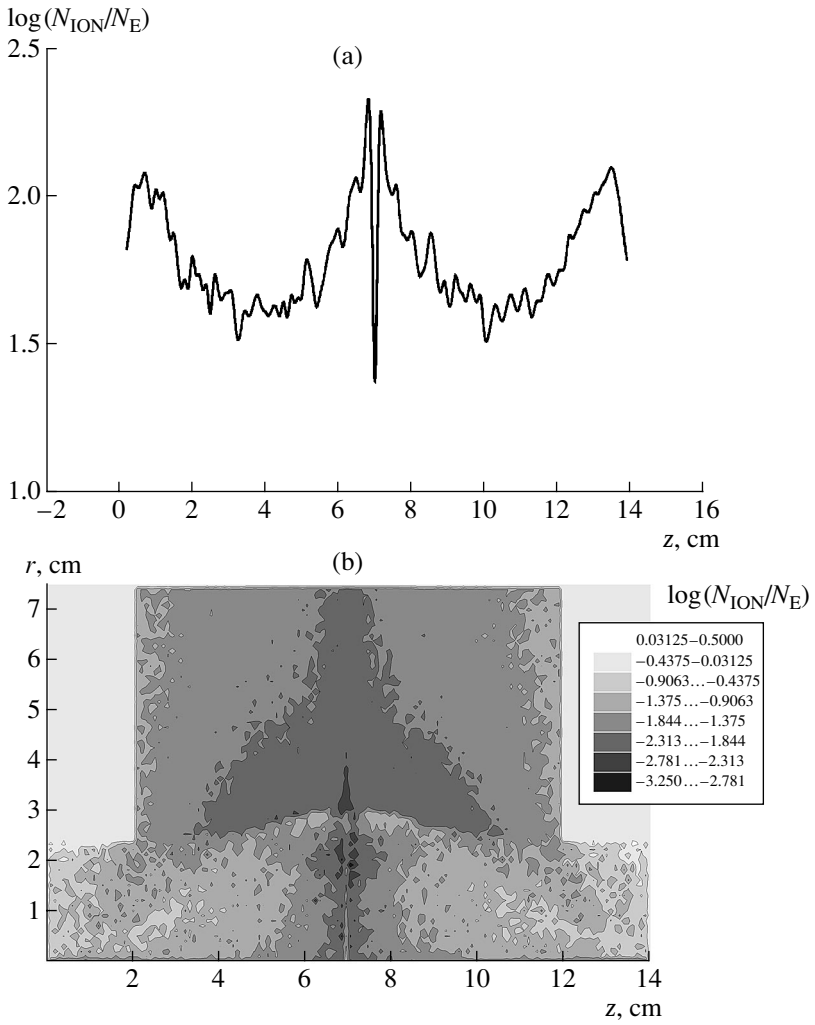

Fig. 3. (a) Axial profile and (b) spatial distribution of the ratio between the steady-state ion and electron densities in the lens at $t = 10^{-5}$ s.

ical steady-state potential distribution. The increase in the potential in the center of the system due to the filling of the working region with a positive charge is ≈300 V.

In the course of the lens formation, the positive argon ions go away from the lens axis along the trajectories close to the electric field lines (Fig. 2a) and occupy the entire lens cavity with time. The electrons in the working region move toward the lens axis and leave the calculation region in the axial direction. Figures 3a and 3b show the ratio between the steady-state electron and positive-ion densities on the lens axis and in the lens volume, respectively. In Fig. 3a, one can see three minima associated with characteristic features of the formation of the ion flow. A deep valley can be seen in the central peak, which is explained by the fact that the ion flux density in the central cross section is the highest and the electrons bunch there due to the lens symmetry. The positive-ion density exceeds the electron density at least by one order of magnitude (the light areas in Fig. 3b), and it is by two to three orders of magnitude higher than the electron density in the region adjacent to the central cross section (the dark areas in Fig. 3b), which testifies that the ion component is predominant during the formation of the space charge distribution.

Figure 4 shows the calculated trajectories of the negative-beam ions in the field of the lens in the steady-state regime. The lens has a high focal power, but there are significant aberrations caused by edge fluxes, which can be avoided under real conditions by limiting the diameter of the output beam and by reducing the influence of the electrodes. The focal length of the lens is 18 cm. At a collector radius of 1 cm, the beam compression ratio attains a value of ≈25, which is substantially higher than that observed in the experiment (about 5). However, this discrepancy can easily be explained taking into account the considerable phase space occupied by the real beam and the initial asymmetry of the beam emerging from the source slit.

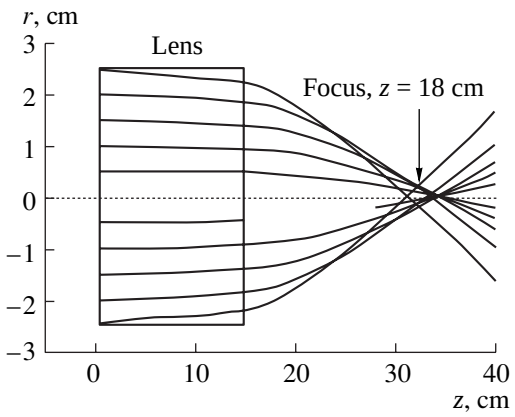

Fig. 4. Calculated trajectories of the negative beam ions in the field of the lens in the steady-state regime.

Thus, we have calculated the distributions of the potential and charged particle densities in the working region of the space-charge lens for focusing a negative-ion beam. The assumptions that the electron density is substantially reduced in the presence of a longitudinal electric field and that an excess positive charge is produced in the lens have been confirmed. The calculated value of the focal length of the lens is close to that measured in the experiment.

4. CONCLUSIONS

(i) The distributions of the space charge and electric field in the space-charge lens for focusing a negative-ion beam have been calculated numerically. The calculations demonstrate the high efficiency of both the inertial confinement of positive ions in the lens and the removal of electrons from the focusing region by a longitudinal electric field. As a result, the density of the positive ions in the lens is two to three orders of magnitude higher than the electron density. The focal length of the lens observed in calculations attains ≈20 cm.

(ii) It has been shown that the calculated values of the focusing electric field and the focal length agree well with the measured values.

(iii) It has been shown experimentally that the geometry of the lens significantly affects the removal of electrons from the lens.

REFERENCES

1. D. Gabor, Nature (London) **160**, 89 (1947).
2. A. I. Morozov, Dokl. Akad. Nauk SSSR **163**, 1363 (1965) [Sov. Phys. Dokl. **10**, 775 (1966)].
3. A. I. Morozov and S. V. Lebedev, *Reviews of Plasma Physics*, Ed. by M. A. Leontovich (Atomizdat, Moscow, 1974; Consultants Bureau, New York, 1980), Vol. 8.
4. A. A. Goncharov, A. N. Dobrovolskiĭ, A. N. Kotsarenko, *et al.*, Fiz. Plazmy **20**, 499 (1994) [Plasma Phys. Rep. **20**, 449 (1994)].
5. V. P. Goretskiĭ, I. A. Soloshenko, and A. I. Shchedrin, Fiz. Plazmy **27**, 356 (2001) [Plasma Phys. Rep. **27**, 335 (2001)].
6. B. I. Volkov and S. A. Yakunin, *Mathematical Problems of Plasma Optics* (Znanie, Moscow, 1982), p. 64.
7. D. Potter, *Computational Physics* (Wiley, New York, 1973; Mir, Moscow, 1975).
8. P. M. Golovinskiĭ and A. I. Shchedrin, Zh. Tekh. Fiz. **59** (2), 51 (1989) [Sov. Phys. Tech. Phys. **34**, 159 (1989)].
9. N. Mott and H. Massey, *Theory of Atomic Collisions* (Clarendon, Oxford, 1965; Mir, Moscow, 1969).

Translated by E.L. Satunina

Plasma Physics Reports, Vol. 29, No. 6, 2003, pp. 485–490. Translated from Fizika Plazmy, Vol. 29, No. 6, 2003, pp. 521–526.

NONIDEAL PLASMA

Oscillations of a Helical Plasma Crystal

N. G. Guseĭn-zade and A. M. Ignatov

Prokhorov Institute of General Physics, Russian Academy of Sciences, ul. Vavilova 38, Moscow, 119991 Russia

Received September 26, 2002

Abstract—Oscillations and the stability of the helical structures of likely charged particles undergoing Coulomb interactions and confined in an axisymmetric potential well are studied theoretically. © *2003 MAIK "Nauka/Interperiodica".*

1. INTRODUCTION

A typical example of a strongly nonideal plasma is provided by ordered structures of charged particles confined by external fields. In plasma physics, such structures are sometimes called quasi-crystals, although they lack the quasi-crystalline order known in solid-state physics [1]. One of the first experimentally observed ordered structures was a system of micron-sized iron and aluminum charged particles in a certain configuration of an alternating and a static field [2]. In later experimental investigations involving laser cooling techniques, Coulomb crystals were observed to form in various types of devices, e.g., in a Penning trap [3, 4], an RF Paul trap [5–7], and storage rings [8, 9]. From a practical standpoint, interest in such systems is associated with a new type of atomic clock [10] and the schemes proposed for implementing a quantum computer [11]. Crystals may also form in a purely electron plasma [12] and a dusty plasma [13].

The nature of ordered structures that arise in various devices is largely governed by the parameters of the external confining field. In this paper, we investigate quasi-one-dimensional structures that form in linear Paul traps and storage rings. The simplest approximation for such structures is to describe them as a system of singly charged ions that is uniform or periodic in a certain direction (e.g., along the z-axis) and whose transverse spreading is prevented by an external parabolic potential. During the laser cooling process, the ion kinetic energy T decreases; as a result, the plasma parameter e^2/aT (where a is the characteristic distance between the particles) amounts to about 10^4. As the parameters of the confining potential change, various structures that form during the cooling process undergo numerous phase transitions. The behavior of such structures has received much experimental, numerical, and analytical study [15]. On the other hand, virtually nothing is known about the oscillations and stability of Coulomb crystals in linear devices.

Here, we develop a theory of linear oscillations of Coulomb crystals exhibiting helical symmetry. We begin with a review of the different equilibrium configurations of charges in a linear device. Then, we derive a general set of linearized equations. Finally, we use these equations to calculate the spectra of oscillations of the five simplest types of crystals.

2. STEADY STATES OF A CRYSTAL

We consider a system consisting of a large number of likely charged particles confined in an external field with the potential $U_{\text{ext}}(\mathbf{r})$, which prevents the system from spreading in the transverse direction. We restrict ourselves to considering the case in which the external potential can be assumed to be independent of one of the coordinates (the z coordinate) and harmonic in the transverse coordinate. This case corresponds to two experimental situations. First, in a Penning trap, as well as in a Paul trap, the shape of any axisymmetric potential well $U_{\text{ext}}(\mathbf{r}) \approx 1/2[K_z z^2 + K(x^2 + y^2)]$ near its bottom is often highly anisotropic, $K_z \ll K$. Accordingly, at $z \approx 0$, the longitudinal component of the external force can be neglected. Second, in a toroidal device or storage ring, charged particles are confined in the vicinity of the closed axis; in this case, toroidal effects can be neglected provided that particle excursions away from the axis are small in comparison with the major radius of the device.

It is acceptable to ignore the distinction between the toroidal and axisymmetric devices in analyzing the small oscillations of a crystal. However, in searching for the spatial configurations of charges that would be most advantageous from the energy standpoint, doing so requires certain care. In a toroidal device, the line density (or the mean distance between the particles) is determined by the total number of particles and the major radius of the torus and is independent of K. On the other hand, in a highly anisotropic device, a decrease in the parameter K, which characterizes particle confinement in the transverse direction, may change the mean interparticle distance even near the bottom of the potential well [14]. In describing the states that are most favorable energetically, we neglect, for simplicity, the dependence of the mean distance between the particles on the confinement parameter K. This dependence

1063-780X/03/2906-0485$24.00

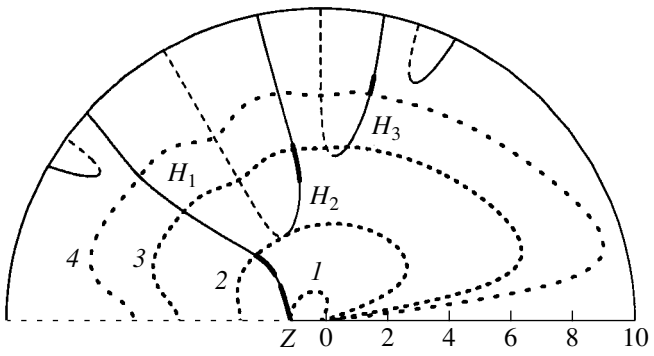

Fig. 1. Extrema of Madelung energy (7) in polar coordinates (u, θ). The solid and dashed curves represent the solutions to Eq. (8), and curves *1–4* are the solutions to Eq. (4) with $\mu =$ (*1*) 1.674, (*2*) 0.305, (*3*) 0.098, and (*4*) 0.058.

can be accounted for through an unessential renormalization of the dimensionless parameter μ, which will be introduced below.

The dynamics of the system is described by the equations

$$m\ddot{\mathbf{r}}_n = -K\mathbf{r}_{\perp n} + q^2 \sum_{\substack{m=-N \\ m\neq n}}^{N} \frac{\mathbf{r}_n - \mathbf{r}_m}{|\mathbf{r}_n - \mathbf{r}_m|^3}, \quad n = -N\ldots N, \quad (1)$$

where $\mathbf{r}_n = (x_n, y_n, z_n)$, $\mathbf{r}_{\perp n} = (x_n, y_n, 0)$, and q and m are the charge and mass of a particle. In writing the formulas, it is convenient to assume that the total number of particles is equal to $2N + 1$.

In the steady state, $\ddot{\mathbf{r}}_n = 0$; accordingly, the problem reduces to that of looking for the coordinates $\mathbf{r}_n$ of the particles with which the right-hand side of Newton's equation (1) vanishes. Let us list some of the simplest configurations that can take place at $N \longrightarrow \infty$. When the external potential is sufficiently high, all particles occur at the axis and form a linear chain (string), in which they have the coordinates

$$\mathbf{r}_n = (0, 0, na). \quad (2)$$

Recall that the distance a between the particles is assumed to be given. It is clear that, by virtue of the symmetry of the system, the total force acting on the nth particle in chain (2) is identically zero.

A somewhat more complicated case is that of a helical configuration, i.e., a helical chain (a helix) of particles with the coordinates

$$\mathbf{r}_n = [R\cos(n\theta), R\sin(n\theta), na]. \quad (3)$$

Substituting coordinates (3) into Eq. (1) and taking the limit $N \longrightarrow \infty$, we can readily see that the balance of the longitudinal forces and the balance of the angular momenta are satisfied exactly and that the condition for the radial force to vanish yields

$$u\left\{\frac{\mu}{4} - \sum_{m=1}^{\infty} \frac{\sin^2\left(\frac{m\theta}{2}\right)}{D_m^{3/2}}\right\} = 0, \quad (4)$$

where

$$D_m = m^2 + u^2\sin^2\left(\frac{m\theta}{2}\right). \quad (5)$$

Here, we have introduced the dimensionless diameter of the helix, $u = 2R/a$. The dimensionless quantity $\mu = Ka^3/q^2$ serves as a control parameter. Equation (4) and its trivial solution $u = 0$, which corresponds to configuration (2), represent only two relationships between the three quantities μ, θ, and u. In other words, the configuration of the system cannot be uniquely determined from the purely mechanical force-equilibrium condition. This ambiguity is resolved by imposing an additional requirement that the total energy of the system be minimum, which naturally applies to systems with dissipation and, in particular, to laser-cooled systems. The total potential energy of the system can be written as $U = \sum_n w_n$, where the energy w_n of an individual particle, which will be called, by analogy with solid-state physics, the Madelung energy, is equal to

$$w_n = \frac{1}{2}K\mathbf{r}_{\perp n}^2 + \frac{q^2}{2}\sum_{m\neq n}\frac{1}{|\mathbf{r}_n - \mathbf{r}_m|}. \quad (6)$$

For both linear chain (2) and helical chain (3), this energy diverges logarithmically as the total number of particles tends to infinity. However, the difference in the Madelung energies of each of these configurations is finite and is, of course, independent of n. In dimensionless form, it is convenient to write this difference as $w_{(h)n} - w_{(s)n} = (q^2/a)\varepsilon(u, \theta)$, where

$$\varepsilon(u, \theta) = \frac{1}{8}\mu u^2 + \sum_{m=1}^{\infty}\left(\frac{1}{D_m^{1/2}} - \frac{1}{m}\right). \quad (7)$$

The values of u that make this function an extremum are given by Eq. (4), and the equation $\partial\varepsilon/\partial\theta = 0$ yields

$$\sum_{m=1}^{\infty}\frac{m\sin(m\theta)}{D_m^{3/2}} = 0. \quad (8)$$

Equations (4) and (8) uniquely determine the dependence of the free parameters u and θ on μ.

Some insight into the extreme points of function (7) is provided by Fig. 1, which presents the solutions to Eq. (8) in polar coordinates (u, θ). The positions of the maxima of $\varepsilon(u, \theta)$ are shown by solid curves, the continuations of which in the form of dashed curves correspond to the minima. The dotted curves refer to the

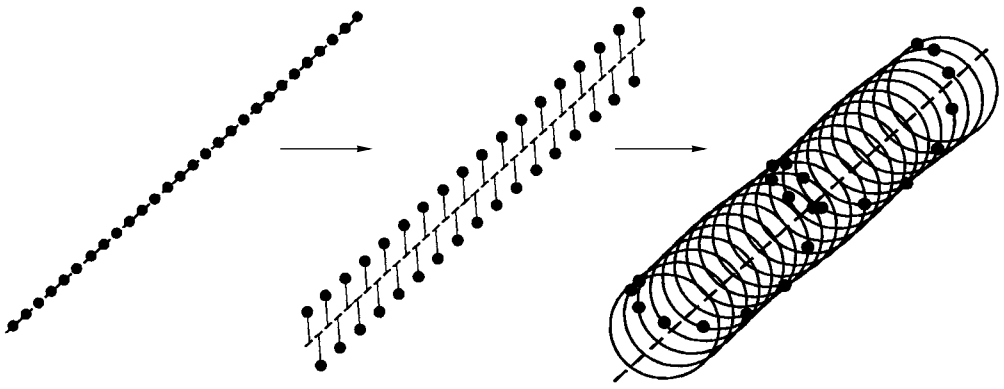

Fig. 2. Evolution of the structure of a Coulomb crystal as the confinement parameter of the device changes.

solutions to Eq. (4) that were obtained for different values of the parameter μ.

For a sufficiently high confining potential ($\mu > \mu_0 \approx 4.209$), the state that is most advantageous from the energy standpoint is that with linear chain (2), which is at the origin of the coordinates in Fig. 1. In the range $\mu_0 > \mu > \mu_1 \approx 1.674$, the most advantageous structure is a zigzag, i.e., structure (3) with $\theta = \pi$. In Fig. 1, the corresponding branch is marked with a *Z*. As μ increases, the size of the zigzag increases from zero to a maximum value of $u_{max} \approx 0.965$. Then, at $\mu < \mu_1$, the following bifurcation occurs: the maxima of Madelung energy (7) are now on the ray $u > u_{max}$, $\theta = \pi$ (Fig. 1) and the minima of this energy lie on the line H_1, corresponding to helical configuration (3) along which the angle θ depends in a certain fashion on μ. The transition from the zigzag to the first helix H_1 is continuous. The two transitions just described are illustrated schematically in Fig. 2.

As the confining potential decreases further, the system undergoes a series of phase transitions. Different helical branches H_2, H_3, … in Fig. 1 are separated from each other by potential barriers. As a rule, phase transitions occur through the formation of more complicated, tetrahedral structures. Altogether, there are ten phase transitions from one to another of the relatively simple structure, such as those shown in Fig. 2. All of these phase transitions are well captured numerically and many of them were observed experimentally. Finally, in the range $\mu \le 0.05$, a system forms that consists of several nested cylindrical shells. The details of the analysis of the Madelung energy for different configurations and the results of numerical simulations can be found in the review by Hasse and Schiffer [15].[1] Table 1 presents the ranges of variation of the parameter μ in which the Madelung energy in different helical structures has an absolute minimum. In Fig. 1, the corresponding portions of the curves are shown by heavy lines. In the gaps between the ranges given in Table 1, the minimum of energy corresponds to a tetrahedral configuration, which is not considered here. It should be noted that H_2 and H_3 helices are nearly isomeric: the difference between the energies in them is about 0.01.

[1] It should be noted that, in [15], the role of the external parameter is played by the dimensionless line particle density λ, which is related to the parameter μ used here by the relationship $\mu = 3/(2\lambda^3)$.

3. DISPERSION RELATION

In order to investigate oscillations of helical structure (3) and its stability, we represent the coordinate of each particle in the form

$$\mathbf{r}_n = a\left[\left(\frac{u}{2} + \delta\rho_n\right)\cos(n\theta + \delta\phi_n),\right.$$
$$\left.\left(\frac{u}{2} + \delta\rho_n\right)\sin(n\theta + \delta\phi_n),\ n + \delta z_n\right]. \quad (9)$$

We insert coordinates (9) into the equation of motion (1) and linearize the resulting equation in small deviations ($\delta\rho_n$, $\delta\phi_n$, δz_n) from the equilibrium positions. As a result, we obtain an infinite set of equations, which is too complicated to present here. Since the group of symmetries of unperturbed helix (3) is Abelian, the linearized set of equations is diagonalized by the substitution

Table 1. Structures with a minimum Madelung energy. Symbol *S* denotes linear chain (2)

Structure type	Intervals of μ
S	(4.207, ∞)
Z	(1.674, 4.207)
H_1	(0.768, 1.674)
H_1	(0.305, 0.559)
H_2	(0.094, 0.143)
H_3	(0.050, 0.058)

$$(\delta\rho_n, \delta\phi_n, \delta z_n) = \exp(-i\omega_p \nu t + isn)(\rho_0, \phi_0, z_0), \quad (10)$$

where we have introduced an analogue of the plasma frequency, $\omega_p = \sqrt{q^2/(ma^3)}$, and the dimensionless oscillation frequency ν. The dimensionless wave vector lies in the first Brillouin zone $-\pi < s < \pi$. Hence, we arrive at a homogeneous set of linear equations:

$$\begin{pmatrix} \nu^2 - \mu + Q_{11} & Q_{12} & Q_{13} \\ -Q_{12} & \frac{1}{4}u^2\nu^2 + Q_{22} & Q_{23} \\ -Q_{13} & Q_{23} & \nu^2 + Q_{33} \end{pmatrix} \begin{pmatrix} \delta r \\ \delta\phi \\ \delta z \end{pmatrix} = \begin{pmatrix} 0 \\ 0 \\ 0 \end{pmatrix}, \quad (11)$$

where the elements of the Hermitian matrix Q are equal to

$$\begin{aligned} Q_{11} &= 2\sum_{m=1}^{\infty} \frac{1-\cos(ms)\cos(m\theta)}{D_m^{3/2}} \\ &\quad - 12u^2 \sum_{m=1}^{\infty} \frac{\cos^2\left(\frac{ms}{2}\right)\sin^4\left(\frac{m\theta}{2}\right)}{D_m^{5/2}}, \\ Q_{22} &= u^2 \sum_{m=1}^{\infty} \frac{\cos(m\theta)\sin^2\left(\frac{ms}{2}\right)}{D_m^{3/2}} \\ &\quad - \frac{3}{4}u^4 \sum_{m=1}^{\infty} \frac{\sin^2(m\theta)\sin^2\left(\frac{ms}{2}\right)}{D_m^{5/2}}, \\ Q_{33} &= -8\sum_{m=1}^{\infty} \frac{\sin^2\left(\frac{ms}{2}\right)}{D_m^{3/2}} \\ &\quad + 12u^2 \sum_{m=1}^{\infty} \frac{\sin^2\left(\frac{ms}{2}\right)\sin^2\left(\frac{m\theta}{2}\right)}{D_m^{5/2}}, \\ Q_{12} &= iu \sum_{m=1}^{\infty} \frac{\sin(ms)\sin(m\theta)}{D_m^{3/2}} \\ &\quad - \frac{3}{2}iu^3 \sum_{m=1}^{\infty} \frac{\sin(ms)\sin(m\theta)\sin^2\left(\frac{m\theta}{2}\right)}{D_m^{5/2}}, \\ Q_{13} &= -6iu \sum_{m=1}^{\infty} \frac{m\sin(ms)\sin^2\left(\frac{m\theta}{2}\right)}{D_m^{5/2}}, \\ Q_{23} &= -3u^2 \sum_{m=1}^{\infty} \frac{m\sin^2(ms)\sin\left(\frac{m\theta}{2}\right)}{D_m^{5/2}}, \end{aligned} \quad (12)$$

and the quantity D_m is given by formula (5).

Equations (11) can be investigated analytically only for a linear chain. The results presented below were obtained from a numerical analysis of other types of chains. The numerical procedure consisted in finding the equilibrium radius u and pitch angle θ for certain values of μ and calculating the eigenvalues and eigenvectors of Eqs. (11) for wavenumbers in the range $0 \le s \le \pi$. Attention was largely focused on determining the intervals of stability of helical configurations, i.e., the intervals of μ values in which $\nu^2 > 0$ for any values of s. Such an analysis is required because a local or a global minimum in the Madelung energy automatically guarantees that the configuration is stable only against long-wavelength perturbations with $s = 0$ but does not guarantee its stability against arbitrary perturbations.

3.1. Linear Chain

For linear ion chain (2), the linearized equations of motion are easy to solve. Since the oscillations of the ions are symmetric, they can be resolved into longitudinal oscillations with $\rho_0 = 0$ and transverse oscillations with $z_0 = 0$ and an arbitrary plane of polarization. The dimensionless oscillation frequencies are determined by the expressions

$$\nu_\parallel^2(s) = 8\sum_{m=1}^{\infty} \frac{\sin^2(ms/2)}{m^3}, \quad (13)$$

$$\nu_\perp^2(s) = \mu - \frac{1}{2}\nu_\parallel^2(s). \quad (14)$$

The spectral curves of the longitudinal and transverse oscillations are shown in Fig. 3. The function $\nu_\parallel^2(s)$ is maximum at $s = \pi$, which indicates that, as the confinement parameter decreases to the value $\mu = \nu_\parallel^2(\pi)/2 = 7\zeta(3)/2 \approx 4.207$, the transverse oscillations with $s = \pi$ lose their stability and a linear chain continuously evolves into a zigzag. This μ value coincides with the stability boundary estimated for a linear chain from energy considerations (Table 1).

3.2. Zigzag

Zigzag chain (3) with $\theta = \pi$ is characterized by three oscillation branches. The polarization of one of them

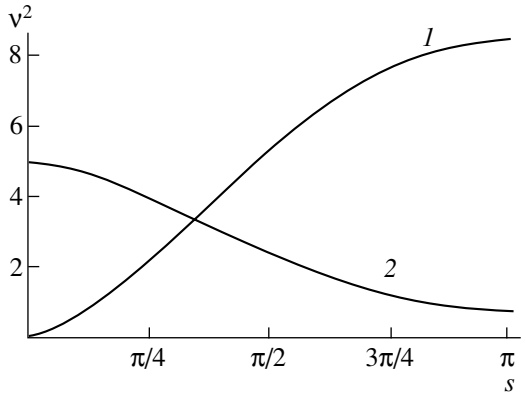

Fig. 3. Spectra (13) and (14) of (*1*) longitudinal and (*2*) transverse oscillations of a linear chain for $\mu = 5$.

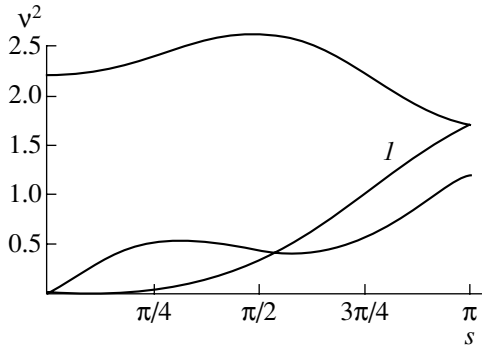

Fig. 4. Spectra of oscillations of a zigzag at the stability boundary for $\mu = 1.674$, $u = 0.965$, and $\theta = \pi$. Spectrum *1* refers to azimuthal oscillations.

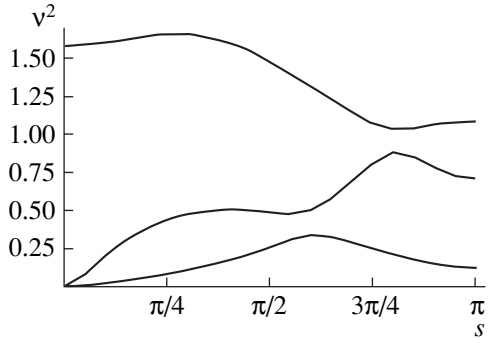

Fig. 5. Spectra of oscillations of helix H_1 for $\mu = 1.04$, $u = 1.405$, and $\theta = 2.548$. The upper curve at $s = 0$ corresponds to purely radial oscillations.

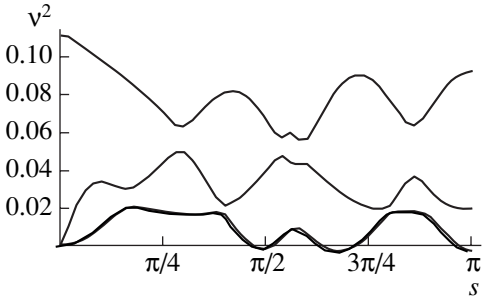

Fig. 6. Spectra of oscillations of helix H_2 for $\mu = 0.06$, $u = 7.264$, and $\theta = 1.753$.

corresponds to purely azimuthal oscillations with $\phi_0 \neq 0$, $\rho_0 = 0$, and $z_0 = 0$. The polarization of the remaining two corresponds to oscillations with $\delta_0 = 0$, $\rho_0 \neq 0$, and $z_0 \neq 0$.

Like a linear chain, a zigzag is stable over the entire range in which it exists. As the confinement parameter decreases to its minimum value $\mu \approx 1.674$, the group velocity of the long-wavelength azimuthal oscillations approaches zero. For $\mu < 1.674$, a long-wavelength instability develops, $(\nu^2/s^2)_{s \to 0} < 0$ (Fig. 4), which corresponds, obviously, to the continuous evolution of a zigzag into helix H_1.

3.3. Helix

As was noted above, there are three different helical configurations that are most advantageous from the energy standpoint; moreover, as the confinement parameter μ changes, the absolute minimum of Madelung energy (7) may jump from branch to branch (Fig. 1).

Helical configurations oscillate in a more complicated fashion than the configurations considered above do. As a rule, the oscillations of the particles are essentially three-dimensional ($\delta_0 \neq 0$, $\rho_0 \neq 0$, $z_0 \neq 0$). The only exception is uniform oscillations with $s = 0$ (i.e., purely radial oscillations), in which case the frequencies of the azimuthal and longitudinal oscillations become zero.

A characteristic example of the dispersion curves for oscillations of helix H_1 is shown in Fig. 5. The intervals of μ values where all of the configurations in question are stable are presented in Table 2. An important point is that, for all configurations, the intervals of stability either coincide with those in which the Madelung energy has an absolute minimum (*S* and *Z* configurations) or exceed them. As μ increases, the helix loses its stability in a more complicated way than the linear chain and zigzag do. As far as we can judge by the numerical results, in most cases, the oscillations that become unstable are those whose wavenumbers are incommensurable with π. A characteristic example of how helix H_2 loses its stability is illustrated in Fig. 6. This type of instability may give rise to more complicated structures, such as helices with additional modulation.

Table 2. Intervals of stability of different helical structures

Structure type	Intervals of μ
S	(4.207, ∞)
Z	(1.674, 4.207)
H_1	(0.708, 1.674)
H_2	(0.084, 0.170)
H_3	(0.033, 0.071)

4. CONCLUSION

The main qualitative conclusion from the above analysis may be formulated as follows. A helical structure whose potential energy has an absolute minimum is stable. On the other hand, as the confinement parameter changes, a crystal may remain stable even when its configuration becomes energetically unfavorable. Since different helical branches are separated from each other by the potential barriers, the crystals may, in principle, evolve into metastable states and the corresponding hysteresis effects may come into play. We can conclude by saying that, whereas the evolutions of a linear chain into a zigzag and of a zigzag into a helix are analogues of phase transitions of the second kind, the evolutions of helices from one configuration into another are analogous to phase transitions of the first kind.

ACKNOWLEDGMENTS

This work was supported in part by the Russian Foundation for Basic Research (project no. 02-02-16439) and the Netherlands Organization for Scientific Research (project no. NWO.047.008.013).

REFERENCES

1. M. Quilichini and T. Janssen, Rev. Mod. Phys. **69**, 277 (1997).
2. R. F. Wueker, H. Shelton, and R. V. Langmuir, J. Appl. Phys. **30**, 342 (1959).
3. S. L. Gilbert, J. J. Bollinger, and D. J. Wineland, Phys. Rev. Lett. **60**, 2022 (1988).
4. J. J. Bolinger, D. J. Wineland, and D. H. E. Dubin, Phys. Plasmas **1**, 1403 (1994).
5. G. Birkl, S. Kassner, and H. Walther, Nature (London) **357**, 310 (1992).
6. J. D. Prestage, G. J. Dick, and L. Maleki, J. Appl. Phys. **66**, 1013 (1989).
7. M. G. Raizen, J. M. Gilligan, J. C. Bergquist, *et al.*, Phys. Rev. A **45**, 6493 (1992).
8. N. Kjærgaard, K. Mølhave, and M. Drewsen, Phys. Rev. E **66**, 015401 (2002).
9. U. Schramm, T. Schätz, and D. Habs, Phys. Rev. E **66**, 036501 (2002).
10. M. E. Poitzesch *et al.*, Rev. Sci. Instrum. **67**, 129 (1996).
11. J. I. Cirac and P. Zoller, Phys. Rev. Lett. **74**, 4091 (1995).
12. J. H. Malmberg and T. M. O'Neil, Phys. Rev. Lett. **39**, 1333 (1977).
13. G. Morfill, H. Tomas, and V. N. Tsytovich, Fiz. Plazmy **28**, 675 (2002).
14. D. H. E. Dubin, Phys. Rev. Lett. **71**, 2753 (1993).
15. R. W. Hasse and J. P. Schiffer, Ann. Phys. (N.Y.) **203**, 419 (1990).

Translated by O.E. Khadin

Plasma Physics Reports, Vol. 29, No. 6, 2003, pp. 491–502. Translated from Fizika Plazmy, Vol. 29, No. 6, 2003, pp. 527–539.

PLASMA ELECTRONICS

Microwave Generation by a Superluminal Source at Limiting Current Densities

Yu. N. Lazarev, P. V. Petrov, and Yu. G. Syrtsova

Zababakhin All-Russia Research Institute of Technical Physics, Russian Federal Nuclear Center, Snezhinsk, Chelyabinsk oblast, 456770 Russia

Received August 12, 2002

Abstract—It is well known that high-power directed wideband electromagnetic radiation in the microwave range can be generated by a superluminal pulse of the electron emission current. The operation of a simple emitting element driven by a superluminal current pulse and consisting of an accelerating diode with a photocathode and a source of ionizing radiation that initiates electron emission from the cathode is considered. It is shown that the parameters of an elementary superluminal source obey scaling relations that are determined by the growth rate of the electron emission current from the photocathode and the parameters of the accelerating diode. The limiting anode current density and the limiting values of the characteristics of electromagnetic radiation achievable in such a system are determined. The effect of the finite dimensions of the accelerating system on the parameters of the emitter is investigated, and the spatiotemporal characteristics of the generated electromagnetic fields are obtained. © *2003 MAIK "Nauka/Interperiodica".*

1. INTRODUCTION

High-power directed wideband electromagnetic (EM) radiation in the microwave range can be generated by means of a superluminal electron emission current pulse [1, 2] produced when the front of the electron emission from the interface between a vacuum and a medium propagates with a velocity v_{ph} higher than the speed of light c. In particular, a superluminal current pulse is generated when a plane metal surface is irradiated by a plane flux of radiation capable of producing electron emission, in which case the phase velocity of the moving emission front is equal to

$$v_{ph} = c/\sin\theta, \quad (1)$$

where θ is the angle of incidence of the radiation.

The spatiotemporal distribution of the electron emission current near the surface is phased in such a way that an emitted EM wave propagates in the same direction as the reflected wave of the ionizing radiation (Fig. 1). At sufficiently large distances R from the source, the amplitude of the emitted EM field is proportional to the second derivative of the surface density of the dipole moment P with respect to time; in turn, this derivative is proportional to the energy of the electrons emitted and the area S of the emitter surface [1, 2]:

$$E^w \sim H^w \sim \ddot{P}S/c^2R, \quad \ddot{P} = \left|d^2\mathbf{P}/dt^2\right|,$$
$$\mathbf{P}(\mathbf{r}, t) = \int dV'(\mathbf{r}-\mathbf{r}')\rho(\mathbf{r}', t), \quad (2)$$

where $\rho(\mathbf{r}, t)$ is the electron density in the dipole layer.

According to formulas (2), the higher the energy of the emitted electrons, the higher the intensity and total energy of the emitted EM radiation. Estimates [2] show that, in order for the energy and intensity of the generated EM radiation be of interest for practical purposes, the energy of the emitted electrons should be on the order of tens of kiloelectronvolts or higher. Under laboratory conditions, the emission current of the high-energy electrons can be generated by separating the processes of the electron production and the formation of the emitting dipole layer. Light or ionizing radiation capable of producing electron emission is used only to initiate the emission of electrons with the minimum possible energy; the electrons emitted are then accelerated to their final energies from hundreds to thousands

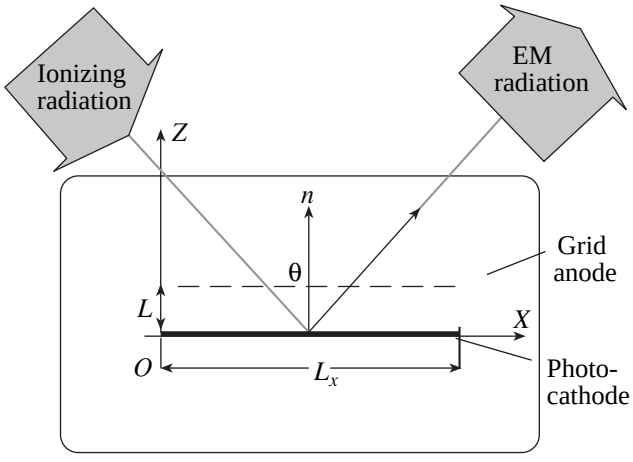

Fig. 1. Elementary microwave source in a vacuum chamber evacuated to a pressure of $p < 0.005$ mm Hg.

1063-780X/03/2906-0491$24.00 © 2003 MAIK "Nauka/Interperiodica"

of kiloelectronvolts by an external electric field. Schematically, an EM radiation source supplied by a superluminal current pulse is a plane accelerating diode with a grid anode irradiated at a certain angle by a plane flux of ionizing or light radiation (Fig. 1). The plane front of the ionizing radiation generates a superluminal current pulse of the electrons emitted from a photocathode. Then, the electrons are accelerated in the interelectrode gap, pass through the grid anode, and form a superluminal current pulse above it. The current pulse so produced generates a high-power directed EM pulse near the anode.

In the theory of a superluminal source [1, 2], the main results were obtained in studying the operating modes of an emitter in which the generated electromagnetic wave did not have any significant effect on the parameters of the accelerating system. However, it is clear that, for high current densities of the accelerated electrons, this effect should be taken into account: when the current density is sufficiently high, the characteristics of the generated EM radiation depend on the parameters of the accelerated diode and, primarily, on the parameters of the limiting current that can be produced above the anode. Although there are many papers devoted to the problem of limiting currents (see [3–5] and the literature cited therein), some features of the generation of EM radiation by a superluminal emission current pulse that do not manifest themselves in the classical schemes of microwave generation remain uninvestigated. In particular, since the EM radiation pulse forms at the front of the emission current, the achievement of high current densities at the anode is determined not by the current density of the emitted electrons but by the growth rate of the emission current.

Our objective here is to investigate the limiting characteristics of the EM radiation generated by an elementary superluminal source. We present analytic estimates and the results of numerical calculations of the parameters of a superluminal current pulse and EM radiation generated when the emission electrons are accelerated in a plane diode operating at high current densities.

2. ANALYTIC MODEL OF THE FORMATION OF AN EMITTING DIPOLE LAYER IN AN ELEMENTARY EMITTER

The feature of an emitting element (Fig. 1) based on the generation of EM radiation by a superluminal current pulse of the electrons accelerated in a plane diode is that it generates two electromagnetic waves, which will be referred to as "directed" and "guided" waves. The interaction of these waves with the emitted electrons governs the magnitude of the anode current and the dipole moment above the anode.

In the free half-space above the anode ($z > L$), the directed electromagnetic wave propagates in the direction in which the ionizing radiation is reflected (Fig. 1). The parameters of the directed wave are determined by the dynamics of the dipole layer of the electrons accelerated in the diode [see Eq. (2)]. It can be assumed that this wave does not affect the anode current amplitude because of the screening effect of the metal grid anode.

A superluminal current pulse produced by the electrons moving in the interelectrode gap also generates an electromagnetic wave that propagates in a plane waveguide formed by the cathode and anode. Being added to the field of the space charge of the emitted electrons, the field of this guided electromagnetic wave reduces the effective accelerating field in the diode and, accordingly, lowers the limiting current density at the anode and the density of the dipole moment of the electrons above it.

The processes of the generation of EM radiation, the formation of the dipole layer, and the electron motion in the accelerating gap should be considered together because they are closely related to each other. A theoretical study of such systems is based mainly on numerical simulations. However, in some cases, the problem of the initial stage of the formation of a dipole layer (before the electron flow velocity becomes multivalued [6]) can be investigated by approximate analytic methods, which make it possible to obtain scaling relations for the main parameters of the electron current and to estimate the limiting current densities at the anode operating in a dynamic mode.

We consider the process of the formation of an electron dipole layer above the grid anode of an infinite plane capacitor in the one-dimensional approximation. We assume that the anode is transparent to electrons and denote by L and φ_0 the distance and the voltage between the electrodes. It is well known that, when the voltage φ_0 is not too high, $e\varphi_0/(mc^2) = \gamma_0 - 1 \ll 1$, the electron motion can be treated as nonrelativistic. In such a diode, the steady-state limiting current density is described by the expression [5]

$$J_0 = \frac{\varphi_0^{3/2}}{9\pi L^2}\sqrt{\frac{2e}{m}}. \quad (3)$$

We assume that, under the action of ionizing radiation incident on the emitting element, the cathode emits electrons with a current density $J_c(t)$ and a zero initial velocity.

2.1. The Case of Normal Incidence of the Ionizing Radiation ($\theta = 0$, $v_{ph} = \infty$)

The normal incidence of ionizing radiation on an emitting element is an exceptional case in which an electromagnetic wave is not generated ($v_{ph} = \infty$) and, accordingly, there is no need to take into account the effect of the fields of the directed and guided electromagnetic waves on the electron motion. Nevertheless, this problem, even being considerably simplified, is of interest because it makes it possible to derive the main

scaling relations for the parameters of the electron current.

Let the cathode ($z = 0$) start emitting electrons into the accelerating gap at the time $t = 0$. We consider only the initial stage of the formation of a dipole layer, up to the time τ_r at which the emitted electrons begin to return to the cathode and the electron flow velocity becomes multivalued. In this stage, the space charge that arises above the cathode by the time τ is equal to

$$Q = \int_0^\tau J_c(t)dt. \tag{4}$$

Since the space charge produced changes the accelerating electric field of the capacitor, the motion of the electrons injected at the time $\tau < \tau_r$ is described by the equation

$$\frac{d^2z(t,\tau)}{dt^2} = \frac{e}{m_e}E(\tau, z), \tag{5}$$

where e and m_e are the charge and mass of an electron. The electric field $E_z(\tau, z)$ acting on an electron emitted from the cathode at the time τ has the form

$$E(\tau, z) = \begin{cases} E_0 - 4\pi\int_0^\tau J_c(t')dt', & 0 < z < L, \\ -\eta[\tau - T^*(\tau)]4\pi\int_{T^*(\tau)}^\tau J_c(t')dt', & z > L. \end{cases} \tag{6}$$

Here, $E_0 = \varphi_0/L$ is the initial accelerating electric field in the diode; $\eta(t) = 0$ ($t < 0$) and 1 ($t \geq 0$) is the Heaviside step function; and $T^*(\tau)$ is the transit time of an electron from the cathode to the anode, so an electron emitted from the cathode at the time τ reaches the anode at the time $t = \tau + T^*(\tau)$.

Since the accelerating field decreases as the space change increases, the electron transit time from the cathode to the anode becomes longer. As a result, the electrons injected from the cathode during the time interval $\Delta\tau$ reach the anode during the time interval $\Delta t = \Delta\tau\left(1 + \left|\frac{dT^*}{d\tau}\right|\right)$. Accordingly, the current density at the anode J_a is related to the current density at the cathode $J_c(\tau)$ by

$$J_a(t) = \frac{J_c(\tau)}{1 + \left|\frac{dT^*}{d\tau}\right|}, \quad t = \tau + T^*(\tau). \tag{7}$$

Of course, for $\left|\frac{dT^*}{d\tau}\right| \ll 1$, the current density may be regarded as conserved: the current density above the anode is equal to that at the cathode and the electron velocity at the anode does not depend on time and is equal to

$$v_0 = \sqrt{\frac{2eLE_0}{m_e}}. \tag{8}$$

In this case, the characteristic time of the formation of the dipole layer, T_p, can be estimated from the current density at the cathode.

If we assume that the current density at the cathode changes linearly with time (at least over the time interval $0 < \tau < \tau_r$),

$$J_c(\tau) = J_t\tau, \tag{9}$$

then we obtain

$$T^*(\tau) = \frac{T_0T_m}{\sqrt{T_m^2 - \tau^2}}, \quad \frac{dT^*(\tau)}{d\tau} = \frac{T_0T_m\tau}{(T_m^2 - \tau^2)^{3/2}},$$
$$T_m = \sqrt{\frac{E_0}{2\pi J_t}}, \quad T_0 = \sqrt{\frac{2m_eL}{eE_0}}. \tag{10}$$

The condition $\left|\frac{dT^*}{d\tau}\right| \ll 1$ is satisfied when

$$a = T_0/T_m \ll 1, \tag{11}$$

i.e., when the transit time of an electron through the interelectrode gap is much shorter than the time scale on which the electric field in the gap changes. This condition can be rewritten in terms of the growth rate of the emission current from the cathode:

$$J_t \ll \frac{J_{0t}}{4\pi} = \frac{J_0}{4\pi T_0} = \frac{eE_0^2}{4\pi m_eL}. \tag{12}$$

Under conditions (11) and (12), the characteristic time of the formation of the dipole layer is $T_p = \left(\frac{m_ev_0}{4\pi eJ_t}\right)^{1/3} = \left(\frac{1}{2\pi J_t}\sqrt{\frac{m_eLE_0}{2e}}\right)^{1/3}$, the surface density of the dipole moment is $P_0 = \frac{mv_0^2}{8\pi e} = \frac{LE_0}{4\pi}$, the time derivatives of the dipole moment density are equal to $\dot{P}_0 = \frac{P_0}{T_p}$ and $\ddot{P}_0 = \frac{P_0}{T_p^2}$, and the characteristic wavelength of the generated EM radiation is $\lambda = 2\pi\lambda\!\!\!^{-} = 2\pi cT_p$.

When the current density at the cathode changes at a high rate, $J_t \sim J_{0t}$, the time scale on which the accelerated field in the interelectrode gap changes is comparable with the electron transit time, $T_m \sim T_0$. The space charge of the electrons emitted from the cathode during the time interval $0 < \tau < T_m$ completely neutralizes the external accelerating field; i.e., the electrons emitted at the times $\tau > T_m$ do not contribute to the anode current. Only after the time $\tau = \tau_r$, at which the electrons begin

to return to the cathode, is the anode current again contributed by the emission from the photocathode. Accordingly, the time scales on which the anode current and the dipole moment density change are determined by the times T_m and T_0.

We assume that the current density changes linearly with time [see expression (9)] and switch to the new dimensionless variables

$$\tau' = \tau/T_m, \quad j_c(\tau') = J_c(\tau)/(J_t T_m),$$
$$\dot{p} = \dot{P}/(J_t T_m^2 v_0), \quad \ddot{p} = \ddot{P}/(J_t T_m v_0), \tag{13}$$
$$v' = v/v_0, \quad a = T_0/T_m.$$

Substituting these variables into equation of motion (5), we obtain the following parametric expressions for the density of the current flowing through the anode and for the time derivatives of the dipole moment density:

$$j_a(\tau') = \frac{j_c(\tau')(1-\tau'^2)^{3/2}}{(1-\tau'^2)^{3/2} + a\tau'}, \tag{14}$$

$$\dot{p} = 1 + \frac{(\tau'^2 - 1 - \tau'^4/4)}{\sqrt{1-\tau'^2}} - \frac{\tau'^5}{20a},$$
$$\ddot{p} = \tau'\sqrt{1-\tau'^2} - \frac{\tau'^5}{4(1-\tau'^2)^{3/2}} - \frac{\tau'^4}{4a}, \tag{15}$$

where the time at which an electron is emitted from the cathode and the time at which it reaches the anode are related by

$$t' = \tau' + a/\sqrt{1-\tau'^2}. \tag{16}$$

Using formulas (14) and (15), we can estimate the maximum values of the anode current and of the time derivatives of the dipole moment density, as well as the times at which the maximum values are achieved:

$$(j_a)_{\max} \approx \frac{1}{2(1 + 4\sqrt{3}a/9)}, \quad t_f' \approx 0.7; \tag{17}$$

$$\dot{p}_{\max} \approx 0.22 - \frac{0.01}{a}, \quad t_f' \approx 0.97a + 0.66; \tag{18}$$

$$\ddot{p}_{\max} \approx \frac{0.36}{1 + 0.52a}, \quad t_f' \approx 0.5 + 0.1a. \tag{19}$$

Figures 2–4 show the electron current and the derivatives of the dipole moment density above the anode, calculated from analytic expressions (17)–(19) and obtained in the one-dimensional numerical modeling with the two-dimensional EMC2D code [7], in which Maxwell's equations and the equations of electron motion are solved self-consistently by a particle-in-cell (PIC) method.

In dimensional form, expressions (17)–(19) become

$$(J_a)_{\max} \approx \frac{\sqrt{J_t E_0}}{2\sqrt{2\pi}\left(1 + \frac{8}{9E_0}\sqrt{\frac{3\pi J_t L m_e}{e}}\right)},$$
$$t_f \approx 0.7T_m = 0.7\sqrt{\frac{E_0}{2\pi J_t}}, \tag{20}$$

$$\dot{P}_{\max} \approx \frac{0.22}{\pi}\sqrt{\frac{eL}{2m_e}E_0^{3/2}}, \quad t_f \approx 0.97T_0 + 0.66T_m, \tag{21}$$

$$\ddot{P}_{\max} \approx \frac{0.36E_0}{1 + \frac{1}{E_0}\sqrt{\frac{\pi m_e L J_t}{e}}}\sqrt{\frac{eLJ_t}{\pi m_e}},$$
$$t_f \approx 0.5T_m + 0.1T_0. \tag{22}$$

Expressions (17)–(22) show that, when the generated EM radiation (the directed and guided waves) has a negligible effect on the motion of accelerated electrons, such parameters as the anode current, the dipole moment, and the EM radiation intensity obey certain scaling relations and their asymptotic values are determined by the parameters of the accelerated diode.

2.2. The Case of Oblique Incidence of the Ionizing Radiation ($\theta \neq 0$, $v_{\text{ph}} < \infty$)

In the case of obliquely incident ionizing radiation, the phase velocity of the emission current from the cathode surface is finite, $c < v_{\text{ph}} < \infty$, which results in the generation of EM waves (directed and guided waves). The field of the guided mode affects the process of electron acceleration in the interelectrode gap, and the field of the directed mode influences the dynamics of the dipole layer above the anode.

We consider the effect of a directed EM wave on the dipole moment above the anode under the assumption that the EM field of the directed wave is screened by the anode and thus has no impact on electron motion in the interelectrode gap. It is clear that the field E^w of the emitted wave can be neglected when it is lower than space-charge field E^{sch}:

$$E^w < E^{\text{sch}}.$$

Near the emitting surface, the component E_z^w of the electric field of the EM wave is determined by the first derivative of the dipole moment [2]:

$$E_z^w \approx \frac{4\pi}{c}\frac{\sin^2\theta}{\cos\theta}\dot{P}(t) \approx \frac{v_0}{c}\frac{\sin^2\theta}{\cos\theta}E_0. \tag{23}$$

In order of magnitude, we have

$$E_z^w \sim \frac{\varepsilon_0}{\chi\tan\theta}, \quad E^{\text{sch}} \sim \frac{\varepsilon_0}{\lambda_D},$$

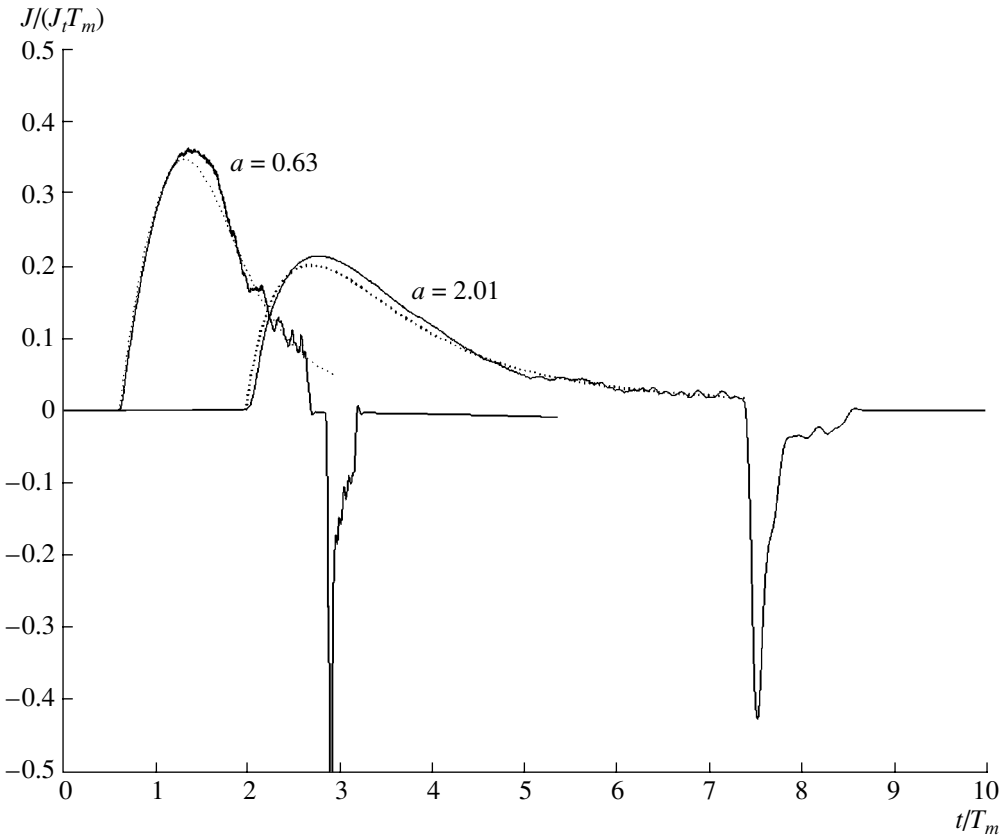

Fig. 2. Time evolutions of the anode current for different growth rates of the current density at the cathode. The solid curves show the results of numerical calculations, and the dotted curves are analytical results.

where $\varepsilon_0 = \dfrac{m_e v_0^2}{2}$ is the maximum energy of the electrons accelerated in the diode and $\lambda_D = v_0 T_m$ is the characteristic dimension of the electron dipole layer.

Consequently, when the angle of incidence of the ionizing radiation satisfies the condition

$$\theta > \arccos\left(\frac{1}{\sqrt{1 + v_0^2/c^2}}\right), \tag{24}$$

the field of the EM wave has a significant effect on the process under consideration: it decreases the derivatives of the dipole moment density and somewhat reduces the duration of the generated EM pulse.

The guided mode of the EM radiation has a greater effect because it influences the electron acceleration process. The reason is that the accelerating field of the diode decreases not only because of the increase in the space charge of the emitted electrons [see expression (6)] but also because of the generation of the EM field component E_z^w. Accordingly, in equation of motion (5), the electric field should be taken in the form

$$E(\tau, z) = E_0 - 4\pi\int_0^\tau J_c(t')dt' - E_z^w(z, \tau), \quad 0 < z < L. \tag{25}$$

Self-consistent PIC computations (Fig. 5) show that, in the case of oblique incidence of the ionizing radiation on an accelerating diode (when EM radiation is generated), the total field of the EM wave and of the space charge increases at a much faster rate and to a greater value than does the space charge field alone in the case of normal incidence. Hence, the guided EM radiation leads to the following effects:

(i) the shortening of the electron transit time T_m from the cathode to the anode and

(ii) the weakening of the accelerating electric field in the interelectrode gap.

Accordingly, both the anode current and the derivatives of the dipole moment decrease.

The amount by which the anode current decreases can be estimated by assuming that the electron acceleration in a diode with the guided mode of the EM radiation is determined not by the initial accelerating electric field E_0 but by a certain effective electric field E_{eff} =

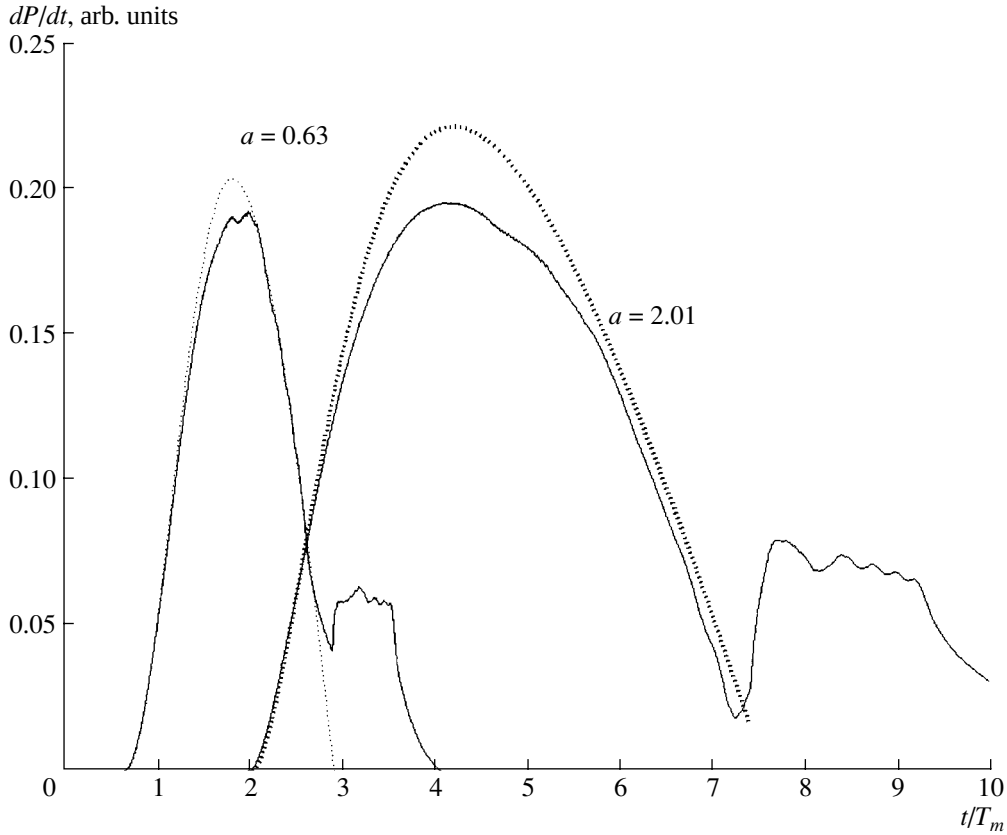

Fig. 3. Time evolutions of the first time derivative of the surface density of the dipole moment for different growth rates of the current density at the cathode. The solid curves show the results of numerical calculations, and the dotted curves are analytical results.

$E_0 - E_z^w$, where the field component E_z^w is given by formula (23):

$$E_{\text{eff}} = E_0\left(1 - \frac{v_0}{c}\frac{\sin^2\theta}{\cos\theta}\right). \tag{26}$$

We assume that the angle of incidence is not too large, $\pi/4 < \theta < \pi/3$, and that the electron motion is nonrelativistic, $\beta_0 = v_0/c \approx 0.5$. Then, we insert E_{eff} into formulas (20)–(22) to see that the amplitude of the anode current and the second derivative of the dipole moment density decrease by a factor of approximately two:

$$(J_a^w)_{\max} \approx \left(1 - \frac{v_0}{c}\frac{\sin^2\theta}{\cos\theta}\right)^{1/2}(J_a)_{\max} \approx 0.5(J_a)_{\max},$$
$$\ddot{P}^w_{\max} \approx \left(1 - \frac{v_0}{c}\frac{\sin^2\theta}{\cos\theta}\right)\ddot{P}_{\max} \approx 0.25\ddot{P}_{\max}. \tag{27}$$

This result is confirmed by numerical calculations with the EMC2D code (Figs. 6, 7).

The above analytic estimates obtained for the generation of microwaves by a superluminal electron emission current pulse formed by a plane diode allow us to draw the following conclusions:

(i) The anode current density and the time derivatives of the dipole moment in an emitting element are determined by the parameters of an accelerating diode and by the growth rate of the electron emission current from the cathode; in turn, this rate depends on the rate of change of the ionizing radiation flux intensity.

(ii) The limiting current at the anode, $(J_a)_{\max}$, is lower than the steady-state limiting current J_0 and the limiting values of the derivatives of the dipole moment are smaller than the corresponding steady-state limiting values because the electron current is limited by not only the space charge field but also by the field of the generated EM wave.

(iii) In a half-space above the anode, the parameters of the anode current and the derivatives of the electron dipole moment obey scaling relations (13), (17)–(19), and (27).

(iv) An increase in the rate of electron emission from the cathode changes not only the amplitude values of the parameters of the dipole layer but also the time dependence of the derivatives of the dipole moment density: the characteristic time scale of the dipole moment and the associated wavelength $\lambda = 2\pi c T_m$ both decrease. This indicates that the spectrum of the gener-

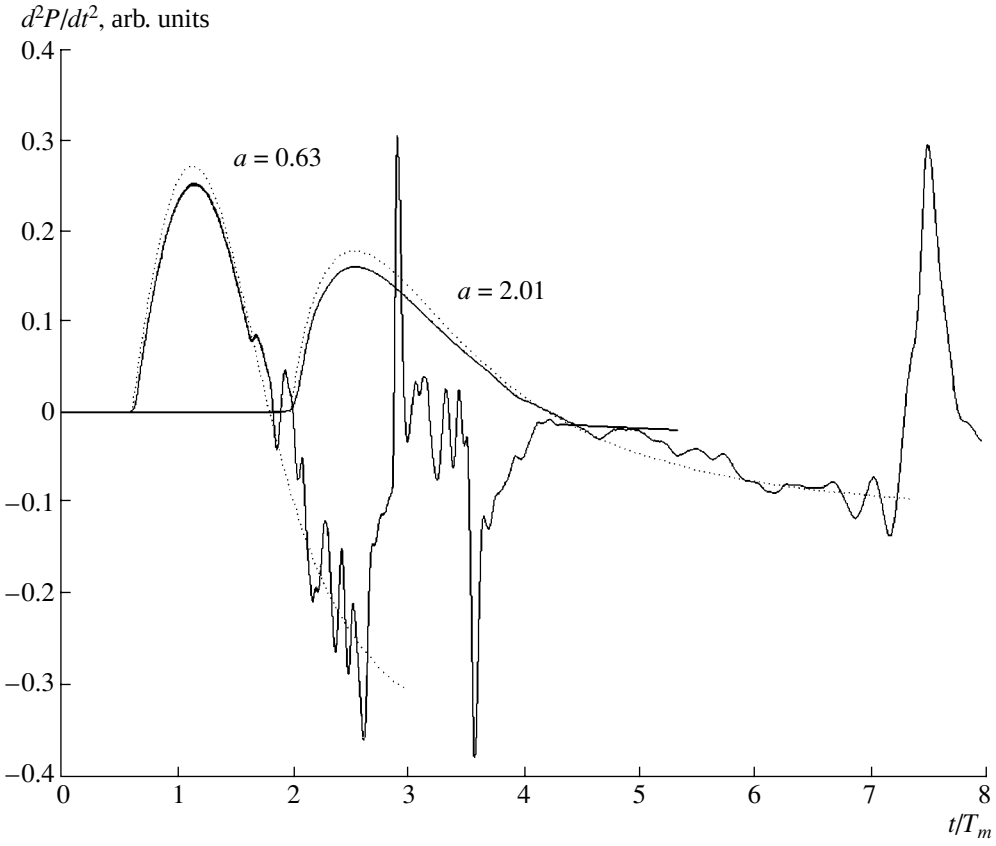

Fig. 4. Time evolutions of the second time derivative of the surface density of the dipole moment for different growth rates of the emission current density at the cathode. The solid curves show the results of numerical calculations, and the dotted curves are analytical results.

ated radiation can be changed by changing the electron emission rate.

3. NUMERICAL SIMULATIONS OF THE MICROWAVE GENERATION AT A HIGH EMISSION RATE

The above estimates have been obtained from a one-dimensional model of an infinitely long emitting element. In actuality, the dimensions of a capacitor used to form superluminal current pulses are usually too small for it to be treated as a plane one with an infinite length and an infinite width. Thus, in [8], the experiments on microwave generation by superluminal current pulses initiated by the front of soft X radiation from a laser–plasma source were carried out with a capacitor with voltage $\varphi_0 = 80$ kV, length $L_x = 80$ cm, width 5 cm, and interelectrode distance $L = 2$ cm. The configuration of this accelerating system was used as the basis for our numerical investigations of the effect of the finite dimensions of an emitter on the parameters of a superluminal source. The investigations were carried out with the EMC2D PIC code [7]. The geometry of the system corresponded to that shown schematically in Fig. 1. The initial electrostatic field of the capacitor were computed by the finite-element method with the help of the MATLAB software package [9] and then were used as the input to the EMC2D code for calculating the dynamics of an electron cloud. It was assumed that electron emission is initiated by the plane front of the ionizing radiation incident at an angle of 60° and that the current density changes linearly according to the law $J_t = 2.5 \times 10^{10}$–5×10^{11} $\frac{\text{A}}{\text{cm}^2\ \text{s}}$ ($a = 0.45$–2.0).

3.1. Effects of the Finite Length of the Emitting Element

Figures 8–10 illustrate the results of calculations of the anode current, the second derivative of the dipole moment, and the rise time of the second derivative [all normalized to their maximum values determined by Eqs. (20)–(22)] as functions of the longitudinal coordinate. The main effect of the finite length of an emitting element is the spatial nonuniformity of the profiles of the anode current and dipole moment density along the capacitor; this effect is associated with the influence of the generated radiation on the electron motion. At the left end of the capacitor (Fig. 1), the EM radiation has an insignificant effect on the formation of the current pulse. However, the larger the distance from the left

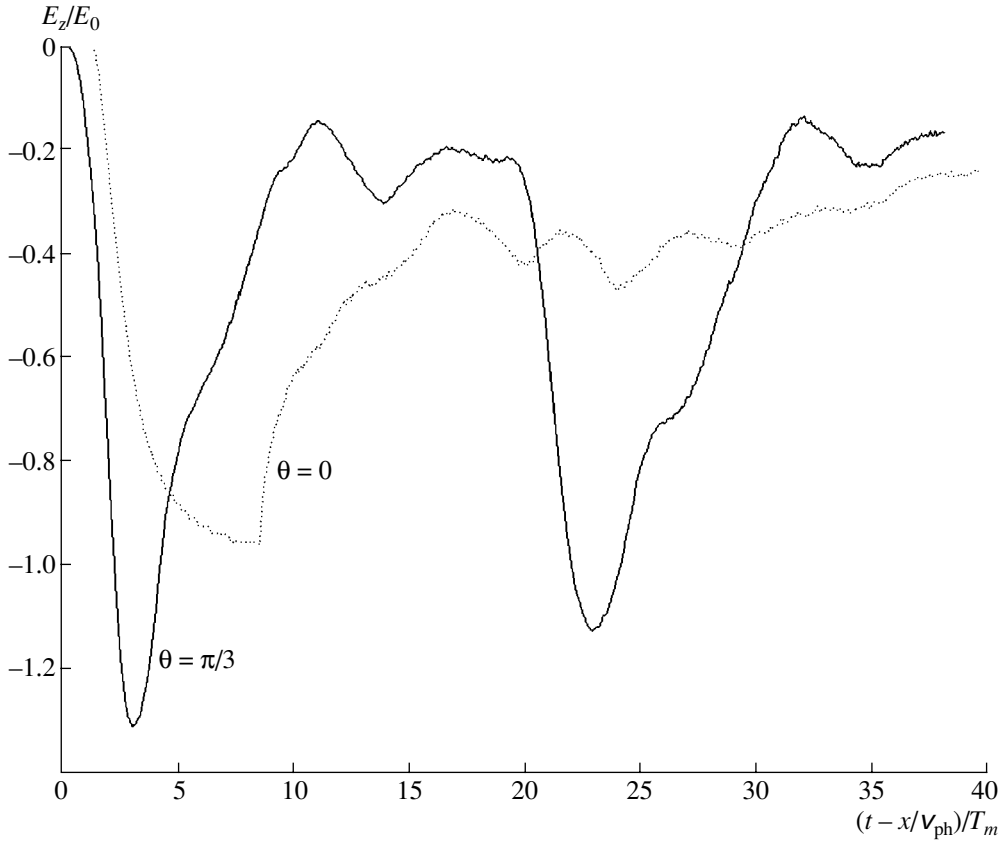

Fig. 5. Time evolutions of the electric field E_z in the middle of the accelerating gap in the case of the oblique ($\theta = \pi/3$) incidence of the ionizing radiation on an infinitely long (one-dimensional) emitting element (with allowance for the generation of EM waves) and in the case of normal ($\theta = 0$) incidence (with no generation of EM waves). The calculations were carried out for $a = 2$.

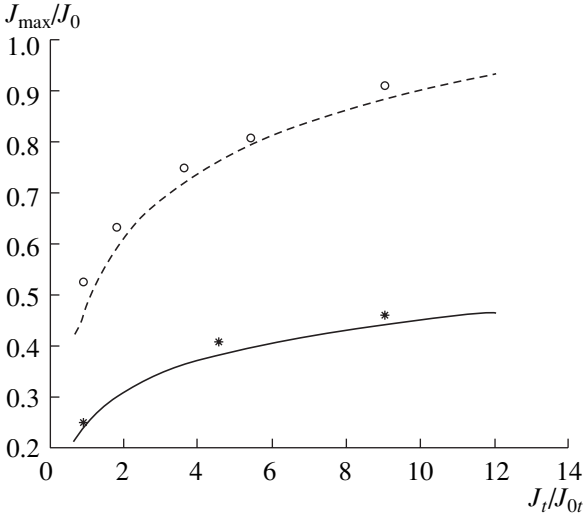

Fig. 6. Anode current density as a function of the growth rate of the emission current density at the cathode in the case of the oblique ($\theta = \pi/3$) incidence of the ionizing radiation on an infinitely long (one-dimensional) emitting element [with allowance for the generation of EM waves, formula (27)] and in the case of normal ($\theta = 0$) incidence [with no generation of EM waves, formula (17)]. The symbols show the results of numerical calculations.

end, the larger the amplitude of the generated EM wave and the closer the parameters of the superluminal current pulse to their limiting values corresponding to an infinitely long emitter (Figs. 6, 7). For an emitter of fixed length, an increase in the rate of electron emission from the cathode is seen to somewhat reduce the degradation of the parameters of the electron dipole moment due to the effect of the guided EM wave (Fig. 9); however, as the length of the emitting surface increases, the parameters in question always approach their asymptotic values given by formulas (27).

3.2. Effects of the Finite Transverse Dimensions of the Emitting Element

For the width of an accelerating diode not to significantly distort the spatiotemporal distribution of the electrons over the dipole layer, it should be much larger than the distance between the electrodes. Calculations show that the anode current and the derivatives of the dipole moment are essentially the same as those predicted by the one-dimensional model. The difference between the numerical and analytical results is the largest at distances from the capacitor edge that are shorter than the distance between the electrodes.

Since the intensity of radiation generated in a distant source region is determined by the second derivative of the surface density of the dipole moment and the emitter area, which is the anode area, the boundary effects associated with the finite width of the capacitor reduce the effective width of the emitting surface by an amount of about $(1–2) \times L$.

3.3. Calculation of the EM Fields

Recall that an elementary microwave source supplied by a superluminal emission current pulse that is formed by an accelerating diode generates two wideband radiation pulses—a directed pulse and a guided pulse.

At sufficiently large distances R from the emitting region, the amplitude of the EM field of the directed wave can be estimated in terms of the delayed potentials. The magnetic field is easier to estimate:

$$\mathbf{H} \simeq \frac{1}{c^2 R}\int dV' \left[\frac{\partial}{\partial t}\mathbf{j}\left(t - \frac{|\mathbf{r}-\mathbf{r}'|}{c}, \mathbf{r}'\right), \frac{\mathbf{r}-\mathbf{r}'}{|\mathbf{r}-\mathbf{r}'|}\right] \approx \frac{1}{c^2 R}\int_{S_a} dS[\ddot{\mathbf{P}} \times \mathbf{n}], \quad (28)$$

where S_a is the anode area.

For an emitting element of infinite width ($-\infty < y < \infty$), this expression yields the following estimate for the magnetic field:

$$H_0 = \frac{L_x \sin\theta}{\sqrt{R}(cT_0)^{3/2}} P_0. \quad (29)$$

Figure 11 presents the results of two-dimensional calculations of the magnetic field in a distant region of the microwave source, $-\infty < y < \infty$ and $R/D = 5$, where $D = L_x \cos\theta$ is the effective length of the radiating element. We can see that, since the parameters of the generated radiation (the derivatives of the dipole moment in Figs. 7, 8) approach their asymptotic values as the growth rate of the emission current increases, the amplitude of the directed EM radiation pulse and its characteristic rise time also approach their limiting values, in which case the field amplitude reaches its maximum and the characteristic wavelength reaches its minimum. A change in the characteristic wavelength of the EM radiation alters its directional pattern, which is characterized by the diffractional divergence angle

$$\theta_D = \frac{\lambda}{D} = \frac{2\pi c T_0}{D}. \quad (30)$$

Figure 12 shows the angular distributions of the maximum radiation flux density with respect to the direction in which the ionizing radiation is reflected for different growth rates of the emission current. As can be seen, an increase in the emission rate and the corresponding decrease in the characteristic radiation wavelength increases the directionality of the EM emission from the source, which radiates energy into a cone with a solid angle of about $2\theta_D$ (Fig. 13).

The characteristic wavelength of the EM radiation generated in the accelerating gap is far longer than the

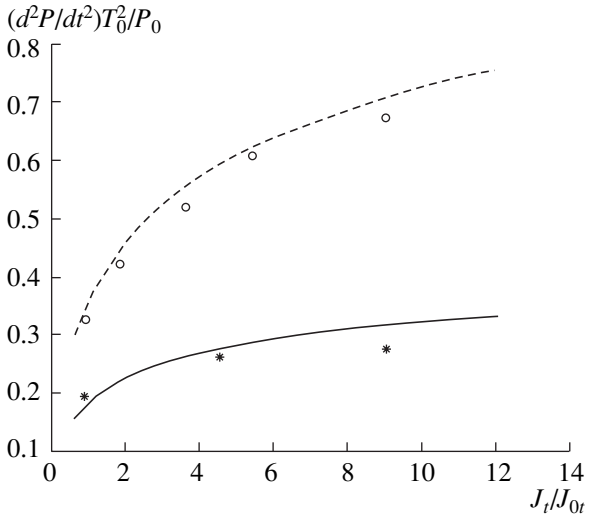

Fig. 7. Second derivative of the electron dipole moment in the half-space above the anode as a function of the growth rate of the emission current density at the cathode in the case of the oblique ($\theta = \pi/3$) incidence of the ionizing radiation on an infinitely long (one-dimensional) emitting element [with allowance for the generation of EM waves, formula (25)] and in the case of normal ($\theta = 0$) incidence [with no generation of EM waves, formula (19)]. The symbols show the results of numerical calculations.

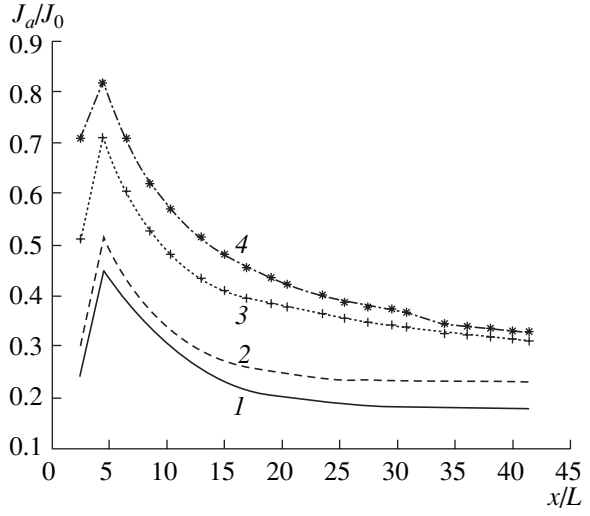

Fig. 8. Profiles of the second derivative of the electron dipole moment along a capacitor in the case of the oblique ($\theta = \pi/3$) incidence of the ionizing radiation for different growth rates of the emission current density at the cathode: a = (*1*) 0.45, (*2*) 0.64, (*3*) 1.42, and (*4*) 2.0.

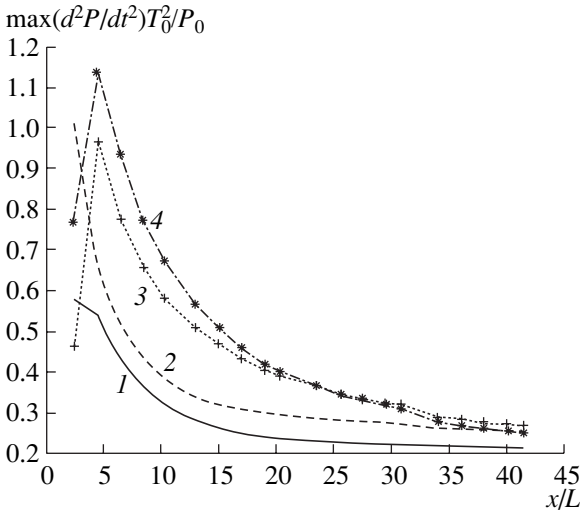

Fig. 9. Profiles of the anode current along a capacitor in the case of the oblique ($\theta = \pi/3$) incidence of the ionizing radiation for different growth rates of the emission current density at the cathode: a = (*1*) 0.45, (*2*) 0.64, (*3*) 1.42, and (*4*) 2.0.

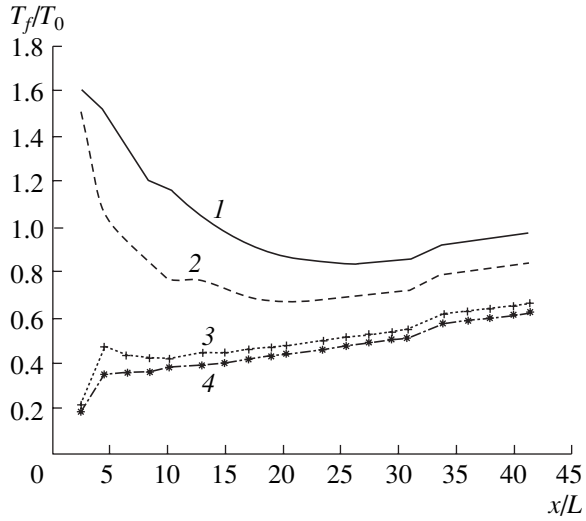

Fig. 10. Rise time of the second derivative of the electron dipole moment as a function of the longitudinal coordinate in the case of the oblique ($\theta = \pi/3$) incidence of the ionizing radiation for different growth rates of the emission current density at the cathode: a = (*1*) 0.45, (*2*) 0.64, (*3*) 1.42, and (*4*) 2.0.

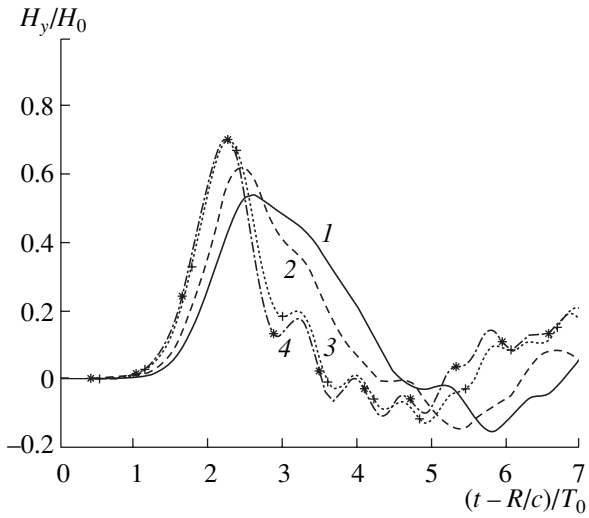

Fig. 11. Time evolutions of the magnetic field of the generated EM radiation propagating in the direction in which obliquely ($\theta = \pi/3$) incident ionizing radiation is reflected for R/D = 5 and for different growth rates of the emission current density at the cathode: a = (*1*) 0.45, (*2*) 0.64, (*3*) 1.42, and (*4*) 2.0.

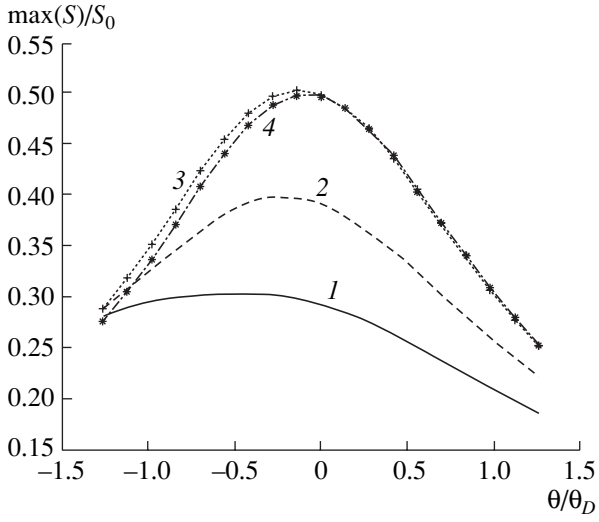

Fig. 12. Angular distributions of the maximum EM radiation flux density for different growth rates of the emission current density at the cathode: a = (*1*) 0.45, (*2*) 0.64, (*3*) 1.42, and (*4*) 2.0.

critical wavelength; i.e., the waveguide formed by the cathode and anode is overcritical. Nevertheless, a guided EM wave can propagate in the waveguide because of the propagation of the emission current along the cathode. As a result, the EM field emitted through the open end of the waveguide is dipolar and coherent with the directed EM wave emitted by a superluminal current source (both of them are generated by the same ionizing radiation pulse and are in phase with one another). Figure 14 illustrates the results from two-dimensional simulations of the generation of EM radiation and its propagation away from an elementary emitter with (a) a screened and (b) an open waveguide end. In both figures, we see the directed EM radiation

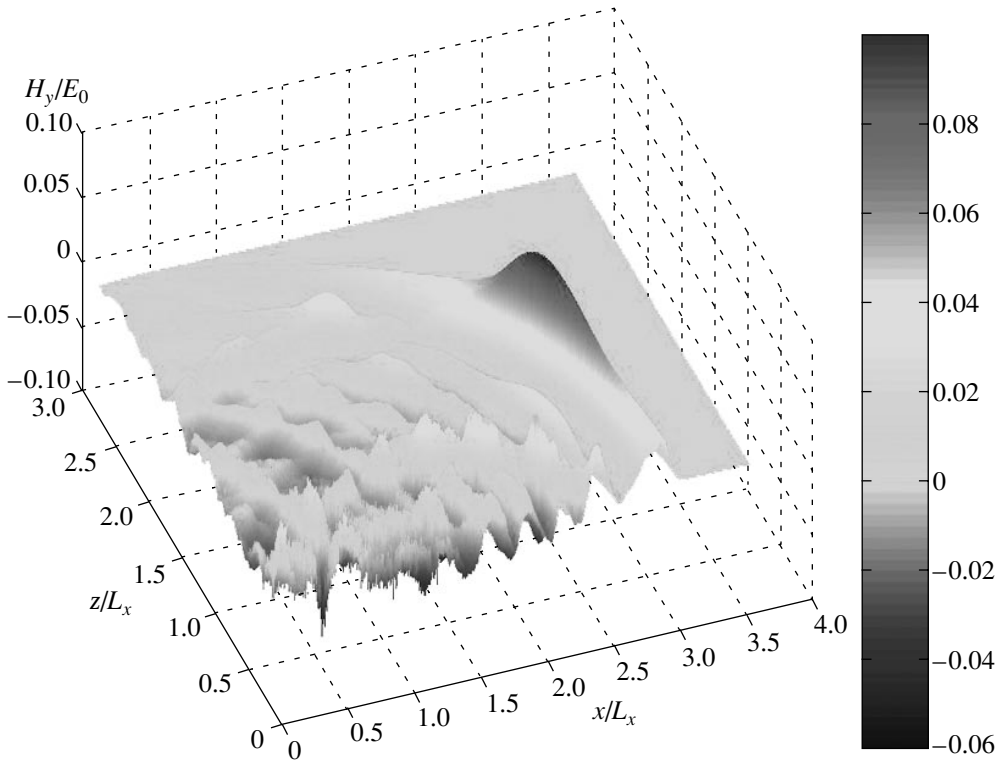

Fig. 13. Spatial distribution of the magnetic field of a directed EM pulse generated by an elementary emitter at the time $t = 5$ ns. The emission current from the cathode increases according to the law $J_t = 5 \times 10^{11}$ A/(cm^2 s) ($a = 2.0$).

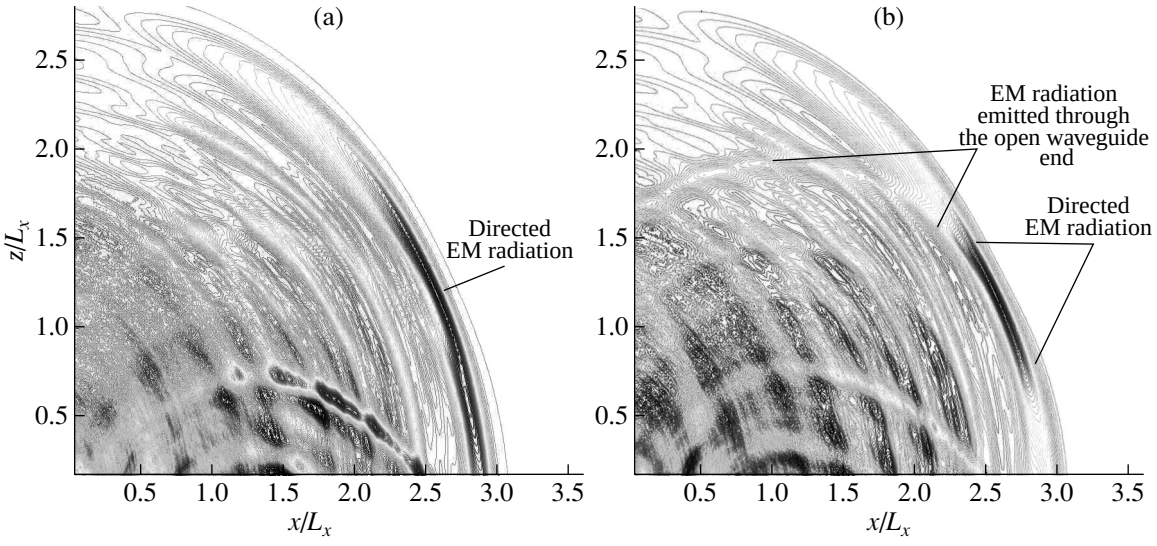

Fig. 14. Spatial distribution of the magnetic field at the time $t = 5$ ns for two versions of an elementary emitter: (a) with a screened and (b) with an open end of the waveguide structure. The emission current from the cathode increases according to the law $J_t = 5 \times 10^{11}$ A/(cm^2 s) ($a = 2.0$).

from a superluminal current source. In Fig. 14b, we also see a cylindrical EM wave emitted through the open end of the waveguide structure. Accordingly, in an emitter with an open waveguide end, the EM field amplitude and the energy flux in the direction in which the radiation is emitted most intensely are seen to sub-

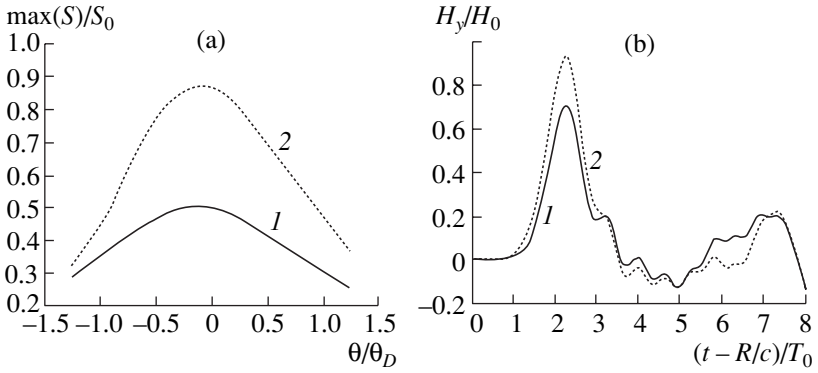

Fig. 15. (a) Angular distributions of the EM radiation flux density and (b) temporal profiles of an EM radiation pulse for two versions of an elementary emitter: (*1*) with a screened and (*2*) an open end of the waveguide structure for $a = 1.42$ and $R/D = 5$. The emission current from the cathode increases according to the law $J_t = 5 \times 10^{11}$ A/(cm^2 s).

stantially exceed those in a system with a screened waveguide end (Fig. 15).

4. CONCLUSION

Our studies have shown that the parameters of an elementary superluminal source obey scaling relations in terms of the growth rate of the electron emission current from the cathode and the parameters of the accelerating diode (the voltage and the distance between the electrodes). The limiting anode current density and the limiting intensity and energy of the EM radiation that can be achieved in such a source have been determined. The maximum achievable anode current density is substantially lower than the steady-state limiting current density because of the additional restrictions on the electron current dynamics that are associated with the influence of the field of the generated EM radiation. The effect of the finite dimensions of the accelerating system on the parameters of the emitter has been investigated. The spatiotemporal characteristics of the emitted EM fields have been obtained as functions of the parameters of the configuration of an accelerating system and the rate of electron emission from the cathode.

ACKNOWLEDGMENTS

This work was supported in part by the International Science and Technology Center (project no. 1158-2000) and the Russian Foundation for Basic Research (project no. 01-02-17629).

REFERENCES

1. Yu. N. Lazarev and P. V. Petrov, Pis'ma Zh. Éksp. Teor. Fiz. **60** (9), 625 (1994) [JETP Lett. **60**, 634 (1994)].
2. Yu. N. Lazarev and P. V. Petrov, Zh. Éksp. Teor. Fiz. **115** (5), 1689 (1999) [JETP **88**, 926 (1999)].
3. A. A. Rukhadze, L. S. Bogdankevich, S. E. Rosinskiĭ, and V. G. Rukhlin, *Physics of High-Current Relativistic Electron Beams* (Atomizdat, Moscow, 1981).
4. L. S. Bogdankevich and A. A. Rukhadze, Usp. Fiz. Nauk **103**, 609 (1971) [Sov. Phys. Usp. **14**, 163 (1971)].
5. A. A. Rukhadze, P. V. Rybak, Ya. K. Khodataev, and V. Shokri, Fiz. Plazmy **22**, 358 (1996) [Plasma Phys. Rep. **22**, 326 (1996)].
6. A. E. Dubinov, Fiz. Plazmy **26**, 439 (2000) [Plasma Phys. Rep. **26**, 409 (2000)].
7. E. V. Diyankova and P. V. Petrov, Preprint No. 99 (All-Russia Research Institute of Experimental Physics, Russian Federal Nuclear Center, Sarov, 1996).
8. A. V. Bessarab, A. V. Kunin, S. P. Martynenko, *et al.*, Tr. RFYaTs–VNIIÉF (Nauchno-Issledovatel'skoe Izd., Sarov, 2001), No. 1, p. 518.
9. *Partial Differential Equation Toolbox User's Guide* (The Mathworks Inc., 1997).

Translated by G.V. Shepekina

Plasma Physics Reports, Vol. 29, No. 6, 2003, pp. 503–511. Translated from Fizika Plazmy, Vol. 29, No. 6, 2003, pp. 540–549.

NONLINEAR PHENOMENA

Nonlinear Scattering of Two Counterpropagating Laser Pulses in an Underdense Plasma

A. A. Frolov

Institute for High Energy Densities, Associated Institute for High Temperatures, Russian Academy of Sciences, Izhorskaya ul. 13/19, Moscow, 125412 Russia

Received November 5, 2002

Abstract—A study is made of the interaction ("collision") of two laser pulses with the same frequency but different durations, propagating toward one another in a low-density plasma. It is found that, in the interaction region, the excitation of small-scale plasma fields localized within a distance on the order of the length of the longer pulse is accompanied by the backscattering of each of the pulses. The frequency shift of the backscattered radiation and its duration depend strongly on the lengths of the interacting pulses. It is shown that the spectrum of the long backscattered radiation "tail" that arises behind the shorter pulse as a result of its interaction with the longer pulse contains satellites shifted from the laser frequency by the plasma frequency. *© 2003 MAIK "Nauka/Interperiodica".*

INTRODUCTION

In recent years, increased attention has been given to the nonlinear effects accompanying the propagation of laser pulses in plasmas. Of particular interest is the investigation of the physical processes occurring in the interaction (collision) between two laser pulses propagating in a plasma toward one another, with the focus on such issues as the amplification of pulses [1, 2], the acceleration of electron bunches [3, 4], the excitation of superstrong wake fields [5], the generation of Bragg mirrors [6], the possibility of deriving information about the structure of the pulses [7], and some other problems [8–11].

In this paper, the nonlinear scattering of two laser pulses during their interaction in an underdense plasma is investigated in one-dimensional geometry. It is shown that, in the interaction region, laser pulses with the same frequency but different lengths generate small-scale plasma perturbations localized within a distance on the order of the length of the longer pulse. In interacting with the small-scale perturbations, each of the laser pulses is backscattered; the frequency shift and duration of the backscattered radiation depend strongly on the lengths of the colliding pulses. In the interaction of two long laser pulses, each of them is backscattered into a pulse whose frequency is equal to the laser carrier frequency and whose duration is determined by the length of the laser pulse propagating in the opposite direction. In the case of short laser pulses, the spectrum of the backscattered pulses contains satellites whose frequencies are shifted from the laser frequency by an amount determined by the plasma frequency and the ratio between the durations of the interacting pulses. In the case of interaction of a long laser pulse with a short counterpropagating laser pulse, the duration of the radiation pulse scattered in the propagation direction of the shorter pulse is determined by the length of the longer pulse. The spectrum of the long backscattered radiation tail that arises behind the shorter laser pulse as a result of scattering contains satellites shifted from the laser frequency by the plasma frequency.

1. SMALL-SCALE PLASMA DENSITY PERTURBATIONS GENERATED IN THE INTERACTION BETWEEN TWO COUNTERPROPAGATING LASER PULSES

We consider two laser pulses with the same frequency but different durations, propagating toward one another along the z-axis in a low-density plasma with the electron density N_{0e} (Fig. 1a). The electric field of laser radiation can be represented as

$$\mathbf{E}_L(z,t) = \frac{1}{2}\exp(-i\omega_0 t) \times [\mathbf{E}_+(z,t)\exp(ik_0 z) + \mathbf{E}_-(z,t)\exp(-ik_0 z)] + \text{c.c.}, \quad (1.1)$$

where $k_0 = (\omega_0/c)\sqrt{\varepsilon(\omega_0)}$; $\varepsilon(\omega) = 1 - \omega_p^2/\omega^2$ is the plasma dielectric function, ω_0 is the laser frequency, $\omega_p = \sqrt{4\pi e^2 N_{0e}/m_e}$ is the plasma frequency ($\omega_0 \gg \omega_p$), e and m_e are the charge and mass of an electron, and c is the speed of light. The amplitudes $\mathbf{E}_\pm(z,t)$ of the electric fields of laser pulses propagating from left to right (the plus sign) and from right to left (the minus sign) are assumed to vary slowly on the spatial and time scales k_0^{-1} and ω_0^{-1}.

When laser pulses begin to overlap, they generate small-scale electron density perturbations $\delta N_e(z,t)$. In

1063-780X/03/2906-0503$24.00

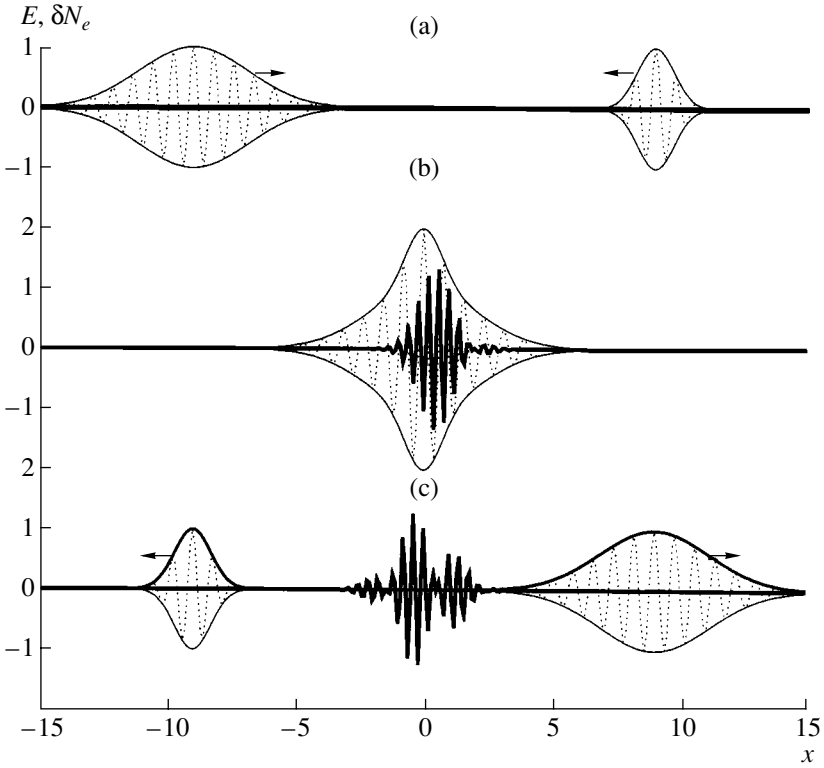

Fig. 1. Schemes illustrating the interaction between a long laser pulse and a short counterpropagating laser pulse and the generation of small-scale plasma fields at different times. The envelopes of the laser electric field and high-frequency oscillations within the laser pulses are represented by light solid curves and dotted curves, respectively. The field amplitudes are given in dimensionless units. The heavy solid curves show the reduced amplitude of the density perturbations, $\frac{\delta N_e}{N_{0e}}\frac{m_e^2\omega_0^2\omega_p^2}{2e^2k_0^2|\mathbf{E}_{0+}\mathbf{E}_{0-}|}$, calculated as a function of the dimensionless coordinate $x = \frac{z}{\sqrt{2}L_-}$ from expression (1.5) at $\omega_p = 0.25\omega_0$ for two laser pulses with the same intensities but different durations $\omega_p\tau_- = \sqrt{2}$, $\tau_+ = 3\tau_-$. Plots (a), (b), and (c) refer to the dimensionless times $\frac{t}{\sqrt{2}\tau_-} = -9$, 0, and 9.

the linear approximation ($\delta N_e \ll N_{0e}$) and under the condition

$$\frac{e^2|\mathbf{E}_{0+}\mathbf{E}_{0-}|}{m_e^2\omega_0^2c^2} \ll \frac{\omega_p^2}{\omega_0^2}, \tag{1.2}$$

the perturbations can be described by the equation [6]

$$\left(\frac{\partial^2}{\partial t^2} + \omega_p^2\right)\frac{\delta N_e}{N_{0e}} = \frac{e^2}{4m_e^2\omega_0^2} \times \frac{\partial^2}{\partial z^2}[(\mathbf{E}_+\mathbf{E}_-^*)\exp(2ik_0z) + (\mathbf{E}_+^*\mathbf{E}_-)\exp(-2ik_0z)]. \tag{1.3}$$

We solve Eq. (1.3) assuming that, in the interaction region, the pulses are Gaussian in shape:

$$\mathbf{E}_+(z,t) = \mathbf{E}_{0+}\exp(-\xi^2/2L_+^2), \quad \mathbf{E}_-(z,t) = \mathbf{E}_{0-}\exp(-\eta^2/2L_-^2), \tag{1.4}$$

where $\xi = z - V_gt$ and $\eta = z + V_gt$ are the spatial coordinates in the comoving frames of reference of the propagating pulses, $V_g = (k_0/\omega_0)c^2$ is the group velocity of the pulses, $L_\pm$ are their lengths, and the vectors $\mathbf{E}_{0\pm}$ characterize their polarization and the maximum amplitudes of their electric fields. The coordinate system is chosen in such a way that, at the initial instant $t = 0$, the functions $\mathbf{E}_+(z,t)$ and $\mathbf{E}_-(z,t)$ are maximum at the point $z = 0$ (Fig. 1b).

With allowance for relationships (1.4), the solution to Eq. (1.3) that satisfies the condition for the electron density to be unperturbed before the two linearly polarized laser pulses start to interact has the form

$$\frac{\delta N_e(z,t)}{N_{0e}} = -\frac{2e^2k_0^2\mathbf{E}_{0+}\mathbf{E}_{0-}}{m_e^2\omega_0^2\omega_p^2} \times \exp\left(-\frac{2z^2}{L_+^2 + L_-^2}\right)\Phi\left(\frac{t}{\tau} + \frac{z}{L}\frac{\tau_+^2 - \tau_-^2}{\tau_+^2 + \tau_-^2}, \omega_p\tau\right)\cos(2k_0z), \tag{1.5}$$

where $\tau = \frac{\sqrt{2}\tau_+\tau_-}{\sqrt{\tau_+^2 + \tau_-^2}}$, $L = V_g\tau = \frac{\sqrt{2}L_+L_-}{\sqrt{L_+^2 + L_-^2}}$, and $\tau_\pm = L_\pm/V_g$ is the duration of the pulses. The time dependence enters solution (1.5) through the function $\Phi(x, a)$ [6]:

$$\Phi(x, a) = a\int_{-\infty}^{x} dy \sin[a(x-y)]\exp(-y^2). \quad (1.6)$$

It should be noted that the amplitude of the density perturbations (1.5) depends on the polarization of the laser pulses and is maximum when the vectors $\mathbf{E}_{0+}$ and $\mathbf{E}_{0-}$ are parallel or antiparallel to each other. When the electric fields of the pulses are mutually orthogonal, $\mathbf{E}_{0+}\mathbf{E}_{0-} = 0$, small-scale electron density perturbations (1.5) are not generated. The reason is that, in this case, the Lorentz force vanishes, because, in the field of either pulse, the electrons move along the magnetic field of the other pulse.

Now, using asymptotic expansions of the function $\Phi(x, a)$, we investigate the spatiotemporal evolution of density perturbations (1.5) generated by laser pulses with different durations τ_+ and τ_-.

In the case of collision between two long laser pulses ($\omega_p\tau_\pm \gg 1$), the parameter $\omega_p\tau$ is large and function (1.6) is described by the asymptotic formula [6]

$$\Phi(x, a) = \frac{a^2}{a^2 + 4x^2}\exp(-x^2) + \frac{\sqrt{\pi}}{2}a\exp\left(-\frac{a^2}{4}\right)\sin(ax), \quad (1.7)$$

which is valid for $a \gg 1, x$. As a result, we arrive at the following expression for density perturbations (1.5):

$$\frac{\delta N_e(z, t)}{N_{0e}} = -\frac{2e^2k_0^2\mathbf{E}_{0+}\mathbf{E}_{0-}}{m_e^2\omega_0^2\omega_p^2} \times \left\{\exp\left(-\frac{2t^2}{\tau_+^2 + \tau_-^2} - \frac{1}{L^2}\left(z + V_g t\frac{\tau_+^2 - \tau_-^2}{\tau_+^2 + \tau_-^2}\right)^2\right) + \frac{\sqrt{\pi}}{2}\omega_p\tau\exp\left(-\frac{2z^2}{L_+^2 + L_-^2} - \frac{\omega_p^2\tau^2}{4}\right) \times \sin\left(\omega_p t + k_p z\frac{\tau_+^2 - \tau_-^2}{\tau_+^2 + \tau_-^2}\right)\right\}\cos(2k_0z). \quad (1.8)$$

The first term in parentheses in expression (1.8) describes quasistatic electron density perturbations, which are excited only during the time interval $\Delta t \approx \sqrt{(\tau_+^2 + \tau_-^2)/2}$ and disappear after the interaction. During the entire interaction process, the amplitude of the density perturbations excited in the interaction between two pulses with the same duration ($\tau_+ = \tau_-$) is maximum at $z = 0$. In the case of pulses with different durations ($\tau_+ \neq \tau_-$), the position of maximum amplitude moves at the velocity $V = -V_g\frac{\tau_+^2 - \tau_-^2}{\tau_+^2 + \tau_-^2}$ in the propagation direction of the shorter pulse. The second term in parentheses in expression (1.8) implies that the plasma oscillations remaining in the interaction region after the interaction process has come to an end are exponentially small.

In the case of collision between two short laser pulses ($\omega_p\tau_\pm \leq 1$) or between a short pulse ($\omega_p\tau_- \leq 1$) and a long pulse ($\omega_p\tau_+ \gg 1$), the parameter $\omega_p\tau$, characterizing the time during which the pulses overlap, is small, $\omega_p\tau \leq 1$. In this case, small-scale plasma perturbations are excited by a short-term driving force (in a shocklike fashion). Using the asymptotic representation [6]

$$\Phi(x, a) = \sqrt{\pi}a\exp(-a^2/4)\sin(ax), \quad (1.9)$$

which is valid for $x > 0$ such that $x \gg 1, a$, we arrive at the following expression for the density perturbations that remain in the interaction region after the interaction process has come to an end:

$$\frac{\delta N_e(z, t)}{N_{0e}} = -2\sqrt{\pi}\omega_p\tau\frac{e^2k_0^2\mathbf{E}_{0+}\mathbf{E}_{0-}}{m_e^2\omega_0^2\omega_p^2} \times \exp\left(-\frac{2z^2}{L_+^2 + L_-^2} - \frac{\omega_p^2\tau^2}{4}\right)\sin\left(\omega_p t + k_p z\frac{\tau_+^2 - \tau_-^2}{\tau_+^2 + \tau_-^2}\right) \times \cos(2k_0z). \quad (1.10)$$

The plasma oscillations that are excited in the interaction of two pulses with the same duration ($\tau_+ = \tau_-$) are long-lived small-scale standing waves. The spatiotemporal evolution of the plasma perturbations generated by two laser pulses with different durations is more complicated. In the interaction between a short and a long laser pulse, small-scale wake plasma fields are excited behind the shorter pulse (Fig. 1b). The small-scale plasma oscillations that remain in the interaction region after the interaction process has come to an end are localized within a distance on the order of the length of the longer pulse (Fig. 1c). In this case, the positions of the zeros of the density perturbation amplitude and of its maxima and minima are determined by the function $\cos(2k_0z)$ and are fixed in space, and the envelope of the small-scale perturbations moves in the propagation direction of the shorter pulse.

2. SCATTERING OF LASER PULSES BY SMALL-SCALE PLASMA FIELDS

In interacting with one another, two laser pulses generate small-scale plasma fields and are backscattered by them. For the pulse propagating from left to right, the electric field $\mathbf{E}_S^+(z, t)$ of the backscattered radiation satisfies the conventional equation of scattering theory [12]:

$$\left(\frac{\partial^2}{\partial t^2} + \omega_p^2 - c^2\frac{\partial^2}{\partial z^2}\right)\mathbf{E}_S^+(z, t) = -\omega_p^2\frac{\delta N_e}{N_{0e}}\left[\frac{1}{2}\mathbf{E}_+\exp(-i\omega_0 t + ik_0 z) + \text{c.c.}\right], \quad (2.1)$$

where the density perturbations δN_e are given by expression (1.5). An analogous equation is valid for a laser pulse propagating in the opposite direction.

To solve Eq. (2.1), we apply the Fourier transformation in time and in the longitudinal coordinate:

$$\mathbf{E}_S^+(z, t) = \int\frac{d\omega dk}{(2\pi)^2}\exp(-i\omega t + ikz)\mathbf{E}_S^+(\omega, k),$$
$$\mathbf{E}_S^+(\omega, k) = \int dt dz\exp(i\omega t - ikz)\mathbf{E}_S^+(z, t). \quad (2.2)$$

With allowance for expressions (1.4), the Fourier transformed electric field of the scattered pulse has the form

$$\mathbf{E}_S^+(\omega, k) = \frac{1}{2}\mathbf{E}_{0+}(2\pi)^{3/2}L_+\frac{\omega_p^2}{\omega^2\varepsilon(\omega) - c^2k^2} \times\int\frac{d\omega' dk'}{(2\pi)^2}\frac{\delta N_e(\omega - \omega', k - k')}{N_{0e}} \times\left\{\delta[\omega' - \omega_0 - (k' - k_0)V_g]\exp\left(-\frac{(\omega' - \omega_0)^2\tau_+^2}{2}\right)\right.$$
$$\left. + \delta[\omega' + \omega_0 - (k' + k_0)V_g]\exp\left(-\frac{(\omega' + \omega_0)^2\tau_+^2}{2}\right)\right\}, \quad (2.3)$$

in which the Fourier transformed density perturbations $\delta N_e(\omega, k)$ can be found from Eq. (1.3):

$$\frac{\delta N_e(\omega, k)}{N_{0e}} = \frac{e^2\mathbf{E}_{0+}\mathbf{E}_{0-}}{4m_e^2\omega_0^2}\frac{\pi k^2 V_g\tau_+\tau_-}{\omega^2\varepsilon(\omega)}\exp\left(-\frac{\omega^2\tau^2}{4}\right) \times\left\{\exp\left[-\left(k - 2k_0 + \frac{\omega}{V_g}\frac{\tau_+^2 - \tau_-^2}{\tau_+^2 + \tau_-^2}\right)^2\frac{L_+^2 + L_-^2}{8}\right]\right.$$
$$\left. + \exp\left[-\left(k + 2k_0 + \frac{\omega}{V_g}\frac{\tau_+^2 - \tau_-^2}{\tau_+^2 + \tau_-^2}\right)^2\frac{L_+^2 + L_-^2}{8}\right]\right\}. \quad (2.4)$$

Taking into account expression (2.4), we integrate over the frequencies ω' and wavenumbers k' in formula (2.3) to obtain

$$\mathbf{E}_S^+(\omega, k) = \frac{ie^2\mathbf{E}_{0+}(\mathbf{E}_{0+}\mathbf{E}_{0-})\pi^{3/2}k_p\tau_-}{16\sqrt{2}m_e^2\omega_0^2[\omega^2\varepsilon(\omega) - c^2k^2]} \times\left\{\exp\left[-\left(k + k_0 - \frac{\omega - \omega_0}{V_g}\right)^2\frac{L_+^2 + L_-^2}{8}\right]\exp\left[-\frac{(\omega - \omega_0)^2\tau_+^2}{2}\right]\right.$$
$$\times\left[L_+^2\left(k - k_0 - \frac{\omega - \omega_0 + \omega_p}{V_g}\right)^2[1 - \text{erf}(i\alpha_-)]\right.$$
$$\left.\times\exp\left(-\frac{\omega_p\tau_+^2}{2}[3(\omega - \omega_0) + 2\omega_p - (k + k_0)V_g]\right)\right.$$
$$\left. - L_+^2\left(k - k_0 - \frac{\omega - \omega_0 - \omega_p}{V_g}\right)^2[1 - \text{erf}(i\alpha_+)]\right.$$
$$\left.\times\exp\left(\frac{\omega_p\tau_+^2}{2}[3(\omega - \omega_0) - 2\omega_p - (k + k_0)V_g]\right)\right] \quad (2.5)$$
$$+\exp\left[-\left(k - k_0 - \frac{\omega + \omega_0}{V_g}\right)^2\frac{L_+^2 + L_-^2}{8} - \frac{(\omega + \omega_0)^2\tau_+^2}{2}\right]$$
$$\times\left[L_+^2\left(k + k_0 - \frac{\omega + \omega_0 + \omega_p}{V_g}\right)^2[1 - \text{erf}(i\beta_-)]\right.$$
$$\left.\times\exp\left(-\frac{\omega_p\tau_+^2}{2}[3(\omega + \omega_0) + 2\omega_p - (k - k_0)V_g]\right)\right.$$
$$\left. - L_+^2\left(k + k_0 - \frac{\omega + \omega_0 - \omega_p}{V_g}\right)^2[1 - \text{erf}(i\beta_+)]\right.$$
$$\left.\times\exp\left(\frac{\omega_p\tau_+^2}{2}[3(\omega + \omega_0) - 2\omega_p - (k - k_0)V_g]\right)\right]\right\},$$

where $k_p = \omega_p/V_g$ is the wavenumber of the plasma oscillations, $\text{erf}(z) = \frac{2}{\sqrt{\pi}}\int_0^z dt\exp(-t^2)$ is the error function of the complex argument, $\alpha_\pm = \frac{\tau_+}{4}[(k + k_0)V_g - 3(\omega - \omega_0) \pm 4\omega_p]$, and $\beta_\pm = \frac{\tau_+}{4}[(k - k_0)V_g - 3(\omega + \omega_0) \pm 4\omega_p]$.

The spectral density $\mathbf{E}_S^+(\omega, z)$ of the electric field of the scattered pulse can be solved for by taking the inverse Fourier transformation of expression (2.5) in the longitudinal coordinate [see the first of formulas (2.2)]. Applying the saddle point method, we find that the main contribution to the integral over the wavenumbers comes from the residue at the pole $k = -\omega\sqrt{\varepsilon(\omega)}/c$, which corresponds to backscattering.

Then, at large distances $z < 0$ from the region where the density perturbations are localized, the Fourier transformed backscattered field has the form

$$\mathbf{E}_S^+(\omega, z) = \frac{\pi^{3/2}\omega_p\tau_+\tau_-}{2\sqrt{2}}k_0L_+\frac{e^2\mathbf{E}_{0+}(\mathbf{E}_{0+}\mathbf{E}_{0-})}{4m_e^2\omega_0^2c^2}$$

$$\times\left\{\exp\left[-i\frac{\omega}{c}\sqrt{\varepsilon(\omega)}z-\frac{(\omega-\omega_0)^2\tau_-^2}{2}\right]\right.$$

$$\times\{[1+\mathrm{erf}(i[\omega-\omega_0+\omega_p]\tau_+)]$$

$$\times\exp(-[\omega-\omega_0+\omega_p]^2\tau_+^2)$$

$$-[1+\mathrm{erf}(i[\omega-\omega_0-\omega_p]\tau_+)]$$

$$\left.\times\exp(-[\omega-\omega_0-\omega_p]^2\tau_+^2)\right\} \qquad (2.6)$$

$$+\exp\left[i\frac{\omega}{c}\sqrt{\varepsilon(\omega)}z-\frac{(\omega+\omega_0)^2\tau_-^2}{2}\right]$$

$$\times\{[1+\mathrm{erf}(i[\omega+\omega_0+\omega_p]\tau_+)]$$

$$\times\exp(-[\omega+\omega_0+\omega_p]^2\tau_+^2)$$

$$-[1+\mathrm{erf}(i[\omega+\omega_0-\omega_p]\tau_+)]$$

$$\times\exp(-[\omega+\omega_0-\omega_p]^2\tau_+^2)\}\}.$$

For the pulse propagating from left to right, the spatiotemporal structure of the backscattered radiation can be evaluated by taking the inverse Fourier transformation of formula (2.6) in time:

$$\mathbf{E}_S^+(z, t) = \sqrt{\pi}k_0L_+\frac{e^2\mathbf{E}_{0+}(\mathbf{E}_{0+}\mathbf{E}_{0-})}{4m_e^2\omega_0^2c^2}$$

$$\times\exp\left[-\frac{\eta^2}{2(L_-^2+2L_+^2)}\right] \qquad (2.7)$$

$$\times\Phi\left(\frac{\eta}{\sqrt{2}L_-\sqrt{1+\tau_-^2/2\tau_+^2}},\frac{\sqrt{2}\omega_p\tau_-}{\sqrt{1+\tau_-^2/2\tau_+^2}}\right)\sin(\omega_0t+k_0z).$$

In deriving expression (2.7) from formula (2.6), we used the following expansion in the small deviation $\Omega = \omega - \omega_0$ from the laser frequency:

$$\frac{\omega}{c}\sqrt{\varepsilon(\omega)}\approx k_0+\frac{\Omega}{V_g}.$$

In this expansion, we neglected the terms of the second order in Ω, which indicates the smallness of the dispersive spreading of the backscattered radiation pulse and is justified under the condition

$$z < k_0L_-^2\frac{\omega_0^2}{\omega_p^2}.$$

Expression (2.7) can also be obtained directly by solving a reduced version of Eq. (2.1) with allowance for relationship (1.5).

For the pulse propagating from right to left, the electric field of the backscattered radiation is obtained in an analogous manner. At large distances $z > 0$ from the interaction region, it has the form

$$\mathbf{E}_S^-(z, t) = \sqrt{\pi}k_0L_-\frac{e^2\mathbf{E}_{0-}(\mathbf{E}_{0+}\mathbf{E}_{0-})}{4m_e^2\omega_0^2c^2}$$

$$\times\exp\left[-\frac{\xi^2}{2(L_+^2+2L_-^2)}\right] \qquad (2.8)$$

$$\times\Phi\left(-\frac{\xi}{\sqrt{2}L_+\sqrt{1+\tau_+^2/2\tau_-^2}},\frac{\sqrt{2}\omega_p\tau_+}{\sqrt{1+\tau_+^2/2\tau_-^2}}\right)\sin(\omega_0t-k_0z),$$

where the function $\Phi(x, a)$ is given by formula (1.6).

Electric fields (2.7) and (2.8) depend on the polarization of laser pulses. The fields have maximum amplitudes when the vectors $\mathbf{E}_{0+}$ and $\mathbf{E}_{0-}$ are parallel or antiparallel to each other and vanish when the vectors $\mathbf{E}_{0+}$ and $\mathbf{E}_{0-}$ are mutually orthogonal.

It follows from expressions (2.7) and (2.8) that, for each of the laser pulses, the ratio of the amplitude of the electric field of the backscattered radiation to the laser field amplitude contains the product of the large quantity $k_0L_\pm$, which is proportional to the number of spatial periods of small-scale plasma perturbations, and the parameter $e^2(\mathbf{E}_{0+}\mathbf{E}_{0-})/4m_e^2\omega_0^2c^2$, which is small by virtue of condition (1.2). In deriving expression (1.5) for density perturbations, the contribution of the scattered fields was assumed to be small and, accordingly, was neglected. Thus, the condition $|\mathbf{E}_S^\pm| < |\mathbf{E}_{0\pm}|$ and inequality (1.2) yield the following restriction on the parameters of the plasma and the laser pulses:

$$\frac{\pi}{4}\frac{\omega_p}{\omega_0}\omega_p\tau_\pm \le 1.$$

Let us analyze how electric fields (2.7) and (2.8) depend on the duration of laser pulses. In the case of a collision between two long laser pulses ($\omega_p\tau_\pm \gg 1$), the

electric field of the backscattered radiation with allowance for asymptotic formula (1.7) has the form

$$\mathbf{E}_S^{\pm}(z,t) = \sqrt{\pi}k_0 L_{\pm}\frac{e^2\mathbf{E}_{0\pm}(\mathbf{E}_{0+}\mathbf{E}_{0-})}{4m_e^2\omega_0^2c^2} \times \exp\left\{-\frac{(z\pm V_g t)^2}{2L_{\mp}^2}\right\}\sin(\omega_0 t \pm k_0 z). \quad (2.9)$$

The small-scale density perturbations excited in the collision are quasistatic, and each of the two laser pulses is backscattered into a radiation pulse whose duration is determined by the length of the laser pulse propagating in the opposite direction and whose frequency is equal to the laser frequency.

An interaction between two short laser pulses ($\omega_p\tau_{\pm} \le 1$) or between a long pulse ($\omega_p\tau_+ \gg 1$) and a short pulse ($\omega_p\tau_- \le 1$) is accompanied by the excitation of plasma oscillations in the interaction region. In this case, the electric fields of the backscattered radiation pulses can be found by using asymptotic representation (1.9):

$$\mathbf{E}_S^{\pm}(z,t) = \frac{\pi k_0 L_+\omega_p\tau_-}{\sqrt{2+\tau_{\mp}^2/\tau_{\pm}^2}}\frac{e^2\mathbf{E}_{0\pm}(\mathbf{E}_{0+}\mathbf{E}_{0-})}{4m_e^2\omega_0^2c^2} \times \exp\left\{-\frac{\omega_p^2\tau_+^2\tau_-^2}{\tau_{\mp}^2+2\tau_{\pm}^2}-\frac{(z\pm V_g t)^2}{2(L_{\mp}^2+2L_{\pm}^2)}\right\} \times\left\{\cos\left[\left(\omega_0-\frac{\omega_p}{1+\tau_{\mp}^2/2\tau_{\pm}^2}\right)t\pm\left(k_0-\frac{k_p}{1+\tau_{\mp}^2/2\tau_{\pm}^2}\right)z\right]\right. \left.-\cos\left[\left(\omega_0+\frac{\omega_p}{1+\tau_{\mp}^2/2\tau_{\pm}^2}\right)t\pm\left(k_0+\frac{k_p}{1+\tau_{\mp}^2/2\tau_{\pm}^2}\right)z\right]\right\}. \quad (2.10)$$

In the case of a collision between short laser pulses, we see from expressions (2.10) that the frequency and wavenumber of each of the backscattered radiation pulses are shifted from the frequency and wavenumber of the laser radiation by the amounts $\omega_0 \pm \frac{\omega_p}{1+\tau_{\mp}^2/2\tau_{\pm}^2}$ and $k_0 \pm \frac{k_p}{1+\tau_{\mp}^2/2\tau_{\pm}^2}$, respectively. The frequency shift is strongly dependent on the ratio between the durations of the laser pulses.

An analysis of the interaction of a long ($\omega_p\tau_+ \gg 1$) and a short ($\omega_p\tau_- \le 1$) laser pulse reveals the following interesting effect. According to formula (2.10), the backscattered electric field of the longer pulse at $\frac{\eta}{L_-} \gg 1$, $\omega_p\tau_-$ has the form

$$\mathbf{E}_S^{+}(z,t) = \frac{\pi k_0 L_+\omega_p\tau_-}{\sqrt{2}}\frac{e^2\mathbf{E}_{0+}(\mathbf{E}_{0+}\mathbf{E}_{0-})}{4m_e^2\omega_0^2c^2} \times \exp\left\{-\frac{\omega_p^2\tau_-^2}{2}-\frac{\eta^2}{4L_+^2}\right\} \times\{\cos[(\omega_0-\omega_p)t+(k_0-k_p)z] -\cos[(\omega_0+\omega_p)t+(k_0+k_p)z]\}. \quad (2.11)$$

According to the same formula, the backscattered electric field of the shorter pulse at $\frac{\xi}{L_+} \gg \frac{\tau_+}{\tau_-}$, $\omega_p\tau_+$ is expressed as

$$\mathbf{E}_S^{-}(z,t) = \pi k_0 L_-\omega_p\tau_-\frac{e^2\mathbf{E}_{0-}(\mathbf{E}_{0+}\mathbf{E}_{0-})}{4m_e^2\omega_0^2c^2} \times \exp\left\{-\omega_p^2\tau_-^2-\frac{\xi^2}{2L_+^2}\right\} \times\left\{\cos\left[\left(\omega_0-2\omega_p\frac{\tau_-^2}{\tau_+^2}\right)t-\left(k_0-2k_p\frac{\tau_-^2}{\tau_+^2}\right)z\right]\right. \left.-\cos\left[\left(\omega_0+2\omega_p\frac{\tau_-^2}{\tau_+^2}\right)t-\left(k_0+2k_p\frac{\tau_-^2}{\tau_+^2}\right)z\right]\right\}. \quad (2.12)$$

The frequency of backscattered electric field (2.12) of the shorter pulse is close to the laser frequency ω_0, the pulse length being comparable with the length L_+ of the longer laser pulse. Consequently, after the interaction, this field has an insignificant impact on the spectral parameters of the longer laser pulse and on its shape. On the other hand, backscattered electric field (2.11) of the longer pulse propagates in the direction of the shorter laser pulse, thereby distorting the shape of the latter and changing its spectrum. As a result, from formula (2.11), we can see that, after the interaction, the spectrum of the backscattered pulse propagating from right to left contains not only the fundamental harmonic at the laser carrier frequency ω_0 but also satellite harmonics at the frequencies $\omega_0 \pm \omega_p$ and the pulse length is determined by the duration of the longer laser pulse. Such an increase in the backscattered pulse length is explained as being due to the scattering of the laser field by the small-scale plasma oscillations that are generated over a distance comparable to the length of the longer laser pulse. The radiation pulse into which the longer laser pulse is backscattered is also long. As a result, when this long backscattered pulse overlaps with

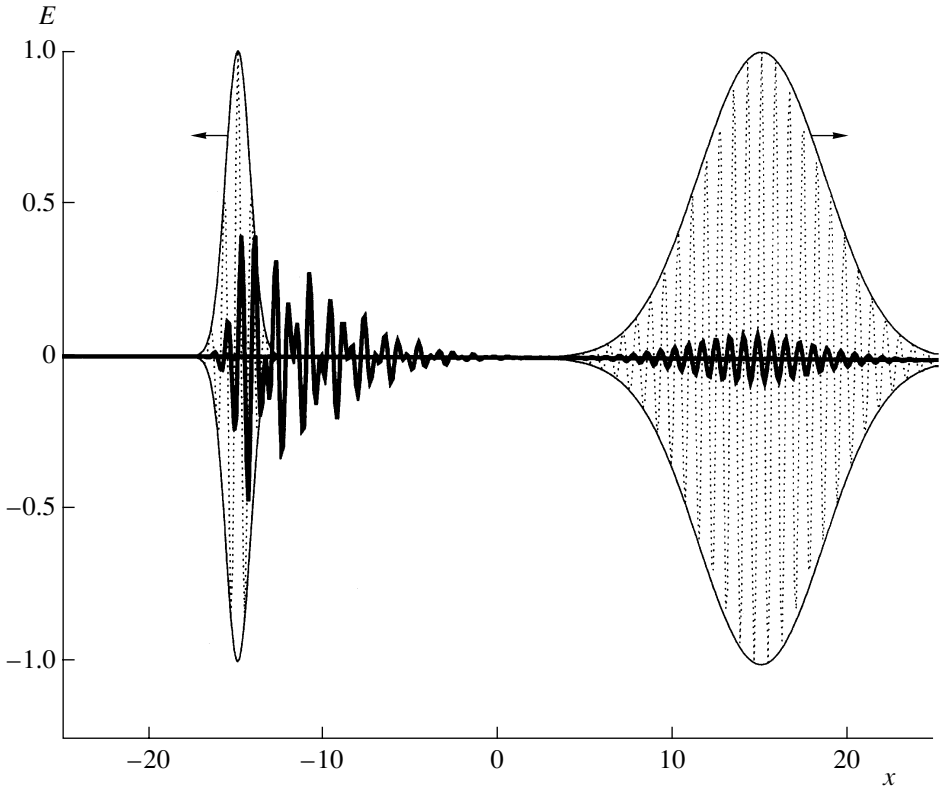

Fig. 2. Laser fields calculated numerically from formulas (1.4), (2.7), and (2.8) as functions of the dimensionless coordinate $x = \frac{z}{\sqrt{2}L_-}$ at the time $\frac{t}{\sqrt{2}\tau_-} = 15$. The electric fields of the laser pulses and backscattered radiation are normalized to the electric fields $E_{0\pm}$ and are shown by light solid curves (and the dotted curves within) and a heavy solid curve, respectively. The calculations were carried out for laser pulses with intensities $I_+ = I_- = 5.1 \times 10^{16}$ W/cm^2 and durations $\omega_p\tau_- = \sqrt{2}$, $\tau_+ = 5\tau_-$ and for a plasma with $\omega_p = 0.25\omega_0$.

the field of the shorter laser pulse, it gives rise to a long radiation tail behind the latter. The results of numerical calculations based on formulas (2.7) and (2.8) are illustrated in Fig. 2, which shows that a long backscattered radiation tail actually arises behind a short laser pulse after its interaction with a long laser pulse.

The spectral features of backscattered laser radiation can be derived from a straightforward analysis of expression (2.6). Simple transformations of this expression in the range of positive frequencies ($\omega > 0$) yield

$$\mathbf{E}_S^+(\omega, z) = \frac{\pi^{3/2}\omega_p\tau_+\tau_-}{2\sqrt{2}}k_0L_+\frac{e^2\mathbf{E}_{0+}(\mathbf{E}_{0+}\mathbf{E}_{0-})}{4m_e^2\omega_0^2c^2} \times \exp\left(-i\frac{\omega}{c}\sqrt{\varepsilon(\omega)}z\right)G_+(\omega), \quad (2.13)$$

where the frequency dependence of the electric field of the backscattered laser radiation is determined by the function $G_+(\omega)$,

$$G_+(\omega) = \exp\left(-\frac{\omega_p^2\tau_+^2\tau_-^2}{\tau_-^2 + 2\tau_+^2}\right) \times \left\{\exp\left[-\left(\omega - \omega_0 + \frac{\omega_p}{1 + \tau_-^2/2\tau_+^2}\right)^2(\tau_+^2 + \tau_-^2/2)\right] \times [1 + \mathrm{erf}(i[\omega - \omega_0 + \omega_p]\tau_+)]\right. \quad (2.14)$$
$$\left. - \exp\left[-\left(\omega - \omega_0 - \frac{\omega_p}{1 + \tau_-^2/2\tau_+^2}\right)^2(\tau_+^2 + \tau_-^2/2)\right] \times [1 + \mathrm{erf}(i[\omega - \omega_0 - \omega_p]\tau_+)]\right\}.$$

Resulting formulas (2.13) and (2.14) show that the spectrum of the backscattered radiation contains satellites at the frequencies $\omega = \omega_0 \pm \frac{\omega_p}{1 + \tau_-^2/2\tau_+^2}$, which depend on the ratio between the durations of the interacting laser pulses.

From expression (2.13) for the electric field, we can find the backscattered radiation energy dW_S^+ per frequency interval $d\omega$:

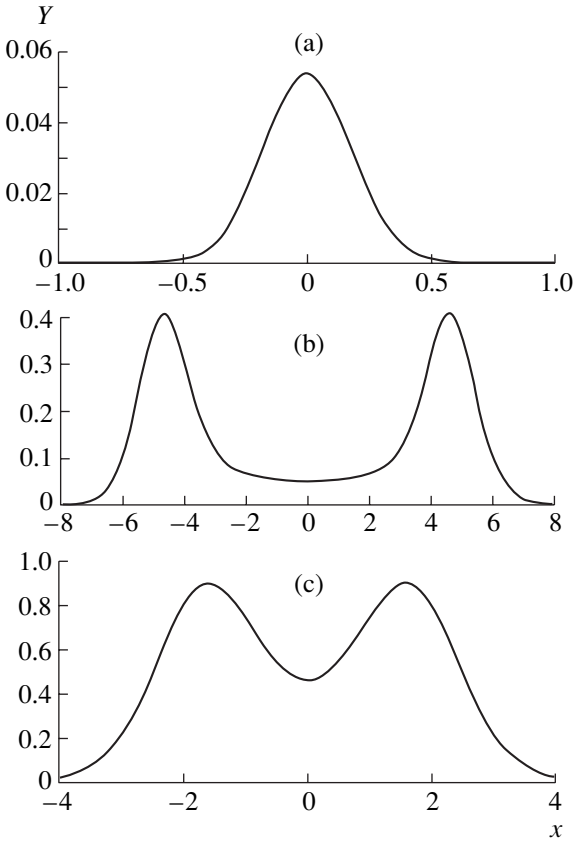

Fig. 3. Dependence of the function $Y = |G_+(\omega)|^2$ on the dimensionless frequency $X = (\omega - \omega_0)\tau_+$ for different ratios between the lengths of the interacting laser pulses: (a) the interaction of two long pulses with the durations $\omega_p\tau_+ = 5$ and $\omega_p\tau_- = 20$, (b) the interaction of a long ($\omega_p\tau_+ = 5$) and a short ($\omega_p\tau_- = 1$) pulse, and (c) the interaction of two short pulses with the durations $\omega_p\tau_+ = 2$ and $\omega_p\tau_- = 0.5$.

$$\frac{dW_S^+}{d\omega} = \frac{\pi^{3/2}\omega_p^2\tau_-^2k_0^2L_+^2}{4}\tau_+W_L^+\frac{e^4(\mathbf{E}_{0+}\mathbf{E}_{0-})^2}{16m_e^4\omega_0^4c^4}|G_+(\omega)|^2, \quad (2.15)$$

where W_L^+ is the energy of the laser pulse propagating from left to right.

The total energy W_S^+ of the backscattered radiation is obtained by integrating expression (2.15) over frequency. For a collision between a long pulse ($\omega_p\tau_+ \gg 1$) and a short counterpropagating pulse ($\omega_p\tau_- \leq 1$), the integral over the frequency spectrum can be taken analytically,

$$\int_0^\infty d\omega|G_+(\omega)|^2 = \frac{2\sqrt{2\pi}}{\tau_+}\exp(-\omega_p^2\tau_-^2), \quad (2.16)$$

and the total backscattered radiation energy is equal to

$$W_S^+ = \frac{\pi^2\omega_p^2\tau_-^2k_0^2L_+^2}{\sqrt{2}}W_L^+\frac{e^4(\mathbf{E}_{0+}\mathbf{E}_{0-})^2}{16m_e^4\omega_0^4c^4}\exp(-\omega_p^2\tau_-^2). \quad (2.17)$$

Figure 3 shows the backscattered radiation spectra calculated for different ratios between the durations of the interacting laser pulses. For two long laser pulses, the frequency of the backscattered radiation coincides with the laser carrier frequency (Fig. 3a). In the case of a collision between a long and a short laser pulse, the backscattering spectrum contains two satellites shifted from the laser frequency by the plasma frequency (Fig. 3b). In the case of two short laser pulses, the spectrum of the backscattered field contains satellites at the frequencies $\omega = \omega_0 \pm \frac{\omega_p}{1 + \tau_-^2/2\tau_+^2}$; however, the spectral peaks are close to one another and partially overlap, which is a consequence of the short pulse lengths (Fig. 3c).

It should be noted that the cold plasma approximation used here is valid for small-scale plasma oscillations under the assumption of a negligible spatial dispersion, i.e., only under the condition

$$\delta^2 = 12\frac{V_T^2}{c^2}\frac{\omega_0^2}{\omega_p^2} \ll 1, \quad (2.18)$$

where $V_T = \sqrt{\frac{T_e}{m_e}}$ is the electron thermal velocity and T_e is the electron temperature. Additionally, the condition that the Landau damping of small-scale plasma oscillations is insignificant during the entire interaction process yields the restrictions

$$\omega_p\tau_\pm < \frac{\delta^3}{3}\exp\left(\frac{3}{2\delta^2} + \frac{3}{2}\right), \quad (2.19)$$

which relate the durations of the laser pulses to the electron temperature.

CONCLUSION

In this paper, a simple one-dimensional hydrodynamic model has been applied to study the nonlinear scattering of two counterpropagating laser pulses in their interaction in a plasma and to investigate the shape of the backscattered radiation pulses and their spectral parameters. In particular, it has been shown that a long backscattered radiation tail arises behind a short laser pulse after its collision with a long laser pulse and that the length of the tail is comparable to the length of the longer pulse. It has also been found that the backscattered radiation spectrum contains satellites shifted from the laser frequency by nearly the plasma frequency. The presence of such satellites may provide the basis for

diagnosing both the plasma and the interacting laser pulses.

Note that the results obtained in one-dimensional geometry change only slightly when the finite transverse dimensions of the laser pulses are taken into account. The difference is that, in three-dimensional geometry, the electromagnetic radiation is scattered in the near-backward (rather than backward) direction, i.e., at such angles θ to the pulse propagation direction that are close to π: $\pi - \theta \le 1/k_0 D$, where D is the diameter of the focal spot of laser light. Another difference lies in the dependence of the amplitude of the electric field of the backscattered laser radiation on the spatial coordinates. However, the main conclusions of the one-dimensional theory, specifically, those concerning the spectral parameters of the backscattered radiation and its longitudinal structure, remain valid in three-dimensional geometry.

Let us estimate the electric field and the energy of radiation backscattered in the interaction of a long laser pulse with intensity $I_+ = 1.2 \times 10^{15}$ W/cm^2, duration $\tau_+ = 330$ fs, and wavelength $\lambda_0 = 0.8$ μm and a counterpropagating, less intense, short laser pulse with intensity $I_- = 1.2 \times 10^{14}$ W/cm^2, duration $\tau_- = 14$ fs, and the same wavelength in a low-density plasma with electron temperature $T_e = 20$ eV and electron density $N_{0e} = 3.2 \times 10^{18}$ cm^{-3}. The amplitude of the plasma density perturbations excited in the interaction region is about $\delta N_e \approx 0.2 N_{0e}$. After the interaction, the radiation pulse propagating from right to left is longer by a factor of 30 times than the original length of the shorter pulse because of the contribution of the backscattered radiation of the longer pulse. Although the electric field amplitude is small, $E_S^+ \approx 0.13 E_{0-}$, backscattered radiation energy (2.17) amounts to about 50% of the energy of the shorter laser pulse. In this case, inequalities (2.18) and (2.19) are satisfied, because the parameter δ^2 is approximately equal to 0.28 and, thus, the small-scale plasma oscillations in question can be described in the cold plasma approximation.

Since the above analysis assumes that the small-scale density perturbations are linear [see Eq. (1.3) and condition (1.2)], it is restricted to laser pulse intensities of 10^{15}–10^{16} W/cm^2 at $\lambda_0 \cong 1$ μm. In fact, however, present-day laser devices can operate at far higher intensities, in which case the electron density perturbations are strongly nonlinear. It can be expected that the backscattering efficiency will increase with laser intensity; hence, it makes sense to speak of the possible reflection of laser pulses from the interaction region.

The above analysis deals exclusively with the excitation of radiation at a frequency close to the laser carrier frequency. However, two interacting laser pulses can also generate low-frequency radiation at a frequency twice the plasma frequency. This issue will be addressed in a separate paper.

ACKNOWLEDGMENTS

I am grateful to L.M. Gorbunov for fruitful discussions and useful remarks. I also thank N.E. Andreev for critical comments and A.N. Vasil'ev and S.V. Kuznetsov for their help in carrying out simulations. This work was supported in part by the Russian Foundation for Basic Research, project nos. 01-02-16723 and 02-02-16110.

REFERENCES

1. V. M. Malkin, G. Shvets, and N. J. Fisch, Phys. Plasmas **7**, 2232 (2000); Phys. Rev. Lett. **84**, 1208 (2000).
2. Y. Ping, I. Geltner, N. J. Fisch, *et al.*, Phys. Rev. E **62**, 4532 (2000).
3. G. Shvets, N. J. Fisch, A. Pukhov, and J. Meyer-ter-Vehn, Phys. Rev. E **60**, 2218 (1999).
4. C. B. Schroeder, P. B. Lee, and J. S. Wurtele, Phys. Rev. E **59**, 6037 (1999).
5. K. Nagashima, J. Koga, and M. Kando, Phys. Rev. E **64**, 066403 (2001).
6. L. M. Gorbunov and A. A. Frolov, Zh. Éksp. Teor. Fiz. **120**, 583 (2001) [JETP **93**, 510 (2001)].
7. I. Y. Dodin and N. J. Fish, Phys. Rev. Lett. **88**, 165001 (2002).
8. G. Shvets and A. Pukhov, Phys. Rev. E **59**, 1033 (1999).
9. B. Shen and J. Meyer-ter-Vehn, Phys. Rev. E **65**, 016405 (2002).
10. Yu. Tsidulko, V. M. Malkin, and N. J. Fisch, Phys. Rev. Lett. **88**, 235004 (2002).
11. L. M. Gorbunov and A. A. Frolov, Fiz. Plazmy **29**, 440 (2003) [Plasma Phys. Rep. **29**, 407 (2003)].
12. L. D. Landau and E. M. Lifshitz, *Electrodynamics of Continuous Media* (Nauka, Moscow, 1982; Pergamon Press, New York, 1984).

Translated by O.E. Khadin

Plasma Physics Reports, Vol. 29, No. 6, 2003, pp. 512–516. Translated from Fizika Plazmy, Vol. 29, No. 6, 2003, pp. 550–554.

PLASMA TURBULENCE

Effect of the External Magnetic Field on the MHD Turbulence Spectra

E. Golbraikh*, S. S. Moiseev†, and A. Eidelman*****

**Center for MHD Studies, Ben-Gurion University of the Negev, Beer-Sheva, Israel*

***Institute for Space Research, Russian Academy of Sciences, Profsoyuznaya ul. 84/32, Moscow, 117810 Russia*

****Mechanical Engineering Department, Ben-Gurion University of the Negev, Beer-Sheva, Israel*

Received September 26, 2002; in final form, January 4, 2003

Abstract—The turbulent properties of conducting fluids in an external constant magnetic field are known to change with increasing field strength. A study is made of the behavior of the second-order structural function of the velocity field in a homogeneous incompressible turbulent fluid in the presence of an external uniform magnetic field. It is shown that, depending on the magnetic field strength, there may be different governing parameters of the system in both the inertial and dissipative intervals of turbulence. This leads to new spectral scalings that are consistent with experimental ones. © *2003 MAIK "Nauka/Interperiodica".*

1. INTRODUCTION

Numerous investigations of turbulent flows of conducting fluids at low Reynolds numbers in an external uniform magnetic field $\mathbf{B}_0$ (see [1] and the literature cited therein) show that the fluid properties charge substantially as the field strength increases. Here, we investigate the behavior of the second-order structural function for the velocity field in a homogeneous incompressible turbulent fluid in the presence of the magnetic field $\mathbf{B}_0$. The one-dimensional second-order structural function is defined by the formula

$$D(r) = \langle [u'(r + r') - u'(r')]^2 \rangle, \quad (1)$$

where u' is the velocity of turbulent fluctuations. In the inertial interval of turbulence, the structural function D is a power function of r:

$$D(r) \sim Ar^{\alpha}, \quad (2)$$

where A is a parameter and α is the scaling index.

As was shown in [2, 3], the α values observed experimentally at different magnitudes of the interaction parameter $N = Ha^2/Re = \sigma B_0^2 L/\rho U$ (where σ is the conductivity of the fluid, ρ is its density, $Ha = B_0(\sigma/\rho\nu)^{1/2}$ is the Hartmann number, $Re = LU/\nu$ is the Reynolds number, L and U are the characteristic length and characteristic velocity, ν is the kinematic viscosity, and B_0 is the strength of the external magnetic field) are equal to 2/3, 4/3, 2, and 8/3. Note that, from a morphological point of view, this sequence forms an arithmetic progression with a difference of 2/3. Below, we will see that, in each turbulent regime, characterized by its own scaling index α, the turbulent energy is transferred along the spectrum by a certain mechanism and there are corresponding governing parameters in the inertial interval of turbulence and the viscous interval of small-scale turbulence.

2. KOLMOGOROV REGIMES OF TURBULENCE

We begin with the most thoroughly studied Kolmogorov turbulent spectrum, which was obtained more than 60 years ago by Kolmogorov under the assumption that, for a developed steady-state homogeneous turbulent flow of an incompressible fluid at a high Reynolds number, the governing parameter in the inertial and viscous intervals is the energy flux along the spectrum. In the viscous interval, there are two governing parameters: the energy flux ε and the viscosity ν, which serves as an additional governing parameter of the turbulent cascade. If the characteristic scale length L_F of an external force that maintains turbulence is much larger than the characteristic length λ_i of the inertial interval, $L_F \gg \lambda_i$, then the structural function of turbulent fluctuations of the velocity field has the form

$$D(r) \sim U^2 f\left(\frac{r}{\lambda}\right), \quad (3)$$

where U is the characteristic velocity of the turbulent fluctuations and λ is their spatial scale.

In the inertial interval, in which the parameters of the system are independent of ν (i.e., we can set $\nu = 0$ in the Navier–Stokes equation), the energy is an integral of motion. Consequently, the energy flux ε along the spectrum is the governing parameter. In essence, Kolmogorov's first hypothesis extends this property to the dissipative interval of turbulent pulsations.

† Deceased.

1063-780X/03/2906-0512$24.00 © 2003 MAIK "Nauka/Interperiodica"

In the dissipative interval, the velocity of turbulent pulsations and their characteristic scale length are equal to $U_\nu = U_k \sim (\varepsilon\nu)^{1/4}$ and $\lambda_\nu = \lambda_k \sim (\nu^3/\varepsilon)^{1/4}$. In the inertial interval, the viscosity drops out of expression (3). As a result, we obtain

$$D(r) \sim \varepsilon^{2/3} r^{2/3}. \quad (4)$$

On the other hand, almost 20 years after the publication of Kolmogorov's works, it was shown that the Euler equation has another integral of motion, namely, the helicity [4],

$$He = \langle \mathbf{u}' \cdot (\nabla \times \mathbf{u}') \rangle, \quad (5)$$

which is associated with the violation of the mirror-image symmetry of homogeneous isotropic turbulence. A helical cascade in the regime of fully developed isotropic turbulence was first investigated by Brissaud *et al.* [5]. If there is a helicity flux η (which may be introduced by analogy with the energy flux ε) in the system, then it can be regarded (together with ε) as a governing parameter in the inertial interval of turbulence. At the same time, in [5], the fluxes ε and η were also assumed to be governing parameters in the dissipative interval. From the experimental and numerical data accumulated over the last 40 years, it has become clear that helical turbulence is encountered as often as conventional Kolmogorov turbulence; this may be attributed to the level of helicity of turbulent pulsations in the system [6]. Interest in helical turbulence increased considerably when it was recognized that it plays a fundamental role in the generation of moderately strong large-scale magnetic fields (see [7] and the references therein) and the formation of large-scale atmospheric vortices (see [1] and the references therein).

By analogy with Kolmogorov's hypothesis, we now consider another case—the one in which, first, the governing parameters for the development of turbulence in the inertial interval are ε and η and, second, in the dissipative interval, to these must be added the viscosity ν. In this case, according to the Π theorem, the characteristic scale of turbulence in the dissipative interval (when the viscosity ν should be accounted for) is equal to

$$\lambda_\eta \sim \varepsilon^\beta \nu^{3(1-\beta)/5} \eta^{-(1+4\beta)/5}, \quad (6)$$

where β is a free parameter.

We take into account the form of function (5) and the asymptotic behavior of the function $D(r)$ in the inertial interval of turbulence and, following conventional practice, set

$$D(r) \sim U_\eta^2 \left(\frac{r}{\lambda_\eta}\right)^\delta, \quad (7)$$

where the velocity scales as $U_\eta \sim \varepsilon^{-\beta} \eta^{-(1+4\beta)/5} \nu^{(2+3\beta)/5}$ (the dependence of the exponents in the formula for U_η on β stems from the fact that, in the dissipative interval, the Reynolds number is approximately equal to unity, $Re(\lambda_\eta) \sim 1$). As a result, we obtain the relationship between the parameters β and δ,

$$\beta = \frac{\delta - 4/3}{\delta + 2}, \quad (8)$$

and the scaling for the structural function,

$$D(r) \sim \left(\frac{\varepsilon^2}{\eta}\right)^{2/3} \left(\frac{\eta}{\varepsilon}\right)^\delta r^\delta. \quad (9)$$

Now, we consider two limiting cases in which, along with ν, either ε or η is a governing parameter in the dissipative interval. It should be noted that, in these cases, the characteristic scale $\lambda \sim \varepsilon/\eta$ of turbulent pulsations and the velocity $U \sim (\varepsilon^2/\eta)^{1/3}$ in the inertial interval depend on the two parameters ε and η, which are both nonzero.

We have derived that, in the first case (which corresponds to Kolmogorov turbulence), the helicity flux η is not a governing parameter; i.e., $\eta = \eta(\varepsilon)$. Therefore, Eq. (9) yields $\delta = 2/3$ and expression (6) gives $\beta = -1/4$. As a consequence, we arrive at Kolmogorov's dependence of the second-order moment in the inertial interval of turbulence:

$$D(r) \sim C_\varepsilon \varepsilon^{2/3} r^{2/3}. \quad (10)$$

In the second case (corresponding helical turbulence), the energy flux ε drops out of expression (6); i.e., $\beta = 0$ and $\delta = 4/3$, and the scaling of the structural function in the inertial interval has the form

$$D(r) = C_\eta \eta^{2/3} r^{4/3}. \quad (11)$$

In scalings (10) and (11), C_ε and C_η are constants. Note that these two scalings are actually observed in experiments (see [1] and the literature cited therein).

Now, using the above expressions for the characteristic scale and velocity of turbulent pulsations, we write the effective Reynolds number as

$$Re_{\text{eff}} \sim \frac{\varepsilon^{5/3}}{\nu \eta^{4/3}}. \quad (12)$$

Since the Reynolds number can be represented as the ratio of the turbulent to the kinematic viscosity (see, e.g., [8]), formula (12) leads to the following fundamentally important conclusion: as the helicity flux (and the helicity itself) increases, the turbulent viscosity in the system decreases according to the law $\eta^{-4/3}$. Note that this conclusion stems exclusively from the sufficiently high level of helical turbulence in the system. An analogous behavior of turbulent fields was also observed in [9].

Hence, when ε is not a governing parameter in the dissipative interval, we obtain $\delta = 4/3$, which corresponds to the helical scaling of the structural function $D(r)$ in the inertial interval. Since such scalings are typical of helical turbulent fields [6], we can conclude that the situation in question, namely, that with $\varepsilon(\eta)$, takes

place in real media. This conclusion is somewhat unexpected in view of the fact that, since Kolmogorov's time, it has become customary to think that ε is the governing parameter in the dissipative interval. For helical turbulence, however, the conclusion reached here is quite natural. In fact, as was shown in many papers (see [1] and the literature cited therein), helical turbulence slows the direct energy transfer from large to small scales, gives rise to reverse energy cascades, reduces turbulent viscosity, etc. As a combined result of all of these processes, the energy flux ε in the dissipative interval depends on the helicity flux η in a way that reflects the behavior of the governing parameters at $\delta = 4/3$ in the inertial interval.

In addition, note that the above interpretation of the scalings obtained differs from the interpretation given in [5] (which, basically, is accepted today). In fact, according to [5], the helical scaling index $\delta = 4/3$ refers exclusively to the case $\varepsilon = 0$. However, this seems highly doubtful, because it is unclear how to treat the energy flux in the inertial interval, which plays the role of the energy source. It is important to take into account the fact that the parameter ε does not disappear in the case under consideration but merely drops out of the expression for the structural function $D(r)$.

3. EFFECT OF THE MAGNETIC FIELD ON THE SCALING FOR TURBULENCE

A growing external magnetic field has a significant effect on the properties of a turbulent flow of conducting fluid. In the presence of an external magnetic field $\mathbf{B}_0$, the homogeneous correlation (and, therefore, structural) function

$$Q(r) = \langle u'(0)u'(r)\rangle \tag{13}$$

depends on the parameter $N = \sigma B_0^2 L/\rho U$ (see, e.g., [7] and the references therein). However, for a magnetic field weak enough that its influence on $Q(r)$ can be neglected, we arrive at spectral scalings close to the Kolmogorov and helical scalings discussed above.

According to [7], the condition for the magnetic field to be sufficiently weak in the first approximation is formulated in terms of the harmonics of the Fourier transformed correlation function:

$$\frac{(\mathbf{k}\cdot\mathbf{B}_0)^2}{\mu\rho_0}\frac{2\eta\nu k^4 - 2\omega^2 + (\mathbf{k}\cdot\mathbf{B}_0)^2/\mu\rho_0}{(\nu_B^2 k^4 + \omega^2)(\nu^2 k^4 + \omega^2)} \ll 1, \tag{14}$$

where $\mathbf{k}$ is the wave vector of turbulent pulsations, $\mathbf{B}_0$ is the external magnetic field, ρ_0 is the fluid density, μ is the magnetic permeability, $\nu_B = 1/\mu_0\sigma$ is the magnetic viscosity, and σ is the electric conductivity of the fluid. However, even sufficiently weak magnetic fields may be important in the generation of helical turbulence [10, 11]. This fundamental effect should be taken into account in investigating helical turbulence since helicity plays an important role in the energy transfer along the spectrum and can substantially affect the magnetic viscosity. Consequently, as the magnetic field increases, condition (14) fails to hold, which, in turn, should change the form of the function $D(r)$.

Recall that, in the absence of an external magnetic field, the mean energy of the turbulent fluctuations and their helicity are the integrals of motion of the Euler equation. In the Euler equation in the inertial interval, a growing external magnetic field is accounted for by an additional term, namely, the Lorentz force:

$$\rho d\mathbf{V}/dt = -\nabla P + \mathbf{j}\times\mathbf{B}, \tag{15}$$

where $\mathbf{j}$ is the current density.

It is easy to show that, for $Re_m = \mu_0\sigma UB_0/\lambda \ll 1$, the Lorentz force and the associated Joule dissipation occur on all scales, in which case the energy and helicity fluxes both become dependent on the magnetic field and, therefore, fail to serve as the governing parameters in the inertial and viscous intervals. At present, there is a vast amount of experimental data obtained from laboratory investigations of turbulence in an external constant magnetic field. On the whole, these investigations were carried out in the two main directions: the fluctuations of the velocity field were measured along [2] and across [3] the magnetic field.

In the first case, the scaling index in correlation function (2) at a sufficiently strong field $\mathbf{B}_0$ was close to $\alpha = 2$, which was explained by the tendency of turbulence to become two-dimensional [2].

In the second case, the scaling index α was close to 8/3; in some papers (see [1] and the literature cited therein), this was attributed to the generation of superhelical turbulence (super-helicity), $\omega_s = \langle(\nabla\times\mathbf{u}')\cdot(\nabla\times\nabla\times\mathbf{u}')\rangle$. In our opinion, however, the difference in the properties of turbulent fluctuations along and across the magnetic field stems from an increase in the anisotropy of the turbulence in the presence of an external magnetic field. In fact, it is obvious from condition (14) that the character of the interaction is different for transverse modes (with $\mathbf{k}\cdot\mathbf{B}_0 = 0$) and longitudinal modes (with $\mathbf{k}\cdot\mathbf{B}_0 \neq 0$): the dissipation of transverse modes is minimal, while the dissipation of longitudinal modes is maximal.

Hence, the effect of Joule dissipation is greatest for the spectral modes whose wave vectors $\mathbf{k}$ are parallel to $\mathbf{B}_0$ and that thus correspond to the longitudinal harmonics of the correlation function. In this case, choosing the parameter $\gamma = \sigma B^2/\rho$, together with the viscosity ν, as a governing parameter in the dissipative interval seems quite logical. Then, using representation (7), we obtain the characteristic velocity of the turbulent pulsations and their characteristic scale, $U \approx (\gamma\nu)^{1/2}$ and $\lambda_B \sim (\nu/\gamma)^{1/2}$, and also arrive at the following scaling for the second-order structural function:

$$D(r) \sim (\gamma r)^2, \tag{16}$$

which corresponds to a α spectrum with a spectral density index of –3. Consequently, the spectral index –3 arises as a result of the increasing influence of the magnetic field on the longitudinal modes of the turbulent field. A similar line of reasoning was earlier suggested in [2].

Note that the spectral index –3 is usually identified with the transition of the turbulence to the two-dimensional regime. In fact, the spectral index –3 is associated with the enstrophy conservation and is characteristic of two-dimensional turbulence, in analogy to the spectral index –7/3, which is associated with the helical properties of a three-dimensional turbulent field. However, in the case of three-dimensional turbulence, the spectral index –3 is associated exclusively with the longitudinal modes.

A conducting fluid in which the turbulent fluctuations of the velocity field are transverse to the magnetic field should be studied in a different manner. In this situation, as the magnetic field increases, the scaling index α changes in a jumplike manner and instead of being equal to 2, it is equal to 8/3, which corresponds to a spectral density index of –11/3 (i.e., to the steeper spectra) [3]. In order to explain the value $\alpha = 8/3$, Branover *et al.* [3] assumed that, in this case, the governing parameter in the inertial interval is the super-helicity flux $\eta_s = d\omega_s/dt$. However, this assumption is based exclusively on the dimensionality of the quantity η_s. In addition, since this quantity is not an integral of motion, it is difficult to understand why it should be conserved and why all the remaining quantities should depend on it.

On the other hand, experimental data show that, as the magnetic field strength increases, the turbulence tends to become intermittent. As this occurs, the properties of the energy flux ε along the spectrum should change. Why we again discuss the behavior of the function ε may be explained as follows: as the magnetic field $\mathbf{B}_0$ increases, the field-aligned fluctuations can decouple from the cross-field fluctuations; i.e., in the first approximation, the longitudinal and transverse fluctuations occur independently of each other and Joule dissipation has essentially no effect on the transverse modes. As a consequence, the parameter γ introduced above ceases to be a governing parameter for describing the development of turbulence.

Now, we again turn to the case in which the energy and helicity fluxes can be the governing parameters in the inertial interval of turbulence. It should be noted, however, that, since the properties of the energy transfer along the spectrum change as the intermittent activity of turbulence increases, the energy flux ε should be treated as a function of the coordinates and time. In other words, instead of ε, it is necessary to consider the function $\varepsilon(\mathbf{x}, t)$, which was studied in many papers, the first being [12, 13]. Usually, this approach reduces to choosing a certain spatial region over which to average the function ε. On the other hand, the energy pumped into the small-scale fluctuations in the system by an external force is independent of the properties of the system. When ε depends on the coordinates, it is more meaningful to switch from the global parameters (such as the densities of the energy and helicity pumped into the system and dissipated there) to the local ones (such as, e.g., the energy and helicity flux densities).

The flux density of the energy pumped into the system is described by the equation

$$\frac{\partial}{\partial V}\left(\frac{dU'^2}{dt}\right) = \varepsilon_V,$$

where U' is the characteristic velocity of the turbulent fluctuations on the spatial scales on which an external force is acting and V is the volume. Under steady-state conditions, this flux density should be canceled by the energy flux density along the spectrum, $\varepsilon_V = -\partial\varepsilon/\partial V$. Consequently, in this case, the parameters ε_V and $\eta_V = \partial\eta/\partial V$ are the governing parameters for the formation of turbulent spectra.

Repeating the above arguments, we find that the expressions for the velocity field components perpendicular to the magnetic field yield the following form of the structural function in the inertial interval:

$$D_\perp(r) \sim (\varepsilon_V^5/\eta_V^4)^{2/3}(\eta_V/\varepsilon_V)^\delta r^\delta. \tag{17}$$

We thus arrive at the following possible scalings for turbulence in two limiting cases:

$$10/3 - \delta = 0 \longrightarrow D_\perp(r) \sim \eta_V^{2/3} r^{10/3}, \tag{18}$$

$$8/3 - \delta = 0 \longrightarrow D_\perp(r) \sim \varepsilon_V^{2/3} r^{8/3}, \tag{18a}$$

the latter of which is a transient one. In the situation in question, the effective Reynolds number analogous to that in formula (12) has the form

$$Re_{\text{eff}} = \frac{\varepsilon_V^{8/3}}{\eta_V^{7/3}\nu}. \tag{19}$$

In the dissipative interval, the scalings of the characteristic parameters differ from those in the inertial interval. In particular, the characteristic scale and velocity of turbulent pulsations obey the scalings

$$\begin{aligned} \lambda_t &\sim \varepsilon_V^\beta \eta_V^{-(1+7\beta)/8} \nu^{3(1-\beta)/8}, \\ U_t &\sim \varepsilon_V^{-\beta} \eta_V^{(1+7\beta)/8} \nu^{(5+3\beta)/8}, \end{aligned} \tag{20}$$

which were derived with allowance for the fact that, at the boundary of the dissipative interval, the Reynolds number is equal to unity. The two limiting cases are now treated as follows. For $\delta = 10/3$, we obtain $\alpha = 0$ and thus arrive at the above scalings for turbulent pulsations: $\lambda_{t\eta} = (\nu^3/\eta_V)^{1/8}$ and $U \sim (\nu^5/\eta_V)^{1/8}$. For $\delta = 8/3$, we obtain $\alpha = -1/7$; i.e., the characteristic scale and velocity of the turbulent pulsations obey the scalings $\lambda_{tV} \sim (\nu^3/\varepsilon_V)^{1/7}$ and $U_{tV} \sim (\nu^4\varepsilon_V)^{1/7}$.

4. CONCLUSION

The results of our study can be summarized as follows. Based on dimensionality considerations, we have investigated MHD turbulence in the different regimes that may occur depending on the relationships between the governing parameters of the system, namely, the energy and helicity fluxes, viscosity, etc. The classical and helical scalings that have been obtained for the second-order structural function are consistent with both the available experimental data on the generation of turbulence and the corresponding numerical results. We have demonstrated that the external magnetic field has a significant impact on the structural properties of turbulent fields in a conducting fluid. We have shown that the transient turbulent regime under analysis is not only peculiar to the dynamics of a conducting fluid in an external magnetic field but can also occur in response to some external action, such as externally induced rotation. The results obtained can be used to interpret the experimental data on MHD turbulence and simulate the generation of turbulence in conducting fluids, e.g., in plasmas.

REFERENCES

1. H. Branover, A. Eidelman, E. Golbraikh, and S. S. Moiseev, *Turbulence and Structures* (Academic, New York, 1999).
2. A. Alemany, R. Moreau, P. L. Sulem, and U. Frisch, J. Mec. **18** (2), 277 (1979).
3. H. Branover, A. Eidelman, M. Nagorny, and M. Kireev, *Progress in Turbulence Research*, Ed. by H. Branover and Y. Unger (AIAA, New York, 1994), Vol. 162, p. 64.
4. J. J. Moreau, C. R. Acad. Sci. (Paris) **252**, 2810 (1962).
5. A. Brissaud, U. Frisch, J. Leorat, *et al.*, Phys. Fluids **16**, 1366 (1973).
6. H. Branover, O. G. Chkhetiani, A. Eidelman, *et al.*, Magnetohydrodynamics **37**, 31 (2001).
7. F. Krause and K.-H. Radler, *Mean-Field Magnetohydrodynamics and Dynamo Theory* (Pergamon Press, Oxford, 1980), p. 321.
8. L. D. Landau and E. M. Lifshitz, *Fluid Mechanics* (Nauka, Moscow, 1986; Pergamon Press, New York, 1987).
9. A. V. Belyan, S. S. Moiseev, and O. G. Chkhetiani, Preprint No. Pr-1845 (Institute for Space Research, Russian Academy of Sciences, Moscow, 1992); A. V. Belyan, S. S. Moiseev, and O. G. Chkhetiani, Dokl. Akad. Nauk **334**, 34 (1994) [Phys. Dokl. **39**, 13 (1994)]; A. Belyan, O. Chkhetiani, E. Golbraikh, and S. Moiseev, Physica A (Amsterdam) **258**, 55 (1998).
10. O. G. Chkhetiani, S. S. Moiseev, and E. I. Gol'braikh, Zh. Éksp. Teor. Fiz. **114**, 946 (1998) [JETP **87**, 513 (1998)].
11. O. G. Chkhetiani and E. Gol'braikh, Zh. Éksp. Teor. Fiz. (in press).
12. A. M. Obukhov, J. Fluid Mech. **13**, 77 (1962).
13. A. N. Kolmogorov, *La Turbulence en Mecanique des Fluides*, Ed. by A. Favre, L. S. G. Kovasznay, R. Dumas, *et al.* (Gauthier-Villars, Paris, 1961), p. 447.

Translated by I.A. Kalabalyk

Plasma Physics Reports, Vol. 29, No. 6, 2003, pp. 517–527. Translated from Fizika Plazmy, Vol. 29, No. 6, 2003, pp. 555–565.

LOW-TEMPERATURE PLASMA

Nonthermal Decomposition of Nitrous Oxide in a High-Current Pulsed Discharge

D. V. Zatsepin, S. M. Starikovskaya, and A. Yu. Starikovskiĭ

Moscow Institute of Physics and Technology, Institutskiĭ proezd 9, Dolgoprudnyĭ, Moscow oblast, 141700 Russia

Received July 3, 2002; in final form, November 21, 2002

Abstract—The kinetics of the nonthermal decomposition of nitrous oxide (N_2O) in a nonequilibrium plasma is investigated experimentally. A numerical model of the process is constructed and used to simulate the decomposition of N_2O in a high-current pulsed discharge. The most important channels for decomposition are revealed by analyzing the results obtained. The role of the charged, electronically excited, and vibrationally excited components is examined. It is shown that the mechanism for the thermally nonequilibrium decomposition of N_2O in a high-current pulsed discharge is governed by the reactions involving ions and electronically excited molecules. © *2003 MAIK "Nauka/Interperiodica".*

1. INTRODUCTION

In recent years, increased attention has been given to the possibility of actively controlling burning process by means of nonequilibrium low-temperature gas-discharge plasmas [1–5]. In our earlier paper [6], we investigated the relative role of the excitation of the vibrational and electronic degrees of freedom of the gas, the ionization of molecules, and their dissociation in controlling the ignition of a H_2–air mixture. We showed that the main governing parameters for ignition under strongly nonequilibrium conditions are the distribution of the discharge energy over different degrees of freedom of the gas and the rate of the relaxation reactions in the initial ignition stage. In particular, we found that the key role in low-temperature oxidation is played by the production of vibrationally and electronically excited molecules in the discharge. Otherwise, as the temperature increases, the efficiency of the excitation of the internal degrees of freedom somewhat decreases, and the key role is played by the dissociation of molecules and the production of chemically active O and H atoms in the discharge stage. This circumstance leads to the idea of using oxygen-carrying polyatomic molecules, which are efficient sources of oxygen under the discharge conditions, as a means of an additional control in initiating ignition by a nonequilibrium pulsed discharge.

Note that one of the best known chemical compounds of this kind is nitrous oxide, N_2O, which is often used as a source of atomic oxygen both at high temperatures and in the processes of plasmochemical deposition of silicon films, in which N_2O is utilized in mixtures with silane [7].

The decomposition of nitrous oxide behind shock waves has been investigated quite thoroughly under both thermally equilibrium and weakly nonequilibrium conditions. The cross sections for the electron impact excitation of nitrous oxides are known fairly well and make it possible to model in detail both the discharge phase and the afterglow stage. That is why, in this study, we attempted to investigate the nonequilibrium regime of the decomposition of N_2O in a plasma of a nanosecond pulsed discharge in order to clarify the effect of reactions involving the electronically excited, charged, and vibrationally excited components on the decomposition kinetics.

In order to better understand the processes that occur in an N_2O plasma in the high-current discharge phase and the discharge afterglow in the pressure range from 1 to 8 torr at room temperature, we experimentally studied the decomposition of nitrous oxide in a system affected by a fast ionization wave. We carried out a numerical modeling of this decomposition process and, by comparing the measured data with the calculated results, analyzed the kinetics of the plasmochemical reactions in the system.

2. EXPERIMENTAL INVESTIGATIONS OF THE DECOMPOSITION OF N_2O IN A PULSED DISCHARGE

The experimental setup used in this study was described in detail in [6]. The discharges were initiated in a 47-mm-diameter and 20-cm-long quartz tube with a high-voltage plane stainless-steel electrode and a low-voltage ring stainless-steel electrode at its ends. The low-voltage electrode was short-circuited to a grounded shield of a feeding cable by eight wide brass bars and was equipped with a CaF_2 window for emission spectroscopy diagnostics. Negative voltage pulses with an amplitude $|U_{gen}| = 13$ kV, a full width at half-maximum (FWHM) of 25 ns, and a rise time of 2 ns were supplied to the high-voltage electrode of the discharge tube from a pulsed-voltage generator at a repetition rate $f = 40$ Hz

1063-780X/03/2906-0517$24.00

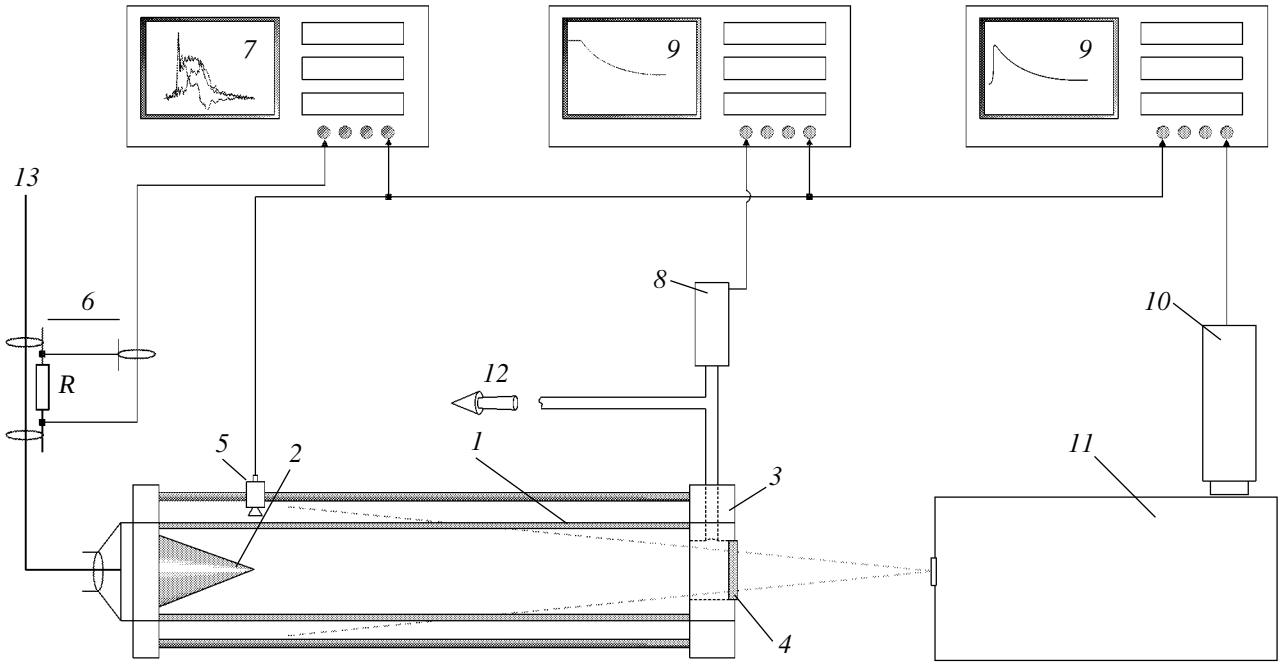

Fig. 1. Experimental device: (*1*) quartz discharge tube, (*2*) high-voltage electrode, (*3*) low-voltage electrode, (*4*) end CaF_2 window, (*5*) capacitive detector, (*6*) back-current shunt, (*7*) TDS-380 oscilloscope, (*8*) pressure gauge, (*9*) C9-8 digital oscilloscope, (*10*) photomultiplier, (*11*) MDR-23 monochromator, (*12*) to a system for pumping out and admitting gas mixtures, and (*13*) 50-Ω coaxial cable for supplying pulsed voltage.

(Fig. 1). In the initial discharge stage, when the conductivity of the discharge plasma is low, a current pulse propagating in a coaxial transmission line is reflected from the open end of the line (i.e., from the high-voltage electrode). As a result, in the stage in which the ionization wave propagates along the discharge gap, the voltage at the high-voltage electrode doubles.

In this stage, the amplitude and shape of the discharge current pulse were measured by a broadband calibrated back-current shunt.

The time-integrated emission signals from the end of the discharge tube were measured by an MDR-23 monochromator.

The absolute value of the pressure during the decomposition of N_2O molecules was measured by an MD × 4S mechanotron.

Figure 2 shows part of the recorded near-ultraviolet spectrum. One can clearly see the spectral bands of the γ system of nitrous oxide.

A complete set of spectroscopic data and the data on the dynamics of the total pressure in the system are illustrated in Fig. 3. Under the same initial conditions, we measured the emission intensities of the second positive system (the $C^3\Pi_u$ transition, $v' = 0 \longrightarrow B^3\Pi_g$, $v'' = 0$; $\lambda = 337.1$ nm) (Fig. 3) and the first negative system (the $B^2\Sigma_u^+$ transition, $v' = 0 \longrightarrow X^2\Sigma_g^+$, $v'' = 0$; $\lambda = 391.4$ nm) of molecular nitrogen, which is the main decomposition product of N_2O. These measurements made it possible to determine the characteristic time of production of molecular nitrogen in the decomposition of N_2O molecules (Fig. 4). The dynamics of the relative density of NO molecules during the decomposition process was measured from the emission intensity corresponding to the transition $NO(A^2\Sigma^+) \longrightarrow NO(X^2\Pi)$ with $\lambda = 237.02 \pm 0.02$ nm. The upper level for this transition is populated by direct electron impact from the ground state of NO molecules and also in chemical reactions involving electronically excited molecules. This circumstance substantially complicates the interpretation of the measured data. Figure 5 shows the half-times of the increase and decrease in the emission intensity of the γ system of NO. Because of the low mean power of the generator of the nanosecond pulses (0.6 W), the gas temperature in the discharge device did not differ appreciably from the temperature of the surrounding air and, in all experiments, was in the range $T = 300 \pm 5$ K.

The data from pressure measurements (Fig. 4) provide additional important information on the conversion rate of a triatomic reagent (N_2O) into bimolecular reaction products.

The total current through the discharge gap can be obtained as a sum of the currents of the incident and reflected pulses. Figure 6 shows the measured incident and reflected current pulses and the calculated transmitted current pulse at an initial gas pressure $p = 4.1$ torr.

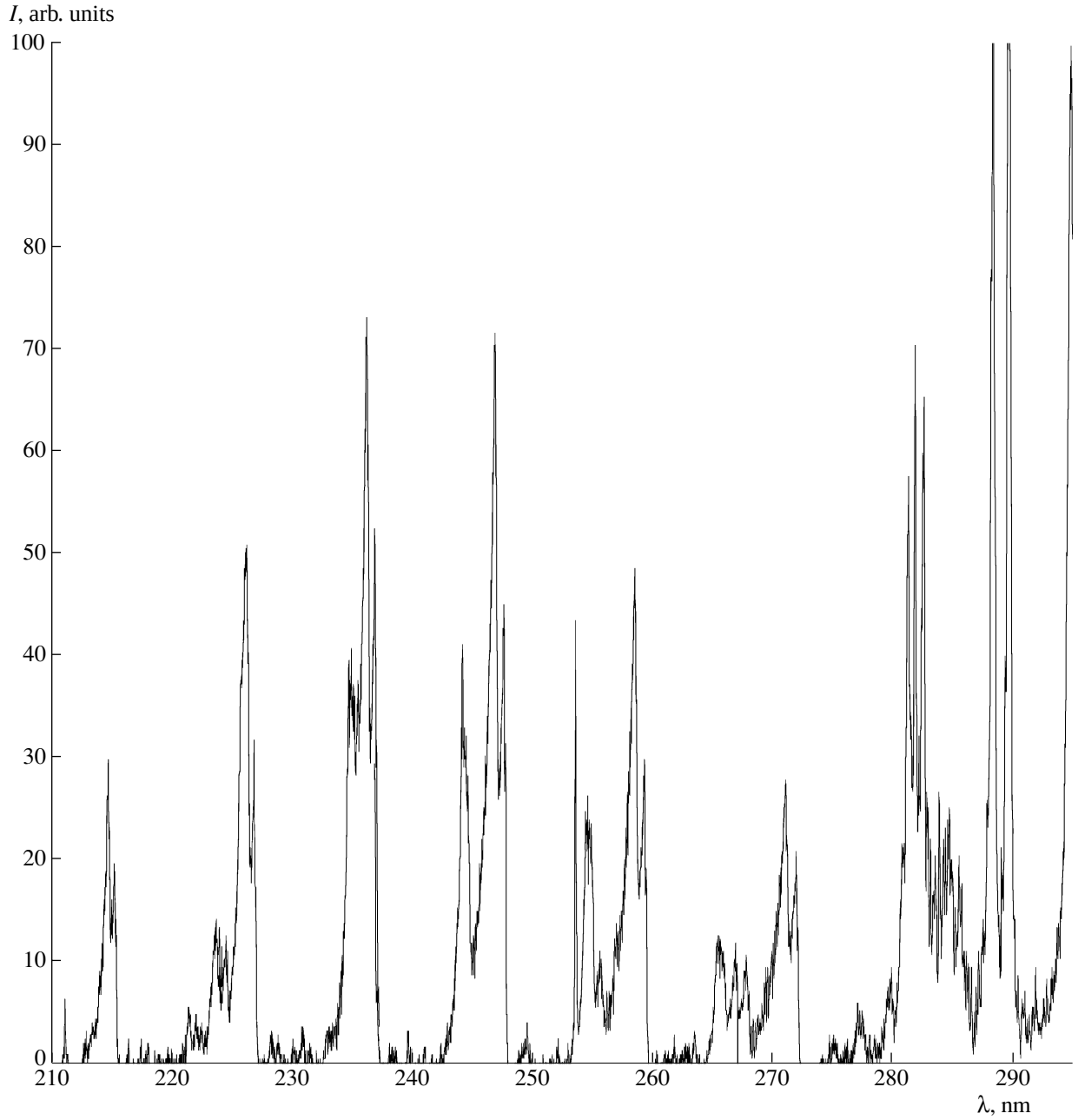

Fig. 2. Emission spectrum from a nanosecond discharge in N_2O at a total pressure of 4 torr 50 s after the start of the decomposition process.

For convenience in comparing the results obtained, the sign of the reflected current pulse is reversed.

Figure 7 displays the maximum amplitude I and the FWHM τ of the current pulse through the discharge gap as functions of pressure. In the pressure range under investigation, the current amplitude in the discharge gap changed from $I = 210$ A at $p = 3$ torr to $I = 110$ A at $p = 7.5$ torr.

The data from measurements of the discharge current and voltage drop across the discharge gap made it possible to estimate the electron density and the reduced electric field after the gap is bridged by a fast ionization wave (Fig. 8). The estimates were carried out in the drift approximation. The electron drift velocity v_d was calculated for a given pulse with allowance for the instantaneous gas composition by solving the Boltzmann equation in the two-term approximation. These data, together with the data on the time behavior of the current density $j = I/S$ through the discharge gap, enabled us to reconstruct the dynamics of the electron

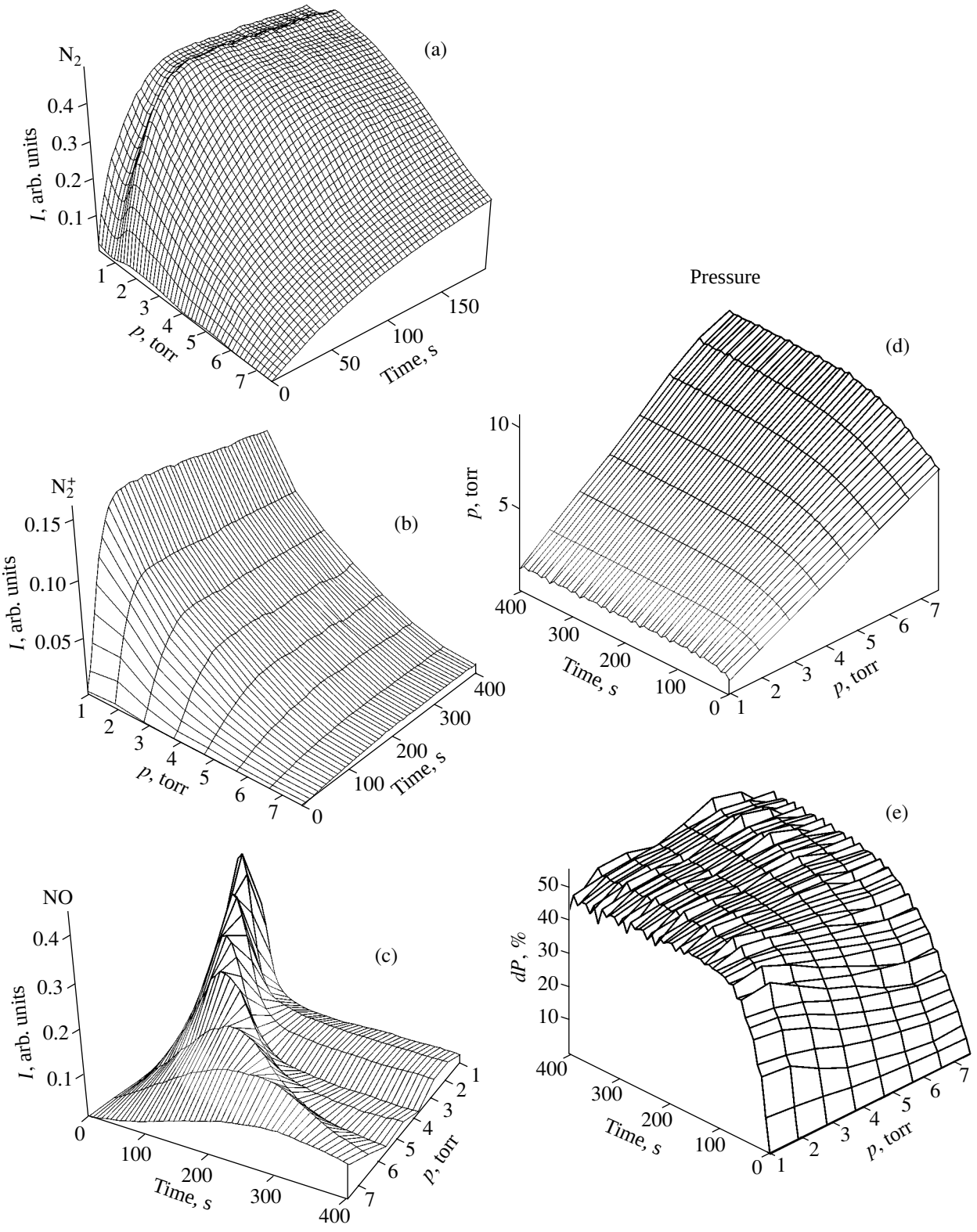

Fig. 3. The measured evolutions of the emission intensities in (a) the second positive nitrogen system (the transition from the $N_2(C^3\Pi_u)$ level), (b) the first negative nitrogen system (the $(N_2^+(B^2\Sigma_u^+))$ level), and (c) the γ system (the $NO(A^2\Sigma^+)$ level) and (d, e) the time evolutions of the gas pressure during the decomposition of N_2O at different initial gas pressures.

density in the high-current discharge phase, $n_e = j/(eV_d)$ (where e is an elementary charge).

In the parameter range under investigation, the reduced electric field in the discharge gap changed from E/n = 300 to 800 Td, which is close to the applicability limit of the two-term approximation for solving the Boltzmann equation in order to calculate the rates of the inelastic processes in the electron–molecule collisions at the lowest pressures in our experiments. The effect of the violation of the two-term approximation (which was observed, e.g., in our earlier paper [6]) should be taken into account when comparing the experimental data and numerical results.

The maximum electron densities were found to lie in the range $n_e \simeq (0.9–2.2) \times 10^{12}$ cm^{-3} (Fig. 8), which correlates well with the results from measurements carried out for other mixtures under similar conditions [8, 9, 6].

3. NUMERICAL MODEL OF THE NONTHERMAL DECOMPOSITION OF N_2O UNDER THE CONDITIONS OF A PULSED DISCHARGE

The calculations were carried out in a direct way; i.e., we computed all subsequent current pulses through the discharge gap with allowance for the changes in the mixture composition during and between the pulses.

The numerical scheme was constructed based on the model developed in [6]. In order to adequately describe the decomposition of N_2O in the presence of NO, N_2, and O_2 molecules, the energy distribution function (EDF) of the electrons was calculated with allowance for the electron-impact excitation of nitric oxide and nitrous oxide molecules. The cross sections for the corresponding processes were taken from [10].

The processes of the relaxation of the vibrationally and electronically excited states, as well as the ion–molecule and molecule–molecule processes, were included in the kinetic scheme in the same manner as was done in [6] in describing the nonthermal oxidation of hydrogen in a H_2–air mixture.

The dependence of the relaxation rate on the degree of vibrational excitation of the reagents and products was taken into account by using the model based on the vibronic-term approximation [11].

The role of the vibrational excitation was taken into account in all the processes involving N_2O, NO, N_2, and O_2 molecules. It was assumed that N_2O molecules are decomposed primarily through the excitation of antisymmetric vibrations (for high vibrational energies and because of the rapid mixing of vibrational modes in an anharmonic interaction, this assumption imposes essentially no restrictions on the dynamics of the EDF near the dissociation threshold).

In the kinetic scheme, every reaction is modeled by a sequence of elementary processes, each of which

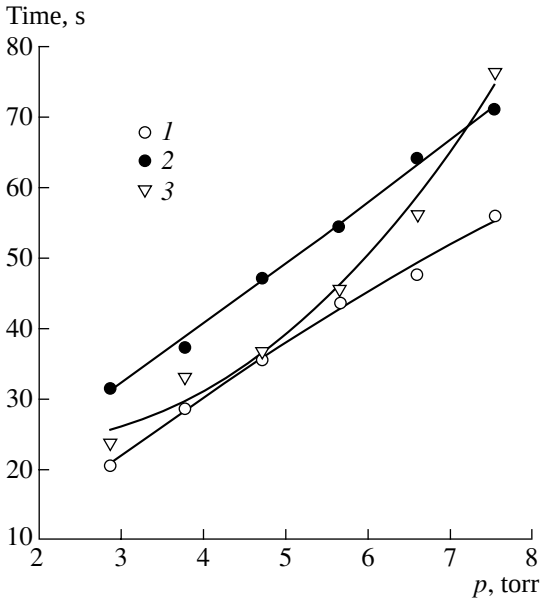

Fig. 4. Characteristic reaction times: the half-times of the increase in the densities of (*1*) $N_2(C^3\Pi_u)$ and (*2*) $N_2^+(B^2\Sigma_u^+)$ molecules and (*3*) the half-time of the increase in pressure. The symbols show the experimental data, and the curves show the calculated results.

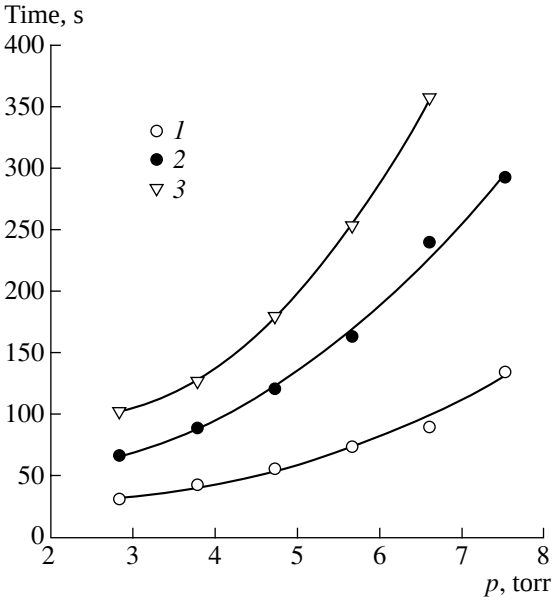

Fig. 5. Dynamics of the density of NO($A^2\Sigma^+$) molecules during the discharge: (*1*) the half-time of the increase in the density, (*2*) the time at which the density becomes maximum, and (*3*) the half-time of the decomposition of NO($A^2\Sigma^+$). The symbols show the experimental data. The curves were obtained by calculating the emission spectrum in the γ band under the assumption that the NO($A^2\Sigma^+$) state is mainly populated via the reaction $N^+ + O_2^- \longrightarrow NO(A^2\Sigma^+) + O$.

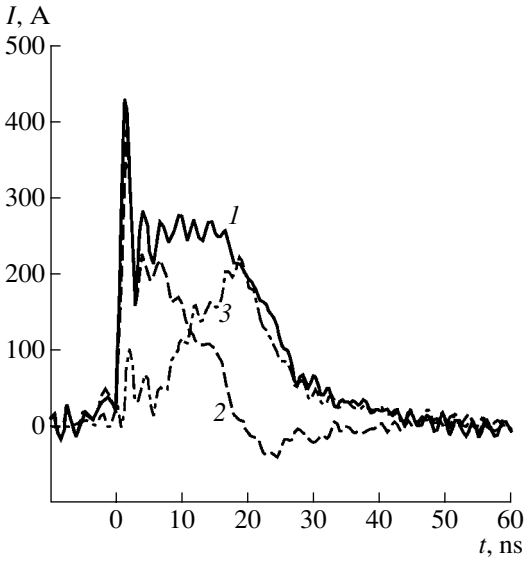

Fig. 6. (*1*) Incident, (*2*) reflected (with the opposite sign), and (*3*) transmitted current pulses at an initial pressure p = 4.1 torr and at U = 26 kV.

determines the rate of the reaction involving reagents in certain vibrationally excited states and producing reagents populated at certain levels.

As an example, the reaction

$$N_2O + O \longrightarrow NO + NO$$

was modeled by the following sequence of elementary processes:

$$N_2O(v_3 = 0) + O \longrightarrow NO(0) + NO(0),$$
$$N_2O(v_3 = 0) + O \longrightarrow NO(1) + NO(1),$$
$$\vdots$$
$$N_2O(v_3) + O \longrightarrow NO(w) + NO(w),$$

whose rate constants were calculated using the algorithm developed in [11].

The remaining reactions incorporated into the kinetic scheme were modeled in an analogous fashion.

The results from calculations of the population dynamics of the individual vibrational states of different molecules in the decomposition process show that the distributions depend nonmonotonically on the energy and that the upper levels are greatly overpopulated. The local peaks in the distributions are associated with the selective depopulation from the upper electronic states to the vibrational levels of the ground state and the recombination fluxes to the upper levels.

The time evolutions of the total pressure and the relative density of $N_2(C^3\Pi_u)$ molecules at an initial pressure p = 4.7 torr are given in Figs. 9 and 10, in which the solid curves show the experimental data and the

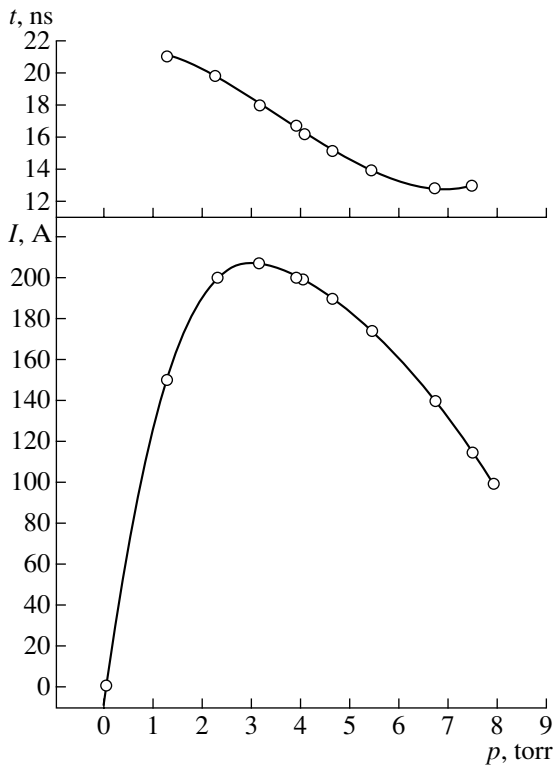

Fig. 7. Mean amplitude of the current pulse and its duration vs. pressure at U = 26 kV.

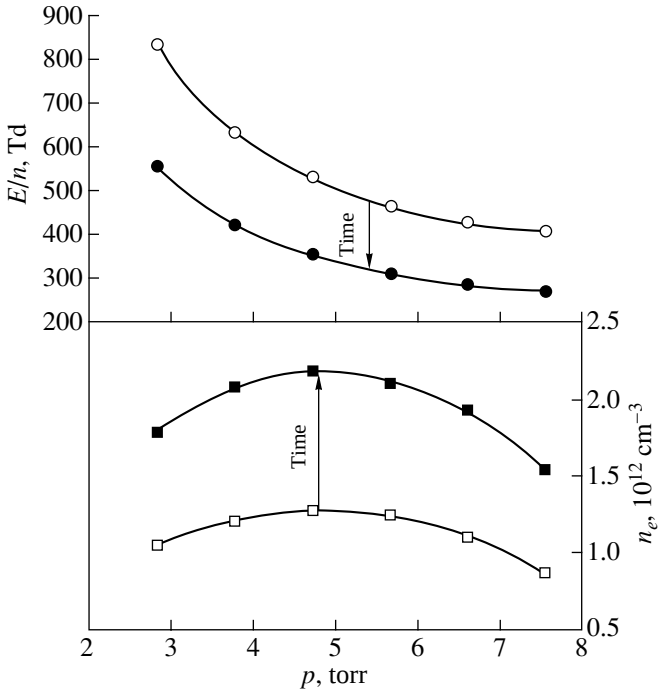

Fig. 8. Reduced electric field and electron density vs. initial pressure for U = 26 kV. The closed circles and closed squares show the initial values, and the open circles and open squares correspond to the values at the end of the decomposition of N_2O molecules.

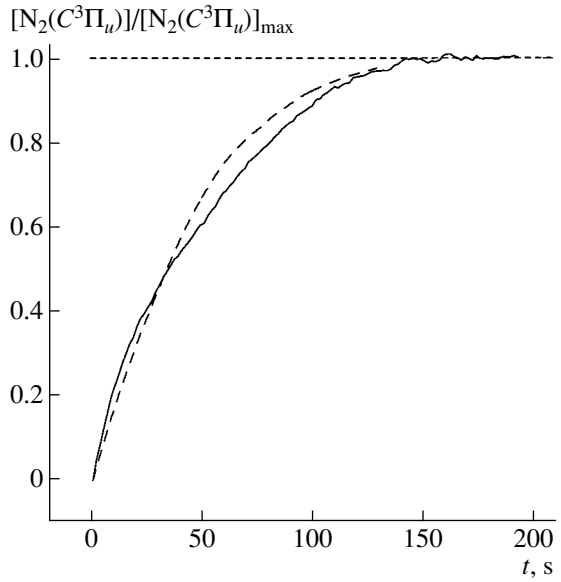

Fig. 9. Comparison between the calculations and the experiment: the measured (solid curve) and calculated (dashed curve) dynamics of the relative density of $N_2(C^3\Pi_u)$ molecules in an N_2O gas at an initial pressure $p = 4.7$ torr and at $U = 26$ kV. Both curves are normalized to the theoretical value of the density of $N_2(C^3\Pi_u)$ molecules in the case of the complete conversion of the initial gas into a mixture of N_2 and O_2 gases.

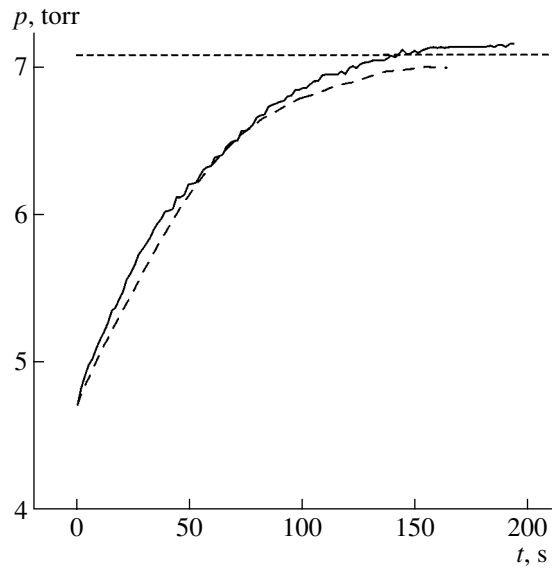

Fig. 10. Comparison between the calculations and the experiment: the measured (solid curve) and calculated (dashed curve) dynamics of the pressure in the mixture resulting from an N_2O gas at an initial pressure $p = 4.7$ torr and at $U = 26$ kV. The horizontal dashed line indicates the theoretical value of the total pressure in the mixture in the case of the complete conversion of the initial gas into a mixture of N_2 and O_2 gases.

dashed curves show the numerical results. The density of $N_2(C^3\Pi_u)$ in Fig. 9 is normalized to the maximum theoretical density of these molecules, and the horizontal dashed line in Fig. 10 indicates the total pressure in the mixture in the case of the complete conversion of the initial gas into a mixture of N_2 and O_2 gases.

Nearly the same shapes of the calculated and measured curves characterizing the production of $N_2(C^3\Pi_u)$ molecules allow us to conclude that, for the conditions of our experiments, the model based on solving the Boltzmann equation in the two-term approximation correctly describes the gas excitation by electron impact. Also, the almost exact coincidence of the time behavior of the experimental and numerical pressure profiles indicates that the model is capable of correctly reconstructing the kinetics of the decomposition of N_2O molecules in the afterglow stage.

The calculated and measured data on the time in which the densities of the main components recorded in our experiments change are compared in Figs. 4 and 5. One can clearly see that, over the entire pressure range under investigation, the proposed model well describes both the rate of conversion of triatomic nitrous oxide into diatomic reaction products (which is evidenced by an increase in pressure during the decomposition of the main reagent; see Fig. 4) and the time evolution of the population of the upper radiating states of nitrogen molecules and atoms.

The situation with the dynamics of the emission intensity of the γ band of NO (Fig. 3) is far more complicated. It is readily seen that the emission from NO increases over a substantially longer time in comparison with the emissions from $N_2(C^3\Pi_u)$ and $N_2^+(B^2\Sigma_u^+)$ (Fig. 5). As a result, the density of $NO(A^2\Sigma^+)$ becomes maximum when the bulk of N_2O molecules have already been decomposed and the density of NO molecules in the ground electronic state is low because of their decomposition in the late discharge stages. This circumstance makes it possible to assert that the $NO(A^2\Sigma^+)$ states are populated through the direct production of the electronically excited nitric oxide molecules rather than through the excitation of NO molecules, e.g., in the reactions $NO + e \longrightarrow NO(A^2\Sigma^+) + e$ or $NO + N_2(A^3\Sigma_u) \longrightarrow NO(A^2\Sigma^+) + N_2$, whose rates are proportional to the instantaneous density of NO molecules in the system. Unfortunately, there are no data on alternative channels of the production of $NO(A^2\Sigma^+)$ molecules. That is why we considered several energetically allowable channels for the production of these excited molecular states. The calculated results that are closest to the experimental data on the dynamics of the emission intensity of the γ band were obtained under the assumption that the $NO(A^2\Sigma^+)$ state is mainly populated in the reaction $N^+ + O_2^- \longrightarrow NO(A^2\Sigma^+) + O$. Since the density of negative oxygen ions O_2^- increases con-

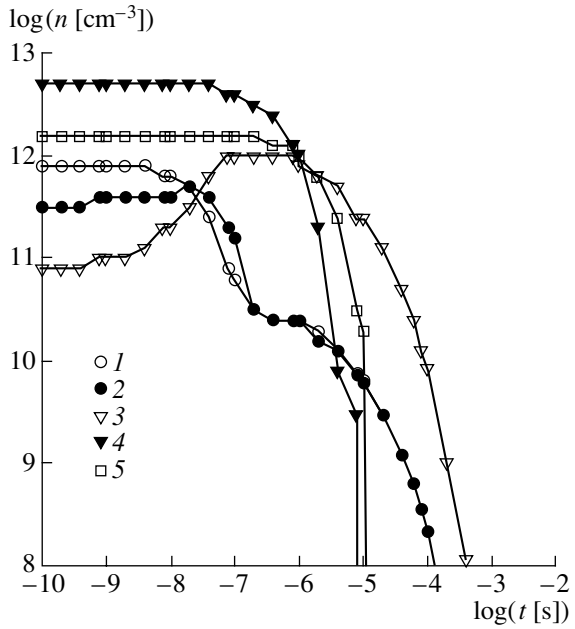

Fig. 11. Dynamics of the densities of the components involved into the fastest reactions in the initial decomposition stage in the discharge afterglow ($[N_2O]/[N_2O]_0 = 1$): (*1*) electrons, (*2*) O^-, (*3*) NO^-, (*4*) $N_2(A^3\Sigma_u^+)$, and (*5*) $N(^2D)$. The initial pressure of the N_2O gas is $p = 4.7$ torr.

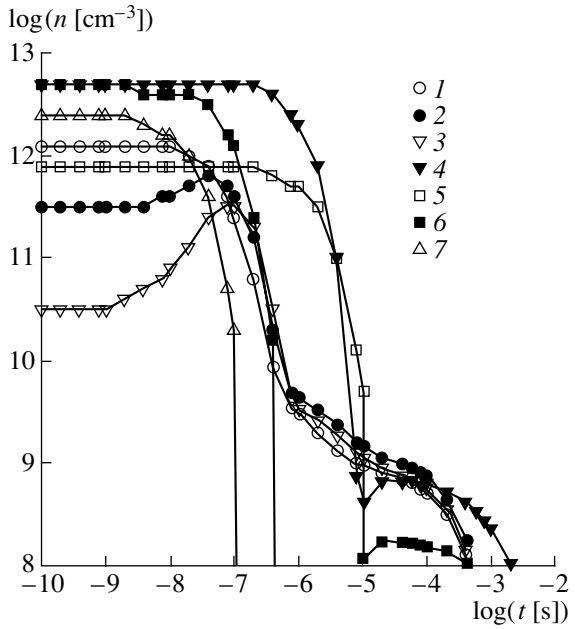

Fig. 12. Dynamics of the densities of the components involved into the fastest reactions in the final decomposition stage in the discharge afterglow ($[N_2O]/[N_2O]_0 = 0.5$): (*1*) electrons, (*2*) O^-, (*3*) NO^-, (*4*) $N_2(A^3\Sigma_u^+)$, (*5*) $N(^2D)$, (*6*) $N_2(B^3\Pi_g)$, and (*7*) $N_2(C^3\Pi_u)$. The initial pressure of the N_2O gas is $p = 4.7$ torr.

tinuously during the discharge, the population of the $NO(A^2\Sigma^+)$ state becomes maximum by the end of the decomposition process; simultaneously, because of a sharp decrease in the density of N^+ atoms after the decomposition of all N_2O molecules, this state is rapidly depopulated in the late discharge stages, which correlates well the experimentally observed population dynamics (Fig. 5). Nevertheless, the question about the possible channels of the excitation of the γ band under our experimental conditions apparently remains open.

4. FLUXES OF ACTIVE PARTICLES AND THE MAIN STAGES OF THE NONTHERMAL DECOMPOSITION OF N_2O IN A PULSED DISCHARGE

In order to single out the most important processes occurring in an afterglow discharge plasma, we analyzed the rates of reactions of the kinetic scheme for the conditions of the first current pulse propagating through the discharge gap originally filled with N_2O at a pressure of 4.7 torr and also for the conditions of the 1560th pulse, which corresponded to the decomposition of 50% of the initial nitrous oxide. To do this, in simulating the discharge kinetics, we calculated the instantaneous densities of the discharge plasma components simultaneously with the absolute rates of all of the reactions (i.e., the rate of the forward reaction minus the rate of the reverse reaction). The reactions that proceed at high absolute rates give rise to particle fluxes in the "reagents–final products" space. This approach allowed us to follow the sequence of the main reactions in which N_2O decomposed into N_2 and O_2.

Figures 11 and 12 show the kinetic curves for the components involved in the fastest reactions in the afterglow plasmas of the above two current pulses.

From these figures, we can clearly see that, in the initial stage of the decomposition of N_2O (when the densities of nitrogen and oxygen molecules in the mixture are low), the kinetics is characteristically different from the kinetics in the late stages (which are dominated by the processes of the excitation of the electronic levels of N_2 molecules in the discharge plasma and their dissociative deexcitation in collisions with N_2O molecules). In particular, the lifetime of the excited $N_2(A^3\Sigma_u)$ molecules increases because of the decrease in the rate of their deexcitation in collisions with N_2O molecules. The lifetime of the negative nitrogen monoxide ions decreases by almost three orders of magnitude because the density of molecular oxygen increases during the decomposition of N_2O and the charge-exchange rate increases. The density of the excited nitrogen atoms $N(^2D)$ decreases markedly for the following reason. In the initial stage, these atoms are efficiently produced in the dissociation of N_2O molecules by electron impact.

However, in the late stages, the density of N_2O molecules decreases; as a result, the rate of this process decreases, thereby reducing the density of $N(^2D)$ atoms. The conversion time of the electrons also becomes somewhat shorter.

The dynamics of the densities of the main neutral components in the afterglow of the first discharge pulse in an N_2O gas at an initial pressure $p = 4.7$ torr is illustrated in Fig. 13. It can be seen that the process proceeds in several stages that are accompanied by the slow decomposition of N_2O and the production of molecular nitrogen and oxygen. During the first pulse, the densities of NO molecules and oxygen atoms in the mixture are relatively high; then, during the decomposition of N_2O, these densities decrease.

As in the case of a system with a reacting H_2–air mixture, the time between the end of each current pulse and the beginning of the next pulse can be divided into four intervals: 0–10^{-7}, 10^{-7}–10^{-5}, 10^{-5}–10^{-3}, and 10^{-3}–25×10^{-3} s.

We performed an analysis of the fluxes of active particles in the fastest chemical conversion reactions during these intervals.

Let us consider the processes that are dominant in each of above four intervals in the afterglow of the first current pulse.

(i) In the first 10^{-7} s after the end of the pulse, the fastest processes are those involved in the electron transfer reactions

$$e^- + N_2O \longrightarrow O^- + N_2, \quad (1)$$

$$O^- + N_2O \longrightarrow NO^- + NO, \quad (2)$$

in which N_2O molecules are efficiently decomposed.

The second fast process is the dissociative quenching of the electronically excited level $N_2(A^3\Sigma_u^+)$ by N_2O molecules.

In this time interval, N_2O molecules are also decomposed in the reaction $N(^2D) + N_2O \longrightarrow NO + N_2$.

(ii) During the second interval (from 10^{-7} to 10^{-5} s), the rate of reactions (1) and (2) increases considerably. However, the decomposition of nitrous oxide is now dominated by the reaction of dissociative quenching of the electronically excited level $N_2(A^3\Sigma_u^+)$ by N_2O molecules.

(iii) The third interval (from 10^{-5} to 10^{-3} s) is characterized by an increasing influence of the secondary processes, namely, the reactions involving O and N atoms.

(iv) For longer times (from 10^{-3} to 25×10^{-3} s), the reactions responsible for the production of N_2 and O_2 molecules in the system become more intense. The most important of these reactions are those involving NO molecules:

$$NO + O + M \longrightarrow NO_2 + M,$$

$$NO_2 + O \longrightarrow NO + O_2,$$

$$NO + N \longrightarrow N_2 + O.$$

The general pattern of the decomposition kinetics changes substantially as the N_2O molecules decompose and the nitrogen, oxygen, and nitric oxide molecules are produced. Although the scheme of the main reactions remains the same, the role of the reactions involving electronically excited nitrogen molecules and oxygen ions increases considerably. The dynamics of the densities of the main reaction products—molecular nitrogen and oxygen—is clearly seen in Fig. 13b. The production of molecular oxygen in the mixture leads, in particular, to a decrease in the density of negative NO^- ions in fast charge-exchange reactions (Fig. 12).

Based on the above analysis, we can conclude that the reactions involving ions and electronically excited particles play a fundamental role in the decomposition of nitrous oxide in a high-current pulsed discharge at low temperatures.

The role of the reactions involving O atoms is relatively unimportant because of the high energy threshold of the reaction

$$N_2O + O \longrightarrow NO + NO.$$

In contrast to an H_2–air mixture, in which the vibrational excitation of H_2 molecules substantially intensifies the oxidation process, the vibrational excitation of the gas does not have any important effect on the decomposition of N_2O molecules.

Under the conditions in question, vibrational excitation cannot play any important role in the decomposition of nitrous oxide by the purely vibrational mechanism [11] for intensifying the monomolecular decomposition because of the high rates of the relaxation of the EDF via the deformation mode at high vibrational quantum numbers.

A decrease in the threshold ($\Theta \simeq 14000$ K) of the reaction $N_2O + O \longrightarrow NO + NO$ also cannot result in any significant (in comparison with other mechanisms) decomposition of N_2O molecules.

The above analysis shows that, under the conditions in question, the nonequilibrium character of the vibrational excitation manifests itself in a quite different manner.

On the one hand, the vibrational excitation of the gas substantially intensifies the reactions of the collisional detachment of electrons from O^-, O_2^-, and NO^- ions. As a result, the recombination of charged particles becomes somewhat more rapid, and reactions (1) and (2) proceed at a slower rate. On the other hand, the vibrational excitation of the gas somewhat increases the mean electron energy in the discharge (because of superelastic collisions) and, accordingly, the population rate of the electronically excited level $N_2(A^3\Sigma_u^+)$,

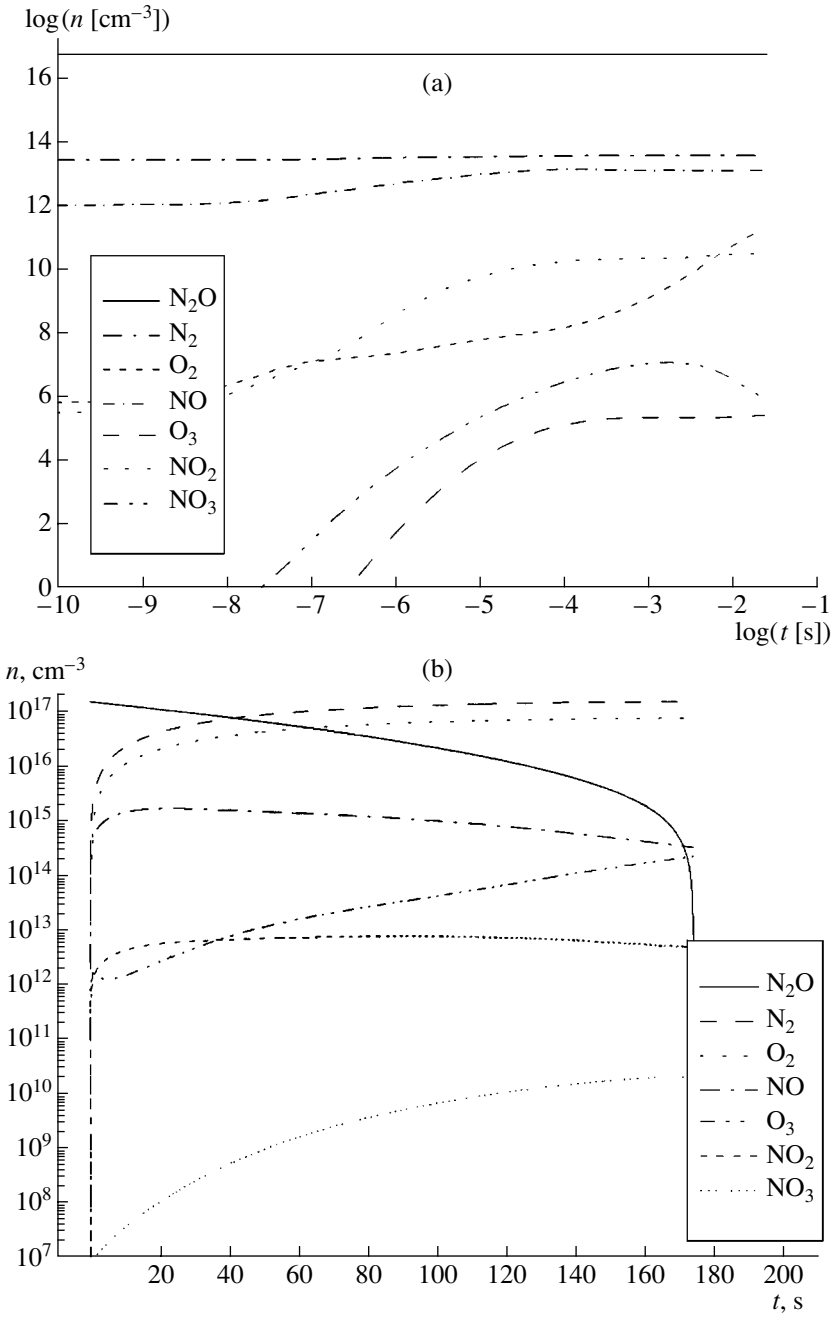

Fig. 13. Dynamics of the densities of the main components (a) in the afterglow of the first discharge pulse and (b) during the decomposition process (the values of the density at the end of each subsequent current pulse are presented): (*1*) molecules, (*2*) atoms, (*3*) electronically excited particles, (*4*) negatively charged particles, and (*5*) positively charged particles. The initial pressure of the N_2O gas is $p = 4.7$ torr.

thereby increasing the rate of the collisional dissociation of N_2O molecules. The rate of direct electron impact ionization of N_2O also increases.

Both of these mechanisms have only an indirect effect on the integral decomposition rate of N_2O molecules and, on the whole, do not significantly change the rate of the decomposition process.

Hence, based on the results obtained in this section, we can conclude that the mechanism for the thermally nonequilibrium decomposition of nitrous oxide (N_2O) in a high-current pulsed discharge is governed by reactions involving the ions and electronically excited molecules.

ACKNOWLEDGMENTS

This work was supported in part by the Ministry of Education of the Russian Federation (project nos. E00-

3.2-427 and E00-5.0-304), the Russian Foundation for Basic Research (project nos. 01-02-17785, 02-02-06523, and 02-03-33376), the International Scientific Technical Center (grant no. 1474), and the U.S. Civilian Research and Development Foundation for the Independent States of the Former Soviet Union (CRDF) (grant no. MO-011-0).

REFERENCES

1. A. F. Panteleev, G. A. Popkov, Yu. N. Shebeko, *et al.*, Fiz. Goreniya Vzryva **27** (1), 26 (1991).
2. N. I. Maiorov, Fiz. Goreniya Vzryva **21** (5), 48 (1985).
3. S. N. Cherepnin, Fiz. Goreniya Vzryva **26** (2), 58 (1990).
4. J. Vinogradov, E. Sher, I. Rutkevich, and M. Mond, Combust. Flame **127**, 2041 (2001).
5. M. Saito, A. Arai, and M. Arai, Combust. Flame **119**, 356 (1999).
6. D. V. Zatsepin, S. M. Starikovskaya, and A. Yu. Starikovskii, Khim. Fiz. **20** (7), 66 (2001).
7. M. Ceiler, B. Kohl, and S. Bidstrup, J. Electrochem. Soc. **142**, 2067 (1995).
8. N. B. Anikin, S. V. Pancheshnyi, S. M. Starikovskaia, and A. Yu. Starikovskii, J. Phys. D **31**, 826 (1998).
9. S. V. Pancheshnyi, S. M. Starikovskaya, and A. Yu. Starikovskii, Fiz. Plazmy **25**, 393 (1999) [Plasma Phys. Rep. **25**, 355 (1999)].
10. M. Hayashi, in *Swarm Studies and Inelastic Electron-Molecule Collisions*, Ed. by L. C. Pitchford, B. V. McKoy, A. Chutjian, and S. Trajmar (Springer-Verlag, New York, 1987).
11. A. M. Lashin and A. Yu. Starikovskii, in *Proceedings of the 26th International Symposium on Combustion, Naples, 1996* (Combustion Inst., Naples, 1996), Rep. 04-077.

Translated by G.V. Shepekina

Plasma Physics Reports, Vol. 29, No. 6, 2003, pp. 528–533. Translated from Fizika Plazmy, Vol. 29, No. 6, 2003, pp. 566–572.

LOW-TEMPERATURE PLASMA

Structure of a Discharge Induced by a Coaxial Microwave Plasmatron with a Gas-Supply Channel in the Inner Electrode

A. Ya. Kirichenko, A. P. Motornenko, and O. A. Suvorova

Usikov Institute of Radiophysics and Electronics, National Academy of Sciences of Ukraine, Kharkov, 61085 Ukraine

Received August 22, 2002; in final form, October 29, 2002

Abstract—The structure of a discharge induced by a coaxial microwave plasmatron with a gas-supply channel in the inner electrode of a coaxial waveguide is investigated. A plasmatron with a power of up to 10 W operates at a frequency of 10 GHz. Depending on the operation regime, the discharge takes either a filament or torch form. A plasma filament arises at low flow rates of the working gas (argon) and occurs at the border of the potential core of the gas jet. A torch discharge occurs at high flow rates and has the form of a hollow cone. In both cases, the discharge arises in the potential core of the gas jet and does not spread beyond it. The distribution of the microwave field in the discharge plasma is determined. © *2003 MAIK "Nauka/Interperiodica"*.

1. INTRODUCTION

The structure of a torch discharge induced by a conventional coaxial microwave plasmatron [1–3] is similar to that of an RF torch discharge [4, 5]. The main difference is that, in an RF torch discharge, the heated gas leaves the discharge region due to upward convection, whereas in a microwave torch, the working gas is blown through the interelectrode channel and then is let out into the atmosphere. When the working gas in a microwave plasmatron is supplied through a special channel in the central electrode [6–10] (rather than through the interelectrode space), the discharge takes a specific form. The plasmatrons of this type are called TIA (Torche á Injection Axiale) plasmatrons. In this case, the edge of the inner electrode (rather than the coaxial outer electrode) acts as a nozzle forming the gas flow. As a result, the microwave discharge is ignited not in the central region of the argon jet, but at the border between the potential core of the jet and the turbulent boundary layer, which contains (besides argon) molecules of the surrounding air. Because of the specific conditions of discharge formation, the discharge structure in such a plasmatron differs significantly from that in a conventional plasma torch [4].

The structure and dynamics of the discharge in various operating regimes of a plasmatron with a gas-supply channel in the central electrode were studied in [8–10]. In [8, 9], the specific features of such a discharge were attributed to the high electron density and the presence of a plasma skin layer, as well as to the effect of the surrounding air. In contrast, in [10], it was suggested that the discharge structure can be strongly affected by the structure of the cold gas jet. In all of these studies, argon at approximately the same flow rate was used as a plasma-forming gas; however, in [8, 9], the discharge was fed with a microwave power of ~1 kW at a frequency of 2.45 GHz, whereas in [10], the power supplied to the discharge did not exceed 10 W and the experiments were performed at a higher microwave frequency (10 GHz).

This paper is aimed at studying the general features of such discharges by a unified approach and acquiring additional data on the microwave field distribution in the discharge at a frequency of 10 GHz and an input power of several watts. Attention is focused mainly on investigating the discharge structure at different flow rates of the plasma-forming gas (argon).

2. EXPERIMENTAL SETUP

In our experiments, we used a plasmatron in which argon was supplied through an axial channel in the inner electrode [6]. The channel diameter was varied from 0.35 to 2 mm. The argon flow rate was no higher than 2 l/min. The output power of the 10-GHz continuous-wave magnetron exciting the discharge was up to 10 W. The discharge plasma was strongly nonequilibrium [6], and the electron energy distribution was far from Maxwellian [8, 9]. Taking into account relatively small plasma dimensions, this somewhat impedes the study of the plasma using conventional investigation techniques. To investigate the microwave field distribution in the discharge, we employed the method of a small perturbing body (vibrating metal string) [11, 12].

Figure 1 presents a schematic of the plasmatron and the block diagram of a system for measuring the microwave field distribution in a discharge. The microwave radiation is fed from magnetron *1* through ferrite valve *2* and attenuator *3* to a plasma torch in the form of coaxial waveguide *4* with nozzle *5* at its end. The end of the coaxial waveguide with an inner electrode 4 mm in diameter and outer electrode 10.5 mm in diameter is

1063-780X/03/2906-0528$24.00

tapered to a cone so that the output opening of the outer electrode decreases to 4 mm and that of the inner electrode decreases to 0.6–2 mm. The shape of the inner electrode apex can be varied by changing the diameter of the gas supply channel. In the feed circuit of the torch, directional coupler *6* is inserted, which receives the total microwave signal reflected from the matching elements of the coaxial waveguide, torch nozzle, and all of the other elements that reside in the surrounding space near the nozzle. The reflected signal is recorded with detector *7*, loading the measurement channel of the directional coupler. Since this signal is time-independent, the input capacitance of oscilloscope *8*, which displays the signal, does not allow it to pass to the oscilloscope input. In the measurements, this signal was used as a reference one.

When a small perturbing body (a sphere, disc, or cylinder) is placed in the microwave field created by the coaxial nozzle in the atmosphere or a discharge plasma, the signal reflected from the perturbing body is added to the reference signal. The amplitude of the reflected signal is proportional to the electric field strength at the position of the perturbing body, and the signal phase is determined by the phase difference between the microwave field at this point and the reference signal. If the perturbing body is immobile, there will be no reflected signal on the oscilloscope screen. However, when the perturbing body is displaced from one point to another, at which the electric field differs in amplitude or phase, the time variations in the electric field will be displayed on the oscilloscope screen.

In our experiment, vibrating steel string *9* (0.3 mm in diameter and 80–100 mm in length) serves as a perturbing body. The string is fixed at its upper end and hangs down freely. The string vibrations are excited with electromagnet *11*, which is placed near the string support and is fed from audio-frequency generator *10*. The audio-frequency oscillator is also used to synchronize the horizontal sweep of the oscilloscope. The signal reflected from the vibrating string provides information about the electric field strength at the string position, and, being superimposed on the reference signal, it also provides information about the phase difference between them.

The electric field profile across the discharge and the amplitude–phase characteristic of the wave propagating along plasma jet *12* are displayed on the oscilloscope screen.

Figure 1 schematically illustrates the string vibrations along the plasma axis. Obviously, such measurements allow us to reveal only the character of the spatial variations in the electric field or the change in the electric field at a given spatial point as the regime of plasmatron feeding is changed or the plasmatron design is modified. It should also be taken into account that the measurement results are averaged over the string segment located in the plasma jet. The abelianization of the measurement results, assuming the discharge to be

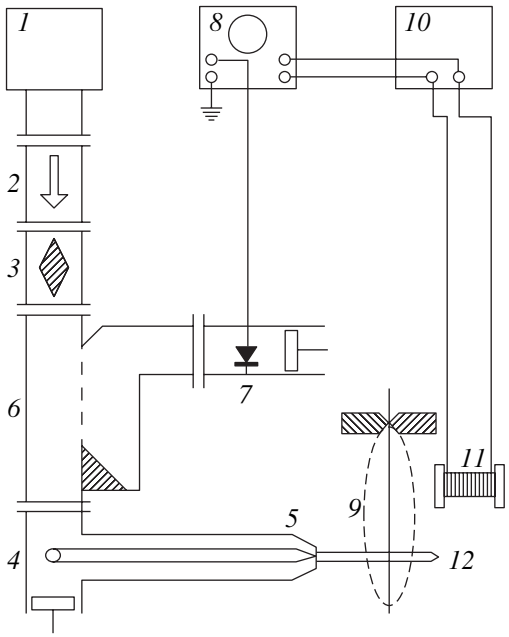

Fig. 1. Schematic of the experimental setup.

cylindrical in shape, allow us to determine the true electric field profile. Since the detector operates at the quadratic segment of its characteristic, the oscilloscope trace reflects the evolution of the electric field squared.

A cathetometer with a magnification of 15–20 was used to monitor the discharge structure and measure its dimensions. The discharge was also photographed.

3. EXPERIMENTAL RESULTS

Photographing the discharge and monitoring its structure with a cathetometer revealed the following features. In the middle of the torch, there is a constriction (waist), which divides the discharge into two parts—a conical part residing on the nozzle and a small cylindrical part, which then transforms into a kind of brush with a blurred end (Fig. 2a). The cone base diameter is determined by the nozzle diameter, i.e., by the diameter of the edge of the inner coaxial electrode. The inner electrode was tapered so that the thickness of the nozzle wall was as small as several tenths of a millimeter. As a result, the electric field at the nozzle edge is fairly strong and highly nonuniform, which leads to the ignition of a microwave discharge. Any eccentricity of the inner electrode with respect to the outer one violates the discharge symmetry.

A specific feature of the conical part of the discharge is that the discharge occurs only in a thin layer on the cone surface, the layer thickness being on the order of the skin depth. From the inside, this layer is adjacent to the conical region occupied by the unexcited working gas. In [8, 9], it was hypothesized that the increase in the electron density N_e, electron temperature T_e, and gas

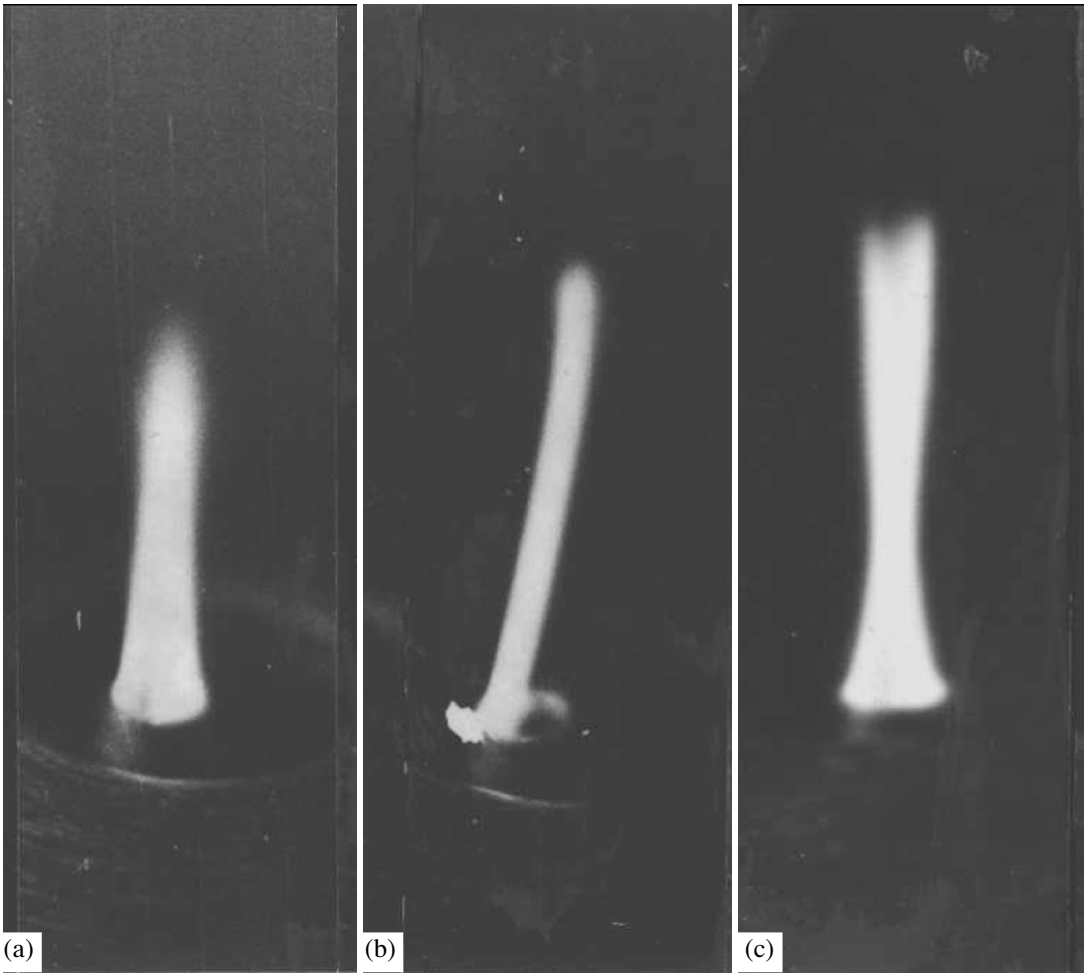

Fig. 2. Photograph of (a) a torch discharge and (b, c) a filament discharge.

temperature T_g at the border of the initial part of the discharge is only due to the penetration of nitrogen or oxygen through the surface of the potential core of the gas jet from the surrounding air. However, this hypothesis seems to be unconvincing; in particular, it does not explain the conical shape of this part of discharge.

It has been found that, in the power range of 2–10 W, the decrease in the argon flow rate to 1.0 l/min results in a qualitative change of the discharge, which converts into a steady-state filament discharge. The photograph of such a discharge is shown in Fig. 2b. The point on the nozzle edge on which the filament base resides is usually located closest to the outer coaxial electrode (it happens because of the violation of the axial electrode symmetry, which is very difficult to avoid in the experiments). It is natural to expect that the microwave field is maximum at this point. The filament is stretched not along the velocity vector of the gas outflowing from the nozzle but is inclined at a small angle (~6°) toward the axis of the inner electrode. The filament radius is around 0.15 mm. Assuming that the filament radius is equal to the skin depth in the discharge plasma, the electron density in the filament turns out to be higher than 10^{12} cm^{-3}, which agrees with the results of [6].

The increase in the argon flow rate at a fixed input power leads to an increase in the filament length until it reaches its maximum value at $Q \approx 1$ l/min.

After the filament has reached its maximum length, a similar filament (initially unstable) inclined at the same angle to the axis arises at the diametrically opposite point of the nozzle edge. The latter filament crosses the former one, forming a scissorlike figure (Fig. 2c). The number of filaments arising and vanishing at the nozzle edge gradually increases with the argon flow rate. At the same time, the rate of filament motion over the perimeter of the nozzle opening also increases. This motion is similar to that of an anode spot on the anode of a voltaic arc. However, the filaments move not in the nozzle plane but along the nozzle perimeter, thereby forming a conical part of the discharge. As a result, a hollow conical discharge region arises near the nozzle (Fig. 2a); such a discharge was previously observed in

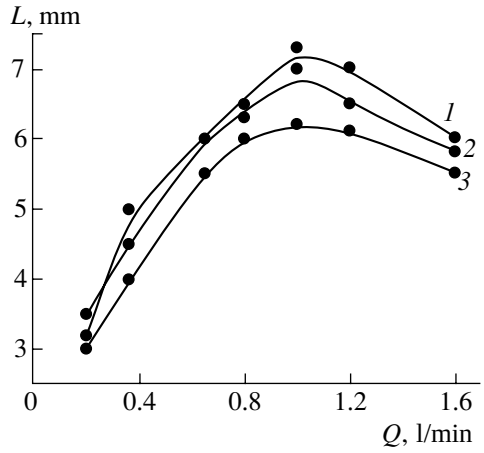

Fig. 3. Plasma filament length L vs. argon flow rate at input powers of (*1*) 5.9, (*2*) 4.5, and (*3*) 3.0 W.

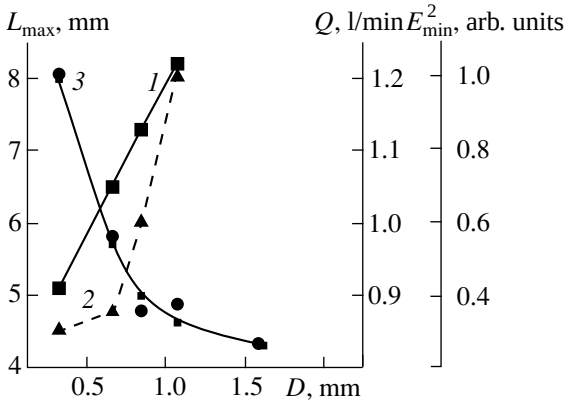

Fig. 4. Maximum discharge length L_{max} and the corresponding values of the argon flow rate Q and the electric field squared E^2 vs. nozzle diameter.

[8–10]. The angle between the cone generatrix and the discharge axis is again ~6°, as in the case with a solitary filament occurring at low argon flow rates. When comparing with the results of [8, 9], it should be remembered that, in those papers, the inclination angle was in the range 4°–8°, which does not contradict the results of our study.

After the filament length L has reached its maximum value, it begins to decrease. This is illustrated in Fig. 3, which shows the plasma filament length as a function of the argon flow rate Q at different input powers P. The dependences were measured for a nozzle with the diameter of the channel in the inner electrode equal to 0.8 mm. Whatever the power, the maximum length of the plasma filament is reached at the same argon flow rate of Q = 1 l/min. We note that a steady-state filament discharge occurs only at argon flow rates in the range Q = 0.2–1.0 l/min. A further increase in the argon flow rate leads to both filament instability and a change in the discharge structure.

The increase in the diameter D of the channel in the coaxial inner electrode (i.e., the diameter of the nozzle opening) leads to an increase in the maximum length of the plasma filament. Simultaneously, the argon flow rate at which this maximum is reached also somewhat increases. Figure 4 shows the maximum filament length L_{max} (curve *1*) and the argon flow rate Q (curve *2*) corresponding to this maximum versus the diameter D of the plasmatron nozzle opening. The dependences were measured at the fixed discharge input power P = 5.9 W. We note that the dependence of the maximum discharge length on the nozzle opening diameter is linear.

The measurements of the electric field profile along the filament show that a surface plasma wave propagates along the filament [11]. As an example, Fig. 5 presents the amplitude–phase characteristics of the wave propagating along the filament for plasmatrons with two different diameters (0.6 and 0.8 mm) of the channel in the inner electrode. In both cases, the input power is 5.3 W and the argon flow rate is 1.0 l/min. Under these conditions, the filament length amounts to 6.0 and 7.5 mm, respectively. It follows from these dependences that, in the latter case, the wave is slower by a factor of 1.25–1.5. In this case (as in the case of a surfatron [13]), the filament discharge is apparently sustained by a slowed-down traveling surface plasma wave. Since, under the same operating conditions, the discharge formed by a nozzle with D = 0.6 mm is shorter than that formed by a nozzle with D = 0.8 mm, the electric field strength in the latter case is somewhat lower.

The increase in the filament length is accompanied by a decrease in the electric field inside the filament. Figure 6 shows the maximum value of the electric field squared E^2 in the filament as a function of the gas flow rate at a fixed power of P = 5.3 W and different nozzle diameters. The electric field was measured at a distance of z = 0.5 mm from the nozzle. Stable plasma filaments

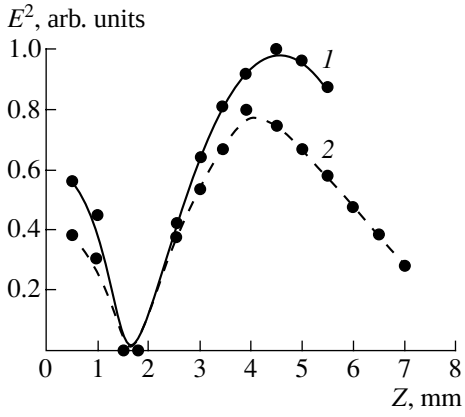

Fig. 5. Profile of the electric field squared E^2 along the discharge axis for nozzle-opening diameters of (*1*) 0.6 and (*2*) 0.8 mm.

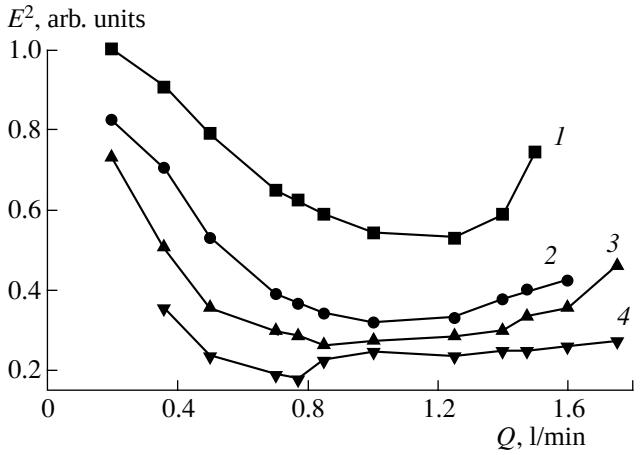

Fig. 6. Electric field squared E^2 in the filament discharge vs. argon flow rate for nozzles with opening diameters of (*1*) 0.35, (*2*) 0.6, (*3*) 0.8, and (*4*) 1.6 mm.

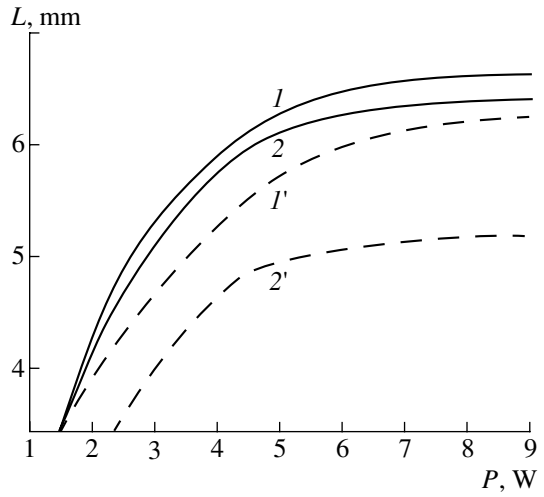

Fig.7. Discharge length L vs. input power P with (curves *1*, *2*) and without (curves *1'*, *2'*) an additional supply of argon through the interelectrode space for two rates of argon supply through the channel in the inner electrode: Q = (*1*, *1'*) 1.4 and (*2*, *2'*) 0.65 l/min.

exist only at the descending branches of these curves. After reaching the minimum on the curve $E = F(Q)$ (which corresponds to the maximum filament length), the filament becomes unstable and begins to move about the nozzle perimeter in a jumplike manner. It is interesting to note that, at the minimum of the curve, the electric field squared $E^2_{\min}$ is approximately inversely proportional to the diameter D of the nozzle opening. This can be seen in Fig. 4, in which the circles show the measured values of $E^2_{\min} = F(D)$ and curve *3* shows the dependence $E^2_{\min} \approx 1/D$. The fairly good agreement between the inversely proportional dependence and the experimental results indicates that the squared electric field E^2 in the filament is inversely proportional to the filament length.

As was noted in [8, 9], the length of the conical part of the discharge depends slightly on the microwave input power, although the total torch length can be varied by varying input power P. The study of the transformation of a filament into a torch shows that, as the input power P and/or argon flow rate Q increase, the length L of a stable steady-state plasma filament gradually increases until it saturates or reaches its maximum value, after which it begins to decrease. A further increase in Q results in the change of the discharge structure. As the input power increases, the dependence $L(P)$ at $Q < 1$ l/min saturates without an appreciable change in the filament structure except for the appearance at its end of an additional reddish glow, whose size increases with P. Seemingly, this extra glow is related to the excitation of nitrogen outside the potential core of argon jet.

4. DISCUSSION OF THE EXPERIMENTAL RESULTS

Observations of the dynamics of the gas jet flowing out of the nozzle [14] show that a potential core in the shape of a cone residing on the nozzle is formed in the jet. Inside the core, the outflowing gas (argon) is not mixed with the surrounding air. In the rest of the jet, intense turbulent mixing of the jet gas with the surrounding air occurs. The cone height is higher by a factor of nearly 4.4–5 than the diameter of the nozzle opening from which the jet is ejected. Hence, the cone half-angle of the potential core is 6°.

Therefore, the discharge filament does not stretch along the gas flow, as is the case of a torch discharge in other types of plasmatrons, but, originating at the nozzle edge, propagates along the conical border of the potential core of the jet. The filament length gradually increases with increasing argon flow rate Q or input power P. A significant fraction of the energy acquired from the microwave field is carried away by the gas flow not only along the filament but also across it. This is an extra channel for thermal energy losses into the surrounding space through the side surface of the filament, thereby appreciably contributing to the loss caused by diffusion. As was shown in [8, 9], the diffusion of the surrounding gas (particularly, nitrogen) into the discharge naturally results in an increase in the gas temperature on the surface of the conical part of the discharge.

In [8], a special chamber filled with argon was used to reduce the effect of nitrogen and oxygen penetrating into the discharge from the surrounding space. In our experiments, similar isolation of the discharge from the surrounding air was accomplished by simultaneously supplying argon through both the axial channel in the central electrode and the interelectrode space. Figure 7 shows the lengths of the filament and torch discharges

as functions of the input power P with (curves *1* and *2*) and without (curves *1*' and *2*') an additional supply of argon through the interelectrode space at a flow rate of $Q' = 1.5$ l/min. In the latter case, argon was supplied only through the channel in the central electrode. In both cases, the filament discharge occurred at $Q = 0.65$ l/min, whereas the torch discharge occurred at $Q = 1.4$ l/min. It can be seen that, when the filament discharge has not yet attained its maximum length, the supply of argon through the interelectrode space increases the discharge length by several tens of percent, whereas in the case of a torch discharge, the extra supply of argon increases the discharge length less significantly.

This result again confirms the influence of the structure of the working gas jet on the characteristics of the discharge under study. The plasma filament is formed at the border of the potential core of the gas jet and stops elongating after leaving the cone region. Then, extra filaments arise, which form the conical part of the discharge. An increase in the microwave power or the argon flow rate does not affect the height of this cone, because it is completely determined by the size of the potential core of the outflowing gas jet. A further increase in the argon flow rate leads to a shortening of the plasma torch because of an increase in the thermal energy losses from the discharge. In this case, the discharge diameter can somewhat increase far from the nozzle.

REFERENCES

1. J. D. Cobine and D. A. Wilbur, J. Appl. Phys. **22**, 835 (1951).
2. S. Murayama, J. Appl. Phys. **39** (12), 5478 (1968).
3. S. P. Martynyuk, A. P. Motornenko, and A. Yu. Usikov, Dokl. Akad. Nauk Ukr. SSR, Ser. A, No. 8, 734 (1975).
4. S. I. Zilitinkevich, Telefoniya i Telegrafiya bez Provodov, No. 6, 652 (1928).
5. R. Grigorovich and D. Kristesku, Opt. Spektrosk. **6** (2), 129 (1959).
6. S. P. Martynyuk and A. P. Motornenko, Dokl. Akad. Nauk Ukr. SSR, Ser. A, No. 2, 161 (1978).
7. M. Moisan, G. Sauve, Z. Zakrzewski, and J. Hubert, Plasma Sources Sci. Technol. **3**, 584 (1994).
8. J. Jonkers, L. J. M. Selen, J. A. M. van der Mullen, *et al.*, Plasma Sources Sci. Technol. **6**, 533 (1997).
9. J. Jonkers, A. Hartgers, L. J. M. Selen, *et al.*, Plasma Sources Sci. Technol. **8**, 49 (1999).
10. A. Ya. Kirichenko, A. P. Motornenko, and O. A. Suvorova, Radiofiz. Élektron. **6** (2), 252 (2001).
11. A. Ya. Kirichenko, A. P. Motornenko, A. F. Rusanov, *et al.*, Zh. Tekh. Fiz. **71** (4), 23 (2001) [Tech. Phys. **46**, 386 (2001)].
12. A. Ya. Kirichenko, A. P. Motornenko, and O. A. Suvorova, Ukr. Fiz. Zh. **46**, 689 (2001).
13. M. Moisan and Z. Zakrzewski, J. Phys. D: Appl. Phys. **24**, 1025 (1991).
14. Shih-I. Pai, *Viscous Flow Theory* (Van Nostrand, Prinston, 1957; Inostrannaya Literatura, Moscow, 1962), Vol. 2.

Translated by N.N. Ustinovskiĭ

Plasma Physics Reports, Vol. 29, No. 6, 2003, pp. 534–537. Translated from Fizika Plazmy, Vol. 29, No. 6, 2003, pp. 573–576.

LOW-TEMPERATURE PLASMA

High-Voltage Stage of a Vacuum Arc

A. V. Zharinov and V. P. Shumilin

Lenin All-Russia Electrotechnical Institute, Krasnokazarmennaya ul. 12, Moscow, 111250 Russia

Received October 31, 2002

Abstract—An elementary theory of the cathode region at the high-voltage stage of an arc discharge is proposed. The theory is based on the balance equations for the particles in an active plasma layer, the power balance at the cathode, and the equation for the Richardson–Dushman electron emission with allowance for the Schottky effect. The most characteristic features of this type of discharge are considered. A non-Langmuir cathode sheath model is proposed for a low-voltage arc on a tungsten electrode. © *2003 MAIK "Nauka/Interperiodica".*

The literature on arc-discharge physics is mainly devoted to low-voltage arcs at voltages on the order of the ionization potential u_i. It is obvious, however, that there is also a high-voltage arc stage (HVAS), which occurs, e.g., during vacuum breakdown, and after which the discharge inevitably transforms into a low-voltage arc.

Theoretical and experimental studies of the HVAS are of interest for the following reasons:

(i) A HVAS seems to be significantly simpler to investigate than a low-voltage arc because the cathode surface can be treated as plane and solid (unmelted). For high-melting cathodes (W, Ta, etc.), evaporation can be ignored in comparison with cathode sputtering. The electron emission is known to be described by the Richardson–Dushman–Schottky (RDS) theory.

(ii) It is likely that studying the HVAS will help to understand some amazing features of a low-voltage arc.

(iii) Experimental studies of the HVAS will allow one to verify the RDS theory within the record ranges of the current densities and electric fields, including those corresponding to the field emission.

(iv) The highest voltage in the HVAS occurs when the electric field at the cathode is zero and the value of i (the ratio of the ion current density at the cathode, j_i, to the density of the electron current at the cathode) is equal to $i_0 = \sqrt{m/M}$, where m and M are the electron and ion masses, respectively. In the regime of a zero electric field, the gas target density n_0 is minimum [1] and is determined by the formula $n_0\sigma_i R \approx i_0 \ll 1$, where σ_i is the ionization cross section and R is the cathode spot radius. For tungsten, we have $i_0 \approx 1.7 \times 10^{-3}$; hence, the mean square scattering angle of the cathode electrons is negligibly small. Thus, in the HVAS, a nearly collisionless electron beam, directed normally to the cathode spot surface, is produced.

As i increases ($i > i_0$) and the surface is deformed, the beam spreads out. Hence, it is possible to experimentally investigate the dynamics of a solid or fluid surface using a technique similar to the Muller electron projector.

(v) The HVAS can be used in various applications; apparently, it has long been used in pulsed accelerators.

All the above considerations inspire one to analyze the quasi-steady HVAS.

The quasi-steady HVAS is described by two elementary algebraic equations

$$jR \approx \frac{e v_0}{\sigma_i(1+\gamma_i)}, \tag{1}$$

$$i(\varphi_p + u_i - \varphi) \approx \varphi + \frac{\lambda T}{jR}. \tag{2}$$

Equation (1) is the existence condition, and Eq. (2) is the heat balance equation at the spot surface. Here, j is the current density in the RDS model at $i > i_0$, e is the elementary charge, v_0 is the mean velocity of the atoms produced due to the cathode self-sputtering (the flux density of these atoms is $q_0 = j_i(1+\gamma_i)/e$), γ_i is the self-sputtering coefficient, φ_p is the discharge voltage, $e\varphi = e\varphi_0 - e\Delta\varphi$ is the work function with allowance for the Schottky effect ($\varphi_0 = 4.5$ V), T is the surface temperature, and λ is the thermal conductivity.

Equation (1) takes into account that the angular expansion of the atomic flow with the flux density q_0 obeys the cosine law [2] and the electron beam is directed normally to the flat surface of the spot of area πR^2 and is practically not scattered. Hence, we have

$$j_i \le \sigma_i j \int_0^\infty n(x)dx \approx \sigma_i j n_0 R.$$

Since $i = j_i/j \ll 1$, then $j \approx$ const, $\sigma_i \approx$ const, and $i \le \sigma_i n_0 R$. Moreover, $n_0 = j_i(1+\gamma_i)/ev_0 = ij(1+\gamma_i)/ev_0$; hence, Eq. (1) is independent of n_0, i, and T (i.e., they can take any values) and depends only on the discharge voltage through $\sigma_i(\varphi_p)$, $v_0(\varphi_p)$, and $\gamma_i(\varphi_p)$. Condition (1) is valid at $R \ge 3d$, where d is the thickness of a one-

dimensional plane cathode sheath with the cathode fall voltage φ_p.

In contrast, when $d/R \geq 3$, the beam is highly diverging, as in the case of a spherical diode. However, even in this case, a condition of type (1) holds accurate to an arbitrary factor or correction function. This is also true for a deformed spot surface. In the general case, the rigorous derivation of the condition of type (1) is not an easy matter.

Below, in the qualitative analysis, we use approximate condition (1), which leads to the following formula for the HVAS minimum current

$$J \approx \frac{\pi}{j}\left[\frac{e v_0}{\sigma_i(1+\gamma_i)}\right]^2. \quad (3)$$

Obviously, the total discharge current is $J_p = \omega J$, where ω is the number of autonomous microarcs and J_p is determined by the load of the external electric circuit.

The literature data on the v_0 and γ_i values are fragmentary and inexact [3]. In a qualitative analysis, it can be assumed that, for tungsten, $\sigma_i \approx 2 \times 10^{-17}$ cm^2; $v_0 \approx 4 \times 10^5$ cm/s; and

$$\gamma_i \approx \frac{10^{-3}\varphi_p}{1 + 10^{-4}\varphi_p}, \quad (4)$$

where φ_p is in volts. Then, the HVAS minimum current (in amperes) is

$$J \approx \frac{3.2 \times 10^7 (1 + 10^{-4}\varphi_p)^2}{j(1 + 10^{-3}\varphi_p)^2},$$

where the electron current density is in A/cm^2.

If $j(T, \varphi_p) = \text{const}$, then the microarc current decreases with increasing voltage: an increase in the voltage φ_p from 10^3 to 5×10^4 V leads to a 24-fold decrease in the current due to the increase in the rate of cathode sputtering. At high voltages ($\varphi_p > 6 \times 10^3$ V), the regime of a zero electric field ($i = i_0 \approx 1.7 \times 10^{-3}$) is feasible. In this regime, the current density j_0 is determined by the Richardson–Dushman law, whereas the current J and radius R exponentially decrease with the voltage (Fig. 1). For example, they decrease from $J \approx 290$ A and $R \approx 0.15$ cm at $\varphi_p = 7230$ V (in this case, $T \approx 4000$ K) to $J \approx 11$ A and $R \approx 6.4 \times 10^{-3}$ cm at $\varphi_p = 8960$ V (in this case, $T \approx 5000$ K). At $i > i_0$, J and R decrease much more rapidly due to the Schottky effect.

It should be stressed that the energy density released at the anode under the action of the electron beam is extremely high. Accordingly, we assume that special measures are taken to prevent the effect of the anode material vapor.

In the literature, the terms "current per spot" and "threshold current" are sometimes used; in fact, these terms refer to the currents equivalent to current (3).

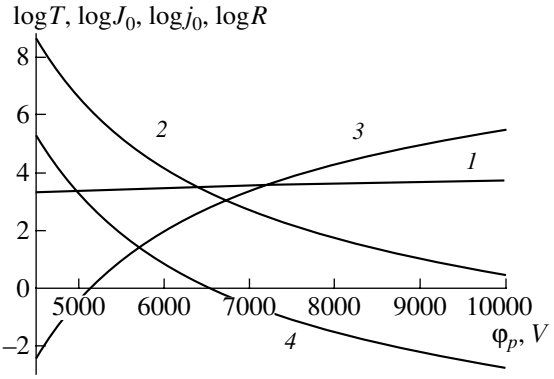

Fig. 1. Decimal logarithms of the (*1*) cathode spot temperature T [K], (*2*) arc current J_0 [A], (*3*) electron current density on the cathode j_0 [A/cm^2], and (*4*) spot radius R [cm] vs. voltage φ_p in the regime of a zero electric field at the cathode.

Even with allowance for the Schottky effect, the HVAS is feasible only at a sufficiently high temperature. For example, if $j > 600$ A/cm^2, then, at $\varphi = 3$ V, we should have $T > 2500$ K.

The Schottky effect leads to a sophisticated interrelation among the HVAS parameters. For a Langmuir cathode sheath, the electric field at the cathode (in volts per centimeter) is

$$E \approx 5700(\varphi_p M)^{1/4}[j(i - i_0)]^{1/2}.$$

Hence, for tungsten ($M \approx 184$ amu) at $\Delta\varphi \approx 3.8 \times 10^{-4}\sqrt{E}$, we have

$$\Delta\varphi \approx 0.055\varphi_p^{1/2} j^{1/4}(i - i_0)^{1/4}. \quad (5)$$

Here, the current density is determined by the formula

$$\vartheta = \tau\exp(-\tau/4), \quad (6)$$

where $\tau = \ln(j/j_0)$, $j_0 = 120T^2\exp(-11\,600\varphi_0/T)$, $\varphi_0 \approx 4.5$ V, and

$$\vartheta T \approx 640\varphi_p^{1/8} j_0^{1/4}(i - i_0)^{1/4}. \quad (7)$$

The values of ϑ lie in the range $0 \leq \vartheta \leq 1.4715$ (Fig. 2). At $\vartheta_{max} = 1.4715$, we have $\tau = 4$ and the current density corresponding to the maximum value of ϑ is equal to $j^* \approx 54.6j_0$; at $\vartheta \longrightarrow 0$, there are two asymptotic values: $j \longrightarrow j_0$ and $j \longrightarrow \infty$. In the range $\vartheta < \vartheta_{max}$, there are two solutions: $j_1 < j^*$ and $j_2 > j^*$. At $T = \text{const}$, the ϑ value increases with increasing $i - i_0$; in this case, we have $dj_1/di > 0$ and $dj_2/di < 0$. Thus, as i and ϑ increase, both solutions tend to j^*. As $i - i_0 \longrightarrow 0$, the current density j_2 tends to infinity because of the decrease in the work function and the transition to field emission becomes feasible. Experimental observations of this transition would be of fundamental importance; however, it is extremely difficult to observe.

One can eliminate T from Eqs. (1), (2), (4), and (7) and obtain the dependence $\vartheta(i)$ at a fixed φ_p. As a

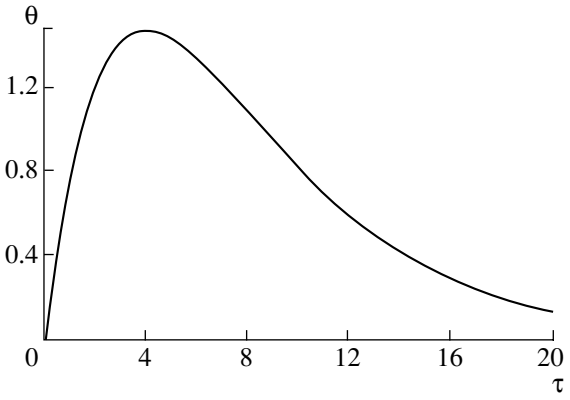

Fig. 2. Parameter θ vs. $\tau = \ln(j/j_0)$.

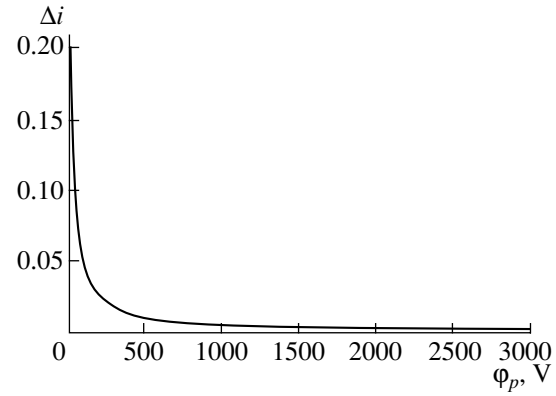

Fig. 3. Dispersion Δi vs. voltage φ_p.

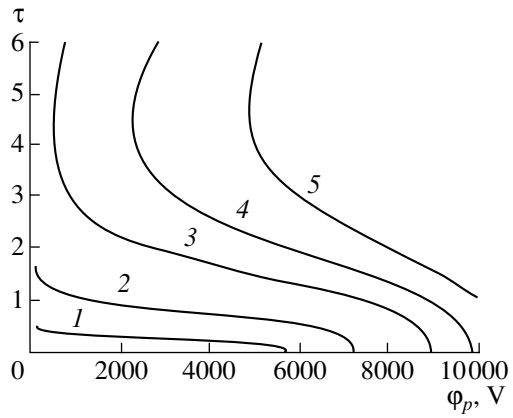

Fig. 4. Dependence of $\tau = \ln(j/j_0)$ on the voltage φ_p at the cathode spot temperatures T = (*1*) 3000, (*2*) 4000, (*3*) 5000, (*4*) 5500, and (*5*) 6000 K.

result, any fixed φ_p value corresponds to certain definite dispersions $\Delta i = i(\varphi_p) - i_0$ and $\Delta J(\varphi_p)$ characterizing the ranges of the admissible i and J values. The dispersions Δi and ΔJ rapidly decrease with increasing voltage. For example, when φ_p increases from 50 to 2000 V, Δi decreases from 0.11 to 2.6×10^{-3}, i.e., by a factor of about 40 (see the dependence in Fig. 3, which was obtained at $\lambda \approx 1.2$ W/(cm K)). Figure 4 presents the solutions to the set of Eqs. (1), (2), (4), and (7) at a fixed temperature. As φ_p increases, the dispersion tends to zero, the Schottky effect disappears, and the current density tends to j_0.

According to Eqs. (3) and (4), the HVAS evolution can start from a single spot with a current of $J \approx 290$ A and radius of $R \approx 0.15$ cm, corresponding to $\varphi_p \approx 7.2 \times 10^3$ V and $T \approx 4000$ K. As i increases, the number of microarcs increases in an avalanche-like manner; the voltage φ_p decreases; and the discharge current $J_p = \omega J$, dispersion, and current density $j = j_0 \exp(t)$ increase. Note that HVAS filamentation develops and J_p grows within the original spot with an initial temperature of 4000 K, rather than on the cold cathode surface.

Obviously, J_p and φ_p vary rapidly in time. Consequently, the filamentation dynamics strongly depends on the intrinsic variable reactance of the microarcs. Thus, the HVAS is also a very sophisticated phenomenon, and an exact non-steady-state theory of the HVAS is still lacking.

In conclusion, let us consider the problem of a field-emission microarc with a current density of $j \sim 10^8$ A/cm^2, which, until now, has been regarded as debatable.

As is the case of the HVAS, the low-voltage tungsten arc is feasible due to cathode sputtering. At the sputtering threshold (e.g., at $\gamma_i \approx 10^{-4}$), the sputtered atoms accumulate near the cathode due to ionization and resonant charge transfer [1]. Equations (1) and (2) also apply to a low-voltage arc at $i \ll 1$. The main distinctive feature of the field-emission arc is the intense Coulomb deceleration of the ions moving to the cathode against the electron flow. As a result, the ions decelerate and the electron beam rapidly spreads out because of scattering. Hence, the Langmuir model of the cathode sheath is not applicable here. In this case, a quasineutral cathode sheath described by the equation

$$\nabla^2 \phi = 4\pi(j/v_e - j_i/v_i) = 0 \qquad (8)$$

can arise. Then, we have $j(r) = \sigma_c d\phi/dr$, where σ_c is the Coulomb conductivity of the plasma,

$$\sigma_c \approx 13 T_e^{3/2}, \qquad (9)$$

with T_e being the electron temperature in eV. On the other hand, we have $j(r) \approx j_E R^2/r^2$ and $T_e(\phi) \approx (T_c + 2\phi/3)$, where T_c is the cathode temperature and j_E is the emission current density. Hence, we obtain

$$j_E \approx 13\left(T_c + \frac{2}{3}\phi\right)^{3/2}\frac{d\phi}{dr}. \qquad (10)$$

It follows from this that, at $\phi \longrightarrow 0$ and $r \sim R$, the electric field at the cathode is

$$\left.\frac{d\phi}{dr}\right|_c \approx \frac{j_E}{13T_c^{3/2}}. \quad (11)$$

At $T_c = 2500$ K ≈ 0.2 eV, we have $E \approx 0.8 j_E$; i.e., in accordance with the Fowler–Nordheim theory, $E \approx 8 \times 10^7$ V/cm at $j_E \approx 10^8$ A/cm^2. After integrating Eq. (10), we obtain

$$j_E R \approx 2.9\varphi_p^{5/2}. \quad (12)$$

According to Eq. (1), at $\varphi_p \ll 10^3$ V, we have

$$jR \approx 3.2 \times 10^3.$$

From here, we obtain $\varphi_p \approx 16.5$ V (for $j_E \approx 10^8$ A/cm^2) and $R \approx 3.2 \times 10^{-5}$ cm. Microspots with such dimensions were mentioned in review [4] and monograph [5].

It is possible that the above estimates are not sufficiently convincing. Nevertheless, the question of a quasineutral cathode sheath is worthy of detailed and comprehensive theoretical consideration.

To conclude, a qualitative analysis of the quasisteady HVAS can stimulate more comprehensive and systematic theoretical and experimental studies aimed at evaluating the fundamental processes in an arc discharge.

ACKNOWLEDGMENTS

We are grateful to A.N. Ermilov for his continuing interest in our study and support. This study was supported in part by the Russian Foundation for Basic Research, project no. 01-02-16014.

REFERENCES

1. A. V. Zharinov, in *Proceedings of XXV International Conference on Phenomena in Ionized Gases, Nagoya, 2001*, Ed. by T. Goto (Nagoya University, Nagoya, 2001), Vol. 3, p. 335.
2. A. V. Zharinov and V. P. Shumilin, Teplofiz. Vys. Temp. **40**, 181 (2002).
3. M. Kaminsky, *Atomic and Ionic Impact Phenomena on Metal Surfaces* (Springer-Verlag, Berlin, 1965; Mir, Moscow, 1967).
4. L. P. Harris, *Vacuum Arcs: Theory and Application*, Ed. by J. M. Lafferty (Wiley, New York, 1980; Mir, Moscow, 1982).
5. G. A. Mesyats, *Ectons* (Nauka, Ekaterinburg, 1993, 1994), Vols. 1–3.

Translated by N.N. Ustinovskiĭ